VIBRATIONS
IN PHYSICAL SYSTEMS

Volume XXVII

Editors

Czesław CEMPEL, Marian W. DOBRY,
Tomasz STRĘK

Poznan 2016

VIBRATIONS IN PHYSICAL SYSTEMS
Vol. 27, 2016

ISSN 0860-6897

EDITORIAL OFFICE
Poznan University of Technology
Institute of Applied Mechanics
ul. Jana Pawla II 24, 61-139 Poznan, Poland
tel. +48 61 665 23 87, fax: +48 61 665 23 07
e-mail: office_am@put.poznan.pl
www.vibsys.put.poznan.pl

Typeset: Tomasz HERMANN
Cover design: Piotr GOŁĘBNIAK

PUBLISHED AND PRINTED
Agencja Reklamowa COMPRINT
ul. Heleny Rzepeckiej 26A, 60-465 Poznan, Poland
Tel. +48 602 266 426, e-mail: comprint@comprint.com.pl, www.comprint.com.pl

The volume was published in the cooperation of the Institute of Applied Mechanics at Poznan University of Technology and Polish Society of Theoretical and Applied Mechanics.
This journal has been indexed in the list of Ministry of Science and Higher Education (5 points).

POZNAN UNIVERSITY OF TECHNOLOGY

**MECHANICAL ENGINEERING
AND MANAGEMENT FACULTY**

INSTITUTE OF APPLIED MECHANICS

**POLISH SOCIETY OF THEORETICAL
AND APPLIED MECHANICS**

XXVII SYMPOSIUM

VIBRATIONS IN PHYSICAL SYSTEMS

2016

XXVII SYMPOSIUM VIBRATIONS IN PHYSICAL SYSTEMS
Bedlewo (near Poznan), May 9–13, 2016

Present edition of Symposium Vibrations in Physical Systems is under auspices of

President of Poznan University of Technology
Tomasz ŁODYGOWSKI

Dean of Mechanical Engineering and Management Faculty
Olaf CISZAK

FINANCIAL SUPPORT
Ministry of Science and Higher Education
Mechanical Engineering and Management Faculty

SPONSORS
• EC Test Systems Sp. z o.o. • COMSOL • Bruel & Kjaer Polska Sp. z o.o.
• Gambit Centrum Oprogramowania i Szkoleń Sp. z o.o. • ENVIBRA Sp. z o.o.

Introduction to the Volume XXVII Collection of Papers of the Conference on Vibrations in Physical Systems – 2016

The phenomena of vibrations, oscillations and waves as physical phenomena are omni-present around us. They are the sign of life, the sign of the operation of machines and devices and they accompany any production processes. Their effects may be harmful, useful and they may also be a source of information on the technical condition of the supervised machines and devices. The successive Volume XXVII of Vibrations in Physical Systems published every second year deals with these widespread phenomena. It comprises the papers presented by specialists from our country but also from abroad at many sessions of XXVII Symposium of Vibrations in Physical Systems organized also every second year. The symposium has been organized since 1960 in Poznan by a local branch of the Polish Society of Theoretical and Applied Mechanics and the Institute of Applied Mechanics at Poznan University of Technology.

This conference is unusual one; we are present in a scientific space 27th times since 1960. This means the subjects we are dealing are still important and still brings the attention of scientific community and co working practitioners. One can say that each successive Volume is a special issue of some scientific Journal devoted mainly to vibration research. Of course, year by year our outlook is evolving; and the scope of current conference has been widened from the previous one, and is currently as follows:

- Mathematical Modelling in Sound and Vibration Analysis
- Experimental Techniques in Sound and Vibration Engineering
- Wave Problems in Solid Mechanics
- Analysis of the Non-Linear Deterministic / Stochastic Vibrations Phenomena
- Computational Methods in Vibration Problems
- Modelling and Identification of Dynamical Systems
- Signal Processing and Analysis
- Active Vibration Control
- Energy Methods in Vibration Engineering
- Vibration and Energy Problems Related to Biomechanics
- Dynamics of Machinery and Rotating Systems
- Vibroacoustics of Machinery, Diagnostics
- Vibrations and Noise of Transport Systems, Vehicles, Roads
- Structural Dynamics, Vibrations of Composite Materials Structures
- Vibration Problems in Environmental Engineering, Vibration of Granular Materials
- Vibrations and Dynamic Stability of Structural Elements, Beams, Plates, Shells
- Flow-induced vibrations, Fluid-structure interaction, Aeroelasticity
- Dynamic behaviour of Vibration Isolation Elements and Systems.

As it is seen the topics of the publications relate to a wide range of issues connected with modelling and identification of mechanical systems, their stability and dynamics of mechanical systems as well as physical phenomena such as propagation of acoustic waves and vibrations in all aspects of science and engineering, beginning from the theory and modelling up to the application subjects in machines, environment and the human body.

The monograph comprises also numerously presented publications relating to the issues of dynamics in biological as well as biological and mechanical systems. They mainly concern mechanical properties of a human body and its organs or parts. Other publications describe the dynamic interaction of power between man and machine (*Hand-held Powered Tools*) or distribution of power and the energy flow in Human-Machine Systems.

Many of the publications present the results of research carried out through simulation with the application of modern digital technologies worked out for the needs of solving linear and nonlinear issues of the dynamics of solid bodies or physical phenomena such as propagation of acoustic waves or dynamics and stability of complicated structures. The publications comprise the results that are analysed from the point of view of the applied methodology or the validity of the obtained data.

There are also some publications devoted to methods of passive, active and semi-active reduction of vibrations and noise and to modelling of vibrations damping with viscous damper. The publications concerning dynamic issues also analysed the stability of the tested mechanical systems.

Other significant publications concern the monitoring of technical facilities with the use of the propagation of elastic waves that allow us to detect cracks in the composite structure under the test and to specify their location.

All the papers comprised in this volume have been reviewed by members of the Scientific Committee, and in some cases by specialists outside the Committee, should the issues concern problems outside the scope of knowledge of the Committee members. We would like to thank all those persons who help us review papers in this published monograph and improve their quality.

Co-editors of the 27th Volume

Czesław CEMPEL
Marian W. DOBRY
Tomasz STRĘK

CONTENTS

INVITED PAPERS

1. **Kajetan DZIEDZIECH, Łukasz PIECZONKA, Phong Ba DAO, Andrzej KLEPKA, Tadeusz UHL, Wiesław J. STASZEWSKI** 13
   STRUCTURAL DAMAGE DETECTION USING NON-CLASSICAL VIBRO-ACOUSTIC APPROACHES

2. **Cezary RZYMKOWSKI** 25
   SELECTED ASPECTS OF THE EXPERIMENTAL METHODS OF IMPACT BIOMECHANICS

PAPERS

3. **Łukasz BĄK, Stanisław NOGA, Feliks STACHOWICZ** 35
   MODELLING AND NUMERICAL SIMULATION OF PARAMETRIC RESONANCE PHENOMENON IN VIBRATING SCREEN

4. **Łukasz BĄK, Feliks STACHOWICZ, Stanisław NOGA, Andrzej SKRZAT** 41
   EFFECT OF EXCITING FORCE AMPLITUDE ON OCCURRENCE OF PARA-METRIC RESONANCE PHENOMENON IN VIBRATING SCREEN

5. **Mirosław BOCIAN, Jerzy KALETA, Daniel LEWANDOWSKI, Michał PRZYBYLSKI** 47
   IMPACT ABSORPTION SYSTEM BASED ON MRE WITH HALBACH ARRAY

6. **Nadiia BOURAOU, Olga LUKIANCHENKO, Sergiy TSYBULNIK, Dmytro SHEVCHUK** 55
   VIBRATION CONDITION MONITORING OF THE VERTICAL STEEL TANKS

7. **Nadiia BOURAOU, Oleksii PAVLOVSKYI, Olha PAZDRII** 61
   IMPROVEMENT OF THE VIBRATION DIAGNOSTICS OF ROTATION SHAFT DAMAGE

8. Piotr CHELUSZKA, Jacek GAWLIK 67
COMPUTER MODELLING OF ROADHEADER'S BODY VIBRATION GENERATED BY THE WORKING PROCESS

9. Zbigniew DĄBROWSKI, Bogumił CHILIŃSKI 75
INFLUENCE OF TORSIONAL-BENDING COUPLING ON TRANSVERSE VIBRATION OF PISTON ENGINE

10. Marian W. DOBRY 83
ENERGY ANALYSIS OF A MECHANICAL SYSTEM WITH A DYNAMIC VIBRATION ABSORBER

11. Marian W. DOBRY, Tomasz HERMANN 91
DIFFERENCES IN POWER DISTRIBUTION IN SUBSYSTEMS OF HUMAN – ANTI-VIBRATION GLOVE – TOOL SYSTEM

12. Łukasz DOMAGALSKI 99
AN ANALYTICAL-NUMERICAL APPROACH TO ANALYSIS OF LARGE AMPLITUDE VIBRATIONS OF SLENDER PERIODIC BEAMS

13. Dariusz GRZELCZYK, Bartosz STAŃCZYK, Jan AWREJCEWICZ 107
ESTIMATION OF THE CONTACT FORCES BETWEEN THE HEXAPOD LEGS AND THE GROUND DURING WALKING IN THE TRIPOD GAIT

14. Tomasz HERMANN, Marian W. DOBRY 115
POWER DISTRIBUTION IN ANTI-VIBRATION GLOVES

15. Eligiusz IDCZAK, Tomasz STRĘK 123
COMPUTATIONAL MODELLING OF VIBRATIONS TRANSMISSION LOSS OF AUXETIC LATTICE STRUCTURE

16. Bartosz JAKUBEK, Roman BARCZEWSKI 129
DETERMINATION OF ACOUSTIC PARAMETERS OF DEVICES WITH EXTENSIVE SOUND SOURCES

17. Bartosz JAKUBEK, Wojciech RUKAT 135
COMPARISON OF VIBRATION IMPACT OF AN IMPACT DRILL ON THE HUMAN BODY UNDER DIFFERENT WORKING CONDITIONS

18. Mateusz JAKUBOWSKI, Paweł FRITZKOWSKI 143
A NEW TOOL FOR TOPOLOGICAL OPTIMIZATION OF
A ROTOR FOR VERTICAL AXIS WIND TURBINES

19. Erik V. JANSSON, Roman BARCZEWSKI, Andrzej KABAŁA . 151
ON THE VIOLIN BRIDGE HILL – COMPARISON OF
EXPERIMENTAL TESTING AND FEM

20. Konrad JAROSZ, Ireneusz CZAJKA, Andrzej GOŁAŚ 161
IMPLEMENTATION OF FFOWCS WILLIAMS AND HAWKINGS
AEROACOUSTIC ANALOGY IN OPENFOAM

21. Jarosław JĘDRYSIAK 169
FREE VIBRATIONS OF MEDIUM THICKNESS
MICROSTRUCTURED PLATES

22. Jarosław JĘDRYSIAK, Ewelina PAZERA 175
VIBRATIONS OF NON-PERIODIC THERMOELASTIC
LAMINATES

23. Jarosław JĘDRYSIAK, Piotr WYRWA 181
HIGHER ORDER VIBRATIONS OF THIN PERIODIC PLATE
BANDS WITH VARIOUS BOUNDARY CONDITIONS

24. Robert KONOWROCKI, Tomasz SZOLC 187
AN ANALYSIS OF THE SELF-EXCITED TORSIONAL
VIBRATIONS OF THE ELECTROMECHANICAL
DRIVE SYSTEM

25. Angelika KOSIŃSKA, Jan AWREJCEWICZ,
Dariusz GRZELCZYK 195
REGULAR AND CHAOTIC DYNAMICS OF
A 4-DOF MECHANICAL SYSTEM WITH DRY FRICTION

26. Krzysztof KULIŃSKI, Jacek PRZYBYLSKI 203
NON-LINEAR VIBRATIONS OF A NON-UNIFORM BEAM
WITH SYMMETRICALLY LOCATED
PIEZOELECTRIC PATCHES

27. Leszek KWAPISZ, Artur MAURIN, Piotr JAKUBOWSKI 211
NUMERICAL MODELLING OF SOUND TRANSMISSION
THROUGH THE WINDOW TYPE PARTITION

28. **Roman LEWANDOWSKI** ... 219
APPROXIMATE METHOD FOR DETERMINATION OF DYNAMIC CHARACTERISTICS OF STRUCTURES WITH VISCOELASTIC DAMPERS

29. **Michał LUDWICKI, Bartłomiej ZAGRODNY, Wiktoria WOJNICZ, Jerzy MROZOWSKI, Jan AWREJCEWICZ** ... 227
INFLUENCE OF ADDITIONAL LOADS ON CHOSEN GAIT PARAMETERS AND MUSCLES ACTIVITY

30. **Wojciech ŁAPKA** ... 237
NUMERICAL ANALYSIS OF PRESSURE DROP AND ACOUSTIC ATTENUATION PERFORMANCE OF TWO HELICOIDAL RESONATORS ARRANGED IN PARALLEL DUCTS WITH DIFFERENT ROTATION ANGLES

31. **Waldemar ŁATAS** ... 245
APPLICATION OF THE CONTINUOUS DYNAMIC ABSORBERS IN LOCAL AND GLOBAL VIBRATION REDUCTION PROBLEMS IN BEAMS

32. **Mykhailo MARCHUK, Taras GORIACHKO, Vira PAKOSH** ... 255
NATURAL FREQUENCIES OF LAYERED ELONGATED CYLINDRICAL PANELS FOR GEOMETRICALLY NONLINEAR DEFORMATION AT DISCRETE CONSIDERATION OF COMPONENTS

33. **Jakub MARCZAK, Jarosław JĘDRYSIAK** ... 265
VIBRATIONS OF PERIODIC SANDWICH PLATES WITH INERT CORE

34. **Maciej MICHAJŁOW, Robert KONOWROCKI, Tomasz SZOLC** ... 273
A SEMI-ACTIVE CONTROL OF LATERAL VIBRATIONS OF THE OVERHUNG ROTOR USING DAMPERS WITH THE MAGNETO-RHEOLOGICAL FLUID

35. **Andrzej MITURA, Krzysztof KECIK** ... 281
INFLUENCES OF SYSTEM PARAMETERS ON ENERGY HARVESTING FROM AUTOPARAMETRIC ABSORBER. NUMERICAL RESEARCH

36. Andrzej MITURA, Krzysztof KECIK 287
INFLUENCES OF SYSTEM PARAMETERS ON ENERGY HARVESTING FROM AUTOPARAMETRIC ABSORBER. EXPERIMENTAL RESEARCH

37. Michał NIEŁACZNY, Wiesław BARNAT 293
EXPERIMENTAL VALIDATION OF THE 3D DYNAMIC UNICYCLE-UNICYCLIST MODEL

38. Martyna RABENDA 301
THE ANALYSIS OF THE IMPACT OF DIFFERENT SHAPE FUNCTIONS IN TOLERANCE MODELING ON NATURAL VIBRATIONS OF THE RECTANGULAR PLATE WITH DENSE SYSTEM OF THE RIBS IN TWO DIRECTIONS

39. Danuta SADO, Jan FREUNDLICH, Anna DUDANOWICZ 309
THE DYNAMICS OF A COUPLED MECHANICAL SYSTEM WITH SPHERICAL PENDULUM

40. Wojciech SOCHACKI, Marta BOLD 317
TRANSVERSE AND LONGITUDINAL DAMPED VIBRATIONS OF HYDRAULIC CYLINDER IN A MINING PROP

41. Krzysztof SOKÓŁ, Sebastian UZNY 325
LOAD BY A FORCE DIRECTED TOWARDS A POSITIVE POLE IN THE ASPECT OF STUDIES ON VIBRATIONS OF A COLUMN WITH CRACK

42. Roman STAROSTA, Grażyna SYPNIEWSKA-KAMIŃSKA, Jan AWREJCEWICZ 333
VIBRATION OF THE OSCILLATOR EXCHANGING MASS WITH SURROUNDING

43. Stanisław STRZELECKI 339
EFFECT OF THE SLEEVE PROFILE ON THE STABILITY OF ROTOR OPERATING IN MULTILOBE JOURNAL BEARINGS

44. Marcin SZCZEPAŃSKI, Wojciech MIGDA, Robert JANKOWSKI 347
TIMBER-FRAME HOUSE RESISTANT TO DYNAMIC LOADS - ANALYSIS OF WALL PANEL FILLED WITH POLYURETHANE FOAM

45. **Janusz SZMIDLA, Ilona CIEŚLIŃSKA-GĄSIOR** 355
FREE VIBRATIONS OF GEOMETRICALLY NONLINEAR COLUMN LOCALLY RESTING ON THE WINKLER ELASTIC FOUNDATION UNDER THE SPECIFIC LOAD

46. **Janusz SZMIDLA, Anna JURCZYŃSKA** 363
FREE VIBRATIONS OF NON-PRISMATIC SLENDER SYSTEM SUBJECTED TO THE FOLLOWER FORCE DIRECTED TOWARDS THE POSITIVE POLE

47. **Michał ŚWIĄTEK, Łukasz DOMAGALSKI, Jarosław JĘDRYSIAK** 369
A STUDY ON NATURAL FREQUENCIES OF TIMOSHENKO BEAM WITH RAPIDLY VARYING STIFFNESS

48. **Marcin ŚWIĄTEK, Jarosław JĘDRYSIAK, ŁUKASZ DOMAGALSKI** 377
INFLUENCE OF SUBSTRUCTURE PROPERTIES ON NATURAL VIBRATIONS OF PERIODIC EULER-BERNOULLI BEAMS

49. **Maciej TABASZEWSKI, Małgorzata WOJSZNIS** 385
ANALYSIS OF VIBRATION TRANSMISSION IN AN AIR-OPERATED DEMOLITION HAMMER

50. **Andrzej URBAŚ, Grzegorz STANCLIK, Jacek KŁOSIŃSKI, Andrzej HARLECKI** 391
DYNAMICS ANALYSIS OF A TRUCK-MOUNTED CRANE WITH THE LUGRE FRICTION MODEL IN THE JOINTS

51. **Sebastian UZNY, Krzysztof SOKÓŁ, Michał OSADNIK** 399
FREE VIBRATIONS OF THE PARTIALLY TENSIONED GEOMETRICALLY NON-LINEAR SYSTEM SUBJECTED TO EULER'S LOAD

Structural Damage Detection Using Non-Classical Vibro-Acoustic Approaches

Kajetan DZIEDZIECH, Łukasz PIECZONKA, Phong Ba DAO, Andrzej KLEPKA, Tadeusz UHL, Wiesław J. STASZEWSKI
Department of Robotics and Mechatronics, AGH University of Science and Technology
Al. Mickiewicza 30, 30-059 Krakow, w.j.staszewski@agh.edu.pl

Abstract

The paper demonstrates how non-classical approaches can be used for structural health monitoring. Wavelet-based modal analysis, various non-classical nonlinear acoustic techniques and cointegration are used for damage detection. These approaches are illustrated using various examples of damage detection in metallic and composites structures.

Keywords: structural damage detection, fatigue cracks, delamination, time-variant modal analysis, nonlinear acoustics, cointegration

1. Introduction

Modern engineering structures utilise new stiffer and stronger materials (e.g. composites) and integrate various hybrid and complex elements (e.g. controllers, electronics, sensors). Such structures often operate under undesirable and harsh conditions. Therefore inspection and maintenance of such structures is a major challenge to designers and end-users. Although many reliable damage detect methods in Structural Health Monitoring have been developed over the last few decades challenges still remain due to ageing (e.g. aircraft structures), limited access (e.g. offshore wind turbines), environmental/operational conditions, intermittent nature of damage and data ambiguity. For example, the main difficulty with the application of ultrasonic guided waves for damage detection in composite materials is that signal changes - produced by defects - tend to be small when compared with those obtained from other effects (e.g. structural features, environmental conditions, variable load) and so are difficult to detect reliably.

Finding a non-classical or unconventional solution could help to overcome many problems and challenges in Structural Health Monitoring. Taking advantage of undesired phenomena (e.g. nonstationarity or nonlinearity) is one of the possible approaches. Looking outside boundaries is the second possible approach used to overcome difficult research problems. The ability to see the problem from a new research perspective is often fundamental to creating breakthroughs in engineering. The paper illustrates how these two non-classical approaches can be used for structural damage detection.

The paper consists of three major parts. Section 2 demonstrates how the time-variant Frequency Response Function can be used to detect abrupt stiffness change in building structures. Examples of damage detection - based on non-classical nonlinear acoustics - are demonstrated in Section 3. The application of cointegration – originally developed in econometrics – for the removal of undesired operational trends from damage detection data is presented in Section 4. Finally, the paper is concluded in Section 5.

2. Detection of Abrupt Changes to Natural Frequencies of Structures

Analysis of vibration and dynamic testing are two critical components of structural design. Traditional vibration analysis relies either on time-domain or frequency-domain approaches. Various methods have been developed for vibration analysis, e.g. [1-3]. Classical vibration analysis assumes that systems/structures are time-invariant, i.e. the output for such systems does not change with a delay in the input. However, this assumption is not valid for many engineering systems with time-variant (global or local) coefficients in the corresponding governing equations. Traditional concepts, analytic methods and experimental techniques of linear time-variant analysis cannot be applied to such systems since modal analysis has been developed for linear time-invariant systems and is not appropriate for time-variant systems. Conventional definitions of modal parameters are not valid for time-variant systems. Varying mass and/or stiffness leads inevitably to varying natural frequencies and mode shapes whereas system responses to harmonic excitations are non-stationary. Such systems do not have even impulse response functions in the classical sense.

A new, non-adaptive concept of the Frequency Response Function (FRF) - based on wavelet analysis - for time variant systems was proposed in [4]. The classical input-output relation was transformed to the wavelet domain to obtained the wavelet-based FRF as

$$H_{\psi}(a,b) = \frac{W_{\psi}[y(t)]}{W_{\psi}[x(t)]} \tag{1}$$

where $W_{\psi}[y(t)]$ and $W_{\psi}[x(t)]$ are the wavelet transforms of the output y(t) and input x(t), respectively. The interpretation of the method - based on the generalised wavelet convolution [5] - was proposed in [4]. Although the wavelet-based extension of the FRF is quite natural and relatively simple, the computation procedure is not as straightforward as Equation (1) implies. Additional data post-processing (i.e. time-frequency domain averaging, ridge extraction, crazy climbers optimisation algorithm) needs to be used in practice in order to obtain the smooth estimate of *H(a,b),* as shown in [6]. The amplitude and phase of the new FRF can be analysed to identify time-variant systems [6] and/or detect abrupt changes to modal parameters [7]. The latter problem is relevant to damage detection since damage often results in local stiffness reduction, leading to the abrupt change of natural frequency. Detection of abrupt changes in natural frequencies from vibration responses of time-variant systems is a challenging task due to the complex nature of physics involved.

The application of the wavelet-based FRF for structural damage detection can be illustrated using a simple example that involves vibration analysis of a three-floor building model. The building model – shown in Figure 1 - consists of three plates connected with four continuous vertical rods. The top plate is additionally connected to the middle plate by a taut string (without any slack) that has been cut in the experiment to simulate an abrupt change of stiffness resulting from structural damage due to earthquake or landslide.

Figure 1. Time-variant three-floor building model

Firstly, the classical experimental analysis was used to analyse vibration of the structure. The random excitation and vibration response were Fourier-transformed to obtain the classical FRF for the undamaged and damaged structure. The results -presented in Figure 2a- clearly show that the FRF changes once the structure is damaged. The snapped string leads to local stiffness reduction that results in the shift of one natural frequency. An additional mode can be also observed when the structure is damaged. Despite all these changes to the classical FRF, structural damage can be identified reliably only when the actual moment of abrupt change of stiffness can be detected. This is illustrated in Figure 2b, where the magnitude of the wavelet-based FRF is presented. The application of the wavelet transform leads to the exact detection of time of the abrupt change of stiffness. The string is snapped after approximately 20 seconds when the experimental modal test is performed. This moment can be clearly identified in the magnitude and phase of the wavelet-based FRF. The magnitude of the wavelet-based FRF also exhibit the change of natural frequency and the extra vibration mode.

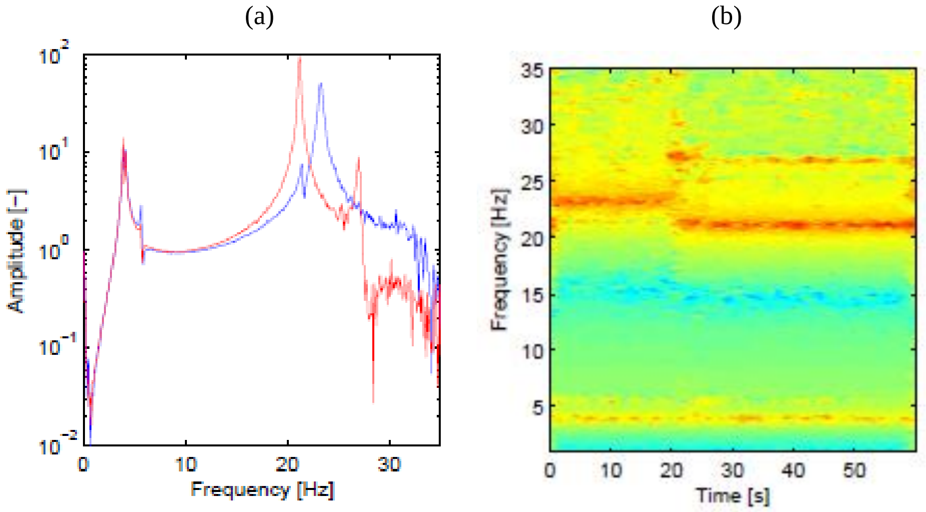

Figure 2. Modal analysis for the three-floor building: (a) classical FRF magnitude for the undamaged (blue line) and damaged (red line) three-floor building; (b) wavelet-based FRF magnitude.

3. Structural Damage Detection Using Non-Classical Nonlinear Acoustics

Ultrasonic testing used for damage detection relies on linear phenomena of wave propagation (e.g. reflection, scattering). Recent years have shown a considerable growth of interest in nonlinear damage detection ultrasonic approaches. Damage-related nonlinear ultrasonic phenomena are quite sensitive but not easy when used for damage detection. This mainly due to the fact that nonlinearities may result not only from cracks but also from other non-damage related effects such as: friction between elements at structural joints or boundaries, overloads, material connections between transducers and monitored surfaces, electronics and instrumentation measurement chain.

Nonlinear acoustics is particularly attractive to detect contact-type damage. This includes fatigue cracks in metals or delamination/debonding in composites. Nonlinear acoustics methods used for damage detection include classical and non-classical approaches. The former methods utilise higher harmonics generation or frequency shifting. These methods are well established and used for many years for material testing. The latter approaches are based on various recently developed non-classical nonlinear phenomena observed in materials. These methods use for example frequency mixing and various approaches based on wave modulation. Non-classical nonlinear phenomena are relatively weak in undamaged and remarkably strong in damage material. Physical mechanisms behind these phenomena are often complex and not easy to explain, as reviewed in [8].

The method based on vibro-acoustic wave modulation [9-11] is one of the most widely used non-classical techniques. When a monitored structure is excited modally (f_L - low-frequency excitation), an ultrasonic wave (f_H - high-frequency excitation) is introduced, as illustrated in Figure 3. Then ultrasonic responses are used for damage detection. Intact (or undamaged) structures exhibit mainly two frequency components associated with the high- and low-frequency excitations. In contrast damage (e.g. fatigue crack in metals or delamination in composites) leads to additional vibro-acoustic wave modulations that can be observed as a pattern of sidebands in ultrasonic response spectra. The frequencies of these additional sideband components are equal to

$$f_{s_n} = f_H \pm n f_L \tag{2}$$

where n = 1,2,3, … . The presence of sidebands and their amplitude indicate possible damage and its severity, respectively. It is important to note that often modulation sidebands can be observed in undamaged specimen due to intrinsic (e.g. material) nonlinearities. However the amplitude of these sidebands increases significantly when damage is present in the structure.

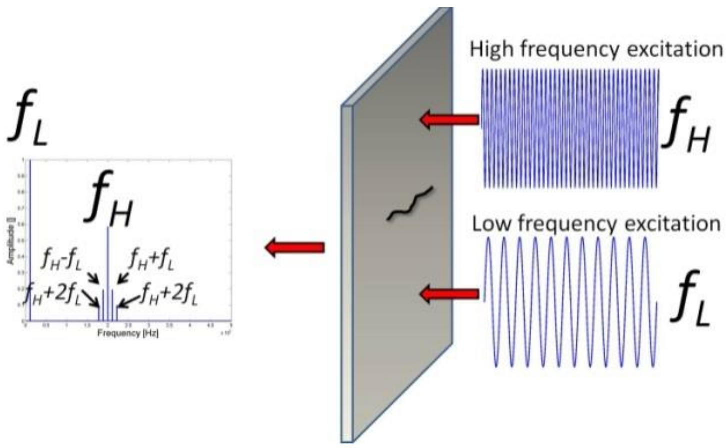

Figure 3. Nonlinear vibro-acoustic wave modulations used for damage detection

The intensity of modulation R = (A1 + A2)/A0, where A1, A2 are the amplitudes of the first pair of sidebands and A0 is the amplitude of the carrier ultrasonic spectral component, can be used as a damage indicator.

Figure 4 demonstrates the application example. An a rectangular (400×150×2 mm) aluminium plate was in the presented application, as shown in Figure 4a. Low-profile *PI Ceramics* PIC-155 piezoceramic transducers of diameter 10 mm and thickness 1 mm were surface-bonded to the plate and used for ultrasonic excitation and response measurement. A *PI Ceramics* PL-055.31 piezoceramic stack actuator (5 × 5 × 2 mm) was additionally bonded on the plate for low-frequency modal excitation. Once the plate was modally excited with the frequency equal to 625 Hz (corresponding to one of the strongest 10th vibration mode), an ultrasonic wave of 60 kHz frequency was introduced to the plate. Figure 4b shows the ultrasonic response spectra for the intact (upper part) and cracked (lower part) plate. A clear pattern of modulation sidebands can be observed when the plate is damaged (11 mm fatigue crack). The intensity of modulation R, defined above, can be used to investigate the severity of damage, as illustrated in [9-11].

(a) (b)

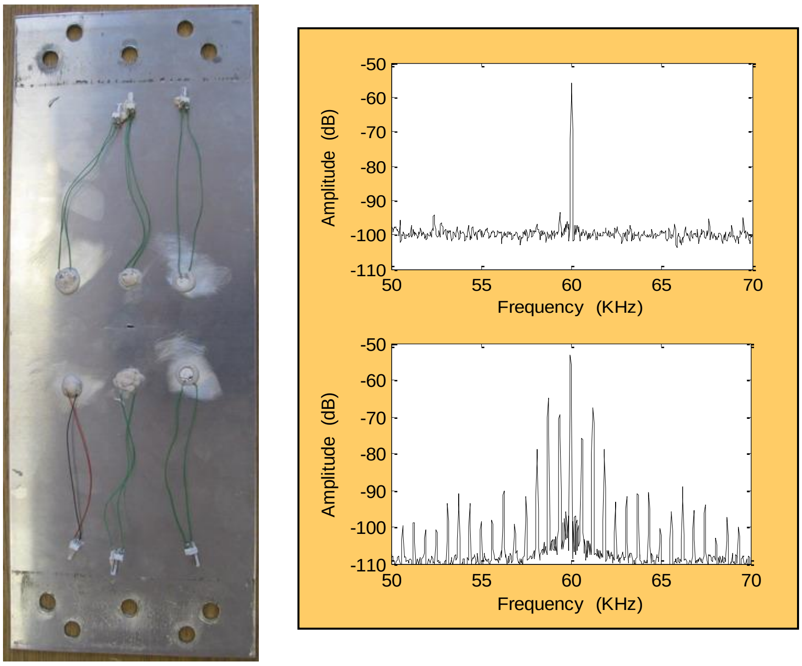

Figure 4. Nonlinear acoustics used for fatigue crack detection: (a) aluminium specimen instrumented with low-profile, surface-bonded piezoceramic transducers; (b) damage detection results for the intact (upper part) and cracked (lower part) plate.

Damage location is one of the major problems when non-classical nonlinear acoustics is used to monitor structures. However, recent studies in [12] demonstrated that modulation sidebands can be used not only to reveal damage or assess its intensity but also to locate damage. An example of damage location based on nonlinear acoustics is illustrated in Figure 5. A rectangular (300×150×2 mm) composite plate (carbon/epoxy prepreg) was impacted in the centre. The impact energy was equal to 3.9 J. The *Monit SHM* vibrothermographic system with the 35 kHz ultrasonic excitation column – was used to reveal butterfly-like delamination in the plate, after impact (Figure 5a). Following these investigations, a non-classical nonlinear acoustic test was performed. Low-profile, surface bonded transducers were used again for low- and high-frequency excitations. Once the plate was excited, ultrasonic responses were gathered The plate was scanned using a 3-D laser vibrometer to analyse sideband amplitudes at various positions. The intensity of modulation R was calculated to reveal the same delamination in Figure 5b.

A new damage detection method was proposed recently in [13] to combine damage location capability offered by Lamb waves and damage sensitivity offered by nonlinear acoustics. Lamb waves are guided plate waves that are widely used for inspecting large areas of structure to reveal damage.

(a) (b)

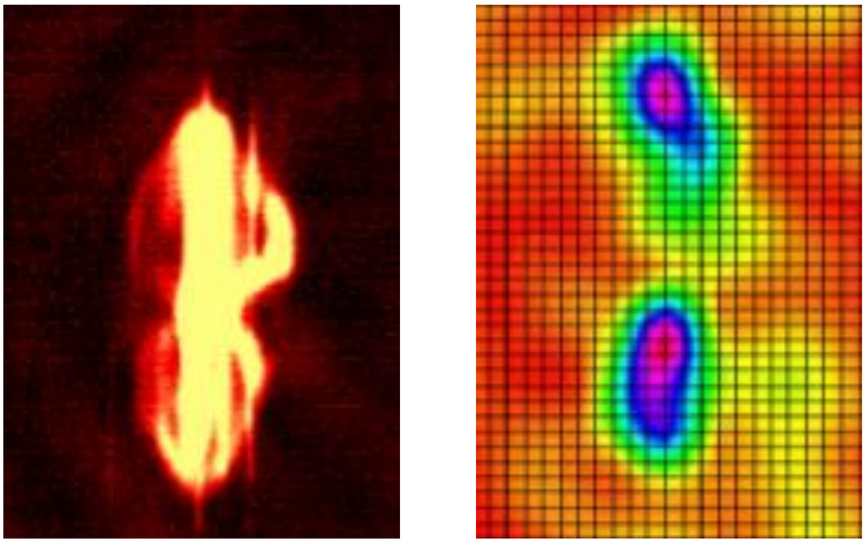

Figure 5. Impact damage detection in composites using. Delamination after 3.9 J impact revealed by: (a) vibrothermography; (b) nonlinear acoustics.

Fatigue testing was used to introduce a crack in the mid span of an 300×20×10 mm aluminium beam (Figure 6). A guided ultrasonic wave (150 kHz) was introduced to the beam when the structure was modally excited (harmonic sinusoidal 10 Hz excitation). Then ultrasonic responses were gathered for two different scenarios of low-frequency excitation, i.e. when the beam was not excited modally and when the beam was excited with the maximum modal amplitude. This measurements were gathered for various positions on the surface of the beam using a 3-D scanning laser vibrometer. Then Ultrasonic responses were band-pass filtered, and their difference was calculated. The RMS values for different measurements are shown in Figure 7, were B-scan (measurements for various positions vs. time) are presented for the intact and cracked beam. The crack is clearly revealed by the increased amplitude of the analysed image (150 mm from the edge of the beam) in Figure 7b.

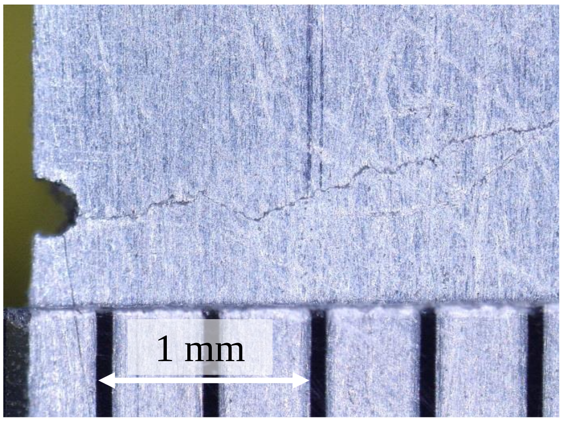

Figure 6. Fatigue crack in an aluminium beam

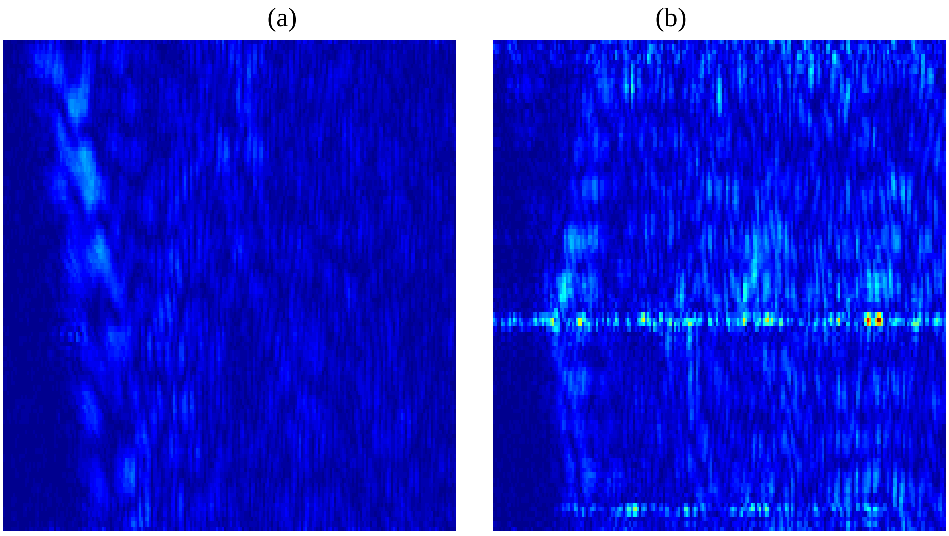

Figure 7. B-scans for the difference signals gathered in the non-linear acoustic test: (a) intact beam; (b) cracked beam

4. Structural Damage Detection Using Non-Classical Nonlinear Acoustics

It is well known that sensor data often needs to be processed and refined before any analysis that can reveal structural damage. Various undesired features – such as noise - are removed from the data. Data drifts, outliers and trends are common undesired nonstationarities. Low-frequency drifts can be removed relatively easy using statistical regression. Unknown trends - caused for example by environmental and operational conditions - are very difficult to remove. These trends often mask damage-related features in analysed signals. For example., it is well known Lamb wave responses - used monitored structures - can be severely affected by temperature changes. Since the majority of Lamb wave based damage detection procedures rely on baseline measurements it is very difficult to find whether signal changes are caused by damage or by temperature. Therefore, compensation for trends - caused for example by temperature or load variation is important to develop methods that are sensitive only to damage but insensitive to other effects.

Various approaches can be used to compensate for undesired effects in the data. The method of cointegration – developed originally from the field of econometrics [14] – has been applied recently in structural damage detection for the removal of undesired environmental and operational effects. temperature effect from bridge vibration data and Lamb wave responses [15-16]. The major idea used in these investigations is based on the concept of stationarity. Time series are considered to be co-integrated if they are themselves non-stationary but their linear combinations are stationary. The method assumes that it is possible for a linear combination of a set of (non-stationary) variables to be stationary if these (non-stationary) variables are integrated of the same order and share common trends. In this context, these variables are said to be co-integrated. Monitored variables are cointegrated to create a cointegrating residual whose stationarity represents normal condition. Then any departure from stationarity can indicate that monitored structures no longer operate under normal condition. More details about this mathematical procedure can be found in [16].

Following the work presented in [16] this section shows an example demonstrating how damage detection can be performed using Lamb wave data corrupted by trends due to temperature. Lamb wave responses were gathered from an aluminium plate with a seeded damage. The seeded damage was a 1 mm hole drilled in the middle of the plate. The plate was exposed to various temperatures in the range between 35 and 70^{0}C. This was sufficient to corrupt the data, so the effects of damage and temperature on Lamb wave responses were undistinguishable. The cointegration procedure was then applied to the corrupted data to obtain the residual vectors. The residual vectors were wavelet-transformed – using the orthogonal wavelet transformed – and the variance of wavelet coefficients were calculated. Figure 8 shows result, where the logarithmic wavelet variance for various wavelet levels is presented for the first three residual vectors of data after cointegration. The results in Figure 8a – for the undamaged plate – exhibit self-similarity through linear variance characteristics. This pattern is broken due to damage in Figure 8b. The temperature trend was removed from the data leaving the nonstationarity related to damage.

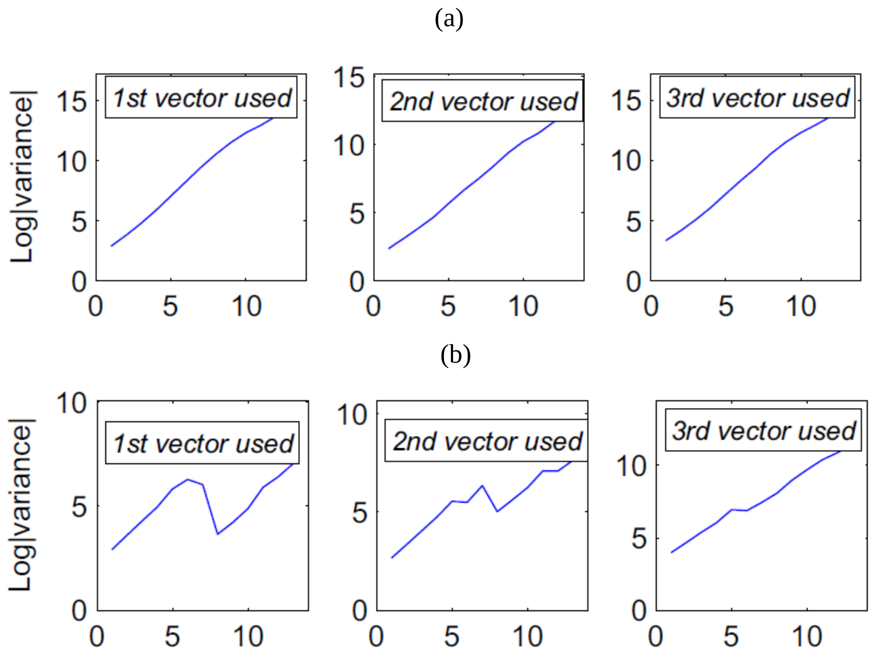

Figure 8. Wavelet variance characteristics calculated from the first three cointegration residuals from Lamb wave data for: (a) intact plate; (b) damaged plate

5. Conclusions

The paper has demonstrated how unconventional modal analysis (wavelet-based FRF), undesired effects (nonlinear phenomena in ultrasonic data) and methods originally developed in other research fields can be applied successfully for structural damage detection. damage detection. Various examples related to structural stiffness reduction, crack detection, impact damage detection have been presented to illustrate that non-classical approaches can often solve damage detection problems for which classical solutions are difficult or impossible. It is anticipated that the work presented will stimulate more research in this area.

Acknowledgments

The authors gratefully acknowledge the financial support provided by the Foundation for Polish Science (Project WELCOME, No 2010-3/2) under the Innovative Economy, National Cohesion Programme, EU.

References

1. A. G. Poulimenos, S. D. Fassois, *Parametric time-domain methods for non-stationary random vibration modelling and analysis - A critical survey and comparison*. Mechanical Systems and Signal Processing, **20** (2006) 763 – 816.
2. P. Orlowski, *Selected problems of frequency analysis for time varying, discrete-time systems using singular value decomposition and discrete Fourier transform*, J. of Sound and Vibration, **278**(4-5) (2009) 903 – 921.
3. B. Basu, S. Nagarajaiah, A. Chakraborty, *Online identification of linear time-varying stiffness of structural systems by wavelet analysis*, Structural Health Monitoring, **7**(1) (2008) 21 – 36.
4. W. J. Staszewski, D.M. Wallace, *Wavelet-based Frequency Response Function for time-variant systems - an exploratory study*, Mechanical Systems and Signal Processing, **47** (2014) 35 – 49.
5. R. S. Pathak, *The Wavelet Transform*, Atlantis Press/World Scientific Paris 2009.
6. K. Dziedziech, W. J. Staszewski, T. Uhl, *Wavelet-based modal analysis for time-variant systems*, Mechanical Systems and Signal Processing, **50-51** (2015) 323 – 337.
7. K. Dziedziech, W. J. Staszewski, B. Basu, T. Uhl, Wavelet-based detection of abrupt changes in natural frequencies of time-variant systems, Mechanical Systems and Signal Processing, **64-65** (2015) 347 – 359.
8. D. Broda, W. J. Staszewski, A. Martowicz, T. Uhl, V. Silberschmidt, *Modelling of nonlinear crack-wave interactions based on ultrasound – a review*, J. of Sound and Vibration, **333**(4) (2014) 1097 – 1118.
9. D. Donskoy, A. Sutin, A. Ekimov, *Nonlinear acoustic interaction on contact interfaces and its use for nondestructive testing*, NDT&E International, **34** (2001) 231 – 238.
10. Z. Parsons, W. J. Staszewski, *Nonlinear acoustics with low-profile piezoceramic excitation for crack detection in metallic structures*, *Smart Materials and Structures*, **15** (2006) 1110 – 1118.
11. A. Klepka, W. J. Staszewski, R. B. Jenal, M. Szwedo, J. Iwaniec, T. Uhl, *Nonlinear acoustics for fatigue crack detection – Experimental investigations of vibro – acoustic wave modulations*, Structural Health Monitoring, **11** (2012) 197 – 211.
12. L. Pieczonka, L. Zietek, A. Klepka, W. J. Staszewski, F. Aymerich, T. Uhl, *Impact damage imaging in composites using nonlinear vibro-acoustic wave modulations*, submitted to Structural Control and Health Monitoring.
13. K. Dziedziech, L. Pieczonka, P. Kijanka, W. J. Staszewski, *Enhanced nonlinear crcak-wave interactions for structural damage detection based on guided ultrasonic waves*, Structural Control and Health Monitoring, (2016), available online before print DOI: 10.1002/stc.1828.
14. R. F. Engle, C. W. J. Granger, *Cointegration and error-correction: representation, estimation and testing*, Econometrica, **55** (1987) 251 – 276.

15. E. J. Cross, K. Worden, Q. Chen, *Cointegration: A novel approach for the removal of environmental trends in structural health monitoring data*, Proc. R. Soc. A **467,** (2011) 2712 – 2732.
16. P. B. Dao, W. J. Staszewski, *Lamb wave based structural damage detection using cointegration and fractal signal processing*, Mechanical Systems and Signal Processing, **49** (2014) 285 – 301.

Selected Aspects of the Experimental Methods of Impact Biomechanics

Cezary RZYMKOWSKI
Warsaw University of Technology
Institute of Aeronautics and Applied Mechanics, ViSEB Lab
ul. Nowowiejska 24, 00-665 Warsaw, czarek@meil.pw.edu.pl

Abstract

Owing to the specificity of the experimental tests conducted in impact biomechanics, whose subjects are volunteers, cadavers or animals, ethical and legal aspects are just as formidable as the restrictions of 'technical nature'. The first part of the paper presents fundamental ethical principles, universally accepted by the international community, which must be followed in the course of conducting biomedical experimental tests (including those that fall under the category of impact biomechanics). The second part is a presentation of the preparation (e.g. to install a great number of measurement sensors, necessary for collection of as much data as possible regarding the behaviour of individual body parts under impact load) and course of experimental tests in which human cadavers were subjected to different loading scenarios of the thorax. The purpose of these tests was to identify the parameters and to validate an advanced simulation model of the human thorax developed within the THOMO project.

Keywords: impact biomechanics, ethical and legal aspects, human cadavers, experimental works

1. Introduction

Impact biomechanics is a field of research dedicated to the examination of phenomena that occur in the bodies of humans (or animals), especially in their musculoskeletal and circulatory systems, as well as in their internal organs, under conditions of loading characterized by short time of duration (usually of few/few tens of milliseconds) and very high amplitudes (such as acceleration reaching few tens/few hundred times the gravitational acceleration).

Experimental tests constitute an important element of the cognitive process in science. This applies also to biomechanics of the human body, including impact biomechanics. However, the specificity of the issues that are investigated by impact biomechanics places certain limitations on the options of experimental tests. This especially concerns tests with the participation of volunteers. In this case, tests conducted under conditions closely imitating real-life incidents could potentially lead to severe injuries or even death.

For this reason, experimental tests in impact biomechanics resemble puzzle pieces – tests avail themselves of both volunteers, animals and post-mortem human subjects (PMHS) that complement each other.

Computer modelling methods, whose rapid advancement is observed in parallel with the increasing computing power of computers and development of specialized software, play an important role as regards correct interpretation and generalization of results obtained from such experimental testing.

Owing to the specificity of these tests, whose subjects are volunteers, cadavers or animals, ethical and legal aspects are just as formidable as the restrictions of 'technical nature'.

2. Ethical and legal aspects of conducting experimental research with the participation of volunteers and with the use of cadavers/biological material

The use of human cadavers or segments/tissues extracted from them in experimental tests raises particularly heated controversies. For moral, ethical and religious reasons, some parts of the public opinion (these parts vary in size depending on the country/cultural circle/religion/...) are convinced that the use of human cadavers (PMHS – Post-mortem Human Subjects) in biomechanics research, including for the purpose of enhancing traffic safety, should not be taking place.

This belief is often supported by the message sent out by the mass media, which tend to purport that dummies and computer models are sufficient to conduct research on systems designed to improve vehicle safety. This is not true – both dummies and computer models (despite the very rapid advancements in the field of modelling over the recent years) are still far from perfect.

Of pivotal significance is the improvement of *biofidelity* of dummies and computer models. This requires tests with the use of PMHS in order to collect data regarding properties of tissues, of the mechanisms of their injuries, as well as the global responses of human bodies, indispensable for their validation.

The use of human cadavers is not only one of the methods of researching crash impact on the injuries of accident victims, but also one of the most important ones. In 1995, King and Viano [1] estimated the number of survivors attributable to the development of safety engineering and they compared this number with the number of PMHS used in biomechanics testing. They have calculated that each PMHS employed in research on the improvement of safety has saved the lives of over 60 people.

Two documents contain a collection of fundamental ethical principles, universally accepted by the international community, which must be followed in the course of conducting biomedical experimental tests (including those that fall under the category of impact biomechanics): *The Nuremberg Code* (1946) [2]and the *Declaration of Helsinki* (1946, as subsequently amended) [3].

The provisions laid down in these documents have been introduced, directly or following relevant adaptations, to the national legislation all over the world.

The above-mentioned documents do not deal directly with the use of cadavers in scientific research, but they do not contain prohibition of such research, either. Given the absence of other legal regulations, it is assumed that they may be expanded to include research with the use of human corps.

The first of the foregoing document, released in 1946 as a result of the Nuremberg Trials in response to information about the criminal medical experiments conducted on prisoners of Nazi concentration camps, sets out what may be referred to as the decalogue (formulated in 10 points) establishing the fundamental principles of conducting (generally speaking) medical experiments on human subjects.

Particular focus, in the form of an extensive commentary, has been placed on its first point: "The voluntary consent of the human subject is absolutely essential".

This provision – of pivotal significance in 1946, that is shortly following the plight of prisoners of WWII concentration camps – still holds as the central tenet.

The second of these documents (*Declaration of Helsinki*), repeatedly amended by experts connected to the Council for International Organizations of Medical Sciences (CIOMS), in collaboration with the World Health Organization (WHO), upholds all the vital principles set out in the *Nuremberg Code*, expanding its scope to cover purely medical research associated with the introduction of new medications and medical procedures. It also offers interpretations and clarifications of the Nuremberg principles. An important new element, formulated in Guideline 2: *Ethical Review Committees*, is the requirement to conduct all research whose subjects are human beings under the close supervision of an appropriate ethical committee/commission.

Human cadavers are only used for biomechanics research in a small number of countries. This is owing to a number of reasons. In some countries, such research is prohibited by law or by religious principles; in others, they are not conducted due to the pressure exerted by the public opinion.

Everywhere where such research is allowed, it is subject to tight supervision and conducted with observance of established rules [4, 5].

In France, the Bioethics Law no. 94-654 of 29 July 1994 concerns the extraction of organs for diagnostics, transplantation or other scientific purposes. It is presumed that, unless otherwise stated, organs may be used for transplantation.

On the other hand, if a body or its individual organs are to be used for purposes other than transplantation or establishment of the causes of death, a relevant consent must be signed and pre-registered (body donation programme).

If the deceased had previously signed consent for the donation of his body for research, his family may not object to this. If the will of the deceased is not known, the decision is made by the family.

In Germany, use of bodies is subject to the law on organ transplantation, even though this piece of legislation does not make any explicit stipulations about whole-body donations.

A part of the PMHS comes from people who had signed a relevant agreement, establishing the scope of purposes for which their bodies may be used after their death. However, in the majority of cases, members of the closest family of the deceased are asked for consent to donate bodies for biomechanics research (this consent must be expressed in writing). Prior to signing, they are informed of the type of load that will impact the body, the expected type and gravity of injury, the type of autopsy which will be carried out, and of the collection and keeping of samples for further testing.

As for the United States, there exists the obstacle of mutually exclusive acts of law, as well as of differences between states.

The violation of bodily integrity (profanation) is prohibited.

In some states, body donation for scientific purposes is allowed, yet under various conditions. In some cases, consent to such donation must be registered prior to death, while the family may still object to it.

In other states, such consent may not be expressed prior to death. It is only after a person has passed away that their family may agree to the use of the body for scientific purposes.

Scientific activities in the area of impact biomechanics is regulated by detailed provisions of law (such as NHTSA Orders 700-3 and 700-4).

In the United States, there are a few places where PMHS research is conducted. Each of these places has their own, strict protocol to be followed. Below are the basic principles in place at one of the Laboratories in the USA.

This particular state has a body donation programme – interested parties sign consent for their bodies to be used for scientific purposes following their death.

Additional consent is necessary for civil-purposes crash tests.

Another consent must be expressed for military-purposes crash tests.

After death, and upon verification of the scope of consent granted by the given person, the coroner/another authorized institution, forwards the information to the Laboratory, and enquires whether they are interested in such particular body.

If so, the Laboratory contacts the closest family members (if possible) and asks whether they agree to the use of the body in the planned tests. The family receives general information only, no specific descriptions of the tests are provided.

If the family's answer is NO (regardless of the consent given by the deceased), the Laboratory withdraws from taking over the body.

If the answer is YES, the body undergoes medical tests (carriage of determined viruses, CT scans, etc.) and, based on the results, it either qualifies to be used in given tests (recorded in the database and placed in a freezer), or is returned.

Prior to the test, a protocol outlining in detail how the body is to be handled, as well as a thorough description of tests to be conducted, is presented to a specially committee.

During these tests, each of the Laboratory employees must follow the internal protocol regarding tests involving biological material (special outfits, covering the face of the deceased, etc.).

In each test, great emphasis is placed on the proper collection, recording and storing of the greatest amount of data possible, both for ongoing and future research, so as to ensure that each test with the use of PMHS renders as much information as possible.

Following the tests, the whole body or its individual segments/tissues may be re-used.

If the body/segments can no longer be used, they are returned to the family (if the family wishes to have it returned), or cremated. Once a year, the Laboratory organizes a scattering ashes ceremony, of which families are also notified.

To sum up:

- Tests with the use of PMHS are an important source of data indispensable for getting to know the mechanisms of how human bodies are injured when subjected to impact loads, which is the necessary condition for further progress in preventing injuries that result from, among others, traffic accidents.

- In order to minimize the critical attitude of some portions of the public opinion toward such research, it must be conducted with observance of ethical principles and in strict conformity with the provisions of law in the each country.
- Ethical Committees, responsible for adopting the test scopes and protocols, as well as for the oversight of these tests, have an important role to fulfil in this respect.
- It is necessary to improve the collection of test results and make them available to all interested science centers in order to avoid repetitions, and to ensure the fulfilment of the principle that guides those willing to donate their body after death to science: <u>donation for science = donation for the humanity</u>.

3. An example of experimental tests with the purpose of identification of parameters and validation of an advanced model of human thorax

What follows is a presentation of the preparation and course of experimental tests in which human cadavers were subjected to impact loads. The purpose of these tests was to identify the parameters and to validate an advanced simulation model developed within the THOMO project [7, 8].

THOMO project (*Development of a Finite Element Model of the Human Thorax and Upper Extremities*), was carried out under FP7 of the European Community (contract number: SCP7-GA-2008-218643), in the period from 2009.01.01 to 2012.10.30, by an international consortium which included 4 research teams: CEESAR – Centre Européend'Etudes de Sécurité et d'Analyse des Risques (Nanterre, France), UVHC – Université de Valenciennes et du Hainaut Cambrésis (Valenciennes, France), UWB – University of West Bohemia (Plzen, Czech Republic) and the Institute of Aeronautics and Applied Mechanics of the Warsaw University of Technology– Virtual Safety Engineering and Biomechanics Laboratory (ViSEB). CEESAR was the project coordinator.

THOMO aimed to develop new, greatly improved models of the human thorax with upper extremities, both 'standard' (5th, 50th and 95th percentile) and 'personalized' (for any type of body build).

The developed models should ensure appropriate (stable, resilient to changes of parameters, natural for biological systems and with proper *biofidelity* properties) behaviour of solutions during simulation tests with their use (the problem of *3-R: Rating, Reliability, Robustness* [6]).

The complicated structure of the thorax model was described with ca. 400 thousand elements, which allowed for a detailed modelling of the thorax anatomy, accounting for many different muscle groups, bones, main blood vessels, etc., as well as for the interactions between them and the varied material properties.

The method used was the Finite Element Method (FEM), implemented in the LS-DYNA package.

Already at the initial stage of drafting the project application, cooperation was initiated with the Global Human Body Model Consortium (GHBMC). This was facilitated by a research group from University of Virginia (USA), which acts as the centre of expertise of GHBMC for the thorax and upper extremities. This cooperation made it possible to exchange data and information about test results and updates introduced based on them, as well as about the research methods used/developed. Results of the THOMO project were implemented in the final human body model developed by GHBMC. The employment of such an advanced model by the automotive industry and by research centres which work for it, including academic centres, should facilitate the design of increasingly safe vehicles, thus reducing the number of traffic accident injuries, especially serious ones, and deaths.

Two basic research directions were pursued under the THOMO project – experimental tests and computer modelling works.

The experimental tests were carried out by French teams: CEESAR (primarily crash tests with the use of whole-body cadavers) and UVHC (research over selected anatomical structures).

This latter research direction focused on the development of simulation computer models (reference 50th percentile model and scaled 5th and 95th percentile models, as well as 'personalized' models). A research group from the ViSEB Laboratory at the Warsaw University of Technology participated in these works (among others, they have developed an effective method of scaling and personalization), as well as groups from UWB and CEESAR. Proper scaling is a particularly important issue in the case of building models of children's bodies. Owing to the virtually complete absence of experimental tests with the use of paediatric PMHS, such models are usually developed based on scaling adult body models (usually of the 5th percentile).

The experimental stage comprised 18 crash tests conducted with the use of both male and female bodies. The tests were designed specifically for the needs of this project. Different loading scenarios of the thorax were tested.

Figure 1. Cadaver ready for the test – side impact onto thorax

Particular attention has been paid to preparing the cadavers for the tests (Figure 1). One important element was to install a great number of measurement sensors/instruments, necessary for collection of as much data as possible regarding the behaviour of individual body parts under impact load.

In order to obtain proper rib strain profiles, over 100 strain gauges (Figure 2) were attached to the ribs and sternum. Accelerometers were also fixed onto the vertebrae T1, T4, T12 and onto the sternum. Pressure transducers were installed in the aorta, pleurae, inferior vena cava, trachea, and stomach in order to analyze the pressure wave transmission through the different organs.

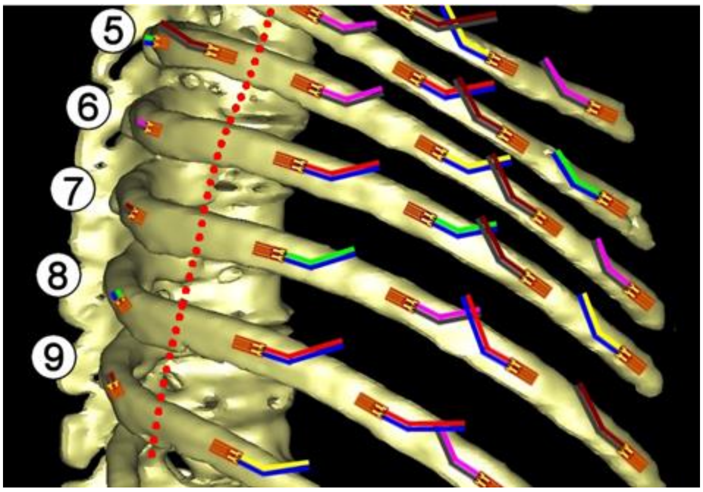

Figure 2. Visualization of the thorax bones, with location of the strain gauges to register strain during crash

Besides the crash tests, also tests regarding ribcage shape and material properties played an important role. In order to obtain correct geometrical data, important from the point of view of durability of the ribcage which protects internal organs, a multistep procedure of scanning thoracic skeleton (Figure 3) was used, with particular focus on the ribs. This has allowed for identification of both differences between individual ribs, as well as of the change of shape (including the change of the cortical bone cross-section area, particularly significant for evaluating the durability) along individual ribs.

The first task was to image the entire thorax with the use of typical computer tomography. Next, external surfaces of individual bones were scanned with the use of a laser 3D scanner. The next step was to cut the examined ribs into segments with a length of 3.5 cm and to scan each segment with the use of micro-CT scanning (μCT), which provides much higher resolution of the obtained images. Based on the micro-CT scanning data, detailed geometrical models were developed, which included both internal and external surfaces and the boundary of the cortical bone, which allowed for, among others, finding characteristics that describe the changing cortical bone cross-section area along individual ribs.

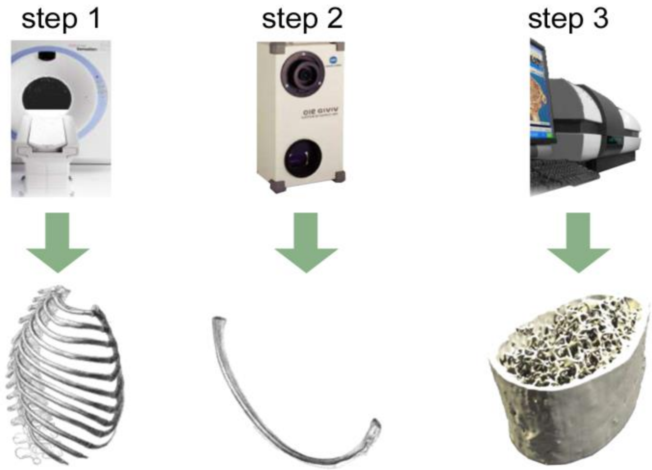

Figure 3. The three-step process of collecting geometrical data of the thorax bones

Information on the external geometry of individual ribs, previously collected with the use of a laser scanner, as well as CT images of the whole thorax, rendered it possible to put together accurate geometrical data for specific segments into a single model of the thoracic skeleton.

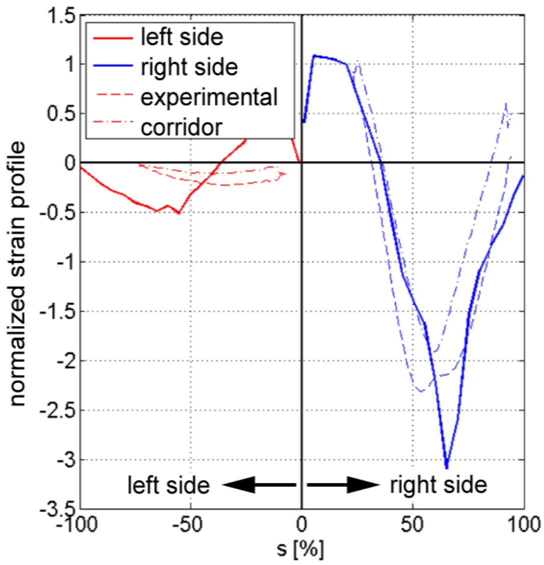

Figure 4. An example of a fifth rib strain profile for the reference model, developed as a result of simulation with the use of the reference model, with side impact, at the moment of maximum ribcage deflection

In order to verify the correctness of computer modelling of the consequences of injuries caused by impact with the amplitude and character typical of traffic accidents, it was important to conduct comparative analyses of the strain profiles and fields in ribs. They were identified in experimental tests with cadavers. Strain gauges had been fixed onto their ribs (Figure 2) and individual experiments were simulated on the computer. The conformity levels have been found satisfactory (Figure 4). The broken lines show the corridor built on the basis of experimental tests conducted under the THOMO project.

4. Conclusions

Based on many years of experience, I can state that:

- The future of research on impact biomechanics and its practical applications rest mainly on virtual methods (based on computer models of the human body).
- Owing to significant limitations, the role of experimental tests will increasingly boil down to identification of parameters and validation of virtual models. However, for many years to come, these tests will continue to serve as a very important source of information.
- Owing to the number and complex nature of the problems (medical, ethical, legal, biomechanical, numerical, equipment-related, etc.), which must be solved in order to develop improved virtual models representing the behaviour of human body under load impact, at a degree enabling reliable assessment of injury risk, works conducted by large interdisciplinary teams are much more likely to succeed, as they combine the necessary experience, computing, experimental, human and financial resources. This is the case of the GHBMC project, for example.

Acknowledgments

This paper is based, in part, on results of the APSN and APROSYS projects co-funded by the European Community FP 6th and the THOMO project co-funded by the European Community FP 7th. The author would like to gratefully thank the European Community and the partners involved in these projects. The contents of this publication are sole the responsibility of the author and do not necessarily represent the views of the EC.

References

1. A. King, D. C. Viano, N. Mizeres, J. D. States, *Humanitarian benefits of cadaver research on injury prevention*, The journal of Trauma: Injury, Infection and Critical Care, **38**(4) (1995) 564 – 569.
2. Trials of war criminals before the Nuremberg Military Tribunals under Control Council law no. 10, Nuremberg, October 1946–April, 1949. (https://www.loc.gov/rr/frd/Military_Law/pdf/NT_war-criminals_Vol-II.pdf)
3. International Ethical Guidelines for Biomedical Research Involving Human Subjects, Council for International Organizations of Medical Sciences, Geneva 2002.

4. Proceedings of the European Passive Safety Network Workshop: *Ethical Guidelines in Biomechanical Testing*, May 22–23, 2001, Lyon-Bron, France.
5. APSN – Advanced Passive Safety Network, FP 6th project, 2004 – 2008, Report D88: *Definition of ethical rules and guidelines for biomechanical research on behalf of APSN*, 2006.
6. APROSYS – Integrated Project on Advanced PROtectionSYStems, FP 6th project, 2004–2009, Deliverables: AP-SP74-0002-K-D741-D743 & AP-SP74-0010C-D742B (access restricted to the APROSYS consortium).
7. THOMO – Development of a Finite Element Model of the Human Thorax and Upper Extremities, FP 7th project 2009–2012, Final Report, 2013, (access restricted to the THOMO consortium).
8. C. Rzymkowski, *Modelowanie i symulacja procesów udarowych w biomechanice* (*Modelling and simulation of impact phenomena in biomechanics*). Prace Naukowe, Mechanika, Zeszyt 262, Oficyna Wydawnicza Politechniki Warszawskiej, Warszawa 2013.

Modelling and Numerical Simulation of Parametric Resonance Phenomenon in Vibrating Screen

Łukasz BĄK
Department of Materials Forming and Processing, Rzeszow University of Technology
Al. Powstańców Warszawy 12, 35-959 Rzeszów,lbak@prz.edu.pl

Stanisław NOGA
Department of Mechanical Engineering, Rzeszow University of Technology
Al. Powstańców Warszawy 12, 35-959 Rzeszów, noga@prz.edu.pl

Feliks STACHOWICZ
Department of Materials Forming and Processing, Rzeszow University of Technology
Al. Powstańców Warszawy 12, 35-959 Rzeszów, stafel@prz.edu.pl

Abstract

In this paper the numerical studies of parametric resonance phenomenon in vibrating screen are presented. Numerical simulations are performed in Ansys Workbench software. Modal analysis is carried out to find the natural frequencies and mode shapes of the sieve. The effect of the excitation frequency on the sieve vibrations in parametric resonance conditions was investigated using the transient analysis. The comparison of numerical and experimental results is presented. It is shown, that two mode shapes of sieve vibrations occur close to the screen operation frequency. Linear dependence between excitation frequency and sieve vibration frequency is obtained. The most stable transient response and the highest vibration amplitude of the sieve is obtained for excitation frequency 47.07 Hz. The range of excitation of parametric resonance is nearly the same as for experimental data.

Keywords: screen, parametric resonance, forced vibrations

1. Introduction

Screening operations are very important part of processing mineral materials. Screens are fundamental instrumentation for minerals separation in order to produce final mineral products for customers. Vibrating screens are one of the most extensively used tools in screening processes. Rapid evolution of vibrating screens occurred in 19th and 20th centuries. Nowadays the level of screens development is stabilized and machine building companies often produce similar screens, and their construction differs in details [10].

The screening process of the naturally wet mineral materials is generally more difficult in comparison to screening of the dry mineral materials. Here, particles of the material combine to form aggregates, that significantly increase the time of the screening process [11]. Therefore, the water supply need to be applied for material particles disintegration. The other solution of this problem is to generate high impact energy by increasing vibration amplitude, that can crush glutted grains of material and degrease adhesion forces between the material and the sieve. The large mass of the conventional screens connected with large amplitude vibration results in reduced life of a machine and increases the energy consumption [9]. Exciting of sieve parametric vibrations in the screen results in the large amplitude vibrations with relatively low energy consumption and can be suitable for screening wet materials.

The first screen with parametrically excited sieve was designed by Slepyan et al. [5]. They also found the mathematical model of the simplified vibrating screen system, where the sieve is modelled as a string connected with two masses [6-7]. The dynamic analysis of vibrating screen was presented in work [1]. The analytical and numerical methods were used to find the sieve natural frequencies and mode shapes. In work [2] the experimental analysis of vibrating screen operation in parametric resonance conditions was presented. In this paper the full plate was used instead of the perforated sieve. Complex dynamic analysis of the large vibrating screen was presented by Zhao et al. [12]. They found optimal dynamic design of the screen by performing structural optimization. Li and Song [4, 8] presented the dynamic analysis of chaotic vibrating screen. Another dynamic analysis of vibrating screen with variable elliptical trace was presented by He and Liu [3]. They analyzed characteristics of the screen by applying multi-degree-of-freedom theory. The kinematic parameters for different motion traces were also determined.

The present paper concerns the dynamic analysis of vibrating screen system with parametrically excited sieve. Numerical simulations were performed to find the effect of excitation frequency on sieve parametric oscillations.

2. Numerical modelling of parametric resonance screen system

As shown in Fig. 1 the model of parametric resonance screen system was prepared according to laboratory parametric resonance screen in Ansys Workbench software [2]. It is simplified to two beams, that are connected with a sieve (plate with rectangular cut-outs). The sieve is fixed inside the beams between the rubber pads. The whole system is suspended by springs with stiffness k equal to 275 N/mm and preload equal to quarter of sieve preload - $F_t/4$.

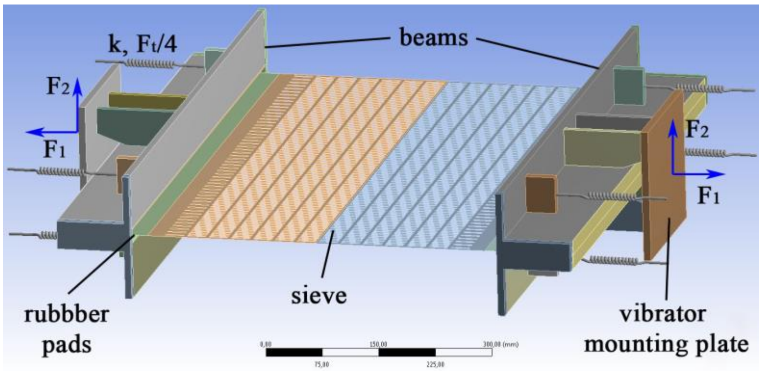

Figure 1. The simplified screen system prepared in Ansys Workbench Design Modeler

The material models of all components was assumed as elastic. In the model, density of external vibrators mounting plates was increased to compensate a mass of electrical vibrators. Contact in the whole model is defined as bonded, except the interactions between the rounded part of the rubber pads and the sieve, where frictionless contact was applied. The finite element model is composed of 131 990 elements. The sieve is modeled by using 4-nodes shell elements. For the beams and the rubber pads meshing the 3-dimentional 20-nodes hexahedron elements and 10-nodes tetrahedron elements were used.

Three steps of numerical analysis were performed in Ansys Workbench software to find the dynamic response of the screen system. In the first step the static structural analysis was carried out in order to apply the sieve preload (F_t) with value 1000 N. For this tension value the natural frequency of the screen system is close to 25 Hz, what was verified experimentally. Then the modal analysis was realized to obtain the natural frequencies of the screen. Afterwards the transient analysis was performed. The time of the analysis equal to 0.4 s was established. This is the minimal time, where the sieve vibrations is being stabilized. Two sinusoidal phase shifted forces (F_1 and F_2) were applied to the beams to simulate the excitation force, which in the real model is generated by rotating eccentric masses (Fig. 1). Excitation frequencies, close to double natural frequency of the screen system were applied with different excitation forces that correspond to the parameters from laboratory parametric resonance screen (Table 1).

Table 1. Excitation parameters used in transient analysis

Excitation frequency, Hz	Magnitude of excitation force, N	Sieve preload, N
41.23	833.6	1000
43.7	936.1	1000
47.07	1086.4	1000
51.13	1282.2	1000
55.82	1528.1	1000
58.74	1692	1000

3. Results and discussion

Two vibration mode shapes occurred close to the screen operation frequency equal to 25 Hz (Fig. 2). The first mode - one side sieve bending, is determined for the natural frequency equal to 25.564 Hz, while the second mode - double side sieve bending is observed for the frequency value of 25.607 Hz. These very close natural frequencies may cause appearance of different mode shapes and lead to unstable vibration amplitude level during the screen operation.

Screen system excitation with frequency close to double natural frequency of the system results in fast vibration amplitude grow (Fig. 3). This phenomenon is observed for all respected cases of excitation frequencies. The most stable transient response of the sieve is obtained for excitation frequency 47.07 Hz. This value is lower than double natural frequency of the screen system obtained in the modal analysis. This is the effect of numerical dumping, which is applied in Ansys Workbench during the problem solving. Numerical dumping eliminates the high frequency modes and stabilizes the numerical integration schemes, but it also affects in lower modes. For all values of excitation force, except 47.07 Hz and 58.74 Hz, the beat phenomenon is observed.

Vibration excitation with a frequency of 58.74 Hz is characterized by unstable sieve motion and the lowest amplitude. Therefore, to obtain stable sieve motion the excitation frequency need to be very close to double natural frequency of the system. The first vibration mode shape is observed for all cases, even when additional loads on the sieve surface were applied to excite the second mode.

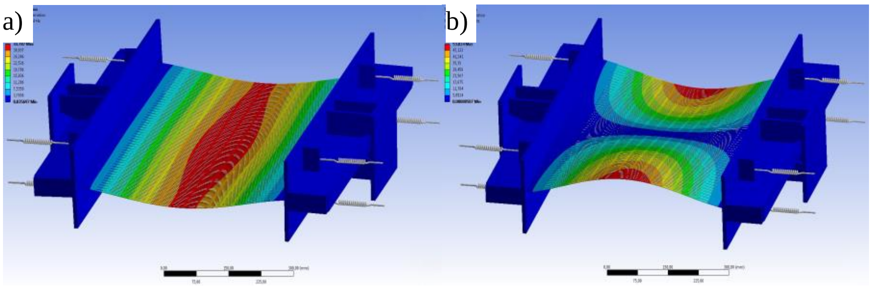

Figure 2. Free vibrations mode shapes of screen system: a) first mode; b) second mode

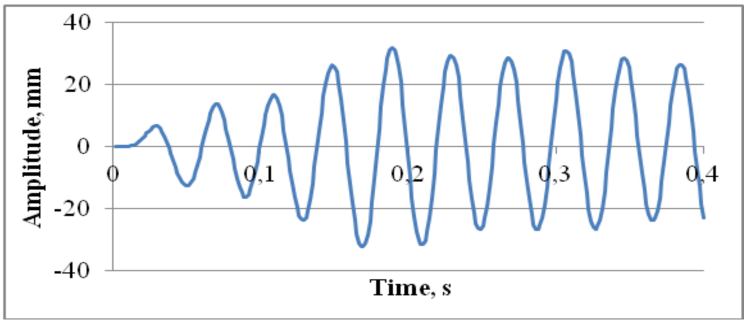

Figure 3. Transient response of the sieve for excitation frequency: 51.13 Hz

The effect of excitation frequency on sieve vibration frequency is presented in Fig. 4. The value of vibration frequency increased with the excitation frequency level. This dependence is nearly linear. The linear character of these relations is confirmed experimentally.

The value of excitation frequency has a significant impact on sieve vibration amplitude (Fig. 5). The vibration amplitude increases together with an increase of excitation frequency level, until its maximal value is obtained. This takes place when the excitation frequency is equal to 47.07 Hz. Further increasing of the excitation frequency results in amplitude decrease. The range of the excitation frequency, where the parametric resonance was observed, is nearly the same for both numerical and experimental data. However, the maximum value of vibration amplitude obtained numerically is almost two times larger than in the experiment. Moreover, the amplitude value in a function of excitation force from experimental data exhibits two local maximums, what cannot be observed in the numerical analysis. This could be the structural damping effect, which was not taken into consideration in the numerical analysis.

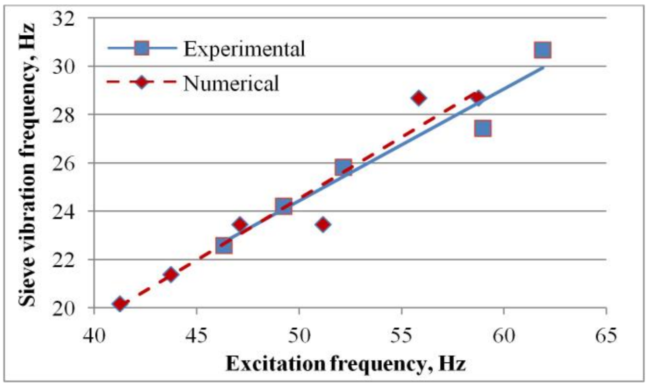

Figure 4. Effect of excitation force on sieve vibration frequency

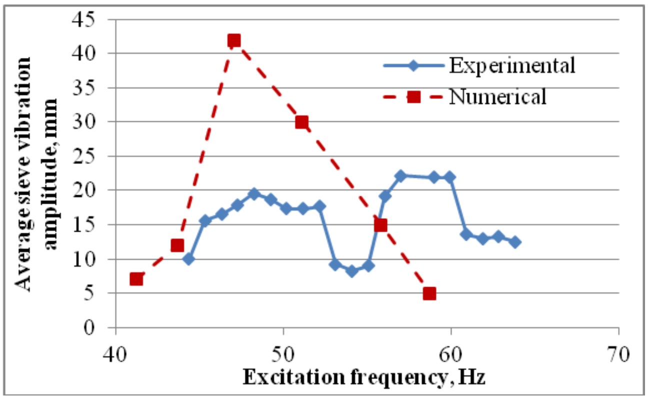

Figure 5. Effect of excitation force on sieve vibration amplitude for different excitation frequencies

4. Conclusions

Two vibration mode shapes occurred close to the screen operation frequency - one side bending and double side bending. This may cause appearance of different mode shapes and lead to unstable vibration amplitude level during the screen operation.

The value of vibration frequency increased with the excitation frequency level. The linear character of this dependence is observed in both numerical and experimental results.

The most stable transient response and the highest vibration amplitude of the sieve is obtained for the excitation frequency of 47.07 Hz. The range of excitation of parametric resonance is nearly the same as for experimental data. Differences of the amplitude level between numerical and experimental results are observed. It is an effect of damping, which is not considered in the numerical simulation.

Acknowledgments

This work was supported by the European Research Agency - 7th FP PEOPLE PROGRAMME Marie Curie Industry-Academia Partnerships and Pathways, grant agreement No. 284544

References

1. Ł. Bąk, S. Noga, A. Skrzat, F. Stachowicz, *Dynamic analysis of vibrating screener system*, Journal of Physics: Conference Series, **451** (2013), article No. 012028.
2. Ł. Bąk, S. Noga, F. Stachowicz, *The Experimental Investigation Of The Screen Operation In The Parametric Resonance Conditions*, Acta Mechanica et Automatica, **9**(4) (2015).
3. X.-M. He, Ch.-S. Liu, *Dynamics and screening characteristics of vibrating screen with variable eliptical trace*, Mining Science and Technology, **19** (2009) 0508 – 0513.
4. Z. Li, *Chaotic vibration sieve*, Mechanism and Maschine Theory, **30** (1995) 613 – 618.
5. V. I. Slepyan, I. G. Loginov, L. I. Slepyan, *The method of resonance excitation of a vibrating sieve and the vibrating screen for its implementation*, Ukrainian patent on invention no. 87369, 2009.
6. L. I. Slepyan, V. I. Slepyan, *Modeling of parametrically excited vibrating,* Journal of Physics: Conference Series, **451** (2013), article No. 012026.
7. L. I. Slepyan, V. I. Slepyan, *Coupled mode parametric resonance in a vibrating screen model*, Mechanical Systems and Signal Processing, **43** (2014) 295 – 304.
8. Y. Song, X.-H. Jiang, J. Song, J.-X. Zhang, *Dynamic analysis of a chaotic vibrating screen*, Procedia Earth and Planetary Science, **1** (2009) 1525 – 1531.
9. K. Sztaba, *Screening*, ŚWT, Katowice 1993 (in Polish).
10. P. Wodziński, *Screens - classification and systematic single-plane screens*, Physicochemical Problems of Mineral Processing, **41** (2007) 237 – 249.
11. P. Wodziński, *Screens and screening*, WPŁ, Łódź 1997 (in Polish).
12. Y.-M. Zhao, Ch.-S. Liu, X.-M. He, Ch.-Y. Zhang, Y.-B. Wang, Z.-T. Ren, *Dynamic design theory and application of large vibrating screen*, Procedia Earth and Planetary Science, **1** (2009) 776 – 784.

Effect of Exciting Force Amplitude on Occurrence of Parametric Resonance Phenomenon in Vibrating Screen

Łukasz BĄK
Department of Materials Forming and Processing, Rzeszow University of Technology
Al. Powstańców Warszawy 12, 35-959 Rzeszów, lbak@prz.edu.pl

Feliks STACHOWICZ
Department of Materials Forming and Processing, Rzeszow University of Technology
Al. Powstańców Warszawy 12, 35-959 Rzeszów, stafel@prz.edu.pl

Stanisław NOGA
Department of Mechanical Engineering, Rzeszow University of Technology
Al. Powstańców Warszawy 12, 35-959 Rzeszów, noga@prz.edu.pl

Andrzej SKRZAT
Department of Materials Forming and Processing, Rzeszow University of Technology
Al. Powstańców Warszawy 12, 35-959 Rzeszów, askrzat@prz.edu.pl

Abstract

The paper considers the effect of exciting force amplitude on occurrence of parametric resonance phenomenon in vibrating screens by using experimental methods. The measuring test is performed for three cases of excitation force levels. For each force level sieve parametric vibrations are excited by using proper excitation frequency. It is shown that an increase of the excitation force results in an increase in the sieve vibration amplitude. The dependence between excitation force and sieve parametric vibrations is nonlinear. The value of excitation force has an effect on the sieve vibration mode shape. Two vibration mode shapes are detected. It is found that the excitation frequency influenced the vibration amplitude. An increase of sieve preload has no effect on the amplitude level, however it results in an increase of the sieve vibration frequency.

Keywords: vibrating screen, parametric resonance, natural frequencies

1. Introduction

In many physical, engineering, electrical and biological systems appearance of parametric resonance in the system is of great interest. Parametric oscillations are the case of system oscillatory motion caused due to time varying (periodic) parameters of the system. These parameters can be stiffness or inertia. Parametric resonance appears when the external excitation is equal to integral multiple of natural frequency of the system. Parametric oscillations for the first time were described by Hill and Mathieu. They elaborated the fundamental theory related to parametric resonance phenomenon (so called Hill's and Mathieu equations). The problem of parametric oscillations was investigated in numerous researches. Many of them are connected with simple structures (e.g. beams or rods) [4, 5, 7, 12]. Bolotin [4] well documented the elementary problems of parametric instability in elastic systems. He also described the damping influence on the regions of stability. Parametric oscillations of preloaded Bernoulli beam with constant transverse load was presented by Osiński [7]. In this research he also considered the case of the beam with periodically changing length. For analysis of parametric vibrations of the beam system, Hagedorn and Koval [5] considered Timoshenko theory. In work of Yang and Chen [12] parametric stability is presented for the beam with periodical axial load. They considered Newton's second law and Boltzmann superposition theorem. A lot of authors have studied the parametric resonance problems for plates and cylindrical shapes by using both analytical and numerical methods. Nguyen [6] presents the parametric resonance problem in simply-supported plate with parametric excitation. In this paper Karman large deflection theory and governing equation are considered. For computation of finite element discretization method is proposed. Dynamic stability analysis of axially moving viscoelastic plates is presented by Tang and Chen [11]. Here the time-dependent speed of plate moving on parametric resonance is investigated.

Most investigations on parametric resonance are carried out to predict the response of the system. Periodic changes of system parameters may result in rapid amplitude grow and lead to fatigue and damage. The examples are gear wheels cooperation, axially loaded slender structures or rolls of ships. However, in some cases the target excitation of resonance brings measurable effects. This is especially in the case of vibrating screens and conveyors, where operation in conditions of resonance can significantly increase the process efficiency. The application of parametric resonance in the screen construction was proposed by Slepyan et al. [8]. In works [9-10] they presented the simplify dynamic screen system consisted of two masses connected by a string. The analytical and numerical analysis of natural vibration of the screen is presented in work [2]. The experimental analysis of the parametric resonance occurrence in screen operation is carried out by Bąk et al. [3]. In this paper the plate without cut-outs is used instead of the sieve. In presented papers the screen system operating in parametric resonance conditions is included.

The paper deals with experimental investigation of the vibrating screen operation in parametric resonance conditions. The changes of the excitation force and the excitation frequencies are executed to measure of their effect on the sieve vibration amplitude.

2. Laboratory parametric resonance screen

The laboratory parametric resonance screen construction (Fig. 1a) is based on the first PR screen designed by Slepyan et al. [8]. The screen system consists of two beams connected by a sieve. The sieve is a simple sheet metal plate with rectangular cut-outs (Fig. 2) made from spring steel grade 1.8159. The rubber pads between the sieve and the beam are applied to limit the bending stresses concentration. Screening surface dimensions are 750 mm length and 500 mm width. This system is suspended on the base frame by set of sixteen springs with stiffness equal to 275 N each one, and the whole machine weight is equal to approx. 200 kg. Excitation force is generated by two electrical vibrators screwed down to the beams. The nominal value of excitation force is equal to 2972 N (for 2954 rpm vibrators rotational speed). This force can be adjusted with 10 % step of its nominal value. Rotational speed of electrical vibrators was read by using laser speedometer. Hence, the excitation frequency has been calculated. The suspension assembly (Fig. 1b) is supplied with strain gauges sleeves, that enable sieve preload measurement. Two piezoelectric accelerometers with the range up to ±1000 g are used for measurement of sieve vibration amplitude and frequency. They are located in two opposite sides of the sieve.

a)

b)

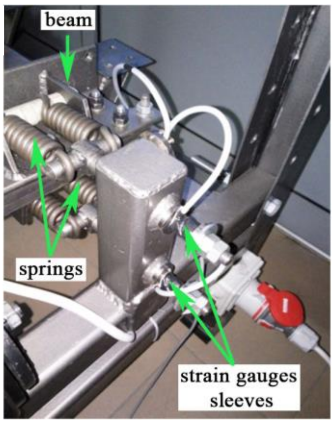

Figure 1. Laboratory parametric resonance screen: a) general view; b) suspension assembly

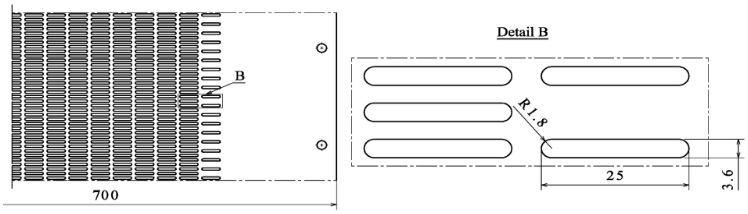

Figure 2. Sieve geometry and cut-outs enlargement

3. Experimental methods

The first step of experimental investigation was carried out for value of sieve preload equal to 1000 N. In this case three levels of excitation force were applied: 30%, 40% and 50% of nominal force. For each value of excitation force the excitation frequency was adjusted until the parametric resonance occurrence.

The second part of the investigation was performed for sieve preload values: 1600 N, 2400 N and 3000 N. Here only 40 % level of excitation force was applied. Data from accelerometers were collected as an acceleration in a function of time. Output signal was processed during the measurement by using Chebyshev filter. Further signal processing was performed in MATLAB software. Fast Fourier Transform was used to find the resonant frequency of the system. Maximum sieve displacement was obtained by double numerical integration of input signal.

4. Results and discussion

The value of sieve vibration amplitude increased with the excitation force level (Fig. 3). For each considered cases this dependence is nonlinear. For the first two values of the excitation frequency (49.24 Hz and 50.21 Hz) there is no significant increase of vibration amplitude. In this case an increase in excitation force of 10 % results in amplitude increase of 33 %. For the two last cases (52.16 Hz and 57.02 Hz) this increase is much greater and respectively is equal to 250% and 325%. Further increasing of excitation force level (from 40% to 50%) has a small effect on the amplitude value. For each considered cases the amplitude increase is less than 20 %.

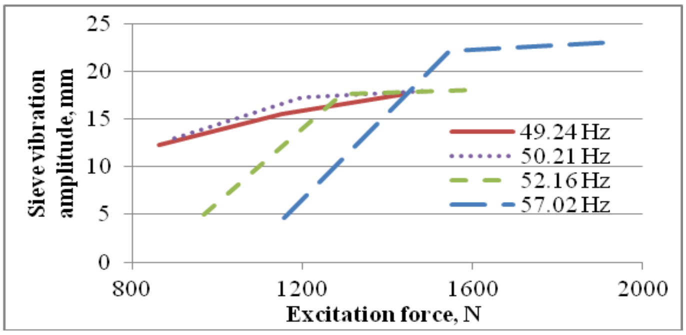

Figure 3. Effect of excitation force on sieve vibration amplitude for different excitation frequencies

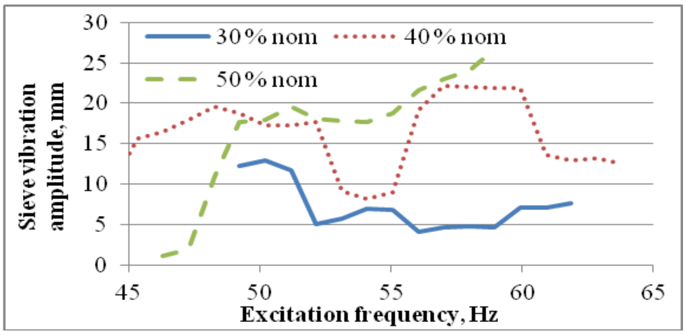

Figure 4. Effect of excitation frequency on sieve vibration amplitude for different excitation forces

The amplitude level increase is caused not only by growing excitation force but also by changes of the excitation frequency (Fig. 4). For the excitation force adjustment on 30% level, parametric resonance is detected for excitation frequencies in a range from 49 Hz to 62 Hz. Here the second mode of natural vibrations was observed [2]. The amplitude reaches the maximum value equal to 13 mm. Further increase of the excitation frequency results in a decrease of the amplitude till 5 mm. The curves of the excitation force levels equal to 40% and 50% are similar. Two local maximum can be distinguished. The first can be observed for the excitation frequency close to 50 Hz. For both excitation force levels the local maximum of amplitude is equal to 19.5 mm. The second one appeared for the frequency near to 59 Hz. Here the increasing of excitation force resulted in 20% increase of the sieve vibration amplitude. For force levels 40% and 50% the first mode of parametric vibrations was observed.

The sieve preload value has no significant effect on the amplitude level (Fig. 5). For each considered tension forces the maximum value of amplitude is within the range between 22 mm and 24 mm, however it is obtained for different excitation frequencies. This is caused by increasing natural frequency of the system due to sieve preload increase [3]. The increase of sieve preload also results in fading of first local maximum of amplitude. For tension forces 2400 N and 3000 N only one local maximum can be visible (Fig. 5).

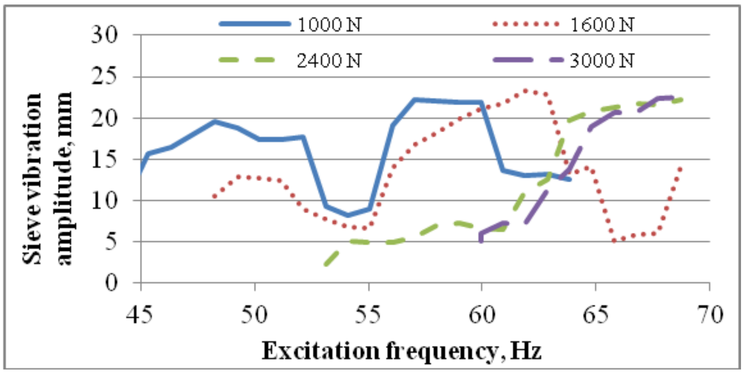

Figure 5. Effect of excitation frequency on sieve vibration amplitude for different sieve preloads

5. Conclusions

The dependence between excitation force and sieve vibration amplitude is nonlinear. Initially the increase of excitation force results in large amplitude grow, further increase has no significant effect on the amplitude value. The amplitude of vibrations excited with 30 % force level is relatively small in comparison with 40 % and 50 % force levels.

Changes of excitation frequency result in sieve vibration amplitude value. It is found that when the excitation force level is equal to 40% or more, two local maximums of amplitude appears for excitation frequencies close to 50 Hz and 59 Hz.

The value of excitation force has an effect on the sieve vibration mode shape. Two mode shapes of parametric vibrations were observed.

An increase of sieve preload results in higher natural frequency of the system, therefore to obtain maximum amplitude higher excitation frequencies must be applied. However, there is no significant effect of preload increase on the amplitude value.

Acknowledgments

This work was supported by the European Research Agency - 7th FP PEOPLE PROGRAMME Marie Curie Industry-Academia Partnerships and Pathways, grant agreement No. 284544

References

1. Y. Başar, C. Eller, W. B. Krätzig, *Finite element procedures for parametric resonance phenomena of arbitrary elastic shell structures*, Computational Mechanics,
2 (1987) 89 – 98.
2. Ł. Bąk, S. Noga, A. Skrzat, F. Stachowicz, *Dynamic analysis of vibrating screener system*, Journal of Physics: Conference Series, **451** (2013), article No. 012028.
3. Ł. Bąk, S. Noga, F. Stachowicz, *The Experimental Investigation Of The Screen Operation In The Parametric Resonance Conditions*, Acta Mechanica et Automatica, **9**(4) (2015).
4. V. V. Bolotin, *The dynamic stability of elastic systems*, Armed Services Technical Information Agency, Arlington 1962.
5. P. Hagedorn, L. R. Koval, *On the parametric stability of a Timoshenko beam subjected to a periodic axial load*, Ingenieur - Archiv, **40** (1971) 211 – 220.
6. H. Nguyen, *Simultaneous resonances involving two mode shapes of parametrically-excited rectangular plates*, Journal of Sound and Vibration, **332** (2013) 5103 – 5114.
7. J. Osiński, *The analysis of parametric vibrations of continuous systems with constant transversal loading by asymptotic method and finite elements,* Journal of Theoretical and Applied Mechanics, **2**(23) (1985) 241 – 254 (in Polish).
8. V. I. Slepyan, I. G. Loginov, L. I. Slepyan, *The method of resonance excitation of a vibrating sieve and the vibrating screen for its implementation*, Ukrainian patent on invention no. 87369, 2009.
9. L. I. Slepyan, V. I. Slepyan, *Modeling of parametrically excited vibrating,* Journal of Physics: Conference Series, **451** (2013), article No. 012026.
10. L. I. Slepyan, V. I. Slepyan, *Coupled mode parametric resonance in a vibrating screen model*, Mechanical Systems and Signal Processing, **43** (2014), 295 – 304.
11. Y. Tang, L. Chen, *Stability analysis and numerical confirmation in parametric resonance of axially moving viscoelastic plates with time-dependent speed*, European Journal of Mechanics A/Solids, **37** (2013) 106 – 121.
12. X. Yang, L. Chen, *Stability in parametric resonance of axially accelerating beams constituted by Boltzmann's superposition principle,* Journal of Sound and Vibration, **289** (2006) 54 – 56.

Impact Absorption System Based on MRE with Halbach Array

Mirosław BOCIAN, Jerzy KALETA, Daniel LEWANDOWSKI, Michał PRZYBYLSKI
Department of Mechanics, Materials Science and Engineering
Faculty of Mechanical Engineering, Wrocław University of Science and Technology
michal.przybylski@pwr.edu.pl

Abstract

This paper presents impact absorption system based on magnetorheological elastomer with Halbach magnetic arrays used for tuning. Its design and results of experimental evaluation are presented together with proposition of a non-linear model to describe the system. In the end validation of the model is presented based on energy and power balance method for its parametrization. This paper presents both novel approach to impact absorption and to modelling of a system based on smart material such as magnetorheological elastomer.

Keywords: Experimental mechanics, smart material, magnetorheological elastomer, magnetic field, modelling, parametrization, simulation

1. Introduction

Magnetorheological elastomer (MRE) is smart material that allows innovative approach to impact and vibration control in mechanical and civil structures. It is a composite material made out of rubber matrix and soft magnetic particles mixture. Application of magnetic field influences change of rheological and mechanical properties of the material as the particles try to arrange themselves into chain like structures inside of the material, along magnetic field vectors. Therefore material properties can be controlled with use of external magnetic field, what can be used in controllable impact and vibration control [1-4]. In the paper design and construction of the impact absorption system based on MRE material and Halbach arrays have been presented. Double dipolar circular Halbach array is an important element of this system as it is innovative method for low power consuming magnetic generator that can be used for stimulation of MRE absorbers and isolators [5, 6]. Testing of presented system have shown its potential for change of resonance frequency and its damping properties. On base of the experimental results a non-linear models of the system have been proposed. For its validation and parametrization energy and power balance method have been used [7, 8]. Results of the parametrization indicate need for search of another model as the results do not match with experiment.

2. Absorption system design

Presented impact absorption system is designed to absorb impact energy and mitigate vibrations occurring after impact. It was thought as single degree of freedom system, however for testing purposes second degree was added. The idea of the system is presented in Figure 1. a), where element between mass M_1 and M_2 is MRE material and spring K correspond to suspension the system is hanging on. The system is based on a magnetorheological elastomer working as damping material. For magnetic stimulation of the MRE material double dipolar circular Halbach arrays were designed and manufactured. Due to need for use of strong magnetic fields all elements used in the test rig are made out of non-magnetic materials, like marble, aluminium and brass. The test system is presented in Figure 1. b).

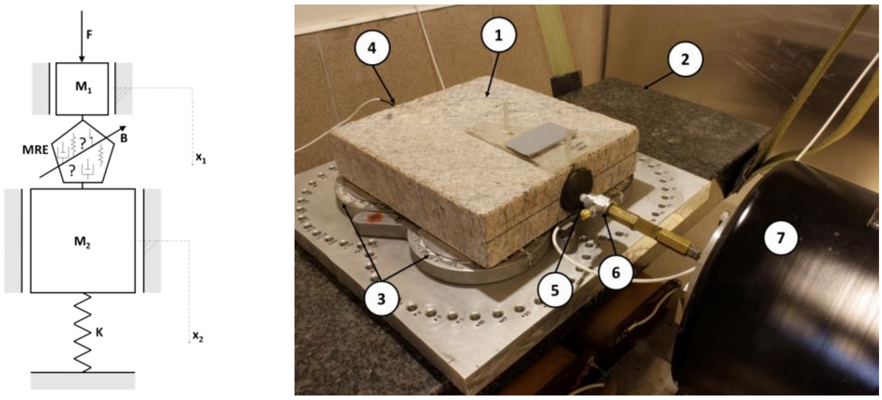

a) b)

Figure 1. Schematic idea of the absorption system a), picture of the absorption system, where: 1 - upper mass (4.25 kg), 2 - bottom mass, 3 - Halbach magnetic arrays, 4 - acceleration sensor, 5 - impact head, 6 - force sensor, 7 - shaker

For measurement purposes system is equipped with two sensors: accelerometer (353A33, PCB) located at the back of the upper mass and force sensor (208A02, PCB) between impact head and shaker. Signals were collected with use of DAQ board (U2355A, Keisight). It was also used to control shaker (2075E, The Modal Shop Inc.) powered by amplifier (SmartAmp Power Amplifier 2100E21 series, The Modal Shop Inc.). Modal shaker was used for controlled impact impulse generation. For programing purposes computer software (VEE 9.32, Keisight) was used [6].

Upper mass was placed on four magnetorheological elastomer dampers surrounded by double dipolar circular Halbach arrays. They were placed on CNC milled aluminium plate with locking holes for Halbach arrays. The base of the system was marble block with weight of almost 40 kg to provide low frequency swing of the system after each excitation.

2.1. Magnetorheological elastomer

Magnetorheological elastomer is a smart material that changes its mechanical and rheological properties under influence of external magnetic field. It is rubber material filled with soft magnetic particles that tend to create chain like structures in the direction of the magnetic field that stimulates the material. MRE material used in the test stand is made out of three components: thermoplastic elastomer matrix Tefabloc TO..222 (Mitsubishi Chemical Performance Polymers), iron particles ASC 300 (Höganäs) and paraffin oil Onida 934 (Shell) in weight ratio 83 : 14 : 3. This material was previously developed and described in papers [9, 10]. Material was prepared using in mixing chamber of Plasti-Corder Lab-Station (Brabender). Samples were made by extrusion pressing. Figure 2. presents picture of the samples and their cross-section showing its uniform structure. Each sample was 15 mm high and had diameter of 25 mm.

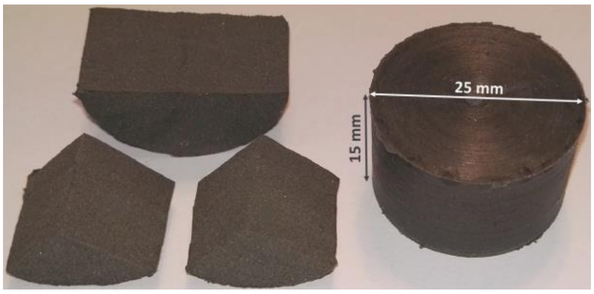

Figure 2. Magnetorheological elastomer sample

2.2. Magnetic field generator

To stimulate magnetorheological elastomer enquired is magnetic field, the stronger it is the bigger change of the materials properties. Therefore for the purpose of the test stand double dipolar circular Halbach arrays were designed and fabricated. Figure 3. a) presents picture of one of the arrays. The circular Halbach array is a set of magnets oriented is a specific way that can generate dipolar magnetic field inside of its opening. By setting two or more such arrays around one another it is possible to change generated magnetic field by rotating them around one another.

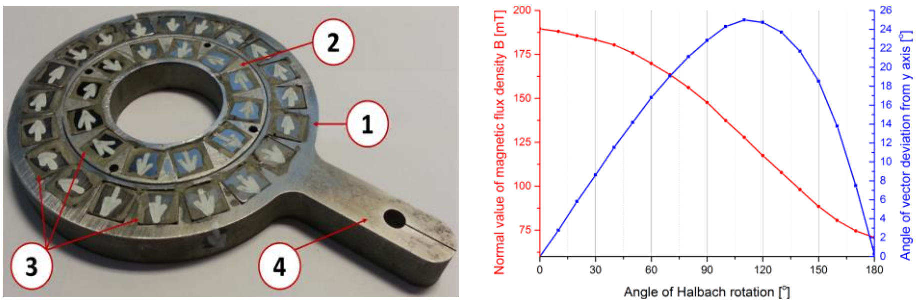

a) b)

Figure 3. a) Double dipolar circular Halbach array, where 1 - outer array frame, 2 - inner array frame, 3 - neodymium magnets, 4 - rotation arm with locking pin hole, b) relation of normal value of magnetic flux density B generated by Halbach array and its angle of deviation from y axis to the angle of rotation of outer array to inner one

Magnetic Halbach arrays used in the study was made out of 32 N48 grade neodymium magnets 12 mm x 12 mm x 12 mm. It allowed to generate magnetic field in range from 190 mT to 70 mT. In Figure 3. b) is presented graph showing change normal value of magnetic flux density B generated versus rotation of the outer array around inner one and change of deviation angle of the magnetic field vector from y axis.

3. Experimental evaluation

Experimental investigation of impact absorption and vibration damping with use of the test stand was conducted for set of impact force and magnetic flux density values. Tests were run in series for different values of magnetic field. After each test setup there was a 20 minute brake that allowed mitigation of vibration caused by the suspension of the system (refer to Figure 1. a)). In the paper are presented results of acceleration time traces for two representative values of impact force and corresponding frequency response functions.

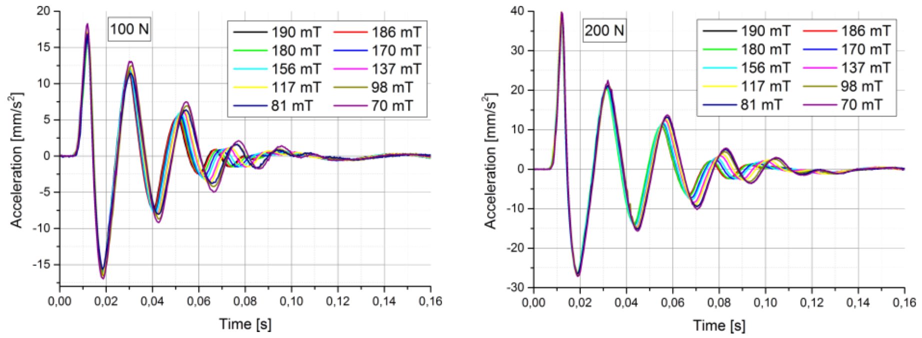

a) b)

Figure 4. Time traces of acceleration of the upper mass for range of magnetic field values for two representative values of impact force: a) 100 N and b) 200 N

Figure 4. presents time traces of acceleration collected with acceleration sensor mounted on the upper mass of the test system. For both values of impact force presented it is visible that the stimulation with stronger magnetic field caused faster damping of the vibrations occurring after impact.

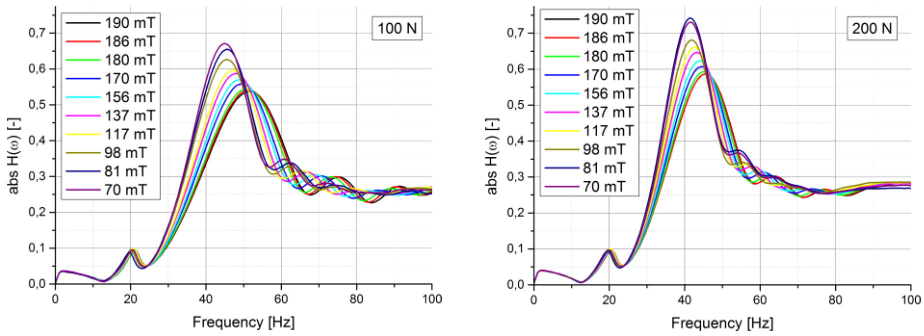

a) b)

Figure 5. Frequency response functions for range of magnetic field values for two representative values of impact force: a) 100 N and b) 200 N

Figure 5. show frequency response functions for range of magnetic fields and two representative values of impact force. It was calculated on base of acceleration and force signals with use of the double channel signal analysing method [6, 11]. On base of presented results it is clearly visible that magnetic field can significantly influence properties of the MRE material and therefore increase its damping properties what can be used for better reduction of vibration in civil and mechanical structures.

4. Parameter estimation

To analyse obtained results a non-linear constitutive model have been proposed. It is four parameter model with one elastic element (C_0) connected with viscous element (K_0) in series and they are connected in parallel with elastic non-linear element (C_1) and viscous element (K_1). For parametrization of this model energy and power balance method is used [7, 12, 13]. Figure 6. presents schematic representation of the model.

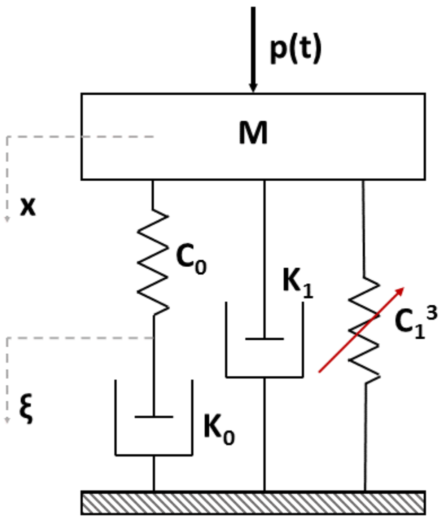

Figure 6. Four parameter constitutive models chosen for analysis of the obtained results [8, 14]

To describe the model following equations are used:

$$C_0 \cdot (x-\xi) = K_0 \cdot \dot{\xi} \tag{1}$$

$$p(t) = C_0(x-\xi) + C_1 \cdot x^3 + K_1 \cdot \dot{x} + m \cdot \ddot{x} \tag{2}$$

$$p(t) = C_1 \cdot x + \frac{K_0 \cdot C_0 + K_0 \cdot C_1}{C_0} \cdot \dot{x} + K_1 \cdot \dot{x}^3 + M \cdot \ddot{x} + \frac{3 \cdot K_0 \cdot K_1}{C_0} \cdot \dot{x}^2 \cdot \ddot{x} + \frac{M \cdot K_0}{C_0} \cdot \dddot{x} - \frac{K_0}{C_0} \cdot \dot{p} \tag{3}$$

$$\alpha_x^p = \left(K_1 + K_0\right) \cdot \alpha_x^{\dot{x}} + \frac{K_0(C_1 + C_0)}{C_0} \cdot \alpha_x^{\dot{x}} + 3\frac{K_0 \cdot C_1}{C_0} \cdot \alpha_x^{x2\dot{x}} + \frac{M \cdot K_0}{C_0} \cdot \alpha_x^{\dddot{x}} - \frac{K_0}{C_0} \cdot \alpha_p^{\dot{x}} \tag{4}$$

$$\alpha_{\dot{x}}^{p} = C_1 \cdot \alpha_{\dot{x}}^{x^3} + \frac{K_0 \cdot K_1}{C_0} \cdot \alpha_{\dot{x}}^{\ddot{x}} + M \cdot \alpha_{\dot{x}}^{\ddot{x}} + 3\frac{K_0 \cdot C_1}{C_0} \cdot \alpha_{\dot{x}}^{x^2\dot{x}} - \frac{K_0}{C_0} \cdot \alpha_{p}^{\ddot{x}} \tag{5}$$

Equations (1) and (2) describe dynamic equilibrium state of the model with non-linear elastic element. On their base equation (3) is created to eradicate ξ from those equations and join them in one. On base of this uniform equation two formulas for the energy and power balance are formulated and are presented in equation (4) and (5). In those equations $\alpha_{\dot{x}}^{x}$ represent area of the hysteresis loop created from displacement x and velocity $\dot{x}$. With use of multiple linear regression parameters of the model are determined and are presented in Table 1. Parameters are presented in form of function where B is normal value of magnetic field used for stimulation of the MRE material.

Table 1. Results from parametrization, where B is value of magnetic field

K_0	K_1	C_0	C_1	Mean squared error
$0.0108\ B^3 - 4.5659\ B^2 + 636.23\ B + 3.34 \cdot 10^4$	$-0.0108\ B^3 + 4.5388\ B^2 - 631.45\ B + 3.29 \cdot 10^4$	$4 \cdot 10^7\ B - 3 \cdot 10^{11}$	$-10^4\ B + 2 \cdot 10^7$	0.999969

On base of those parameters simulation have been done with initial parameters matching those from experiment. The unexpected result was that scatter instead of tending to zero what means that the model does not match presented results and therefore presented parameters are wrong. Nevertheless presented method gives a promising approach for modelling and parametrization of the presented system, with use of different model.

5. Conclusions

This paper presents design, construction and an approach to modelling of the system. The impact absorption system is based on magnetorheological elastomer is and active smart magnetic material that presents controllable damping properties. To control its properties double dipolar circular Halbach arrays have been designed and fabricated. They allow to change generated magnetic field in a range from 70 mT to 190 mT. Experimental testing of the system have proven its possibility to shift frequency resonance by more than 10 Hz and to effectively reduce vibrations occurring in the system after impact. An approach to modelling with use of the energy and power balance method have been made, however obtained results do not match with experimental results and indicate need for search of a different model.

References

1. Y. C. Li, J. C. Li, T. F. Tian, W. H. Li, *A highly adjustable magnetorheological elastomer base isolator for applications of real-time adaptive control*, Smart Materials and Structures, **22** Sep (2013).
2. J. Yang, H. P. Du, W. H. Li, Y. C. Li, J. C. Li, S. S. Sun, et al., *Experimental study and modeling of a novel magnetorheological elastomer isolator*, Smart Materials and Structures, **22** Nov (2013).
3. Y. C. Li, J. C. Li, *A Highly Adjustable Base Isolator Utilizing Magnetorheological Elastomer: Experimental Testing and Modeling*, Journal of Vibration and Acoustics-Transactions of the Asme, **137** Feb (2015) 011009.
4. S. S. Sun, H. X. Deng, J. Yang, W. H. Li, H. P. Du, G. Alici, et al., *An adaptive tuned vibration absorber based on multilayered MR elastomers*, Smart Materials and Structures, **24** Apr (2015).
5. M. Bocian, J. Kaleta, D. Lewandowski, M. Przybylski, *Design concept of test stand for determining properties of magnetorheological elastomer*, Acta Mechanica et Automatica, **7** (2013) 131 – 134.
6. M. Bocian, D. Lewandowski, J. Kaleta, M. Przybylski, *Test setup for examination of magneto-mechanical properties of magnetorheological elastomers with use of a novel approach*, Archives of Civil and Mechanical Engineering, **16** (2016) 294 – 303.
7. M. Bocian, M. Kulisiewicz, S. Piesiak, *Wykorzystanie nieliniowych modeli zdegenerowanych w identyfikacji elementów sprezysto-tłumiacych maszyn*, presented at the IV Konferencja Naukowa pt. *Problemy Rozwoju Maszyn Roboczych*, Zakopane, 2001.
8. M. Panek, *Własciwosci dynamiczne kosci długich. Badania, modele, identyfikacja*, PhD, Wydział Mechaniczny, Wrocław University of Science and Technology, Wrocław, 2013.
9. J. Kaleta, M. Krolewicz, D. Lewandowski, M. Przybylski, *Investigations of Magnetorheological Elastomers Subjected to Cyclic Loading*, in Fracture and Fatigue of Materials and Structures, **598** J. Galkiewicz, Ed., ed, 2014, 81 – 85.
10. P. Zajac, J. Kaleta, D. Lewandowski, A. Gasperowicz, *Isotropic magnetorheological elastomers with thermoplastic matrices: structure, damping properties and testing*, Smart Materials & Structures, **19** Apr (2010) 1 – 7.
11. M. Bocian, J. Kaleta, D. Lewandowski, M. Przybylski, *Test stand and method for determination of the usefulness of the magnetorheological composites in active suspension systems*, in Fracture and Fatigue of Materials and Structures. **598** J. Galkiewicz, Ed., ed, 2014, 7 – 12.
12. M. Kulisiewicz, *Modeling and identyfication of nonlinear mechanical systems under dynamic complex loads*, Oficyna wydawnicza Politechniki Wrocławskiej, 1994.
13. S. Piesiak, *Identyfikacja układów mechanicznych w dziedzinie nieliniowych i zdegenerowanych modeli dynamicznych*, Oficyna wydawnicza Politechniki Wrocławskiej, 2003.

14. W. Derski and S. Ziemba, *Analiza Modeli Reologicznych*, vol. I. Warszawa: Państwowe Wydawnictwo Naukowe, 1968.

Vibration Condition Monitoring of the Vertical Steel Tanks

Nadiia BOURAOU
National Technical University of Ukraine Kyiv Polytechnic Institute
37 Peremogy Pr., Kyiv, Ukraine, 03056, burau@pson.ntu-kpi.kiev.ua

Olga LUKIANCHENKO
Kyiv National University of Construction and Architecture
31 Povitroflotsky Pr., Kyiv, Ukraine, 03680, tush_lu@mail.ru

Sergiy TSYBULNIK
National Technical University of Ukraine Kyiv Polytechnic Institute
37 Peremogy Pr., Kyiv, Ukraine, anteri0r@yandex.ru

Dmytro SHEVCHUK
National Technical University of Ukraine Kyiv Polytechnic Institute
37 Peremogy Pr., Kyiv, Ukraine, 00012066@ukr.net

Abstract

This paper presents the results of numerical analysis and physical simulation of the vertical steel tank for usage in the vibration condition monitoring system. For purposes of the numerical analysis the tank is considered as the double steel cylinder consisting of the inner and outside shells. The discrete model of a tank is developed. The estimations of stress and deformation are obtained when the following vertical loads are exerting: weight of the fuel, weight of the tank roof and other structural elements or equipment. The physical model of a tank is used for physical simulation. The impulse responses of this model are measured and analyzed for different levels of tank filling. The methods of Prony and Steiglitz-McBride are used for estimation of the vibration damping factor which depends on the level of tank filling.

Keywords: vertical steel tank, numerical analysis, stress, deformation, vibration analysis, damping factor

1. Introduction

Ensuring safe operation is a very important problem for many complex objects located in hard-to-reach regions and influenced by the dynamic excitation.

As a complex object we will consider a vertical weld-fabricated steel tank with environmentally hazardous substances, whose operation is associated with various internal and external influences. For example, such tank was installed at the Ukrainian Antarctic Station Vernadsky. Modal (natural modes and shapes) and dynamic (vibration) characteristics of the tank are caused by the structural and technological conditions of its assembling. In addition, these characteristics also depend on the external dynamic excitations (wind load, earthquake load), temperature variations, and the changes of the fuel level in the tank.

The following factors make such tanks extremely dangerous for people and the environment: (a) defects caused by fabrication, transportation, or installation, (b) changes of mechanical characteristics of the used materials under the influence of dynamic excitation, (c) damages in the tank structure, which can lead to the fuel leakage.

The condition monitoring system is developed for prevention of the tank failure and environmental pollution [1]. The bases of such system are: vibration measuring subsystem, control subsystem, signal processing and decision making subsystem, subsystem for simulation, determination and prediction of parameters and characteristics of the mode of deformation.

The purposes of this work are: a) numerical analysis of the vertical steel tank when the vertical loads are exerting, b) physical simulation of the tank, analysis of the impulse response and determination of features of changes in the tank model condition.

2. Development and analysis of tank model

We consider the testing object (tank) as the double steel cylinder which consists of the inner shell and the outside shell. The shells consist of welded walls, besides there are steel tubes for fuel dispensing and tank unloading.

We use Finite Element (FE) Analysis to design the discrete model of the tank, which can be representative of an actual object. For this purpose we consider the walls of shells made from steel with the following properties: density 7850 kg/m^3; modulus of elasticity 2,05 10^5 N/m^2; Poison's ratio 0,3; shear modulus $0{,}79 \cdot 10^5$ N/m^2. Each wall is modeled by the set of the quadrilateral plane FE with six degrees of freedom. Mechanical data of weld seams are accepted the same as of the material of walls. Therefore, additional finite elements for simulation of weld seams are not used. The NASTRAN is used for design of discrete model of the tank, the presence of weld seams is ensured by the simulation of walls in the form of surfaces (bodies). Two mentioned tubes connect the inner and outside shells are modeled by two rod FE "tube", two quadrilateral FE are replaced by eight triangle FE at the attaching point. Thus, the developed discrete model of tank consists of 3548 FE and 3393 nodes. The discrete model of tank is presented in Figure 1.

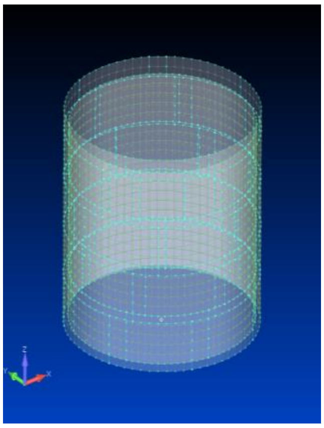

Figure 1. Discrete model of vertical steel tank as a double cylinder

The aim of analysis of the developed model is to estimate the mode of deformation when the vertical loads are exerting. We consider the following loads: weight of the fuel, weight of the tank roof and other structural elements or equipment.

Results of analysis of the stress and deformation of inner tank caused by weight of the fuel are presented in Table 1, values of the stress and deformation do not exceed the allowable values.

Table 1. Dependencies of stress and deformation on weight of the fuel

Characteristic of tank condition	Cases of fuel filling as part of tank volume			
	1/4	1/2	3/4	1
Stress, MPa	12	27	41	56
Deformation, mm	0,207	0,476	0,728	0,978

Maxima of stress and deformation of the inner tank are obtained at the bottom of walls for the four cases of fuel filling. Fig 2 shows the result of estimation of the mode of deformation for full filling.

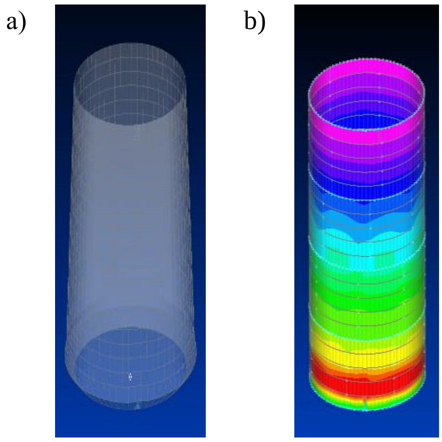

Figure 2. Mode of deformation of inner tank full filling: a) deformation; b) stress

The results of analysis of the stress and deformation of the tank as a double cylinder caused by weight of the tank roof and other structural elements or equipments are presented in Fig. 3. Maxima of stress (0,6MPa) and deformation (0,016 mm) are observed in elements of the bottom of walls and in elements of the top of the tank ring (in part in weld seams). The obtained value of load caused by weight of the tank roof and other equipments is considerably less than the bound of calculated stress. Received results show that the surface pressure caused by weight of the fuel on the tank's wall stresses the model elements much more than the axial load weight of the tank roof and other equipment.

Thus, for the purposes of further research, different levels of tank filling can be considered as a cause of changes in the tank condition.

a)
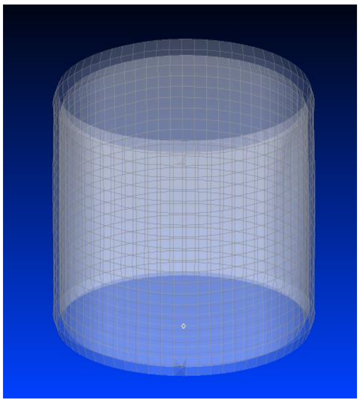
b)
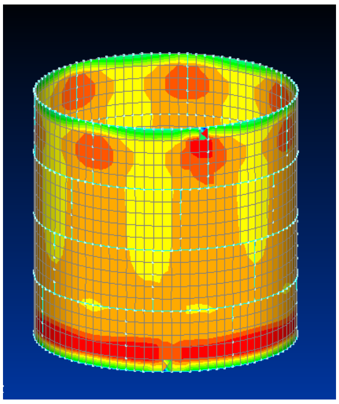

Figure 3. Mode of deformation of tank as a double cylinder caused by weight of the tank roof and equipments: a) deformation; b) stress

3. Physical simulation of tank and analysis of impulse responses

A small-size vertical steel container, with capacity of 0,04m^3, is considered as a physical model of a tank. We use the vibration method of free oscillations, which consists in the impact excitation of the testing object and further analysis of object's impulse response. The unit of two MEMS MS8002.D accelerometers are used to measure the impulse responses in two directions: in horizontal plane and vertical plane [2]. Figure 4a shows the physical model of the tank with mounted unit of accelerometers, and Figure 4b illustrates the object's simulation model, on the surface of which the spots of impact excitation are indicated as "x" and the spots of impulse responses measurement are indicated as "o".

a)

b)
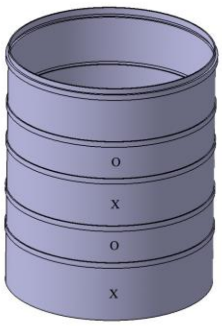

Figure 4. Models of tank: a) physical model of tank with mounted unit of accelerometers; b) three-dimensional simulation model

Measurements of the object's impulse responses are carried out for the mentioned above cases of liquid filling. The example of Welch periodogram of impulse response is presented in Fig. 5 (impact is in the orthogonal direction to axes of sensitivity of both accelerometers, container is empty). Figure 5 shows the presence of two spectral components in the frequency band (300 Hz, …, 500 Hz), whose amplitudes exceed the others.

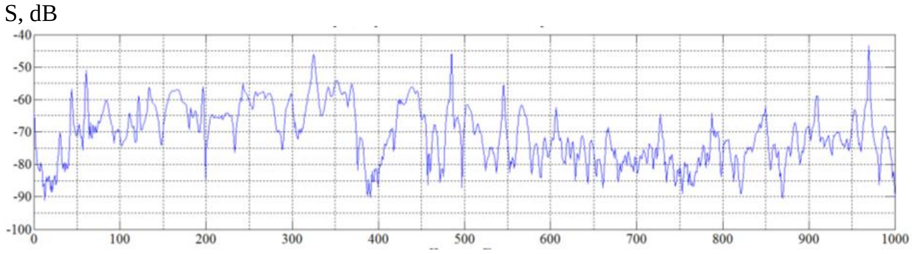

Figure 5. Welch periodogram of impulse response under impact in the orthogonal direction to axes of sensitivity of both accelerometers

The methods of Prony and Steiglitz-McBride are used for analysis of the impulse responses and estimation of vibration damping factor depending on the level of liquid filling. In conformity with Prony's method, the impulse response, consisting of the N samples**,** is approximated by the model of sum of q complex exponents [3]:

$$\hat{x}[n]=\sum_{k=1}^{q} A_k \exp[(\alpha_k + j2\pi f_k)(n-1)T + j\theta_k] \tag{1}$$

where T is a sampling period; n is a number of time step; $A_k, \alpha_k, f_k, \theta_k$ indicate the amplitude, damping factor, frequency, and phase angle of k component respectively.

The equation (1) can be presented in the form of z-transform:

$$\hat{x}[z]=\sum_{k=1}^{q} \frac{h_k z}{z_k(z-z_k)} \tag{2}$$

where $h_k = A_k \exp(j\theta_k)$; $z_k = \exp[(\alpha_k + j2\pi f_k)T]$ and $z = \exp(j2\pi fT)$.

Estimations of the unknown parameters $A_k, \alpha_k, f_k, \theta_k$ are obtained by using the estimations of coefficients of the discrete transfer function of certain filter with the finite pulse characteristic. The N-sampling impulse response of testing object is used as the filter pulse characteristic h(k). It is necessary to assure the identical equality of the discrete transfer function of the filter to transformation (2), if Prony's method is used.

The method of Steiglitz-McBride [4] also allows synthesizing the filter if the pulse characteristic is given. But this method does not demand the identical equality (2), in this case the following condition is fulfilled:

$$\sum_{k=0}^{N} |h(k)-h_*(k)|^2 \to \min \tag{3}$$

where $h_*(k)$ is the pulse characteristic of recursive filter with given polynomials order of numerator and denominator of the discrete transfer function.

The following data are used for estimation of vibration damping factor by the method of Steiglitz-McBride: N=4096 and q=10. Results of estimation of frequency and damping factor for two low-frequency components of impulse responses are presented in Table 2 for different levels of liquid filling.

Table 2. Estimations of frequencies and damping factors (modulus) depending on the level of liquid filling

Cases of liquid filling as part of tank volume		0	1/4	1/2	3/4	1
Component 1	Frequency, Hz	340	354	327	367	337
	Damping factor	20	36	39	54	102
Component 2	Frequency, Hz	445	476	444	465	449
	Damping factor	2	11	14	34	45

It can be seen, the increase of liquid filling results in increase of damping of components of the impulse response. This fact can be used as feature of changing of the tank condition during the vibration condition monitoring of vertical steel tanks.

4. Conclusions

The numerical analysis of the vertical steel tank is carried out when vertical loads are exerting. Received results show that surface pressure caused by weight of the fuel on wall of tank stresses of elements of tank model much more than axial load weight of the tank roof and other elements and equipment.

The physical simulation of tank is done. Impulse responses of tank's physical model are measured and analyzed for different levels of liquid filling. Estimations of vibration damping factor are obtained by the method of Steiglitz-McBride for different levels of liquid filling. Received results show that increase of liquid filling results in increase of damping of components of the impulse response.

Results of the presented work can be used for vibration condition monitoring of vertical steel tanks.

References

1. UA Patent 73310 Ukraine, IPC G01M 7/00, *Information-diagnostic complex for monitoring and forecasting of the technical condition of civil engineering structures* /Inventors Bouraou N. I., Tsybulnik S. A., Shevchuk D. V. and other, Filed 30.12.2011, Pub. Date 25.09.2012.
2. N. I. Bouraou, S. A.Tsybulnik, D. V.Shevchuk, *The investigation of model of the vibration measuring channel of the complex monitoring system of vertical steel tanks*, EEJET, **5/9** (2015) 45 – 52.
3. S. L. Marple, Jr., *Digital spectral analysis with applications,* Prentice Hall, New Jersey 1987.
4. Ljung, Lennart, *System Identification: Theory for the User*. Prentice Hall, New Jersey 1999.

Improvement of the Vibration Diagnostics of Rotation Shaft Damage Based on Fractal Analysis

Nadiia BOURAOU
National Technical University of Ukraine Kyiv Polytechnic Institute
37 Peremogy Pr., Kyiv, Ukraine, burau@pson.ntu-kpi.kiev.ua

Oleksii PAVLOVSKYI
National Technical University of Ukraine Kyiv Polytechnic Institute
37 Peremogy Pr., Kyiv, Ukraine, *a_pav@ukr.net*

Olha PAZDRII
National Technical University of Ukraine Kyiv Polytechnic Institute
37 Peremogy Pr., Kyiv, Ukraine

Abstract

This work is devoted to further research and improvement of the vibration diagnostics of the initial crack-like damage of rotation shaft in aviation gas-turbine engines (GTE). We propose to use fractal analysis of the accelerating shaft response in order to increase the damage detection efficiency. Responses of the accelerating shaft are derived by using simulation in absence and in presence of the initial traverse crack. The responses of the cracked shaft have sub-critical peaks; the increase in size of a crack leads to the increase in peak values of the vibration amplitude in the range of sub-harmonic resonances. The Hurst exponent is obtained for the time series in the range of sub-harmonic resonances. The research shows that a small change in the crack size results in considerable change of the Hurst exponent, which allows to detect the mentioned sub-harmonic resonances of the measured signal in order to identify the initial crack-like damage of the rotation shaft.

Keywords: gas-turbine engine, cracked shaft, vibration diagnosis, fractal analysis, Hurst exponent

1. Introduction

This paper is a continuation of the previous researches [1,2] dedicated to development of the multilevel vibration control system of aviation gas-turbine engines (GTE) and its practical implementation. The system mentioned above comprises the following three levels: (i) the first (main) level - for current control and awareness of the actual levels of vibration at the harmonics of the rotor rotation, (ii) the second (auxiliary) level - for diagnostics of the initial crack-like damages of the engine blades and (iii) the third (auxiliary) level - for diagnostics of the initial crack-like damage of the rotor's shaft during startup at the acceleration to operating speed. In order to diagnose the damage of the rotor's shaft, the peak values of vibration amplitude in the range of sub-harmonic resonances of accelerating cracked shaft response are used as fault features. Therefore, the narrow-band digital tracking filter was developed in order to extract the main rotor harmonic vibration at the non-steady-state mode, as presented in [2]. The peak values of vibration amplitudes are determined after filtration in the field of sub-harmonic resonances. The received values are compared with the threshold and the decision on the presence or absence of a crack in the shaft is made.

We propose to improve the diagnostics of the initial crack-like damage of the rotating shaft by using fractal analysis of the accelerating shaft response in order to increase the efficiency of the damage detection. It is very important for detection of the initial crack-like damage and especially in case of the low signal-to-noise ratio.

Fractal analysis is a promising signal processing method used for the noise-like signals [3]. The analysis of fractal and multifractal properties of time series allows obtaining simple and suitable characteristics of the investigated signals, such as the fractal dimension, Hurst exponent, and other characteristics (correlation dimension, embedding dimension), if necessary. Changes of the mentioned characteristics can be used to detect the local changes in the measured signal which are generated by the initial crack-like damage of the rotation shaft.

2. Estimation the Hurst exponent

We propose to use the Hurst exponent of the accelerating shaft response as a faul feature. The oldest and best-known method to estimate the Hurst exponent is *R*/*S* analysis [4]. Ratio *R*/*S* indicates ratio of the range *R* to the standard deviation S of the analyzed time series. The procedure of estimation of the Hurst exponent presented in [4] is as follows:

1. It is necessary to find the mean *E* and the standard deviation *S* of the analyzed time series Z_i ($i = 1, \dots, n$).
2. The data of the series Z_i has to be normalized by subtracting the sample mean

$$X_i = Z_i - E$$

3. Create the cumulative time series for $i = 1, \dots, n$:

$$Y_i = \sum_{j=1}^{i} X_j$$

4. Find the range

$$R = max(Y_1, \dots Y_n) - min(Y_1, \dots Y_n)$$

5. Calculate the mean value (*R*/*S*) of the series of length *n*.
6. Obtain the value of Hurst exponent *H*, taking into consideration that the *R*/*S* statistic asymptotically follows the relation

$$R/S \approx \tau^H ,$$

where τ is a time interval of the analyzed time series Z_i.

The value of Hurst exponent allows to recognize a persistent process ($H > 0,5$) and anti-persistent process ($H < 0,5$), for a Gaussian noise $H = 0,5$.

3. Simulation and analysis of accelerating shaft response

The equations of motion for a Jeffcott rotor with a cracked shaft in presence of the gravity forces and unbalance excitation, and subject to constant acceleration, were presented and investigated in [5]. The following from among the equations of motion mentioned above are used for simulating of the accelerating shaft response:

- in inertial coordinate system (*xyz*):

$$\begin{pmatrix} M & 0 \\ 0 & M \end{pmatrix}\begin{Bmatrix} \ddot{z} \\ \ddot{y} \end{Bmatrix}+\begin{pmatrix} F & 0 \\ 0 & F \end{pmatrix}\begin{Bmatrix} \dot{z} \\ \dot{y} \end{Bmatrix}+\begin{pmatrix} K_{11} & K_{12} \\ K_{21} & K_{21} \end{pmatrix}\begin{Bmatrix} z \\ y \end{Bmatrix}=\begin{Bmatrix} Mg \\ 0 \end{Bmatrix}+M\varepsilon\begin{Bmatrix} \dot{\theta}^2 \cos\theta+\ddot{\theta}\sin\theta \\ \dot{\theta}^2 \sin\theta-\ddot{\theta}\cos\theta \end{Bmatrix}, \tag{1}$$

where **M** is the mass matrix; **F** is the damping matrix; **K** is the stiffness matrix; z and y are the displacements; θ is the angle of orientation of unbalance mass ε relative to the axes z;

- in body-fixed rotating coordinate frame ($\xi\eta\varsigma$):

$$\begin{pmatrix} M & 0 \\ 0 & M \end{pmatrix}\begin{Bmatrix} \ddot{\xi} \\ \ddot{\eta} \end{Bmatrix}+\begin{pmatrix} F & -2M\omega(t) \\ 2M\omega(t) & F \end{pmatrix}\begin{Bmatrix} \dot{\xi} \\ \dot{\eta} \end{Bmatrix}+\begin{pmatrix} K-f(\psi)\Delta K_{\xi}-M\omega^2(t) & -F\omega(t) \\ F\omega(t) & K-M\omega^2(t) \end{pmatrix}\begin{Bmatrix} \xi \\ \eta \end{Bmatrix}=$$

$$=Mg\begin{Bmatrix} \cos\Phi \\ -\sin\Phi \end{Bmatrix}+M\varepsilon\omega^2(t)\begin{Bmatrix} \cos\beta \\ \sin\beta \end{Bmatrix}+M\varepsilon a\begin{Bmatrix} \sin\beta \\ -\cos\beta \end{Bmatrix}, \tag{2}$$

where $\omega(t)$ is the instantaneous speed of rotation; a is the constant acceleration of rotation; Φ is the angle of position of the rotating coordinate frame ($\xi\eta\varsigma$) relative to the inertial coordinate frame (*xyz*); β is the angle of orientation of unbalance mass ε with respect to crack; ΔK_{ξ} is the shaft rigidity decrease at the crack presence; $f(\psi)$ is the function for crack accounting to the shaft stiffness according to the crack angular position ψ.

The transformation between the inertial and rotating coordinate frames is carried out according to the following dependence:

$$\begin{pmatrix} z \\ y \end{pmatrix}=\begin{pmatrix} \cos\Phi & -\sin\Phi \\ \sin\Phi & \cos\Phi \end{pmatrix}\begin{pmatrix} \xi \\ \eta \end{pmatrix}. \tag{3}$$

The model of the transverse crack is a function of "breathing", the relative rigidity changing of the shaft $\Delta K = \Delta K_{\xi}/K$ depends on the cross location of crack section and stress-strain area of the shaft.

The computer simulation of the accelerating shaft response in absence ($\Delta K = 0$) and in presence of a small crack ($\Delta K = 0{,}005,...,0{,}1$) is carried out by using the transformed equations (2) to non-dimensional form and dependence (3). The time plots of non-steady-state vibration of the rotating shaft are shown in Figure 1 for the following data: $\Delta K = (0; 0{,}01; 0{,}05; 0{,}1)$ and $\psi = \beta = 0^0$. These plots are represented in the relative scale on the ordinate axis (non-dimensional vibration amplitude z) and on the abscissa (non-dimensional time τ). Value $\tau = 1000$ corresponds to transition through critical frequency of rotation. It can be seen that the initial transverse crack results in presence of 1/2 order sub-critical peak, and the increase of the crack parameter ΔK leads to the increase in sub-critical peak values of vibration amplitude.

Simulated signals were processed using the above presented procedure of estimation of the Hurst exponent. We used two separate parts of each signal for the analysis: a) a sample of 500 values of non-dimensional vibration amplitude z in the range of sub-harmonic resonances and b) a sample of 500 values of non-dimensional vibration amplitude z in the range of main resonance. Figure 2 represents the dependence of obtained values of Hurst exponent H on the relative rigidity changing ΔK of the shaft for the mentioned samples.

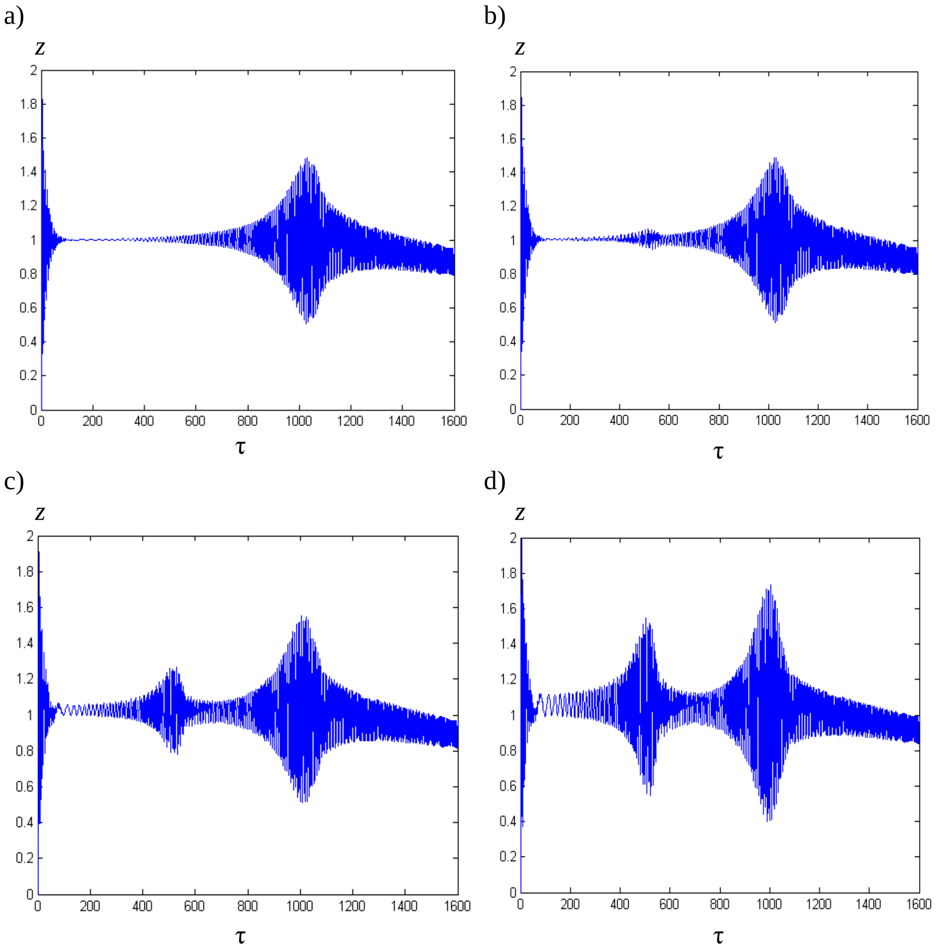

Figure 1. Non-dimensional vibration amplitude of accelerated rotor at the ΔK = 0 (a), ΔK = 0,01 (b), ΔK = 0,05 (c) and ΔK = 0,1 (d)

In general, the Hurst exponent is decreasing at the increasing of a crack parameter ΔK for both analyzed parts of simulated signal. It can be seen in Figure 2b that the initial transverse crack results in small changing of Hurst exponent of signal in the range of main resonance (decreasing is about 19%). In the range of sub-harmonic resonances (Fig. 2a) the value of Hurst exponent is decreasing to a considerable extent, this decreasing is more than 3 times at the interval of relative rigidity changing ΔK = 0,005, …, 0,1. In the case of ΔK < 0,005, the Hurst exponent dependence on ΔK is not informative for crack detection.

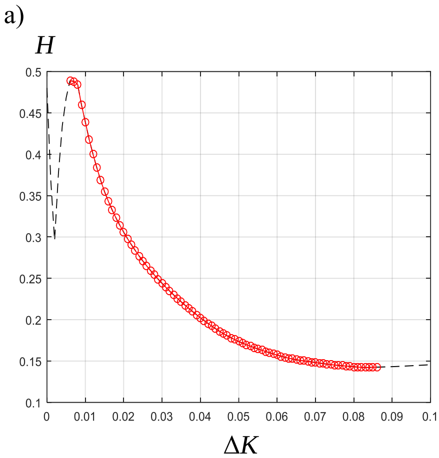

Figure 2. The Hurst exponent dependencies on relative rigidity changing ΔK in the range of sub-harmonic resonances (a) and in the range main resonance (b)

Another simulation and fractal analysis of signals are carried out taking into account of additive Gaussian noise. The value of noise standard deviation is selected 10^{-2}, in this case the value of signal to noise ratio (SNR) is different for each simulated signal. The noisy vibration amplitudes z_n in the range of sub-harmonic resonances for $\Delta K = 0$ and $\Delta K = 0{,}05$ are illustrated in Fig. 3.

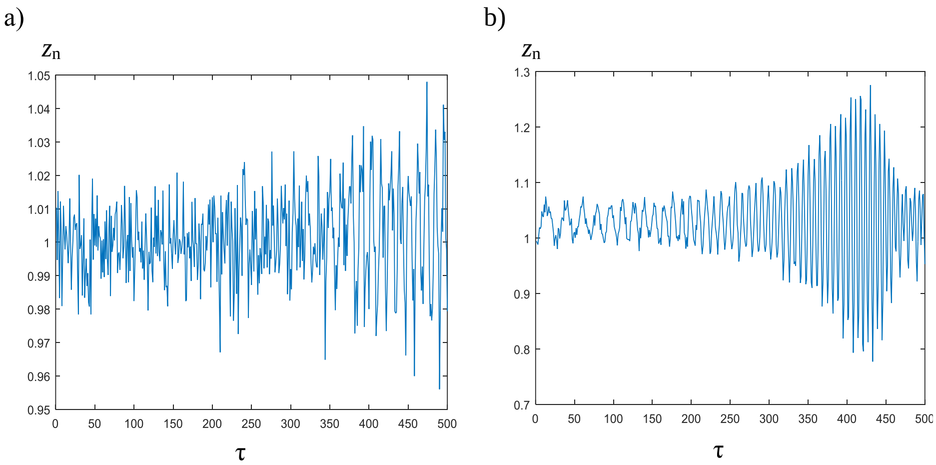

Figure 3. Non-dimensional noisy vibration amplitude in the range of sub-harmonic resonances at the $\Delta K = 0$ (a) and $\Delta K = 0{,}05$ (b)

Fig. 4 shows dependence of values of Hurst exponent H on the relative rigidity changing ΔK, which are obtained for the noisy vibration amplitudes z_n in the range of sub-harmonic resonances. The presented result show, that values of Hurst exponent is decreasing at the increasing crack parameter ΔK. The form of depengence is simiral to the graph represented in Figure 2a, the changing of Hurst exponent is more than 3 times in the presented interval of ΔK. Taking into account of additive Gaussian noise eliminates method error of Hurst exponent estimation at the $\Delta K < 0,005$.

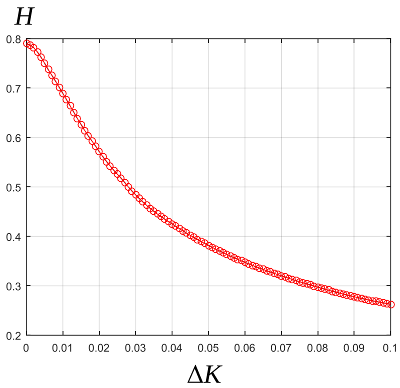

Figure 4. The Hurst exponent dependence on ΔK for the noisy vibration amplitudes in the range of sub-harmonic resonances

4. Conclusions

Research presented in this paper shows that a small change in the relative rigidity changing of shaft in presence of the initial crack-like damage results in considerable change of the Hurst exponent. This fact allows to detect the small sub-harmonic resonances of the noisy measured signal and to identify the initial crack-like damage of the rotation shaft. The usage of proposed approach to improvement of diagnostics of the crack-like damage will promote to ensure awareness of GTE.

References

1. O. Pavlovskyi, N. Bouraou, L. Iatsko, *Multilevel vibration control system of aviation gas-turbine engines*, Vibrations in Physical Systems, **25** (2012) 323 – 328.
2. O. Pavlovskyi, N. Bouraou, *On-board vibration diagnostics of shaft damage of the aviation engine*, Vibrations in Physical Systems, **26** (2014) 229 – 234.
3. J. Feder, *Fractals*, Plenum Press, New York, 1988.
4. M. A. Sanchez Granero, J. E. Trinidad Segovia, J. Garcia Perez, *Some comments on Hurst exponent and the long memory processes on capital markets*, Physica A, **387** (2008) 5543 – 5551.
5. J. Sawicki, X. Wu, G. Baaklini, A. Gyekenyesi, *Vibration-based crack diagnosis in rotating shafts during acceleration through resonance*, Proc. of SPIE, **5046** (2003) 1 – 10.

Computer Modelling of Roadheader's Body Vibration Generated by the Working Process

Piotr CHELUSZKA
Institute of Mining Mechanisation, Faculty of Mining and Geology
Silesian University of Technology, Akademicka 2, 44–100 Gliwice
piotr.cheluszka@polsl.pl

Jacek GAWLIK
Institute of Mining Mechanisation, Faculty of Mining and Geology
Silesian University of Technology, Akademicka 2, 44–100 Gliwice
jacek.gawlik@polsl.pl

Abstract

Boom–type roadheaders represent heavy working machines used in underground mines for the drilling of dog headings, for tunnelling and – to a certain extent – for surface mining. The key working process carried out by such roadheaders is rock mining. This process, especially when cutting rocks with low workability, causes strong vibration excitations and dynamic loads not only in a roadheader cutting system, but within its entire construction. The article presents a dynamic model of a boom–type roadheader body. Four vibrating masses, representing the key subassemblies of the studied object and a seat together with a roadheader operator, are distinguished in a spatial physical model with a discrete structure. They are subject to the activity of an excitation from the loads generated in the cutting process. A mathematical model is comprised of 19 non-linear ordinary differential quotations of the second order. The model was implemented in the MATLAB/Simulink environment, in which a simulation model was created. The article presents the examples of results of numerical simulations using the established model.

Keywords: roadheader, dynamic model, dynamic loads, vibrations

1. Introduction

Roadheaders are working machines used in mechanised technologies for drilling dog headings and chamber headings in underground mines and tunnels in civil engineering. Roadheaders are multi–functional machines designed for the mechanisation of the basic activities connected with the drilling of mine headings, namely tunnels. The activities encompass, in particular, rock cutting, loading the mined rock into the means of transport, transporting the mined rock from the heading face, as well as mechanised erection of a dog heading support. For this reason, such machines are subject to the activity of vibration excitations originating from different sources, with their varied intensity. As the key process carried out by such type of machine is the mechanical cutting of rock, the vibrations they are susceptible to and the dynamic loads of their construction are basically caused by interactions taking place in the machine–mined rock configuration. Such an activity is not limited here only to a drive of the working units directly performing the cutting process, but is transmitted by such working units' load-carrying structure onto the roadheaders' other subassemblies. The vibrations excited by and the dynamic loads generated by the cutting process of rocks with especially low workability, are having the greatest effect on the durability and reliability of not only the roadheader cutting system, but also its other subassemblies and systems.

The dynamic state of the group of heavy working machines discussed is analysed here not only to draw conclusions concerning the improvement of their construction. The investigations of roadheaders' dynamics are of high significance also for ensuring the operational safety and ergonomics of such type of mining machines. Such investigations include, notably, those aimed at identifying the magnitude and character of the excited vibrations transferred onto an operator's station for evaluating the impact of mechanical vibrations on a human organism and an operator's vibration isolation [1,7], or examining the stability of the discussed machines. A roadheader may lose its stability as a result of the vibrations generated in a working process, and a serious hazard may be posed for people working in the confined space of dog headings or tunnels (this concern also applies to numerous mobile machinery, for instance cranes [4]). The vibrations excited by roadheader operation, transferred through a substrate (the floor plane of a heading being driven) to the environment may also be a source of paraseismic vibrations (tremors) [5]. Such vibrations are propagated in rock mass, in the surrounding of a place where mining works are carried out. Such vibrations may affect the environment adversely.

This article touches upon the issue of modelling of vibrations and dynamic loads of boom–type roadheaders. Such machines are a sub–group of mining roadheaders, used for excavation of dog headings, equipped with working units in the form of cutting heads with small dimensions, in relation to the cross section area of the headings excavated with them. The heads are mounted at the end of a boom which is inclined in two mutually perpendicular planes. Cuttings heads can be moved this way along the heading face surface along any track. Rock mining is carried out in this case by way of cutting – by means of picks mounted on a cutting head, where the rotary motion of a cutting head is caused by a drive system.

The research works pursued until now have been related to the dynamics of selected subassemblies of a roadheader or its components – mainly the cutting system: cutting heads, their drive and a load–carrying structure (e.g. [2,3,6,9]). The reasons given above allow to conclude, however, that the entire object should be treated as a whole – as a complex dynamic system, taking into account the dynamic impact onto its substrate. The article presents a dynamic model of a boom–type roadheader body. For the purpose of numerical investigations of the roadheader's dynamics, the mathematical model created was implemented in the MATLAB/Simulink environment, in which a simulation model was created. The article presents the examples of computer simulations accompanying the execution of a working process of cutting the heading face surface of the dog heading being drilled.

2. Physical model

The construction of a boom–type roadheader body supports the creation of discrete physical models. Four rigid bodies connected with each other with weightless viscoelastic elements are distinguished in a physical model of the studied object (Fig.1).

The bodies represent the key parts of a roadheader boom, i.e.: roadheader casing (1), movable part of the turntable (2) and a boom with cutting heads (3), and a seat together with an operator seating on it (4). A movable part of the turntable with a vertical axis of rotation is fitted rotationally to the roadheader casing (body). In case of the considered roadheader construction, the movable part of the turntable is provided with a bearing relative to the fixed part (of the roadheader casing) by means of two bearings – a axial and radial bearing. The rotary motion of a movable part of the turntable is carried out here with an actuating–rack–and–pinion mechanism. The activity of such a mechanism is modelled in the form of the concentrated force $P_{SO} = f\left(\dot{\varphi}_{OZ}\right)$ applied to point 13. The direction in which the force is acting is parallel to the axis X_O of the system of coordinates $X_OY_OZ_O$. A roadheader boom is mounted to the movable part of the turntable by means of two slide bearings and is supported with two hydraulic lifting actuators – a right one (SPP) and left one (SPL).

The roadheader components mentioned above are considered as rigid bodies with the mass of, respectively, m_K, m_O, m_W and m_{FO}, concentrated in their centres of gravity (in the points: S_{CK}, S_{CO}, S_{CW} and S_{CFO}) and with the moments of inertia of, respectively: I_{KX}, I_{KY} and I_{KZ}, (roadheader casing) I_{OX}, I_{OY} and I_{OZ} (movable part of the turntable) and I_{WX}, I_{WY} and I_{WZ} (boom). The values of moments of inertia of the turntable and boom were determined in relation to the axis of the system of coordinates $X_OY_OZ_O$.

The activity of the roadheader casing on the substrate was modelled as six viscoelastic constraints with the specific rigidity k_i and the damping coefficient c_i (for i=1,…,4) applied in the points marked with numbers from 1 to 4. Four of them (nominated with index Z) are transmitting loads perpendicular to the substrate. Two of them (nominated with index X and Y) – are transmitting loads in the plane parallel to the substrate, in the direction of the axis X_K and Y_K of the system of coordinates $X_KY_KZ_K$ connected with the roadheader body.

The susceptible mounting of the movable part of the turntable in relation to its fixed part was modelled as six viscoelastic constraints applied in the points numbered 5 to 10. They represent the considered way of its bearing. Out of six viscoelastic elements, fours are situated in the vertical direction and arranged at the pitch diameter of the axial slide bearing raceway (located in the upper part of the turntable). The activity of a radial bearing situated in the lower part of the turntable is modelled by means of other two constraints (situated horizontally, perpendicular to each other). The bearing of the boom on the turntable is presented as five viscoelastic elements applied in points 11 and 12. The constraints are representing reactions acting in the place where a boom is fitted to a turntable in slide bearings. As already mentioned, the boom is supported with two hydraulic actuators. The actuators' dynamics is shown as indicated in the work [8]. The mounting of the operator's seat to the roadheader casing is modelled by means of a single viscoelastic element with the rigidity k_{FO} and the damping factor c_{FO}. It was assumed that the seat–operator system has only a single degree of freedom (this results from the mounting construction).

The physical spatial model created has nineteen degrees of freedom. The temporary location of a roadheader casing modelling solid is described with the six coordinates:

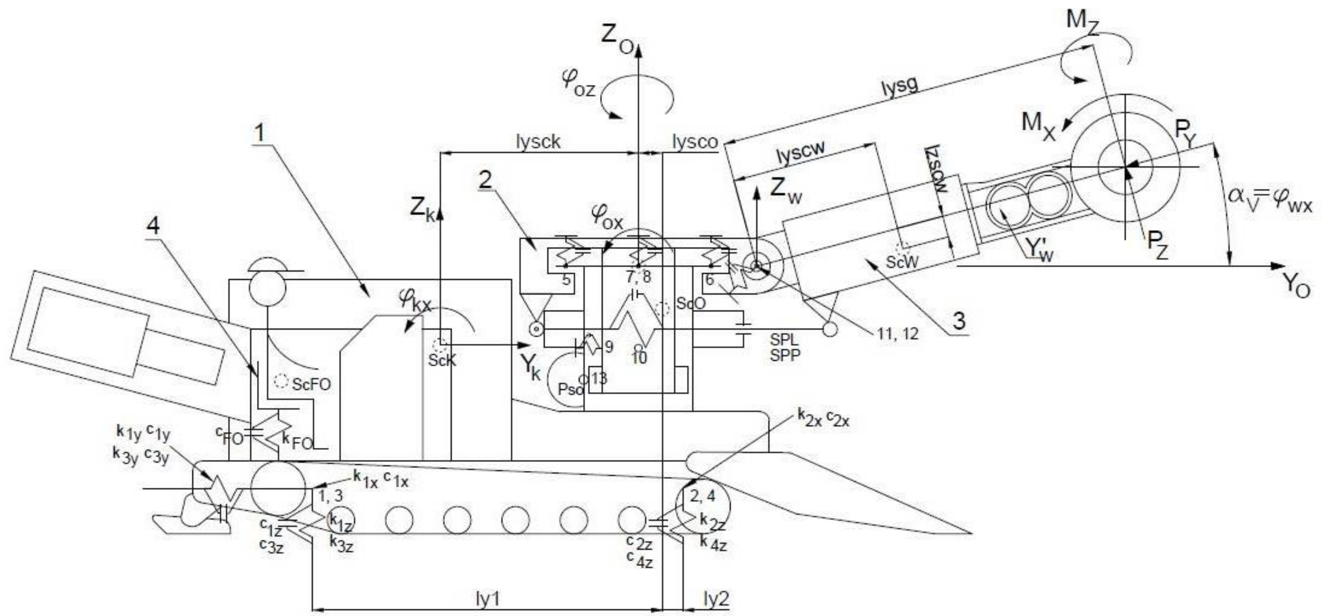

Figure 1. Physical model of roadheader body (view of the YZ plane): 1 – roadheader casing, 2 – movable part of the turntable, 3 – boom with cutting heads, 4 – seat together with roadheader operator

three translation coordinates – x_K, y_K and z_K, and three rotation coordinates – φ_{KX}, φ_{KY}, and φ_{KZ} (six degrees of freedom). The following designations for coordinates were used for the movable part of the turntable: x_O, y_O, z_O (for translation movement) and φ_{OX}, φ_{OY}, φ_{OZ} (for rotational movement). The following translation coordinates are describing the situation of the boom: x_W, y_W, z_W and the rotation coordinates: φ_{WX}, φ_{WY}, φ_{WZ}. The vibrating motion of the seat together with the operator is described by the translation coordinate z_{FO} measured in the direction of the axis Z_K of the system of coordinates connected with the roadheader body.

Vibration excitations are acting on the masses distinguished in the physical model in the form of an external load, which are the result of carrying out the working process (cutting the heading face of the drilled dog heading). This load was reduced to the intersection point of the boom longitudinal axis with an axis of rotation of the cutting heads and was described with six components – three concentrated forces (P_X, P_Y and P_Z) and three moments of forces (M_X, M_Y and M_Z). The time curves of this excitation are generated in a separate computer programme for the set values of parameters for the execution of this cutting process.

3. Mathematical model

The motion equations in the developed physical model were entered using the Lagrange second degree equation:

$$\frac{d}{dt}\left(\frac{\partial E_K}{\partial \dot{q}_j}\right)+\frac{\partial E_P}{\partial q_j}=Q_j-R_j \qquad \text{, for } j=1,2,\ldots,19 \tag{1}$$

where: E_K – kinetic energy of the system; E_P – potential energy of the system; Q_j – the external generalised force corresponding to the coordinate q_j; R_j – the generalised resistance force corresponding to the coordinate q_j; q_j and $\dot{q}_j$ – the generalised (translation or rotation) coordinate and its first derivative

A mathematical model describing motion in the established physical model of the studied object consists of a system of 19 ordinary nonlinear second–order differential equations, which have the following form in the matrix–vector form:

$$\mathbf{M}\cdot\ddot{\mathbf{q}}+\mathbf{C}\cdot\dot{\mathbf{q}}+\mathbf{K}\cdot\mathbf{q}=\mathbf{Q} \tag{2}$$

where: **M**, **C**, **K** – mean, respectively, the matrix of: inertia, damping and rigidity; **Q** – vector of external forces; whereas $\mathbf{q},\dot{\mathbf{q}},\ddot{\mathbf{q}}$ – vectors of generalised coordinates and their subsequent derivatives. The vector of generalised coordinates **q** has the following form here:

$$\mathbf{q}=\left[x_K, y_K, z_K, \varphi_{KX}, \varphi_{KY}, \varphi_{KZ}, x_O, y_O, z_O, \varphi_{OX}, \varphi_{OY}, \varphi_{OZ}, x_W, y_W, z_W, \varphi_{WX}, \varphi_{WY}, \varphi_{WZ}, z_{FO}\right]^T \tag{3}$$

The motion equations were entered into MATLAB/Simulink software after executing relevant conversions. Three layers can be distinguished in a hierarchy structure of the so obtained simulation model. Functionally interrelated sub-systems are situated in the master layer (Fig.2), which are representing the vibrating elements distinguished in a physical model (roadheader casing, turntable, boom and seat with an operator), a block responsible for recording calculations results (to workspace) and blocks responsible for calculating, in successive steps, numerical integration of motion equations of temporary values of dynamic parameters of actuators lifting the boom (Lsp, P_SP) and the force developed by a boom rotation mechanism actuator (Pso). The second layer of the simulation model consists of blocks in which motion equations are implemented for each of vibrating masses (Fig.3). Motion equations are integrated numerically in the lowest (third) layer by means of appropriate function blocks (integrators) (Fig.4). The values of coordinates of each of the masses are established in successive integration steps as a result of solving a motion equation iteratively. Motion equations are integrated numerically by means of a fourth order Runge–Kutta algorithm with a constant integration step.

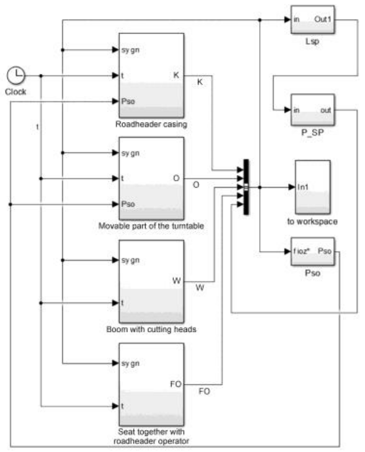

Figure 2. Master layer of simulation model in MATLAB/Simulink environment

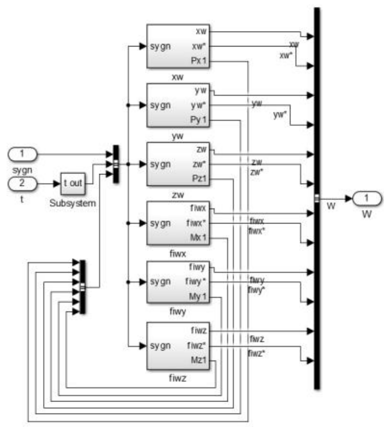

Figure 3. Second layer of simulation model

4. The examples of simulation results

Figures 5 and 6 show the selected results of computer simulations of roadheader body dynamics using the developed simulation model. The motion of the boom together with a movable part of the turntable was started in the right direction in the considered time interval, after the lapse of 0.5 s of the simulation. The cutting heads performed 3 revolutions over the next 2.5 s of the simulation. During this motion, the roadheader body was loaded with forces exciting vibrations generated by a cutting process. The cutting of the rock with the compressive strength of R_C=80 MPa with the web of z=0.13 m was simulated here. As seen, the working process carried out by the roadheader is a source of strong vibrations of its components, in particular – a boom. The angular speed of boom deflection was established at the average level of 0.033 rad/s, whereas the amplitude of such speed vibrations (understood as the variability range) was 0.05 rad/s. During this time interval the boom turned about the axis of rotation of the turntable through an angle of ~5 deg.

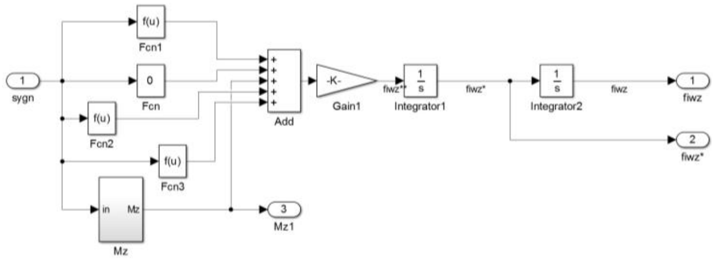

Figure 4. Structure of the lowest (third) layer of simulation model with the example of equation describing the rotation motion of the boom along the axis Z

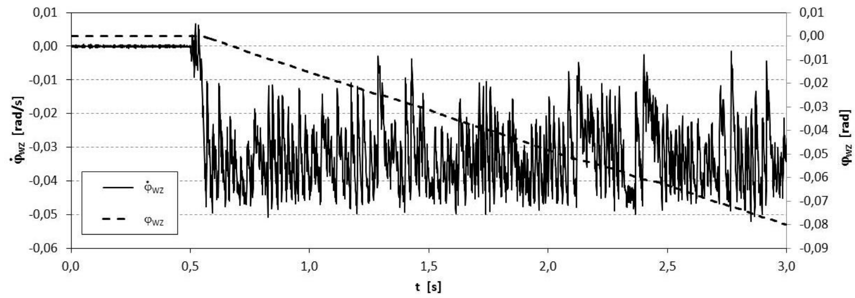

Figure 5. Boom angular speed and its angular displacement curve relative to the axis Z

Due to the dynamic properties of the studied object resulting from its construction (especially with the use of hydraulic actuators), the boom subjected to the activity of a variable external load is performing intensive lateral vibrations (Fig.6). This is important considering the dynamic state of the studied machine as well as the working process it performs. The roadheader body's vibrations result in periodical changes in parameters for which this process is performed. Changes in cutting conditions have, on the other hand, influence of the character and magnitude of excitation of vibrations of the roadheader body. This is because strong feedback exists in the system of the roadheader and the working process carried out by it.

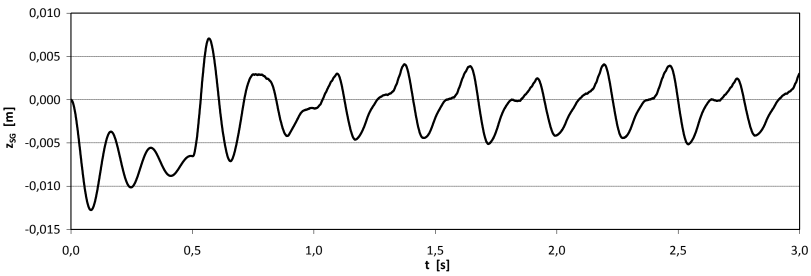

Figure 6. Curve of the coordinate of the boom axis intersection point with the axis of rotation of cutting heads in the direction of the axis Z

5. Conclusions

The dynamic model created allows to perform simulation investigations in order to determine dynamic loads in the selected constructional nodes of a boom–type roadheader body and to analyse its vibrations generated in a working process. Experimental verification is necessary, however, to be able to use it practically for research purposes. The conformity of the results obtained by way of a computer simulation with the actual dynamic characteristics of the modelled object will be established based on the outcomes of experimental investigations. Dynamic characteristics will be measured with an experimental station developed for this aim by the Institute of Mining Mechanisation, Faculty of Mining and Geology, Silesian University of Technology. The R–130 roadheader (manufactured by FAMUR S.A.) will be the object of investigations. Vibrations will be excited in the body of the machine as a result of the cutting process of a block made of equivalent materials.

Acknowledgments

The work has been implemented under the research project titled “Control of roadheader cutting heads movement for reduction of energy consumption of mining and dynamic loads“ co–financed by the National Centre for Research and Development under the Applied Research Projects (agreement no. PBS3/B2/15/2015).

References

1. M. W. Dobry, T. Hermann, *A comparison of human physical models used in the ISO 10068:2012 standard based on power distribution – PART 2,* Vibrations in Physical Systems, **26** (2014) 57 – 64.
2. M. Dolipski, P. Cheluszka, *Dynamika układu urabiania kombajnu chodnikowego*, Wydawnictwo Politechniki Śląskiej, Gliwice 2002.
3. M. Dolipski, P. Cheluszka, P. Sobota, *Numerical tests of roadheader's boom vibrations*, Vibrations in Physical Systems, **26** (2014) 65 – 72.
4. J. Janusz, J. Kłosiński, *Wpływ wybranych strategii sterowania ruchami roboczymi żurawia samojezdnego na jego stateczność*, Acta Mechanica et Automatica, **4**(2) (2010) 74 – 80.
5. J. Kogut, *Analiza spektrum odpowiedzi drgań drogowych*, Praca doktorska, Politechnika Krakowska, Kraków 1999.
6. X. Li, B. Huang, C. Li, S. Jiang, *Dynamics analysis on roadheader cutting head based on LS–DYNA,* Journal of Convergence Information Technology, **7**(23) (2012) 333 – 340.
7. I. Maciejewski, *Active control of working machines seat suspension aimed at health protection against vibration*, Proc. Appl. Math. Mech., **7** (2007) 4130017 – 4130018, doi: 10.1002/pamm.200700345.
8. B. Podsiadła (red.), *Modelowanie i badania zjawisk dynamicznych wysięgników teleskopowych i żurawi samojezdnych*, WNT, Warszawa 2000.
9. X. H. Wei, M. Xie, *Dynamic analysis on the longitudinal roadheader's cutting system*, Advanced Materials Research, **619** (2013) 160 – 163.

Influence of Torsional-Bending Coupling on Transverse Vibration of Piston Engine

Zbigniew DĄBROWSKI
Institute of Machinery Design Fundamentals
Faculty of Automotive and Construction Machinery Design
Warsaw University of Technology
ul. Narbutta 84, Warsaw, zdabrow@simr.pw.edu.pl

Bogumił CHILIŃSKI
Institute of Machinery Design Fundamentals
Faculty of Automotive and Construction Machinery Design
Warsaw University of Technology
ul. Narbutta 84, Warsaw, bogumil.chilinski@gmail.com

Abstract

The article presents the analysis of the influence of bending-torsional coupling of vibrations in the crankshaft on transverse vibrations of the engine body. In practice, there is used a simplified model, wherein transverse and torsional oscillations are analyzed independently. With the use of the model of deformable crankshaft, the authors show the influence of bending-torsional coupling on the frequency structure of transverse vibrations. The introduction presents the problem of vibrations in combustion engines and their modelling. Further, there is presented the elastic model of the crankshaft, together with the applied assumptions and equations of motion describing vibrations in one cylinder combustion engine . Next chapter shows numerical simulation results with their initial analysis. The whole paper is summarized with conclusions about calculations and the possibility to use the results in practice.

Keywords: Bending-torsional vibrations of the crankshaft, modeling of crank system, analytical solutions, numerical simulations.

1. Introduction

Dynamics of crank system is a very important technical problem. Basic parameters of the engine and its work are directly related to this system. In the case of motion with a constant velocity of the crankshaft, it is easy to determine the forces and displacements which appear in the crankshaft. The dynamics of crank system in unsteady motion requires many studies [1-4].

Due to the complex geometry of the rotor and "complicated" construction of the crank mechanism there exists a coupling between vibrations occurring in the engine [5-8]. In practice this phenomenon considerably hinders the analysis, due to the coupling of individual degrees of freedom. Therefore, in order to make calculations there is used the most commonly applied simplification based on rejecting any dependencies connecting bending and torsional vibrations in engines. Such an approach is used in preliminary design calculations. However, in the case of problems connected with an operation it may be insufficient [9-13]. Moreover, in practice, measured vibrations are different from theoretical model results.

This issue is important because there may appear new critical areas due to the coupling of bending-torsional vibrations. What is more, torsional vibrations affect significantly transverse displacements. This motion influences the vibrations of the whole body. In practice there appear a shift and modulations of particular frequencies of eigen vibrations of uncoupled system. This shows the presence of nonlinear or parametric effects in the considered object [14-16].

The authors propose to apply this phenomenon to analyze torsional vibrations of the engine based on the spectra of transverse displacements of the body. This problem is important because the measurement of angular vibrations of the crankshaft of a combustion engine is more difficult than the measurements of transverse vibrations.

2. The dynamic model of piston engine with an elastic crankshaft

Due to the complex geometric and material structure it is convenient to replace the continuous mass system, which is the crankshaft, with a discrete model. In such cases, the masses are usually reduced to selected constructional nodes, whereas the remaining part of the object is treated as a massless deformable structure.

Of course, the model of the system of point masses is a significant simplification of the continuous system, which is characterized by infinite (but countable)set of eigen values. The number of eigen frequencies in the case of discrete systems is the finite number . Therefore, it is not possible to replace "fully" the continuous system with a model of point masses. However, it is possible to make an equivalent reduction in a selected frequency band, for example, in the range of low frequencies. In practice, such a simplification does not lead to serious errors. At the same time, it must be emphasized that this method significantly simplifies the calculations.

Single crank of the crankshaft of the piston engine is presented schematically in Figure 1.

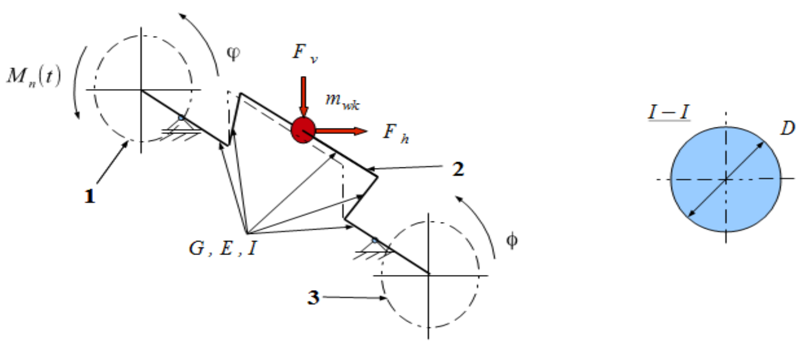

Figure 1. The model of the crankshaft of one piston. 1 - 2 flywheel - crankshaft, 3 - pulley

In constructions of real combustion engines, very rigid crankshafts are used. Basically due to the precision required from crank mechanisms. Even small changes in the angular position of the crank may affect the process of combustion in a given system, which directly influences its dynamics. In addition, in vibrating systems there is a risk of resonance with a basic harmonic of extortion which comes from gas forces [17-19]. In this case, oversizing of the crankshaft allows to move the frequency of eigen vibrations into the area of higher components of drive moment.

Due to high rigidity of crank system, it can be assumed that with a good approximation, deformations occurring in the crank systems are very small. This allows to use the model of linear-elastic system for calculations [20,21]. Figure 2 shows the displacement of the crank described in the moving coordinate system.

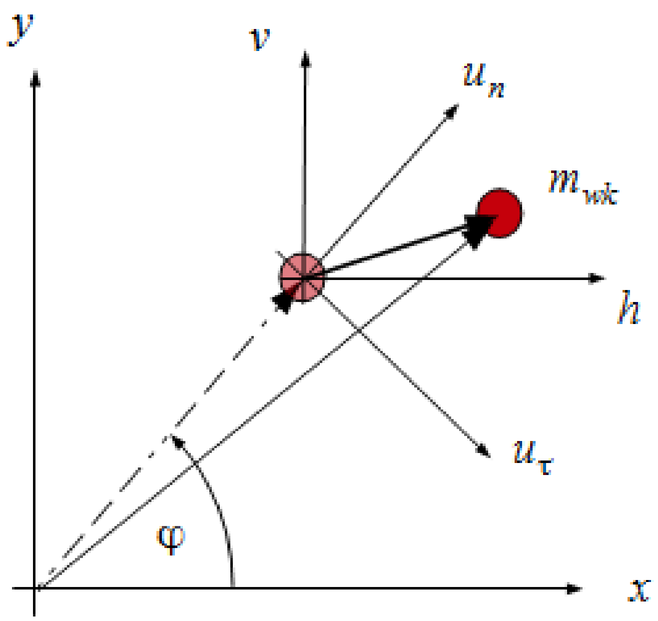

Figure 2. Displacement of crank of the crankshaft

In Figures 1 and 2 there are used the following generalized coordinates describing the dynamics of the analyzed model of the crank:

ϕ – rotation angle of the flywheel of the engine,
φ –rotation angle of the disc of torsional vibration damper,
h – horizontal deformation of the crank,
v – vertical deformation of the crank.

Generalized forces in selected constructional bands may be determined on the basis of the equations:

$$F = K \cdot u \tag{1}$$

where:

K – stiffness matrix,
F – generalized force vector,
u – displacement generalized vector.

Due to the symmetry conditions and the load system, the stiffness matrix has a simplified form:

$$K = \begin{bmatrix} k_{nn} & 0 & 0 \\ 0 & k_{\tau\tau} & -k_{\tau\theta} \\ 0 & -k_{\tau\theta} & k_{\theta\theta} \end{bmatrix} \tag{2}$$

It is possible to find motion equations for the system presented in Figure 1with the use of any formalism of analytical mechanics. Due to the linearity of the model and holonomic constraints appearing in the system, there are used Lagrange equations of second kind. On this basis, the following dynamic model is determined:

$$(I_{kl} + m_{wk}R^2)\ddot{\phi} + m_w R\ddot{u}_\tau + k_{\tau\theta}u_\tau + k_{\theta\theta}(\phi - \varphi) = M_0 \tag{3}$$

$$m_w\ddot{u}_\varphi + m_w R\ddot{\phi} + k_{\tau\tau}u_\tau - k_{\tau\theta}(\varphi - \phi) = P_\tau \tag{4}$$

$$I_{kP}\ddot{\varphi} + \left[-k_{\theta\tau}u_\tau + k_{\theta\theta}(\varphi - \phi)\right] = 0 \tag{5}$$

$$m_w\ddot{u}_r - m_w R\ddot{\phi}^2 + k_{rr}u_r = P_r \tag{6}$$

3. Simulation analysis of transverse vibrations of the crankshaft

The series of numerical simulations was carried out for a proposed system of equations. Transverse vibrations of the crankshaft without the coupling of bending and torsional vibrations presented in plot 3 are taken as a point of reference.

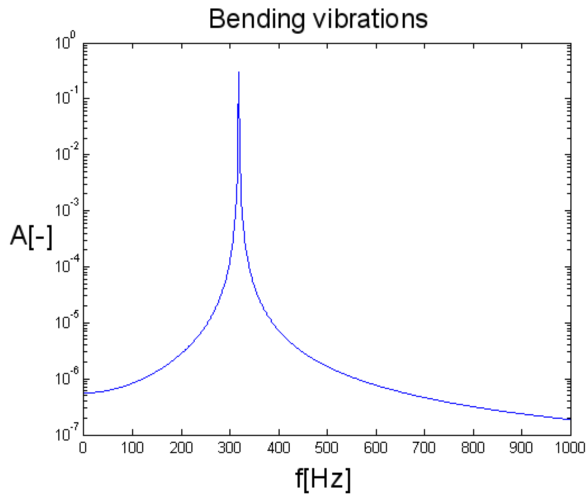

Figure 3. Bending vibrations of the crankshaft of the system without coupling

In the case when the coupling is taken into account, the spectral structure of transverse vibrations is much more complex. The spectrum of displacement of transverse vibrations in a moving coordinate system is shown in plot 4. It is possible to observe additional frequencies connected with torsional vibrations.

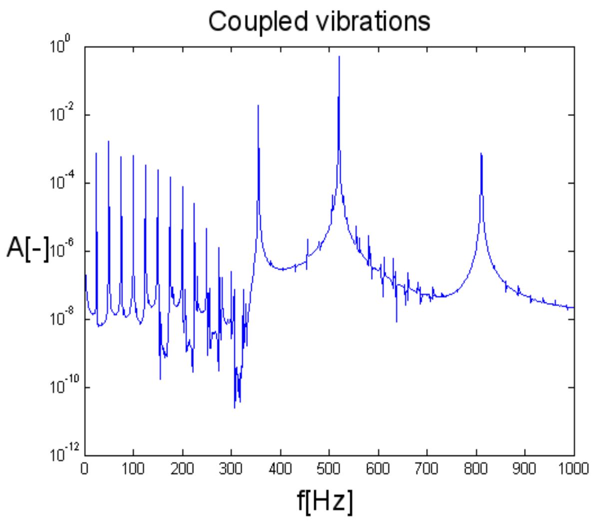

Figure 4. Bending vibrations of the crankshaft system with a coupling

4. Conclusion

The phenomenon of coupling of bending and torsional vibrations in vibrating systems is usually omitted in model calculations. Such calculations are justified at the design stage, when it is necessary to pre-define the basic dimensions of the system for further designing process. However, the dynamics of motion of the real crankshaft system is much more complex. As a result, the authors proposed a model which takes into account more phenomena and allows for more detailed analysis of vibrations occurring in combustion engines.

The proposed system of dynamics equations in moving coordinate system is possible to be solved analytically. Part of the equations is uncoupled and linear.

The simulations clearly show the impact of taking into account the coupling on transverse displacements of the crankshaft. The frequencies of torsional vibrations are transferred to bending oscillations. This allows to draw conclusions about the frequencies occurring in the spectral structure of angular vibrations only on the basis of the measurements of body vibration [22-24]. The proposed model can be used successfully in the diagnostics of combustion engines [25-27].

References

1. A. Grzędziela, *Modeling of propeller shaft dynamics at pulse load*, Polish Maritime Researches, **15**(4) (2008) 52 – 58.
2. R. Burdzik, Ł. Konieczny, Z. Stanik, P. Folęga, A. Smalcerz, A. Lisiecki, *Analysis of impact of chosen parameters on the wear of camshaft*, Archives of Metallurgy And Materials, **59**(3) (2014) 957 – 963.
3. Z. Dąbrowski, J. Dziurdź, C*omparative analysis of torsional vibrations of the crankshaft and transverse vibrations of motor body*, Logistyka, **6** (2014) 2965 – 2972 (in Polish).
4. Z. Dąbrowski, *Machine shafts*, PWN, Warsaw, 1999 (in Polish).
5. B. Chiliński, *Analysis of disturbance torque influence on critical state in rotational systems*, Transportation Problems, **8**(4) (2013) 137 – 146.
6. M. Desbazeille, R. B. Randall, F. Guillet, M. El. Badaoui, C. Hoisnard, *Model-based diagnosis of large diesel engines based on angular speed variations of the crankshaft*, Mechanical Systems and Signal Processing, **24** (2010) 1529 – 1541.
7. P. Charles, J. K. Sinha, F. Gu, L. Lidstone, A. D. Ball, *Detecting the crankshaft torsional vibration of diesel engines for combustion related diagnosis*, Journal of Sound and Vibration, **321** (2009) 1171 – 1185.
8. Z. Dabrowski, M. Zawisza, *Investigations of the vibroacoustic signals mechanical defects sensitivity is not recognized by the OBD system in diesel engines*, Solid State Phenomena, **180** (2012) 194 – 199.
9. R. Burdzik, *Research on the influence of engine rotational speed to the vibration penetration into the driver via feet – Multidimensional Analysis*, Journal of Vibroengineering, **15**(4) (2013) 2114 – 2123.

10. R. Burdzik, *Monitoring system of vibration propagation in vehicles and method of analyzing vibration modes*, in: J. Mikulski (Ed.), Telematics in the transport environment, CCIS 329, Springer, Heidelberg, (2012) 406 – 413.
11. G. Klekot, *Application of vibro-acoustic energy propagation measures to monitor status of the object and as a tool in the manage of noise*, Radom: ITE, 2012 (in Polish).
12. R. Burdzik, Ł. Konieczny, R*esearch on structure, propagation and exposure to general vibration in passenger car for different damping parameters*, Journal of Vibroengineering, **15**(4) (2013) 1680 – 1688.
13. P. Czech, G. Wojnar, R. Burdzik, Ł. Konieczny, J. Warczek, *Application of the discrete wavelet transform and probabilistic neural networks in ic engine fault diagnostics*, Journal of Vibroengineering, **16**(4) 2014 1619 – 1639.
14. W. Batko, Z. Dabrowski, J. Kiciński, *Nonlinear Effects in Technical Diagnostics*, Radom ITE-PIB 2008.
15. B. Chiliński, R. Pakowski, *Analysis of bending and torsinal vibroations of rotors with using perturbation methods*. In: Kleiber M et. al., editor. 3rd Polish Congress of Mechanics and 21st International Conference on Computer Methods in Mechanics - PCM-CMM. Short papers, Polish Society of Theoretical and Applied Mechanics, **1**(2) 2015 15 – 17.
16. B. Chiliński, *Analysis of disturbance torque influence on critical state in rotational systems*, Transportation Problems, **8**(4) (2013) 137 – 146.
17. S. Wierzbicki, *Laboratory control and measurement system of a dual-fuel compression ignition combustion engine operating in a cogeneration system*, Solid State Phenomena, **210** (2014) 200 – 205.
18. S. Wierzbicki, M. Śmieja, *Visualization of the parameters and changes of signals controlling the operation of common rail injectors*, Solid State Phenomena, **210** (2014) 136 – 141.
19. Z. Dąbrowski, H. Madej, *Masking mechanical damages in the modern control systems of combustion engines*, Journal of KONES Powertrain and Transport, **13**(3) (2006) 53 – 60, in Polish with an abstract in English, Retrieved June 19, 2013.
20. B. Chiliński, M. Zawisza, *Modelling of lateral-torsional vibrations of the crank system with a damper of vibrations*, Vibroengineering Procedia, **6**(6) (2015) 61 – 65.
21. Z. Dąbrowski, B. Chiliński, *Identification of a model of crank shaft with a damper of torsional vibrations*, Vibroengineering Procedia, **6**(6) (2015) 50 – 54.
22. P. Deuszkiewicz, J. Pankiewicz, J. Dziurdź, M. Zawisza, *Modeling of powertrain system dynamic behavior with torsional vibration damper*, Advanced Materials Research, **1036** (2014) 586 – 591.
23. W. Homik, J. Pankiewicz, *Examinations of torsional vibration dampers used in reciprocating internal combustion engines*, Polish Journal of Environmental Studies, Olsztyn, **20**(5A) (2011) 108 – 111.
24. W. Homik, *Broadband Torsional Dampers*, Wydawnictwo Naukowe Instytutu Technologii Eksploatacji - PIB, Rzeszów, 2012, (in Polish).

25. G. Peruń, J. Warczek, R. Burdzik, B. Łazarz, *Simulation and laboratory studies on the influence of selected engineering and operational parameters on gear transmission vibroactivity*, Key Engineering Materials, **588** (2014) 266 – 275.
26. Ł. Konieczny, R. Burdzik, T. Figlus, *The possibility to control and adjust the suspensions of vehicles*, J. Mikulski (Ed.): Activities of Transport Telematics, TST, CCIS, **395** (2013) 378 – 383. Springer, Heidelberg (2013) (Ed. Jerzy Mikulski, Berlin: Springer, 2013, (Communications in Computer and Information Science **395**).
27. Z. Dąbrowski, M. Zawisza, *diagnostics of mechanical defects not recognised by the OBD system in self-ignition engines*, Combustion Engines – Silniki Spalinowe **3** (2011) (146) (in Polish).

Energy Analysis of a Mechanical System with a Dynamic Vibration Absorber

Marian Witalis DOBRY
Poznan University of Technology, Institute of Applied Mechanics
24 Jana Pawła II Street, 60-965 Poznan, marian.dobry@put.poznan.pl

Abstract

The study relates to the phenomenon of power distribution in mechanical systems equipped with a dynamic vibration absorber. It is one of the methods of eliminating vibrations in a mechanical system, which stabilises its operation. This solution helps to reduce dynamic stress in subsystems of a vehicle's suspension or stabilise the motion of flying machines, such as helicopters. The article describes the phenomenon of power distribution of structural forces, which has not been described so far. The phenomenon reveals the power distribution in a dynamic structure of a system of interest and can be used to determine the rate of energy flow as a function of the dynamic state resulting from the selection of dynamic parameters of the vibration absorber. The energy analysis applied in the study is based on an energy-based optimization method of adjusting the dynamic vibration absorber to the main mechanical system without changing its dynamic parameters, as is the case, for example, in turbine rotor balancing.

Keywords: energy flow, dynamics of machines, elimination of energy flow

1. Introduction

The phenomenon of power distribution of structural forces in mechanical systems with a dynamic vibration absorber has not been recognised so far [5]. It is a holistic approach, which makes it possible to control and optimize energy flow in order to ensure effective stabilisation of the main mechanical system thanks to the influence of the dynamic vibration absorber. The analysis of power distribution can be used in mechanical and biomechanical systems to optimize the structural design, to evaluate the amount of energy absorbed by particular elements and, globally, by entire systems, and as a diagnostic tool at every life stage of these systems [2, 3, 4].

2. The physical model of the dynamics of the system of interest

Dynamic analysis of a mechanical system with a dynamic vibration absorber requires a physical model with two degrees of freedom. The first point of reduction is mass M, which models the mass of the main mechanical system, which is to be stabilized, while the second point of reduction corresponds to mass “m” of the dynamic vibration absorber, connected with mass M through a damping-energy dissipating element. Vibrations are generated by the driving force $F(t)$, which excites mass M. The physical model of such a mechanical system is shown in Figure 1. The purpose of the absorber is to minimize the vibration amplitude of the main subsystem. The tuning parameters of the absorber are determined by the dynamics of the system of interest. For this purpose a dynamic mathematical model of the system has been formulated.

3. The mathematical model of the dynamics of the system of interest

The mathematical model was derived using Lagrange equations of the second kind given by [1]:

$$\frac{d}{dt}\left(\frac{\partial E}{\partial \dot{q}_j}\right)-\frac{\partial E}{\partial q_j}=Q_j-\frac{\partial V}{\partial q_j}-\frac{\partial \Phi}{\partial \dot{q}_j}; \quad j=1,2,\ldots s; \tag{1}$$

where:

s – the number of degrees of freedom,

ϕ – the power of forces of energy dissipation,

E – kinetic energy of the mechanical system,

V – potential energy of the mechanical system,

Q_j – generalised active forces,

q_j – generalised coordinates,

$\dot{q}_j$ – generalised velocities.

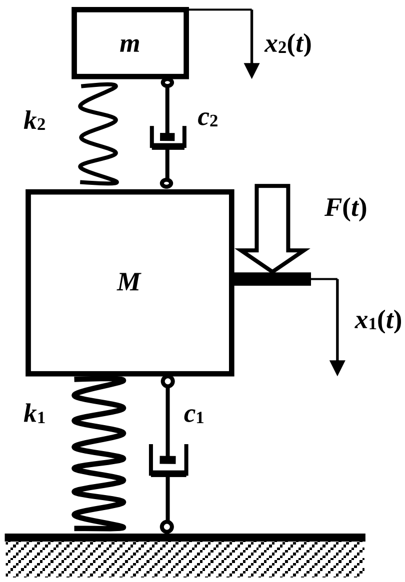

M – reduced mass of the main system

k_1 – reduced coefficient of elasticity of the main system

c_1 – reduced damping coefficient of the main system

$F(t)$ – the driving force with a variable frequency

m – reduced mass of the dynamic vibration absorber

k_2 – reduced coefficient of elasticity of the dynamic vibration absorber

c_2 – reduced damping coefficient of the dynamic vibration absorber

Figure 1. The physical model of a mechanical system with a dynamic vibration absorber

As mentioned earlier, the mechanical system of interest has two degrees of freedom, hence $s = 2$. The following generalised coordinates have been assumed:
$q_1 = x_1(t)$ – the location coordinate of mass M of the stabilized mechanical system,
$q_2 = x_2(t)$ – the location coordinate of mass m of the attached dynamic vibration absorber.

The mathematical model of forces acting in the system consists of two differential equations of forces given by (2):

$$\begin{aligned}&M\ddot{x}_1(t)+(c_1+c_2)\dot{x}(t)+(k_1+k_2)x(t)-k_2x_2(t)-c_2\dot{x}(t)=F_0\sin[2\pi f(t)t];\\&m\ddot{x}_2(t)+c_2\dot{x}_2(t)+k_2x_2(t)-c_2\dot{x}_1(t)-k_2x_1(t)=0\end{aligned}\tag{2}$$

The first equation describes forces acting in a stabilized mechanical system, the second one describes forces acting in the additional system of the dynamic absorber attached to the main system. When dynamic forces acting in the mechanical system are known, it is possible to formulate an energy model. The model was formulated by applying the First Principle of Power Distribution in a Mechanical System (PPDiMS) [2, 3].

4. The energy model of power distribution in a mechanical system with a dynamic vibration absorber

The above-mentioned principle can be used to derive equations of power distribution in the mechanical system. The energy model of the system of interest consists of two equations of power given by:

$$\begin{aligned}&M\ddot{x}_1(t)\dot{x}_1(t)+(c_1+c_2)\dot{x}_1^2(t)+(k_1+k_2)x(t)\dot{x}_1(t)-k_2x_2(t)\dot{x}_1-c_2\dot{x}_2(t)\dot{x}_1(t)=\\&=F_0\dot{x}_1(t)\sin[2\pi f(t)t];\\&m\ddot{x}_2(t)\dot{x}_2+c_2\dot{x}_2^2(t)+k_2x_2(t)\dot{x}_2(t)-c_2\dot{x}_1(t)\dot{x}_2(t)-k_2x_1(t)\dot{x}_2(t)=0\end{aligned}\tag{3}$$

The first equation describes how the powers of all structural forces change over time, that is: the power of inertial forces, the power of dissipative forces, the power of elastic forces and the power of the driving force, which excites the motion of the mechanical system.The equation also accounts for the powers of the elastic and dissipative coupling with the vibration absorber.

The second equation describes power distribution at the reduction point connected with the mass of the dynamic absorber and the power of forces involved in the elastic and dissipative coupling with the main system.

The equation of energy flow can be derived from the First Principle of Energy Flow in a Mechanical System based on integral equations given by (3).
Given the energy models of the system of interest, one can solve the energy model and determine power distribution and energy flow in its dynamic structure for specific data.

$$
\begin{aligned}
&\int_0^{t_S}\left[M\ddot{x}_1(t)\dot{x}_1(t)\right]dt+\int_0^{t_S}\left[(c_1+c_2)\dot{x}_1^2(t)\right]dt+\int_0^{t_S}\left[(k_1+k_2)x(t)\dot{x}_1(t)\right]dt=\\
&=\int_0^{t_S}\left[k_2x_2(t)\dot{x}_1\right]dt+\int_0^{t_S}\left[c_2\dot{x}_2(t)\dot{x}_1(t)\right]dt+\int_0^{t_S}\left[F_0\dot{x}_1(t)\sin(2\pi f_w t)\right]dt;\\
&\int_0^{t_S}\left[m\ddot{x}_2(t)\dot{x}_2(t)\right]dt+\int_0^{t_S}\left[c_2\dot{x}_2^2(t)\right]dt+\int_0^{t_S}\left[k_2x_2(t)\dot{x}_2(t)\right]dt=\\
&\int_0^{t_S}\left[c_2\dot{x}_1(t)\dot{x}_2(t)\right]dt+\int_0^{t_S}\left[k_2x_1(t)\dot{x}_2(t)\right]dt;
\end{aligned}
\tag{3}
$$

5. The solution of the energy model of power distribution in a mechanical system with a dynamic vibration absorber

The above models were solved usingnumerical simulation implemented in the MATLAB/simulink environment. An original simulation programme called SPED was developed for this purpose. The programme makes use of the Elementary Processor of Energy Flow MWD, which implements two principles: the First Principle of Power Distribution in a Mechanical System (PPDiMS) and the First Principle of Energy Flow in a Mechanical System (FPEFiMS) [2, 3, 4].

Example analytical calculations were done for the following data:

M = 10 kg, k_2 = 3948 N/m, c_2 = 1.257 Ns/m, m = 1 kg,
k_1 = 3.948E+004 N/m, c_1 = 252.6 Ns/m, $F(t)$ = 100 sin [2πf(t)t]

The SPED programme enables a synchronous solution of the mathematical model of the system's motion, power distribution and energy flow in the mechanical system.

Figure 2 shows the results of the simulation of the dynamics of the system of interest, comparing values of acceleration, velocity and displacement of the reduction points of the dynamic vibration absorber and the main system. Response characteristics were obtained by inducing the motion of the main system through a sinusoidal driving force with amplitude of 100 N and with a frequency varying at the rate of 1 Hz/s.

Analysis of all kinematic quantities indicates mutual interactions between the subsystems. The effect of the main subsystem on the dynamic vibration absorber is evident for all characteristics once the driving frequency reaches the resonant frequency of the main system and is manifested by extended characteristics of all kinematic quantities. The strong effect of the dynamic vibration absorber is especially evident in the characteristics of the main subsystem. One significant change is manifested by reduced values of all kinematic quantities for a frequency of 10 Hz, which the absorber was tuned to. It is precisely the purpose of the dynamic vibration absorber, which ensures stabilization of the main subsystem's motion by reducing its vibration amplitudes.

To facilitate comparative analysis of the motion of the main(stabilized) subsystem, Figure 3 shows dimensionless dynamic characteristics of vibration amplitudes relative to the static deflection of the main subsystem. The horizontal line at a height of 1 divides the chart into two sections: the area of amplified vibrations of the main subsystem for values greater than 1 and the area of vibration elimination for values less than 1.

$$x_{stat} = \frac{F_{z0}}{k_1} \quad [m] \tag{4}$$

where: F_{z0} – reduced amplitude of the driving force inducing the motion of the main subsystem, k_1 – reduced coefficient of elasticity of the main system.

Results of the dynamic analysis for the dynamic vibration absorber

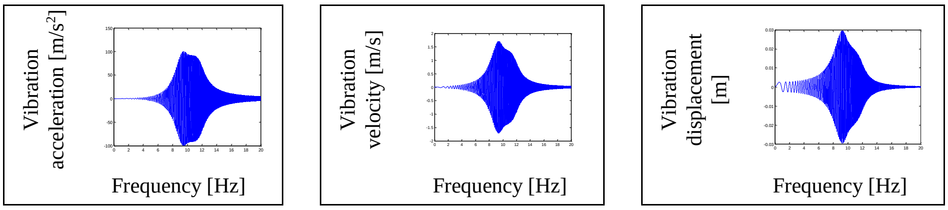

Results of the dynamic analysis for the main mechanical system with a dynamic vibration absorber

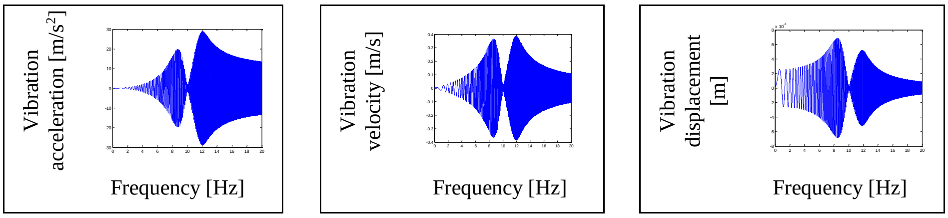

Figure 2. Results of the dynamic analysis of a mechanical system (stabilized) with a dynamic vibration absorber during a harmonic test with a driving force $F(t) = 100 \sin [2\pi F(t)]$ with a constant rate of frequency switching $f = 1$ Hz/s in the range 0-20 Hz.

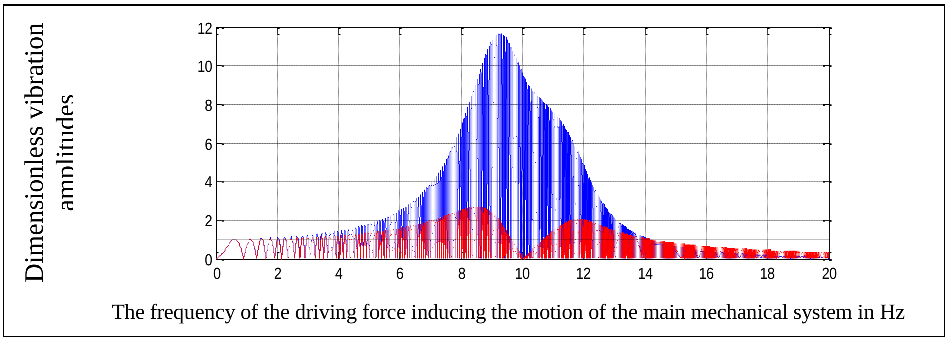

Figure 3. Dimensionless characteristics of amplitude and frequency of the mechanical system with a dynamic vibration absorber

Analysis of Figure 3 indicates that the frequency band where vibration elimination occurs in the main subsystem is very narrow and its middle lies at 10 Hz, which is the frequency the absorber was tuned to.The vibrations of the main subsystem were reduced by 89.3% relative to the static deflection that would be produced if a static force with an amplitude equal to that of the driving force was applied to it.This means that the dynamic coefficient for a frequency of 10 Hz amounts to **0.107**. It is a well-known fact that an absorber eliminates the amplitude of vibrations at a specific frequency, which makes it a selective absorber. This limits the application of the absorber to machines and devices that operate at constant (stabilized) frequency.

6. Amplitude and frequency characteristics of powers of structural forces in a mechanical system with a dynamic vibration absorber

The above properties of a dynamic vibration absorber were also confirmed by a novel dynamic analysis in the domain of power distribution of structural forces acting at reduction points.Figure 4 shows instantaneous powers of inertial, dissipative and elastic forces as functions of frequency in the range 0-20 Hz. In other words, these are amplitude and frequency characteristics of powers for the above mentioned structural forces.

The distribution of instantenous power at the reduction point of the dynamic vibration absorber in [W]

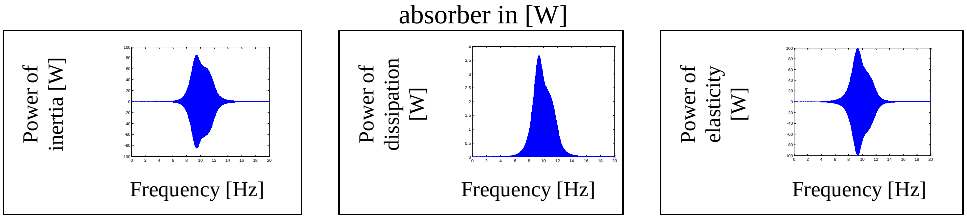

The distribution of instantenous power at the reduction point of the main mechanical system

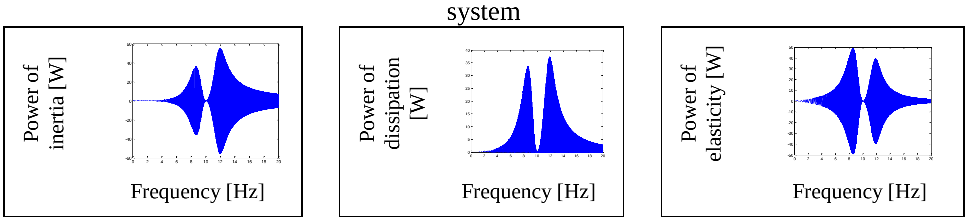

Figure 4. The distribution of instantaneous power in the dynamic structure of the(stabilized)mechanical system with a dynamic vibration absorber during a harmonic test with a constant rate of switching frequency f = 1 Hz/s

The figures indicate that the power of structural forces in the main subsystem for the frequency of 10 Hz (effective operation of the absorber) is close to 0 and amounts to: Nbg(10 Hz) = 0.2 [W], Nstg(10 Hz) = 0.125 [W] and Nspg(10 Hz) = 0.114 [W]. This means that the rate of energy flow is very low and suspension elements of the main subsystem are exposed to little dynamic load.Fatigue depends on the amount of energy transferred through structural elements of the suspension of the main (stabilized)subsystem.

7. The effectiveness of eliminating energy flow in a stabilized subsystem

The effectiveness of eliminating energy flow in a stabilized subsystem by means of a dynamic vibration absorber can be expressed in the form of a dimensionless characteristic of elasticity, which relates the power of elasticity at both reduction points to the maximum power at the frequency for which the power of elasticity in the main subsystem is the smallest – Fig. 5.

Figure 5 shows the factor by which the power of elasticity is reduced when the absorber reaches the point of its effective operation; the factor reduction is expressed as a ratio of maximum power of energy characteristics obtained in both systems to the maximum power of elasticity in the main subsystem observed at the driving frequency, i.e. at the point of elimination. The chart shows a high degree of power reduction, which confirms the specific effect in which the subsystem of the dynamic absorber affects the main subsystem (stabilized) in the domain of power.A properly tuned dynamic vibration absorber effectively eliminates energy flow in elastic elements of the suspension of the main subsystem. A comparison of both characteristics of instantaneous powers of elasticity clearly reveals that this kind of power is neutralized by the dynamic absorber. In the frequency band where elimination occurs, instantaneous elastic power reaches a maximum value, which is 872 times greater than the peak power obtained for instantaneous elastic power in the main subsystem (stabilized).

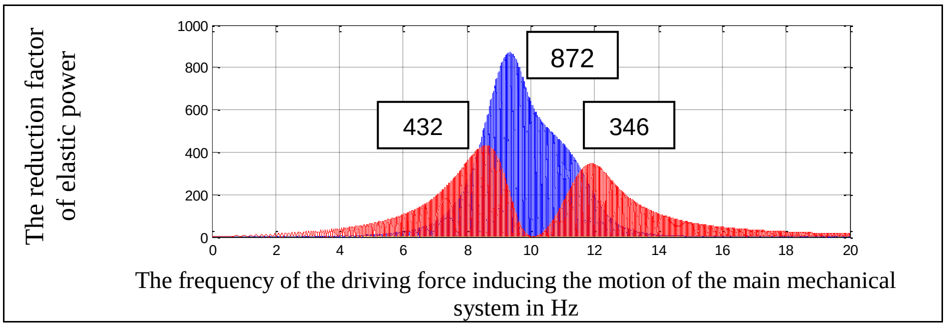

Figure 5. The reduction factor of the power of elastic forces in a mechanical system with a dynamic vibration absorber expressed as a function of the ratio of the driving frequency to the maximum instantaneous power obtained for optimal parameters of the absorber

It can also be concluded that in the design of a dynamic vibration absorber one should ensure that its elastic element is not exposed to stress exceeding permissible values.

Elastic power can be regarded as a measure of fatigue load exerted on suspension (elastic) structures of the main subsystem. A dynamic absorber contributes to increasing the durability and reliability of the suspension of the main (stabilized)subsystem.

8. Conclusions

Based on the results of energy analysis of the mechanical system with a dynamic vibration absorber, one can formulate a few important conclusions.

1. The dynamic analysis conducted in the study explains the phenomenon of power distribution and energy flow in a mechanical system with a vibration absorber.
2. The energy analysis has demonstrated a considerable reduction in the flow of all kinds of energy in the stabilized subsystem for the selected frequency which the vibration absorber was tuned to.
3. The optimal energy flow in the main (stabilized) subsystem depends on its damping ratio.
4. The dynamic absorber absorbs energy introduced into the system by the driving force in the optimal range of vibration elimination and has a strong effect on the main (stabilized) subsystem by reducing the flow of energy transferred to it.
5. The elimination of the flow of elastic energy in the main subsystem and in the absorber, which was computed in relation to the maximum instantaneous elastic power for the optimal frequency of vibration elimination, amounted to, respectively: in the main system – 432, and in the subsystem of the absorber – 872.

Acknowledgments

The study was partly financed by the Ministry of Science and Higher Education as a project entitled: *Energy informational considerations of vibroacoustics, diagnostics and biomechanics of systems*. Study code: 02/21/DSPB/3478

References

1. R. H. Cannon jr., *Dynamika układów fizycznych*, Wydawnictwa Naukowo-Techniczne, Warszawa 1973.
2. M. W. Dobry, *Optymalizacja przepływu energii w systemie Człowiek – Narzędzie – Podłoże*, Ph.D. Thesis, Poznan University of Technology, Poznan, 1998.
3. M. W. Dobry, *Podstawy diagnostyki energetycznej systemów mechanicznych i biomechanicznych*, Wydawnictwo Naukowe Instytutu Technologii Eksploatacji – PIB, Radom 2012.
4. M. W. Dobry, *Energy efficiency of passive vibroisolation in machines and devices*, Vibroengineering Procedia, JVE International Ltd., Kaunas, Lithuania, **3** (2014) 117 – 123.
5. C. M. Harris, Ch. E. Crede, *Shock and Vibration Handbook*, chapt. 30 – 33, McGRAW – HILL, New York 1976.

Differences in Power Distribution in the Subsystems of the Human – Anti-Vibration Glove – Tool System

Marian Witalis DOBRY
Poznan University of Technology, Institute of Applied Mechanics
24 Jana Pawła II Street, 60-965 Poznan, marian.dobry@put.poznan.pl

Tomasz HERMANN
Poznan University of Technology, Institute of Applied Mechanics
24 Jana Pawła II Street, 60-965 Poznan, tomasz.hermann@put.poznan.pl

Abstract

The article continues the analysis presented in the article „Power distribution in anti-vibration gloves" [6], which described the approach adopted to construct an energy model of the Human – Glove – Tool system (H – G – T). The outcome of the analysis was the power distribution calculated only for the anti-vibration glove. This article continues the energy analysis for another subsystem of the H – G – T system – the human physical model. The energy method was also used to calculate the power distribution in its dynamic structure in order to account for interactions between the elements of the H – G – T system. The results obtained in the study indicate that the power distribution in the human physical model and in the glove model is completely different.

Keywords: biomechanical system, hand-arm vibrations, power distribution, energy method

1. Introduction

Every physical model corresponds to the real system in terms of key features selected by the researcher, which are relevant for a given research problem. At the beginning of the modelling process one always starts with a number of simplifying assumptions, which, however, should not lead to approximations that distort the modelling goal. Ideally, one should only introduce simplifications that result in a simple model and facilitate the process of drawing conclusions while providing an accurate representation of the real system [1].

In this case, the problem becomes particularly interesting when one studies the discrete models used for analysing the impact of vibrations on the human body [7, 8, 10, 11]. The models differ from one another in terms of structure, because they are made up of a different number of mass, damping and elastic elements. This is a significant difference, because there is a relationship between an object's structure and its function. It should be emphasized that it is a cause and effect relationship. Hence, only models displaying structural similarity can guarantee the most reliable information about the real system [9]. It follows, then, that one should not create models with arbitrary structures that represent the real system's response only approximately.

The problem in question is important when one wants to determine the strain exerted on the dynamic structure of the model. The reason why this is a significant consideration is because this value should properly reflect the strain exerted on the real system. In this case, we use the response generated by the system, of course, but we also take into account the model's structure and the value of its dynamic parameters.

In the case analysed in the study it is assumed that the model is an energy transformation system. A similar approach, though applied to machines, was adopted by Cempel [2, 5], who described it in his works. In this article the approach is combined with the energy method implemented according to the theory developed by Dobry [3, 4].

The aim of the analysis was to determine the degree of difference between the load exerted on the dynamic structures of the human physical model and glove model. This assessment was based on three kinds of powers identified theoretically and related to the forces of inertia, dissipation and elasticity. This made it possible to determine which of the two subsystems of the H – G – T system was exposed to a higher dynamic load.

2. The human energy model

The dynamic load of the human physical model, which is a component of the H – G – T system, was calculated using the energy method. The H – G – T system was composed of the human physical model and the glove model specified in the ISO 10068:2012 standard [11].

Using the energy model of the H – G – T system, it is possible to identify the power distribution in the dynamic structure of the human physical model. A detailed description of the process of constructing the energy model and the application of the First Principle of Power Distribution in a Mechanical System [3, 4] is presented in another article [6]. The energy model of the H – G – T system (Fig. 1) represented by equations of power, is given by [6]:

$$
\begin{aligned}
&j=1, && m_0\ddot{z}_0\dot{z}_0+(c_0+c_1)\dot{z}_0^2+(k_0+k_1)z_0\dot{z}_0-c_1\dot{z}_1\dot{z}_0-k_1z_1\dot{z}_0=0\\
&j=2, && m_1\ddot{z}_1\dot{z}_1+(c_1+c_2+c_3)\dot{z}_1^2+(k_1+k_2+k_3)z_1\dot{z}_1-c_1\dot{z}_0\dot{z}_1-k_1z_0\dot{z}_1-\\
& && -c_2\dot{z}_2\dot{z}_1-k_2z_2\dot{z}_1-c_3\dot{z}_3\dot{z}_1-k_3z_3\dot{z}_1=0\\
&j=3, && m_2\ddot{z}_2\dot{z}_2+(c_2+c_4)\dot{z}_2^2+(k_2+k_4)z_2\dot{z}_2-c_2\dot{z}_1\dot{z}_2-k_2z_1\dot{z}_2-c_4\dot{z}_4\dot{z}_2-k_4z_4\dot{z}_2=0\\
&j=4, && m_{3\mathrm{R}}\ddot{z}_3\dot{z}_3+(c_3+c_5)\dot{z}_3^2+(k_3+k_5)z_3\dot{z}_3-c_3\dot{z}_1\dot{z}_3-k_3z_1\dot{z}_3-c_5\dot{z}_5\dot{z}_3-k_5z_5\dot{z}_3=0\\
&j=5, && m_{4\mathrm{R}}\ddot{z}_4\dot{z}_4+(c_4+c_6)\dot{z}_4^2+(k_4+k_6)z_4\dot{z}_4-c_4\dot{z}_2\dot{z}_4-k_4z_2\dot{z}_4-c_6\dot{z}_5\dot{z}_4-k_6z_5\dot{z}_4=0\\
&j=6, && m_{\mathrm{RT}}\ddot{z}_5\dot{z}_5+(c_5+c_6)\dot{z}_5^2+(k_5+k_6)z_5\dot{z}_5-c_5\dot{z}_3\dot{z}_5-k_5z_3\dot{z}_5-\\
& && -c_6\dot{z}_4\dot{z}_5-k_6z_4\dot{z}_5=F(t)\dot{z}_5
\end{aligned}
\tag{1}
$$

The energy method makes it possible to determine the dynamic load for each of the subsystems of the H – G – T system, taking into account the influence of the other subsystems. This article focuses on only one subsystem, i.e. the human body, which was analysed by means of the energy method.

For this purpose, one should isolate from the energy model for the whole dynamic structure of the H – G – T system the power introduced into the human physical model. Consequently, in the following calculations it is necessary to take into account only those dynamic parameters that were used to model the behaviour of the human body (the part marked off in Figure 1). The dynamic parameters for the human physical model and the glove model, i.e. m_i, k_i, c_i are specified in the ISO 10068:2012 standard [11].

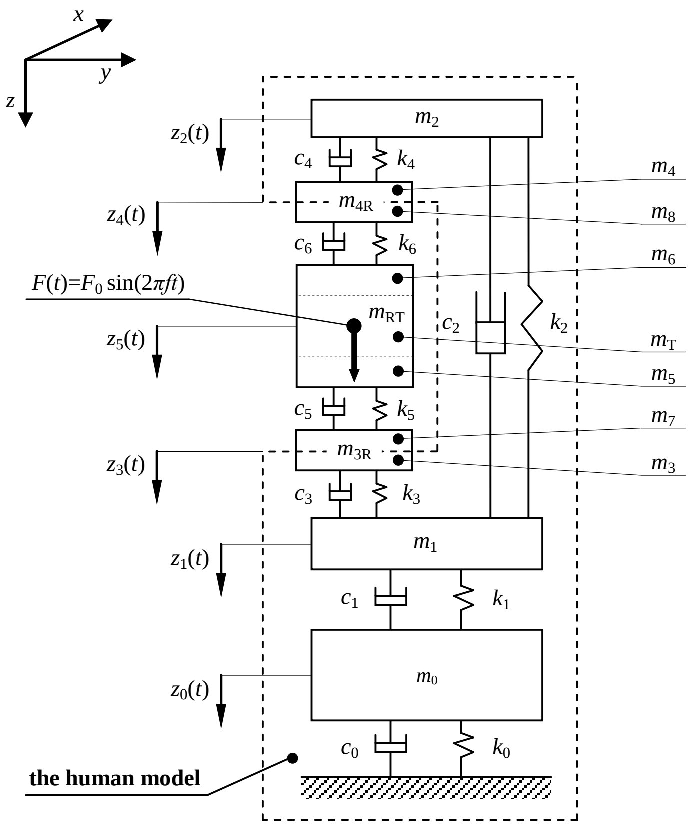

<u>where:</u>

$\left.\begin{array}{l} \boldsymbol{m_0, m_1, m_2, m_3, m_4} \\ \boldsymbol{k_0, k_1, k_2, k_3, k_4} \\ \boldsymbol{c_0, c_1, c_2, c_3, c_4} \end{array}\right\}$ **<u>dynamic parametersof the human model</u>**

$\left.\begin{array}{l} m_5, m_6, m_7, m_8 \\ k_5, k_6, c_5, c_6 \end{array}\right\}$ dynamic parametersof the glove model

m_T – tool mass

<u>Reduction points:</u> $m_{RT} = m_5 + m_6 + m_T$;

$m_{3R} = m_3 + m_7$; $m_{4R} = m_4 + m_8$.

Figure 1. The physical model of the biomechanical H – G – T system, obtained by combining the physical models from the ISO 10068:2012 standard [11] with the tool model

RMS values of power, calculated as a sum of powers at all points of reduction for the human model are defined as follows:
– the power of inertia expressed in [W]:

$$P_{\mathrm{H-INE}} = \sqrt{\frac{1}{t}\int_0^t \left[m_0 \ddot{z}_0 \dot{z}_0\right]^2 \mathrm{d}t} + \sqrt{\frac{1}{t}\int_0^t \left[m_1 \ddot{z}_1 \dot{z}_1\right]^2 \mathrm{d}t} + \sqrt{\frac{1}{t}\int_0^t \left[m_2 \ddot{z}_2 \dot{z}_2\right]^2 \mathrm{d}t} + \sqrt{\frac{1}{t}\int_0^t \left[m_3 \ddot{z}_3 \dot{z}_3\right]^2 \mathrm{d}t} + \sqrt{\frac{1}{t}\int_0^t \left[m_4 \ddot{z}_4 \dot{z}_4\right]^2 \mathrm{d}t} \tag{2}$$

– the power of dissipation expressed in [W]:

$$P_{\mathrm{H-DIS}} = \sqrt{\frac{1}{t}\int_0^t \left[(c_0 + c_1)\dot{z}_0^2\right]^2 \mathrm{d}t} + \sqrt{\frac{1}{t}\int_0^t \left[(c_1 + c_2 + c_3)\dot{z}_1^2\right]^2 \mathrm{d}t} + \sqrt{\frac{1}{t}\int_0^t \left[(c_2 + c_4)\dot{z}_2^2\right]^2 \mathrm{d}t} + \sqrt{\frac{1}{t}\int_0^t \left[c_3 \dot{z}_3^2\right]^2 \mathrm{d}t} + \sqrt{\frac{1}{t}\int_0^t \left[c_4 \dot{z}_4^2\right]^2 \mathrm{d}t} \tag{3}$$

– the power of elasticity expressed in [W]:

$$P_{\mathrm{H-ELA}} = \sqrt{\frac{1}{t}\int_0^t \left[(k_0 + k_1) z_0 \dot{z}_0\right]^2 \mathrm{d}t} + \sqrt{\frac{1}{t}\int_0^t \left[(k_1 + k_2 + k_3) z_1 \dot{z}_1\right]^2 \mathrm{d}t} + \sqrt{\frac{1}{t}\int_0^t \left[(k_2 + k_4) z_2 \dot{z}_2\right]^2 \mathrm{d}t} + \sqrt{\frac{1}{t}\int_0^t \left[k_3 z_3 \dot{z}_3\right]^2 \mathrm{d}t} + \sqrt{\frac{1}{t}\int_0^t \left[k_4 z_4 \dot{z}_4\right]^2 \mathrm{d}t} \tag{4}$$

3. The results of the energy method

In the case under consideration the energy model was solved for the same conditions as in the previous article [6]. The biodynamic model of the H – G – T system was exposed to a sinusoidally varying driving force $F(t)$ with an amplitude of 115 N. The analysis was conducted assuming the value of frequency f = 20 Hz and tool mass m_T = 6 kg. As a result, it was possible to compare power distributions for the human model and the glove model.

The energy model was solved using numerical simulation for time t = 100 seconds. Integration was carried out using algorithm ode113 (Adams) with a tolerance of 0.0001. Simulations were implemented in the MATLAB/simulink environment with integration time steps ranging from a maximum value of 0.0001 to a minimum of 0.00001 second.

Figure 2 shows the structural power distribution for the human physical model and the glove model. The results for the glove model come from the previous article [6]. In the case of the human physical model and the glove model the percentage share of each type of power was calculated by relating the each type of power to the total power, equal to the sum of power generated in the two subsystems. The relationship can be expressed by the following formula:

$$S_{\mathrm{Z}}=\frac{P_{\mathrm{Z}i}}{P_{\mathrm{H-INE}}+P_{\mathrm{H-DIS}}+P_{\mathrm{H-ELA}}+P_{\mathrm{G-INE}}+P_{\mathrm{G-DIS}}+P_{\mathrm{G-ELA}}}\cdot 100\% \tag{5}$$

where:

- $P_{\mathrm{Z}i}$ – RMS value of the power of inertia, dissipation or elasticity determined at all points of reduction for the given model,
- $P_{\mathrm{G-Z}i}$ – RMS value of the power of inertia, dissipation or elasticity determined at all points of reduction for the glove model [6],
- $P_{\mathrm{H-Z}i}$ – RMS value of the power of inertia, dissipation or elasticity determined at all points of reduction for the human model (2) ÷ (4).

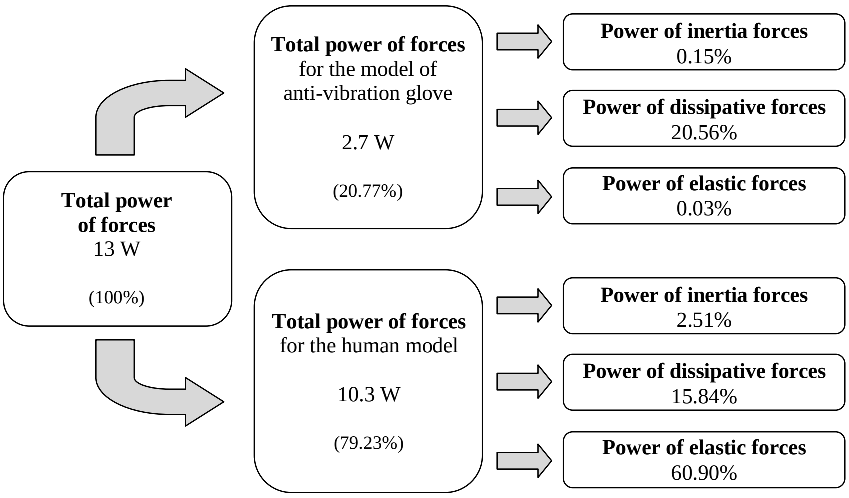

Figure 2. The structural power distribution of forces for the human model and the glove model [6] for the operating frequency of the tool f = 20 Hz

The results shown in Figure 2 indicate that the total power determined for the human model and the glove model for the operating frequency of the tool f = 20 Hz is equal to 13 W. The resulting value can be further decomposed into two total powers of forces introduced into both subsystems, i.e. for the human model and the glove model. The energy method demonstrated that the strain exerted on the dynamic structures in the analysis was different. It is worth noting that the total power for the human model is over 3.81 times larger than that calculated for the glove model.

More importantly, the results indicate that the power distribution computed for both models is completely different. This is reflected by the percentage share of each kind of power in each subsystem. For the glove model, the powers are ordered as follows: the power of dissipative forces – 20.56%, the power of inertial forces – 0.15% and the power of elastic forces – 0.03%. In the case of the human physical model the order is completely different. The contributions of the three kinds of power are ordered as follows: the power of elastic forces – 60.90%, the power of dissipative forces – 15.84% and the power of inertial forces – 2.51%.

It is worth noting that only one kind of force is comparable in quantitative terms. Quantitative comparison of powers between the models is presented in Figure 3.

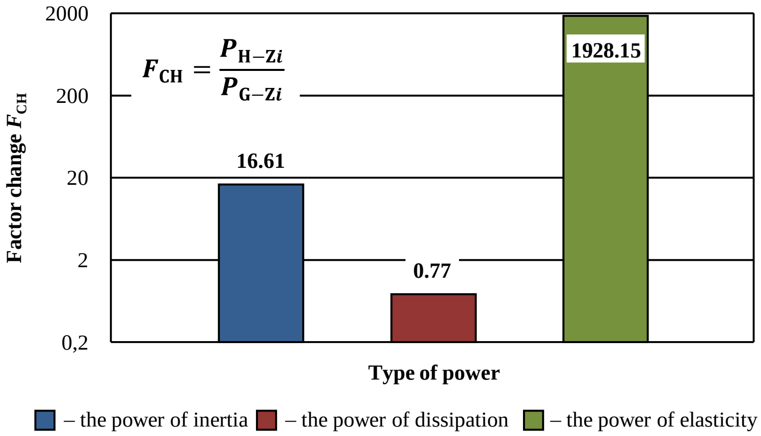

Figure 3. Quantitative comparison of three kinds of powers between the human model and the glove model for the operating frequency of the tool f = 20 Hz

The results shown in Figure 3 indicate that the only kind of power that is quantitatively comparable is the power of dissipation. More importantly, it is the only kind of power that is greater for the glove model than for the human model. The comparison results are quite different the powers of inertia and dissipation: in this case the factor change is equal to 16.61 for the power of inertia and 1928.15 for the power of elasticity. The values of the two kinds of forces computed for the dynamic structure of the tool are exactly as many times smaller than the results obtained for the structural human model.

4. Summary

The study has resulted in computing the power distribution for the human model, which is part of the biodynamic H – G – T system. More importantly, the results provide the basis for a comparative assessment of this subsystem with the values obtained for the anti-vibration glove. In this way it was possible to demonstrate that out of the two subsystems of the H – G – T system, it is the human operator who is exposed to more dynamic load. The results indicate the human dynamic structure receives 3.81 times more load than the glove.

Moreover, the analysis conducted in the study reveals that the disparate character of the load exerted on the two subsystems of the H – G – T system. The dynamic structure of the anti-vibration glove experiences a loss (dissipation) of energy, or its conversion into heat. In the human physical model, the dominant power component is related to the forces of elasticity. This is important because the computed power of forces can be related to specific changes in the human body [4]. The power of elastic forces should be linked to elastic elements in the human body. It should be emphasized that the elements of the human biological structure exposed to the greatest amount of dynamic stress are tendons, joints and muscles. When people are exposed to vibrations, it is these body parts that are adversely affected first and show pathological changes.

In the following stages of research the analysis will be extended to include other selected operating frequencies of the tool. As a result, curves of factor changes will be computed to enable a quantitative comparison of the powers of inertia, dissipation and elasticity between the different models. On this basis it will be possible to assess changes in the structural power distribution of forces in the subsystems of the H – G – T system in terms of the operational frequencies used in power hand-held tools.

Acknowledgments

The study was partly financed by the Ministry of Science and Higher Education as a project entitled: *Energy informational considerations of vibroacoustics, diagnostics and biomechanics of systems.*

Study code: 02/21/DSPB/3465

References

1. R. H. Cannon jr., *Dynamika układów fizycznych*, Wydawnictwa Naukowo-Techniczne, Warszawa 1973.
2. C. Cempel, *Minimalizacja drgań maszyn i ich elementów*, w: Współczesne zagadnienia dynamiki maszyn, Ossolineum, Wrocław 1976.
3. M. W. Dobry, *Optymalizacja przepływu energii w systemie Człowiek - Narzędzie - Podłoże*, Ph.D. Thesis, Poznan University of Technology, Poznan 1998.
4. M. W. Dobry, *Podstawy diagnostyki energetycznej systemów mechanicznych i biomechanicznych*, Wydawnictwo Naukowe Instytutu Technologii Eksploatacji – PIB, Radom 2012.
5. Z. Engel, W. M. Zawieska, *Hałas i drgania w procesach pracy: źródła, ocena, zagrożenia*, CIOP – PIB, Warszawa 2010.
6. T. Hermann, M. W. Dobry, *Power distribution in anti-vibration gloves*, Vibrations in Physical Systems, **27** (2016) 115 – 122.
7. A. M. Książek, *Analiza istniejących modeli biodynamicznych układu ręka – ramię pod kątem wibroizolacji człowieka – operatora od drgań emitowanych przez narzędzia ręczne*, Czasopismo Techniczne, **2** (1996) 87 – 11.
8. S. Rakheja, J. Z. Wu, R. G. Dong, A. W. Schopper, *A comparison of biodynamic models of the Human hand-arm system for applications to hand-held power tools*, Journal of Sound and Vibration, **249**(1) (2002) 55 – 82.

9. B. Żółtowski, *Badania dynamiki maszyn*, MARKAR – B. Ż, Bydgoszcz 2002.
10. ISO 10068:1998, *Mechanical vibration and shock – free, mechanical impedance of the human hand-arm system at the driving point*.
11. ISO 10068:2012, *Mechanical vibration and shock – mechanical impedance of the human hand-arm system at the driving point*.

An Analytical-Numerical Approach to Analysis of Large Amplitude Vibrations of Slender Periodic Beams

Łukasz DOMAGALSKI
Department of Structural Mechanics, Łódź University of Technology
al. Politechniki 6, 90-924 Łódź, Poland, lukasz.domagalski@p.lodz.pl

Abstract

The paper is devoted to analysis of geometrically nonlinear vibrations of beams with geometric and material properties periodically varying along the axis. The 1-D Euler-Bernoulli theory of beams with von Kármán nonlinearity is applied. An analytical-numerical model based on non-asymptotic tolerance modelling approach and Galerkin method is applied. The linear natural frequencies and mode shapes are determined and the results are confirmed by comparison with a finite element model. Forced damped vibrations analysis in the large deflection range is performed to illustrate complex behaviour of the system.

Keywords: nonlinear vibrations, periodic beams, averaging, tolerance modelling

1. Introduction

Structures with physical properties arranged periodically or almost periodically in the body domain are often found in engineering and in the nature. Properly designed, they have many advantages, such as favourable mass to stiffness ratio. Furthermore, considering problems of dynamics, we can point out the frequency filtering properties of such structures, i.e. existence of frequency band gaps.

In this paper, vibrations of beams with periodically varying geometric and material properties along the longitudinal axis are considered. Equations of motion of such structures have highly oscillating, periodic, often non-continuous coefficients.

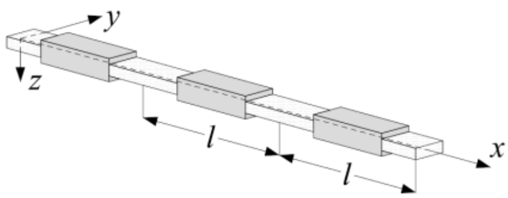

Figure 1. A fragment of a periodic beam

There are numerous special techniques in analysis of periodic media, many of them based on strict mathematical asymptotic homogenization [1]. Extensive work has been done in homogenization of periodic beams, cf. [4]. The theoretical foundation of the analytical-numerical model used here is the non-asymptotic tolerance modelling approach to analysis of microstructured periodic or almost periodic media. It is based mainly on the concepts of slowly-varying and tolerance periodic functions, and the indiscernibility relation, cf. [6]. The resulting partial differential equations with constant coefficients are then transformed into a set of ordinary differential equations using Galerkin method and then numerically integrated via the Runge-Kutta-Fehlberg method. The resulting model is an extension of a simplified one, presented in [3]. The new concept is the notion of a weakly slowly-varying function, cf. [5]. Some of the results of analysis geometrically nonlinear equilibrium problems of thin periodic plates via the tolerance modelling are confirmed in [2].

2. Equations of motion

The object under consideration is a linearly elastic, piecewise-prismatic beam. Let *Oxyz* be an orthogonal Cartesian coordinate system, the *Ox* axis coincides with the axis of the beam, the cross section of the beam be symmetric with respect to the plane of the load *Oxz*, the load acts in the direction of the axis *Oz*. The beam is assumed to be made of small repetitive elements, called periodicity cells, each of which is defined as $\Delta\equiv[-l/2,l/2]$, where $l<<L$ is the length of the cell and named the microstructure parameter.

The assumptions of the Euler-Bernoulli theory of beams with von Kármán terms serve as a basis. The effects of axial and rotational inertia are neglected, as we investigate slender elements and we are interested in analysis of transverse vibrations. Let $\partial^k=\partial^k/\partial x^k$ be the *k*-th derivative of a function with respect to the *x* coordinate. Let the transverse deflection, the longitudinal displacement, tensile and flexural stiffness, the damping coefficient, mass of the beam per unit length, transverse load and dissipative force by $w = w(x,t)$, $u_0 = u_0(x,t)$, $EA = EA(x)$, $EJ = EJ(x)$, $c = c(x)$, $\mu = \mu(x)$, $q = q(x,t)$, $p = p(x,t)$, the system of nonlinear coupled differential equations for the longitudinal displacements u_0 and the transverse deflection w can be written as:

$$\begin{aligned} &\partial^2\left(EJ\partial^2 w\right) - EA\left(\partial u_0 + \tfrac{1}{2}\left(\partial w\right)^2\right)\partial^2 w + c\dot{w} + \mu\ddot{w} = q. \\ &\partial\left[EA\left(\partial u_0 + \tfrac{1}{2}\left(\partial w\right)^2\right)\right] = 0, \end{aligned} \tag{1}$$

The coefficients EA, EJ, μ, c, and in some cases the load q, are highly oscillating, often non-continuous functions of the x coordinate.

3. Introductory concepts and basic assumptions of the tolerance modelling

To become acquainted with the basics of the method, the reader is referred to the book [6]. Here, only the fundamental concepts are presented.

Let $\Delta(x) = x + \Delta$, $\Omega_\Delta = \{x \in \Omega : \Delta(x) \subset \Omega\}$ be a cell with centre at $x \in \Omega_\Delta$. The averaging operator for an arbitrary integrable function f is defined by:

$$< f > (x) = \frac{1}{|\Delta|} \int_{\Delta(x)} f(y)dy, \quad x \in \Omega_\Delta, \quad y \in \Delta(x). \tag{2}$$

It is assumed that each of the unknown displacements w and u_0 can be decomposed into its averaged and fluctuating part, the latter of which is a finite sum of products of fluctuation shape functions (*FS*) and fluctuation amplitudes:

$$\begin{aligned} w(x,t) &= W(x,t) + h^A(x)V^A(x,t), \quad A = 1,\ldots,N, \\ u_0(x,t) &= U(x,t) + g^K(x)T^K(x,t), \quad K = 1,\ldots,M, \end{aligned} \tag{3}$$

where the functions $W(\cdot), V^A(\cdot) \in WSV_d^2(\Omega,\Delta)$, $U(\cdot), T^K \in SV_d^1(\Pi,\Delta)$ are new basic unknowns, being weakly slowly-varying or slowly-varying functions in x; the fluctuation shape functions $h^A(\cdot) \in FS_d^2(\Omega,\Delta)$, $g^K(\cdot) \in FS_d^1(\Omega,\Delta)$ are postulated *a priori* in every problem under consideration. The new basic kinematic unknowns $W(\cdot)$ and $U(\cdot)$ are called the macrodeflection and the in-plane macrodisplacements, respectively; $V^A(\cdot)$ and $T^K(\cdot)$ are additional kinematic unknowns, called the fluctuation amplitudes.

4. The averaged equations

4.1. The tolerance model

After substitution the micro-macro decomposition (3) into equations (1), the next step of modelling is averaging these equations over an arbitrary periodicity cell with weights 1, h^A and g^K. After some manipulations we arrive at the following system of equations:

$$\begin{aligned} &\langle EJ\rangle\partial^4 W + \langle EJ\partial^2 h^A\rangle\partial^2 V^A + 2\langle EJ\partial h^A\rangle\partial^3 V^A + \langle EJh^A\rangle\partial^4 V^A \\ &-\langle N\rangle\partial^2 W - \langle N\partial h^A\rangle\partial V^A + \langle c\rangle\dot{W} + \langle\mu\rangle\ddot{W} + \langle ch^A\rangle\dot{V}^A + \langle\mu h^A\rangle\ddot{V}^A - \langle q\rangle = 0, \end{aligned} \tag{4}$$

$$\begin{aligned} &\langle EJh^A\rangle\partial^4 W - 2\langle EJ\partial h^A\rangle\partial^3 W + \langle EJ\partial^2 h^A\rangle\partial^2 W + \langle N\partial h^A\rangle\partial W + \langle\mu h^A\rangle\ddot{W} - \langle qh^A\rangle + \\ &+\langle ch^A\rangle\dot{W} + \langle EJh^A h^B\rangle\partial^4 V^B + 2\left[\langle EJh^A\partial h^B\rangle - \langle EJh^B\partial h^A\rangle\right]\partial^3 V^B + \langle ch^A h^B\rangle\dot{V}^B \\ &+2\left[\langle EJ\partial h^B\partial^2 h^A\rangle - \langle EJ\partial h^A\partial^2 h^B\rangle\right]\partial V^B + \langle EJ\partial^2 h^A\partial^2 h^B\rangle V^B + \langle N\partial h^A\partial h^B\rangle V^B \\ &+\left[\langle EJ\partial^2 h^B h^A\rangle + \langle EJ\partial^2 h^A h^B\rangle - 4\langle EJ\partial h^A\partial h^B\rangle\right]\partial^2 V^B + \langle\mu h^A h^B\rangle\ddot{V}^B = 0, \end{aligned} \tag{5}$$

where the averaged axial forces $\langle NF(y)\rangle$, $F(y) = \{1, \partial h^A, \partial h^A\partial h^B\}$, are independent of x:

$$\begin{aligned} \langle NF(y)\rangle = &\int_0^L V^D V^C dx \times \\ &\times\tfrac{1}{2}\left(\langle EA\partial h^C\partial h^D F(y)\rangle - \langle EA\partial g^L\rangle\langle EA\partial g^K\partial g^L\rangle^{-1}\langle EA\partial g^K\partial h^C\partial h^D F(y)\rangle\right) \\ &+\left(\langle EA\partial h^C F(y)\rangle - \langle EA\partial g^L\rangle\langle EA\partial g^K\partial g^L\rangle^{-1}\langle EA\partial g^K\partial h^C F(y)\rangle\right)\int_0^L V^C\partial W dx \\ &+\left(\langle EAF(y)\rangle - \langle EA\partial g^L\rangle\langle EA\partial g^K\partial g^L\rangle^{-1}\langle EA\partial g^K F(y)\rangle\right)\left(\Delta_0 + \tfrac{1}{2}\int_0^L \partial W\partial W dx\right). \end{aligned} \tag{6}$$

Equations (4-5) with denotations (6) stand for a system of 2+N differential equations for the macrodeflection $W(\cdot)$ and for its fluctuation amplitudes $V^A(\cdot)$. As the axial inertia terms are neglected, the axial displacement $U(\cdot)$ and its fluctuation $T^K(\cdot)$ can be eliminated. The coefficients of these equations are constant, some and of them depend on the size l of the periodicity cell. Note that the elimination of axial displacement dependent terms is possible only when end displacements are restrained, but not necessarily equal to zero.

4.2. The tolerance-asymptotic model

In cases when we restrict ourselves to investigate the low frequency vibrations, we can pass with the periodicity cell length to zero, $l \rightarrow 0$. Then, some of the coefficients of equations (4)-(5) vanish. Introducing the following denotations:

$$\begin{aligned} D^{eff} &\equiv \langle EJ \rangle - \langle EJ\partial^2 h^A \rangle \langle EJ\partial^2 h^A \partial^2 h^B \rangle^{-1} \langle EJ\partial^2 h^B \rangle, \\ B^{eff} &\equiv \langle EA \rangle - \langle EA\partial g^K \rangle \langle EA\partial g^K \partial g^L \rangle^{-1} \langle EA\partial g^L \rangle, \end{aligned} \tag{7}$$

equations of the tolerance-asymptotic model take the form:

$$\begin{aligned} & D^{eff}\partial^4 W - \overline{N}\partial^2 W + C\dot{W} + M\ddot{W} - Q = 0, \\ & \overline{N} = \frac{B^{eff}}{2L}\int_0^L \partial W \partial W dx + \frac{B^{eff}}{L}\Delta_0, \quad \Delta_0 = \int_0^L \partial U dx = U(L) - U(0) \end{aligned} \tag{8}$$

The usefulness of the above formulation is restricted to analysis of long-wave modes, for which the length scale effect is not of high importance. Nevertheless, in many practically important issues such approximation is acceptable.

5. Applications

Let us investigate a piecewise-prismatic beam of length L, and periodically variable cross-section, as it is shown in Figure 2. The material of the beam is elastic and homogeneous.

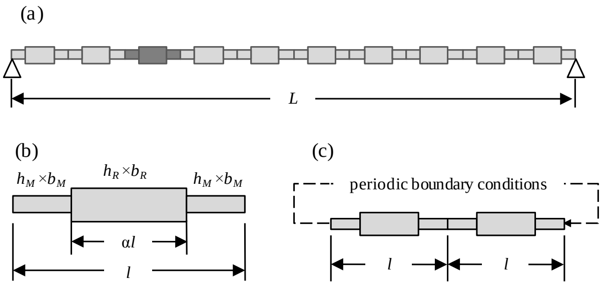

Figure 2. Scheme of the analysed beam (a), a periodicity cell (b), and periodic boundary conditions (c)

The fluctuation shape functions were obtained from a finite element analysis of a two-cell system. Each subsection of a periodicity cell was divided into two elements based on Hermite polynomials and the periodic boundary conditions were assumed, as indicated in Figure 2(c). The obtained mode shapes can be divided into two groups of even (*ESF*) and odd (*OSF*) shape functions, cf. Figure 3.

The solutions to the tolerance model and the load were assumed as finite sums:

$$\begin{Bmatrix} W(x,t) \\ Q(x,t) \end{Bmatrix} = \sum_{m=1}^{M_w} \begin{Bmatrix} W_m(t) \\ Q_m(t) \end{Bmatrix} X_m(x), \quad \begin{Bmatrix} V^A(x,t) \\ Q^A(x,t) \end{Bmatrix} = \sum_{n=1}^{M_V^A} \begin{Bmatrix} V_n^A(t) \\ Q_n^A(t) \end{Bmatrix} Y_n^A(x), \quad A = 1,\ldots,N, \tag{9}$$

where the functions X_m and Y^A_n were chosen to satisfy the boundary conditions of a simply supported beam:

$$X_m(x) = \sin(m\pi x/L), \quad Y_n^A(x) = \begin{cases} \sin(n\pi x/L) & \text{for } A \in ESF, \\ \cos[(n-1)\pi x/L] & \text{for } A \in OSF. \end{cases} \tag{10}$$

That leads to the following system ordinary differential equations of second order:

$$[\mathbf{K}_0 + \mathbf{K}_{NL}(\mathbf{y})]\mathbf{y} + \mathbf{C}\dot{\mathbf{y}} + \mathbf{M}\ddot{\mathbf{y}} = \mathbf{f}. \tag{11}$$

After dropping the nonlinear, damping and forcing terms the linear natural frequencies and mode shapes are determined from analysis of the generalized eigenvalue problem. The results of comparison with a full finite element model of a beam are presented in Section 5.1.

Then, the nonlinear model based on the asymptotic approximations (8) is applied in analysis of damped forced vibrations. It is justified only when the forcing frequency is of the order of the few lowest natural frequencies of the beam. The analysed equations and used denotations are given by formulas (12) and (13), respectively.

$$\begin{aligned} &\omega_m^{\,2} w_m(t) + \ddot{w}_m(t) + 2\beta \dot{w}_m(t) + \\ &\quad + \gamma_m \sum_n n^2 w_n(t)^2 w_m(t) + P_m w_m(t) - p_m f_0 \cos \Omega t = 0, \end{aligned} \tag{12}$$

$$\begin{aligned} &\omega_m = \left(\frac{m\pi}{L}\right)^2 \sqrt{\frac{D^{eff}}{M}}, \quad \gamma_m = \frac{m^2}{4}\left(\frac{\pi}{L}\right)^4 \frac{B^{eff}}{M}, \\ &P_m = \left(\frac{m\pi}{L}\right)^2 \frac{B^{eff}}{M}\frac{\Delta_0}{L}, \quad \beta = \frac{C}{2M}, \quad p_m = \frac{q_m}{M}. \end{aligned} \tag{13}$$

The results of analysis are briefly described in Section 5.2.

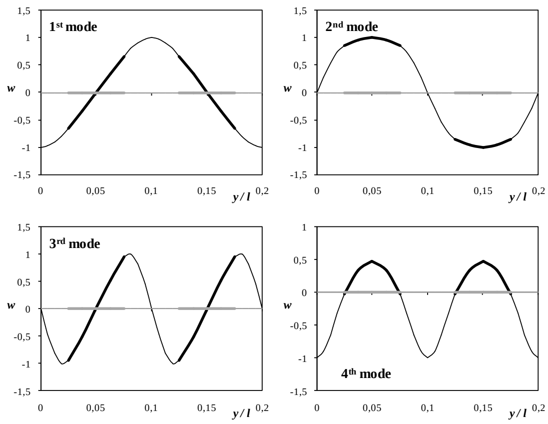

Figure 3. The first four modes of a two-cell system used as fluctuation shape functions

5.1. Natural linear frequencies and mode shapes

The object of this section is to perform a limited confidence check of the model accuracy. The analysed beam (cf. Figure 2) has length $L = 1.0$ m, the elastic modulus is $E = 205$ GPa, the mass density $\rho = 7850$ kg/m3. The cross section is rectangular: $b_M = b_R = 10$ mm, $h_M = 5$ mm, $h_R = 10$ mm, other geometric parameters of the cell are $l = 1/10$ m, $\alpha = 1/2$.

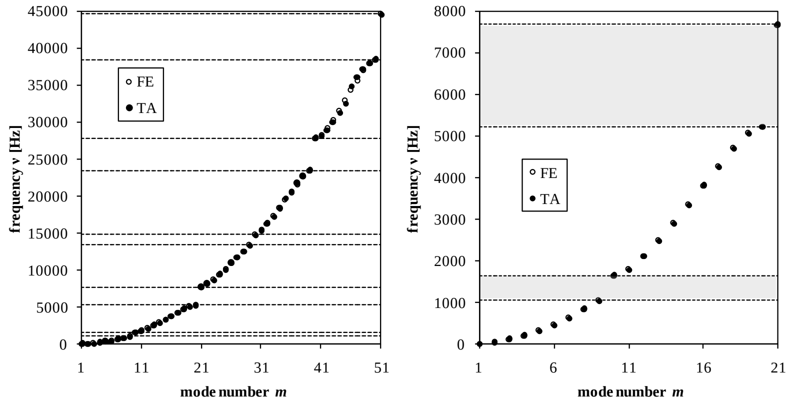

Figure 4. Comparison of first 51 (left) and first 21 (right) natural frequencies obtained from tolerance (closed circles) and finite element model (open circles)

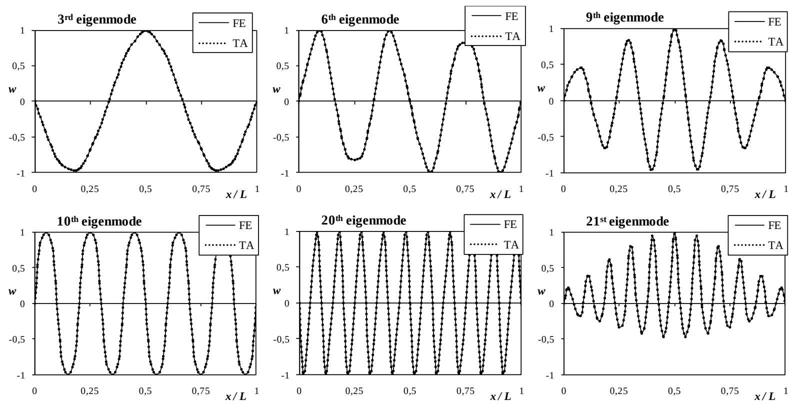

Figure 5. Comparison of chosen natural modes of considered beam obtained from tolerance (TA - dotted lines) and finite element (FE - solid lines) model.

The first four of 23 modes of a two-cell assemblage used as fluctuation shape functions are shown in Figure 3. For comparison, a finite element model of the full beam has been formulated. The natural frequencies and mode shapes were determined from the equation $\det(\mathbf{K}_0 - \omega^2\mathbf{M})=0$, cf. (11). Figure 4 presents the comparison between tolerance modelling (TA) and finite element (FE) results for first 51 frequencies and its close-up in the range of first 21 frequencies, where the lower band-gaps are more visible. The 3rd, 6th, 9th, 10th, 20th and 21st natural modes obtained from both models are depicted in Figure 5. The results are in good agreement. It has to be mentioned that all the upper and lower boundaries of band gaps correspond to the first (n=1) modes of fluctuation amplitudes, cf. relationships (9) and (10). The proposed model gives satisfactory results not only in the low frequency range.

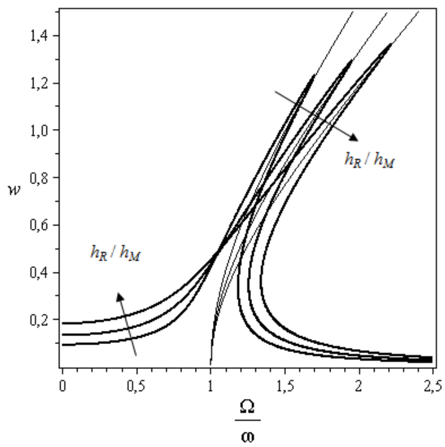

Figure 6. Backbone and amplitude-frequency curves

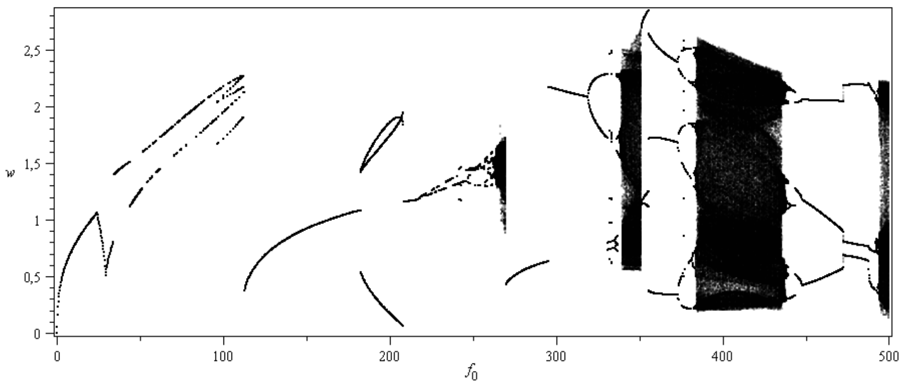

Figure 7. Bifurcation diagram of central deflection w versus forcing amplitude f_0

5.2. Nonlinear vibrations analysis

Let us consider a problem of forced damped vibrations of a beam introduced in the beginning of this section, governed by the equations (12). The material and geometric parameters remain the same, although three cases were considered here: a) $\alpha = 4/5$, $h_R / h_M = 13/8$; b) $\alpha = 1/2$, $h_R / h_M = 2$; c) $\alpha = 1/5$, $h_R / h_M = 3$. That is, the total mass of the beam is kept constant, but the effective bending and axial stiffness is: $D^{eff} = \{55.259;\ 37.963;\ 26.538\}$ Nm^2, and $B^{eff} = \{1.481;\ 1.367;\ 1.196\}\times 10^7$ N, and the first natural linear frequencies are $\omega_1 = \{95.617;\ 79.253;\ 66.263\}$ rad/s. The coefficient of the external damping was assumed to be $c = 2.5$ Ns/m.

First, the one-term approximation of to the equations (12) has been used to determine the backbone curves and amplitude-frequency response curves shown in Figure 6. Light forcing amplitude ($f_0 = 4.25$) and forcing frequency near the fundamental frequency was assumed. Next, five-term approximation to these equations has been applied in analysis of long-term forced vibrations for case (b). The forcing frequency is equal to the first natural frequency of the beam. The bifurcation diagram with forcing amplitude f_0 as a parameter is displayed in Figure 7. Complicated behaviour of the system is exposed, including periodic oscillations, symmetry breaking and saddle-node bifurcations, as well as period-doubling routes to chaos. More detailed analysis of the results will be presented and discussed in forthcoming papers.

6. Conclusions

It can be concluded that the presented model properly describes the crucial dynamic characteristics of beams with periodic structure and it can be used as a reliable tool in parametric analysis of vibration problems. The advantage of proposed approach is that it allows for the construction of models of low degree of freedom number.

Acknowledgement

The authors are grateful for the support provided by the National Science Centre, Poland (Grant No. 2014/15/B/ST8/03155).

References

1. A. Bensoussan, J. L. Lions, G. Papanicolaou, *Asymptotic analysis for periodic structures*, North-Holand, Amsterdam 1978.
2. Ł. Domagalski, M. Gajdzicki, *Moderately large deflections of thin densely ribbed plates*, in: W. Pietraszkiewicz, J. Górski (eds.), Shell Structures: Theory and Applications, Taylor & Francis Group, London, **3** (2014) 77 – 80.
3. Ł. Domagalski, J. Jędrysiak, *Nonlinear vibrations of periodic beams*, Vibrations in Physical Systems, **26** (2014) 73 – 78.
4. A. G. Kolpakov, *The governing equations of a thin elastic stressed beam with a periodic structure*, Journal of Applied Mathematics and Mechanics, **63**(3) (1999) 495 – 504.
5. B. Tomczyk, C. Woźniak, *Tolerance models in elastodynamics of certain reinforced thin-walled structures*, in: Z. Kołakowski, K. Kowal-Michalska (eds.), Statics, Dynamics and stability of Structural Elements and Systems, TUL PRESS, Łódź, **2** (2012) 123 – 153.
6. C. Woźniak et al. (eds.), *Mathematical modeling and analysis in continuum mechanics of microstructured media*, Wydawnictwo Politechniki Śląskiej, Gliwice 2010.

Estimation of the Contact Forces Between the Hexapod Legs and the Ground During Walking in the Tripod Gait

Dariusz GRZELCZYK
Department of Automation, Biomechanics and Mechatronics
Lodz University of Technology, TUL, 1 /15 Stefanowski Str., 90-924 Lodz
dariusz.grzelczyk@p.lodz.pl

Bartosz STAŃCZYK
Department of Automation, Biomechanics and Mechatronics
Lodz University of Technology, TUL, 1 /15 Stefanowski Str., 90-924 Lodz
bartosz.stanczyk@dokt.p.lodz.pl

Jan AWREJCEWICZ
Department of Automation, Biomechanics and Mechatronics
Lodz University of Technology, TUL, 1 /15 Stefanowski Str., 90-924 Lodz
jan.awrejcewicz@p.lodz.pl

Abstract

The paper is devoted to the dynamical modelling of the hexapod robot walking on a flat and hard ground. The main goal is to determine time series of reaction forces acting on individual legs of the robot during tripod gait often used both by the six-legged insects as well as mobile walking robots found in engineering applications. The movement of the considered robot is realized by the kinematic excitation of its legs using the so-called Central Pattern Generator (CPG) method. The paper demonstrates that there are different contact forces and overload acting on the robot, resulting from different models working as a CPG. The mentioned forces belong to the important issues that should be taken into account when the robot locomotion on the unknown terrain is planned.

Keywords: Multi-legged robot, six-legged robot, hexapod, tripod gait, contact forces, reaction forces

1. Introduction

Legged locomotion is the most common locomotion form in nature and numerous animals species use this method for travelling on our planet. For many researchers, it became the inspiration for the construction of walking machines for engineering applications [1,2]. It should be noted that there are lots of biological inspirations and constructed robots in the scientific literature (including hexapod-type robots), and interesting state-of-the-art in this area can be found in recent paper [3]. Lately, also eight-legged robots have become popular, for instance a biomimetric robot called Scorpion [4], or searching and rescuing robot Halluc II [5]. The mentioned eight-legged robots are popular and usually studied based on the six-legged walking machines. Hexapod robots, due to their simplicity, statical and dynamical stability as well as due to large configuration of various possible gaits (described by the so-called MhGee formula [6]) have been studied by many researchers over the past decades. However, in comparison to the wheeled vehicles, legged locomotion is characterized by more non-uniform distribution of reaction forces acting between the mentioned mobile machines and the ground. Namely, in the case of wheeled motion, usually all the wheels touch the ground at the same time, and the appropriate contact pressure distribution is almost the same in each phase of the machine movement. In turn, in the case of the legged locomotion, reaction forces between the ground and legs forming the support polygon of the robot vary in a periodic manner. In addition, fluctuations of the robot gravity center have a significant impact on the reaction forces between the legs of the robot and the ground, due to present additional dynamic load resulting from the movement of the individual elements of the robot in the gravitational field of the Earth. In the case of relatively small contact surfaces of the robot leg tips with the ground and the simultaneous transport of an additional mass by the robot, the problem of the reaction forces acting on the ground may be significantly important for this system. In engineering calculations, the appropriate mathematical models are rarely used, since engineers usually employ commercial software, such as SimMechanics module of MATLAB [7,8]. This is why in this paper the mentioned problem has been considered in more detail by adopting the appropriate dynamic robot model, taking kinematic excitation of the robot legs, and focusing on the reaction forces acting along the direction of the gravity field. The problem of controlling individual robot legs has been presented in our previous paper [10] and in this work is not considered in detail.

2. Model of the Hexapod Robot for the Tripod Gait

Figure 1 shows a model of the considered hexapod robot embedded in the gravity field with coefficient g, supported by three legs forming the support polygon. The robot consists of a body with mass M_B and six identical legs denoted as L1, L2, L3 (on the left) and R1, R2, R3 (on the right). Each leg of the robot contains three links with masses m_1, m_2 and m_3, respectively. In the case of the tripod gait, the robot legs are divided into two groups, i.e.: the group A (solid legs L1, L3 and R2) and group B (dashed legs R1, R3 and L2). The movements of all robot legs are controlled by the same CPG model, however, the signals applied to the group B of the legs (joint angles $\varphi_{1B}(t)$, $\varphi_{2B}(t)$, $\varphi_{3B}(t)$) are out of phase with respect to signals applied to the group A (joint angles $\varphi_{1A}(t)$, $\varphi_{2A}(t)$, $\varphi_{3A}(t)$), with shift phase equal to 180°, and vice versa. For this reason, in one phase the robot is supported by the legs from group A, and in another phase - by the legs from group B. As a result, ground reaction forces to respective foot robot appear on different legs. In addition, due to the symmetry of the considered system, we can assume that the reaction forces in legs L1 and L3 are the same, as well as are the reaction forces in legs R1 and R3. In the considered case we assume that the robot walks on a relatively hard ground. This is why it can be assumed that there is no rotation of the robot body, and therefore the corresponding rotational movements and moments of inertia of the robot body can be neglected. The presented robot consists of many connected parts (including six identical legs). Without loss of generality, and to increase transparency of illustration, only one leg has been precisely described in Fig 1.

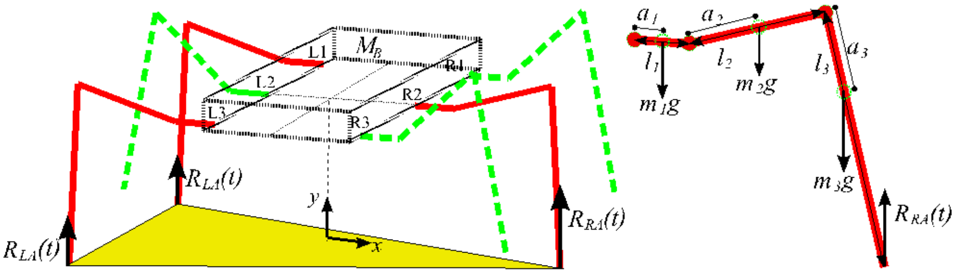

Figure 1. Model of the considered hexapod robot

Equations of motion of the hexapod robot considered in Fig. 1 in y direction can be written as follows

$$2R_{LA}(t)+R_{RA}(t)=\left(6\sum_{i=1}^{3}m_i+M_B\right)g+M_B\ddot{y}_C(t)+$$
$$+2\sum_{i=1}^{3}m_i\ddot{y}_{iLA}(t)+\sum_{i=1}^{3}m_i\ddot{y}_{iRA}(t)+2\sum_{i=1}^{3}m_i\ddot{y}_{iRB}(t)+\sum_{i=1}^{3}m_i\ddot{y}_{iLB}(t) \tag{1}$$

if $h_A(t)\geq h_B(t)$, and

$$2R_{RB}(t)+R_{LB}(t)=\left(6\sum_{i=1}^{3}m_i+M_B\right)g+M_B\ddot{y}_C(t)+$$
$$+2\sum_{i=1}^{3}m_i\ddot{y}_{iLA}(t)+\sum_{i=1}^{3}m_i\ddot{y}_{iRA}(t)+2\sum_{i=1}^{3}m_i\ddot{y}_{iRB}(t)+\sum_{i=1}^{3}m_i\ddot{y}_{iLB}(t) \tag{2}$$

if $h_A(t)<h_B(t)$, where

$$h_A(t)=\left|l_2\sin\varphi_{2A}(t)-l_3\sin(\varphi_{3A}(t)-\varphi_{2A}(t))\right|, \tag{3}$$

$$h_B(t)=\left|l_2\sin\varphi_{2B}(t)-l_3\sin(\varphi_{3B}(t)-\varphi_{2B}(t))\right|, \tag{4}$$

$$y_C(t)=\begin{cases}h_A(t) & \text{if} \quad h_A(t)\geq h_B(t)\\ h_B(t) & \text{if} \quad h_A(t)<h_B(t)\end{cases}, \tag{5}$$

$$y_{1RA}(t)=y_{1LA}(t)=y_{1RB}(t)=y_{1LB}(t)=y_C(t), \tag{6}$$

$$y_{2RA}(t)=y_{2LA}(t)=y_C(t)+a_2\sin\varphi_{2A}(t), \tag{7}$$

$$y_{2RB}(t)=y_{2LB}(t)=y_C(t)+a_2\sin\varphi_{2B}(t), \tag{8}$$

$$y_{3RA}(t)=y_{3LA}(t)=y_C(t)+l_2\sin\varphi_{2A}(t)-a_3\sin(\varphi_{3A}(t)-\varphi_{2A}(t)), \tag{9}$$

$$y_{3RB}(t)=y_{3LB}(t)=y_C(t)+l_2\sin\varphi_{2B}(t)-a_3\sin(\varphi_{3B}(t)-\varphi_{2B}(t)). \tag{10}$$

Next, taking into account symmetrical distribution of the robot legs and partial compensation of their mutual movements, we assume that $R_{RA}(t)\approx 2R_{LA}(t)$ and

$R_{LB}(t) \approx 2R_{RB}(t)$. The exact solution to this problem requires consideration of additional equations for moments of the forces generated by the individual reaction forces, gravity forces acting on the mass centers and inertial forces resulting from movements of individual elements of the robot legs in the considered coordinate system. This problem requires more complicated numerical algorithm and will be the subject of our further research.

3. Numerical Results

This section presents numerical simulations obtained with the use of Mathematica 10 software. Parameters of the considered robot gait are the same as in our previous paper [10], namely: the stride length of 60 mm, the stride height of 30 mm. However, the mentioned simulations have been obtained for two different periods of the single robot stride equal to 2 s and 1 s, respectively. In the first case the average velocity of the robot movement in the forward direction is 30 mm/s and in the second one is equal to 60 mm/s. This approach allows for additional investigation of the influence of robot velocity on the estimated contact forces. The aforementioned kinematic excitation of the robot legs is realized using four different CPG models based on simple mechanical oscillators, namely: Hopf oscillator, van der Pol oscillator, Rayleigh oscillator as well as oscillator describing stick-slip vibrations (further referred to as a stick-slip oscillator) [10]. Other parameters required for numerical simulations are presented in Table 1.

Table 1. Parameters of the considered hexapod robot

Quantity	Symbol	Unit	Value
Mass of the robot body (without legs)	M_B	kg	2.00
Masses of the robot leg parts	m_1 ; m_2 ; m_3	kg	0.12; 0.05; 0.15
Lengths of the robot leg links	l_1 ; l_2 ; l_3	m	0.027; 0.07; 0.12
Displacements of the mass centers	a_1 , a_2 , a_3	m	0.0135; 0.035; 0.04
Gravity coefficient	g	m/s^2	9.81

Figure 2 depicts the trajectories plotted by the robot gravity center (fluctuations $y_C(t)$ of the robot gravity center in the vertical direction) and trajectories plotted by the tips of the robot legs (group A - solid line, group B - dashed line). As can be seen, in the case of first three oscillators controlling robot legs, considerable fluctuations of the robot gravity center can be observed. These fluctuations have a great impact on the contact forces acting on the individual legs of the robot due to its acceleration/deceleration in the vertical direction.

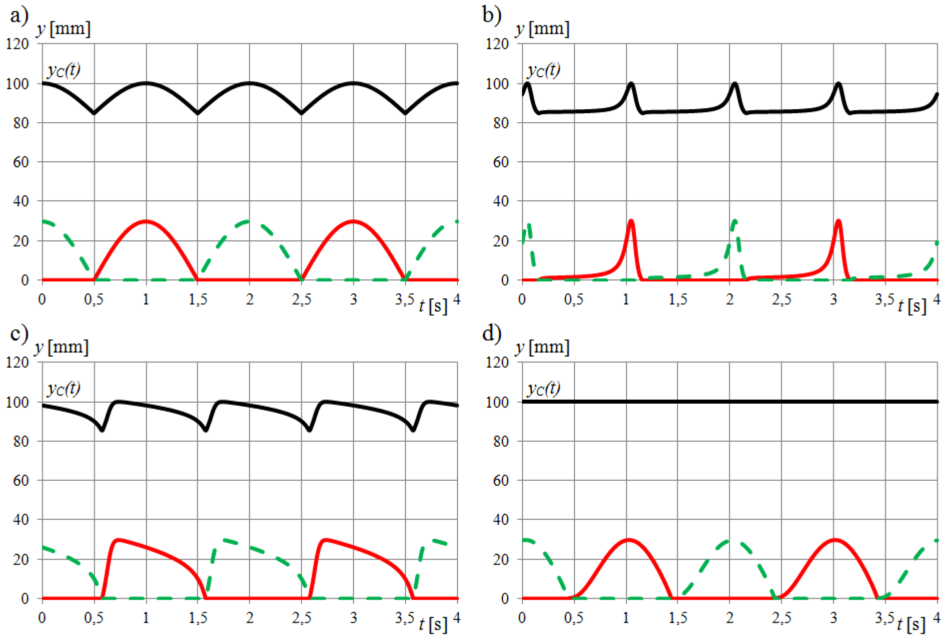

Figure 2. Fluctuations of the robot gravity center $y_C(t)$ and trajectories plotted by the robot legs for the period of the single robot stride equal to 2 s: a) Hopf oscillator; b) van der Pol oscillator; c) Rayleigh oscillator; d) stick-slip oscillator. Solid line - group A of the robot legs; dashed line - group B of the robot legs

Figure 3 shows time series of contact forces acting on the robot legs for the period of the single robot stride equal to 2 s. Due to the previously adopted assumptions, the largest contact reactions forces between the legs and the ground occur in the central legs (L2 and R2), and this is why only these reactions are presented (reaction forces in the lateral robot legs are two times smaller). The presented curves show that the appropriate reaction forces oscillate (increase and decrease) around the reaction force resulting from the weight of the robot (when none of its components is moved). As can be seen, the most frequent oscillations (overloads) occur in the case of using van der Pol oscillator and the Rayleigh one as a CPG model. In turn, the lowest fluctuations exist when the stick-slip oscillator is applied. Similar conclusions can be achieved considering the reaction forces shown in Fig. 4, where the appropriate curves have been obtained for two times larger velocity of the robot movement. However, for larger velocities of the robot movement, there are larger dynamic overloads and the appropriate reaction forces. This occurs due to faster and more frequent oscillations of the robot gravity center and other elements of its legs. As can be seen, the stick-slip oscillator does not have this disadvantage (there is only slight dynamical overload in comparison to other CPG models).

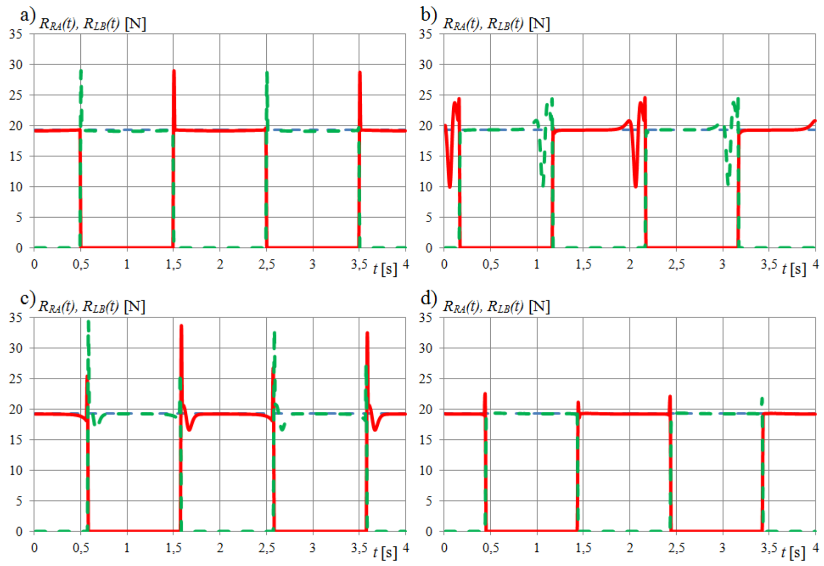

Figure 3. Time series of the reaction forces for the period of the single robot stride equal to 2 s: a) Hopf oscillator; b) van der Pol oscillator; c) Rayleigh oscillator; d) stick-slip oscillator. Solid line denotes $R_{RA}(t)$, whereas dashed line denotes $R_{LB}(t)$

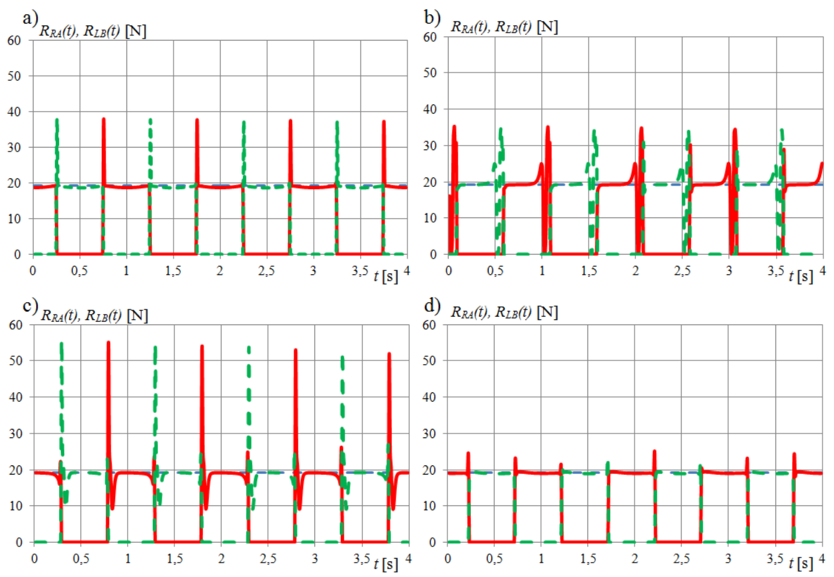

Figure 4. Time series of the reaction forces for the period of the single robot stride equal to 1 s: a) Hopf oscillator; b) van der Pol oscillator; c) Rayleigh oscillator; d) stick-slip oscillator. Solid line denotes $R_{RA}(t)$, whereas dashed line denotes $R_{LB}(t)$

4. Conclusions

In the paper, time series of the reaction forces acting on the individual robot legs and occurring undesirable dynamic overloads caused mainly by strong fluctuations of the center of gravity of the robot are obtained numerically. The robot movement has been kinematically excited by different well-known mechanical oscillators working as the CPG models, and to simulate the robot locomotion the tripod gait has been chosen. The choice of such a type of the robot gait has its justification. First, this type of gait is most commonly used by both the six-legged insects as well as six-legged walking machines in engineering applications. Second, in the case of the tripod gait, in general, at each moment of the robot movement the support polygon is formed only by three legs and the corresponding reaction forces are greater than in the case of other gaits (for instance, in case of tetrapod gait or wave gait). In addition, the choice of a relatively hard ground has also its justification, since this type of surface generates larger reaction force and correspondingly greater dynamic overload. In the considered type of gait and movement on the hard ground, the largest reaction forces and dynamic overload are expected, which justifies the choice to study this kind of the robot gait and this type of the ground. Different reaction forces and overload acting on the robot, being the result of using different CPG models to control its motion, have been illustrated and discussed. However, it should be noted that the obtained reaction forces have been obtained by double differentiation of displacements of the gravity centers of individual elements of the robot. The exact value of reaction forces at the moment of changing of supported legs depends strongly on the stiffness and damping of both the ground and construction of the robot. Nevertheless, the obtained simulations allow to compare the generated reaction forces for different CPG models which control the robot motion. The obtained information can be used in the future for analyzing the strength of the robot legs, being important for trouble-free uses and extension of life and operational time of the robot. Reaction forces occurring on the contact surfaces between the robot legs and the ground belong to one of the most important issues which should be taken into account.

Acknowledgments

The work has been supported by the National Science Centre of Poland under the grant MAESTRO 2 no. 2012/04/A/ST8/00738 for years 2012-2016.

References

1. T. Zielińska, *Biological inspiration used for robots motion synthesis*, J. Physiol-Paris, **103** (2009) 133 – 140.
2. T. Zielińska, C. M. Chew, P. Kryczka, T. Jargilo, *Robot gait synthesis using the scheme of human motion skills development*, Mech. Mach. Theory, **44**(3) (2009) 541 – 558.
3. X. Chen, L. Wang, X. Ye, G. Wang, H. Wang, *Prototype development and gait planning of biologically inspired multi-legged crablike robot*, Mechatronics, **23** (2013) 429 – 444.

4. B. Klaassen, R. Linnemann, D. Spenneberg, F Kirchner, *Biomimetic walking robot SCORPION: control and modeling,* Robot. Auton. Syst., **41** (2002) 69 – 76.
5. http://www.pinktentacle.com/2007/07/halluc-ii-8-legged-robot-vehicle/
6. R.B. McGhee, *Vehicular legged locomotion,* Adv. in Autom. and Robot., (1985).
7. E. Burkus, P. Odry, *Mechanical and Walking Optimization of a Hexapod Robot using PSO,* IEEE 9th International Conference on Computational Cybernetics, July 8-10, 2013, Tihany, Hungary.
8. D. Thilderkvist, S. Svensson, *Motion Control of Hexapod Robot Using Model-Based Design,* MSc Thesis. Department of Automatic Control, Lund University, SE-221 00 LUND, Sweden.
9. D. Grzelczyk, B. Stańczyk, J. Awrejcewicz, *On the Hexapod Leg Control with Nonlinear Stick-Slip Vibrations,* App. Mech. and Mat., **801** (2015) 12 – 24.
10. D. Grzelczyk, B. Stańczyk, J. Awrejcewicz, *Prototype, control system architecture and controlling of the hexapod legs with nonlinear stick-slip vibrations*, Mechatronics (2016), http://dx.doi.org/10.1016/j.mechatronics.2016.01.003.

Power Distribution in Anti-Vibration Gloves

Tomasz HERMANN
Poznan University of Technology, Institute of Applied Mechanics
24 Jana Pawła II Street, 60-965 Poznan, tomasz.hermann@put.poznan.pl

Marian Witalis DOBRY
Poznan University of Technology, Institute of Applied Mechanics
24 Jana Pawła II Street, 60-965 Poznan, marian.dobry@put.poznan.pl

Abstract

The article analyses power distribution in an anti-vibration glove. The glove of interest was modelled in a biodynamic model of the Human – Glove – Tool system. The model was a combination of the human model and the glove model specified in the ISO 10068:2012 standard and the model of the vibration tool. To determine the power distribution in the glove, its energy model was developed. The power distribution in the model was determined using numerical simulation in order to show how power was distributed in the dynamic structure of the anti-vibration glove. Three kinds of powers were distinguished, which are related to forces of inertia, dissipation and elasticity. It turned out that out of the three kinds of powers identified in the anti-vibration glove, only one is dominant: namely the power of dissipation.

Keywords: biomechanical system, hand-arm vibrations, power distribution, energy method

1. Introduction

The first important stage of modelling consists in a systematic analysis of the real object. One should remember that the researcher's awareness, knowledge and needs affect the degree to which he or she simplifies the reality. This implies that the process of modelling depends, above all, on the degree of simplification which is applied to the real object. What is more, a model always replaces the object of study and only resembles it with respect to certain characteristics selected by the researcher [8].

A model can be similar to the real object in terms of structure. This means that the model represents features of the internal structure which it shares with the real object. Another kind of similarity is functional compatibility. Unfortunately, this kind of model does not lend itself to a precise assessment of its structure [8]. These facts are especially important when one wants to select a model to determine the impact of vibrations on the human body.

Nowadays the human response to vibration can be analysed using of a range of discrete human models that are available in the literature [6, 7, 10, 11]. These models differ from one another with respect to the number of degrees of freedom, the number of components making up the dynamic structure and the way they are connected. In other words, all of these models have different structures and differ in the way they transmit, dissipate and store vibration energy. In this study the analysis of the impact of vibration on the human body is based on the human model from the ISO 10068:2012 standard [11], which was used as part of the bigger biodynamic model of the Human – Glove – Tool system (H – G – T).

The approach presented in this article is completely different from those adopted to analyse anti-vibration gloves so far. Until recently studies of anti-vibration gloves were limited to computing coefficients to measure the effectiveness of vibroisolation [5]. This approach only involved comparing system responses and determining factor changes between them as a result of applying the anti-vibration glove. What is more, exact requirements for anti-vibration gloves are specified in the relevant standards [4, 9, 12].

This article, in contrast, describes an analysis of the flow of energy through the glove, which was treated as an energy transformation system. A similar approach, though applied to machines, was adopted by Cempel, who described it in his works [1, 4]. This article, however, describes the idea of analysing the flow of vibroacoustic energy related to dynamic properties of the system under consideration, which can be used to analyse mechanical and biomechanical systems. The theory developed by Dobry makes it possible to switch from the dynamic analysis implemented in the domain of amplitudes of kinematic quantities to the energy analysis implemented in the power domain [2, 3].

The power distribution in the anti-vibration glove was determined using the energy method. The aim of the analysis was to check whether the discrete model of the anti-vibration glove adopted from the ISO 10068:2012 standard [11] has an appropriate structure. The energy method consists in identifying three kinds of powers related to forces of inertia, dissipation and elasticity. The theoretically determined power distribution in the dynamic structure of the glove will make it possible to identify what happens to the energy of vibration only in the glove as a subsystem of the entire biomechanical H – G – T system.

2. The structure of the energy model

Figure 1 shows the combined H – G – T biodynamic model. The analysis is based on the human and glove models from the ISO 10068:2012 standard [11] The models selected are discrete models containing points of reduction connected through damping and elastic elements. The values of dynamic parameters for both models, that is m_i, k_i and c_i (Fig. 1) specified in the ISO 10068:2012 standard [11].

The human model from the said standard was used to determine values of vibrations along three directions, i.e. along the „x”, „y” and „z” axes. This article describes a simplified case limited to one dominant direction of vibrations, i.e. along the „z” axis, which is the most significant one in tests of many tools.

The H – G – T model must also include a model of the vibration tool. In this case, the tool was limited to one concentrated mass m_T and a sinusoidally varying driving force $F(t)$ acting on the H – G – T system. Hence, the model is assumed to represent a hypothetical situation of an operator using a grinder with an unevenly worn-out grinding disc. Additionally, the dashed line denotes the subsystem analysed by the energy method (Fig. 1), that is the anti-vibration glove.

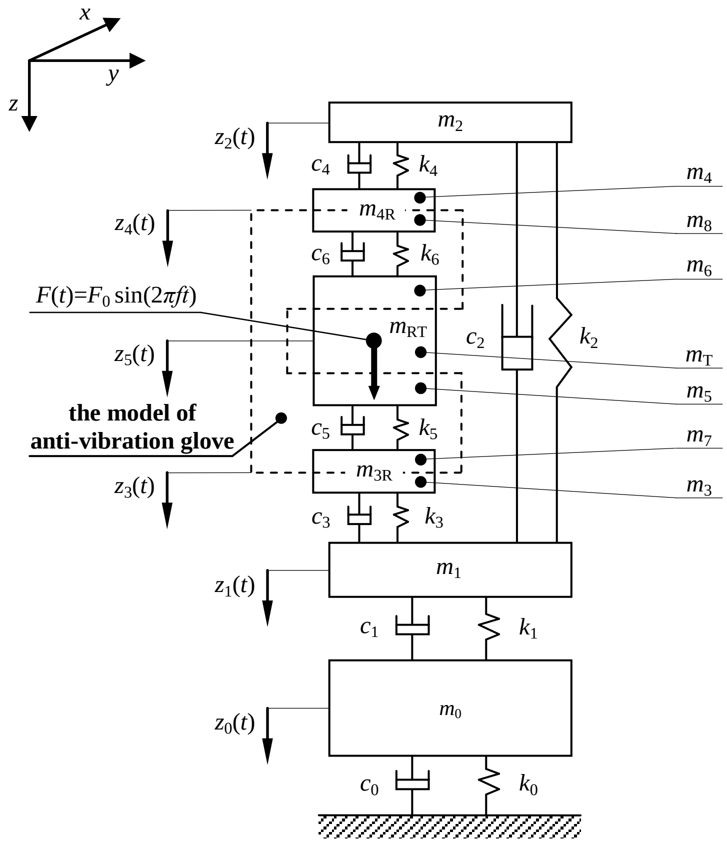

where:

m_0, m_1, m_2, m_3, m_4; k_0, k_1, k_2, k_3, k_4; c_0, c_1, c_2, c_3, c_4 – dynamic parameters in the human physical model

$\boldsymbol{m_5}$**,** $\boldsymbol{m_6}$**,** $\boldsymbol{m_7}$**,** $\boldsymbol{m_8}$; $\boldsymbol{k_5}$**,** $\boldsymbol{k_6}$**,** $\boldsymbol{c_5}$**,** $\boldsymbol{c_6}$ – **dynamic parameters in the glove model**

m_T – tool mass

Points of reduction: $m_{RT} = m_5 + m_6 + m_T$;

$m_{3R} = m_3 + m_7$; $m_{4R} = m_4 + m_8$.

Figure 1. The physical model of the biomechanical H – G – T system, obtained by combining the physical models from the ISO 10068:2012 standard [11] with the tool model

In the first step, a mathematical model of the dynamic structure was derived, using Lagrange equations of the second kind given by:

$$\frac{d}{dt}\left(\frac{\partial E}{\partial \dot{q}_j}\right)-\frac{\partial E}{\partial q_j}=Q_j+Q_{jP}+Q_{jD} \qquad j=1,2,\ldots,s \tag{1}$$

where: E – kinetic energy of the system, q_j – generalized coordinates,
$\dot{q}_j$ – generalized velocities, Q_j – active external forces, Q_{jP} – potential forces,
Q_{jD} – forces of dissipation, s – the number of degrees of freedom.

The mathematical model was fed with generalized coordinates. For the model of the H – G – T system (Fig. 1), the generalized coordinates were as follows:

j = 1, $q_0 = z_0(t)$ – displacement of mass m_0,
j = 2, $q_1 = z_1(t)$ – displacement of mass m_1,
j = 3, $q_2 = z_2(t)$ – displacement of mass m_2,
j = 4, $q_3 = z_3(t)$ – displacement of mass m_{3R},
j = 5, $q_4 = z_4(t)$ – displacement of mass m_{4R},
j = 6, $q_5 = z_5(t)$ – displacement of mass m_{RT}.

After adopting the generalized coordinates, it was possible to derive differential equations of motion for the H – G – T model. The mathematical model in matrix form is given by:

$$\mathbf{M}\ddot{\mathbf{q}}(t)+\mathbf{C}\dot{\mathbf{q}}(t)+\mathbf{K}\mathbf{q}(t)=\mathbf{F}(t) \tag{2}$$

where:

– matrix of displacements: – matrix of masses: – matrix of forces:

$$\mathbf{q}(t)=\begin{bmatrix} z_0(t)\\ z_1(t)\\ z_2(t)\\ z_3(t)\\ z_4(t)\\ z_5(t)\end{bmatrix} \qquad \mathbf{M}=\begin{bmatrix} m_0 & 0 & 0 & 0 & 0 & 0\\ 0 & m_1 & 0 & 0 & 0 & 0\\ 0 & 0 & m_2 & 0 & 0 & 0\\ 0 & 0 & 0 & m_{3R} & 0 & 0\\ 0 & 0 & 0 & 0 & m_{4R} & 0\\ 0 & 0 & 0 & 0 & 0 & m_{RT}\end{bmatrix} \qquad \mathbf{F}(t)=\begin{bmatrix} 0\\ 0\\ 0\\ 0\\ 0\\ F(t)\end{bmatrix}$$

– matrix of damping:

$$\mathbf{C}=\begin{bmatrix} (c_0+c_1) & -c_1 & 0 & 0 & 0 & 0\\ -c_1 & (c_1+c_2+c_3) & -c_2 & -c_3 & 0 & 0\\ 0 & -c_2 & (c_2+c_4) & 0 & -c_4 & 0\\ 0 & -c_3 & 0 & (c_3+c_5) & 0 & -c_5\\ 0 & 0 & -c_4 & 0 & (c_4+c_6) & -c_6\\ 0 & 0 & 0 & -c_5 & -c_6 & (c_5+c_6)\end{bmatrix}$$

– matrix of stiffness:

$$\mathbf{K}=\begin{bmatrix}(k_0+k_1) & -k_1 & 0 & 0 & 0 & 0\\ -k_1 & (k_1+k_2+k_3) & -k_2 & -k_3 & 0 & 0\\ 0 & -k_2 & (k_2+k_4) & 0 & -k_4 & 0\\ 0 & -k_3 & 0 & (k_3+k_5) & 0 & -k_5\\ 0 & 0 & -k_4 & 0 & (k_4+k_6) & -k_6\\ 0 & 0 & 0 & -k_5 & -k_6 & (k_5+k_6)\end{bmatrix}$$

The next step in modelling the H – G – T system involved creating the energy model. The model was formulated by applying the First Principle of Power Distribution in a Mechanical System [2, 3]. The principle enables the switch from the dynamic model to the energy model implemented in the power domain. The model was derived using differential equations of motions (2). The energy model of the H – G – T system (Fig. 1), consists of equations of power given by:

$$\begin{aligned}
&j=1, && m_0\ddot{z}_0\dot{z}_0+(c_0+c_1)\dot{z}_0^2+(k_0+k_1)z_0\dot{z}_0-c_1\dot{z}_1\dot{z}_0-k_1z_1\dot{z}_0=0\\
&j=2, && m_1\ddot{z}_1\dot{z}_1+(c_1+c_2+c_3)\dot{z}_1^2+(k_1+k_2+k_3)z_1\dot{z}_1-c_1\dot{z}_0\dot{z}_1-k_1z_0\dot{z}_1-\\
& && -c_2\dot{z}_2\dot{z}_1-k_2z_2\dot{z}_1-c_3\dot{z}_3\dot{z}_1-k_3z_3\dot{z}_1=0\\
&j=3, && m_2\ddot{z}_2\dot{z}_2+(c_2+c_4)\dot{z}_2^2+(k_2+k_4)z_2\dot{z}_2-c_2\dot{z}_1\dot{z}_2-k_2z_1\dot{z}_2-c_4\dot{z}_4\dot{z}_2-k_4z_4\dot{z}_2=0\\
&j=4, && m_{3\mathrm{R}}\ddot{z}_3\dot{z}_3+(c_3+c_5)\dot{z}_3^2+(k_3+k_5)z_3\dot{z}_3-c_3\dot{z}_1\dot{z}_3-k_3z_1\dot{z}_3-c_5\dot{z}_5\dot{z}_3-k_5z_5\dot{z}_3=0\\
&j=5, && m_{4\mathrm{R}}\ddot{z}_4\dot{z}_4+(c_4+c_6)\dot{z}_4^2+(k_4+k_6)z_4\dot{z}_4-c_4\dot{z}_2\dot{z}_4-k_4z_2\dot{z}_4-c_6\dot{z}_5\dot{z}_4-k_6z_5\dot{z}_4=0\\
&j=6, && m_{\mathrm{RT}}\ddot{z}_5\dot{z}_5+(c_5+c_6)\dot{z}_5^2+(k_5+k_6)z_5\dot{z}_5-c_5\dot{z}_3\dot{z}_5-k_5z_3\dot{z}_5-\\
& && -c_6\dot{z}_4\dot{z}_5-k_6z_4\dot{z}_5=F(t)\dot{z}_5
\end{aligned}\tag{3}$$

The energy model of the H – G – T system was derived using a program implemented in the MATLAB/simulink environment in order to compute curves of powers of inertia, dissipation and elasticity. The energy method makes it possible to analyse each subsystem separately, while taking into account the impact of the other subsystems. For this reason, when analysing the energy model for the whole dynamic structure of the H – G – T system, one should only consider the part of power which is transferred to the anti-vibration glove. In the computations it was necessary to include only those dynamic parameters, which were used to model the glove – the fragment of the model marked off in Fig. 1. RMS values of powers, calculated as sums of powers at all points of reduction in the glove model, were defined as follows:

– the power of inertia expressed in [W]:

$$P_{\mathrm{G-INE}}=\sqrt{\frac{1}{t}\int_0^t\left[(m_5+m_6)\ddot{z}_5\dot{z}_5\right]^2\mathrm{d}t}+\sqrt{\frac{1}{t}\int_0^t\left[m_7\ddot{z}_3\dot{z}_3\right]^2\mathrm{d}t}+\sqrt{\frac{1}{t}\int_0^t\left[m_8\ddot{z}_4\dot{z}_4\right]^2\mathrm{d}t}\tag{4}$$

– the power of dissipation expressed in [W]:

$$P_{\mathrm{G-DIS}} = \sqrt{\frac{1}{t}\int_0^t \left[c_5 \dot{z}_3^2\right]^2 \mathrm{d}t} + \sqrt{\frac{1}{t}\int_0^t \left[c_6 \dot{z}_4^2\right]^2 \mathrm{d}t} + \sqrt{\frac{1}{t}\int_0^t \left[(c_5 + c_6)\dot{z}_5^2\right]^2 \mathrm{d}t} \qquad (5)$$

– the power of elasticity expressed in [W]:

$$P_{\mathrm{G-ELA}} = \sqrt{\frac{1}{t}\int_0^t \left[k_5 z_3 \dot{z}_3\right]^2 \mathrm{d}t} + \sqrt{\frac{1}{t}\int_0^t \left[k_6 z_4 \dot{z}_4\right]^2 \mathrm{d}t} + \sqrt{\frac{1}{t}\int_0^t \left[(k_5 + k_6) z_5 \dot{z}_5\right]^2 \mathrm{d}t} \qquad (6)$$

3. The results of the energy method

In the study the biodynamic model of the H – G – T system was exposed to a sinusoidally varying driving force $F(t)$ with an amplitude of 115 N. The analysis was conducted assuming the value of frequency f = 20 Hz, and tool mass m_{T} = 6 kg.

The energy model was solved using numerical simulation for time t = 100 seconds. Integration was carried out using algorithm ode113 (Adams) with a tolerance of 0.0001. Simulations were implemented in the MATLAB/simulink environment with integration time steps ranging from a maximum value of 0.0001 to a minimum of 0.00001 second.

Figure 2 presents the resulting structural power distribution in the anti-vibration glove. The percentage share of each kind of power was determined by relating it to the total power in the glove. The relationship is expressed by the following formula:

$$S_{\mathrm{Z}} = \frac{P_{\mathrm{Z}}}{P_{\mathrm{G-INE}} + P_{\mathrm{G-DIS}} + P_{\mathrm{G-ELA}}} \cdot 100\% \qquad (7)$$

where:

P_{Z} – RMS value of the power of inertia, dissipation or elasticity determined at all points of reduction in the anti-vibration glove.

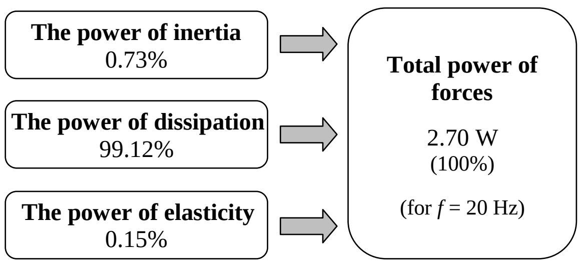

Figure 2. Structural power distribution in the anti-vibration glove for frequency of the driving force f = 20 Hz

The results reveal the power distribution in the dynamic structure of the subsystem under consideration. The results presented in Figure 2 indicate that the dominant role of the power of dissipation forces. The percentage share of the power of dissipation for the frequency of the driving force $f = 20$ Hz exceeded 99% of total power.

This means that the dynamic structure of the glove experiences energy loss (dissipation), with kinetic energy being converted to heat. This implies that the amount of energy transferred to the human body is limited. In other words, the energy method has successfully demonstrated a positive influence of the anti-vibration glove in the H – G – T system. Moreover, the dynamic structure of the glove was correctly modelled, which is confirmed by the results that are consistent with expectations. The study suggests that an anti-vibration glove should be made using materials characterized by high energy dissipation. This implies that the glove should be capable of dissipating large amounts of energy.

4. Summary

The study has resulted in determining the structural power distribution in the anti-vibration glove for the operating frequency $f = 20$ Hz. The results indicate the dominant role of only one kind of power. It turns out that the power of dissipation accounts for over 99% of total power in the glove.

More importantly, the analysis correctly confirmed the anti-vibration properties of the glove. The model structure ensures energy dissipation, which is responsible for decreasing the vibration energy transferred to the human body. This property should be taken into consideration in choosing materials for the manufacturing of anti-vibration gloves.

Further studies will be devoted to specifying the power distribution in the human physical model. Knowing power distributions in these two subsystems will make it possible to assess the level of dynamic load they are exposed to. Another goal will be to calculate the ratio change in the distribution of the three kinds of powers in the dynamic structure of the human and glove model.

Acknowledgments

The study was partly financed by the Ministry of Science and Higher Education as a project entitled: *Energy informational considerations of vibroacoustics, diagnostics and biomechanics of systems*.

Study code: 02/21/DSPB/3478

References

1. C. Cempel, *Minimalizacja drgań maszyn i ich elementów*, w: Współczesne zagadnienia dynamiki maszyn, Ossolineum, Wrocław 1976.
2. M. W. Dobry, *Optymalizacja przepływu energii w systemie Człowiek – Narzędzie – Podłoże*, Ph.D. Thesis, Poznan University of Technology, Poznan, 1998.
3. M. W. Dobry, *Podstawy diagnostyki energetycznej systemów mechanicznych i biomechanicznych*, Wydawnictwo Naukowe Instytutu Technologii Eksploatacji – PIB, Radom 2012.

4. Z. Engel, W. M. Zawieska, *Hałas i drgania w procesach pracy – źródła, ocena, zagrożenia*, CIOP – PIB, Warszawa 2010.
5. J. Koton, J. Szopa, *Rękawice antywibracyjne – ocean skuteczności i zasady doboru do stanowisk pracy*, Bezpieczeństwo Pracy: nauka i praktyka, **11** (1999) 2 – 5.
6. A. M. Książek, *Analiza istniejących modeli biodynamicznych układu ręka – ramię pod kątem wibroizolacji człowieka – operatora od drgań emitowanych przez narzędzia ręczne*, Czasopismo Techniczne, **2** (1996) 87 – 114.
7. S. Rakheja, J. Z. Wu, R. G. Dong, A. W. Schopper, *A comparison of biodynamic models of the Human hand-arm system for applications to hand-held power tools*, Journal of Sound and Vibration, **249**(1) (2002) 55 – 82.
8. B. Żółtowski, *Badania dynamiki maszyn*, MARKAR – B. Ż, Bydgoszcz 2002.
9. EN ISO 10819:1996, *Mechanical vibration and shock. Hand-arm vibration. Method for the measurement and evaluation of the vibration transmissibility of gloves at the palm of the hand.*
10. ISO 10068:1998, *Mechanical vibration and shock – free, mechanical impedance of the human hand-arm system at the driving point*.
11. ISO 10068:2012, *Mechanical vibration and shock – mechanical impedance of the human hand-arm system at the driving point*.
12. PN-EN ISO 10819:2000, *Drgania i wstrząsy mechaniczne. Drgania oddziałujące na organizm człowieka przez kończyny górne. Metoda pomiaru i oceny współczynnika przenoszenia drgań przez rękawice na dłoń operatora.*

Computational Modelling of Vibrations Transmission Loss of Auxetic Lattice Structure

Eligiusz IDCZAK
Institute of Applied Mechanics, Poznan University of Technology
ul Jana Pawla II 24, 60-965 Poznań, Poland
eligiusz.j.idczak@doctorate.put.poznan.pl

Tomasz STREK
Institute of Applied Mechanics, Poznan University of Technology
ul Jana Pawla II 24, 60-965 Poznań, Poland
tomasz.strek@put.poznan.pl

Abstract

In this article dynamical properties of auxetic lattice structures will be analysed. Auxetic structures are materials, which have negative Poisson's ratio and some of these have got specific dynamic properties. Their dynamic behaviour in the frequency domain will be also shown in this article. The possibility of isolation of auxetics will show the factor VTL – Vibration Transmission Loss.

Keywords: auxetics, negative Poisson's ratio, dynamic analysis, VTL factor

1. Introduction

Auxetic materials are materials characterized by negative Poisson's ratio which means that they expand during stretching and shrinks during compressing in the transverse directions to direction of compressing or stretching force. The Poisson's ratio (PR) of isotropic is between -1 and +0.5. Anisotropic materials have non-bounded range for Poisson's ratio.

Materials with negative Poisson's ratio (NPR), at present often referred to as auxetics, have been known for over 100 years and the key to this auxetic behaviour is the negative Poissons ratio [1]. In early 1900s a German physicist Woldemar Voigt was the first to report this property [2] and his work suggested that the crystals somehow become thicker laterally when stretched longitudinally, nevertheless it was ignored for decades.

Gibson [3] in 1982 realized the auxetic effect in the form of the two-dimensional silicone rubber or aluminum honeycombs is deformed by flexure of the ribs. The first mechanical [4] and thermodynamical [5] models were presented by Almgren in 1985 and Wojciechowski in 1987.

Evans et al. paper [6] introduces the term auxetic, from the root word for growth, to describe transverse expansion under uniaxial (longitudinal) tensile load. Re-entrant foams were reported for the first time by Lakes [7]. A negative Poisson ratio implies the substances with negative Poisson's ratio that can be readily compressed but are difficult to bend [8].

Nowadays, it is known that negative Poisson's ratio may also characterize many other structures with other shape and geometries [9]. In the literature are described also: fibre materials, centre-symmetric or gradient honeycombs, chiral structures, auxetic laminates, composites or lattice-like cell structures - sometimes are also designed the combinations of this arts of auxetics. All of them have negative Poisson's ratio. Some of these because of their auxeticity exhibit extraordinary dynamic properties and have great attention by the scientists from many countries [10-19].

Ruzzene et al. [18] in their work have presented the structural and acoustic analysis of truss-core beams. They obtained the optimal geometry of truss-core with the best as possible acoustic behaviour. Their numerical model was created by employing dynamic shape functions derived exactly from the distributed parameter model of beam elements.

Joshi et al. [15] in their works has presented dynamic, acoustic analysis of auxetic composites and its dependency on geometry or number of single repeated cells of material. Structures with negative Poisson's ratio may have unknown and unexpected dynamic behaviour e.g they can be a good isolator or protector from the resonance. The parameter which circumscribed isolation properties is Vibration Transmission Loss, which shows the range of frequency where the structure doesn't transmit vibrations. In order to determine this factor it is useful to define Vibration Transmission Coefficient τ_υ. The Vibration Transmission Loss (VTL) is given by the formula:

$$VTL = 10\log_{10}\frac{1}{\tau_\vartheta} \tag{1}$$

where τ_υ is Vibration Transmission Cofficient (VTC) given by:

$$\tau_\vartheta = \frac{\int_0^{Lt} \omega^2 [u_y(x,\omega)]_t [u_y(x,\omega)]_t \, dx}{\int_0^{Lb} \omega^2 [u_y(x,\omega)]_b [u_y(x,\omega)]_b \, dx} \tag{2}$$

where: ω is frequency [Hz], $u_y(x,\omega)$ - displacement in *y*-direction, indices *t*, *b* – top and bottom layer of auxetic structure. L_t and L_b are lengths of top and bottom boundary of structure.

2. Numerical results

Auxetic lattice-like structure is designed for the analysis of dynamical properties. The structure is built of a repeated unit cell which has geometry parameters as follows: height a, width b and parameter c – height of the notch in the bottom. The Poisson's ratio of this cell is negative and equals -0.915. The single cell can be multiplicated and analysed as complex 3D structure (see Figure 2). This lattice-like structure was tested to find vibration transmission factors. For the simulations the following values were taken: a = 1 m, b = 0.5 m, c = 0.3 m.

In order to facilitate the analysis only one quarter of the 3D structure is considered The boundary conditions are: constant displacement 0.1 m on the top, on the one side of x-axis, y-axis and bottom - roller boundary and on the rest boundaries - free boundary condition.

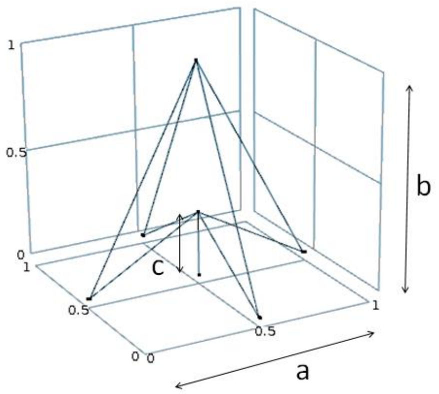

Figure 1. Three-dimensional auxetic unit cell

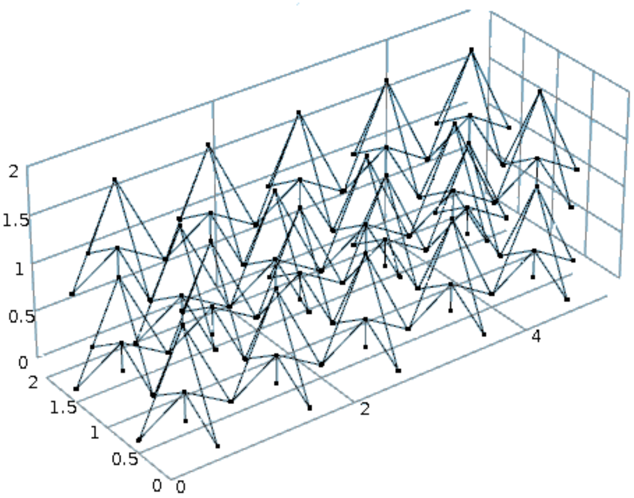

Figure 2. Three-dimensional auxetic structure

The results of simulation by the frequency analysis of the auxetic structure are presented in Figures 3 and 4. These diagrams can be used to analyse the possibility of using the structure to reduce the level of vibrations.

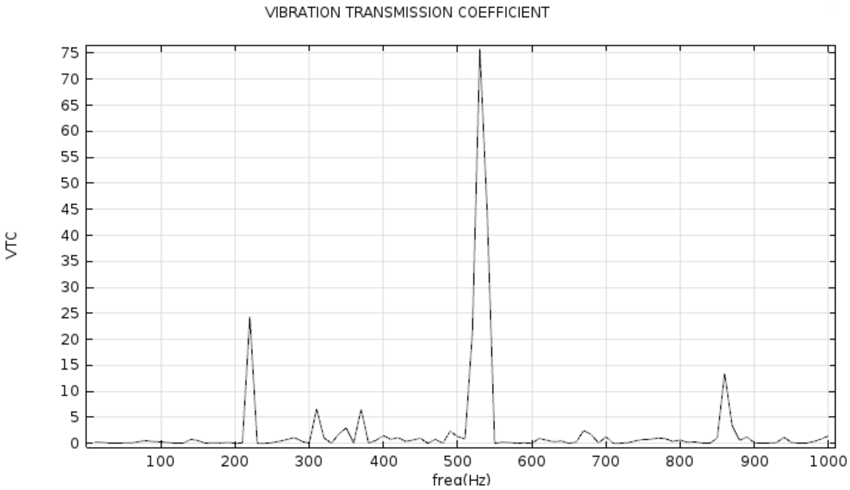

Figure 3. Vibration Transmission Coefficient (VTC) of auxetic structure

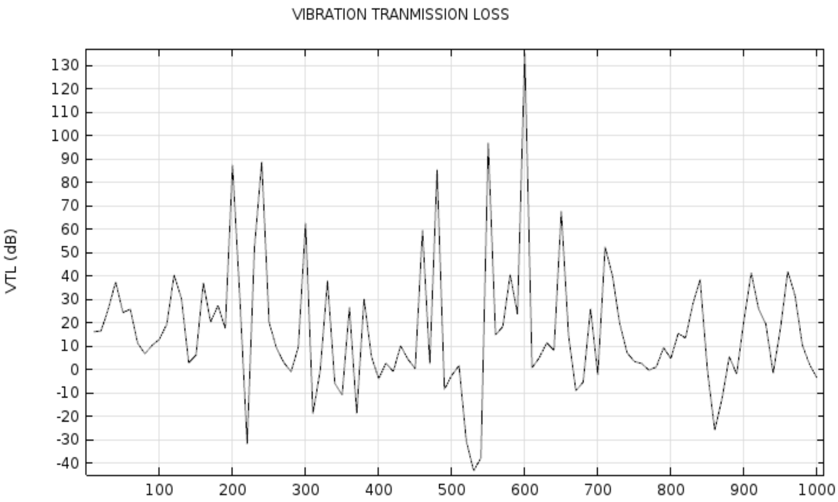

Figure 4. Vibration Transmission Loss (VTL) of analysed auxetic structure

3. Conclusions

A finite element model was developed to evaluate the effective properties and dynamic response of the auxetic lattice structure. The influence of the parameter structure on effective properties and dynamic response (VTL) of structure was investigated.

To cover a wide range of structural resonances, the excitation frequencies of sandwich panels varied from 0 to 1000 Hz. The range of frequency vibration which are most damped is around 200 Hz and 600 Hz. The values of Vibrations Transmission Loss for these frequencies are 90 and 130 decibels respectively. The numerical experiment confirms also the transmission loss of auxetics by some frequencies.

If the geometry parameters are changing e.g. by increasing the value of c twice - to 0.15 m – the auxetic effect is smaller: Poisson's ratio is -0,2. The value of the VTL is greater in 0-1000 Hz and dampens vibration better as in the previous case. Minimal value of VTL in this situation is about -10 dB for frequency 500 Hz. In this case we observe strengthening of vibration.

Acknowledgments

This work has been supported by grants of the Ministry of Science and Higher Education in Poland: 02/21/DSPB/3477/2016 and 02/21/DSMK/3480/2016. The simulations were carried out at the Poznan University of Technology.

References

1. A. E. H. Love, *A Treatise on the Mathematical Theory of Elasticity*, Cambridge University Press (1892).
2. W. Voigt, *Lehrbuch der Kristallphysik*, Leipzig Berlin, B. G. Teubner-Verlag (1928).
3. L. J. Gibson, M. F. Ashby, G. S. Schajer and C. I. Robertson, *The Mechanics of Two-Dimensional Cellular Materials*, Proc R Soc A, **382** (1982) 25 – 42.
4. R. F. Almgren, *An isotropic three-dimensional structure with Poisson's ratio* $=-1$, Journal of Elasticity, **15** (1985) 427 – 430.
5. K. W. Wojciechowski, *Constant thermodynamic tension Monte Carlo studies of elastic properties of a two-dimensional system of hard cyclic hexamers*, Molecular Physics, **61** (1987) 1247-1258.
6. K. E. Evans, M. A. Nkansah, I. J. Hutchinson, S. C. Rogers, S. C, *Molecular network design*, Nature (**353)** 124 (1991).
7. R. S. Lakes, *Foam structures with a negative Poisson's ratio*, Science, **235** (1987) 1038 – 1040.
8. J. Cherfas, *Stretching the Point*, Science, **247** Issue 4943 630 (1990).
9. E. Idczak, T. Strek, Transmission Loss of Auxetic Lattices Vibration Applied Mechanics and Materials, **797** (2015) 282 – 289.
10. A. Spadoni, M. Ruzzene, F. Scarpa, *Dynamic response of chiral truss-core assemblies*, J. of Intelligent Material Systems and Structures, **17**(11) (2006) 941 – 952.

11. T. Strek, H. Jopek, M. Nienartowicz, *Dynamic response of sandwich panels with auxetic cores*, Phys. Status Solidi B, **252**(7) (2015) 1540 – 1550.
12. K. E. Evans, K. L. Alderson, *Auxetic materials: the positive side of being negative*, Engineering Science & Education Journal, **9**(4) (2000) 148 – 154.
13. A. Alderson, K. L. Alderson, *Auxetic materials*, Proceedings of the Institution of Mechanical Engineers, Part G: Journal of Aerospace Engineering, **221**(4) (2007) 565 – 575.
14. K. C. Cheung, N. Gershenfeld, *Reversibly Assembled Cellular Composite Materials*, Science, **341**(13) (2013) 1219 – 1221.
15. H. Joshi, *Finite Element Analysis of effective mechanical properties, vibration and acoustic performance of auxetic chiral core sandwich structures*, All Theses. Paper 1723, Clemson University, Clemson, South Carolina, 2013.
16. K. Bertoldi, P. M. Reis, S. Wilshaw, T. Mullin, *Negative Poisson's Ratio Behavior induced by an Elastic Instability*, Adv. Mater., **22** (2010) 361 – 366.
17. J. T. B. Overvelde, S. Shan, K. Bertoldi, *Compaction Through Buckling in 2D Periodic, Soft and Porous Structures: Effect of Pore Shape*, Adv. Mater., **24** (2012) 2337 – 2342.
18. A. Spadoni, M. Ruzzene, *Structural and Acoustic Behavior of Chiral Truss-Core Beams*, Journal of Vibration and Acoustics, **128**(5) (2006) 616-626.
19. R. R Galgalikar, *Design automation and optimization of honeycomb structures for maximum sound transmission loss*, Clemson University (2012).

Determination of Acoustic Parameters of Devices with Extensive Sound Sources

Bartosz JAKUBEK
Poznan University of Technology, Institute of Applied Mechanics
24 Jana Pawla II, 60-965 Poznan, bartosz.jakubek@put.poznan.pl

Roman BARCZEWSKI
Poznan University of Technology, Institute of Applied Mechanics
24 Jana Pawla II, 60-965 Poznan, laboratoria@tlen.pl

Abstract

In most cases, while the sound power level of machines and devices is determined, it is assumed that tested objects are sound sources which can fit in a so-called reference box. Such an approach takes into account the influence of local sources. Although it does not allow their localization, separate noise measurement and evaluation. There are devices which have two or more relevant sound sources. In this paper this type of devices has been defined as devices with extensive sound sources (DESS). The tested device is a functional unit but its local sound sources are distant from each other. The results showed that determining the sound power level only is not sufficient for proper parameterization of noise emitted by DESS.

Keywords: devices with extensive sound sources (DESS), sound power level, biomedical devices

1. Introduction

The determination of acoustic parameters of devices with extensive sound sources (DESS), limited only to the sound power level (L_{WA}), may be inadequate to this kind of devices. Under the term of DESS we mean the technical object that has the possibility of various spatial arrangement of its components. In addition, these components are together a functional unit and they can not work separately. In many cases, each of the device's components could be treated as a separate sound source which usually emits sound of a different nature.

Due to the specific design of this kind of devices it is worth mentioning that:

- it is impossible to clearly define what type of measuring surface should be used in the procedure of determination of L_{WA} (see Figure 1),
- description of the acoustic features of a device basing only on one parameter, for example L_{WA}, will not fully characterize the influence of the device on the environment and it will not provide sufficient information needed for creation of acoustic maps (by numerical simulations) e.g. in the planned installation place.

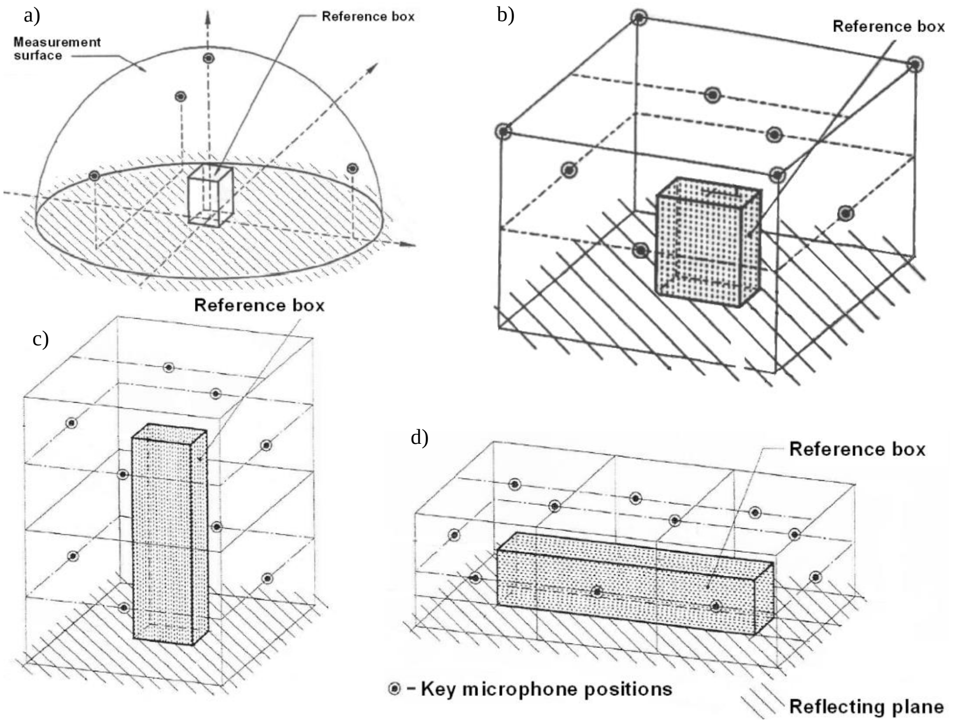

Figure 1. Examples of microphone positions and measurement surface, while determination of sound power level according to ISO 3746 : 2011; a) hemisphere, b) parallelepiped surface for a small machine, c) parallelepiped surface for a tall machine, d) parallelepiped surface for a long machine [1]

2. Research methodology

Vacuum cleaners, sets of pneumatic devices or biomedical devices such as smoke evacuators can be examples of DESS. A more accurate parameterization of noise emitted by the last mentioned is necessary because of high requirements concerning the acoustic climate in areas such as operating rooms. Such devices are used to remove smoke and particles carried by it (bacteria, viruses) created during operation or electrosurgical procedures. The system typically includes a suction pump unit with air filtration system, a working tool (electrocoagulator or electroscalpel) with an air sucking tip and a flexible hose connecting the components. The pump and the working tool are usually placed in different locations within the operating room, in addition each of the components emit sound of a different character (Figure 2).

It is worth noting that due to the surgeon's necessity to maintain long-term concentration during procedures or surgeries, it is important to limit noise in the operational environment. Following recommendations from PN-N-01307: 1994 [2], relating to the performance of precision work it can be assumed that the equivalent sound pressure level (L_{Aeq}) in this case should not exceed 65 dB. It is also worth noting that the recommendations for noise in the operating room in the United States are more restrictive. According to ANSI / ASA S12.2-2008 [3] L_{Aeq} should not exceed 44 dB. It should be emphasized that this is only a recommendation not a requirement. The results of the research presented by Kaczmarska, Łuczak and Sobolewski [4] have shown that the presence of low-frequency noise (even L_{Aeq} = 52 dB and L_{Geq} = 62 dB) while performing precision work can cause fatigue and somnolence.

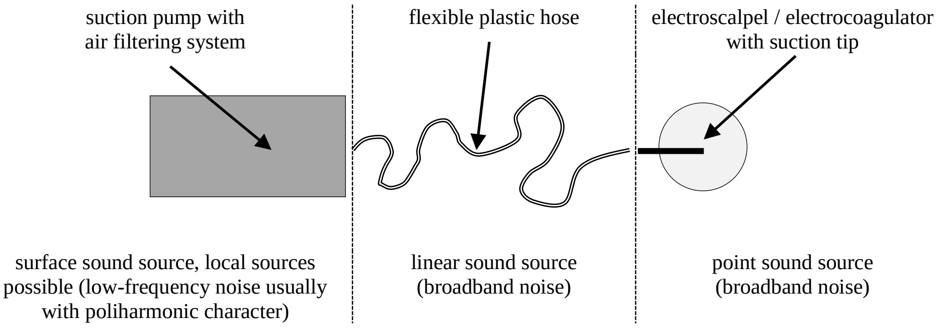

Figure 2. Components of smoke evacuator an example of DESS and specifics of noise emitted by them

For the measurement an equipment set consisting of Roga R50 microphone (ICP), data acquisition module VibDAQ 4+ and DSP structure elaborated in DASYLab® was used. An influence of environmental conditions in laboratory was taken into account according to ISO 3746: 2011 (A = 54,56 m^3/s, K_{1A} = 0,03 dB, K_{2A} = 2,13 dB).

3. Research results

The research included the determination and comparison of the L_{WA} (Figure 3) of tested device treated as:

- compact arrangement (all components were placed close to each other in a reference box in accordance to ISO 3746: 2011),
- extensive sound source; testing was carried with various configurations of the spatial arrangement of device's components, as it occurs in the real conditions in the operating room.

Figure 4 contains sound pressure levels (L_p) in octave bands. The values correspond to the levels on the measurement surface of 1m^2. The following conclusions has been drawn on the basis of comparison of the test results.

- The noise emitted by the suction pump has a low-frequency character (polyharmonic) associated with rotational frequency (and its superharmonics) of the electric motor (Figure 6). The dominant amplitude components of the noise are included in frequency range that does not exceed 500 Hz.
- The noise emitted by the suction tip is a broadband noise covering the frequency range from 4 kHz up to 16 kHz.

- An important data that should be taken into account in the parameterization of noise emitted by the device is the radial spectra of the sound emitted mainly by the suction pump unit (Figure 5).

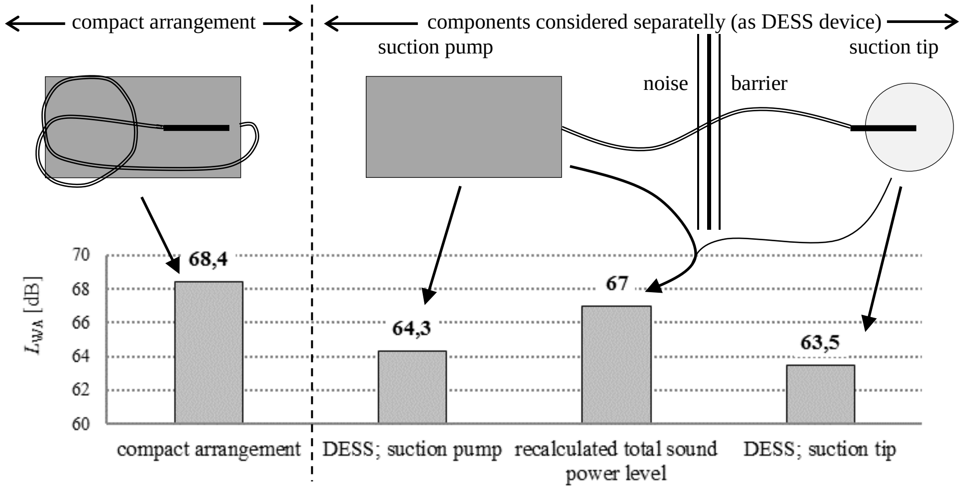

Figure 3. Spatial arrangement of components during testing and theirs L_{WA}

Taking under consideration that components emit noise of different character, reduction of the level of emitted noise require an individual approach to each source. Another problem is the determination of L_{WA} of device that is characterized by various regime of work. Testing should include all operating modes that can occur during surgery or chirurgical procedures. This is connected with the necessity of using a relatively long averaging time and/or determining the duration of each operating mode such as suction, choking airflow, idle.

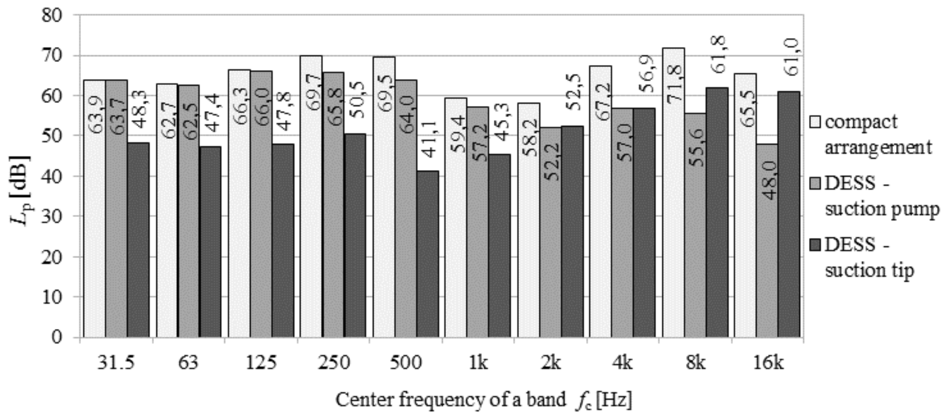

Figure 4. Noise emitted by tested device treated as compact arrangement and as DESS (average acoustic pressure level correspondent to measurement surface of 1m^2)

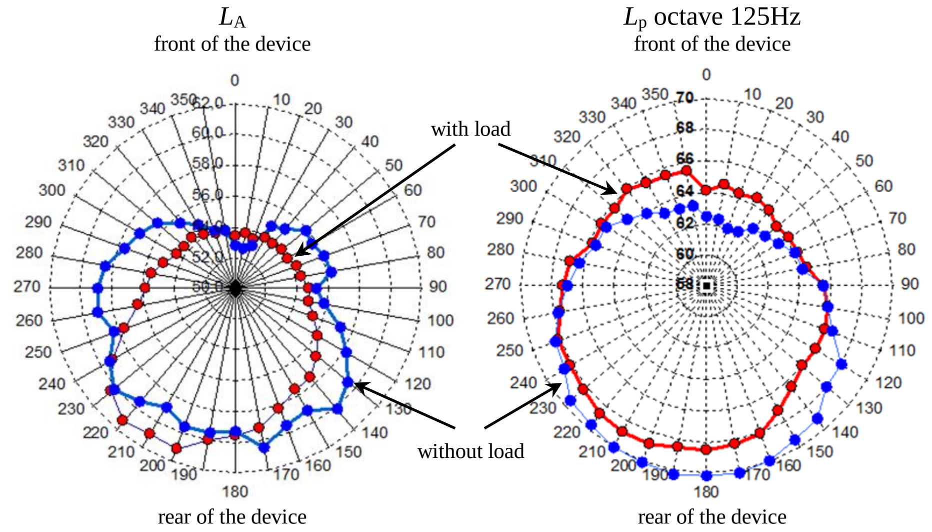

Figure 5. Radial spectra of noise emitted by suction pump; without load (hose not connected), with load (hose and tool connected)

Sound power level of the tested device (compact arrangement case) determined in accordance to ISO 3746 : 2011 is equal to 68.4 dB. In the case of the machine's components tested separately L_{WA} of suction pump equals 64.3 dB and L_{WA} of suction tip equals 63.5 dB. While the total sound power level of both components after recalculation would be 67 dB. The difference between the device's L_{WA} (compact arrangement case) and the recalculated total L_{WA} (separated sound sources case) probably results from that a part of acoustic energy emitted by the hose is not included. In comparison to other potential sources of noise in the operating room [5-8] it can be stated that the noise emitted by the tested device can have a significant influence on the acoustic climate in the operating room.

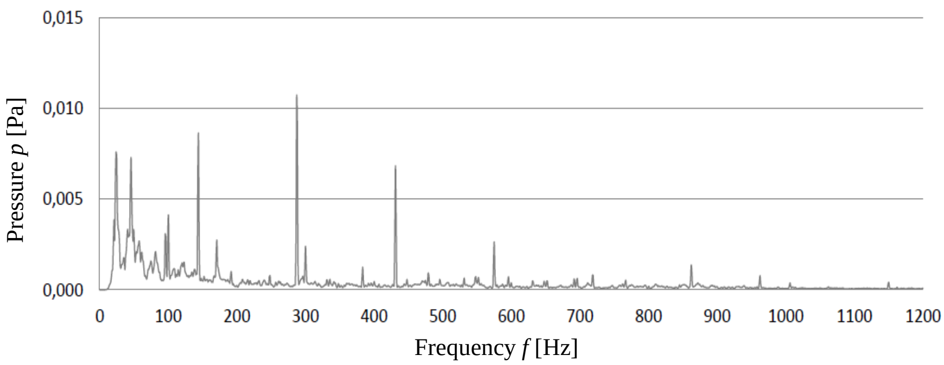

Figure 6. Narrowband spectrum of acoustic pressure measured 1m above the suction pump unit

4. Conclusions

- Treating components as autonomous but simultaneously influencing sound sources allows obtaining data helpful at the prototype research stage and minimize the noise emitted by the each device's component. Finally, this approach gives the possibility of noise reduction in the area of surgeon's operation. As well as, it allows meeting the noise requirements in areas of such a kind. It can be done by e.g. the appropriate placement of the device's components within the operating room.
- An extended data set should include among others:
  - L_{WA} (total and individual for device's components, which can be treated as local noise source),
  - radial spectra of noise emitted by device's components,
  - typical arrangement of components and operator in installation place (e.g. operating room),
  - duration of typical tasks performed using the device.

  That parameters may allow the creation of reliable acoustic maps of operating rooms at the design stage using simulation software.
- The results of the carried out research may be helpful in developing the methodology of L_{WA} determination for DESS.

Acknowledgement

This paper was partially financially supported in the year 2016 by research project 02/21/DSPB/3478.

References

1. ISO 3746 : 2011, Acoustics – Determination of sound power levels of noise sources using sound pressure – Survey method using an enveloping measurement surface over a reflecting plane.
2. PN-N-01307 : 1994, Hałas – Dopuszczalne wartości parametrów hałasu w środowisku pracy – Wymagania dotyczące wykonywania pomiarów
3. ANSI/ASA S12.2-2008, Criteria for Evaluating Room Noise.
4. A. Kaczmarska, A. Łuczak, A. Sobolewski, *Uciążliwość hałasu niskoczęstotliwościowego*, Bezpieczeństwo Pracy, **6** (2006) 11 – 15.
5. J. M. Kracht, I. J. Busch-Vishniac, J. E. West, *Noise in the operating rooms of Johns Hopkins Hospital*, Journal of the Acoustical Society of America, **12**(5) (2007) 2673 – 2680.
6. H. Love, *Noise exposure in the orthopaedic operating theatre: a significant health hazard*, ANZ Journal of Surgery, **73** (2003) 836 – 838.
7. N. Shankar, K. L. Malhotra, *Noise in the operation theatre: intensity and sources*, Indian Journal of Physiology and Pharmacology, **43**(2) 1999 263 – 266.
8. C. Tsiou, G. Efthymiatos, T. Katostaras, *Noise in the operating rooms of Greek hospitals*, Journal of the Acoustical Society of America, **123**(2) (2008) 757 – 765.

Comparison of Vibration Impact of an Impact Drill on the Human Body under Different Working Conditions

Bartosz JAKUBEK
Poznan University of Technology, Institute of Applied Mechanics
24 Jana Pawła II Street, 60-965 Poznan, bartosz.jakubek@put.poznan.pl

Wojciech RUKAT
Poznan University of Technology, Institute of Applied Mechanics
24 Jana Pawła II Street, 60-965 Poznan, wojciech.rukat@put.poznan.pl

Abstract

Currently there is a wide range of different kinds of power tools on the market. In the case of impact drills the major threat to the user's health are vibration and acoustic impacts. Knowing that the actual drilling conditions may vary significantly from standardized conditions. It is important to determine the actual maximum level of dangerous factors present during drilling. Furthermore, it is also very important to link that factors to the conditions in which they occur. Among many factors affecting the level of vibration of an impact drill, change of the working position, the length of the drill bit and the diameter of the drill bit were verified in this paper. Verification was based on a comparison of vector-weighted mean values of acceleration of vibrations $\bar{a}_{\mathrm{RMS}}$ registered on the handles of the impact drill, while drilling in concrete, under different working conditions.

Keywords: impact drill, local vibrations, concrete drilling, drill bit, different working conditions

1. Introduction

Impact Drills are one of the most common power tools used both professionally and at home. The manufacturer's declaration of levels of vibration and noise are taken into account in industrial conditions for legal reasons [1]. However, in the case of private use, the lack of awareness of safe use can be observed or the threats are just ignored.

Vibration levels declared by the manufacturers are determined in the specific standardized conditions. According to EN 60745 the procedure requires a drill bit diameter of 8 mm and a working length of 100 mm. While drilling vertically, downward the force acting on the device must be between 120 N and 180 N. [2]. However, the actual drilling conditions often significantly differs from the standardized conditions, which are the basis of manufacturers' declarations of vibrations. Therefore, the value of acceleration of vibrations given by the manufacturer should be treated with caution. Due to the harmful impact of vibration on human health [3,4] the proper selection of personal protective equipment, determination of allowable time of exposure or even the decision to stop using the device is vital.

There are a number of factors affecting the level of vibrations emitted by an impact drill. These factors can be divided into three groups associated with:

- machined material and the way of its foundation (concrete, brick, stone, etc.),
- operator's personal features (physique, experience),
- device and tool (build and additional equipment).

The factors affecting the level of vibration emitted during drilling were discussed in many publications [5-10]. But there is no information about the influence of different diameters and working lengths of the drill bit in terms of the measurement of acceleration of vibrations.

2. Measurements

A series of holes was drilled in reinforced concrete beams (vibration-compacted concrete) in the experiment. Drilling was done vertically, downwards and horizontally. The operator's positions are shown on Figure 1.

Figure 1. The stand and the operator while drilling vertically – on the left, while drilling horizontally – on the right

Triaxial vibration transducer ICP 604B31 and SVAN 911A analyser were used to register the vibration signal. Spatial orientation of the measurement directions, related to a tool, is following:

- the X direction (axis) corresponds to the longitudinal axis of the spindle of the drill,
- the Y direction (axis) corresponds to the longitudinal axis of the rear handle of the drill (a handle rigidly connected with the tool's body),
- the Z direction (axis) is mutually perpendicular to the other two [11].

During the tests 620W impact drill HITACHI DH 22 PH was used. To determine the impact of the forced change of the operator's position Ø12mm drill was used. In order to determine the effect of the diameter of the drill bit the following tools were used: Ø8mm, Ø12mm, Ø16mm and Ø20mm. Examination of the effect of drill bit's diameter on the vibration was carried out in the vertical direction, downwards. To determine the effect of the length of the drill bit on the values of vibration a set of Ø12 mm drill bits was used. The set includes the following bits: 125/165mm, 250/315mm, 400/460mm, 520/600mm and 900/1000 mm (working/total length). In this case drilling was done only in the horizontal direction.

Each comparison required as constant conditions as possible. One experienced operator drilled in a single beam (one for each comparison). The operator was 27-year old, 175cm tall and 78kg weight male. The maximum power of the device was used. The drilling direction was controlled by laser. In order to eliminate the influence of temporary changes in the downforce, the average of multiple measurements was adopted as the result. The total measurement time was approximately 300s in the comparison of drilling directions, and 180s for the rest. Transient states were omitted in the measuring sequences.

3. Research results

The results of the measurements are presented below. The following charts show the impacts of: forced change of the operator's position, the length of the drill bit and the diameter of the drill bit on the values of vibrations.

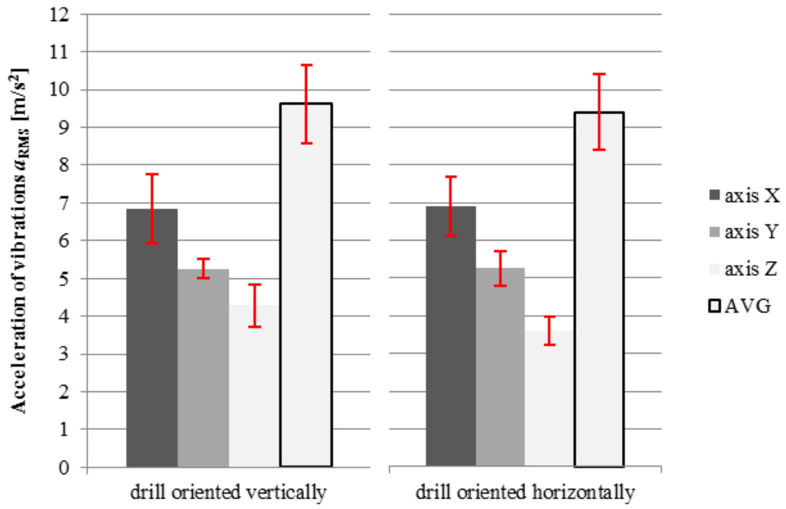

Figure 2. Acceleration of vibrations of the front handle of the impact drill deepening on drilling direction

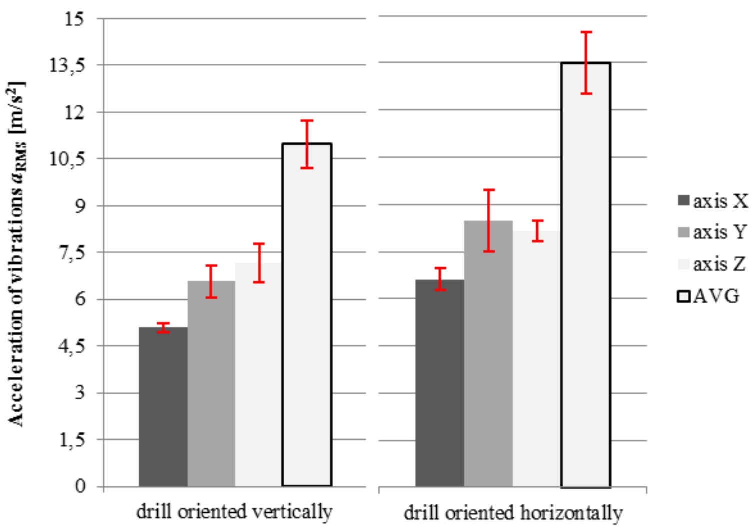

Figure 3. Acceleration of vibrations of the rear handle of the impact drill deepening on drilling direction

As it can be seen in Figure 2. the change of operator's position due to change of drilling direction has no impact on the value of acceleration of vibrations measured on the rear handle. The highest vibrations were measured along the x-axis. The repeatability of the results determined by the formula (1) equals 97.7%.

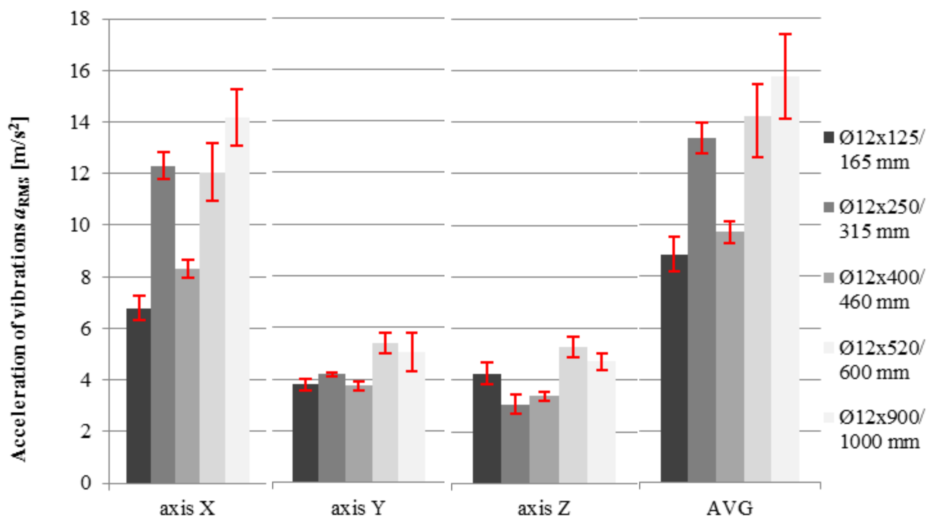

Figure 4. Acceleration of vibrations of the front handle of the impact drill deepening on drill bit length

$$\frac{\bar{a}_{\mathrm{RMS}} - \left|a_{\mathrm{RMS\_H}} - a_{\mathrm{RMS\_V}}\right|}{\bar{a}_{\mathrm{RMS}}} \cdot 100\%, \tag{1}$$

Where $\bar{a}_{\mathrm{RMS}}$ is the arithmetic mean of $a_{\mathrm{RMS\_H}}$ and $a_{\mathrm{RMS\_V}}$,

$a_{\mathrm{RMS\_H}}$ is vector-weighted mean value of acceleration of vibrations measured while drilling horizontally,

$a_{\mathrm{RMS\_V}}$ is vector-weighted mean value of acceleration of vibrations measured while drilling vertically.

In the case of the front handle, an increase of acceleration of vibrations was observed, what confirms the conclusions of other work [10]. This is caused by the change of the angle between the arm and the forearm of the operator's left hand. In the case of vertical drilling the arm is straight. During horizontal drilling, the left arm is bent at the elbow (see Figure 1.). The repeatability of results in the case of front handle equals 79.3%.

With the increase of the length of the drill bit an increase of the acceleration of vibrations of the rear handle is observed. Maximum vibration values were measured along the x-axis.

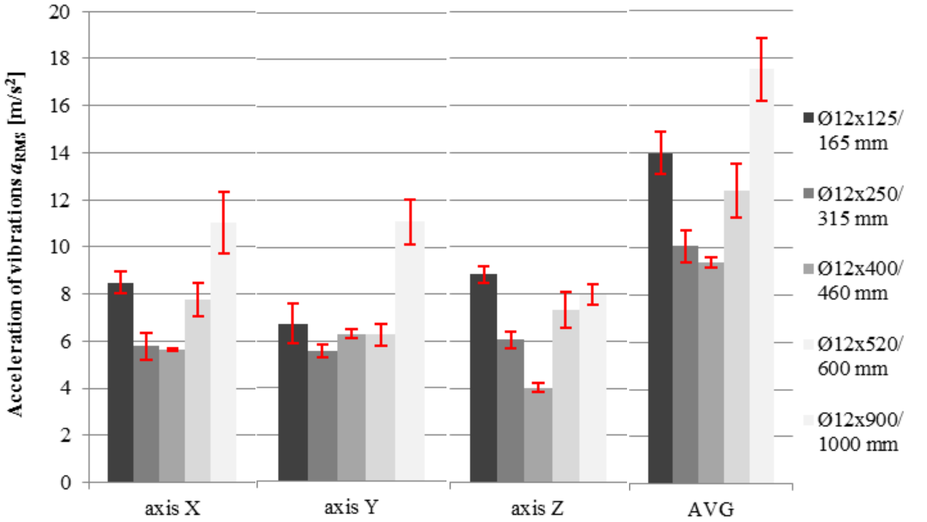

Figure 5. Acceleration of vibrations of the rear handle of the impact drill deepening on drill bit length

It is impossible to describe the nature of the dependence between the length of the drill bit and the values of acceleration of vibrations of the front handle. Initially the values of acceleration of vibrations tend to decrease, followed by their increase. In the case of the longest drill bits, such high $\bar{a}_{\mathrm{RMS}}$ values were caused by the buckling of the drill bit. The buckling was probably triggered by the action of the downforce, which was misaligned with the drill bit's axis [12,13]. Verification of exceeding the critical buckling force was not possible.

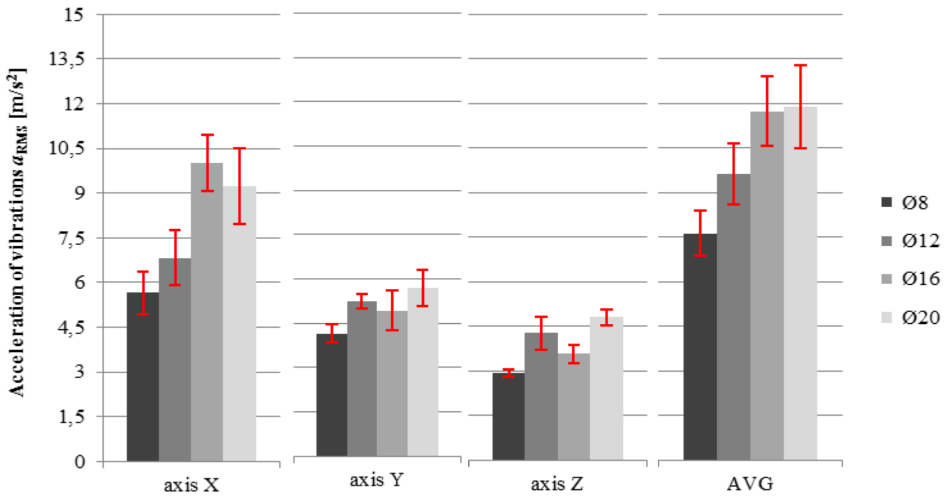

Figure 6. Acceleration of vibrations of the front handle of the impact drill deepening on drill bit diameter

With the increase of the drill bit diameter an increase of the acceleration of vibrations of the rear handle is observed. Maximum vibration values was measured in the X axis. In this case, the coefficient of determination R^2 equals 0.91 which indicates a very strong dependence between the level of vibration of the rear handle and drill bit diameter.

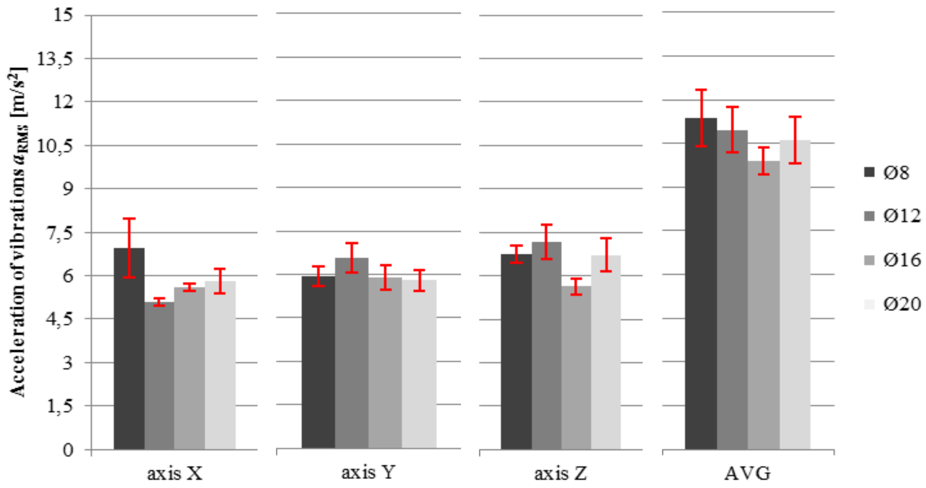

Figure 7. Acceleration of vibrations of the rear handle of the impact drill deepening on drill bit diameter

On the basis of Figure 7. it can be stated that the vibration level measured on the front handle does not change with increasing diameter of the drill bit. Vibration values are similar in different directions. The measurement results are consistent with previous work. [11].

In order to meet the paper fundaments the drill bit Ø12×125/165mm was used three times (three different beams). The convergence of the results were calculated with the use of additional data. Percent convergence of results determined on the basis of formula (1) equals 96.41% for the rear handle, and 94.02% for the front handle. The average absolute error of the vector-weighted mean value of acceleration of vibrations $\overline{a}_{\mathrm{RMS}}$ is 0.9 m/s^2, and the average relative error is 7.88%.

Table 1. The time limit for drilling in different working conditions

Handle	direction of drilling	Drill bit description							
		Ø8 mm	Ø12× 125 mm	Ø12× 250 mm	Ø12× 400 mm	Ø12× 520 mm	Ø12× 900 mm	Ø16 mm	Ø20 mm
right	vertical	65.0 min	40.6 min	-----	-----	-----	-----	×	×
	horizontal	-----	42.6 min	×	39.7 min	×	**×**	-----	-----
left	vertical	×	31.3 min	-----	-----	-----	-----	38.5 min	33.5 min
	horizontal	-----	×	37.2 min	42.9 min	×	**×**	-----	-----

The table above shows the time limit for drilling in different working conditions in relation to Exposure Limit Value (ELV) [1]. The symbol × indicates conditions that do not allow the use of the drill without personal protective equipment. In two cases that are in bold, $\overline{a}_{\mathrm{RMS}}$ of drill’s handle exceeded the manufacturer's declaration (13.2 ± 1.5 m/s^2) with maximum uncertainty included.

4. Conclusions

There were no changes in the acceleration of vibrations on the rear handle associated with the change of the operator’s position and direction of drilling observed. At the same time an 30% increase occurred for the front handle. This is connected with forced bend of elbow joints in left arm.

Vibrations of the drill’s handle depend on the length of the drill bit but the nature of this dependence is not clear. Vibration levels dangerous for operator and exceeding the ELV were observed for the longest drills and it was caused by the buckling of the drill bit.

The change of the drill bit diameter has no effect on the level of vibration of the front handle. Yet, the dependence between the change of the drill bit diameter and the level of vibration of the rear handle is increasing.

The increase of the diameter of the drill bit, as well as the change of drilling direction and the change of operator’s position from vertical to horizontal extend the time of drilling and cause a loss of productivity of the process – both are connected with power demand.

In practice there may occur a combination of factors at the same time, which will result in vibration emitted by the device exceeding the ELV as well as the occurrence of health hazard to the operator, despite secure level of vibration declared. In one case the acceleration of vibrations of both handles significantly beyond the manufacturer's declaration were measured.

Acknowledgement

This paper was financially supported in the year 2016 by research project 02/21/DSMK/3470.

References

1. J. Skowroń, *Weryfikacja wartości NDN dla drgań mechanicznych o działaniu ogólnym i miejscowym*, Bezpieczeństwo Pracy Nauka i Praktyka, **6** (2000) 22 – 23.
2. EN 60745-2-1:2010, *Hand-held motor-operated electric-tools – Safety; Part 2-1: Particular requirements for drills and impact drills*.
3. G. Björing, L. Johansson, G. Hägg, *Surface pressure in the hand when holding a drilling machine under different drilling conditions*, International Journal of Industrial Ergonomics, **29** (2002) 255 – 261.
4. B. Harazin, *Occupational exposure to whole-body vibration in Poland*, Occupational Medicine (Medycyna Pracy), **6** (2002) 465 – 472.
5. B. Huang, J. Kuang, P. Yu, *Effect of crack on drilling vibration*, Journal of sound and vibration, **322** (2009) 1100 – 1116.
6. S. Keith, A. Brammer, *Rock-drill handle vibration: measurement and hazard assessment*, Journal of Sound and Vibration, **174**(4) (1994) 475 – 491.
7. G. Neely, L. Burström, M. Johansson, *Subjective responses to hand-arm vibration: implication for frequency-weighting and gender differences*, Proceedings of the 7th Annual Meeting of the International Society of Psychophysics, (2001) 553 – 558.
8. R. Oddo, T. Loyau, P. Boileau, Y. Champoux, *Design of a suspend handle to attenuate rockdrill hand-arm vibration: model development and validation*, Journal of Sound and Vibration, **275** (2004) 623 – 640.
9. D. Rempel, D. Star, A. Barr, I. Janowitz, *Overhead drilling: Comparing three bases for aligning a drilling jig to vertical*, Journal of Safety Research, **41** (2010) 247 – 251.
10. E. P. Shanks, S. M. Hewitt, P. M. Pitts, *Investigation of the relationship between vibration emission and in-use vibration for electrical tools*, Health & Safety Laboratory, Canadian Acoustics (Acoustique Canadienne), **39**(2) (2011) 104 – 105.
11. B. Jakubek, W. Rukat, *Influence of a tool's working diameter on the level of handle vibrations of an impact drill*, Vibroengeineering PROCEDIA, **6** (2015) 288 – 291.
12. J. Łabędź, P. Rusek, *Ocena niebezpieczeństwa wyboczenia narzędzia przy obróbce otworów a stali 40H wiertłami długimi o małych średnicach*, Przegląd Mechaniczny, **9** (2008) 25 – 28.

A New Tool for Topological Optimization of a Rotor for Vertical Axis Wind Turbines

Mateusz JAKUBOWSKI
Poznan University of Technology (Graduate in the field of Mechatronics)
ul. Jana Pawła II 24, 60-965 Poznań, mateusz@konstrubowski.pl

Paweł FRITZKOWSKI
Institute of Applied Mechanics, Poznan University of Technology
ul. Jana Pawła II 24, 60-965 Poznań, pawel.fritzkowski@put.poznan.pl

Abstract

A computer program for topological optimization of a rotor for vertical axis wind turbines of various type is presented. The tool is based mainly on two external modules: the GMSH mesh generator and the OpenFOAM CFD toolbox. Interpolation of rotor blades geometry and computational model of the airflow through a turbine are briefly discussed. Moreover, a simple optimization algorithm is described. Exemplary results for a H-type rotor are presented. Finally, potential directions for the software development are indicated.

Keywords: vertical axis wind turbines; topological optimization; computational fluid dynamics

1. Introduction

Vertical axis wind turbines (VAWT) have great potential in the area of renewable energy generation, although they are relatively rarely used in industry. Modern manufacturing methods make production of complex geometric shapes increasingly cheaper. Thus, topological optimization of rotor blades can provide quite valuable results that are realizable in practice.

Aerodynamics of turbines is complicated and sensitive to slight changes in shape. Therefore, the software for finding the best possible geometry of a rotor is of high importance for design engineers. There are many commercial systems (usually based on the finite element method) that allow one to solve a wide variety of problems in the field of computational fluid dynamics (CFD). However, the general purpose character of such programs makes particular tasks rather burdensome: computational model preparation, geometry parameterization, etc. In this light, developing a specialized optimization tool seems to be an attractive and challenging idea.

From the programming and numerical viewpoint, CFD-related problems are very demanding. A common (but not always occurring) feature of vertical turbines, i.e. a uniform cross-section of a rotor along the axis of rotation (see Fig. 1), simplifies the problem considerably. In any case, it was decided to create the program with a use of commonly available components: free, open source packages which fulfill the crucial and hardest tasks.

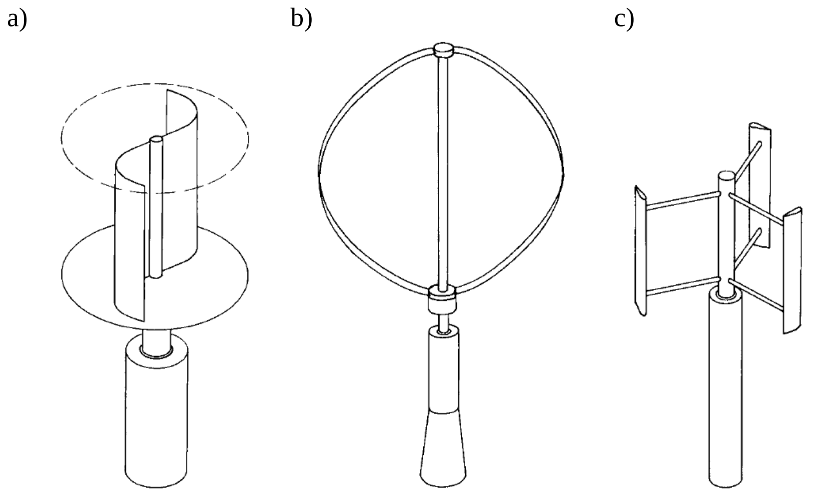

Figure 1. Basic types of rotors for VAWT [1, 4]: a) the Savonius rotor, b) the Darrieus rotor, c) the H-type rotor

2. The OPTIMIZER software

The computer program *Optimizer* developed by the first author has a graphical user interface and was written in the Python programming language. The application accomplishes the following tasks: drawing the initial geometric model of a rotor, generating and previewing a discrete numerical model, changing the simulation and solver settings, results archiving, conducting simulation related to the direct problem (air flow through a wind turbine), optimization of the rotor shape, and results visualization. *Optimizer* employs external modules: the *GMSH* mesh generator and the solvers of the *OpenFOAM* environment. The program window with sample data can be seen in Fig. 2.

In order to reduce the number of parameters describing the rotor geometry, it was decided to use interpolation of curves that pass through some control points specified by user. More precisely, the method known as Piecewise Cubic Hermite Interpolation (PCHI) is used [3]. On each subinterval the given curve is interpolated by a third degree polynomial of Hermite type. To form a smooth contour of a blade, continuity of the first and second derivatives of neighbouring polynomials is ensured at the nodal points. Obviously, this constraint is cancelled in case of a corner vertex (see Fig. 3). All in all, user defines the shape of a single blade and the number of blades.

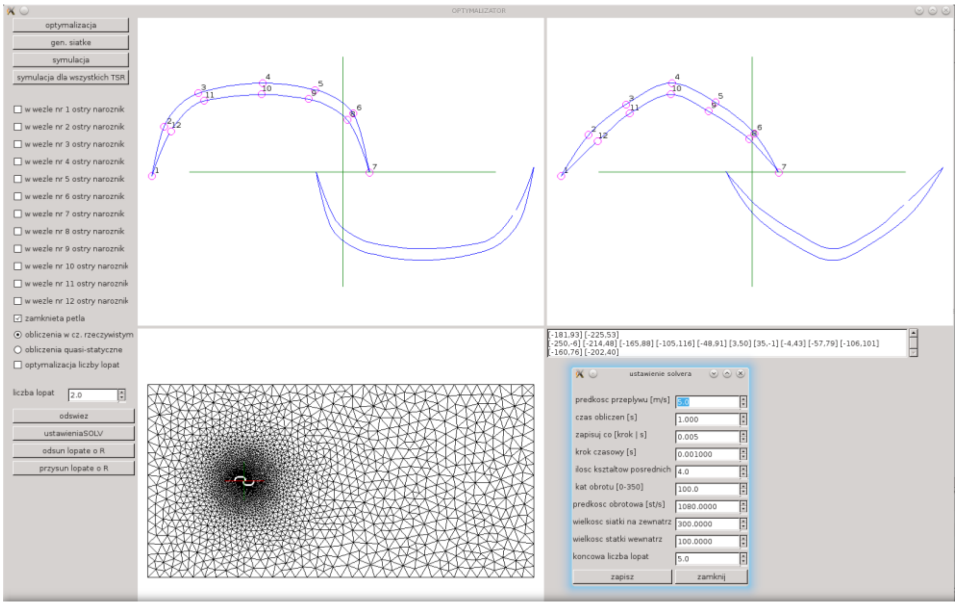

Figure 2. Graphical interface of *Optimizer*

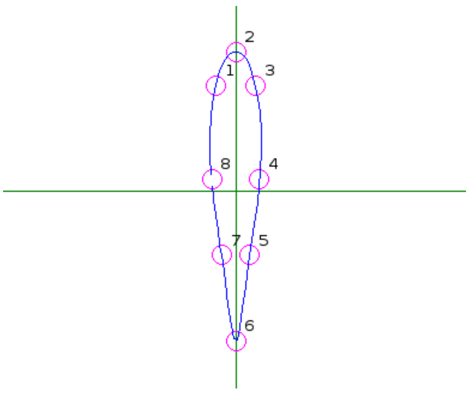

Figure 3. Shape of a blade of the H-type rotor generated via PCHIP

3. Computational model and solver

A schematic view of a virtual wind tunnel is presented in Fig. 4. The problem domain is divided into two parts. The central one includes the rotor and its close neighbourhood, thus, it rotates during simulation. The non-moving subdomain constitutes an outer, dominant part. The interface between the two regions forms a circle centered at the rotor axis.

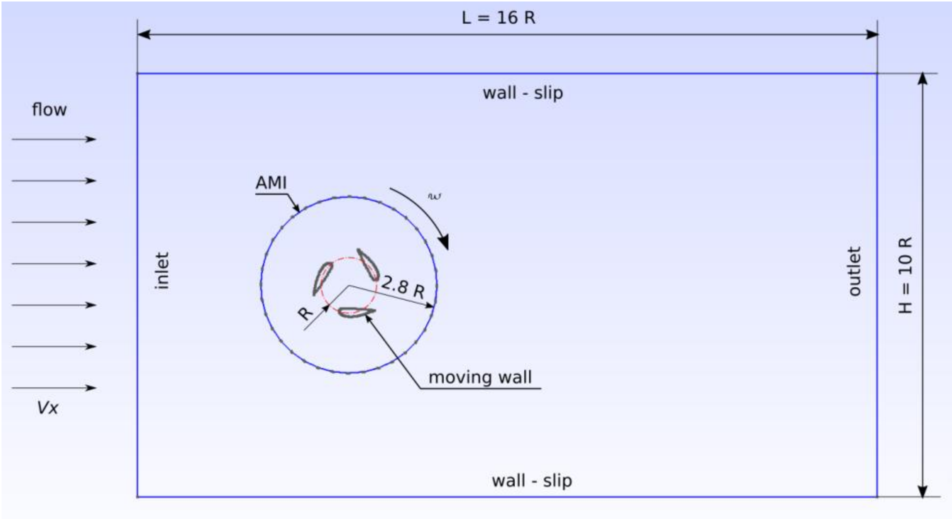

Figure 4. The domain and boundary conditions for the problem

Airflow through the wind turbine is described by the Navier-Stokes equations; the fluid is assumed to be incompressible [4]. On the left boundary, uniform inflow velocity of the air is defined. At the bottom and top walls the slip condition is specified, which prevents the fluid from leaving the domain. The outlet condition corresponds to zero relative pressure. AMI stands for Arbitrary Mesh Interface, and is used to model the mutually sliding subdomains.

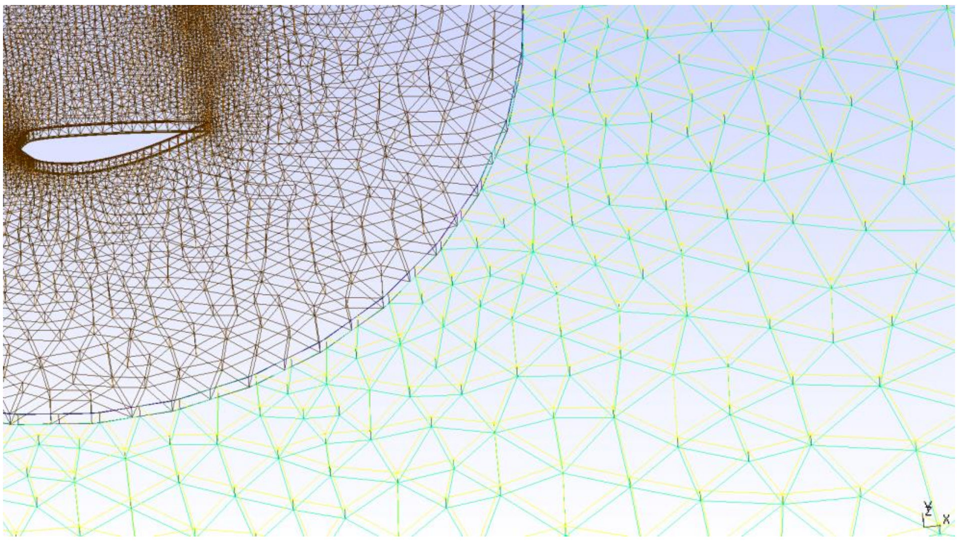

Figure 5. An exemplary finite volume mesh

In general the planar domain is discretized by triangular cells. Additionally, quadrilateral cells are used in the boundary layers on the blades. The solver employed to cope with the initial-boundary value problem is based on the finite volume method (FVM). Since a three-dimensional computational domain is required, the planar one is extruded by a unit distance. Therefore, the final discrete model consists of prismatic finite volumes (see Fig. 5).

Within the *OpenFOAM* environment, the solver *pimpleDyMFoam* allows for dynamic meshes. It is an implementation of the so called PIMPLE algorithm: a combination of the standard PISO (Pressure Implicit Split Operator) and SIMPLE (Semi Implicit Method for Pressure Linked Equation) algorithms. To guarantee continuity of physical quantities on the interface between moving and stationary cells, an additional interpolation is used.

4. Optimization algorithm

The algorithm for topological optimization of rotor blades is made of two modules: a generator of new rotor geometries, and an analyzer and selector of the best solution. The former one requires the following user-defined input data: the start and end blade shapes as well as the number of intermediate profiles (resolution). The algorithm analyzes the given geometries and prepares a set of new shapes according to the simple principle illustrated in Fig. 6. The left and right triangles represent the start and end profiles, respectively. The middle triangle, in turn, illustrates the only intermediate shape (a special case is shown). Starting from the initial shape, translation vectors for all control nodes are determined, which leads to a new interpolated geometry. The number of translations is equal to the number of intermediate profiles.

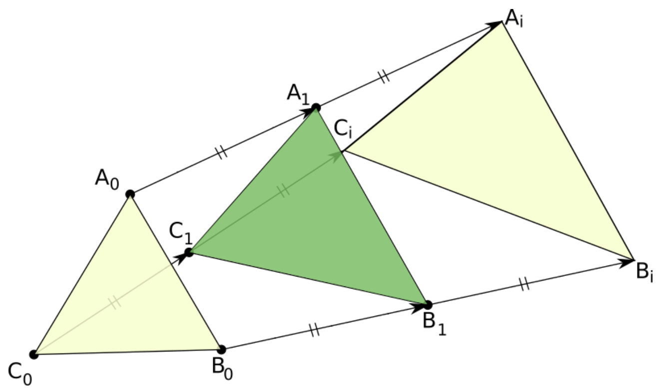

Figure 6. Illustration of the start, intermediate and end shapes

As the comparison criterion (an objective function), the power coefficient is used:

$$C_p = \frac{P_r}{P_w}. \tag{1}$$

The power of the rotor and the wind flowing past the rotor are given by

$$P_r = \omega T\ , \quad P_w = \frac{1}{2}\rho A V_x^3\ , \tag{2}$$

where: ω – angular velocity of the turbine, T – torque generated by the rotor, ρ – air density, A – rotor area in the cross-section normal to the airflow direction, V_x – airflow velocity. If the defined start and end shapes ensure a constant rotor diameter during optimization, this criterion can be simplified and replaced with the torque at the rotor shaft. The torque value is specified on the basis of pressure field at the blades, and is saved to file in real time. As simulations related to all the prepared profiles are completed, the program analyzes the results and presents the best solution.

5. Results

The *Optimizer* software was tested by solving several direct and optimization problems related to the Savonius and H-type rotors. Results of these studies are thoroughly discussed in Ref. [2]. Here, only one example is presented.

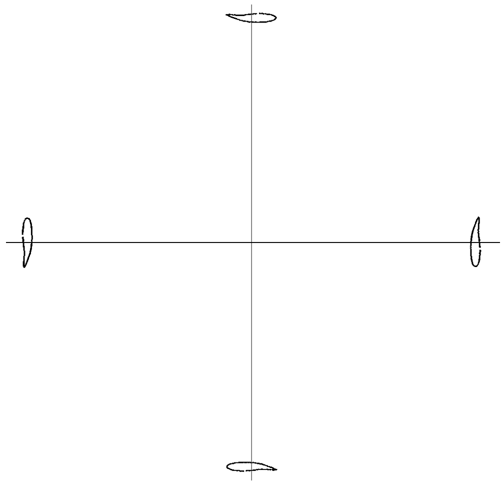

Figure 7. Initial geometry of the NS2L4 rotor

Consider blade shape optimization for a H-type rotor denoted by the code NS2L4 (see Fig. 7). Geometry of the start, end and intermediate profiles is illustrated in Fig. 8. The corresponding values of the rotor torque and power are shown in Fig. 9. As can be seen, the best solution (in terms of the torque criterion) is denoted by SERIES-4. A detailed analysis of the results has indicated that this blade variant generates the weakest vortices. Time history of the torque T for the initial and optimized shapes is presented in Fig. 10. The simulations were performed for R = 700 mm, V_x = 21.6 km/h. Fluid-structure interaction was analyzed for time $0 \le t \le 2$ s. The optimization lasted 17 690 s.

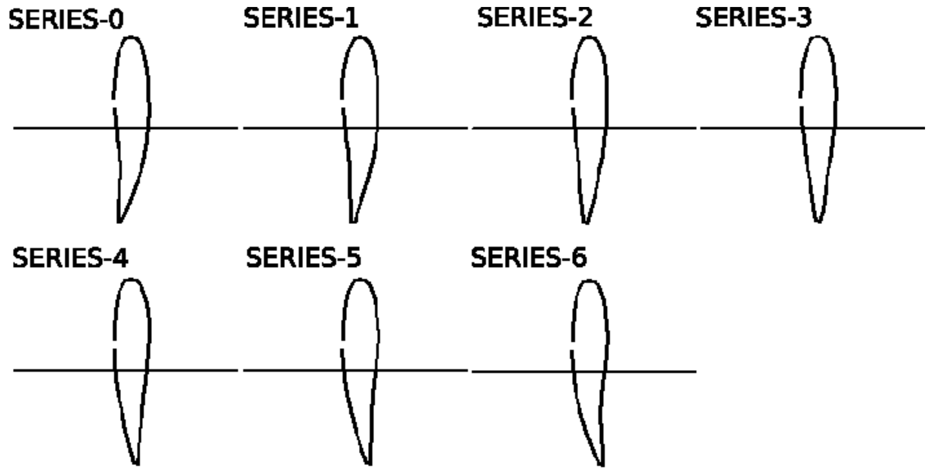

Figure 8. Blade profiles in consecutive iterations

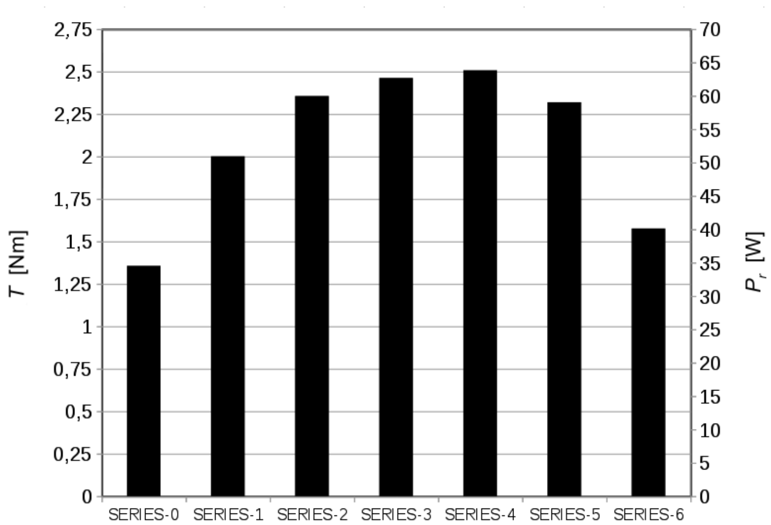

Figure 9. Maximal torque and power (steady-state) of the rotor in consecutive iterations

6. Conclusions

The presented software is a specialized tool that can be applied for topological optimization of various types of VAWTs. To create a true alternative to commercial systems, the program should be improved by increasing functionality of the preprocessor and postprocessor. Nevertheless, *Optimizer* is a solid basis for implementation of advanced optimization approaches, e.g. artificial neural networks (ANN) or genetic algorithms (GA).

a)

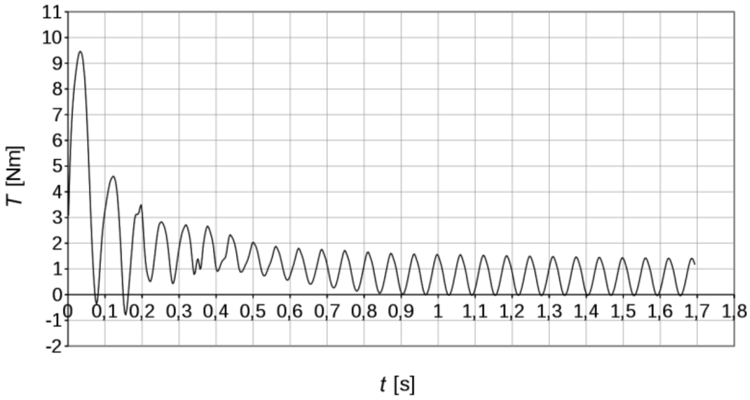

b)

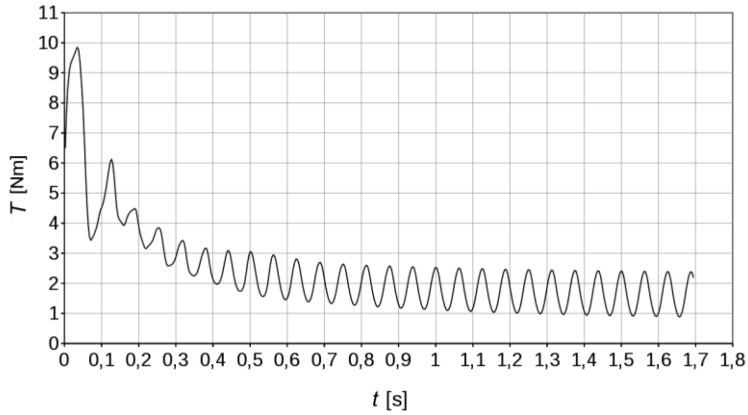

Figure 10. Time history of the rotor torque for SERIES-0 and SERIES-4

References

1. E. Hau, *Wind Turbines – Fundamentals, Technologies, Application, Economics,* Springer, Berlin 2014.
2. M. Jakubowski, *Software for topological optimization of a rotor for a vertical axis wind turbine*, Master thesis, Poznan University of Technology, Poznan 2015.
3. N. Madden, *Lecture 10: Piecewise Hermite Interpolation*, National University of Ireland, Galway 2010.
4. A. P. Schaffarczyk, *Introduction to Wind Turbine Aerodynamics*, Springer, Berlin 2014.

On the Violin Bridge Hill – Comparison of Experimental Testing and FEM

Erik V. JANSSON
Department of Speech, Music and Hearing, KTH
SE-10044 Stockholm, Sweden, erik.jansson2@ownit.nu

Roman BARCZEWSKI
Poznan University of Technology – Institute of Applied Mechanics
Jana Pawła II 60-965 Poznań, Poland, roman.barczewski@put.poznan.pl

Andrzej KABAŁA
Poznan University of Technology – Institute of Applied Mechanics
Jana Pawła II 60-965 Poznań, Poland, kabalaandrzej@gmail.com

Abstract

Italian violins of the golden era and French violins are different. Measurements of bridge mobility show that the Italian violins have a local maximum (a hump) at approx. 2,5 kHz in the bridge mobility. The French violins do not show this maximum. The arching along the centre line is different. The Italian violins are flat between the f-holes while the French ones are arched. Does this difference in design explain the difference in bridge mobility and tone? Proposed FEM simulation and digital signal post-processing of the time series are promising methods of the virtual testing of various violin models. These techniques may give an answer for the question above and they should be helpful in achieving high tonal quality of violin.

Keywords: Bridge mobility, top plate arching, experiments and FEM

1. Introduction

A large number of wooden blanks was free for further experiments. It was planned to use the blanks to investigate the influence of material properties on the top plate of the violin. In introductory pilot experiments it turned out that the geometry influenced more than the material properties. Therefore it was decided to cut a large number of rectangular plates to the same measures and to investigate the effects of f-holes in each plate. The f-hole shapes were simplified to three rectangular sections making various perturbations possible in simple ways.

Thereby it was found that the longer parts along the wood fibres and the lower transversal parts of the f-holes gave small effects. The largest influence was given by the upper transversal parts. The influence of two f-holes was well given by f-holes in shape of two letters, uppercase L:s, one upside down and the other in mirror image (Fig. 1). The findings were in line with previous f-hole experiments on an assembled violin. Thus the influence of f-hole geometry had been mapped [1] as well as thickness previously. The violin top is not flat but arched. No way to explain the influence of differences in arching had been found. In this report we present experiments and FEM analysis of “arched” plates. The experiments indicate the effect of arching which can be tested by FEM. The traditional way of violinmaking does not offer investigation of arching, only of thickness.

The frequency range of the so called bridge hill is of special interest. The fundamental bridge resonance was presented by Reinicke [2 and 3]. The resonance was found at approximately 2,5 kHz. In this frequency range the ear can register small level changes of a played tone. The 2,5 kHz-range is most interesting. In experiments with violins it turned out that at least for this very violin the shape of the bridge was of minor influence. A plate bridge i.e. a bridge with only a plate and two feet gave the same hump at 2,5 kHz. The plate bridge resonance frequency was far above that of the normal bridge. Thereby it was asked whether does the 2,5 kHz hump would be described as a body-hill rather than bridge-hill (BH) [4]. This plate bridge thus makes it possible to measure body properties with no addition of complex violin bridge properties. In this paper we are mainly interested in body properties and we use the plate bridge in the experiments and the FEM. This makes experimental modelling and FEM of arching attractive.

The bridge-body properties and their influence on the 2,5 kHz hump found in good violins have been modelled as coupled circuits [5]. The bridge is modelled as a mass-spring resonator coupled to the violin body. The body properties are modelled by means of averages. So called skeleton technique is used and the influences of bridge and body properties are predicted. It is suggested to start measuring a violins input mobility using plate bridges [6]. This approach is the background of experimenting. Physical models can be more easily built for experiments as will be reported here.

Measurements of Italian violins from the “golden era” show clear BH humps in the 2.5 kHz range [7]. Similar measurements of later French violins do not show the BH. Possibly it is the difference in lengthwise arching between the “golden” Italian (flat not arched) and the French (more arched) violins. Good old Polish violins also have a BH [8].

The BH also shows up in spectra of played test music, i.e. the common test music the prelude of the Bruch violin concerto. Such attest was made with the concert master Bernt Lysell of the Swedish radio and his Italian Guadagnini showing a BH but not a French violin by Leon Bernardel, see Figure 1 [9]. The test playings were preformed in the main concert studio of the orchestra. The two Stradivari violins and the J. Guarnerius del Gesu violin in the Strad3D playing tests also show a BH [10]. This background makes the influence of arching the main question of the present project. What influence has the lengthwise arching on the BH?

2. Experiments

A half of wooden blank for a guitar top was selected and cut into two pieces. One piece was made with measures close to earlier experiments and a second smaller piece for pilot experiments. The smaller piece was soaked in water and its mass (weight) was noted as function of time. After twelve hours the amount of water absorbed was close to maximum. Drying the plate in hot air oven at 80°C for 2 hours dried the plate. Therefore it was decided to soak the test the plate in water for twelve hours, clamp it in a bent form and dry it for two hours to make the larger plate arched.

The test plate was first arched by soaking, placing a 5 mm diameter rod under the bridge line and clamped to a grid, 0 mm, at the shorter sides, and dried in the oven. After removing the clamps a 3 mm arch remained. The "rectangular" simplified f-holes were cut and a plate bridge glued to the centre of the plate see Figure 1.

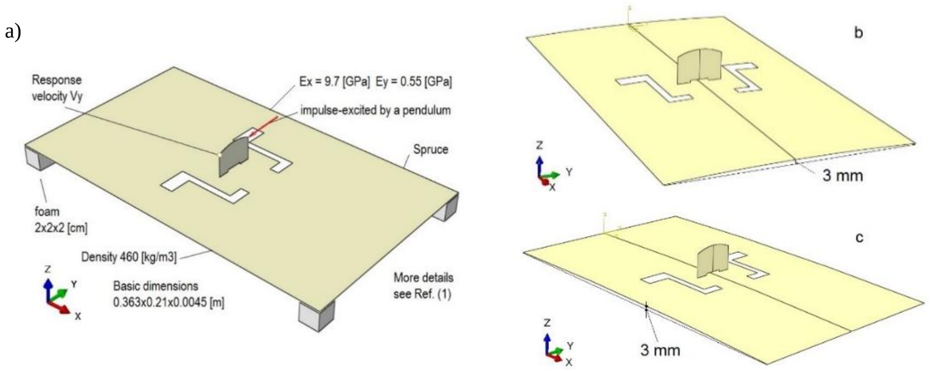

Figure 1. Plate with "f-holes"; a) sketch of bridge and supports
b) center line bending; c) bridge line bending

Secondly the plate was flattened by doing the same procedure but slightly bent in the opposite direction. The plate was now flat after drying. Finally the rod was placed under the centre line, see figure 1b and a 3 mm arching along the centreline was obtained.

In each case the plate was placed on soft supports at its corners. This was found close to free edges in measurements. In the acoustical measurements the bridge was impulse-excited by a pendulum hitting the bridge in the y-direction. A small magnet, mass approximately 30 mg was waxed to the other, opposite bridge corner. The resulting velocity, time history, in the y-direction was recorded by an electrical coil over a small airgap; see recorded time histories in Figure 2. By means of FFT the frequency spectra of the time histories were obtained, see Figure 3. The Figure 3a thus represents the frequency response of the plate bent with maximum arch along the bridge line, Figure 3b the plate "flat" and Figure 3c the plate bent along its centre line. In Figure 3a compared to Figure 3b flat plate it can be seen that the response level in the 2,5 kHz range is the lowest, i.e. the lowest for the "French" arching.

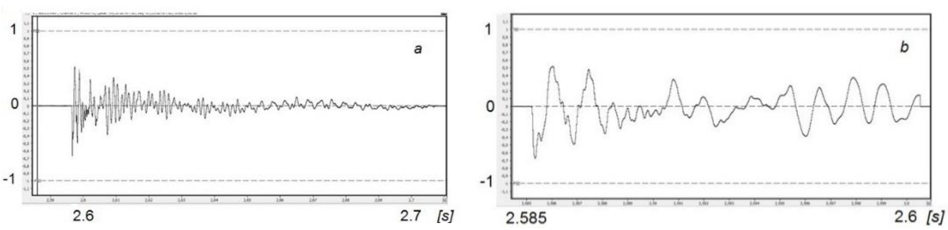

Figure 2. Time history (velocity) of plate flat a) initial 0,1 s and b) initial 0,015 s

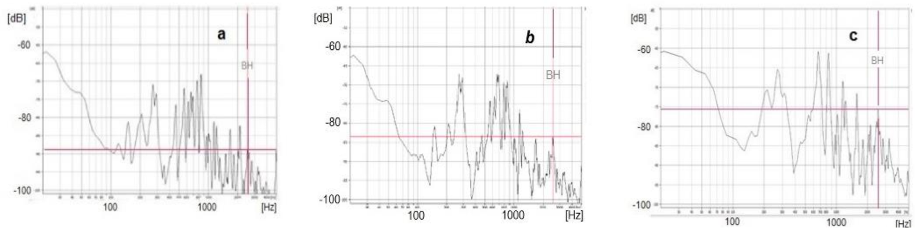

Figure 3. Frequency response of bridge time histories (velocity) for: a) plate bent as in Figure 1c; b) plate flattened; c) plate bent as in Figure 1b

3. FEM simulation

The geometry and properties of the plate applied for the experiment described above are used to create a discrete model in the FEM study. The basic difference between FEM model and experiment is application of the springs and dashpots instead of the foam to model boundary condition of the plate. It is shown in Figure 1a and Figure 4b.

Plate (spruce)	Young's modulus	$E_L = E_x = 9{,}7$ GPa; $E_R = E_y = 0{,}55$ GPa
	Density $\rho = 460$ kg/m^3, Poisson's r. $\nu_{xy} = 0{,}44$; $\nu_{xz} = 0{,}33$, $\nu_{yz} = 0{,}42$	
Bridge (maple)	Young's modulus	E= 10 GPa
	Density $\rho = 600$ kg/m^3, Poisson's ratio $\nu = 0{,}43$	

Additional properties were given from [11]

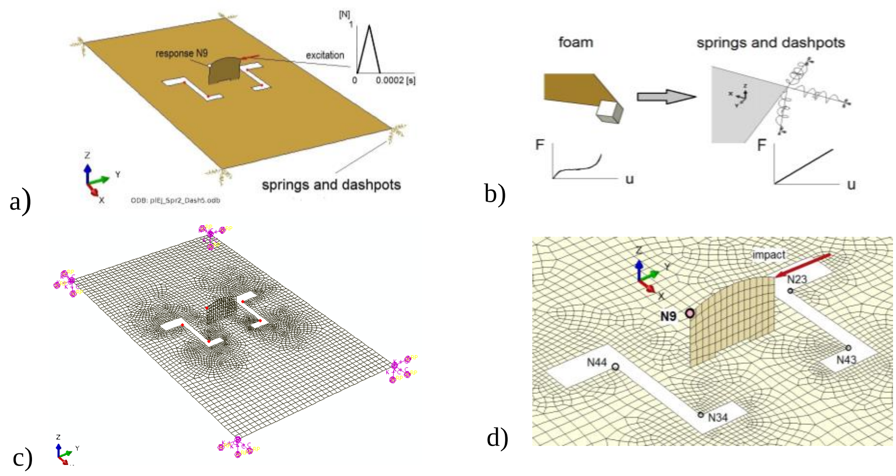

Figure 4. FEM model of the plate; a) shell model of the plate, b) support of the corners – foam (experiment) and springs (FEM), c) discrete model of the plate – 4016 shell elements type 4SR, d) "f-holes" and bridge with numbers of the output nodes

FEM model of the plate and boundary conditions are shown in Figure 4. Loads – excitation: see Fig. 4a and Table 1. The procedure *Dynamic*, *Explicit* of ABAQUS/Explicit System was used to lead simulation of the plate vibration. Selected results of FEM simulations are shown in Figure 5.

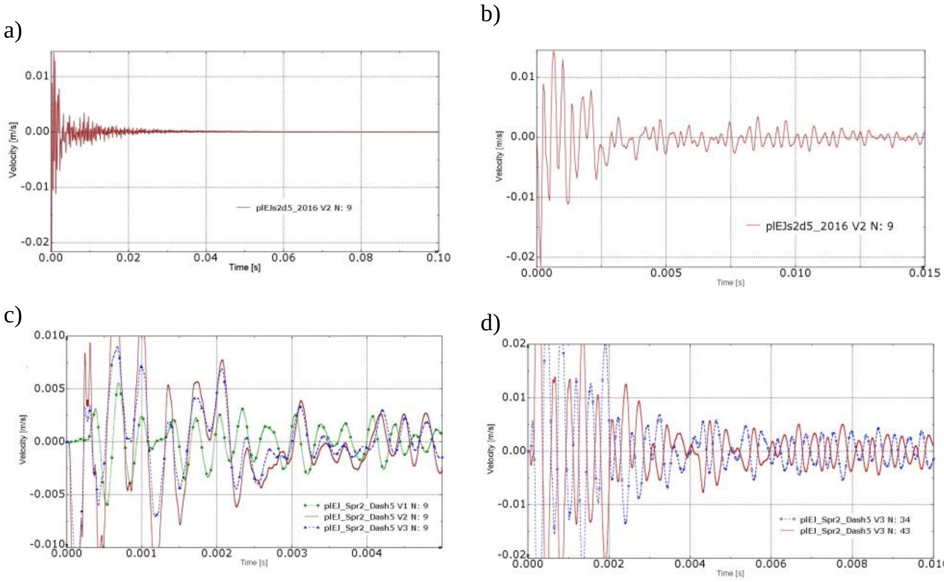

Figure 5. Time history (velocity) of the plate a) response of V_y in node N9 (see Fig. 4d) - initial 0,1s; b) response of V_y in node N9 initial 0,015 s; c) comparison of response V_x, V_y, V_z in node N9, d) comparison of response V_z in nodes N34, N43 (see Fig. 4d)

4. Signal post-processing

The FEM simulation gives results in the form of the time series (see Fig. 5). The mobility (admittance) can be obtained by digital signals processing (DSP) of excitation signal (force – see Fig. 4a) and the response signal of the tested model (velocity – e.g. Fig. 5a). A simplified algorithm of DSP procedures has been outlined in Figure 6. In the first step the output data from FEM simulation is windowed. Then, by FFT procedure the time signals are transformed into frequency domain. The transmittance (in this case module of the mobility in [ms^{-1}/N]) is obtained by dividing the response spectrum by the excitation spectrum. In the last step, magnitude of mobility is converted from linear to logarithmic scale which is more useful for comparisons of results of experiments and numerical simulations. The reference value equal to 1 ms^{-1}/N has been used. The sampling frequency used in the DSP system was equal to 20 kHz. It results from the time step of FEM analysis (Δt = 0,0005 s). The rectangle time window of the size of 2048 samples has been applied. Taking into account these parameters we can state that only a short signal sequences (of excitation and response about 0,1 s) has been used to determine the admittance (see Fig. 5a).

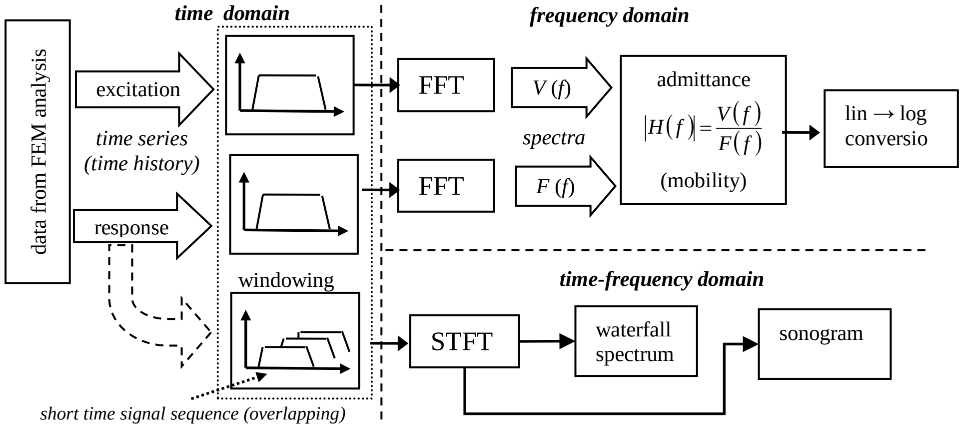

Figure 6. Simplifies scheme of digital signal post-processing used to the mobility determination of the violin bridge (based on FEM results)

The first 10 milliseconds of analyzed signals (excitation and response) are shown in Figures 7a and 7c. The short triangle force impact equal to 1 N and duration of 0,2 ms is visible in Figure 7a. Spectra of the excitation and the response are presented in Figures 7b and 7d respectively.

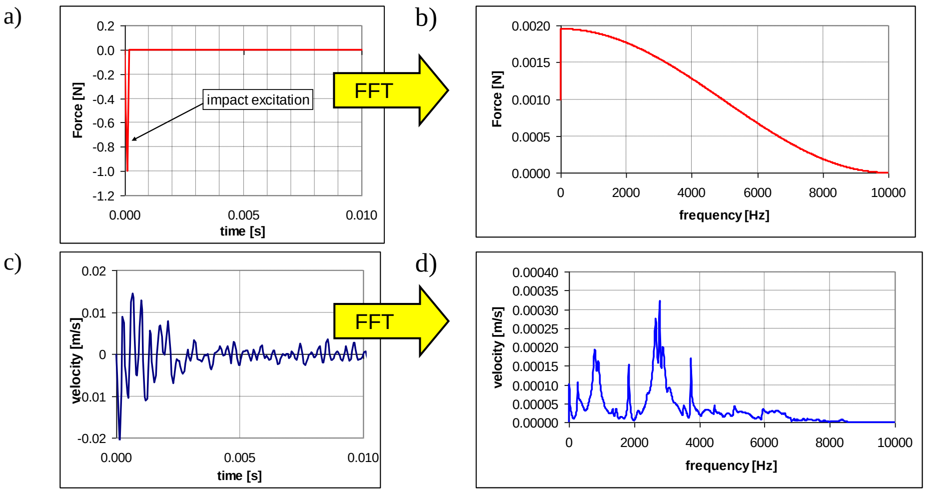

Figure 7. Example results of signals post-processing (flat plate; see Fig. 4) signals from FEM simulation : a) excitation signal c) response (V_y in node N9); spectra obtained by FFT: b) spectrum of excitation signal d) spectrum of response

The frequency range of spectral analysis and spectral resolution results directly from settings of DSP parameters. A sampling frequency f_s determines the frequency range. In this case it is limited to 10 kHz (½ f_s – Nyquist frequency). However a usable frequency range of the admittance may be lower. The frequency range depends on the shape and the duration of the virtual impact excitation which will be used for dynamic testing of FEM model. In practice the duration can not be shorter than Δt. The frequency resolution Δf (of spectra as well as the admittance) is determined by the sampling frequency and the number of signal samples (N) in the time window ($\Delta f = f_s/N$). Taking into account values of both these parameters the resolution Δf is approximately equal to about 10 Hz. It is worth mentioning that DSP software has been elaborated in the DASYLab® environment (*Data Acquisition System Laboratory*).

The mobility (admittance) in linear and logarithmic scale of the magnitude has been shown in Figure 8. In Figures 8a and 8b the BH ("Bridge Hill") frequency range has been marked.

a)

b)

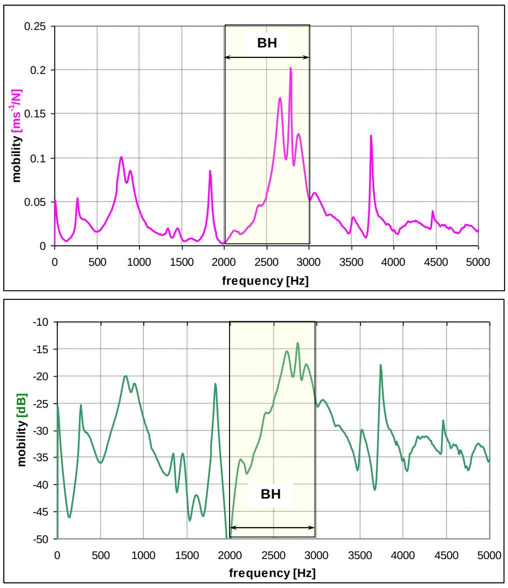

Figure 8. The final result of DSP – mobility (admittance) of violin FEM model;
a) linear scale b) logarithmic scale (flat plate see Fig. 4 – corresponding to response of V_y in node N9)

The Short Time Fourier Transform (STFT) was applied as auxiliary analysis which shows well the nature of the response signal in the frequency and time domain. This type of analysis has been described in [12]. Some optimization techniques of STFT can be found in [13]. An interesting approach to the time-frequency analysis and obtaining of a time-variant frequency response function is proposed in [14]. The methods mentioned above can be useful in development of new testing methods as well as parameterization of the vibroacoustical properties of violins.

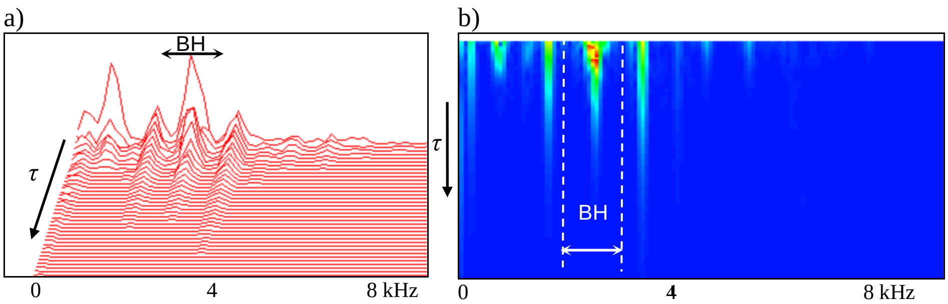

Figure 9. Violin model testing. The results of STFT analysis of the response signal presented in Fig. 5a . (where: BH is a frequency band pass of the "Bridge Hill"; τ is the shift of the time window); a) waterfall spectrum b) sonogram

5. Comparison of FEM – experiment

The basic differences between FEM and experimental testing are shown in Table 1.

Table 1. Comparison FEM - Experiment

FEM	Experiment
Structure	
The structure is divided into finite elements. All elements have the same properties.	The continuity of the structure. Local inhomogeneous density and other according to wooden properties.
Basic material properties	
Young's modules (E_L, E_R) are constant.	Young's modulus (E_L, E_R) are inhomogeneous according to local properties of the wooden plate. The average values of Young's modules are the same as in FEM
Boundary conditions	
The plate is supported on the springs and dashpots in axis directions (k_{spring} = 200 N/m) – linear – see Figure 4a,b,c 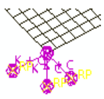	The plate is based on the foam ankles. The foam stiffness is unknown (typical nonlinear) – see Figure 1a and Figure 4b
Load – excitation	
Impact force F = -1N (triangle, time=0.0002s) – see Figure 4a,d 	Excited by a mechanical pendulum – see Figure 1a

6. Conclusions

Experiments were made with a rectangular wood-plate with a simplified bridge and simplified f-holes. The bridge was impulse excited by a mechanical pendulum and the velocity response was measured. By FFT the velocity response was transformed into frequency response. The plate was bent in three steps, first across the fibres with maximum arch along the bridge line, secondly flattened and finally bent along the fibres with maximum arch height along the centre line. Minimum level in the 2,5 kHz, the BH range, was found for the plate with the arch along the bridge line, somewhat higher for the flattened plate and the highest level for the plate arched along the centre line. The experimental results were subjectively evaluated and need independent verification and an explanation.

The comparison of the experiment results that are shown in Figure 3b and in [1, Figure 6c] to the transformed FEM results shown in Figure 8 confirms that typical BH exists near frequency of 2,8 kHz. Despite the differences shown in Table 1 the results of the experimental investigation and FEM coincide for the flat plate.

Preliminary FEM simulations of the bent plates that are shown in Figure 1b and Figure 1c do not confirm experiment results exactly that are shown in Figure 3a and Figure 3c. Further research are planned to clarify the reasons of the differences. Perhaps the methods of bending plates used in the experiment had introduced changes in the material properties of the plates. FEM models ought to be checked beside of this.

Acknowledgment

This paper was partially financially supported in the year 2016 by research project 02/21/DSPB/3478.

References

1. F. Durup, E. V. Jansson, *The quest of the violin bridge hill*. Acustica - Acta Acustica (2004), **91** (2005) 206 – 213.
2. W. Reinicke, *Die Übertragungseigenschaften des Streichinstrumentenstegs,* Doctoral dissertation, Technical University of Berlin, 1973.
3. L. Cremer, *The physics of the violin*, chapter 9, MIT Press, Cambridge MA, 1985.
4. E. V. Jansson, B. K. Niewczyk, *On the acoustics of the violin bridge or body hill*, J. Catgut Acoust. Soc. Series **23** (1999) 23 – 27.
5. J. Woodhouse, *On the "Bridge hill" of the Violin*, Acustica-Acta Acustica, **91** (2005) 155 – 165.
6. J. Woodhouse, *The acoustics of the violin*, a review Rep. Prog. Phys. 77 (2014) 115901 (42pp).
7. E. V. Jansson, *Admittance measurements of 25 high quality violins*, Acustica - Acta Acustica, **83** (1997) 337– 341.
8. E. V. Jansson, B. K. Niewczyk, A. Knast, *An investigation of old violins in Poznan and Krakow*, unpublished report.

9. E. V. Jansson, *On the prominence of the violin bridge hill in notes of played music*, J. Violin Soc. Am. VSA papers Summer 2009 XXII, No 1, 169 – 176.
Better ref E. Jansson, *On projection: long-time-average spectral analysis of four played violins* JVS VSA papers Summer 2006, Vol. XX, No 2, 143 – 154.
10. S. Zygmuntowicz, *Strad3D DVD*, 2009.
11. E. K. Askenazi, Anisotropy of woods and wood materials, Forest industry (*"Lesnaiia Promyslennost"*), Moscow 1978.
12. S. Qian, D. Chen, *Joint time-frequency analysis: methods and applications*, Upper Saddle River, NJ, Prentice-Hall 1996.
13. K. Dziedzich, W. Staszewski, T. Uhl, Time–*frequency analysis of time-variant systems*, Diagnostyka, **14**(1) (2013) 37 – 42.
14. R. Barczewski, *Diagnostic oriented methods of short time processing of vibroacoustical signals*, Publishing House of Poznan University of Technology, monograph, No 504, Poznan, 2013.

Implementation of Ffowcs Williams and Hawkings Aeroacoustic Analogy in OpenFOAM

Konrad JAROSZ
AGH University of Science and Technology
Faculty of Mechanical Engineering and Robotics
Department of Power Systems and Environmental Protection Facilities
Al. Mickiewicza 30, 30-059 Kraków, jaroszk@agh.edu.pl

Ireneusz CZAJKA
AGH University of Science and Technology
Faculty of Mechanical Engineering and Robotics
Department of Power Systems and Environmental Protection Facilities
Al. Mickiewicza 30, 30-059 Kraków, iczajka@agh.edu.pl

Andrzej GOŁAŚ
AGH University of Science and Technology
Faculty of Mechanical Engineering and Robotics
Department of Power Systems and Environmental Protection Facilities
Al. Mickiewicza 30, 30-059 Kraków, ghgolas@cyf-kr.edu.pl

Abstract

This paper presents the development of post-processing aeroacoustics utility for OpenFOAM, based on Ffowcs Williams-Hawkings aeroacoustic analogy. Although the FH-W analogy is well known for almost 50 years, there is a lack of open-source software which is using it, hence decision to perform this implementation. This is the veryfirst version of utility, so only one formulation of FH-W were implemented. Presented application allows to compute far-field acoustic pressure from near field CFD solution. Validation is based on NASA Tandem Cylinder Case. Comparison of the results from simulation show fairly good agreement with experimental data.

Keywords: *aeroacoustics, CFD, FH-W analogy, CAA, OpenFOAM, FVM*

1. Introduction

Engineering problems like far-field noise prediction of aircraft landing gear or helicopter rotor it is still a challenge, despite there is a constant progress in computational aeroacoustics(CAA). Complexity of these cases and large distances to far-field, causes that accurate solution of acoustic fluctuations propagation inside computational domain would beineffective.

There is a way to bypass this difficulty by introducing some integral methods. Those methods are using data obtained from time-dependent CFD(computational fluid dynamics) solution or PIV measurements. That data should be accurate enough to capture all potential noise sources. The next step is to use anaeroacoustic analogy to propagate near-field results(sources)to the far-field observers. This paper is a try to extend the research conducted in [10].

It is worth mentioning that apart from the technical aspects of modeling of the sound distribution, more and more research uses the modeling of wave phenomena to the sound synthesis [11].

2. Lighthill equation

The Lighthill analogy[1][2] is applicable to unbounded, incompressible, low Mach number flow. These equations are derived from Navier-Stokes[7] equations, which are reorganised into inhomogeneous wave equation, in form presented below:

$$\frac{\partial^2 \rho}{\partial t^2} - a_0^2 \nabla^2 \rho = \frac{\partial^2}{\partial x_i \partial x_j} T_{ij} \tag{1}$$

$$T_{ij} = \rho u_i u_j + p_{ij} - a_0^2 \rho \delta_{ij} \tag{2}$$

The source term from equation (1) and described in equation (2) has been named a Lighthill stress tensor. It contains acoustical sources, which are represented as a flow parameters. Mathematically speaking, equation (1) is a hyperbolic differential equation, which describes acoustic wave propagation with speed of sound a_0. Because of assumptions that were made, these analogy have some obvious limitations:

- propagation of sound is through unbounded domain,
- level of sound pressure is relatively small,
- acoustic wave have no influence on the flow.

So it is clear, that Lighthill analogy is applicable only on subsonic flows.

3. Ffowcs-Williams Hawkings analogy

FH-W analogy[3] is an extended version of Lighthill analogy. It introduces the so called source surfaces, which are taken into account when computing the sound pressure level at the observer. Those surfaces can be set as surfaces of solid body(impermeable) or as a any free surface located in domain(permeable). In contradiction to Lighthill analogy, FH-W analogy allows the motion of the bodies inside fluid domain, that fact extends its applicability to predict noise generated by rotors. Analogy is govern by equations below:

$$\begin{aligned} &\frac{1}{a_0} \frac{\partial^2 (\rho - \rho_0)}{\partial t^2} - \nabla^2 (\rho - \rho_0) = \frac{\partial}{\partial t}[Q_n \delta(f)] - \frac{\partial}{\partial x_i}[L_i \delta(f)] + \\ &+ \frac{\partial^2}{\partial x_i \partial x_j}[T_{ij} H(f)] \end{aligned} \tag{3}$$

Where Q_n and L_i are defined as:

$$Q_n = Q_i \hat{n}_i = [\rho_0 v_i + \rho(u_i - v_i)]\hat{n}_i \tag{4}$$

$$L_i = L_{ij} \hat{n}_i = [P_{ij} + \rho u_i (u_j - v_j)]\hat{n}_i \tag{5}$$

The source surface mentioned before(also called integration surface) is described as $f(x,t)=0$ and $\hat{n}_i = \nabla f$ is a unit normal vector pointed out from surface f. In equations (4) and (5) $v_i$denotes the velocity of surface *f*, while u_i is the velocity of the fluid at the integration surface. If the source surface is equal to the solid body surface then $u_i=v_i$.

In equation (5) there is a compressible stress tensor:

$$P_{ij} = (p - p_0)\delta_{ij} - \tau_{ij} \tag{6}$$

Because of the contribution of the last term of equation (6) to total acoustic power is relatively small, it can be neglected. Also we can assume that the disturbances of density outside the source surface are also small, so the term $(\rho\text{-}\rho_0)$ can be replaced by p', which is considered to be acoustic pressure.

4. Formulation 1A

For a complex geometry it is hard to find the direct solution of equation (3). Therefore some numerical formulations of FH-W analogy were introduced.One of them is formulation 1A proposed by Farassant[5][6]. It is suitable for moving solid bodies in fluid at rest. That formulation was developed to improve prediction of noise generated by helicopter rotor.

The acoustic pressure p'that is generated by solid body with subsonic velocity, measured by observer in position x and time t is given by:

$$p'(x,t) = p'_T(x,t) + p'_L(x,t) \tag{7}$$

$$\begin{aligned} 4\pi p'_T(x,t) = &\int_{f=0} \left[\frac{\dot{Q}_n + Q_{\dot{n}}}{r(1-M_r)^2} \right]_{ret} dS + \\ &+ \int_{f=0} \left[\frac{Q_n (r\dot{M}_r + a_0(M_r - M^2))}{r^2(1-M_r)^3} \right]_{ret} dS \end{aligned} \tag{8}$$

$$\begin{aligned} 4\pi p'_L(x,t) = &\int_{f=0} \left[\frac{\dot{L}_r}{r(1-M_r)^2} \right]_{ret} dS + \\ &+ \int_{f=0} \left[\frac{L_r - L_M}{r^2(1-M_r)^3} \right]_{ret} dS + \\ &+ \int_{f=0} \left[\frac{L_r (r\dot{M}_r + a_0(M_r - M^2))}{r^2(1-M_r)^3} \right]_{ret} dS \end{aligned} \tag{9}$$

Where M denotes Mach number of a source, with components $M_i=v_i/a_0$, the dot "·" means time derivative with respect to emission time τ. Other components of equations (8) and (9) are following:

$$M_r = M_i r_i \quad \dot{M}_r = \frac{\partial M_i}{\partial \tau} r_i$$

$$Q_n = Q_i \hat{n}_i \quad \dot{Q}_n = \frac{\partial Q_i}{\partial \tau} \hat{n}_i \quad Q_{\dot{n}} = Q_i \frac{\partial \hat{n}_i}{\partial \tau} \tag{10}$$

$$L_i = L_{ij} \hat{n}_i \quad \dot{L}_r = \frac{\partial L_i}{\partial r} \hat{r}_i \quad L_r = L_i \hat{r}_i \quad L_M = L_i M_i$$

Subscript *ret* means that the integral is evaluated at the emission time. The retarded time equation has a form presented below:

$$g = \tau_{ret} - t + \frac{r}{a_0} = 0 \tag{11}$$

Where $r = |x - y(ret)|$, and is a distance between observer and the source at the emission time.

5. Formulation GT

In case, that could be defined as flow inside wind tunnel, there is situation when both observer and source remain motionless. Only fluid has a velocity. Also there is a need to assume that mean flow velocity has a direction $+x_1$, which leads to $U_0 = (U_{01}, 0, 0)$. These situation is equivalent to situation when source and observer are in motion with velocity $-U_0$ but the fluid is at rest. With those assumptions there is an ability to use special case of formulation A1.

For source in subsonic, rectilinear and uniform motion equation (11) given by Garrick [4] simplifies to form:

$$\tau_{ret} = t = \frac{R}{a_0} \tag{12}$$

And distance between source and observer is given by:

$$R = \frac{-M_0(x_1 - y_1) + R^*}{\beta^2} \tag{13}$$

Where:

$$R^* = \sqrt{(x_1 - y_1)^2 + \beta((x_2 - y_2)^2 + (x_3 - y_3)^2)} \tag{14}$$

$$\beta = \sqrt{1 - M_0^2} \tag{15}$$

In this particular case R is an effective acoustic distance, rather than geometric. Components of unit distance vector are defined as:

$$\hat{R}_1 = \frac{-M_0 R^* + (x_1 - y_1)}{\beta^2 R} \quad \hat{R}_2 = \frac{(x_2 - y_2)}{R} \quad \hat{R}_3 = \frac{(x_3 - y_3)}{R} \quad M_R = M_i \hat{R}_i \tag{16}$$

Variables Q_n and L_i are identical as in equations (4) and (5), but in this formulation velocity of integration surface v_i is replaced by $-U_{0i}$, because all of the velocity components has to expressed in stationary reference frame. So equations (4) and (5) could be rewrite as:

$$Q_n = [\rho_0 U_{0i} + \rho(u_i + U_{0i})]\hat{n}_i \tag{17}$$

$$L_i = [P_{ij} + \rho u_i (u_j + U_{0j})]\hat{n}_i \tag{18}$$

In contradiction to formulation 1A, distance between source and observer is not a function of time, so *R=const* also as other variables which depend on time.Those variables which are not function of time could be computed at initial step.Also derivatives of those variables could be neglected.That leads to simplification of computation. Simplified equations (8) and (9) could be written as:

$$\begin{aligned} 4\pi p'_T(x,t) &= \int_{f=0}\left[\frac{\dot{Q}_n}{R(1-M_R)^2}\right]_{ret} dS + \\ &+ \int_{f=0}\left[\frac{Q_n + a_0(M_R - M^2)}{R^2(1-M_R)^3}\right]_{ret} dS \end{aligned} \tag{19}$$

$$\begin{aligned} 4\pi p'_L(x,t) &= \int_{f=0}\left[\frac{\dot{L}_R}{R(1-M_R)^2}\right]_{ret} dS + \\ &+ \int_{f=0}\left[\frac{L_R - L_M}{R^2(1-M_R)^3}\right]_{ret} dS + \\ &+ \int_{f=0}\left[\frac{L_R(M_R - M^2)}{R^2(1-M_R)^3}\right]_{ret} dS \end{aligned} \tag{20}$$

6. Numerical implementation

In the first version of the utility presented in this paper, the GT formulation were implemented. The decision were made to make this application working as a post-processing utility of OpenFOAM(open source FVM software). Due to fact that acoustic pressure measured at the observer is a function of time, the CFD simulation,which will provide input data, needs to be time dependent. Each cell of finite volume mesh will be treated as a separate acoustic source region.

The retarded time equation (12) could be resolved in 2 ways. In the first option, commonly called retarded time algorithm, receive time t is set, and then the emission time τ_{ret} has to be found, and finally the integrals are evaluated. Considering a numerical calculations this could be confusing, because of the possibility of not having input data at computed emission time.

The second approach is to set constant emission times, which in fact will be equal to CFD time steps, then appropriate receive times needs to be calculated. That algorithm was described in [6].

For purpose of these implementation, the second approach was chosen. In constant emission time algorithm, there is a need to interpolate calculated data of each source region at the same receive times. That is necessary to correctly sum noise deriving from all sources.

The last simplification in this version of utility, is to allow use only solid body surfaces(impermeable) as a source surfaces. It will reduce the computational complexity of utility. Equation (7) will be simplified to form:

$$p'(x,t) = p'_L(x,t) \tag{21}$$

Computations made with usage of theaeroacuostical analogies have that advantage, that observer could be located outside of computational domain. That allows to reduce size of computational mesh, and simulate only area of interest. But there is also a disadvantage, those analogies does not take into account the reflections of the acoustic wave. They are also "blind" to solid reflecting surfaces. The final decision, if use or not to use, always depend on user.

7. Validation of implementation

To check if implemented analogy works properly, some validation was performed.It was a CFD simulation of tandem cylinder case, which is well described in [8], also a experimental data are available[8]. Geometry and flow parameters of the test case are presented below. All microphones are located at the center plane of the span.

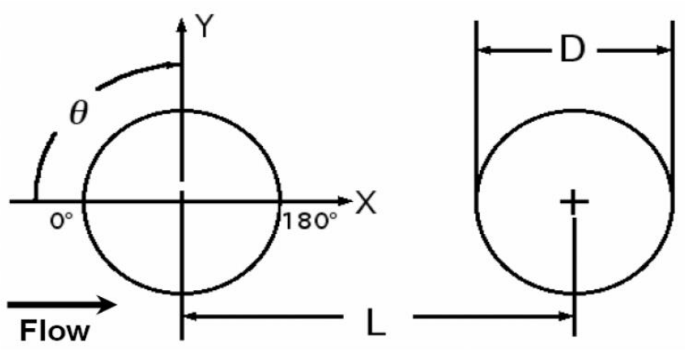

Figure 1. Configuration of test case

- D = 0.05715 [m] L=3.7 D Re=166000 M=0.128 (44 m/s)
- Span = 12 D
- Mic. A(-8.33D, 27.815D) Mic.B(9.11D, 32.49D) Mic.C(26.55D, 27.815D)

To obtain results, transient simulation with Spalart-Allmaras[7][9] turbulence model was performed. Due to fact that used solver demands Courant number lower than 1 and very fine quality of computational mesh (around 5 million of finite volume elements), time step value was $\Delta t=10^{-5}s$. Because $y+$ parameter value were lower than 1, no wall functions were used. Simulation results served as input to implemented utility. Computation took almost 2 weeks on Zeus HPC cluster (24 cores).

Results from microphone B are shown on Figure 2. There is slight difference between simulation and experimental data, but the dominant frequency is almost the same(around 170 Hz), with similar levels. Better results could be obtained with more accurate computational grid. But that needs more hardware resources to use, and also drastically extends simulation time.

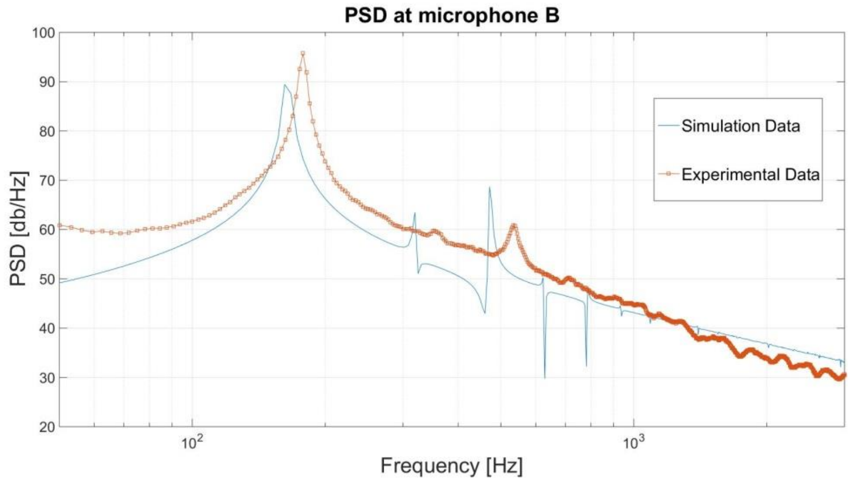

Figure 2. PSD at microphone B

8. Conclusions

Benchmark test that was conducted, shows that presented implementation of FH-W analogy works more or less properly. It is a desirable tool for predicting acoustic pressure at far-field observer. Acoustic analogies allows to compute acoustic pressure outside of numerical domain, what causes in significant reduce in computation time. The next will be an implementation of 1A formulation, which extend utility potential to permeable surfaces and more general cases, for example helicopter rotor noise.

Acknowledgments

This paper was supported in part by Cyfronet AGH infrastructure.

References

1. M. J. Lighthill, *On Sound Generated Aerodynamically I. General Theory*, Proceedings of the Royal Society A: Mathematical, Physical and Engineering Sciences, **211**(1107) (1952) 564 – 587.
2. M. J. Lighthill, *On Sound Generated Aerodynamically II. Turbulence as a Source of Sound*, Proceedings of the Royal Society A: Mathematical, Physical and Engineering Sciences, **222**(1148) (1954).
3. J. E. Ffowcs Williams, D. L. Hawkings, *Sound generation by turbulence and surfaces in arbitrary motion*, Proc. R. Soc. Lond. A, **264** (1969) 321 – 342.

4. I. E Garrick, E. W. Watkins, *A Theoretical Study of the Effect of Forward speed on the Free Space Sound Pressure Field Around Helicopters*, Tech. Rep. TR-1198, NACA, 1954.
5. F. Farassant, *Derivation of Formulation 1 and 1A of Farassant*, Tech. Rep. TM-2007-214853, NASA, 2007.
6. K S. Brentner, F.Farassant, *Modeling aerodynamically generated sound of helicopter rotors*, Prog. Aerospace Sci., **39** (2003) 83 – 120.
7. D. C. Wilocox, T*urbulence Modeling for CFD*, 2006.
8. D. P. Lockard, M. M Choudhari, M. R Khorrami, D. H Neuhart, F. V. Hutcheson, T. F Brooks, D. J. Stead, *Aeroacoustic Simulations of Tandem Cylinders with Subcritical Spacing*, AIAA-2008-2862, 2008.
9. P. R. Spalart, S. R. Allmaras, *A One-Equation Turbulence Model for Aerodynamic Flows*, AIAA Paper 92-0439, 1992.
10. I. Czajka, K. Jarosz, K. Suder-Dębska, *Modelling of an aerodynamic noise of a horizontal axis wind turbine using ANSYS/Fluent and OpenFOAM packages*, 7th forum acusticum 2014, Kraków 7-12.09.2014.
11. M. Pluta, B. Borkowski, I. Czajka, K. Suder-Dębska, *Sound synthesis using physical modeling on heterogeneous computing platforms*, Acta Physica Polonica. A, **128** (2015).

Free Vibrations of Medium Thickness Microstructured Plates

Jarosław JĘDRYSIAK
Department of Structural Mechanics, Łódź University of Technology
al. Politechniki 6, 90-924 Łódź, jarek@p.lodz.pl

Abstract

A problem of free vibrations of medium thickness microstructured plates, which can be treated as made of functionally graded material on the macrolevel is presented. The size of the microstructure of these plates is of an order of the plate thickness. Averaged governing equations of these plates can be obtained using the tolerance modelling technique, cf. [18, 19, 9]. Because, the derived tolerance model equations have the terms dependent of the microstructure size, this model describes the effect of the microstructure size. Results can be evaluated introducing the asymptotic model. Calculated results can be compared to those from the finite element method or a similar tolerance model of thin plates, cf. [9].

Keywords: medium thickness functionally graded plates, microstructure, tolerance modelling

1. Introduction

In this paper, medium thickness functionally graded plates with microstructure are investigated. Their microstructure is in planes parallel to the plate midplane along one, i.e. the x_1-axis direction. It is assumed that plate properties along the perpendicular direction are constant. Moreover, the size of the microstructure is assumed to be of an order of the plate thickness. An example of these plates is shown in Figure 1, cf. [12].

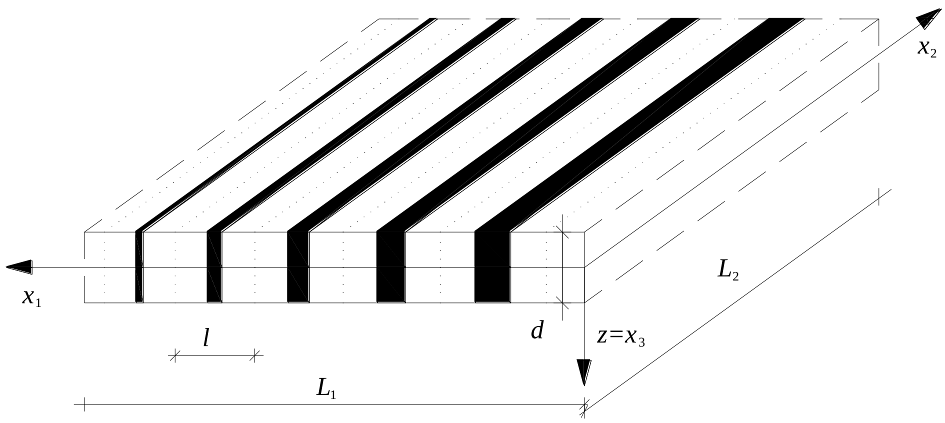

Figure 1. Fragment of a medium thickness functionally graded plate with the microstructure, cf. [12]

These plates consist of many small elements along the x_1-axis with a span equal l, cf. Figure 2, ($x \equiv x_1$). Such elements are called the cells. Their length l describes the size of the microstructure and is called the microstructure parameter.

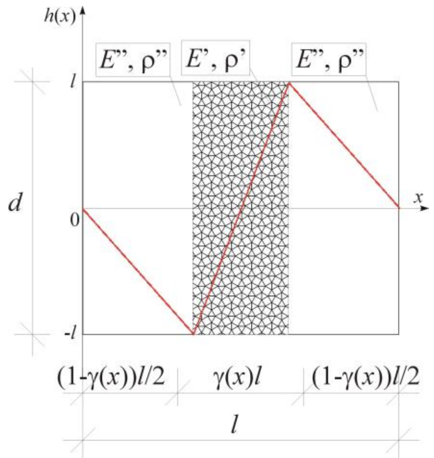

Figure 2. Element of the plate with a fluctuation shape function, cf. [12]

Thermomechanical problems of functionally graded media are often described applying various averaging approaches, which are used for macroscopically homogeneous structures, cf. Jędrysiak [7, 8]. Models of periodic plates based on the asymptotic homogenization method play a role between them, cf. Kohn and Vogelius [14]. In a series of papers there are shown applications of other methods, which describe various problems of thermoelasticity of beams, plates and shells, e.g. frequencies of functionally graded plates using a meshless method by Ferreira et al. [5], vibrations of functionally graded shells by Tornabene and Viola [17], thermoelasticity of functionally graded plates by Akbarzadeha [1], dynamics of beams with functionally graded core by Bui et al. [3], buckling of sandwich beams with variable properties of a core by Grygorowicz et al. [6]. However, the effect of the microstructure size is neglected in governing equations of these models.

In order to take into account this effect the tolerance averaging technique can be applied, cf. [18, 19, 7]. Various periodic structures are modelled by using this method in many papers, e.g. medium thickness periodic plates by Baron [2], higher order vibrations of thin periodic plates by Jędrysiak [7], nonlinear thin periodic plates by Domagalski and Jędrysiak [4], vibrations of periodic three-layered plates by Marczak and Jędrysiak [15]. The tolerance method is also adopted and successfully used to analyse different functionally graded structures, e.g. thermoelastic problems of laminates, plates and shells with functionally graded structure by Jędrysiak [8] or Michalak [16], stability of thin functionally graded plates by Jędrysiak and Michalak [11], vibrations of thin transversally graded plates by Kaźmierczak and Jędrysiak [13], vibrations of thin functionally graded plates with the size of the microstructure of an order of the plate thickness by Jędrysiak [9, 10], Jędrysiak and Pazera [12].

2. Modelling foundations

By $Ox_1x_2x_3$ the orthogonal Cartesian coordinate system is denoted and t is the time coordinate. Let us introduce arguments: $\mathbf{x}\equiv(x_1,x_2)$, $z\equiv x_3$; and p as a loading along z-axis. The region of the undeformed plate is described by $\Omega\equiv\{(\mathbf{x},z):-d/2\le z\le d/2,\mathbf{x}\in\Pi\}$, with the midplane Π and the plate thickness d. The "basic cell" $\Delta\equiv[-l/2,l/2]$ is defined in the interval $\Lambda=(-L_1/2,L_1/2)$ on the x_1-axis, with l as the span of cell Δ, called *the microstructure parameter*. Parameter l is assumed to satisfy the conditions $d\sim l<<L_1$.

Let properties of the plate: a mass density μ, a rotational inertia ϑ and bending stiffnesses $d_{\alpha\beta\gamma\delta}$, be tolerance-periodic functions in x defined as:

$$\begin{aligned} &\mu(x)\equiv\int_{-d/2}^{d/2}\rho(x,z)dz, && \vartheta(x)\equiv\int_{-d/2}^{d/2}\rho(x,z)z^2dz,\\ &b_{\alpha\beta\gamma\delta}(x)\equiv\int_{-d/2}^{d/2}c_{\alpha\beta\gamma\delta}(x,z)z^2dz, && d_{\alpha\beta}(x)\equiv\tfrac{5}{6}\int_{-d/2}^{d/2}c_{\alpha3\beta3}(x,z)dz. \end{aligned} \tag{1}$$

Under assumptions of the Hencky-Bolle-type plates theory equations for deflection $u(\mathbf{x},t)$ and rotations $\phi_\alpha(\mathbf{x},t)$, $\alpha=1,2$, of functionally graded plates under consideration can be written in the following form:

$$\begin{aligned} &\partial_\beta(b_{\alpha\beta\gamma\delta}\partial_\delta\phi_\gamma)-d_{\alpha\beta}(\partial_\beta u+\phi_\beta)-\vartheta\ddot{\phi}_\alpha=0,\\ &\partial_\alpha[d_{\alpha\beta}(\partial_\beta u+\phi_\beta)]-\mu\ddot{u}=-p. \end{aligned} \tag{2}$$

The above equations have highly oscillating, tolerance-periodic, non-continuous coefficients being functions in x.

3. Tolerance modelling

3.1. Modelling concepts

In the tolerance averaging technique there are used some basic concepts, defined in books, cf. [18, 19, 8].

Denote $\Delta(x)\equiv x+\Delta$, $\Lambda_\Delta=\{x\in\Lambda\colon \Delta(x)\subset\Lambda\}$, as a cell at $x\in\Lambda_\Delta$. The first concept is *the averaging operator* for an arbitrary integrable function f, defined by

$$< f >(x,x_2)=\tfrac{1}{l}\int_{\Delta(x)} f(y,x_2)dy,\quad x\in\Lambda_\Delta. \tag{3}$$

For function f being tolerance-periodic in x, averaged value by (3) is a slowly-varying function in x.

Following the aforementioned books other introductory concepts are denoted as: a set of tolerance-periodic functions by $TP_\delta^\alpha(\Lambda,\Delta)$, a set of slowly-varying functions by $SV_\delta^\alpha(\Lambda,\Delta)$, a set of highly oscillating functions by $HO_\delta^\alpha(\Lambda,\Delta)$, where $\alpha\ge 0$, δ is a tolerance parameter. Very important concept is *the fluctuation shape function* $g(\cdot)$, called of the 1-st kind of that function, if it is: a continuous highly oscillating function, $g\in FS_\delta^1(\Lambda,\Delta)$, with a piecewise continuous and bounded gradient $\partial^1 g$; and it depends on l as a parameter and satisfies conditions: $\partial^k g\in O(l^{\alpha-k})$ for $k=0,1,\ldots,\alpha$, $\partial^k g\equiv g$, and $<\mu g>(x)\approx 0$ for every $x\in\Lambda_\Delta$, $\mu>0$, $\mu\in TP_\delta^1(\Lambda,\Delta)$.

3.2. Fundamental assumptions of the tolerance modelling

Two fundamental modelling assumptions stand a base of the tolerance modelling, cf. the books edited by Woźniak et al. [18, 19] and for thin functionally graded plates [8, 9, 13].

The first assumption of them is *the micro-macro decomposition*, where the plate displacements are decomposed as:

$$u_3(\mathbf{x},z,t)=u(\mathbf{x},t)=w(\mathbf{x},t),\\ u_\alpha(\mathbf{x},z,t)=z[\varphi_\alpha(\mathbf{x},t)+g(x)\theta_\alpha(\mathbf{x},t)],\qquad \alpha=1,2; \tag{4}$$

with new basic kinematic unknowns: *macrodeflection* $w(\cdot,x_2,t)\in SV^1_\delta(\Lambda,\Delta)$, *macrorotations* $\varphi_\alpha(\cdot,x_2,t)\in SV^1_\delta(\Lambda,\Delta)$, and *the fluctuation amplitudes* $\theta_\alpha(\cdot,x_2,t)\in SV^1_\delta(\Lambda,\Delta)$; $g(\cdot)$ as the known *fluctuation shape function*, having the form of a saw-type function of x, cf. Figure 2.

The tolerance averaging approximation is the second assumption, in which it is assumed that terms of an order of $O(\delta)$ are treated as negligibly small, cf. [18, 19, 8], e.g. for $f\in TP^1_\delta(\Lambda,\Delta),\quad g\in FS^1_\delta(\Lambda,\Delta),\quad F\in SV^a_\delta(\Lambda,\Delta), a=1,2,$ in: $<f>(x)=<\bar{f}>(x)+O(\delta),$ $<fF>(x_1)=<f>(x_1)F(x_1)+O(\delta),\ <f\partial_\alpha(gF)>(x)=<f\partial_\alpha g>(x)F(x)+O(\delta)$.

3.3. The outline of the tolerance modelling procedure

The tolerance modelling procedure is shown in the books: for composites in [18, 19], for plates in [8]. Here, an outline of this method is shown.

In the tolerance modelling a few basic steps can be distinguished. In the first step micro-macro decomposition (4) is used. Than averaging operator (3) is applied to the resulting formula, and the tolerance averaged lagrangean $<\Lambda_g>$ is derived:

$$\begin{aligned}<\Lambda_g>=&\tfrac{1}{2}(<\mu>\dot{w}\dot{w}+<\vartheta>\dot{\varphi}_\alpha\dot{\varphi}_\beta\delta_{\alpha\beta}+\underline{<\vartheta gg>\dot{\theta}_\alpha\dot{\theta}_\beta\delta_{\alpha\beta}})-\\ &-\tfrac{1}{2}(<b_{\alpha\beta\gamma\delta}>\partial_\alpha\varphi_\beta\partial_\gamma\varphi_\delta+2<b_{\alpha\beta1\delta}\partial_1 g>\partial_\alpha\varphi_\beta\theta_\delta+<b_{1\beta1\delta}\partial_1 g\partial_1 g>\theta_\beta\theta_\delta+\underline{<b_{2\beta2\delta}gg>\partial_2\theta_\beta\partial_2\theta_\delta})-\\ &-\tfrac{1}{2}(<d_{\alpha\beta}>\partial_\alpha w\partial_\beta w+<d_{\alpha\beta}>\partial_\alpha w\varphi_\beta+<d_{\alpha\beta}>\varphi_\alpha\varphi_\beta+\underline{<d_{\alpha\beta}gg>\theta_\alpha\theta_\beta})+<p>w\end{aligned} \tag{5}$$

In the next step using the principle of stationary to (5) the Euler-Lagrange equations for $w(\cdot,x_2,t)$, $\varphi_\alpha(\cdot,x_2,t)$, $\theta_\alpha(\cdot,x_2,t)$ can be obtained:

$$\begin{aligned}&-\frac{\partial}{\partial t}\frac{\partial<\Lambda_g>}{\partial\dot{w}}-\partial_\alpha\frac{\partial<\Lambda_g>}{\partial\,\partial_\alpha w}+\frac{\partial<\Lambda_g>}{\partial w}=0,\\ &-\frac{\partial}{\partial t}\frac{\partial<\Lambda_g>}{\partial\dot{\varphi}_\alpha}-\partial_\alpha\frac{\partial<\Lambda_g>}{\partial\,\partial_\alpha\varphi_\beta}+\frac{\partial<\Lambda_g>}{\partial\varphi_\alpha}=0,\\ &-\frac{\partial}{\partial t}\frac{\partial<\Lambda_g>}{\partial\dot{\theta}_\alpha}-\partial_2\frac{\partial<\Lambda_g>}{\partial\,\partial_2\theta_\alpha}+\frac{\partial<\Lambda_g>}{\partial\theta_\alpha}=0.\end{aligned} \tag{6}$$

4. Model governing equations

Substitute the tolerance averaged lagrangean (5) to the Euler-Lagrange equations (6). Than, the system of equations for $w(\cdot,x_2,t)$, $\varphi_\alpha(\cdot,x_2,t)$, $\theta_\alpha(\cdot,x_2,t)$ is derived in the following form:

$$\begin{aligned}&\partial_\beta(<b_{\alpha\beta\gamma\delta}>\partial_\delta\varphi_\gamma)+\partial_\beta(<b_{\alpha\beta\gamma1}\partial_1 g>\theta_\gamma)-<d_{\alpha\beta}>(\partial_\beta w+\varphi_\beta)-<\vartheta>\ddot{\varphi}_\alpha=0,\\ &\partial_\alpha(<d_{\alpha\beta}>(\partial_\beta w+\varphi_\beta))-<\mu>\ddot{w}=-p,\\ &-<b_{\alpha1\gamma\delta}\partial_1 g>\partial_\delta\varphi_\gamma-(<b_{\alpha1\beta1}\partial_1 g\partial_1 g>+\underline{\underline{<d_{\alpha\beta}gg>}})\theta_\beta+\underline{\underline{<b_{\alpha2\gamma2}gg>}}\partial_{22}\theta_\gamma-\underline{<\vartheta gg>}\ddot{\theta}_\alpha=0.\end{aligned} \tag{7}$$

Equations (7) together with micro-macro decomposition (4) determine *the tolerance model of dynamics of medium thickness functionally graded plates with the microstructure size of an order of the plate thickness*. The underlined terms depend on the microstructure parameter l. Hence, the effect of the microstructure size on dynamic problems of these plates is taken into account. All coefficients of equations (7) are slowly-varying functions in $x \equiv x_1$ in contrast to equations (2), which have non-continuous, highly oscillating and tolerance-periodic coefficients. The basic unknowns w, φ_α, θ_α, $\alpha=1,2$, are slowly-varying functions in x. It can be observed that boundary conditions have to be formulated for *the macrodeflection* w and *the macrorotations* φ_α on all edges, and for *the fluctuation amplitudes* θ_α only for edges normal to the x_2-axis.

Using the asymptotic modelling procedure, shown in [19, 8, 13], or neglecting the underlined terms in equations (7), the following equations of *the asymptotic model* are derived:

$$
\begin{aligned}
&\partial_\beta(<b_{\alpha\beta\gamma\delta}>\partial_\delta\varphi_\gamma)+\partial_\beta(<b_{\alpha\beta\gamma1}\partial_1 g>\theta_\gamma)-<d_{\alpha\beta}>(\partial_\beta w+\varphi_\beta)-<\vartheta>\ddot{\varphi}_\alpha=0,\\
&\partial_\alpha(<d_{\alpha\beta}>(\partial_\beta w+\varphi_\beta))-<\mu>\ddot{w}=-p,\\
&-<b_{\alpha1\gamma\delta}\partial_1 g>\partial_\delta\varphi_\gamma-<b_{\alpha1\beta1}\partial_1 g\partial_1 g>\theta_\beta=0.
\end{aligned}
\tag{8}
$$

These equations have smooth, slowly-varying coefficients in the contrast to equations (2). The asymptotic model equations describe vibrations of medium thickness plates under consideration on the macrolevel only.

5. Final remarks

In this contribution there are derived two systems of averaged equations of medium thickness plates with functionally graded macrostructure, which have the microstructure size of an order of the plate thickness. These equations are obtained using two modelling procedures – the tolerance modelling and the asymptotic modelling. These modelling approaches are based on the known Hencky-Bolle-type plates assumptions. Using these procedures the governing equations with non-continuous, tolerance-periodic functional coefficients of x_1 can be replaced by the systems of differential equations with slowly-varying, continuous coefficients of x_1 for each model.

The tolerance model, which governing equations take into account the effect of the microstructure size, makes it possible to analyse not only macrovibrations, but also microvibrations, related to the microstructure of the functionally graded plates.

Equations of the tolerance model have a physical sense for unknowns w, φ_α, θ_α, being slowly-varying functions in x_1. It can be treated as a certain *a posteriori* condition of physical reliability for the model.

On the other side, *the asymptotic model*, because its governing equations neglect the aforementioned effect, describes only macrovibrations of these plates under consideration.

Some applications to special dynamic problems of medium thickness functionally graded plates, which have the microstructure size of an order of the plate thickness will be presented in forthcoming papers.

References

1. A. H. Akbarzadeha, M. Abbasib, M. R. Eslami, *Coupled thermoelasticity of functionally graded plates based on the third-order shear deformation theory*, Thin-Walled Struct., **53** (2012) 141 – 155.

2. E. Baron, *Mechanics of periodic medium thickness plates*, Publishing House of Silesian Univ. Techn., Gliwice 2006 [in Polish].
3. T. Q. Bui, A. Khosravifard, C. Zhang, M. R. Hematiyan, M. V. Golu, *Dynamic analysis of sandwich beams with functionally graded core using a truly meshfree radial point interpolation method*, Engng. Struct., **47** (2013) 90 – 104.
4. Ł. Domagalski, J. Jędrysiak, *On the tolerance modelling of geometrically nonlinear thin periodic plates*, Thin Walled Struct., **87** (2015) 183 – 190.
5. A. J. M. Ferreira, R. C. Batra, C. M. C. Roque, L. F. Qian, R. M. N. Jorge, *Natural frequencies of functionally graded plates by a meshless method*, Comp. Struct., **75** (2006) 593 – 600.
6. M. Grygorowicz, K. Magnucki, M. Malinowski, *Elastic buckling of a sandwich beam with variable mechanical properties of the core*, Thin-Walled Struct., **87** (2015) 127 – 132.
7. J. Jędrysiak, *Higher order vibrations of thin periodic plates*, Thin-Walled Struct., **47** (2009) 890 – 901.
8. J. Jędrysiak, *Thermomechanics of laminates, plates and shells with functionally graded structure*, Publishing House of Lodz Univ. Techn., Lodz 2010 [in Polish].
9. J. Jędrysiak, *Modelling of dynamic behaviour of microstructured thin functionally graded plates*, Thin-Walled Struct., **71** (2013) 102 – 107.
10. J. Jędrysiak, *Free vibrations of thin functionally graded plates with microstructure*, Engng. Struct., **75** (2014) 99 – 112.
11. J. Jędrysiak, B. Michalak, *On the modelling of stability problems for thin plates with functionally graded structure*, Thin-Walled Struct., **49** (2011) 627 – 635.
12. J. Jędrysiak, E. Pazera, *Free vibrations of thin microstructured plates*, Vibr. Phys. Systems, **26** (2014) 93 – 98.
13. M. Kaźmierczak, J. Jędrysiak, *A new combined asymptotic-tolerance model of vibrations of thin transversally graded plates*, Engng. Struct., **46** (2013) 322 – 331.
14. R. V. Kohn, M. Vogelius, *A new model for thin plates with rapidly varying thickness*, Int. J. Solids Struct., **20** (1984) 333 – 350.
15. J. Marczak, J. Jędrysiak, *Tolerance modelling of vibrations of periodic three-layered plates with inert core*, Comp. Struct., **134** (2015) 854 – 861.
16. B. Michalak, *Thermomechanics of solids with a certain inhomogeneous microstructure*, Publishing House of Lodz Univ. Techn., Lodz 2011 [in Polish].
17. F. Tornabene, E. Viola, *Free vibration analysis of functionally graded panels and shells of revolution*, Meccanica, **44** (2009) 255 – 281.
18. C. Woźniak, B. Michalak, J. Jędrysiak, *Thermomechanics of heterogeneous solids and structures*, Publishing House of Lodz Univ. Techn., Lodz 2008.
19. C. Woźniak, et al. (eds.), *Mathematical modeling and analysis in continuum mechanics of microstructured media*, Publishing House of Silesian Univ. Techn., Gliwice 2010.

Vibrations of Non-Periodic Thermoelastic Laminates

Jarosław JĘDRYSIAK
Department of Structural Mechanics, Łódź University of Technology,
al. Politechniki 6, 90-924 Łódź, jarek@p.lodz.pl

Ewelina PAZERA
Department of Structural Mechanics, Łódź University of Technology,
al. Politechniki 6, 90-924 Łódź, ewelina.pazera@p.lodz.pl

Abstract

Vibrations of non-periodic thermoelastic laminates, which can be treated as made of functionally graded material with macroscopic properties changing continuously along direction, x_1, perpendicular to the laminas on the macrolevel are considered. Three models of these laminates are presented: the tolerance, the asymptotic-tolerance and the asymptotic. Governing equations of two first of them involve terms dependent of the microstructure size. Hence, these models (the tolerance, the asymptotic-tolerance) describe the effect of the microstructure. Averaged governing equations of these laminates can be obtained using the tolerance modelling technique, cf. Jędrysiak [1]. Because the model equations have functional, but slowly-varying coefficients calculations for examples can be made numerically or by using approximated methods.

Keywords: nonperiodic laminates, thermoelasticity, vibrations, microstructure, tolerance modelling

1. Introduction

The objects under consideration are non-periodic laminates, made of two components, which are non-periodically distributed along a direction normal to laminas. Cells of them are composed of two sublaminas of different materials. Macroscopic properties of these laminates are assumed to be continuously varied along this direction, cf. Figure 1. A microstructure can be realised as uniform, l=const, or non-uniform, l=l(x), distribution of laminas (Figures 1b, 1c), cf. Jędrysiak [2]. Hence, these laminates can be called *transversally* or *functionally graded laminates*, cf. Jędrysiak and Radzikowska [3].

Although a microstructure of these laminates is not periodic, thermomechanical problems of them can be investigated using micromechanical models proposed for composites with idealised geometries, e.g. periodic. Hence, the behaviour of these media can be analysed by certain modified methods, which are also applied to macroscopically homogeneous composites. Some of these methods are explained by Suresh and Mortensen [4] or Reiter et al. [5]. Between them techniques based on the asymptotic homogenization, [6], or on concepts of microlocal parameters, [7], can be mentioned. Various alternative approaches are proposed to describe the behaviour of functionally graded materials, such as the higher-order theory shown by Aboudi et al [8]. Unfortunately, governing equations of most of these approaches neglect *the effect of the microstructure size* on the overall behaviour of these laminates.

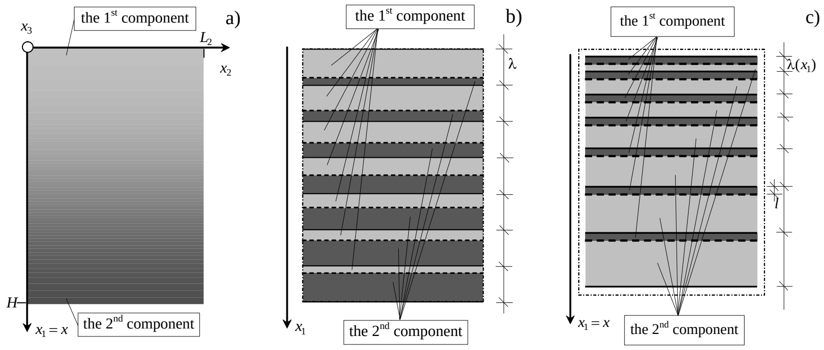

Figure 1. A part of the laminate: a) the macro-level, b) the micro-scale with uniform distribution of laminas, c) the micro-scale with non-uniform distribution of laminas; [2]

Here, in order to describe this effect the tolerance modelling is applied, cf. the books by Woźniak and Wierzbicki [9], edited by Woźniak et al. [10, 11] and by Jędrysiak [1].

This method was proposed and used to investigate different thermomechanical problems of periodic media, e.g. for thermoelastic processes by Ignaczak [12] or Baczyński [13]. Examples of analysis various periodic structures can be found in [10]. Moreover, the tolerance modelling is successfully used to investigate thermomechanical problems of functionally graded media with a microstructure in a series of papers, e.g. for vibrations of thin microstructured plates by Jędrysiak [1]; for heat conduction problems by Ostrowski and Michalak [14], Jędrysiak and Radzikowska [3], Jędrysiak [2]; for thermoelasticity problems by Jędrysiak [1, 15], Pazera and Jędrysiak [16]. All these problems are described for FG-type structures by differential equations with highly oscillating, tolerance-periodic, non-continuous, functional coefficients. The tolerance modelling leads from these equations to the system of differential equations with slowly-varying coefficients. Some applications of this approach for transversally graded structures are also shown in books by Jędrysiak [1], Michalak [17].

The main aim is to present and apply the governing equations of the tolerance model, the asymptotic-tolerance model and the asymptotic model to the problem of vibrations of a functionally graded laminated layer. The equations of two the first aforementioned models (the tolerance and the asymptotic-tolerance) involve terms, which describe the effect of the microstructure size on the overall behaviour of these laminates.

2. Modelling foundations

Denote by $Ox_1x_2x_3$ the orthogonal Cartesian coordinate system and by t the time coordinate. Let: $\mathbf{x}\equiv(x_2,x_3)$, $x\equiv x_1$. The region of the undeformed laminate is described by $\Omega\equiv(-L/2,L/2)\times(-L_2/2,L_2/2)\times(-L_3/2,L_3/2)$, with the lengths L, L_2, L_3 along the x, x_2-, x_3-axis, repectively. The "basic cell" $\Delta\equiv[-l/2,l/2]$ is defined in the interval $\Lambda=(-L/2,L/2)$ along the x-axis, with l as the length of cell Δ, called *the microstructure parameter*. Parameter l is assumed to satisfy the condition $l<<L$.

Denote by c_{ijkl}, ρ, b_{ij}, k_{ij}, c elasticity modulus, a mass density, thermoelasticity modulus, heat conduction coefficients, a specific heat, respectively, which can be assumed to be highly-oscillating, non-continuous functional coefficients of x. Introduce displacements u_i (i,j,k,l=1,2,3) and temperature θ.

Thermoelasticity problems of composites can be describe by the following equations:

$$\begin{aligned} &\partial_j(c_{ijkl}\partial_l u_k)-\rho\ddot{u}_i=\partial b_{ij}\theta+b_{ij}\partial_j\theta,\\ &\partial_j(k_{ij}\partial_i\theta)=c\dot{\theta}+T_0 b_{ij}\partial_j\dot{u}_i, \end{aligned} \tag{1}$$

which have highly-oscillating, tolerance-periodic, non-continuous coefficients being functions in x.

3. Modelling concepts

Some basic concepts, defined in books [1, 10-11], are applied in the tolerance modelling.

Denote $\Delta(x)\equiv x+\Delta$, $\Lambda_\Delta=\{x\in\Lambda\colon \Delta(x)\subset\Lambda\}$, as a cell at $x\in\Lambda_\Delta$. The first concept is *the averaging operator* for an arbitrary integrable function f, defined by

$$<f>(x,x_2)=\frac{1}{l}\int_{\Delta(x)} f(y,x_2)dy,\quad x\in\Lambda_\Delta. \tag{2}$$

Averaged value of function f being tolerance-periodic in x, calculated by (2) is a slowly-varying function in x.

Following [1, 10, 11] more introductory concepts are introduced and applied: tolerance-periodic functions $TP_\delta^1(\Lambda,\Delta)$, slowly-varying functions $SV_\delta^1(\Lambda,\Delta)$, highly oscillating functions $HO_\delta^1(\Lambda,\Delta)$, with δ as a tolerance parameter. *The fluctuation shape function* $g(\cdot)\in FS_\delta^1(\Lambda,\Delta)$, is a very important concept, which is a continuous highly oscillating function, dependent on l; has a piecewise continuous and bounded gradient $\partial^1 g$; satisfies conditions: $g\in O(l)$, $\partial^1 g\in O(l^0)$; $<\mu g>(x)\approx 0$ for $x\in\Lambda_\Delta$, $\mu>0$, $\mu\in TP_\delta^1(\Lambda,\Delta)$.

4. The outline of the modelling procedures

The various modelling procedures based on the concepts of the tolerance modelling are shown in the books [1, 11]. Here, the outline of them is presented.

- *The outline of the tolerance modelling procedure*

Two fundamental assumptions are formulated in the tolerance modelling procedure. The first assumption of them is *the micro-macro decomposition*, where the displacements and the temperature are decomposed as:

$$u_i(x,\mathbf{x},t)=w_i(x,\mathbf{x},t)+h(x)v_i(x,\mathbf{x},t),\qquad \theta(x,\mathbf{x},t)=\vartheta(x,\mathbf{x},t)+g(x)\psi(x,\mathbf{x},t), \tag{3}$$

with new basic unknowns: *the macrodisplacements* w_i, *the macrotemperature* ϑ, and *the fluctuation amplitudes of displacements* v_i, and *temperature* ψ, which all of them are slowly-varying functions in x; $h(x)$, $g(x)$ are the known fluctuation shape functions, assumed here as saw-like functions.

The tolerance averaging approximation is the second assumption, in which it is assumed that terms of an order of $O(\delta)$ are negligibly small, cf. [1, 10, 11], e.g. in: $<f\partial_1(gF)>(x)=<f\partial_1 g>(x)F(x)+O(\delta)$, $<fF>(x)=<f>(x)F(x)+O(\delta)$, for $f\in TP_\delta^1(\Lambda,\Delta)$, $g\in FS_\delta^1(\Lambda,\Delta)$, $F\in SV_\delta^1(\Lambda,\Delta)$.

Substituting micro-macro decompositions (3) to governing equations (1), by doing averaging (2), after some manipulations the governing equations of the averaged models can be derived.

- *The outline of the asymptotic-tolerance modelling procedure*

This modelling procedure, cf. [1, 11], can be divided into two steps. The first step is to apply the asymptotic modelling approach to obtain the asymptotic model solutions in the form:

$$u_{0i}(x,\mathbf{x},t) = w_i(x,\mathbf{x},t) + h(x)v_i(x,\mathbf{x},t), \qquad \theta_0(x,\mathbf{x},t) = \vartheta(x,\mathbf{x},t) + g(x)\psi(x,\mathbf{x},t). \tag{4}$$

It is derived the system of differential equations only for the macrodisplacements and the macrotemperature. In the second step there are introduced the additional micro-macro decompositions to these equations,:

$$u_i(x,\mathbf{x},t) = u_{0i}(x,\mathbf{x},t) + f(x)r_i(x,\mathbf{x},t), \qquad \theta(x,\mathbf{x},t) = \theta_0(x,\mathbf{x},t) + d(x)\chi(x,\mathbf{x},t), \tag{5}$$

with functions: w_i, v_i, ϑ, ψ (known from the asymptotic model solution); new unknown slowly-varying functions: r_i, χ; fluctuation shape functions f, d similar to h, g.

Using these modelling procedures, shown explicitly in [1, 11], the equations of the tolerance model, the asymptotic model and the asymptotic-tolerance model for functionally graded laminates can be derived. These model equations are written in the next section.

5. Model governing equations

Hence, the tolerance modelling procedure, cf. [1, 11, 15], leads to the system of governing equations in the following form:

$$\begin{aligned}
&\partial_j(<c_{ijkl}>\partial_l w_k + <c_{ijk1}\partial h> v_k) - <\rho>\ddot{w}_i = \partial<b_{i1}>\vartheta + <b_{ij}>\partial_j\vartheta,\\
&-\underline{c_{i\alpha k\beta}hh>\partial_\alpha\partial_\beta v_k} + <c_{i1k1}\partial h\partial h> v_k + <c_{i1kl}\partial h>\partial_l w_k + \underline{<\rho hh>\ddot{v}_i} =\\
&\qquad = -<b_{i1}\partial g>\vartheta + \underline{<b_{i\beta}gh>\partial_\beta\psi},\\
&\partial_j(<k_{ij}>\partial_i\vartheta + <k_{1j}\partial g>\psi) = <c>\dot{\vartheta} + <T_0 b_{ij}>\partial_j\dot{w}_i + <T_0 b_{i1}\partial h>\dot{v}_i,\\
&\underline{<k_{\alpha\beta}gg>\partial_\alpha\partial_\beta\psi} - <k_{i1}\partial g>\partial_i\vartheta - <k_{11}\partial g\partial g>\psi = \underline{<cgg>\dot{\psi}} + \underline{<T_0 b_{i\beta}hg>\partial_\beta\dot{v}_i},
\end{aligned} \tag{6}$$

with all coefficients being slowly-varying functions in x. These equations together with micro-macro decompositions (3) determine *the tolerance model of thermomechanics of functionally graded laminates*. The underlined terms depend on the microstructure parameter l. Hence, equations (6) describe the effect of the microstructure size of these laminates. The basic unknowns w_i, v_i, ϑ, ψ, i=1,2,3, are slowly-varying functions in x. It can be observed that boundary conditions have to be formulated for *the macrodisplacements* w_i and *the macrotemperature* ϑ on all edges, and for *the fluctuation amplitudes* v_i, ψ only for edges normal to the x_2- and the x_3-axis.

Using the asymptotic-tolerance modelling procedure, cf. [1, 11], governing equations take the form:

$$\begin{aligned}
&\partial_j(<c_{ijkl}>\partial_l w_k + <c_{ijk1}\partial h> v_k) - <\rho>\ddot{w}_i = \partial<b_{i1}>\vartheta + <b_{ij}>\partial_j\vartheta,\\
&\underline{<c_{i\alpha k\beta}ff>\partial_\alpha\partial_\beta r_k} - \underline{<\rho ff>\ddot{r}_i} - <c_{i1k1}\partial f\partial f> r_k = <c_{i1k1}\partial h\partial f> v_k + <c_{i1kl}\partial f>\partial_l w_k + <b_{i1}\partial f>\vartheta,\\
&\partial_j(<k_{ij}>\partial_i\vartheta + <k_{1j}\partial g>\psi) = <c>\dot{\vartheta} + <T_0 b_{ij}>\partial_j\dot{w}_i + <T_0 b_{i1}\partial h>\dot{v}_i,\\
&\underline{<k_{\alpha\beta}dd>\partial_\alpha\partial_\beta\chi} - <k_{11}\partial d\partial d>\chi = <k_{i1}\partial d>\partial_i\vartheta + <k_{11}\partial g\partial d>\psi + \underline{<cdd>\dot{\chi}} + \underline{<T_0 b_{i\beta}fd>\partial_\beta\dot{r}_i},\\
&<c_{i1k1}\partial h\partial h> v_k = -<c_{i1kl}\partial h>\partial_l w_k - <b_{i1}\partial g>\vartheta, \qquad <k_{11}\partial g\partial g>\psi = -<k_{i1}\partial g>\partial_i\vartheta.
\end{aligned} \tag{7}$$

These equations have smooth, slowly-varying coefficients in the contrast to equations (1). Equations (7) together with micro-macro decompositions (4)-(5) stand *the asymptotic-tolerance model of thermomechanics of functionally graded laminates*. These equations take into account the effect of the microstructure size of these laminates, since the underlined terms depend on the microstructure parameter l. The basic unknowns w_i, r_i, ϑ, χ, i=1,2,3, are slowly-varying functions in x. It can be observed that boundary conditions have to be formulated for *the macrodisplacements* w_i and *the macrotemperature* ϑ on all edges, and for *the fluctuation amplitudes* v_i, ψ only for edges normal to the x_2- and the x_3-axis.

Using the asymptotic modelling procedure, cf. [1, 11], the following governing equations can be derived:

$$
\begin{aligned}
&\partial_j(<c_{ijkl}>\partial_l w_k + <c_{ijk1}\partial h> v_k) - <\rho>\ddot{w}_i = \partial <b_{i1}>\vartheta + <b_{ij}>\partial_j\vartheta,\\
&\partial_j(<k_{ij}>\partial_i\vartheta + <k_{1j}\partial g>\psi) = <c>\dot{\vartheta} + <T_0 b_{ij}>\partial_j\dot{w}_i + <T_0 b_{i1}\partial h>\dot{v}_i,\\
&<c_{i1k1}\partial h\partial h> v_k = -<c_{i1kl}\partial h>\partial_l w_k - <b_{i1}\partial g>\vartheta,\\
&<k_{11}\partial g\partial g>\psi = -<k_{i1}\partial g>\partial_i\vartheta.
\end{aligned}
\tag{8}
$$

The above equations have smooth, slowly-varying coefficients and together with micro-macro decompositions (4) determine *the asymptotic model of thermomechanics of functionally graded laminates*. These equations neglect the effect of the microstructure size of these laminates. It can be observed that boundary conditions have to be formulated for *the macrodisplacements* w_i and *the macrotemperature* ϑ on all edges. The asymptotic model equations describe thermoelasticity of these laminates on the macrolevel only.

6. Remarks

In this note three systems of averaged governing equations of functionally graded laminates are shown. These equations are derived using different modelling procedures – the tolerance modelling, the asymptotic modelling and a combination of them – the asymptotic-tolerance modelling. These procedures lead from the governing equations of thermoelasticity in laminates, with coefficients being non-continuous, tolerance-periodic functions in x to the systems of differential equations having slowly-varying coefficients of x for each model.

Two of presented models – *the tolerance* and *the asymptotic-tolerance*, make it possible to analyse the effect of the microstructure size in thermoelasticity problems of these laminates. Both of these models can describe not only macrovibrations, but also microvibrations, related to the microstructure of the functionally graded laminates.

However, *the asymptotic model*, since its model equations neglect the above effect, describes only macrovibrations of these composites.

Because the equations of all models have still functional coefficients, but slowly-varying, solutions of them can be found analytical only for special cases of distribution of properties of laminates, or using approximate methods. It will be shown in forthcoming papers.

References

1. J. Jędrysiak, *Thermomechanics of laminates, plates and shells with functionally graded structure,* Publishing House of Lodz Univ. Techn., Lodz 2010 [in Polish].
2. J. Jędrysiak, *Stationary heat conduction in transversally graded laminates with uniform and non-uniform distribution of laminas*, Building Physics in Theory and Practice, **5/3** (2010) 17 – 20.
3. J. Jędrysiak, A. Radzikowska, *On the modelling of heat conduction in a non-periodically laminated layer*, J. Theor. Appl. Mech., **45** (2007) 239 – 257.
4. S. Suresh, A. Mortensen, *Fundamentals of functionally graded materials*, The University Press, Cambridge 1998.
5. T. Reiter, G. J. Dvorak, V. Tvergaard, *Micromechanical models for graded compositematerials*, J. Mech. Phys. Solids, **45** (1997) 1281 – 1302.
6. V. V. Jikov, C. M. Kozlov, O. A. Oleinik, *Homogenization of differential operators and integral functionals*, Springer Verlag, Berlin-Heidelberg 1994.
7. S. J. Matysiak, *On certain problems of heat conduction in periodic composites*, Z. Angew. Math. Mech., **71** (1994) 524 – 528.
8. J. Aboudi, M. J. Pindera, M. Arnolds, *Higher-order theory for functionally graded materials,* Comp., **30** (1999) 777 – 832.
9. C. Woźniak, E. Wierzbicki, *Averaging techniques in thermomechanics of composite solids*, Publishing House of Częstochowa Univ. of Techn., Częstochowa 2000.
10. C. Woźniak, B. Michalak, J. Jędrysiak, *Thermomechanics of heterogeneous solids and structures,* Lodz, Publishing House of Lodz Univ. Techn. 2008.
11. C. Woźniak, et al. (eds.), *Mathematical modeling and analysis in continuum mechanics of microstructured media,* Publishing House of Silesian Univ. Techn., Gliwice 2010.
12. J. Ignaczak, *A spatial decay estimate for transient thermoelastic process in a composite semispace*, J. Therm. Stresses., **23** (2000) 1 – 14.
13. Z.F. Baczyński, *Dynamic thermoelastic processes in microperiodic composites*, J. Therm. Stresses., **26** (2003) 55 – 66.
14. P. Ostrowski, B. Michalak, *A contribution to the modelling of heat conduction for cylindrical composite conductors with non-uniform distribution of constituents*, Int. J. Heat Mass Transfer, **92** (2016) 435 – 448.
15. J. Jędrysiak, *On the tolerance modelling of thermoelasticity problems for transversally graded laminates*, Arch. Civ. Mech. Engng., 11 (2011) 61 – 74.
16. E. Pazera, J. Jędrysiak, *Thermoelastic phenomena in transversally graded laminates*, Comp. Struct., **134** (2015) 663 – 671.
17. B. Michalak, *Thermomechanics of solids with a certain inhomogeneous microstructure*, Publishing House of Lodz Univ. Techn., Lodz 2011 [in Polish].

Higher Order Vibrations of Thin Periodic Plate Bands with Various Boundary Conditions

Jarosław JĘDRYSIAK
Department of Structural Mechanics, Łódź University of Technology, al. Politechniki 6, 90-924 Łódź, jarek@p.lodz.pl

Piotr WYRWA
Department of Structural Mechanics, Łódź University of Technology, al. Politechniki 6, 90-924 Łódź, piotr.wyrwa@p.lodz.pl

Abstract

In this contribution there are considered thin periodic plates. The tolerance averaging method, cf. [12, 13, 4], is applied to model problems of vibrations of these plates. Hence, the effect of the microstructure size is taken into account in model equations of the tolerance model. Calculations are made for periodic plate bands using this model and the asymptotic model for various boundary conditions.

Keywords: periodic plates, effect of microstructure size, higher order vibrations, tolerance modelling

1. Introduction

Thin periodic plate bands are main objects under consideration. These plate bands have a periodic microstructure along their spans on the microlevel, cf. Figure 1.

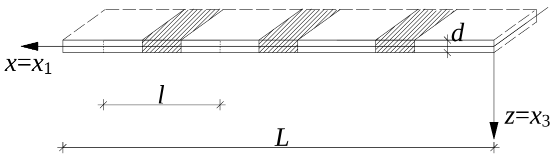

Figure 1. Fragment of a thin periodic plate band

Plate bands of this kind are consisted of many repeated small elements. Every element can be treated as a thin plate band with span l along the x_1-axis. This span describes the size of the microstructure and is called *the microstructure parameter l*. It is necessary to distinguish that in various problems of such plate bands *the effect of the microstructure size* cannot be neglected. These plates are modelled using different averaging approaches, e.g. based on the asymptotic homogenization, cf. [7]. However, most averaged equations of these plates neglect the effect of the microstructure size.

In order to take into account this effect *the tolerance averaging technique*, cf. [12] and [13], can be applied. Different applications of this method to analyse various periodic structures are shown in a series of papers, e.g. [1-3], [8-11]. This approach is also successfully adopted to functionally graded structures, e.g. [4-6].

The main aim of this note is to present governing equations of the *tolerance model* and the *asymptotic model* of thin periodic plates. Equations of these models can be derived using the tolerance modelling procedure and the asymptotic modelling procedure, respectively. In an example there are analysed lower and higher free vibration frequencies of periodic plate bands with various boundary conditions.

2. Modelling foundations

Set $\mathbf{x}\equiv(x_1,x_2)$, $x\equiv x_1$, $z\equiv x_3$. Let us consider a periodic plate band with span L along the x-axis. Hence, all properties of the plate can be periodic functions of x, but are independent of x_2. Denote a plate deflection by $w(x,t)$, loads normal by p and a derivative with respect to x by $\partial(\cdot)$. The region $\Omega\equiv\{(x,z): -d(x)/2\leq z\leq d(x)/2, x\in\Lambda\}$ denotes the undeformed plate band, with an interval $\Lambda=[0,L]$ and the plate thickness $d(\cdot)$. The *periodicity cell* on Λ is denoted by $\Delta\equiv[-l/2,l/2]\times\{0\}$.

Properties of the plate band are determined by periodic functions of x: a mass density per unit area μ, a rotational inertia ϑ and bending stiffnesses $b_{\alpha\beta\gamma\delta}$ in the form:

$$\mu(x)\equiv\int_{-d/2}^{d/2}\rho(x,z)dz,\qquad \vartheta(x)\equiv\int_{-d/2}^{d/2}\rho(x,z)z^2dz,\qquad b_{\alpha\beta\gamma\delta}(x)\equiv\int_{-d/2}^{d/2}c_{\alpha\beta\gamma\delta}(x,z)z^2dz. \tag{1}$$

Denoting $b\equiv b_{1111}$ and using the Kirchhoff-type plates theory assumptions the known four order differential equation for deflection $w(x,t)$ of periodic plate band can be derived:

$$\partial\partial(b\partial\partial w)+\mu\ddot{w}-\partial(\vartheta\partial\ddot{w})=p, \tag{2}$$

with highly oscillating, periodic, non-continuous coefficients being functions of x.

3. The outline of the tolerance modelling

Averaged equations thin periodic plates can be obtained using the tolerance modelling procedure (or the asymptotic procedure), with the basic concepts, defined in books, cf. [12, 13, 4].

Let $\Delta(x)\equiv x+\Delta$, $\Lambda_\Delta=\{x\in\Lambda: \Delta(x)\subset\Lambda\}$, be a cell at $x\in\Lambda_\Delta$. The averaging operator for an arbitrary integrable function f is defined by

$$<f>(x)=\frac{1}{l}\int_{\Delta(x)}f(y)dy,\quad x\in\Lambda_\Delta. \tag{3}$$

If a function f is periodic in x, then averaged value by (3) is constant.

Following the above books there can be introduced a set of tolerance-periodic functions $TP_\delta^\alpha(\Lambda,\Delta)$, a set of slowly-varying functions $SV_\delta^\alpha(\Lambda,\Delta)$, a set of highly oscillating functions $HO_\delta^\alpha(\Lambda,\Delta)$, ($\alpha\geq0$, δ is a tolerance parameter). Denote by $h(\cdot)$ a continuous highly oscillating function, $h\in FS_\delta^2(\Lambda,\Delta)$. Function $h(\cdot)$ is called *the fluctuation shape function* of the 2-nd kind, if it depends on l as a parameter and satisfies conditions: $\partial^k h\in O(l^{\alpha-k})$ for $k=0,1,\ldots,\alpha$, $\partial^k h\equiv h$, and $<\mu h>(x)\approx0$ for every $x\in\Lambda_\Delta$, $\mu>0$, $\mu\in TP_\delta^1(\Lambda,\Delta)$.

Using the above concepts, two fundamental assumptions of the tolerance modelling can be formulated, cf. Woźniak et al. [12, 13] and for thin periodic plates [3].

The first assumption is *the micro-macro decomposition*, in which it is assumed that the plate deflection can be decomposed as:

$$w(x,z,t)=W(x,t)+h^A(x)V^A(x,t),\qquad A=1,\ldots,N. \tag{4}$$

Functions $W(\cdot,t), V^A(\cdot,t) \in SV_\delta^2(\Lambda,\Delta)$ are basic kinematic unknowns, called *the macrodeflection* and *the fluctuation amplitudes*, respectively; $h^A(\cdot)$ are the known *fluctuation shape functions*, which can be assumed as trigonometric functions.

The second assumption is *the tolerance averaging approximation*, i.e. terms of an order of $O(\delta)$ can be treated as negligibly small, cf. [12, 13, 3], e.g. for $f \in TP_\delta^2(\Lambda,\Delta)$, $h \in FS_\delta^2(\Lambda,\Delta)$, $F \in SV_\delta^2(\Lambda,\Delta)$, in: $< f >(x) = < \bar{f} >(x) + O(\delta)$, $< fF >(x) = < f >(x)F(x) + O(\delta)$, $< f\partial(hF) >(x) = < f\partial h >(x)F(x) + O(\delta)$.

The tolerance modelling procedure can be found in the books [12, 13, 4]. Here, it is shown only an outline of this method.

In the tolerance modelling two basic steps can be introduced. In the first step micro-macro decomposition (4) is applied. In the second step averaging operator (3) is used to the resulting formula. Hence, the tolerance averaged lagrangean $< \Lambda_h >$ is obtained:

$$\begin{aligned} < \Lambda_h > = -\tfrac{1}{2}\{ & (< b > \partial\partial W + 2 < b\partial\partial h^B > V^B)\partial\partial W + < \vartheta > \partial\dot{W}\partial\dot{W} + \\ & + < B\partial\partial h^A \partial\partial h^B > V^A V^B - < \mu > \dot{W}\dot{W} + \\ & + (\underline{< \vartheta \partial h^A \partial h^B >} - \underline{< \mu h^A h^B >})\dot{V}^A \dot{V}^B\} + < p > W, \end{aligned} \tag{5}$$

with underlined terms, which depend on the microstructure parameter l.

4. The outline of the asymptotic modelling

In the asymptotic modelling, cf. [13], [4], the asymptotic procedure is applied. Using the asymptotic decomposition $w_\varepsilon(x,y,t) = U(y,t) + \varepsilon^2 \tilde{h}_\varepsilon^A(x,y)Q^A(y,t)$ in equation (2) and bearing in mind the limit passage $\varepsilon \to 0$ terms $O(\varepsilon)$ are neglected in final equations.

Using the above asymptotic decomposition and averaging operator (3) to the resulting formula, the asymptotic averaged lagrangean $< \Lambda_0 >$ is obtained:

$$\begin{aligned} < \Lambda_0 > = -\tfrac{1}{2}\{ & (< b > \partial\partial W + 2 < b\partial\partial h^B > V^B)\partial\partial W + < \vartheta > \partial\dot{W}\partial\dot{W} + \\ & + < B\partial\partial h^A \partial\partial h^B > V^A V^B - < \mu > \dot{W}\dot{W}\} + < p > W. \end{aligned} \tag{6}$$

This model does not describe effects of the microstructure size.

5. Governing equations of presented models

Equations of two models are presented here: *the tolerance model*, *the asymptotic model*.

Substituting $< \Lambda_h >$, (5), to the proper Euler-Lagrange equations, after some manipulations we arrive at the following system of equations for $W(\cdot,t)$ and $V^A(\cdot,t)$:

$$\begin{aligned} & \partial\partial(< b > \partial\partial W + < b\partial\partial h^B > V^B) + < \mu > \ddot{W} - < \vartheta > \partial\partial\ddot{W} = < p >, \\ & < b\partial\partial h^A > \partial\partial W = - < B\partial\partial h^A \partial\partial h^B > V^B - (\underline{< \mu h^A h^B >} + \underline{< \vartheta \partial h^A \partial h^B >})\ddot{V}^B. \end{aligned} \tag{7}$$

Equations (7) together with micro-macro decomposition (4) stand *the tolerance model of thin periodic plate bands*. These equations describe free vibrations of these plates and take into account the effect of the microstructure size on them by the underlined terms dependent on the microstructure parameter l. In contrast to equation (2), which has non-continuous, highly oscillating and periodic coefficients, equations (7) have constant coefficients. The basic unknowns W, V^A, $A=1,\ldots,N$, are slowly-varying functions in $x \equiv x_1$. It can be observed that boundary conditions have to be formulated only for *the macrodeflection W* on all edges.

Using the asymptotic modelling procedure, shown in [13, 4], equations of an approximate model, without the effect of the microstructure size, can be obtained in the following form:

$$\begin{aligned}&\partial\partial(<b>\partial\partial W+<b\partial\partial h^B>V^B)+<\mu>\ddot{W}-<\vartheta>\partial\partial\ddot{W}=<p>,\\&<b\partial\partial h^A>\partial\partial W=-<B\partial\partial h^A\partial\partial h^B>V^B.\end{aligned}\tag{8}$$

Equations (8) stand the governing equations of *the asymptotic model* of periodic plate bands. It can be observed that these equations can be also derived by neglecting the underlined terms in equations (7). The asymptotic model equations have also constant coefficients, but they describe free vibrations of thin plates under consideration on the macrolevel only.

6. Applications – free vibrations of periodic plate bands with various boundary conditions

Let us consider a thin periodic plate band with span L along the x-axis, neglecting the loading p, p=0. The material properties of this plate are independent of the x_2-coordinate. Let us assume the constant plate thickness d.

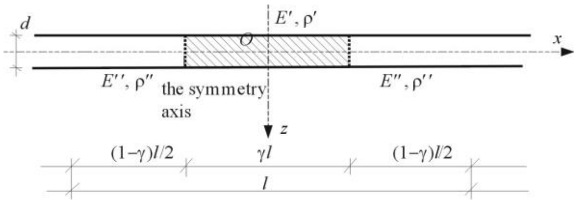

Figure 2. A cell of the plate band

It is assumed that the plate band is made of two different homogeneous isotropic materials, with properties described by Young's moduli E'', E' and mass densities ρ'', ρ':

$$E(y)=\begin{cases}E', & \text{for}\quad y\in((1-\gamma)l/2,(1+\gamma)l/2),\\ E'', & \text{for}\quad y\in[0,(1-\gamma)l/2]\cup[(1+\gamma)l/2,l],\end{cases}\tag{8}$$

$$\rho(y)=\begin{cases}\rho', & \text{for}\quad y\in((1-\gamma)l/2,(1+\gamma)l/2),\\ \rho'', & \text{for}\quad y\in[0,(1-\gamma)l/2]\cup[(1+\gamma)l/2,l],\end{cases}\tag{9}$$

where γ is a distribution parameter of material properties, cf. Figure 2; the Poisson's ratio $\nu\equiv\nu''=\nu'$ is constant.

Our considerations are restricted to only one fluctuation shape function, i.e. A=N=1. Denote $h\equiv h^1$, $V\equiv V^1$. Hence, micro-macro decomposition (4) has the form:

$$w(x,t)=W(x,t)+h(x)V(x,t),\tag{10}$$

where the fluctuation shape function $h(x)$ assumed for the cell shown in Figure 2, takes the form:

$$h(y)=l^2[\cos(2\pi y/l)+c],\qquad y\in\Delta(x),\quad x\in\Lambda,\tag{11}$$

with parameter c is a constant determined by $<\mu h>=0$:

$$c=\sin(\pi\gamma)(\rho'-\rho'')\{\pi[\rho'\gamma+\rho''(1-\gamma)]\}^{-1}.\tag{12}$$

Under denotations:

$$\begin{array}{lll} \breve{B} = < b >, & \hat{B} = < b\partial\partial h >, & \overline{B} = < b\partial\partial h\partial\partial h >, \\ \breve{\mu} = < \mu >, & \overline{\mu} = l^{-4} < \mu hh >, & \breve{\vartheta} = < \vartheta >, \quad \overline{\vartheta} = l^{-2} < \vartheta\partial h\partial h >, \end{array} \tag{13}$$

tolerance model equations (7) can be written as:

$$\begin{array}{l} \partial\partial(\breve{B}\partial\partial W + \hat{B}V) + \breve{\mu}\ddot{W} - \breve{\vartheta}\partial\partial\ddot{W} = 0, \\ \hat{B}\partial\partial W + \overline{B}V + l^2(l^2\overline{\mu} + \overline{\vartheta})\ddot{V} = 0, \end{array} \tag{14}$$

however, asymptotic model equations (8) take the form of one equation:

$$\partial\partial[(\breve{B} - \hat{B}^2/\overline{B})\partial\partial W] + \breve{\mu}\ddot{W} - \breve{\vartheta}\partial\partial\ddot{W} = 0. \tag{15}$$

Certain approximate formulas of free vibrations frequencies for periodic plate bands with various boundary conditions can be obtained applying the known Ritz method, cf. [4-6]. Using this method the maximal strain energy Y_{max} and the maximal kinetic energy K_{max} are determined. For the plate band solutions to equations (14) and (15), which are applied in the Ritz method, can be assumed in the form:

$$W(x,t) = A_W\Xi(\alpha x)\cos(\omega t), \qquad V(x,t) = A_V\Theta(\alpha x)\cos(\omega t), \tag{16}$$

where: α is a wave number; ω is a free vibration frequency; functions $\Xi(\cdot)$ and $\Theta(\cdot)$ are eigenvalue functions for the macrodeflection and the fluctuation amplitude, respectively, which have to satisfy the proper boundary conditions for x=0, L. Denote the first and second order derivatives of functions $\Xi(\cdot)$ and $\Theta(\cdot)$ by:

$$\partial\Xi(\alpha x) \equiv \alpha\tilde{\Xi}(\alpha x), \quad \partial\Theta(\alpha x) \equiv \alpha\tilde{\Theta}(\alpha x), \quad \partial\partial\Xi(\alpha x) \equiv \alpha^2\overline{\Xi}(\alpha x), \quad \partial\partial\Theta(\alpha x) \equiv \alpha^2\overline{\Theta}(\alpha x). \tag{17}$$

Moreover, let us introduce denotations:

$$\begin{array}{l} \breve{B} = \frac{d^3}{12(1-\nu^2)}[E''(1-\gamma) + \gamma E']\int_0^L [\overline{\Xi}(\alpha x)]^2 dx, \quad \hat{B} = \frac{\pi d^3}{3(1-\nu^2)}(E' - E'')\sin(\pi\gamma)\int_0^L \overline{\Xi}(\alpha x)\Theta(\alpha x)dx, \\ \overline{B} = \frac{(\pi d)^3}{3(1-\nu^2)}\{(E' - E'')[2\pi\gamma + \sin(2\pi\gamma)] + 2\pi E''\}\int_0^L [\Theta(\alpha x)]^2 dx, \\ \breve{\mu} = d[(1-\gamma)\rho'' + \gamma\rho']\int_0^L [\Xi(\alpha x)]^2 dx, \qquad \breve{\vartheta} = \frac{d^3}{12}[(1-\gamma)\rho'' + \gamma\rho']\int_0^L [\tilde{\Xi}(\alpha x)]^2 dx, \\ \overline{\mu} = \frac{d}{4\pi}\{(\rho' - \rho'')[2\pi\gamma + \sin(2\pi\gamma)] + 2\pi\rho''\}\int_0^L [\Theta(\alpha x)]^2 dx + \\ \qquad + \frac{d}{\pi}(\rho' - \rho'')c[\pi c\gamma - 2\sin(\pi\gamma)]\int_0^L [\Theta(\alpha x)]^2 dx + d\rho'' c^2\int_0^L [\Theta(\alpha x)]^2 dx, \\ \overline{\vartheta} = \frac{\pi d^3}{12}\{(\rho' - \rho'')[2\pi\gamma - \sin(2\pi\gamma)] + 2\pi\rho''\}\int_0^L [\Theta(\alpha x)]^2 dx, \end{array} \tag{18}$$

Using the conditions of the Ritz method:

$$\frac{\partial(\mathrm{Y}_{max} - \mathrm{K}_{max})}{\partial A_W} = 0, \quad \frac{\partial(\mathrm{Y}_{max} - \mathrm{K}_{max})}{\partial A_V} = 0, \tag{19}$$

and make some manipulations we arrive at the following formulas:

$$\begin{array}{l} (\omega_{-,+})^2 \equiv \dfrac{l^2(l^2\overline{\mu} + \overline{\vartheta})\alpha^4\breve{B} + (\breve{\mu} + \alpha^2\breve{\vartheta})\overline{B}}{2(\breve{\mu} + \alpha^2\breve{\vartheta})l^2(l^2\overline{\mu} + \overline{\vartheta})} \mp \\ \qquad \mp \dfrac{\sqrt{[l^2(l^2\overline{\mu} + \overline{\vartheta})\alpha^4\breve{B} - (\breve{\mu} + \alpha^2\breve{\vartheta})\overline{B}]^2 + 4(\alpha^2\hat{B})^2 l^2(\breve{\mu} + \alpha^2\breve{\vartheta})(l^2\overline{\mu} + \overline{\vartheta})}}{2(\breve{\mu} + \alpha^2\breve{\vartheta})l^2(l^2\overline{\mu} + \overline{\vartheta})}, \end{array} \tag{20}$$

of *the lower frequency* ω_- *of free macro-vibrations* and *the higher frequency* ω_+ *of free micro-vibrations*, respectively, in the framework of *the tolerance model*.

Calculations can be made for various cases of boundary conditions:

- the simply supported plate band: $\Xi(0) = \partial\partial\Xi(0) = \Xi(L) = \partial\partial\Xi(L) = 0$;
- the plate band clamped on both edges: $\Xi(0) = \partial\Xi(0) = \Xi(L) = \partial\Xi(L) = 0$;

- the clamped-hinged plate band: $\Xi(0)=\partial\Xi(0)=\Xi(L)=\partial\partial\Xi(L)=0$;
- the cantilever plate band: $\Xi(0)=\partial\Xi(0)=\partial\partial\Xi(L)=\partial\partial\partial\Xi(L)=0$.

7. Remarks

In this paper *the tolerance model governing equations of thin periodic plate bands* are presented and applied to analyse free vibrations of them. The tolerance modelling replaces the governing differential equation with non-continuous, periodic coefficients by the system of differential equations with constant coefficients, which involve terms with the microstructure parameter. The tolerance model describes the effect of the microstructure size on vibrations. Hence, there are calculated the lower free vibration frequency and the higher free vibration frequency, which is related to the microstructure, for plate bands with various boundary conditions. These calculations are made using the procedure of the Ritz method.

References

1. Ł. Domagalski, J. Jędrysiak, *On the elastostatics of thin periodic plates with large deflections,* Meccanica, **47** (2012) 1659 – 1671.
2. Ł. Domagalski, J. Jędrysiak, *Nonlinear vibrations of periodic beams*, Vibr. Phys. Syst., **26** (2014) 73 – 78.
3. J. Jędrysiak, *Higher order vibrations of thin periodic plates*, Thin-Walled Struct., **47** (2009) 890 – 901.
4. J. Jędrysiak, *Thermomechanics of laminates, plates and shells with functionally graded structure*, Łódź, Wyd. Politechniki Łódzkiej 2010 [in Polish].
5. J. Jędrysiak, E. Pazera, *Free vibrations of thin microstructured plates*, Vibr. Phys. Syst., **26** (2014) 93 – 98.
6. M. Kaźmierczak, J. Jędrysiak, *Tolerance modelling of vibrations of thin functionally graded plates*, Thin-Walled Struc., **49** (2011) 1295 – 1303.
7. R. V. Kohn, M. Vogelius, *A new model for thin plates with rapidly varying thickness*, Int. J. Solids Struct., **20** (1984) 333 – 350.
8. J. Marczak, J. Jędrysiak, *Analysis of vibrations of plate strip with concentrated masses using tolerance averaging technique*, Vibr. Phys. Syst., **26** (2014) 161 – 168.
9. J. Marczak, J. Jędrysiak, *Tolerance modelling of vibrations of periodic three-layered plates with inert core*, Comp. Struct., **134** (2015) 854 – 861.
10. B. Michalak, *Dynamics and stability of wavy-type plates*, Łódź, Wyd. Politechniki Łódzkiej 2001 [in Polish].
11. B. Tomczyk, *On the modelling of thin uniperiodic cylindrical shells*, J. Theor. Appl. Mech., **41** (2003) 755 – 774.
12. C. Woźniak, B. Michalak, J. Jędrysiak (eds.), *Thermomechanics of heterogeneous solids and structures*, Łódź, Wyd. Politechniki Łódzkiej 2008.
13. C. Woźniak, et al. (eds.), *Mathematical modelling and analysis in continuum mechanics of microstructured media*, Gliwice, Wyd. Politechniki Śląskiej 2010.

An Analysis of the Self-Excited Torsional Vibrations of the Electromechanical Drive System

Robert KONOWROCKI and Tomasz SZOLC
Institute of Fundamental Technological Research of the Polish Academy of Sciences
ul. A. Pawińskiego 5B, 02-106 Warszawa, rkonow@ippt.pan.pl, tszolc@ippt.pan.pl

Abstract

This paper presents a dynamic analysis of torsional vibrations of the railway drive system. A dynamic electromechanical drive model has been created and then integrated with the railway wheelset-rail system to simulate self-excited torsional vibrations of the considered system. Results of this analysis are used in order to investigate the drive system's sensitivity to torsional oscillations. Here, the dynamic electromechanical interaction between the electric driving motor and the rotating wheelset is considered. This investigation has proved that the torsional stiffness and damping of drivetrain system strongly affect amplitudes of the self-excited vibrations. A self-excited vibrations affecting on an energy consumption of the electric motor of the considered system are studied

Keywords: torsional vibrations, electromechanical coupling, wheel-rail adhesion, wheelset drivetrain dynamic

1. Introduction

Mechanical vibrations and deformations are phenomena associated with an operation of majority of railway vehicle drivetrain structures. The knowledge about torsional vibrations in transmission systems of railway vehicles is of a great importance in the fields dynamics of mechanical systems [1]. Torsional vibrations in the railway vehicle drive train are generated by several phenomena. Generally, these phenomena are very complex and they can be divided into two main parts. To the first one belongs the electromechanical interaction between of the railway drive system including the: electric motor, gears, the driven part of disc clutch and driving parts of the gear clutch [2]. To the second one belong torsional vibrations of the flexible wheels [3, 4] and wheelsets caused by variation of adhesion forces in the wheel-rail contact zone [5]. An interaction of the adhesion forces has nonlinear features which are related to the creep value and strongly depends on the wheel-rail zone condition and track geometry (when driving on a curve section of the track). In many modern mechanical systems torsional structural deformability plays an important role. Often the study of railway vehicle dynamics using the rigid multibody methods without torsionally deformable elements are used [6]. This approach does not allow toanalyse self-excited vibrations which have an important influence on the wheel-rail longitudinal interaction [7].

A dynamic modelling of the electrical drive systems coupled with elements of a driven machine or vehicle is particularly important when the purpose of such modelling is to obtain an information about the transient phenomena of system operation, like a run-up, run-down and loss of adhesion in the wheel-rail zone. In this paper most attention is paid to the modelling of an electromechanical interaction between the electric driving motor and the railway wheelset as well as to an influence of the self-excited torsional vibrations in the considered drive system.

2. Mathematical modeling of the wheelset and the electric motor

In order to investigate a character of self-excited torsional vibrations in the electric railway vehicle powertrain and a dynamic mutual coupling between the wheelset and the electric motor, a possibly realistic and reliable electromechanical model of the railway drivetrain is applied. The mechanical drive system is representedby a torsionally vibrating system of four-DOFs. The scheme of the considered model is shown in Figure 1.

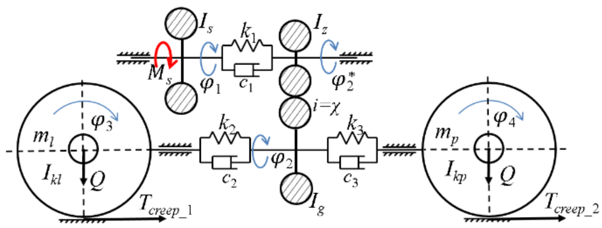

Figure 1. Scheme of the dynamic model of the railway wheelsetdrive system

A mathematical model of the single torsionally deformable railway wheelset under torsional vibrations induced by the traction motor and various adhesion frictional effects occurring in wheel-rail contact zones has been derived by means of the second-orderLagrange's equations in the generalized coordinates $\varphi_i(t)$. These coordinates describe angular displacements of the drivetrain components of the wheelset. Here, there will be presenteda torsional dynamic analysis of the single wheelset running on a geometrically perfect straight section under various operational conditions determined by longitudinal slip $s_i$of both wheels, vertical wheel forces $Q+m\cdot g$and vehicle velocity v. The drive torque and the retarding one due to the creep forces in contact of the rails with with the wheels complements the conservative railway drive model on the right side (1) and it can be expressed as

$$\mathbf{I}\ddot{\varphi}(\mathrm{t}) = (\mathbf{K}_{wheelset} + \mathbf{K}_{gear})\varphi(\mathrm{t}) + (\mathbf{C}_{wheelset} + \mathbf{C}_{gear})\dot{\varphi}(\mathrm{t}) = \mathbf{M}_{drive} - \mathbf{M}_{creep}\ , \tag{1}$$

where $\mathbf{I}$ denotes the mass matrix containing mass moments of inertia of rotating elements of the drive system, the matrices$\mathbf{K}_{wheel}$, $\mathbf{K}_{gear}$, $\mathbf{C}_{wheel}$and $\mathbf{C}_{gear}$ express the torsional stiffness and damping properties of the wheelset, disc-clutch and of the gearbox wheel, respectively.Vector $\mathbf{M}_{drive}$contains the electromagnetic torque generated by an asynchronous motor described in the following part of the paper and vector $\mathbf{M}_{creep}$contains the traction torque generated by longitudinal tangential loads in the wheel-rail zones.Their form can be expressed as

$$T_{creep\_i} = \mu_i(s_i)\cdot(Q + m_i g), \quad i = 1{,}2\ , \tag{2}$$

where Q is the normal load imposed on the single wheel, r is the wheel radius and $\mu(s_i)$ is the traction coefficient expressed in Eq. (4). Its maximum value is called an adhesion coefficient. The longitudinal creepage of the wheels is defined in the following form

$$s_0 = (\frac{3.6\omega_i r}{v} - 1), \quad s_i = s_0 + (\frac{3.6\dot{\varphi}_i r}{v} - 1), \quad i = 1,2, \tag{3}$$

where s_0 and s_i are the longitudinal creepage before and duringdisturbances, respectively. Symbol ω_i is the angular speed of the i-th wheel,i-indexmeansthe left and therightwheel and $v$denotes forward wheelset velocity in km/h obtained by the equivalent angular speed of wheelset axle $\dot{\varphi}_2$ at the contact point.

In equation (1) the traction torque including torques $M_{creep\_1,2}$ on left and right wheel of the wheelset have nonlinear properties. These propertiesare dependenton a profile of adhesion characteristic describing a contact in the wheel-rail zones. Depending on the adopted various maintenance, operation and weather conditions, this characteristic can take into considerationvarious forms of creepage curves, as shown in Fig. 2. The creepage curve applied for the carried out investigations has been plotted in Fig. 3 and it can be expressed by the following equation

$$\mu(s_i) = 0.3*[(a + \exp(-s_i) + \tanh(\frac{b}{c} \cdot s_i)/2 + (d \cdot \mathrm{atan}(e \cdot s_i)) + \exp(f \cdot s_i))], \quad i = 1,2. \tag{4}$$

For dry and wet weather conditions in the wheel-rail zone parameters of Eq. 4 have numerical values contained in Table 1.

Table 1. Parameters for traction coefficient in Eg. (4)

Quantity	a	b/c	d	e	f
dry	-1	100	1.75	0.7	-7
wet	-2	25	1.25	1	-0.5

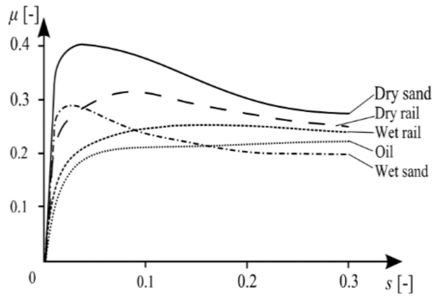

Figure 2.Adhesion-creep characteristic ofthe railway conditions [8]

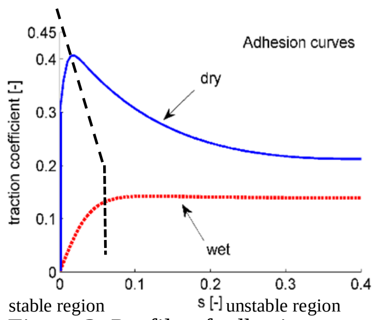

Figure 3. Profile of adhesion curves using in investigations

The adhesion curve can be divided into two regions, see Fig. 3. The first regionis characterized by a rapidly rising slope of the curve is the stable region. The second one, due to a negative damping results in visible decreasingslope,can lead to self-excited oscillations in the wheel-rail contact zone. This phenomenon makes the driven wheelset slipping on the rails of a railway track. Consequently, when a tangential force between the wheel and the rail exceedsan adhesion force in the wheel-rail contact zone, the self-excited torsional vibrations of the wheelset occur. Such a phenomenon has a very large impact on the relative rotation between the wheel and the axle due to a lack of friction in press fitting [9] and it can make vehicle derailed. Additional dynamic torsional overloadsproduce disturbances in the wheelset drive system, which has a influence on the traction moment of a railway vehicle. This characteristic of the traction moment is also dependent on electrical parameters of the motor, power supply and its regulation.A modeling of the electrical part of a drivetrain is a very difficult and complex task. For a simple solution it is possible to use a linearization around of the working point static characteristic of thedriving motor. But, in the case of a more advanced analysis of transient phenomena in the drivetrainan accurate circuit model of the electric motor is needed [10,11].The asynchronous motors are very commonly applied as railway vehicles driving sources. From the viewpoint of electromechanical coupling investigation, for an introductory approach the properly advanced circuit model of the electric motor seems to be required, similarly as e.g. in [12]. In the case of the symmetrical three-phase asynchronous motor electric current oscillations in its windings are described by the six circuit voltage equations. In order to simplicity of their form they are transformed into the system of four Park's equations in the so called'*αβ-dq*' reference system

$$\begin{bmatrix} \sqrt{\frac{3}{2}}U\cos(\omega_e t) \\ \sqrt{\frac{3}{2}}U\sin(\omega_e t) \\ 0 \\ 0 \end{bmatrix} = \begin{bmatrix} L_s+\frac{1}{2}L_m & 0 & \frac{3}{2}L_m & 0 \\ 0 & L_s+\frac{1}{2}L_m & 0 & \frac{3}{2}L_m \\ \frac{3}{2}L_m & 0 & L'_r+\frac{1}{2}L_m & 0 \\ 0 & \frac{3}{2}L_m & 0 & L'_r+\frac{1}{2}L_m \end{bmatrix} \cdot \begin{bmatrix} i_\alpha^s(t) \\ i_\beta^s(t) \\ i_d^r(t) \\ i_q^r(t) \end{bmatrix} + \\ + \begin{bmatrix} R_s & 0 & 0 & 0 \\ 0 & R_s & 0 & 0 \\ 0 & \frac{3}{2}pL_m\dot{\varphi}_1(t) & R_r & p\dot{\varphi}_1(t)\left(L'_r+\frac{1}{2}L_m\right) \\ -\frac{3}{2}pL_m\dot{\varphi}_1(t) & 0 & -p\dot{\varphi}_1(t)\left(L'_r+\frac{1}{2}L_m\right) & R_r \end{bmatrix} \cdot \begin{bmatrix} i_\alpha^s(t) \\ i_\beta^s(t) \\ i_d^r(t) \\ i_q^r(t) \end{bmatrix}, \tag{5}$$

where U denotes the power supply voltage, ω_e is the supply voltage circular frequency, L_s, L_r' are the stator coil inductance and the equivalent rotor coil inductance, respectively, L_m denotes the relative rotor-to-stator coil inductance, R_s, R_r are the stator coil resistance and the equivalent rotor coil resistance, respectively, p is the number of pairs of the motor magnetic poles, $\dot{\varphi}_1(t)$ is the current rotor angular speed including the average and vibratory component and i_α^s, i_β^s are the electric currents in the stator windings reduced to the electric field equivalent axes α and βandi_d^r, i_q^r are the electric currents in the rotor windings reduced to the electric field equivalent axes d and q, [12]. Then, the electromagnetic torque generated by such a motor can be expressed by the following formula

$$M_s = \frac{3pL_m\left(i_\beta^s \cdot i_d^r - i_\alpha^s \cdot i_q^r\right)}{2}. \tag{6}$$

In our approach the interaction between the electromagnetic and mechanical systems of the considered powertrain coupled mutually through electromagnetic torque M_s and angular rotor velocity $\dot{\varphi}_1$ is shown in Eqs. (5) and (6).In order to control the electric motor assumed in the applied drive system model the field-oriented control methods has been used [13].According to the above, this set of coupled electromechanical Eqs. (1), (5) and (6) is going to be simultaneously solved by means of a selected direct integration method for electric parameters including: resistance of the stator and the rotor equal R_s=0.288Ω, R_r=0.158Ω. The relative inductance, inductance of the stator windings and inductance of the rotor windings are respectively equal to L_m = 0,0412 H, L_s = 0,0425 H and L_r = 0,0418 H.The asynchronous motor has 4 pole pairs and its supply voltage is equal to 3 kV with 60 Hz supply frequency. In the considered case, the Runge-Kuttafourth-order method will be applied for motion equations of the electromechanical model assumed in this way.

3. Numerical results

In the computational example railway drivetrain system with the torsionally flexiblewheelset is used as an object of considerations. This wheelset of a total weight 1500 kg and a load of the single wheel equal to Q=40kN is driven by the asynchronous motor by means of the disc-clutch with torsional stiffness and dampingcoefficient k_1=3000 kNm, c_1=100 Ns/m.The spur gear stage of the ratio i=1:6reduces a rotational speed of the wheelset into $\dot{\varphi}_2^* = \dot{\varphi}_2 \cdot \chi$. There is assumed that the minimum radius of the wheelset axle and the half of length of the axle are respectively equal to 0.08 and 0.75 m. This axle is made of steelP35G. The torsional stiffness of this axis has been determined equal to k_2=k_3= 6.9e7 Nm/rad.More parameters applied in this investigations are also given in the Table 2.

Table 2. Simulationbaseparameters

χ	c_2	c_3	I_s	I_z	I_g	I_{kl}	I_{kr}
0.16	50 Ns/m	50 Ns/m	2.1 kgm^2	20.2 kgm^2	43 kgm^2	78 kgm^2	78 kgm^2

The simulation model described above can be used to simulate several differentconditions of operation, i.e. motor acceleration, deceleration, load change, faultcondition, etc. However, due the limitedsize, only selected results arepresented here. An amplitude of self-excited vibrations is an important evaluating indicator to measure the vibration magnitude. Some drive system parameters influencing the amplitude of the self-excited torsional vibration are shown in Figs. 4 and 5. Figure 4a and 4c present the result of the self-excited vibration amplitudes and the spectrum of them at various damping between the drivetrain system and the wheelset wheels. As shown in this figure, the vibration amplitude decreases with an increaseof damping level where the dominant frequency of the vibration is kept constant. An increase ofthe damping can restrain this amplitude and shorten the convergence time of the torsional vibrations, but it is not affected whether the self-excited vibration occurs or not.The same effect can be observed on time-histories of the currents of the stator windings shown in Figs. 4b and 4 d.Figure 5a shows a result of the self-excited vibration amplitudes at different equivalent stiffness betweenthe drivetrain and the wheelset wheels of wheelset.

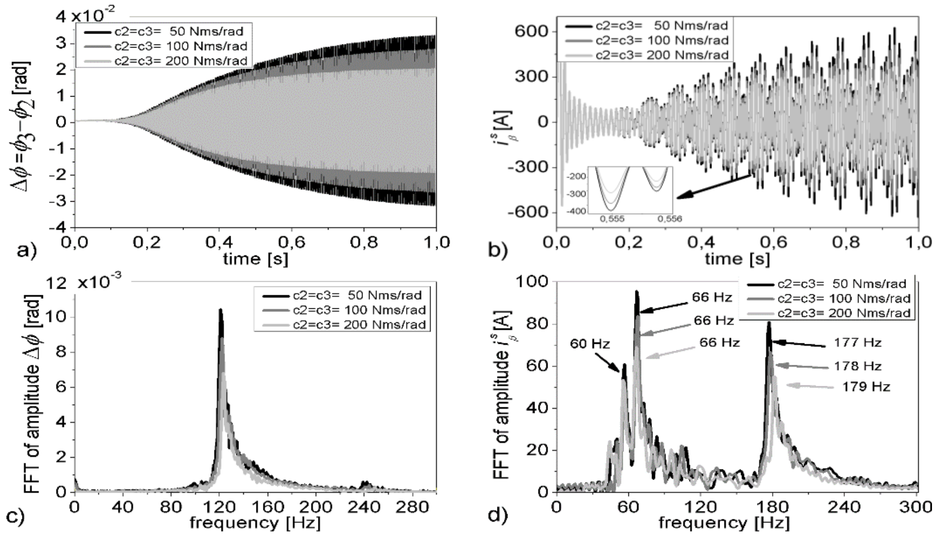

Figure 4. Self-excited torsional vibration amplitudes of the mechanical and electricparameters at various torsional damping ofwheelset drivetrain. Time-history (a) and amplitude spectrum (c) of the difference between the angular displacements of the left and right wheelset wheel. Time-history (b) and amplitude spectrum (d) of the electric currents in the stator winding

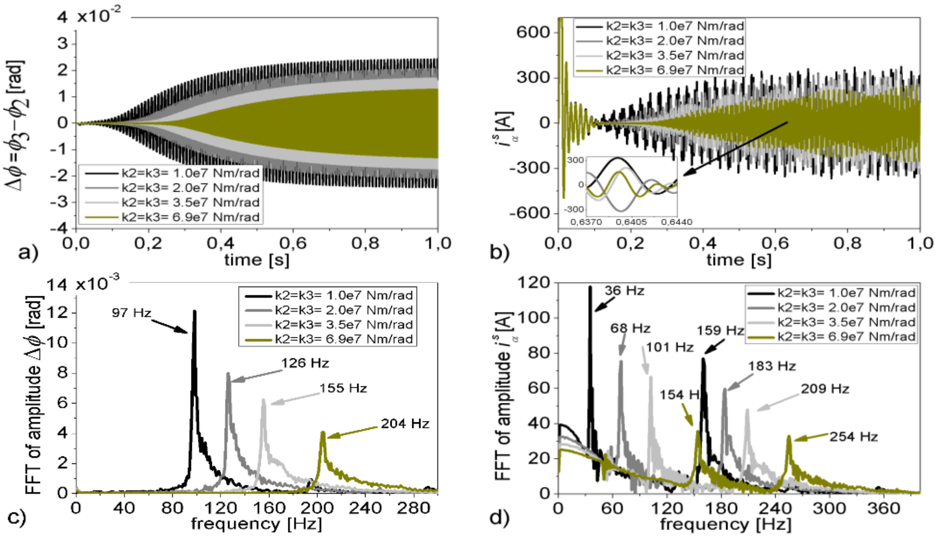

Figure 5. Self-excited torsional vibration amplitudes of the mechanical and electricparameters at various torsional stiffness ofwheelset drivetrain. Time-history (a) and amplitude spectrum (c) of the difference between the angular displacements of the left and right wheelset wheel. Time-history (b) and amplitude spectrum (d) of the electric currents in the stator winding

As shown in this figure(Fig 5.), the vibration amplitude decreases with an increase of $k_2$and k_3. It indicates that where increasing the torsional stiffness of drivetrain system, it is influences on the stability of the vibration and its shifting dominant frequency of the vibration in the higher range of the spectrum (Fig. 5c).

Considering the electrical parameter values of motor obtained from the above investigations it is worth highlighting that the self-excitation torsional vibrations affected on the entire electromechamicaldrivtrain system and they have a significant influence on the amount of theoretically expected electric energy P_{el}consumed by the driving motor.In the case of the investigated system, this energy can be determined by the electromotive forces induced in the asynchronous motor phases by voltages and currents in the stator windings. This energy can be defined [7].

$$P_{el} = \frac{1}{t_k} \int_0^{t_k} [U_{ds}(t) \cdot i_{\alpha}^s(t) + U_{qs}(t) \cdot i_{\beta}^s(t)]\, dt \quad , \tag{7}$$

where $U_{ds}(t)= \sqrt{\frac{3}{2}}U\cos(\omega_e t)$, $U_{qs}(t)= \sqrt{\frac{3}{2}}U\sin(\omega_e t)$, and $i_{\alpha}^s(t)$, $i_{\beta}^s(t)$, denote the voltages and currents in the stator circuits of the electric motor phases transformed into the reference system of Park's equations, $t_k$is the total duration time of the each variant of an analysis and the remaining symbols have been already defined in Eqs. (5) and (6). Table 3illustrates the amounts of electric energy consumed by the drivetrain motor during the consideredtest scenariosat various of parametersthe drive system discussed above.

Table 3. Amounts of electric energy consumed by the asynchronous motor during the assumed four scenarios of the investigation using the assumed drivetrain models

stiffnes of drivtrain [Nm/rad]	1e7	2e7	3.5e7	6.9 e7
stiffness-energy consumed [kWs]	62,35	70,44	76,65	78,93
damping of drivtrain [Nms/rad]	50,00	100,00	150,00	200,00
damping-energyconsumed [kWs]	78,93	88,37	88,59	93,02

From a comparison of the results shown in Table 3it follows that, when the torsional stiffness increase, more electric energy have been consumed. This fact can be substantiated by change amplitude of the time-histories of the difference between the angular displacements of the left and right wheelset wheel characteristics of presented in Fig. 5.

4. Final remarks and preview

In this paper, an electromechanical model of the railway vehicle drive system has been performed. This model has been used to investigate self-excited torsional vibrations occurring in this system. In the investigations their influence of the torsional vibration on the electric parameters of the drive motor are also considered.From obtained results it follows that a reductionof the self-excited vibration amplitudes by means of increasing the damping and stiffness between the driving motor and the wheelset and torsion stiffness of wheelset occur.The results obtained using numerical simulations indicated that the self-excited torsional vibrations in the considered drive system are strongly dependent on the characteristics of the adhesion coefficient in wheel-rail contact zone. A circuit model of the electric motor in the considered drive system enable us to obtain values of electrical parameter characterizing the driving motor.The information concerning a frequency variation of the current in the driving motor stator can be used for monitoring and identification of self-excited vibration in the wheelset drivetrain system. The further work will be denoted to an assumption of the vehicle model with the drivetrain system and it will be carried out experimentally verification on real railway vehicle.

References

1. R. Bogacz, T. Szolc, H. Irretier, *An application of torsional wave analysis to turbogenerator rotor shaft response*, J. Vibr. Acou. - Trans. of the Asme, **114**(2) (1992) 149 – 153.
2. O. Ahmedov, V. Zeman, M. Byrtus, *Modelling of vibration and modal properties of electric locomotive drive*, Eng. Mech., **19**(2/3) (2012) 165 – 176.
3. S. Noga, R. Bogacz, T. Markowski, *Vibration analysis of a wheel composed of a ring and a wheel-plate modelled as a three-parameter elastic foundation*, J.SoundVib., **333**(24) (2014) 6706 – 6722.
4. R. Bogacz, R. Konowrocki, *On new effects of wheel-rail interaction*, Arch. Appl. Mech, **82** (2012) 1313 – 1323.
5. V. Zeman, Z. Hlavac, *Dynamic wheelset drive load of the railway vehicle caused by shortcircuit motor moment*, App. & Comp. Mech., **3**(2) (2009) 423 – 434.
6. B. S. Branislav, *Simulation of torsion moment at the wheel set of the railway vehicle with the traction electromotor for wavy direct current*, Mech. Trans. Com., **3** (2008) 6 – 9.
7. J. Liu, H. Zhao, W. Zhai, Mechanism of self-excited torsional vibration of locomotive driving system, Front. Mech. Eng.China, **5**(4) (2010) 465 – 469.
8. A. K. Kumar, Method and system of limiting the application of sand to a railroad rail, U.S. Patent 7,290,870B2, Nov. 6, (2007).
9. S. Friedrich, M. Traupe, *Dynamic Torsional Loads on Wheelsets. Recent Findings for the Assessment*, Fatigue Strength and Simulation, T.TVI 24, Milan (2014).
10. T. Szolc, R. Konowrocki, M. Michajłow, A. Pręgowska, *An investigation of the dynamic electromechanical coupling effects in machine drive systems driven by asynchronous motors*, Mech. Syst. Signal Process., **49** (2014) 118 – 134.
11. R. Konowrocki, T. Szolc, A. Pochanke, A. Pręgowska, *An influence of the stepping motor control and friction models on precise positioning of the complex mechanical system*, Mech. Syst. Signal Process., **70-71** (2016) 397 – 413.
12. K. L., Shi, T. F., Chan, Y. K., Wong, L.S Ho, *Modelling and simulation of the three-phase induction motor using Simulink*, Int. J. Elect. Eng. Edu., **36** (1999) 163 – 172
13. L. Lipiński, *Applying simulation models for operation analysis and selection of controller settings in traction drives with induction motors*,Electrical Machines - Transactions Journal, **1**(94) (2012) 75 – 80 (in Polish).

Vibrations in Physical Systems Vol. 27 (2016)

Regular and Chaotic Dynamics of a 4-DOF Mechanical System with Dry Friction

Angelika KOSIŃSKA
Lodz University of Technology, Department of Automation Biomechanics and Mechatronics, 1/15 Stefanowski Street, 90-924 Lodz
angelika.kosinska@dokt.p.lodz.pl

Jan AWREJCEWICZ
Lodz University of Technology, Department of Automation Biomechanics and Mechatronics, 1/15 Stefanowski Street, 90-924 Lodz
jan.awrejcewicz@ p.lodz.pl

Dariusz GRZELCZYK
Lodz University of Technology, Department of Automation Biomechanics and Mechatronics, 1/15 Stefanowski Street, 90-924 Lodz
dariusz.grzelczyk@ p.lodz.pl

Abstract

In this paper the model of four degree-of-freedom mechanical sliding system with dry friction is considered. One of the components of the mentioned system rides on driving belt, which is driven at constant velocity. This model corresponds to a row of carriage laying on a guideway, which moves at constant velocity with respect to the guideway as a foundation. From a mathematical point of view the analyzed problem is governed by four second order differential equations of motion, and numerical analysis is performed in Mathematica software. Some interesting behaviors are detected and reported using Phase Portraits, Poincaré Maps and Lyapunov Exponents. Moreover, Power Spectral Densities obtained by the Fast Fourier Transform technique are reported. The presented results show different behaviors of the system, including periodic, quasi-periodic and chaotic orbits.

Keywords: periodicity, quasi-periodicity, chaos, hyper-chaos, non-regular vibrations

1. Introduction

The comprehension and characterization of dynamical systems belong to a challenging subject in recent years [1], and also nowadays these investigations are still continued. In many real systems (for instance, sliding linear guide systems, brakes, clutches, piston rings in a cylinder, and many other) friction phenomenon and stick-slip effect as a result of relative sliding velocity between surfaces of bodies rubbing themselves have a great impact on the strength of mechanical elements of these systems as well as their dynamics. And although there are numerous papers related to the mentioned problems in the literature, not all effects, associated with the friction phenomenon, have been sufficiently understood so far. In many cases, the presence and the manifestation of some effects depends on the structure of the considered system. In general, friction belongs to the complex processes and depends on various parameters like relative sliding velocity, normal load or surface properties. As an example, a review on different applied in the literature dry friction models can be found in [4], or in the recent paper [5].

The presented in this paper studies are a continuation and extension of research related to the mechanical model presented in [2,3]. In comparison to the mentioned papers, here other new numerical simulations obtained for other system parameters are presented and discussed. In addition, in contrary to the previous numerical investigations, beyond using Phase Portraits and Lyapunov Exponents, also other methods are used and applied like Poincaré Maps and Power Spectral Densities (PSDs).

The rest of the paper is organized as follows. In section 2 mechanical model of the considered system and its equations of motion in the non-dimensional form are introduced. In section 3 assumptions of numerical computations, the applied approximations of non-smooth functions, as well as parameters of the considered system are introduced. Numerical results of our investigations are presented in section 4. Finally, conclusions of our investigations are presented in the last section 5.

2. Mechanical Model and Non-Dimensional Form

The analyzed in this paper four degrees-of-freedom model is shown in Fig. 1.

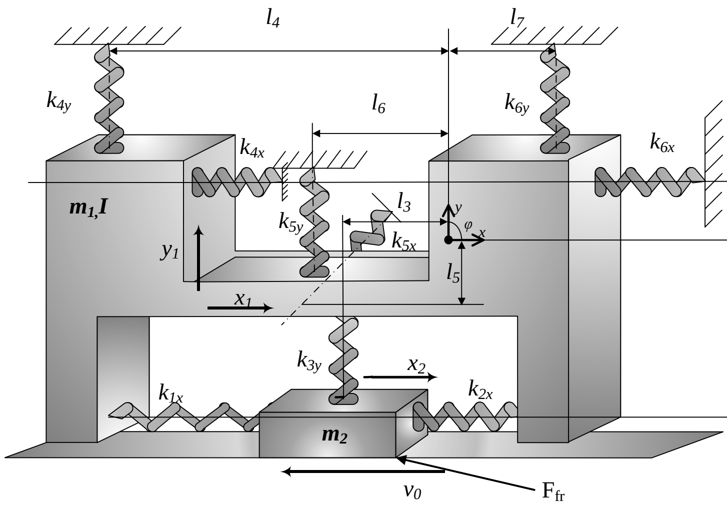

Figure 1. The considered 4-DOF model with dry friction

The state of the considered dynamical system is described by the following variables: x_1, $v_1 = \dot{x}_1$, y_1, $z_1 = \dot{y}_1$, φ, $\omega = \dot{\varphi}$, x_2 and $v_2 = \dot{x}_2$. The body of mass m_1 can rotate about the pivot axis S (moment of inertia about the pivot axis S of this mass is equal to I). The whole system is characterized by lengths l_i (i = 1,2,...,6) and springs with stiffness coefficients k_{ix}, k_{jy} (i =1,2,4,5,6; j =3,4,5,6). Moreover, additional body of mass m_2 is placed on the belt as a foundation, which moves with a constant velocity v_0. Between the mentioned mass m_2 and the belt dry friction force occurs, which is a function of the relative sliding velocity $v_0 - \dot{x}_2$. Equations of motion of the system are obtained using the second kind of Lagrange equations (presented in detail in [2]) and have the following non-dimensional form

$$\begin{cases} \ddot{x}_1 + a_1 x_1 + a_2\varphi - a_3 x_2 = 0, \\ \ddot{y}_1 + b_1 y_1 - b_2\varphi + f_g = 0, \\ \ddot{\varphi} + c_1 x_1 - c_2 y_1 + c_3\varphi - c_4 x_2 = 0, \\ \ddot{x}_2 - x_1 - \varphi + x_2 = f_k(v_0 - \dot{x}_2)\cdot[f_g - (e_1 y_1 - e_2\varphi)]\cdot \mathbf{1}(f_g - (e_1 y_1 - e_2\varphi)), \end{cases} \tag{1}$$

where x_1, $\dot{x}_1$, y_1, $\dot{y}_1$, φ, $\dot{\varphi}$, x_2, $\dot{x}_2$ denote now non-dimensional state variables. Other non-dimensional parameters and functions of Eqn. (1) are introduced in section 3.

3. The Applied Approximations and Parameters

Numerical simulations are obtained in Mathematica software via the fourth order Runge-Kutta method, and the trajectories are started from zeros initial conditions. The values of non-dimensional system parameters are as follows:

$$a_1 = 0.08,\ a_2 = 0.03,\ a_3 = 0.04,\ b_1 = 0.09,\ b_2 = 0.03,\ c_1 = 0.03,\ c_2 = 0.03,$$
$$c_3 = 0.06,\ c_4 = 0.03,\ f_g = 0.01,\ e_1 = 1.38,\ e_2 = 0.47,\ v_0 = \text{var.},$$

and their estimation is explained in [2]. Kinetic friction function $f_k(v_0 - v_2)$ in our model is described by the Stribeck function. Since the classical signum function is discontinuous, it has been approximated by the hyperbolic tangent function with control parameter ε in the following way

$$f_k(v_0 - v_2) = \mu_0 \tanh\left(\frac{v_0 - v_2}{\varepsilon}\right) - \alpha(v_0 - v_2) + \beta(v_0 - v_2)^3 \tag{2}$$

with fixed parameters $\mu_0 = 0.8$, $\alpha = 15{,}59$, $\beta = 4252{,}12$ and $\varepsilon = 10^{-4}$. Because the unit step function $\mathbf{1}(f_g - (e_1 y_1 - e_2\varphi))$ is also discontinuous, the following approximation is also applied in our computations

$$f_n(f_g - (e_1 y_1 - e_2\varphi)) = \left[\tanh\left(\frac{f_g - (e_1 y_1 - e_2\varphi)}{\varepsilon}\right)\right]^3 \cdot \mathbf{1}(f_g - (e_1 y_1 - e_2\varphi)). \tag{3}$$

4. Results

Figs. 2-4 present numerical simulations for different parameter v_0. The presented results vary from each other, depending on the used value of v_0 parameter.

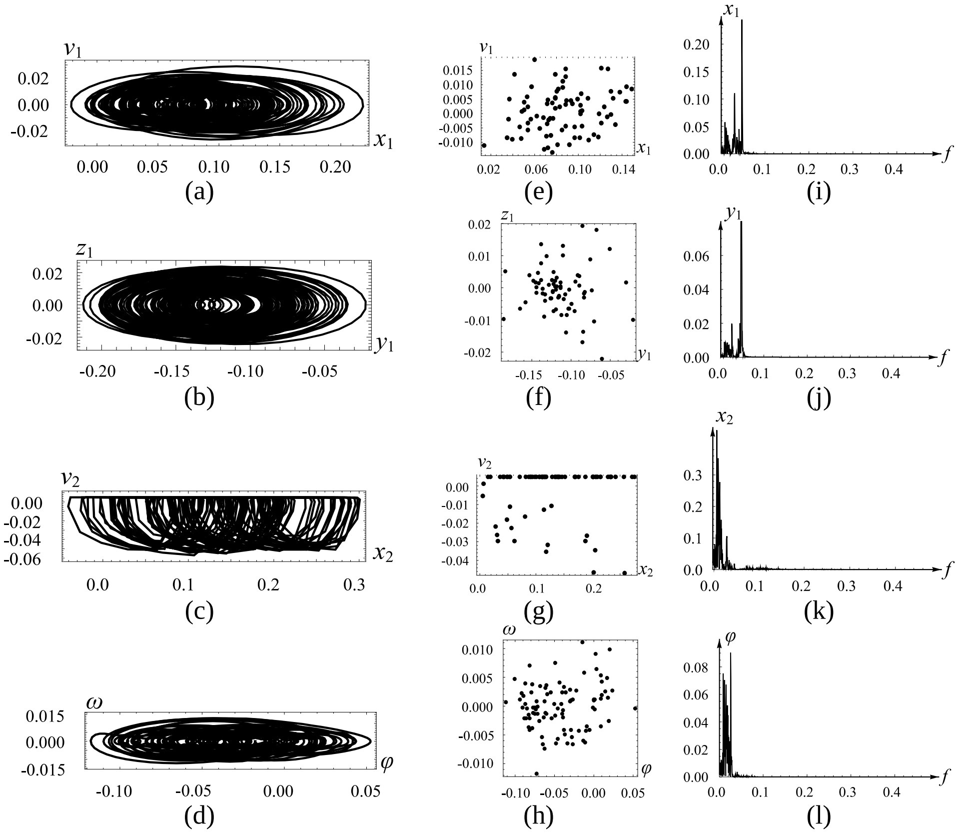

Figure 2. Phase portraits (a,b,c,d), Poincaré sections (e,f,g,h) and PSDs (i,j,k,l) for $v_0 = 0.005$ in time interval $\tau \in (20000,22000)$

As can be seen, for $v_0 = 0.005$ the character of motion is chaotic. Presented in Fig. 2 phase portraits, Poincaré sections and PSDs confirm its irregular dynamics. The chaotic attractor has different forms on different Poincaré maps. Moreover, it should be emphasized that the characters of motion differ is very sensitive to the changes of the belt velocity v_0. In particular stick-slip chaotic dynamics is clearly exhibited by the phase portrait shown in Fig. 2c and the Poincaré map reported in Fig. 2g.

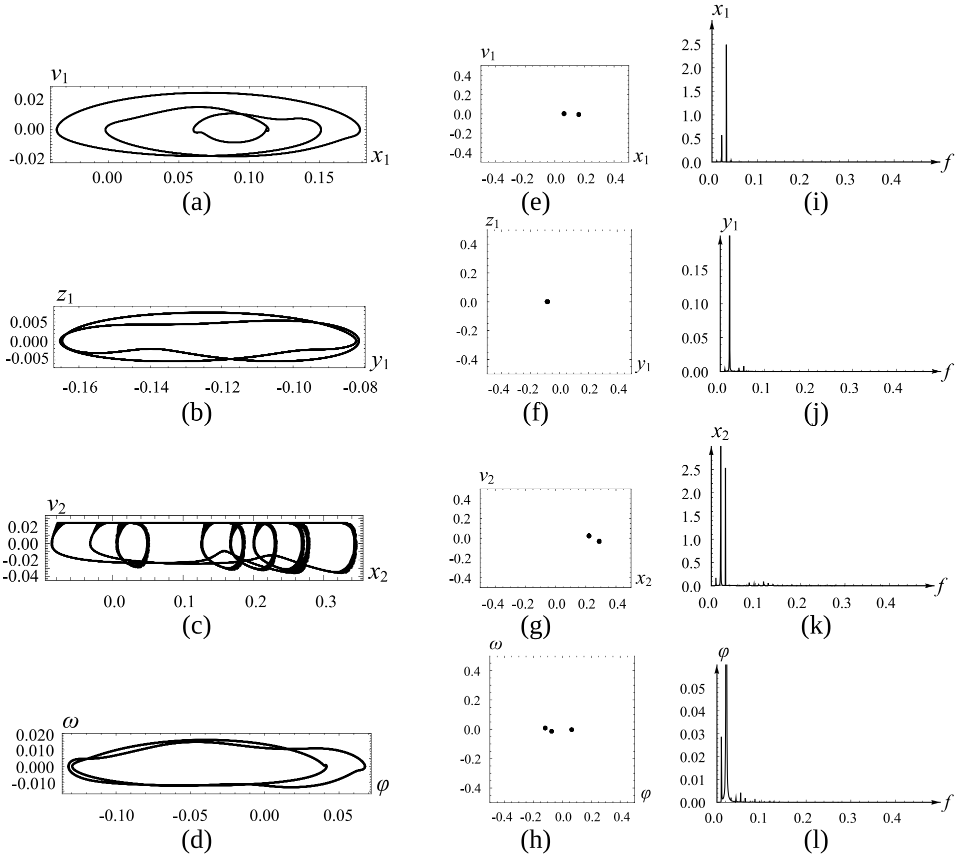

Figure 3. Phase portraits (a,b,c,d), Poincaré sections (e,f,g,h) and PSDs (i,j,k,l) for $v_0 = 0.025$ in time interval $\tau \in (20000,22000)$

When $v_0 = 0.025$, for variable x_1 there is a periodic-two cycle orbit, which is represented by two points in the Poincaré section (Fig. 3e) and is depicted as the trajectory crosses itself in phase portrait (Fig. 3a). The same situation occurs for state variable x_2. While for y_1 a period-one harmonic appears (Fig. 3f), it is worth noting that this is a closed curve in the phase plane (Fig. 3b). A three cycle period behavior is presented for ω (Fig. 3d,h).

Frequencies, at which the energies are strong and at which variations energies are weak, are shown in the Fig. 3 (i,j,k,l) for $v_0 = 0.025$. For the following state variables: x_1, y_1, x_2 and ω the energy is the strongest at two, single, two and three frequencies, respectively.

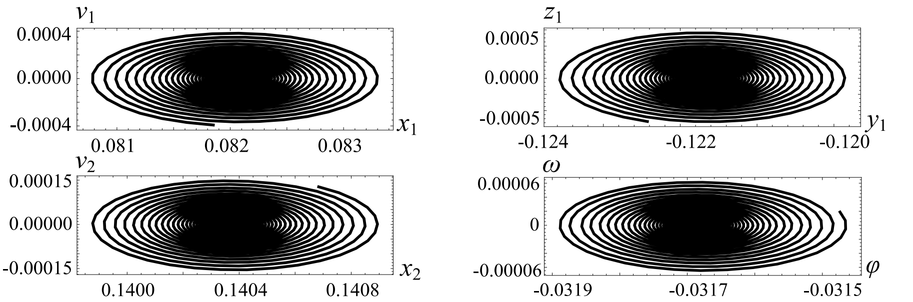

Figure 4. Trajectories of the system for $v_0 = 0.05$ in time interval $\tau \in (10000,12000)$

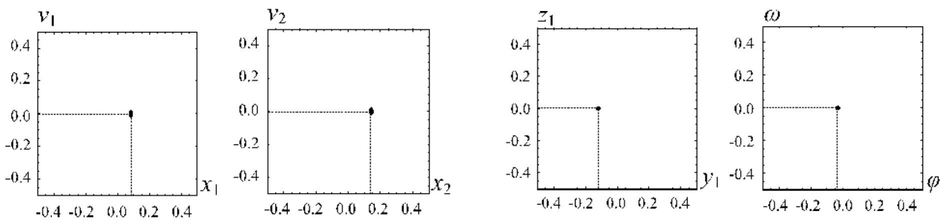

Figure 5. Poincaré sections for $v_0 = 0.05$ in time interval $\tau \in (20000,22000)$

Another character of motion is detected for $v_0 = 0.05$. Fig. 4 shows the transient states for chosen time interval, which indicate that the trajectories of the system go to the fixed points. After avoiding the mentioned transient states, the Poincaré sections are also obtained and presented in Fig. 5, and they prove that the system goes to steady state.

Table 1. Lyapunov exponents for different parameter v_0

v_0	λ_1	λ_2	λ_3	λ_4	λ_5	λ_6	λ_7	λ_8
0.005	0.0069	0.0027	0.0001	-0.0010	-0.0030	-0.0077	-0.0206	-33.00
0.025	0.0000	-0.0026	-0.0027	-0.0095	-0.0358	-0.0384	-0.0960	-19.52
0.032	0.0002	-0.0004	-0.0011	-0.0080	-0.0149	-0.0324	-0.1333	-15.81
0.04	0.0000	-0.0022	-0.0026	-0.0160	-0.0198	-0.0421	-0.0850	-7.8248
0.05	-0.0043	-0.0045	-0.0100	-0.0102	-0.1195	-0.1197	-0.1764	-2.2371

Our numerical investigations are also conducted by calculations of the max. Lyapunov exponents, which are depicted in Tab. 1. Moreover, as an example, time histories of max. Lyapunov exponents for two different parameter v_0 are reported in Fig. 6. The

Lyapunov exponents for each values of v_0 has been obtained using the Gram-Schmidt reorthonormalization time $\Delta T = 0.5$, after avoiding the transition state and starting numerical computations from zeros initial conditions. Chaotic characters of motions are detected for v_0 equal to 0.005 and 0.032, while the periodic behavior are detected for v_0 equal to 0.025, 0.04 and 0.05. For $v_0 = 0.05$ the trajectories goes to the fixed points.

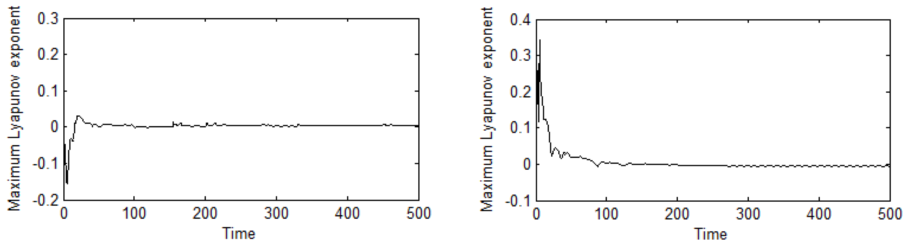

Figure 6. Time histories of max. Lyapunov exponents of the system for different values of velocity v_0 equal to: (a) 0.005 and (b) 0.05

5. Conclusions

Mathematical model of 4-DOF mechanical sliding systems with dry friction is considered. From a mathematical point of view the mentioned system is presented as a nonlinear system of equations of motion. Dynamics of the analyzed system is carried out for a set of system parameters and various non-dimensional control parameter. Interesting dynamics behaviors of the considered system are reported using standard tools dedicated to the both qualitative and quantitative theories of nonlinear differential equations. There are many technical devices in engineering applications, where we deal with stick-slip induced vibrations. The considered in this paper system can be treated as a model, which corresponds to a row of carriage laying on a guideway and moved at constant velocity with respect to the guideway as a foundation. As this paper shows, there are many possible behaviors of this system, and also it is very sensitive to the changes of the belt (foundation) velocity. It is therefore can be anticipated that also the movement of the real system of this type with various velocities of foundation, may vary considerably. In result, it can cause strongly nonlinear vibrations (regular or chaotic) that moving to the various components of the system may lead to its damage. Therefore the considered system can be used in engineering practice to predict its vibrations, and consequently to its protection.

Acknowledgments

The work has been supported by the National Science Centre of Poland under grant MAESTRO2 no. 2012/04/A/ST8/00738 for years 2012-2016.

References

1. J. Abdo, M. Tahat, A. Abouelsoud, M. Danish, *The effect of frequency of vibration and humidity on the stick–slip amplitude*, International Journal of Mechanics and Materials in Design, **6** (2010) 45 – 51.
2. D. Grzelczyk, J. Awrejcewicz, G. Kudra, *Dynamics of mechanical sliding system with dry friction*, Machine Dynamics Research, **38**(3) (2014) 61 – 70.
3. A. Kosińska, J. Awrejcewicz, D. Grzelczyk, *Dynamics of two coupled 4-DOF mechanical linear sliding systems with dry friction*, Dynamical Systems - Control and Stability, Eds. J. Awrejcewicz, M. Kaźmierczak, J. Mrozowski, P. Olejnik, TU of Lodz, Lodz, (2015) 327 – 340 (978-83-7283-708-0).
4. J. A. C. Martins, J. T. Oden, F.M.F. Simoes, *A study of static and kinetic friction*. International Journal of Engineering Science, **28**(1) (1990) 29 – 92**.**
5. J. Awrejcewicz, P. Olejnik, *Analysis of dynamics systems with various friction laws*, Applied Mechanics Reviews, **58**(6) (2005) 389 – 411.

Non-Linear Vibrations of a Non-Uniform Beam with SymmetricallyLocated Piezoelectric Patches

Krzysztof KULIŃSKI
Częstochowa University of Technology, Institute of Mechanics and Machine Design Foundations, Dąbrowskiego 71,42 200 Częstochowa, krzysztku@gmail.com

Jacek PRZYBYLSKI
jacek.pr@imipkm.pcz.pl

Abstract

In this paper the non-linear vibration behaviour and its modification due to the piezoelectric actuation of a beam with varying cross section and resting on an elastic foundation has been discussed. Due to assumed end conditions the stretching force emerges during the system vibrations. That force can be modified by an axial residual force to enhance or reduce the value of vibrations frequency of the beam. The system is divided onto three segments with the central segment consisted of the core beam and two colocally and perfectly bonded piezo patches. In order to obtain the approximate solutions of the non-linear frequency of the systems the Lindstedt-Poincare method has been utilized. Vast number of numerical results shows that not only the structural parameters of the system have significant effect on its non-linear vibration behaviour at a given amplitude but also the residual force and the elastic foundation modulus.

Keywords: non-linear vibrations, piezoactuators, amplitude-frequency relation, Winkler foundation

1. Introduction

The non-linear lateral vibrations of beam structures have been the subject of interest of many researchers. From the engineering point of view the beam-type structures are very interesting due to their wide application in civil and mechanical engineering, automotive, aviation, aeronautics industry, medical systems and equipment and many more. It is well known that any mechanical structure or its part should be protected from exposure to long time periods of resonance. Piezoelectric materials which are also called “smart materials” allow to modify the vibration frequency and buckling load of a given structure due to the inverse piezoelectric effect. That effect result in dimension changes of piezoelement which depend on the applied electric field vector. It should be noted that direct piezoelectric effect is also widely utilized in many areas of life such as sound processing, pacemakers, airbags, lighters etc.

As the research precursor of non-linear frequency studies shall be deemed to Wojnowsky-Krieger [1] whose thesis concerned the effect of the axial force on the non-linear frequency of simply supported beams. In the subsequent years there were vast number of literature positions published and experimental studies performed concerning the problem of the non-linear vibrations. Azrar et al. [2] presented mathematical approach concerning the second order approximation to obtain the non-linear vibration frequency for pinned-pinned and clamped-clamped beams which are close to the exact solution in a large amplitude frequency range. Moreover authors presented a very thorough discussion about increasing the accuracy of the obtained amplitude-frequency solutions. Benamar et al. [3] proposed a general model of the non-linear vibrations at large amplitudes for standardly supported beams to describe the influence of amplitude on both the mode shapes and the natural frequency. It was observed that near the clamps there were a great increase in beam curvatures which caused increased deflection resulting in highly non-linear increase of bending strain. A vast literature overview concerning the active, passive, semi-active and hybrid vibration control of the systems was presented by Song et al [4]. It was stated that piezoelectric materials despite some limitations have many advantages such as low-cost, low weight and ease of implementation. On the basis of Faria [5] as well as Zehetner and Irschik [6] considerations it can be stated that only for the beams which ends are mounted to prevent their axial displacement, both the stability and vibration frequency can be modified by piezoelectric actuation. Oguamanan et al. [7] investigated the influence of piezoelectric material in plane stress on beams mechanical performance. Authors showed that in systems where piezoelectric material was bonded both to the upper and bottom surface of the beam, especially the first frequency can be significantly modified. It was observed that depending on the applied electric field vector direction, vibration frequency can be enhanced or reduced. Moreover authors demonstrated that piezoactuators localized near the beam supports, give slightly more effective control of the system vibrations. The influence of piezoactuators length, its localization and the piezoelectric force on the amplitude-nonlinear frequency relationship in a slender pinned-pinned beam has been studied by Przybylski [8]. It was proved that stretching piezoelectric force result in an increase of the natural frequency and decrease of non-linear frequency, whereas compressive piezo-force resulted in opposite system behaviour. A broader literature overview with wider area of study of slender systems with bonded piezoelectric materials can be found in [9].

In this paper the influence of vibrations amplitude, piezosegment length and Winkler elastic foundation modulus on the non-linear frequency for a pinned-pinned and clamped-clamped beams is investigated. Moreover the non-linear vibration adjustment due to piezoelectric actuation is examined. The object of study is a three segment system made of aluminium host beam with two symmetrically piezo patches bonded perfectly on the upper and bottom surface of the central segment. In order to obtain approximate solutions the Lindstedt-Poincare method has been utilized.

2. Problem formulation

The main objective of this work is to formulate and solve the problem of the non-linear vibrations of a stepped beam resting on the Winkler elastic foundation and to estimate the influence of both the structural parameters and the piezoelectric actuation on the non-linear frequency-amplitude relationship. Due to the moderately large amplitude of vibrations, the von Karman theory has been applied according to which during transversal vibrations, the axial inertia effect can be treated as insignificant.

The scheme of three-segmented system composed of a core beam with both ends clamped and two piezoelectric patches bonded along the central segment is shown in Fig. 1.

a) b)

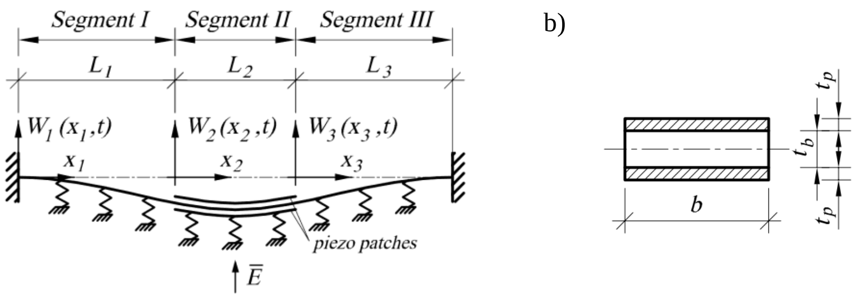

Figure 1. Scheme of clamped-clamped beam resting on elastic Winkler foundation with two piezoelectric patches colocally mounted along the central segment (a), piezosegment cross-section (b)

The applied voltage, symbolized by the electric field vector **E** in Fig. 1, is exactly the same for the upper and bottom piezo actuator which results in the axial stretching/compressive force being generated dependently on the electric field vector sense. A derivation of the residual force equation appearing along the stepped beams with *n*-pairs of piezoelectric actuators has been presented in [9]. According to these considerations for the three segmented system the residual force can be described as follows

$$F_r = F\left[1+\eta\left(\frac{L}{L_2}-1\right)\right]^{-1} \tag{1}$$

where: η denotes the relation of the piezosegment axial stiffness to that of the beam, $F = -2be_{31}V$ is the piezoelectric force induced by piezoceramic patches of width b, when piezo material is characterised by constant e_{31} and the applied voltage is equal to V, L is the length of the beam, L_2 is the length of piezosegment. According to von Karman theory and the actuality that algebraic sum of the axial displacement of three segments is equal to zero, the force which stretches the beam during its transverse vibration can be expressed as

$$S(t) = \frac{1}{2}\left[\sum_{i=1}^{3}\frac{L_i}{E_i A_i}\right]^{-1}\sum_{i=1}^{3}\int_0^{L_i}\left(\frac{\partial W_i(x_i,t)}{\partial x_i}\right)^2 \tag{2}$$

Introducing both residual piezo-force F_r and dynamic force $S(t)$ into the governing equation of motion for the i-th segment, that equation takes the following non-dimensional form

$$\frac{\partial^4 w_i(\xi_i,\tau)}{\partial \xi_i^{\,4}} \pm \varphi_i\left(f_r^2+s^2(\tau)\right)\frac{\partial^2 w_i(\xi_i,\tau)}{\partial \xi_i^{\,2}} + \mu_i\omega^2\,\frac{\partial^2 w_i(\xi_i,\tau)}{\partial \tau^2} + \beta w_i(\xi_i,\tau) = 0, \quad \text{for} \;\; i = 1,2,3 \tag{3}$$

where the dimensionless parameters are defined as

$$w_i(\xi_i,\tau)=\frac{W_i(x_i,t)}{L},\quad \xi_i=\frac{x_i}{L},\quad l_i=\frac{L_i}{L},\quad \varphi_i=(1+r_m)^{-\frac{1}{2}(j^{2i}+1)},\quad r_m=\frac{E_pI_p}{E_bI_b},$$

$$j=\sqrt{-1},\quad f_r^2=\frac{F_rL^2}{E_bI_b},\quad s^2(\tau)=\frac{\lambda}{2}\left(\sum_{i=1}^{3}\eta^{-\frac{1}{2}(j^{2i}+1)}l_i\right)^{-1}\sum_{i=1}^{3}\int_0^{l_i}\left[\frac{\partial w_i(\xi_i,\tau)}{\partial \xi_i}\right]^2 d\xi_i\,,$$

$$\lambda=A_bL^2/I_b,\quad \mu_i=\left(\frac{\alpha_1+(\eta-1)\alpha_2}{\alpha_1(1+r_m)}\right)^{\frac{1}{2}(j^{2i}+1)},\quad \alpha_1=\frac{E_p}{E_b},\quad \alpha_2=\frac{\rho_p}{\rho_b},\quad \eta=\frac{E_bA_b+E_pA_p}{E_bA_b},\tag{4}$$

$$\omega^2=\Omega^2L^4\frac{\rho_bA_b}{E_bI_b},\quad \tau=\Omega t,\quad \beta=\frac{kL^4}{E_bI_b}$$

Following notation has been assumed: E_pI_p, E_bI_b - the bending stiffness of piezo patches and that of a beam, respectively, A_p, A_b - the cross section area of piezopatches and beam, respectively, ρ_p, ρ_b - the material densities of the actuators and beam, respectively, ω - the natural frequency of the system, t is time, k denotes the Winkler foundation modulus.

The non-dimensional boundary conditions for a pinned-pinned beam are:

$$w_1(\xi_1,\tau)\big|_{\xi_1=0}=w_1^{II}(\xi_1,\tau)\big|_{\xi_1=0}=w_3(\xi_3,\tau)\big|_{\xi_3=l_3}=w_3^{II}(\xi_3,\tau)\big|_{\xi_3=l_3}=0\tag{5}$$

whereas for a clamped-clamped beam take the form:

$$w_1(\xi_1,\tau)\big|_{\xi_1=0}=w_1^{I}(\xi_1,\tau)\big|_{\xi_1=0}=w_3(\xi_3,\tau)\big|_{\xi_3=l_3}=w_3^{I}(\xi_3,\tau)\big|_{\xi_3=l_3}=0\tag{6}$$

where: I and II are the Roman numerals denoting the order of the derivative with respect to the space variable ξ.

The continuity conditions are independent from the type of supports and describe the equality of the transversal force, moments, slopes and displacements between segments:

$$w_i(\xi_i,\tau)\big|_{\xi_i=l_i}=w_{i+1}(\xi_{i+1},\tau)\big|_{\xi_{i+1}=0},\quad w_i^{I}(\xi_i,\tau)\big|_{\xi_i=l_i}=w_{i+1}^{I}(\xi_{i+1},\tau)\big|_{\xi_{i+1}=0},$$

$$(1+r_m)^{\frac{1}{2}\left[j^{2i}+1\right]}w_i^{Rn}(\xi_i,\tau)\Big|_{\zeta_i=l_i}=(1+r_m)^{\frac{1}{2}\left[j^{2(i+1)}+1\right]}w_{i+1}^{Rn}(\xi_{i+1},\tau)\Big|_{\xi_{i+1}=0},\ i=1,\,2\,,\,Rn=II,III\tag{7}$$

3. Approximate solutions

In order to obtain approximate solutions of the non-linear boundary problem the Lindstedt-Poincare method has been utilized, according to which relevant quantities are expanded into exponential series with respect to the small amplitude parameter ε

$$w_i(\xi_i,\tau)=\sum_{n=1}^{N}\varepsilon^{2n-1}w_{i2n-1}(\xi_i,\tau)+\mathrm{O}\left(\varepsilon^{2N+1}\right)\tag{8}$$

$$s^2(\tau)=\sum_{n=1}^{N}\varepsilon^{2n}s_{2n}^2(\tau)+\mathrm{O}\left(\varepsilon^{2(N+1)}\right)\tag{9}$$

$$\omega^2 = \omega_0^2 + \sum_{n=1}^{N} \varepsilon^{2n} \omega_{2n}^2 + \mathrm{O}\left(\varepsilon^{2(N+1)}\right) \tag{10}$$

where separation of space and time variable are described as:

$$w_{ij}(\xi_i,\tau) = \sum_{k=1}^{b} \overset{(2k-1)}{w_{ij}}(\xi_i)\cos(2k-1)\tau\,,\ \text{for}\ \ b = \frac{j-1}{2}+1\ \ \text{and}\ \ j = 1,3,5,\ldots \tag{11}$$

$$s_j^2(\tau) = \sum_{k=1}^{c} \overset{(2k-2)}{s_j^2}\ \cos 2(k-1)\tau\,,\ \text{for}\ \ c = \frac{j}{2}+1\ \ \text{and}\ \ j = 2,4,6,\ldots \tag{12}$$

Introducing expansions from (8-10) into the equation of motion (3) and axial dynamic force $s^2(\tau)$ expressed in (4) and then equating the terms of respective ε exponents to zero, an infinite set of equations of motion and axial force is obtained.

By solving the first pair of equations from the infinite set of equations with use of boundary conditions (5-6) an infinite number of solutions for the natural frequency is obtained, whereas from the third equation after applying the orthogonally condition the second term of frequency ω_2 can be obtained. The relationship of non-linear frequency ω and amplitude ε are determined on the basis of equation (10), with a customary limit up to the second order.

4. Numerical results

In this chapter the numerical results concerning the non-linear frequency-amplitude relationship for clamped-clamped and pinned-pinned beams with piezosegment centrally localised are presented. All analysis can be performed by using the non-dimensional quantities, but to show its usefulness for engineering applications it has been assumed that the host beam thickness $t_b = 3.0$ [mm] and piezo patches $t_p = 0.5$ [mm] each, whereas both the beam and piezo patches width $b = 20$ [mm]. The influence of adhesive layer thickness has been taken as negligibly small. The beam was made of a homogeneous elastic isotropic aluminium, while piezoceramic actuators were made of a homogeneous elastic transversely isotropic P41 material (Annon Piezo Technology Ltd. Co.). Electromechanical properties of the adopted materials for the numerical analysis are shown in Tab. 1.

Table 1. Material properties of beam and piezo patches

Property	**Unit**	**Beam**	**Piezoceramic**
E	GPa	70.00	83.33
ρ	kg/m^3	2720	7450
d_{31}	C/N	-	$1.00\cdot10^{-10}$
U_{max}	V/mm	-	2000

The first group of plots presented in Fig. 2 shows the influence of structural parameters of the beam and the elastic foundation stiffness modulus on the mentioned relationship, whereas in Fig. 3 the role of piezoelectric actuation in modification the obtained curves for the system with piezosegment of length l_2 = 0.80.

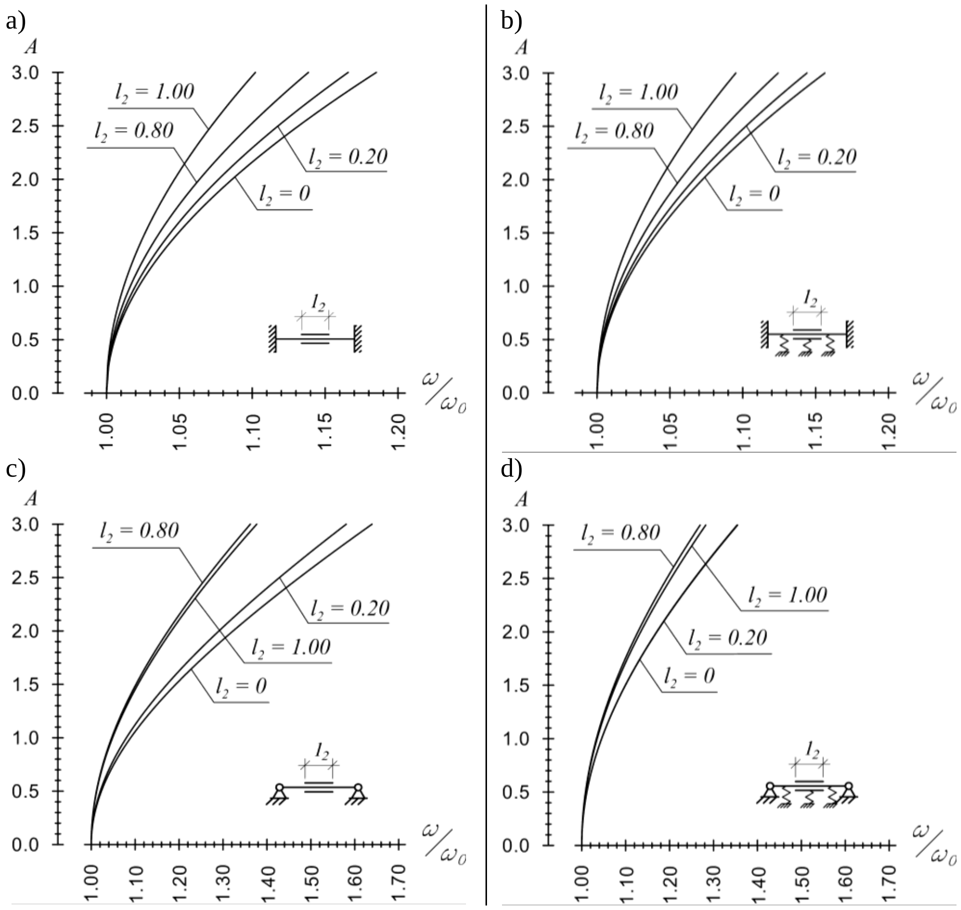

Figure 2. The influence of piezosegment length on amplitude – non-linear frequency relationship in clamped-clamped (a, b) and pinned-pinned (c, d) beams; remaining parameters: Winkler elastic foundation modulus β = 0 (a, c), β = 100 (b, d)

Comparing the curve courses for the clamped-clamped support (Fig. 2a, b) it can be stated than the longer the piezosegment length the smaller the amplitude influence on the non-linear frequency. For the pinned-pinned beam (Fig. 2c,d) at the whole range of the amplitude, the non-linear frequency is lower for the piezosegment of length l_2 = 0.80 than for the piezosegment mounted at the entire beam (l_2 = 1.00), whereas for the lengths l_2 = 0.0 and l_2 = 0.20 the vibrations aims to be the same with increased elastic foundation modulus. In both clamped-clamped and pinned-pinned system together with an increase of the elastic foundation modulus, the non-linear frequency decreases at the whole range of amplitudes and for any value of the piezo patches length.

In order to examine the piezoelectric actuation influence on the non-linear frequency – amplitude relationship two values of piezoelectric force has been chosen $f^2 = \pm\pi^2$. It should be noted that the range of non-dimensional residual force resulting from the applied electric field is far below the depoling field for the piezoceramic material.

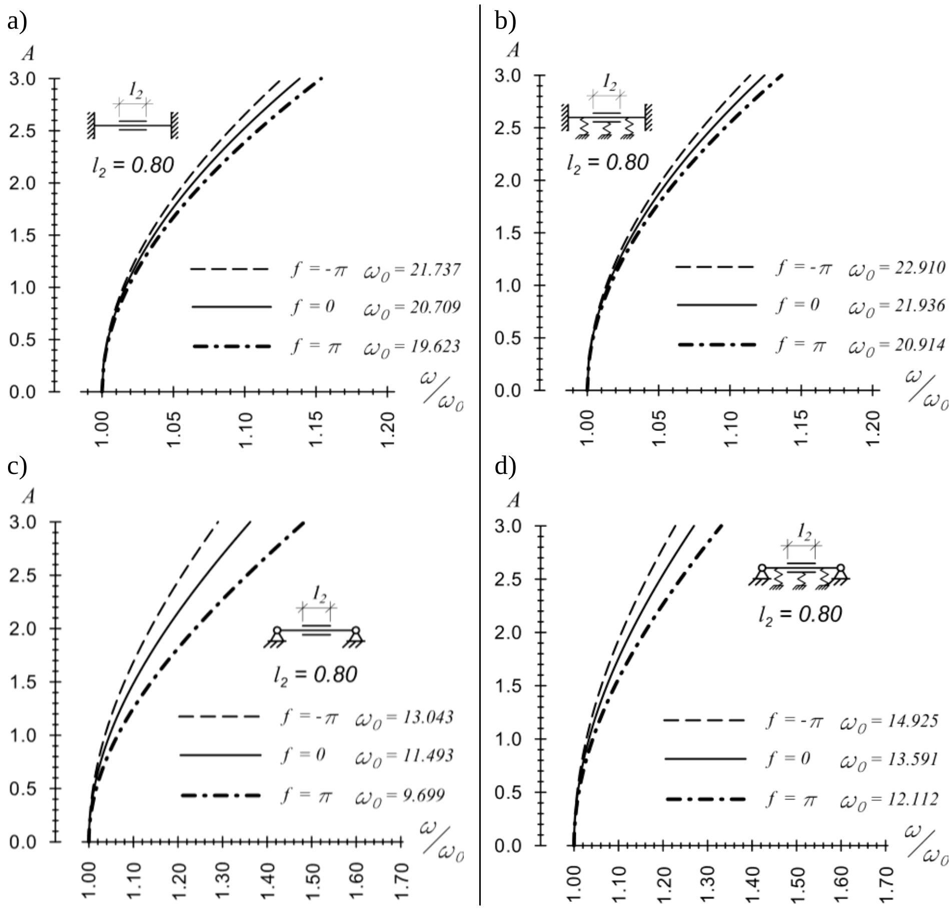

Figure 3. The influence of piezoelectric actuation on the amplitude-non-linear frequency relationship for clamped-clamped (a, b) and pinned-pinned (c, d) beams; remaining parameters: Winkler elastic foundation modulus $\beta = 0$ (a, c), $\beta = 100$ (b, d)

As it is presented in Fig. 3 in both cases (clamped-clamped and pinned-pinned beam) at any given amplitude and elastic foundation modulus the tensile piezoelectric force reduce the non-linear frequency, while the natural frequency is increased comparing to the beam without piezoactuation, whereas compressive piezo-force acts in an opposite way. Moreover the higher stiffness of Winkler elastic foundation the lower value of non-linear frequency at the whole range of amplitude. It should also be noted that more significant affection of Winkler elastic foundation on the non-linear frequency – amplitude relationship for systems with lower external support stiffness.

5. Conclusions

In this study the problem of non-linear vibrations for the non-uniform Euler-Bernoulli beams has been discussed. Moreover the enhancement and reduction of non-linear vibrations due to the piezoelectric actuation has been examined. It should be noted that performed studies can be useful in the manufacture of elements which are responsible of controlling static and dynamic response of structures.

It was also shown in this paper that regardless of system external support, the higher value of Winkler foundation modulus parameter results in decreasing of the non-linear frequency. There was also proved that piezoelectric actuation can enhance the non-linear vibration frequency via compressive force induced, while the natural frequency is increased and the opposite system behaviour is obtained for the tensile piezo-force.

References

1. S. Wojnowsky-Krieger, *The effect of an axial force on the vibration of hinged beams*, J. of Applied Mechanics, **17** (1950) 35 – 36.
2. L. Azrar, R. Benamar, R. G. White, *Semi-analitycal approach to the nonlinear dynamic response problem of S-S and C-C beams at large vibrations amplitudes. Part I: General theory and application to the single mode approach to free and forced vibration analysis*, J. of Sound and Vibr., **224** (1999) 183 – 207.
3. R. Benamar, M. Bennouna, R. G. White, *The effects of large vibration amplitudes on the mode shapes and natural frequencies of thin elastic structures. Part I: Simply supported and clamped-clamped beams*, J. Sound. and Vibr., **149** (1991) 179 – 195.
4. G. Song, V. Sethi, H-N. Li, *Vibration control of civil structures using piezoceramic smart materials: A review*., J. of Engng. Struct., **28** (2006) 1513 – 1524.
5. A. R. Faria, *On buckling enhancement of laminated beams with piezoelectric actuators via stress stiffening*., J. of Comp. Struct., **65** (2004) 187 – 192.
6. C. Zehetner, H. Irschik, *On the static and dynamic stability of beams with an axial piezoelectric actuation*, Smart Struct. and Syst., **4** (2008) 67 – 84.
7. D. Oguamanam, S. Almeida, J. Hansen, *Stress stiffening effect in laminated beams with piezoelectric actuators*, J Intell Mater Syst. Struct., **9** (1998) 137 – 145.
8. J. Przybylski, *Non-linear vibrations of a beam with a pair of piezoceramic actuators*, J. of Engng. Struct., **31** (2009) 2687 – 2695.
9. J. Przybylski, *Static and dynamic problems of slender mechanical systems with integrated piezoceramic elements*, Wydawnictwo Politechniki Częstochowskiej, Częstochowa 2012 (in Polish).

Numerical Modelling of Sound Transmission Through the Window Type Partition

Leszek KWAPISZ
Institute of Fluid Flow Machinery PAS, Gdansk, Fiszera 14 St., kwapi@imp.gda.pl

Artur MAURIN
Institute of Fluid Flow Machinery PAS, Gdansk, Fiszera 14 St., amaurin@imp.gda.pl

Piotr JAKUBOWSKI
Ship Design and Research Centre CTO S.A, Gdansk, Szczecińska 65 St.
piotr.jakubowski@cto.gda.pl

Abstract

The approach to numerical modelling of sound transmission through window type partitions is investigated in the paper. The laboratory conditions of reverberation room are simulated. The numerical and experimental results are compared. The impact of different model parameters on the sound insulation levels are evaluated.

Keywords: sound transmission, acoustic insulation, window, numerical simulation

1. Introduction

There are several basic approaches to sound insulating: increasing the distance between source and receiver, using noise barriers to reflect or absorb the energy of the sound waves, using damping structures such as sound baffles, or using active antinoise sound generators. Those approaches are implemented through a variety of techniques: vibration isolation, sound insulation, sound absorption and vibration damping. The window type partition is primarily a mass barrier with sound insulation properties.

There were several attempts to simulate sound insulation properties of partitions numerically. In the literature, this type of problems are usually referred to as vibroacoustic or structural-acoustic effects with fluid interaction. Davidson [1] investigated structure-acoustic effect, which involved a flexible structure coupled to an enclosed acoustic fluid. Ruber et al. [2] have investigated of a tuned vibration absorber with high damping for increasing acoustic panels sound transmission loss in low frequency range. Sakuma et al. [3] performed a numerical investigation of the niche effect in sound insulation measurement. Their numerical results demonstrate that sound reduction index decreases below the critical coincidence frequency due to niches, while it increases above the frequency. It was also confirmed that the effect of the two sided niche with a centrally located specimen is largest at low frequencies.

Dimino et al. [4] investigated a vibroacoustic design of an aircraft-type active window. An experimental modal analysis was carried out to determine both single partition and coupled fluid-structure modal frequencies used to validate the finite element model. The sound radiation characteristics of the window prototype via numerical procedure of coupling boundary and finite element methods was proposed to solve the coupled acoustic structure problem in the exterior acoustic domain. The above publications did not considered the standardised sound insulation measurement procedure, therefore the obtained results were difficult to be compared comprehensively.

Gimeno [5] studied the acoustic insulation of domestic windows, with the objective to compare the experimental and numerical methods. The calculations were made in COMSOL. Obtained results were not completely satisfactory, due to 2D numerical model restrictions and certain differences in boundary conditions between the numerical model and experimental measurements.

In this paper, a 3D approach to numerical modelling of sound transmission through a domestic windows, based on laboratory measurement standardised procedure EN ISO 20140-3, was investigated.

2. Laboratory measurements

The airborne sound insulation of domestic windows can be evaluated from laboratory measurements of the sound reduction index according to EN ISO 20140-3 norm [6]. The results acquired in laboratory can be used to compare the properties of sound insulation of building elements, to classify such items according to their capabilities of acoustic insulation, help design building products which require certain acoustic properties and estimate the in situ performance in complete buildings. The measurements are performed in laboratories in which sound transmission via flanking paths is suppressed. However, the results of measurements made in accordance with this standard cannot be applied directly to the field situation without accounting for other factors, such as flanking transmission, boundary conditions and total loss factor. The laboratory measurements are made using octave or one-third-octave bands.

The airborne sound insulation measurement, known as the reverberation room method, takes into consideration two chambers: a source chamber and a receiving chamber separated by a test element. It is assumed that all sound is transmitted via the test element, and that the structure of the transmission suite itself plays no role other than defining the space for the source and receiving rooms.

The transition coefficient τ, is defined as the ratio of the sound power transmitted by the test element W_2, to the sound power of the source W_1, expressed in Watts:

$$\tau = \left(\frac{W_2}{W_1} \right) \tag{1}$$

The sound reduction index R expressed in decibels is the inverse of the wall's transmission factor. In the laboratory measurements the index R is determined by measuring sound pressure level L_1 and L_2 in the two rooms. The following is obtained [6]:

$$R = L_1 - L_2 + 10\log\frac{S}{A} \quad \text{(dB)} \tag{2}$$

Where: L_1 is the average sound pressure level in the source chamber (dB),
L_2 is the average sound pressure level in the receive chamber (dB),

S is the test area (m^2),

A is the equivalent sound absorption area in the receiver chamber (m^2).

Dijckmans and Vermeir [7], carried out an extensive parametric study with a wave based model to numerically investigate the fundamental repeatability and reproducibility in such acoustical measurements through the different partitions. The effect on the uncertainty of single number quantities by including low frequencies (50-80 Hz) was discussed. Furthermore, their parametric study gave information to what extent it is possible to predict the sound insulation by laboratory results. In the low-frequency range, the sound transmission level as measured in the laboratory was not representative for results *in situ*. The same partition can give different sound transmission values, depending on the geometry and dimensions of the chambers or the partition. This source of uncertainty should be taken into further consideration.

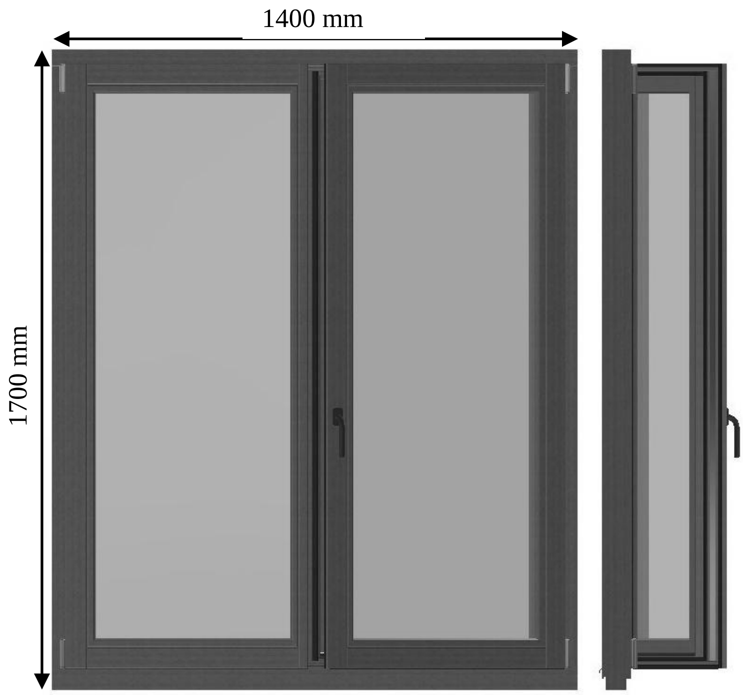

Figure 1. The CAD model of analysed window

The window frame (Figure 1), analysed in *Ship Design and Research Centre CTO*, has overall dimensions of . The default frame thickness 'G' is 78 mm and default frame height 'H' is 98 mm. The width of the central pillar is 82 mm. The default frame material is Meranti wood with density of 800 kg/m^3 and sound speed of 4500 m/s. The window glass material has density of 2500 kg/m^3 and sound speed of 5580 m/s. Three types of glazing where installed and measured: 4/12/4/12/4, 8/12/4/12/6 and 4/16/4. Every odd number in the sequence defines the glass thickness in mm, while every even number defines the distance in mm between subsequent glasses. The laboratory measurement results were discussed and compared further in section 4.

3. Numeric model

The window frame with three glazing types from laboratory measurements were modelled and enclosed in calculation space created in ANSYS Workbench environment, bisecting it into source and receiving domains. As the considered window has two planes of symmetry, the calculation space was restricted to 1/4 of the window (Figure 2). Using the symmetric boundary conditions significantly reduced the computational cost of the model, giving the results for whole window.

The introduced calculation space boundary condition is the wall that is around the model. Perfectly Matched Layer (PML) is utilised to obtain an absorption condition. Acoustic Mass Source with amplitude of 0.01 kg/m^2s is located at rear wall of source domain, ensuring a parallel wave excitation as required in [6].

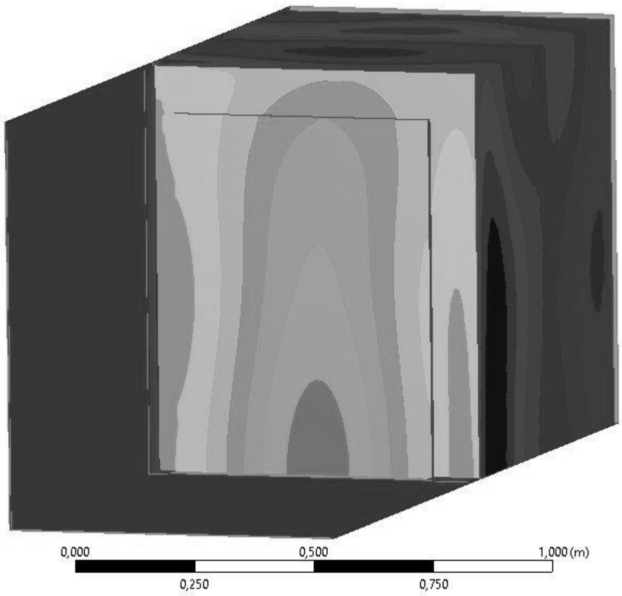

Figure 2. The calculation space with sound pressure level results for 500 Hz excitation

The frequencies of interest were those between 50Hz and 5000Hz, influence the mesh size (Figure 3): at least five elements should be used to model the shortest wavelength (0,06806 m at 5000 Hz), therefore size of the element is assumed to be 0,01 m. The assumed FE size was next validated by comparing with higher density meshes. The ANSYS FLUID 220, a higher order 3-D 20-node solid element that exhibits quadratic pressure behaviour, was used in the analysis (for more details see ANSYS online help documentation).

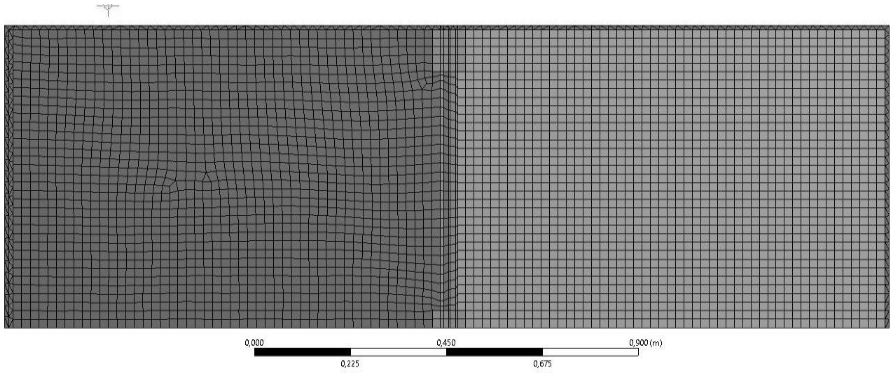

Figure 3. Geometry of the model (half-bottom view) and finite element size

In the numerical calculations, the sound reduction index R is defined as [6]:

$$R = 10\log\frac{W_1}{W_2} \quad \text{(dB)} \tag{3}$$

Where the W_1 is sound power calculated in the source domain and the W_2 is the sound power calculated in receiver domain. The sound power in the model was determined by setting up ANSYS acoustic power monitors in both domains. This approach, (acoustic power instead of acoustic pressure in the laboratory measurements [6]), allows to reduce dimensions of the source and receiver domains to minimum.

4. Numerical results

An Acoustic Harmonic Analysis in ANSYS Workbench environment was conducted. The experimental and numerical results were calculated in one-third-octave band (21 frequencies in range between 50 and 5000 Hz), however the reference glazing manufacturer data results were given in octave bands in range 125 to 4000 Hz (6 frequency values represented in the below diagrams in solid black). When comparing measured data, care must be taken to differentiate between measured data for glazing and measured data for windows. The reason is that the overall sound insulation performance of a window is affected by the window frame and the sealing of the glazing. The variety of measurement results acquired in CTO laboratories caused by sealing differentiation is represented on the diagrams below by group of the same-coloured lines.

Figure 4 represents the comparison between the group of six experimental measurements for glazing 4/12/4/12/4 with different sealing configurations – “CTO 444” (grey) – and the numerical results “ANSYS 444”. The visible difference for the low frequencies between (50-80 Hz) may occur due to measurement uncertainties described in [7]. Even if it was possible to measure the source and transmitted intensity correctly, the problem of reproducibility at low frequencies remains. The theoretical sound reduction index R - defined as the ratio between source and transmitted sound power - is also influenced by all the parameters which determine the modal composition of the sound fields and the modal coupling. One way to reduce the variations in low-frequency measurements is the use of more octave band values. As more modes are present in an octave band, variations in the sound transition values should be smaller [7]. The another significant difference was observed for 3200 and 5000 Hz frequencies probably due to the fact that measurements do not account for indirect transmissions and loss factor effects.

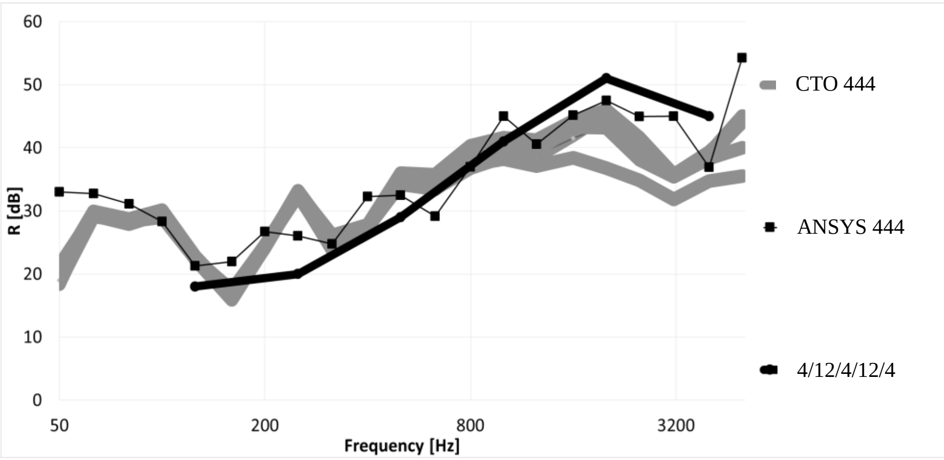

Figure 4. The comparison of numerical ANSYS 444 and experimental CTO 444 results for 4/12/4/12/4 type of window glazing

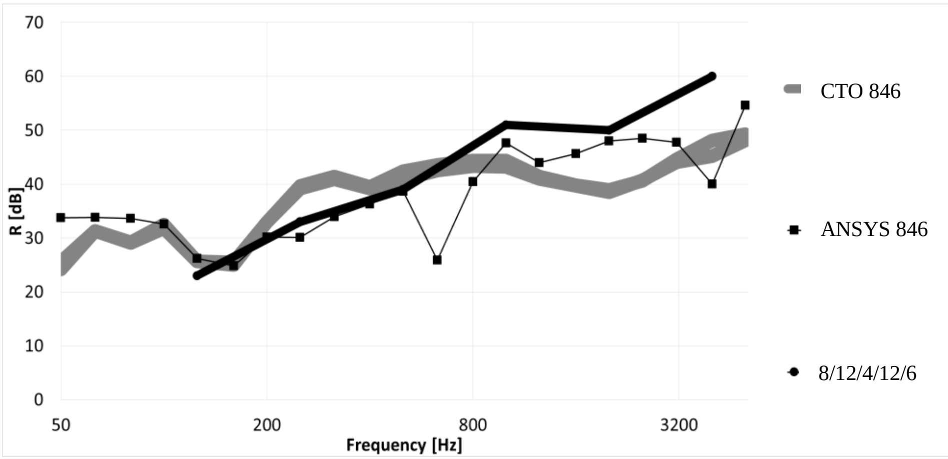

Figure 5. The comparison of numerical ANSYS 846 and experimental CTO 846 results for 8/12/4/12/6 type of window glazing

Figure 5 represents the comparison between two experimental measurements for 8/12/4/12/6 glazing with different sealing configurations – “CTO 846” (grey) – and the numerical results “ANSYS 846”. The same, low frequency differences can be observed.

The significant difference at 630 Hz most probably occur due to the coincidence effect. The discrepancies in the range between 200-400 Hz and 1250-3150 Hz were associated with seals.

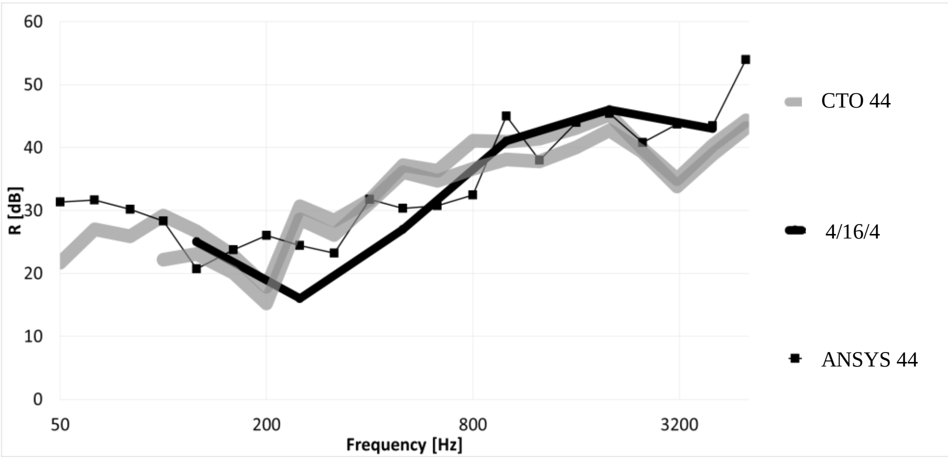

Figure 6. The comparison of numerical ANSYS 44 and experimental CTO 44 results for 4/16/4 type of window glazing

Figure 6 represents the comparison between two experimental measurements for different glazing sealing configuration – „CTO 44" (grey) – and the numerical results „ANSYS 44". Once again, the low frequency differences can be observed. As the different window models were studied, we may conclude that although the experimental and numerical results follow similar pattern, there were not exactly the same. There are several possible reasons for that.

The reverberation room method for measuring sound insulation performance of glazing and window type partitions involves the "niche effect" as a bias error factor [3]. It is known that the niche effect occurs when a specimen is mounted inside an aperture in the common wall between two chambers, and the dependence of the measured transmission loss on the specimen position in the aperture is not negligible. This effect is difficult to account for in experiment as well as in numerical calculations. A vibroacoustic coupling analysis should be employed in the future study to investigate this effect, where one or two-sided niches are modelled as thin boundaries around the specimen. The vibration damping mechanism of window seals and window frame-wall fixing was not accounted for in numerical model.

The nonlinear sound absorption of the window frame material should be also modelled. Generally, at lower frequency (<500Hz), the sound absorption coefficient of dense wood material is low and at higher frequency (>500 Hz), the sound absorption coefficient is high. However, especially at higher frequencies, the sound absorption coefficient of lower density species may be greater [8]. This nonlinearity of sound absorption coefficient for wood should be incorporated in future studies.

5. Conclusions

The proposed numerical approach, although simplified (it does not contain damping effects of the window fixation, nonlinearities of material sound absorption coefficient and does not consider acoustic coupled effects) gave satisfactory results in the mapping of the experimental sound insulation curves of windows.

The detailed comparison between numerical and experimental results exposed, that numerical results are not exactly the same as in the experimental method. There are still several modelling aspects to account for.

The achieved numerical accuracy should be useful when examining trends in sound insulation as a function windows design parameters, such as different glazing types, frame dimensions, frame material type, etc.

In the future numerical studies can be completed, however not without additional expense of computational cost, which may be disadvantageous in when rapid assessment of the given window configuration is needed.

Acknowledgments

The research work was supported by scientific project no. PBS2/B2/9/2013 “The Influence of parameters of construction on the sound insulation of windows”.

References

1. P. Davidson, *Structure-Acoustic Analysis; Finite Element Modelling and Reduction Methods*, Doctoral Thesis, Division of Structural Mechanics, LTH, Lund University, Box 118, SE-221 00 Lund, Sweden.
2. K. Ruber, S. Kanapathipillai, N. Feng, R. Randall, *Investigations of a Tuned Vibration Absorber with High Damping for Increasing Acoustic Panels Sound Trans-mission Loss in Low Frequency Range*, Proceedings of ACOUSTICS 2011 2-4 November 2011, Gold Coast, Australia.
3. T. Sakuma, K. Adachi, Y. Yasuda, *Numerical investigation of the niche effect in sound insulation measurement*, Inter Noise 2011, 4-7 September, Osaka, Japan.
4. I. Dimino, A. Vigliotti, M.H.F. Aliabadi, A. Concilio, *Vibro-Acoustic Design Of an Aircraft-Type Active Window*, Journal of Theoretical and Applied Mechanics, **50** (1) (2012) 169 – 192, Warsaw 2012, 50th anniversary of JTAM.
5. S. R. Gimeno, *Study of the Acoustic Insulation through Domestic Windows*, tesis de master, GANDÍA, 5 de Septiembre de 2012.
6. EN 20140-3, *Acoustics - Measurement of sound insulation in buildings and of building elements - Part 3: Laboratory measurements of airborne sound insulation of building elements*.
7. A. Dijckmans, G. Vermeir, *Numerical investigation of the repeatability and reproducibility in building acoustical measurements*, Department of Civil Engineering, KU Leuven, Kasteelpark Arenberg 40, B-3001 Heverlee, Belgium.
8. J. I. Mohammad, N. Johari, M. H. Fouladi, *Numerical Investigation on the Sound Absorption Coefficients of Malaysian Wood*, Proceedings of 20th International Congress on Acoustics, ICA 2010, 23-27 August, Sydney, Australia.

Approximate Method for Determination of Dynamic Characteristics of Structures with Viscoelastic Dampers

Roman LEWANDOWSKI
Poznan University of Technology, 60-695 Poznan, ul. Piotrowo 5
roman.lewandowski@put.poznan.pl

Abstract

An approximate method for determination of dynamic characteristics of structures with viscoelastic dampers is proposed in this paper. A fractional derivative is used to describe the dynamic behaviour of viscoelastic dampers. The method is based on a continuous dependency of the sensitivity of eigenvalue on a certain artificially introduced parameter which scaled up the influence of the damping term in the eigenvalue problem. Some results of a representative calculation are also presented and briefly discussed.

Keywords: structures, viscoelastic dampers, generalized fractional model, dynamic characteristics

1. Introduction

Natural frequencies, non-dimensional damping ratios and modes of vibration are the fundamental dynamic characteristics of every structural system. These quantities are obtained after solving appropriately defined eigenvalue problems. It is a well known procedure when the damping of systems can be neglected or when the so-called proportional damping could be assumed. The problem is much more complex when damping takes place because the eigenvalue problem is often nonlinear and because complex calculations are involved. The procedure of determination of dynamic characteristics is even more complicated when the fractional derivative modes are used to describe viscoelastic (VE) dampers. In this case, usually, an advanced procedure, called the continuation method, is used to solve the nonlinear eigenvalue problem [1, 2]. Adhikari [3] used the Neumann expansion method to obtain first and second order approximations for complex eigenvectors.

In this paper, the method of determination of an approximate solution to the nonlinear eigenvalue problem describing the dynamic properties of structures with fractional dampers is presented. The method used a solution to the classical eigenvalue problem without damping and a differential equation to calculate the natural frequencies and non-dimensional damping ratios sought. Only a partial solution to the classic eigenvalue problem is needed. The method presented is an extension of the method recently proposed by Lazaro [4] but, in contrast to that method, only a partial solution to the classic eigenvalue problem is necessary and the method is extended to the case of a system of which the viscoelastic properties of dampers or materials are described by fractional derivatives. A previous approach in a similar direction was presented, also by Lazaro, in [5].

2. Equation of motion of structures with viscoelastic (VE) dampers

The elastic, planar frame structures with VE dampers are considered. The fractional model, shown in Fig. 1, is used as a model of dampers. It consists of the fractional Kelvin element which is connected in parallel with the fractional Maxwell element. The rhombus shown in the figure denotes the viscoelastic or springpot element [6]. This model of damper can be regarded as a generalized one. A set of specific models arise from it: the simple fractional Maxwell (when $k_0 = c_0 = 0$), the fractional Kelvin model (when $k_1 = c_1 = 0$) and the fractional Zener model (when $c_0 = 0$). This means that almost all of the fractional models known in the literature up to now are taken into account by the above fractional model. Here k_0, k_1 and c_0, c_1 are the stiffness and damping factors of damper, respectively, and α is the order of the fractional derivative; ($0 < \alpha \le 1$). Well known classic rheological models of damper are obtained for $\alpha = 1$.

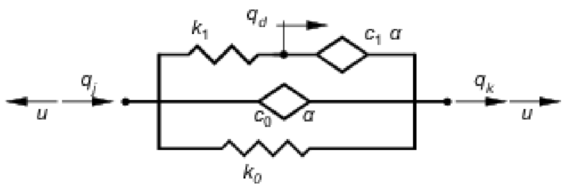

Figure 1. Mechanical diagram of the fractional model of damper

The total force in this model, $u(t) = u_0(t) + u_1(t)$, is the sum of forces that occur in the Kelvin element $u_0(t)$ and the force in the fractional Maxwell element $u_1(t)$, i.e.:

$$u_0(t) = k_0(q_k(t) - q_j(t)) + c_0 D_t^\alpha (q_k(t) - q_j(t)) , \tag{1}$$

$$u_{1s}(t) = k_1(q_d(t) - q_j(t)) , \qquad u_{1d}(t) = c_1 D_t^\alpha (q_k - q_d(t)) , \tag{2}$$

where the symbol $D_t^\alpha(\bullet)$ denotes the Caputo or Riemann-Liouville fractional derivative of $(\bullet)$ of the order α with respect to time t. The symbol $q_d(t)$ denotes the so-called “internal variable” (see also [6, 7]). It is easy to find that $u_{1s}(t) = u_{1d}(t) = u_1(t)$.

The equation of motion of structures with VE dampers could be written in the following form (see also [6, 7]):

$$\mathbf{M}\ddot{\mathbf{q}}(t) + \mathbf{C}D_t^\alpha \mathbf{q}(t) + \mathbf{K}\mathbf{q}(t) = \mathbf{P}(t) \tag{3}$$

Here, $\mathbf{M}$, $\mathbf{C}$, $\mathbf{K}$ are the $(n \times n)$ global mass, damping and stiffness matrices, respectively. $\mathbf{P}(t)$ is the vector of excitation forces and $\mathbf{q}(t)$ is the $(n \times 1)$ global vector of displacements, which contains also all internal variables $q_d(t)$. For the sake of simplicity, the damping properties of structure are neglected. The mass and damping matrices are often singular and the stiffness matrix is positively defined.

Assuming that $\mathbf{P}(t) = \mathbf{0}$ and applying the Laplace transform (with zero initial conditions), the following nonlinear eigenvalue problem is obtained from Eq (3):

$$(s^2\mathbf{M}+s^{\alpha}\mathbf{C}+\mathbf{K})\overline{\mathbf{q}}=\mathbf{0} \tag{4}$$

where s is the Laplace variable and $\overline{\mathbf{q}}$ is the Laplace transform of $\mathbf{q}(t)$.

3. Approximate method of solution to the nonlinear eigenvalue problem

First of all, the artificial parameter p is introduced and Eq. (4) is rewritten as:

$$\mathbf{D}(s(p),\, p)\overline{\mathbf{q}}(p)=(s^2\mathbf{M}+s^{\alpha}\, p\mathbf{C}+\mathbf{K})\overline{\mathbf{q}}=\mathbf{0} \tag{5}$$

For $p=1$, the solution to the eigenvalue problem (4) is obtained whereas for $p=0$, Eq. 5 is reduced to the following linear eigenvalue problem

$$(s^2\mathbf{M}+\mathbf{K})\overline{\mathbf{q}}=\mathbf{0} \tag{6}$$

which has a well known set of solutions of the type $s=\mathrm{i}\omega$, $\overline{\mathbf{q}}=\mathbf{a}$, where ω and $\mathbf{a}$ are the natural frequency and mode of vibration, respectively, and $\mathrm{i}=\sqrt{-1}$. Let us note that the influence of the damper's stiffness is still incorporated in the stiffness matrix $\mathbf{K}$. It is assumed that the eigenvector $\overline{\mathbf{q}}$ fulfills the following normalization condition:

$$\overline{\mathbf{q}}^T(p)[2s(p)\mathbf{M}+\alpha s^{\alpha-1}p\mathbf{C}]\overline{\mathbf{q}}(p)=1 \tag{7}$$

Now, the sensitivity of the solution to the eigenvalue problem with respect to changes of parameter p will be analyzed. After differentiating Eqs (5) and (7) with respect to parameter p, the following set of equations are obtained (see also [7]):

$$(s^2\mathbf{M}+s^{\alpha}p\mathbf{C}+\mathbf{K})\frac{\partial\overline{\mathbf{q}}}{\partial p}+(2s\mathbf{M}+\alpha s^{\alpha-1}p\mathbf{C})\,\overline{\mathbf{q}}\,\frac{\partial s}{\partial p}=-s^{\alpha}\mathbf{C}\,\overline{\mathbf{q}} \tag{8}$$

$$\overline{\mathbf{q}}^T(2s\mathbf{M}+\alpha s^{\alpha-1}p\mathbf{C})\frac{\partial\overline{\mathbf{q}}}{\partial p}+\frac{1}{2}\overline{\mathbf{q}}^T[2\mathbf{M}+\alpha(\alpha-1)s^{\alpha-2}p\mathbf{C}]\overline{\mathbf{q}}\frac{\partial s}{\partial p}=-\frac{1}{2}\alpha s^{\alpha-1}\overline{\mathbf{q}}^T\mathbf{C}\overline{\mathbf{q}} \tag{9}$$

from which the sensitivity of the eigenvector $\partial\overline{\mathbf{q}}/\partial p$ and the sensitivity of the eigenvalue $\partial s/\partial p$ can be found.

Equation (8) is multiplied by $\overline{\mathbf{q}}^T$ and transformed to the following form:

$$\frac{\partial s}{\partial p}=-s^{\alpha}(p)\frac{A(\overline{\mathbf{q}}(p))}{B(s(p),\overline{\mathbf{q}}(p))} \tag{10}$$

$$A(\overline{\mathbf{q}}(p))=\overline{\mathbf{q}}^T\mathbf{C}\,\overline{\mathbf{q}}\ ,\qquad B(s(p),\overline{\mathbf{q}}(p))=\overline{\mathbf{q}}^T(2s\mathbf{M}+\alpha\, s^{\alpha-1}p\mathbf{C})\,\overline{\mathbf{q}} \tag{11}$$

The functions $A(\overline{\mathbf{q}}(p))$ and $B(s(p),\overline{\mathbf{q}}(p))$ are expanded in the Taylor's series in the vicinity of $p=0$, i.e.:

$$A(\overline{\mathbf{q}}(p))=A(0)+\left.\frac{\partial A(\overline{\mathbf{q}}(p))}{\partial p}\right|_{p=0},\quad B(s(p),\overline{\mathbf{q}}(p),\, p)=B(0)+\left.\frac{\partial B(s(p),\overline{\mathbf{q}}(p),\, p)}{\partial p}\right|_{p=0} \tag{12}$$

where

$$A(0)=\mathbf{a}^T\mathbf{C}\,\mathbf{a}\ ,\qquad B(0)=2\mathrm{i}\omega\,\mathbf{a}^T\mathbf{M}\mathbf{a} \tag{13}$$

Moreover, taking into account that both the eigenvalue s and the eigenvector $\overline{\mathbf{q}}$ depend on p, we can write:

$$\frac{\partial B}{\partial \mathrm{p}} = 2\overline{\mathbf{q}}^T (2s\mathbf{M} + \alpha\, s^{\alpha-1} p\mathbf{C}) \frac{\partial \overline{\mathbf{q}}}{\partial p} + \overline{\mathbf{q}}^T \left[2\mathbf{M} + \alpha\,(\alpha - 1) s^{\alpha-2}\, p\mathbf{C}\right] \overline{\mathbf{q}} \frac{\partial s}{\partial p} + \alpha\, s^{\alpha-1} \overline{\mathbf{q}}^T \mathbf{C} \overline{\mathbf{q}} \quad (14)$$

$$\frac{\partial A}{\partial p} = 2\, \mathbf{q}^T \mathbf{C}\, \frac{\partial \mathbf{q}}{\partial p} \quad (15)$$

The values of the above derivatives at $p = 0$ are:

$$\left.\frac{\partial B}{\partial \mathrm{p}}\right|_{p=0} = 4\mathrm{i}\omega\, \mathbf{a}^T \mathbf{M} \left.\frac{\partial \overline{\mathbf{q}}}{\partial p}\right|_{p=0} + 2\mathbf{a}^T \mathbf{Ma} \left.\frac{\partial s}{\partial p}\right|_{p=0} + \alpha\,(\mathrm{i}\omega)^{\alpha-1} \mathbf{a}^T \mathbf{Ca} \quad (16)$$

$$\left.\frac{\partial A}{\partial p}\right|_{p=0} = 2\, \mathbf{a}^T \mathbf{C} \left.\frac{\partial \mathbf{q}}{\partial p}\right|_{p=0} \quad (17)$$

The sensitivities $\partial \mathbf{q} / \partial p$ and $\partial s / \partial p$, calculated at $p = 0$, can be determined from Eqs (8) and (9). In the vicinity of $p = 0$, these equations take the following form:

$$(\mathbf{K} - \omega^2 \mathbf{M}) \left.\frac{\partial \overline{\mathbf{q}}}{\partial p}\right|_{p=0} + 2\mathrm{i}\omega\, \mathbf{Ma} \left.\frac{\partial s}{\partial p}\right|_{p=0} = -(\mathrm{i}\omega)^{\alpha}\, \mathbf{C}\, \mathbf{a} \quad (18)$$

$$2\mathrm{i}\omega\, \mathbf{a}^T \mathbf{M} \left.\frac{\partial \overline{\mathbf{q}}}{\partial p}\right|_{p=0} + \mathbf{a}^T \mathbf{Ma} \left.\frac{\partial s}{\partial p}\right|_{p=0} = -\frac{1}{2} \alpha (\mathrm{i}\omega)^{\alpha-1} \mathbf{a}^T \mathbf{Ca} \quad (19)$$

from which the sought quantities could be determined.

Finally, Eq (10) could be rewritten in the form of the following differential equation:

$$\frac{\partial s}{\partial p} = -s^{\alpha}\, \frac{a_0 + a_1 p}{b_0 + b_1 p} \quad (20)$$

where

$$a_0 = \mathbf{a}^T \mathbf{C}\, \mathbf{a} \;, \qquad b_0 = 2\mathrm{i}\omega\, \mathbf{a}^T \mathbf{Ma} \;, \qquad a_1 = 2\, \mathbf{a}^T \mathbf{C} \left.\frac{\partial \mathbf{q}}{\partial p}\right|_{p=0} \quad (21)$$

$$b_1 = 4\mathrm{i}\omega\, \mathbf{a}^T \mathbf{M} \left.\frac{\partial \overline{\mathbf{q}}}{\partial p}\right|_{p=0} + 2\mathbf{a}^T \mathbf{Ma} \left.\frac{\partial s}{\partial p}\right|_{p=0} + \alpha\,(\mathrm{i}\omega)^{\alpha-1} \mathbf{a}^T \mathbf{Ca} \quad (22)$$

It should be noted that, for $p = 0$, the normalization condition (7) is reduced to $2\mathrm{i}\omega\, \mathbf{a}^T \mathbf{Ma} = 1$, which means that $b_0 = 1$. Moreover, from Eq (19)

$$4\mathrm{i}\omega\, \mathbf{a}^T \mathbf{M} \left.\frac{\partial \overline{\mathbf{q}}}{\partial p}\right|_{p=0} + 2\mathbf{a}^T \mathbf{Ma} \left.\frac{\partial s}{\partial p}\right|_{p=0} + \frac{1}{2} \alpha\,(\mathrm{i}\omega)^{\alpha-1} \mathbf{a}^T \mathbf{Ca} = 0 \quad (23)$$

which means that $b_1 = 0$.

Finally, Eq (20) is reduced to

$$\frac{\partial s}{\partial p} = -s^{\alpha}(a_0 + a_1 p) = f(s, p) \tag{24}$$

and only the constant a_1 depends on α .

The solution to Eq (24) must fulfill the following initial condition: for $p = 0$ $s(0) = \mathrm{i}\omega$ or $s(0) = -\mathrm{i}\omega$, depending on which complex conjugate solution is sought.

Before describing the method for solving Eq (24), the special case $\alpha = 1$ will be discussed. It means that dampers are described by classic rheological models and Eq (24) takes the following form:

$$\frac{\partial s}{\partial p} = -s\,(a_0 + a_1 p) \tag{25}$$

Solution to Eq (25) fulfilling the described above initial conditions is given by

$$s(p) = \pm\mathrm{i}\omega \exp\,(a_0 p + \tfrac{1}{2} a_1 p^2) \tag{26}$$

It means that, for $p = 1$, the following approximate solution to the eigenvalue of the nonlinear eigenvalue problem (4) is obtained:

$$\hat{s} = \pm\mathrm{i}\omega \exp\,(a_0 + \tfrac{1}{2} a_1) \tag{27}$$

The above result is identical with the one obtained in [4].

An implicit version of the Euler method is used to solve Eq (24) numerically. First of all, the increment of p is chosen and denoted by h. Moreover, a set of points are chosen on the p axis in such a way that $p_{n+1} = p_n + h$ and the notation $s(p_n) = s_n$ is used. According to the Euler method

$$s_{n+1} = s_n + [\,f(s_n, p_n) + f(s_{n+1}, p_{n+1)}\,]\,h/2 \tag{28}$$

and for $n = 0$, $s(0) = s_0 = \pm\mathrm{i}\omega$.

The simple iteration method is adopted for solving the nonlinear algebraic equation (28) with respect to s_{n+1}. The initial approximation of s_{n+1} is calculated from the formula:

$$s_{n+1}^{(0)} = s_n + hf(s_n, p_n) \tag{29}$$

and the (i+1)-th approximation of s_{n+1} is given by

$$s_{n+1}^{(i+1)} = s_n + [\,f(s_n, p_n) + f(s_{n+1}^{(i)}, p_{n+1)}\,]\,h/2 \tag{30}$$

where the superscript denotes the number of iteration.

The iteration is continued until the following inequality is fulfilled:

$$\left|\mathrm{Re}(s_{n+1}^{(i+1)} - s_{n+1}^{(i+1)})\right| \le \varepsilon \left|\mathrm{Re}(s_{n+1}^{(i+1)})\right| \;, \qquad \left|\mathrm{Im}(s_{n+1}^{(i+1)} - s_{n+1}^{(i+1)})\right| \le \varepsilon \left|\mathrm{Im}(s_{n+1}^{(i+1)})\right| \tag{31}$$

where ε is the assumed accuracy of calculation.

Having the eigenvalue $s = \mu + \mathrm{i}\eta$, the natural frequency ω and the non-dimensional damping ratio γ is determined from

$$\omega^2 = \mu^2 + \eta^2 \;, \qquad \gamma = -\mu/\omega \tag{32}$$

The approximation of eigenvector $\overline{\mathbf{q}}$ is given by

$$\overline{\mathbf{q}} = \mathbf{a} + \left.\frac{\partial \overline{\mathbf{q}}}{\partial p}\right|_{p=0} \tag{33}$$

4. Representative results

Results for a four-storey shear frame with two dampers located at the first and fourth storeys will be presented. The fractional Kelvin model is used for describing the dampers. The following data are used for describing the frame: (i) the storeys' stiffness are: $k_1 = k_2 = 26.0 \cdot 10^6$ [N/m], $k_3 = k_4 = 20.0 \cdot 10^6$ [N/m]; (ii) the storeys' masses are: $m_1 = m_2 = m_3 = m_4 = 34.0 \cdot 10^3$ [kg]. The first-floor damper's parameters are: $\alpha = 0.8$, $k_{0,1} = 10.0 \cdot 10^6$ [N/m], $c_{0,1} = 0.4 \cdot 10^6$ [Ns$^{\alpha}$/m] and the damper's parameters for the fourth floor are: $\alpha = 0.8$, $k_{0,2} = 6.0 \cdot 10^6$ [N/m], $c_{0,2} = 0.2 \cdot 10^6$ [Ns$^{\alpha}$/m].

The system matrices are: $\mathbf{M} = diag[m_1,\ m_2,\ m_3,\ m_4]$,

$$\mathbf{K} = \begin{bmatrix} k_1 + k_2 + k_{0,1} & -k_2 & 0 & 0 \\ -k_2 & k_2 + k_3 & -k_3 & 0 \\ 0 & -k_3 & k_3 + k_{0,2} & -k_4 - k_{0,2} \\ 0 & 0 & -k_4 - k_{0,2} & k_4 + k_{0,2} \end{bmatrix} \tag{34}$$

$$\mathbf{C} = \begin{bmatrix} c_{0,1} & 0 & 0 & 0 \\ 0 & 0 & 0 & 0 \\ 0 & 0 & c_{0,2} & -c_{0,2} \\ 0 & 0 & -c_{0,2} & c_{0,2} \end{bmatrix} \tag{35}$$

The natural frequencies of frame without dampers are in the first column of Table 1, whereas in the next column, there are the natural frequencies resulting from Eq (6) when the stiffness matrix is the sum of the stiffness of frame and dampers.

Table 1. Natural frequencies of frame

Frame without dampers	From Eq (6)	Difference
$\omega_1 = 9.27367$ rad/s	$\omega_1 = 9.90121$ rad/s	6.77%
$\omega_2 = 25.35547$ rad/s	$\omega_2 = 27.9594$ rad/s	10.27%
$\omega_3 = 39.20204$ rad/s	$\omega_3 = 43.15206$ rad/s	10.07%
$\omega_4 = 48.9857$ rad/s	$\omega_4 = 50.51930$ rad/s	3.13%

Results of calculation are presented in Table (2). The exact vales of eigenvalues are obtained by means of the continuation method described in [1]. The second column collect results obtained by means of Eq (24). Very similar results are obtained and differences are not greater than 0.2 %. Moreover, in Table 3, the exact and approximate natural frequencies and non-dimensional damping ratios are compared. It is evident that the approximate results have an very good accuracy.

Although in Table 4, the eigenvalues of frame with dampers are stated, now, the dampers are described with the help of a classic Kelvin model ($\alpha = 1.0$, and other damping data are as stated previously). In the second column, the eigenvalues calculated from Eq (27) are presented. Moreover, the exact values of natural frequencies and non-dimensional damping ratios are shown. Exact eigenvalues are obtained using the classical approach given in [6].

A comparison of the eigenvalues obtained from the formula derived by Lazaro in [4] with the ones resulting as the solution to the differential equation (24) is presented in Table 5.

Table 2. Eigenvalues for a frame with the fractional Kelvin dampers ($\alpha = 0.8$)

Eigenvalues (exact results)	Eigenvalues – Euler Eq (24)	Differences
$s_{1,5} = -0.112501 \pm \mathrm{i}\ 9.94280$	$s_{1,5} = -0.11262 \pm \mathrm{i}\, 9.94295$	$0.11\% + \mathrm{i}\, 0.00\%$
$s_{2,6} = -1.11279 \pm \mathrm{i}\ 28.3731$	$s_{2,6} = -1.11240 \pm \mathrm{i}\, 28.3720$	$0.03\% + \mathrm{i}\, 0.00\%$
$s_{3,7} = -2.61179 \pm \mathrm{i}\, 43.9430$	$s_{3,7} = -2.61042 \pm \mathrm{i}\, 43.9405$	$0.05\% + \mathrm{i}\, 0.00\%$
$s_{4,8} = -1.58018 \pm \mathrm{i}\, 50.9182$	$s_{4,8} = -1.57899 \pm \mathrm{i}\, 50.9174$	$0.08\% + \mathrm{i}\, 0.00\%$

Table 3. Natural frequencies and non-dimensional damping ratios – comparison of exact and approximate results for a frame with the fractional Kelvin dampers ($\alpha = 0.8$)

Frequency (exact results)	Damping ratio (exact results)	Frequency (approximate results)	Approximate damping ratio
$\omega_1 = 9.94344\,\mathrm{rad/s}$	$\gamma_1 = 0.01131$	$\omega_1 = 9.94359\,\mathrm{rad/s}$	$\gamma_1 = 0{,}01133$
$\omega_2 = 28.3949\,\mathrm{rad/s}$	$\gamma_2 = 0.03919$	$\omega_2 = 28.3938\,\mathrm{rad/s}$	$\gamma_2 = 0.03918$
$\omega_3 = 44.0205\,\mathrm{rad/s}$	$\gamma_3 = 0.05933$	$\omega_3 = 44.0118\,\mathrm{rad/s}$	$\gamma_3 = 0.05930$
$\omega_4 = 50.9427\,\mathrm{rad/s}$	$\gamma_4 = 0.03102$	$\omega_4 = 50.9418\,\mathrm{rad/s}$	$\gamma_4 = 0.03100$

Table 4. Eigenvalues for frame with classic Kelvin dampers ($\alpha = 1.0$)

Eigenvalues (exact results)	Eigenvalues - Eq (27)	Frequency [rad/s]	Damping ratio
$s_{1,5} = -0.19179 \pm \mathrm{i}\, 9.9133$	$s_{1,5} = -0.19196 \pm \mathrm{i}\, 9.88545$	$\omega_1 = 9.91516$	$\gamma_1 = 0.019343$
$s_{2,6} = -2.3712 \pm \mathrm{i}\, 28.114$	$s_{2,6} = -2.31103 \pm \mathrm{i}\, 27.6169$	$\omega_2 = 28.2138$	$\gamma_2 = 0.084044$
$s_{3,7} = -5.7509 \pm \mathrm{i}\, 42.729$	$s_{3,7} = -5.73843 \pm \mathrm{i}\, 42.8072$	$\omega_3 = 43.1142$	$\gamma_3 = 0.133387$
$s_{4,8} = -3.4508 \pm \mathrm{i}\, 49.919$	$s_{4,8} = -3.45254 \pm \mathrm{i}\, 49.9294$	$\omega_4 = 50.0381$	$\gamma_4 = 0.068963$

5. Concluding remarks

The proposed method enables determination of the dynamic properties of structures with VE dampers in a simple way. The dampers' behavior is described with the help of fractional derivatives. A partial solution to the classic eigenvalue problem is necessary in the proposed method. Only one eigenvector and the corresponding eigenvalue of problem (6) are necessary to determine the conjugated eigenvalue and eigenvector for the structure with VE dampers. The results of an extensive calculation, which is not presented in this paper due to the limitation of space, indicate that the accuracy of the method is good for a range of damper's parameters used in practice.

Table 5. Eigenvalues for frame with classic Kelvin dampers ($\alpha = 1.0$) – comparison of the results obtained from Eq (24) (the Euler method) and Eq (27)

Eigenvalues – Euler Eq (24)	Eigenvalues - Eq (27)	Differences
$s_{1,5} = -0.19250 \pm \mathrm{i}\, 9.91326$	$s_{1,5} = -0.19196 \pm \mathrm{i}\, 9.88545$	$0.28\% + \mathrm{i}\, 0.28\%$
$s_{2,6} = = -2.35233 \pm \mathrm{i}\, 28.1094$	$s_{2,6} = -2.31103 \pm \mathrm{i}\, 27.6169$	$1.79\% + \mathrm{i}\, 1.78\mathrm{i}\, \%$
$s_{3,7} = -5.72822 \pm \mathrm{i}\, 42.7318$	$s_{3,7} = -5.73843 \pm \mathrm{i}\, 42.8072$	$0.18\% + \mathrm{i}\, 0.18\%$
$s_{4,8} = -5.55776 \pm \mathrm{i}\, 50.1042$	$s_{4,8} = -5.58168 \pm \mathrm{i}\, 50.3188$	$0.43\% + \mathrm{i}\, 0.43\%$

Acknowledgments

The study is partially supported by the National Science Centre, Poland, as part of Project No. DEC/2013/09/B/ST8/01733, carried out in the years 2014–2016 and partially supported by the Poznan University of Technology as part of grant No. 01/11/DSPB/606.

References

1. R. Lewandowski, Z. Pawlak, *Dynamic analysis of frames with viscoelastic dampers modelled by rheological models with fractional derivatives*, J. Sound and Vibration, **330** (2011) 923 – 936.
2. Z. Pawlak, R. Lewandowski, *The continuation method for the eigenvalue problem of structures with viscoelastic dampers*, Comp. Struct., **125** (2013) 53 – 61.
3. S. Adhikari, *Modal analysis of linear asymmetric non-conservative systems*, J. Eng. Mech., **125** (1999) 1372 – 1379.
4. M. Lazaro, *Eigensolutions of non-proportionally damped systems based on continuous damping sensitivity*, J. Sound and Vibr., **363** (2016) 532 – 544.
5. M. Lazaro, *Dynamic analysis of frame structures with viscoelastic layers: New closed-form solutions of eigenvalues and a viscous approach*, Eng. Struct., **54** (2013) 69 – 81.
6. R. Lewandowski, *Reduction of vibration of building structures*, PWN, Warszawa 2014 (in Polish).
7. R. Lewandowski, M. Łasecka-Plura, *Design sensitivity analysis of structures with viscoelastic dampers*, Comp. Struct., **164** (2016) 95 – 107.

Influence of Additional Loads on Chosen Gait Parameters and Muscles Activity

Michał LUDWICKI
Department of Automation, Biomechanics and Mechatronics, Łódź University of Technology, Stefanowskiego str. 1/15 Łódź, michal.ludwicki@p.lodz.pl

Bartłomiej ZAGRODNY*
*Department of Automation, Biomechanics and Mechatronics, Łódź University of Technology, Stefanowskiego str. 1/15 Łódź, *contact author bartlomiej.zagrodny@p.lodz.pl*

Wiktoria WOJNICZ
Department of Mechanics and Mechatronics, Gdansk University of Technology, Narutowicza str.11/12, Gdańsk, wiktoria.wojnicz@pg.gda.pl

Jerzy MROZOWSKI
Department of Automation, Biomechanics and Mechatronics, Łódź University of Technology, Stefanowskiego str. 1/15 Łódź, jerzy.mrozowski@p.lodz.pl

Jan AWREJCEWICZ
Department of Automation, Biomechanics and Mechatronics, Łódź University of Technology, Stefanowskiego str. 1/15 Łódź, jan.awrejcewicz@p.lodz.pl

Abstract

This paper is devoted to human motion analysis and comparison of chosen kinematics parameters during normal gait with and without additional load in a form of backpack. A stability in both cases were compared in both frontal and sagittal planes, by applying a video tracking system. Experimental tests performed on treadmill, passive markers, placed on volunteers bare skin were used. Additionally, an infra-red camera was employed to evaluate muscle activity and its groups involved in the movement. The change of body temperature and distribution of the thermal maps were observed. Analysing these thermograms, loading of different muscle groups was evaluated. During the experiment, an attempt to correlate a results obtained from a thermal imaging camera and video tracking system were made. It is shown that thermal imaging can help to evaluate an asymmetry in muscle load and in some cases can help to detect pathological cases, what was confirmed with motion analysis. Advantages and disadvantages of this method were also described.

Keywords: thermovision, motion capture, motion analysis, ergonomics, gait stability

1. Introduction

Motion analysis plays a key role in understanding of locomotion and some phenomena that occur during the movement. To obtain more information of musculo-skeletal system functionality than just motion trajectories, typically a force platform [9] and/or an electromyography (EMG) method is applied (e.g. [1]). However, to record the signal, a complicated and expensive measurement technique should be employed. Moreover in this method it is obligatory to use an electrodes placed on the skin in a specific muscle area. EMG signal is vulnerable for noise (e.g. cross-talking phenomenon) [4]. For this reason, in this research, both a visual motion analysis and an infra-red imaging is used to evaluate the activity of the chosen muscle groups. This method is also widely used, see for example in papers [2, 5, 6, 8]. In contrary to EMG, there is no need for any electrodes, cables or special recording units, that would disturb the movement; moreover it is a non-contact method, and results can be obtained almost immediately.

2. Methods

2.1. Experiment description

Volunteers were asked not to perform any intensive activities to avoid muscle fatigue. Normal gait on the treadmill without any load and with additional load in a form of a backpack were performed. Both experiments were done with the same velocity (chosen by volunteer) for ten minutes. Video in two planes of motion (sagittal and frontal) were recorded; also thermograms were taken before and after each test.

2.1. Video analysis

In order to analyze recorded videos an authorial software was used during the experiment. It allowed to detect and track position of both passive and active type markers. Examples of the marker placement and its representation after lightening and image filtering, are shown in Fig. 1a and 1b.

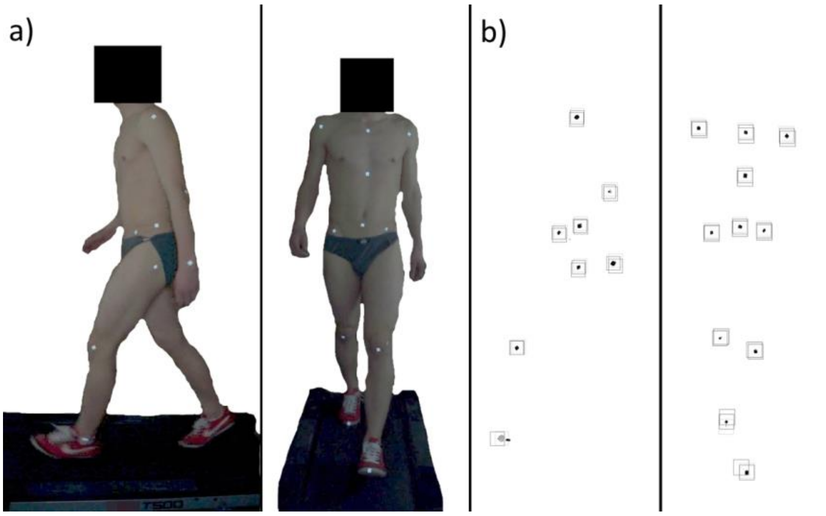

Figure 1. Example of video frame and detected passive markers for front and side of the body: a) markers distribution on the body; b) markers after lightening, filtering and position identification

Light, flat, reflective, passive type markers were chosen, and placed on a volunteer bare skin. This, in authors opinion, helps to prevent movement of the markers, relative to the joint. Moreover, their masses not affect the dynamics of locomotion and no special costume were needed, which would constrain the movement. Example of the front and side body markers detection are presented in Fig. 1c. The following parameters were recorded during treadmill gait:

- k_1 – angle of torso longitudinal axis deviation,
- k_2 – angle of shoulder girdle tilt,
- k_3 – angle of pelvis tilt,
- k_4, k_5 – angle of forearm and arm flexion/extension,
- R_{max} – wrist horizontal displacement,
- X_{max} – step length,
- Y_{max} – shoulder vertical displacement.

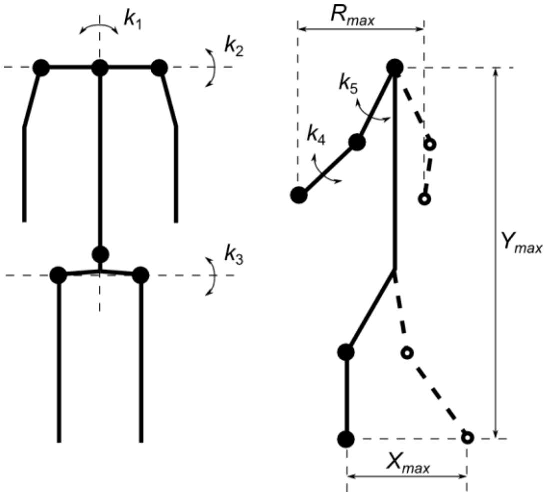

Figure 2. Measured parameters (see text for more details)

After about a half of the exercise time, 1.5 minute was recorded and then 20 seconds were chosen for further analysis. Depending on the visibility of detected markers, approx. 20 to 260 steps were recognised. Even if the number of steps identified was small (in the worst case approx. 20), no additional recordings were performed to prevent any unnecessary fatigue affecting the volunteer.

2.2. Video analysis results

Results, obtained from video analysis are presented in Figures 3-5. It can be noticed that for each volunteer each of the examined parameters have changed, i.e. angles of limb flexion/extension decreased (see Fig. 5), but length of the step increased. Similarly, mean amplitude value of torso longitudinal axis and pelvis oscillation decreased, what was compensated with shoulder girdle movability (see Fig. 4). Reason of such differences is an additional load and probably that volunteers were more accustomed to the treadmill gait after first try (without load). However, it is necessary to emphasise that each of the volunteer had an earlier experience with this type of exercise.

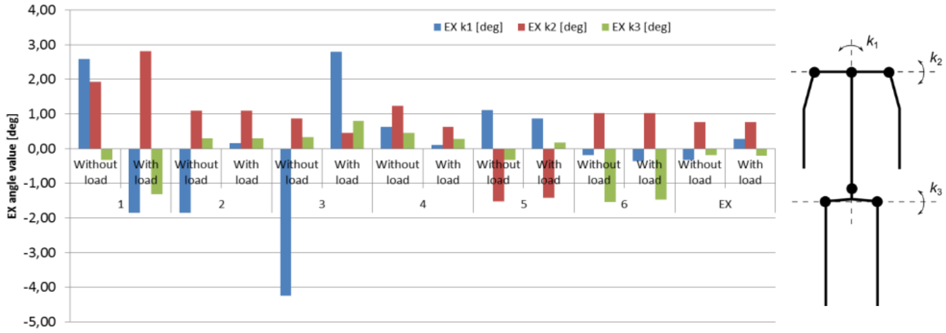

Figure 3. Motion capture results (mean values): longitudinal axis deviation (k_1), shoulder girdle (k_2) and pelvis tilt (k_3); during gait without and with load for each of six volunteers

It can be seen (see Fig. 3) that most volunteers longitudinal axis deviation (k_1) direction changes to the opposite one after adding a load. This alternation is also visible in mean values. Possible explanation is the change of mass distribution of the load. The volunteers tried to compensate this asymmetrycity by rising left or right shoulder. At the same time, shoulder girdle tilt (k_2) and pelvis tilt (k_3) did not changed significantly. The minimal decrease of both value due to the additional load and limit of the movement was expected. It was noticed in almost all volunteers except the first one. Fig. 4 presents mean amplitude values of axes (k_1, k_2, k_3). Unlike the mean values from fig. 3, here it can be easily seen that movability of the longitudinal body axis after adding a load decreases significantly.

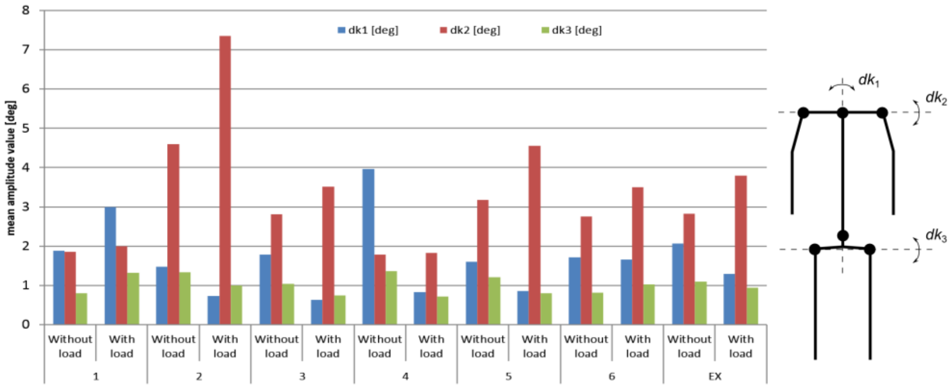

Figure 4. Motion capture results (mean amplitude) in a front view: longitudinal axis deviation (dk_1), shoulder girdle (dk_2) and pelvis tilt (dk_3); during gait without and with load for each of six volunteers

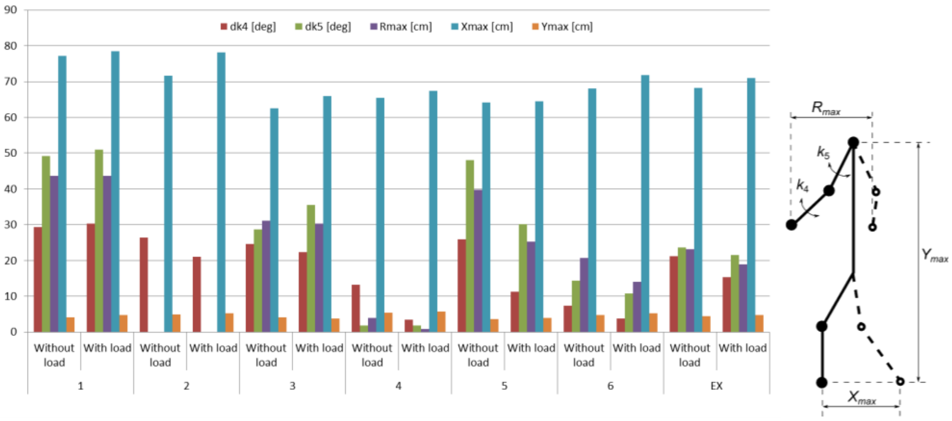

Figure 5. Motion capture results (mean values) in side view: angles of forearm and arm flexion/extension (k_4, k_5), hand horizontal displacement (R_{max}), stride length (X_{max}) and shoulder vertical displacement (Y_{max}); during gait without and with load for each of six volunteers

In Fig. 5, it can be seen, that adding load after free gait causes that the angles of forearm and arm flexion/extension (k_4, k_5) and also hand horizontal displacement (R_{max}) decreases significantly. The hypothesis is that decreasing the amplitude of the arms movement helps to compensate the shoulders load. Simultaneously, stride length increased to improve the stability of the gait. Shoulder vertical displacement (Y_{max}) did not changed significantly what is similar to the results published in reference [1].

2.3. Thermography

In addition to the motion capture method an infra-red analysis was performed. Changes of the body temperature and skin were observed. Acclimatization time was set to about 20 minutes. Volunteers were dressed in the same way as during the examination. Aim of this experiment was to point muscle groups involved in movement and symmetry of the muscular system activity. An example of thermogram before and after each type of experiment are presented in Figures 6-9, an example of muscle activity asymmetry is shown in Fig. 10.

2.3. Thermography results

For each of thermograms series for each volunteer a body surface temperature were measured (see Fig. 11), additionally an attempt was made to distinguish a muscle groups or muscles, which are especially active during gait with additional load, are mentioned below thermograms. Examples of the thermograms where these muscles are seen (more distinct temperature change was observed) are shown in Figures 6-9.

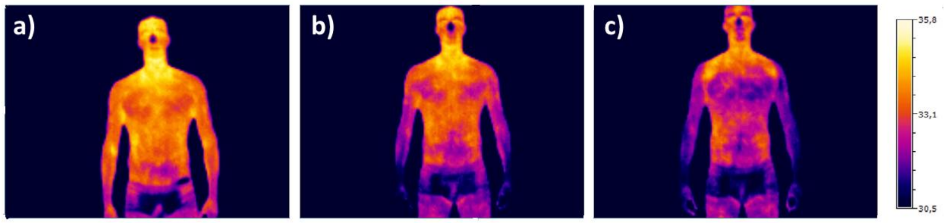

Figure 6. Example of muscle activity observed in infrared, temperature in [°C] – chest, muscles: *serratus, obliquus external abdominis*; a) before experiment, b) after gait without load, c) after gait with load

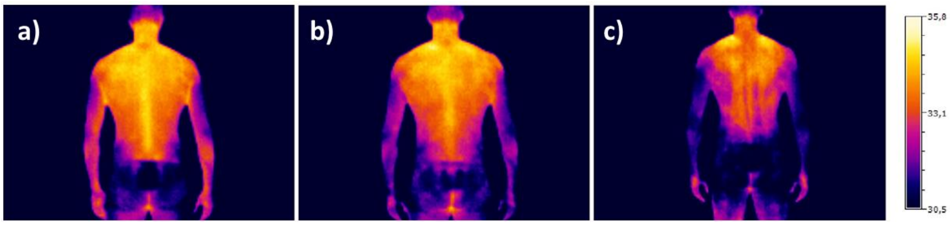

Figure 7. Example of muscle activity observed in infrared, temperature in [°C] – back muscle: *trapezius*; a) before experiment, b) after gait without load, c) after gait with load

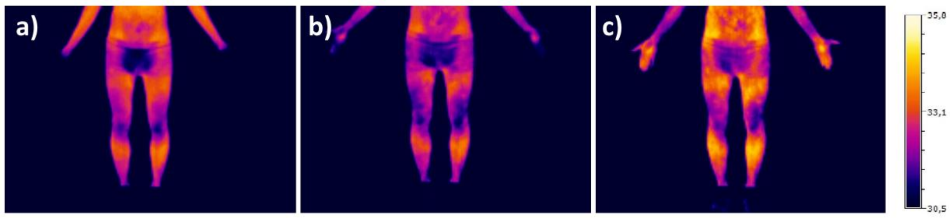

Figure 8. Example of muscle activity observed in infrared, temperature in [°C] – front of the legs muscles: *rectus femoris, pektineus, adductor longus, tibialis anterior, soleus*; a) before experiment, b) after gait without load, c) after gait with load

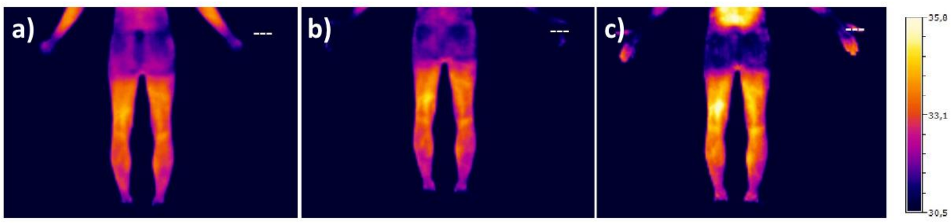

Figure 9. Example of muscle activity observed in infrared, temperature in [°C] – back of the legs muscles: *biceps femoris, semimembranosus, gastrocnemius*; a) before experiment, b) after gait without load, c) after gait with load

Moreover, when an asymmetry of gait was observed during video analysis, an asymmetry of the temperature distribution were observed. Thus implicates that both methods (video analysis and thermography) can help to detect asymmetry of the body movement and muscles load. Disadvantage of thermographic method is that it is sensitive to many factors. For example, sweat secretion results in an uneven cooling of the skin, as observed during experiment (also by other authors, see [8]); see Fig. 8c – some colder and warmer "dots" are seen. Also a backpack insulates the heat transfer from the back and it is necessary to stabilize temperature and humidity in the laboratory. Moreover, it is mandatory to "prepare" volunteer in a very specific way (requirements are described among others in works [5, 6]). Muscle asymmetry can be also observed in Figures 6-9 and in Fig. 10. In this case, it can be seen that left leg carried more load in both cases – gait without and with additional load. In all cases, where asymmetry were observed also a asymmetrical wear of shoe soles for left and right foot were noticed. In all cases asymmetry of gait parameters were confirmed by infra-red imaging. Remarkably, similar method was used in a paper [10] for evaluating compensation of asymmetrical load applied to the pectoral girdle.

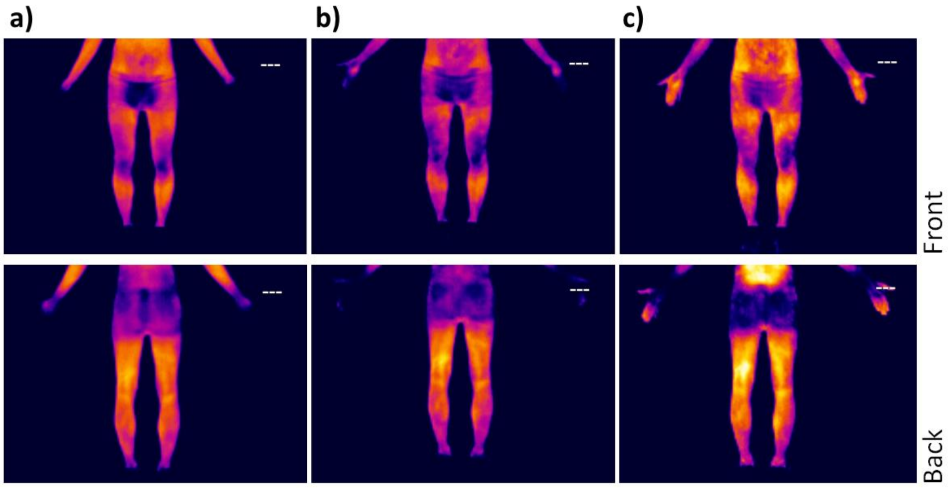

Figure 10. Examples of muscle activity asymmetry; a) before experiment, b) after gait without load, c) after gait with load for front and back of the body; in this example left leg was more loaded in both cases

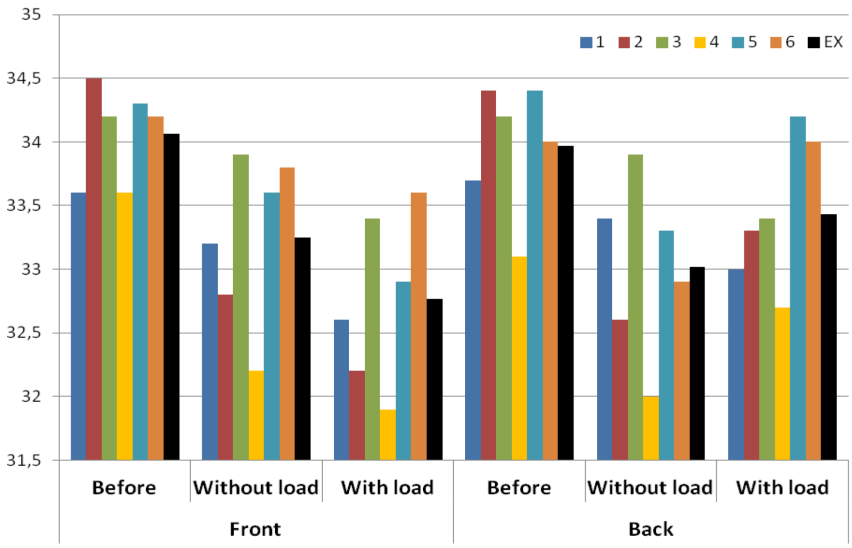

Figure 11. Results of thermographic measurements, temperature in [°C]: front and back of the body shell just before experiment, after gait without and with load for each of volunteer and mean value

3. Additional measurements

During experiment some additional measurements were made: temperature of the body core, systolic and diastolic blood pressure, pulse and blood oxidation. Results are shown in Fig. 12. It can be observed that these parameters were almost constant.

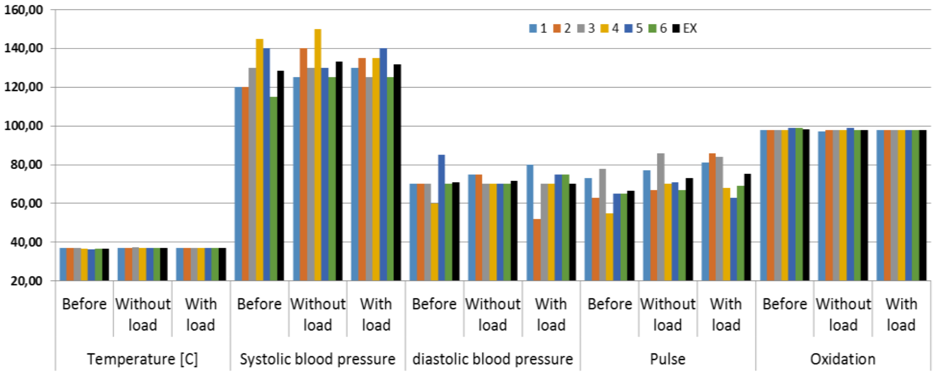

Figure 12. Results of additional measurements: core temperature, systolic and diastolic blood pressure, pulse and oxidation

4. Concluding remarks

A method of complex movement analysis with evaluation of muscle activity has been employed and presented. Its advantages and disadvantages have been discussed. Additionally, a video analysis has been carried out and the obtained results have been validated via comparison with the results reported in other publications. The change in several gait parameters like maximal angle of deviation and the angle vs. time in case of the gait with and without load has been detected and monitored. For example, EX of angle of the main body axis changes from -0.32 deg in case of gait without load up to +0.29 deg with load. Exemplary results are presented in Fig. 3. Changes in muscle activity and overall body temperature have been also observed and reported. The infra-red imaging can also give a qualitative information about symmetry of muscular system load. Moreover, other important detected issues follow:

- Marker-based motion tracking methods are the most effective and precise ones, in comparison to e.g. special inertial sensors, which belong to relatively heavy and inconvenient [7].
- It was observed that many parameters have changed during gait with additional load: stability, pelvis and pectoral girdle tilt, step length (and frequency).
- An activity of muscle groups can be observed in infra-red and groups of muscles involved in the movement can be indicated.
- Asymmetry of the gait is correlated with temperature changes and revealed by infra-red measurements – thermography can be proposed as a method for evaluating various gait pathology.
- In case of gait with an additional load in the form of backpack a lower pectoral girdle tilt and higher value of pelvis tilt was observed.
- The sign of the longitudinal axis deviation (k_1) in most volunteers changes after adding a load. Possible explanation is the change of mass distribution of the load or some asymmetric placement of backpack belts or load.

Acknowledgments

The work has been supported by the National Science Centre of Poland under the grant OPUS 9 No. 2015/17/B/ST8/01700 for years 2016-2018.

References

1. Ch. Schulze et all, *Biomechanical Study of the influence of the weight equipment on selected trunk muscles*, Acta of Bioengineering and Biomechanics, **15**(3) (2013) 45 – 51.
2. J. Anwajler, K. Dudek, *Evaluation of activity of a chosen group of muscles on the basis of temperature changes on the skin's surface* (in Polish), Acta Bio-Optica et Informatica Medica, **15** (2009) 20 – 22.
3. K. Watanabe, T. Asaka, Y. Wang, *Effects of Backpack Load and Gait Speed on Plantar Force During Treadmill Walking*, International Proceedings of Chemical, Biological and Environmental Engineering, **29** (2012) 105 – 110.

4. C. J. De Luca, *The use of surface electromyography in biomechanics*, Journal of Applied Biomechanics, **13**(2) (1997) 135 – 163.
5. G. Broniarczyk – Dyla, *Several remarks on skin thermometry*, Dermatological Review, **61** (1974) 89 – 93.
6. M. Tkaćova, R. Hudak, P. Foffova, J. Zicak, *An importantance of camera – subject distance and angle in musculoskeletal applications of medical thermography*, Acta Electrotechnica et Informatica, **10**(2) (2010) 57 – 60.
7. A. Seaman, J. McPhee, *Comparison of Optical and Inertial Tracking of Full Golf Swings*, Procedia Engineering, **34** (2012) 461 – 466.
8. G. Tanda, *The use of infrared thermography to detect the skin temperature response to physical activity*, Journal of Physics: Conference Series, **655** (2015) 1 – 10.
9. A. Cappozzo, *Gait analysis methodology*, Human Movement Science, **3** (1984) 27 – 50.
10. J. Awrejcewicz, Sz. Byczek, B. Zagrodny, *Influence of the asymmetric loading of the body during the march on the temperature distribution* (in Polish), Acta Bio-Optica et Informatica Medica, Biomedical Engineering, **18**(2) (2012) 74 – 79.

Numerical Analysis of Pressure Drop and Acoustic Attenuation Performance of Two Helicoidal Resonators Arranged in Parallel Ducts with Different Rotation Angles

Wojciech ŁAPKA
Poznan University of Technology, Institute of Applied Mechanics
Jan Paweł II 24 Street, 61-139 Poznań, wojciech.lapka@put.poznan.pl

Abstract

The paper presents a numerical analysis of pressure drop and acoustic attenuation performance (transmission loss) of two identical acoustic helicoidal resonators arranged in parallel ducts with different rotation angles. The air stream is divided from one cylindrical duct of a diameter *D*=140mm to a two parallel cylindrical ducts of diameter *d*=125mm with two helicoidal resonators inside – one per one duct. The ratio of helicoidal pitch *s* of helicoidal resonators to a cylindrical duct diameter *d* equals *s/d*=1,976. Other geometrical relationships of helicoidal resonators, as a mandrel diameter d_m to duct diameter ratio d_m/d=0.024, thickness *g* of helicoidal profile *g/d*=0.0024, and the number of helicoidal turn *n*=0,695 for both resonators. The investigated range of rotation angles covered the three characteristic positions of helicoidal resonators gaps, when considering the air stream distribution from central large duct with diameter *D*. The value of normal inflow velocity *v*[m/s] equaled 1 for all investigated cases.

Keywords: helicoidal resonators, pressure drop, acoustic attenuation, parallel ducts, flow distribution, numerical analysis

1. Introduction

The newly patented solution of acoustical helicoidal resonator [1] has a specific feature of a narrowband sound attenuation and multi resonances. The acoustical properties of this solution and basic dimensions are quite well described in many publications [2-7, 9-12, 14-17]. The flow properties of this solution were described mainly for one helicoidal resonator inside cylindrical duct [8, 9, 13, 14, 16]. In the paper [15] were mentioned the possibilities of inserting a few ducts with acoustically tuned helicoidal resonators for the same blade-passing frequency of fan in ducted system. From the acoustical point of view it is determined by the plane wave propagation condition, which must be satisfied for a proper work of helicoidal resonator (acoustical resonance). From the fluid dynamics point of view the pressure drop depends on many conditions of inserted helicoidal resonators, as example most important here relationship between helicoidal pitch *s*and numbers of helicoidal turns *n*. But the transition of air flow stream into few ducts induces more complications, as example distribution inside duct of helicoidal resonators and other obstacles.

Also this work presents the numerical analysis of transmission loss (*TL*) characteristics and pressure drop for specific three cases of rotation angles of two identical helicoidal resonators with constant *s/d* ratio that equals 1,976 and numbers of helicoidal turns *n=0,695* arranged in parallel cylindrical ducts.

2. Description of investigated models

In this chapter are characterized investigated acoustical (2.1) and CFD turbulent flow (2.2) models of two identical helicoidal resonators placed inside a cylindrical ducts arranged in parallel just past the transition from one duct with larger diameter D=140mm to two parallel ducts with diameters d=125mm, as presented in Figure 1. In both subchapters the three dimensional (3D) models were analysed.

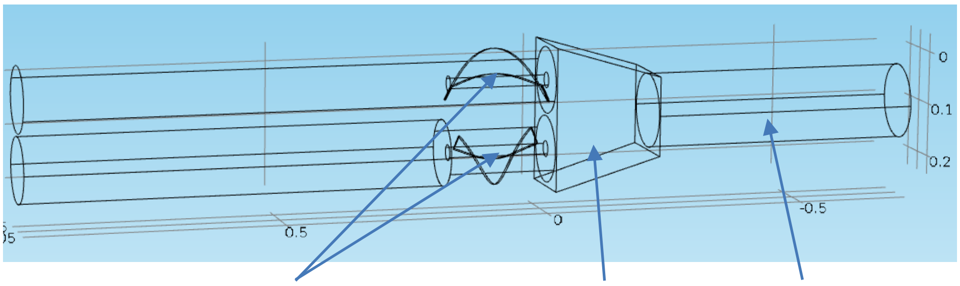

Figure 1. Example view on numerically represented and considered ducted system with two identical helicoidal resonators with s/d=1,976 and n=0,695 arranged in parallel ducts past the transition from one larger duct

The ducted system consists of a straight cylindrical ductsand the transition with lengthl_2=200mm. The ratio of helicoidal pitch s of helicoidal resonators to cylindrical duct diameter d equals s/d=1,976, and the number of helicoidal turns n=0,695. The geometrical relationships of helicoidal resonator, as a mandrel diameter d_m to duct diameter ratio d_m/d=0.024 and thickness g of helicoidal profile g/d=0.0024, were constant as well. The length of the cylindrical duct with diameter D at the inlet sideequaled 500mm, and the outlet parallel ducts with diameter d=125mm equaled 1000mm.As it is presented in figure 1 the helicoidal resonators were placed right past the transition, and the closest edges of helicoidal profiles were situated in the distance of 10mm from the end of transition.

Three cases of rotation of helicoidal resonators were analyzed in this paper, as it is presented in Figure 2. Case 1 represents the situation when helicoidal resonators are placed in the same way inside cylindrical ducts. Case 2 represents the situation when the characteristic gaps of the rest part 0,305 of helicoidal turns are placed externally, and Case 3 represents the situation when those gaps are placed internally.

Case 1: rotation angles
- both resonators 70°,
- gaps oriented on the same side,

Case 2: rotation angles
- left resonator 60°,
- right resonator 240°.
- gaps oriented externally,

Case 3: rotation angles
- left resonator 240°,
- right resonator 60°,
- gaps oriented internally.

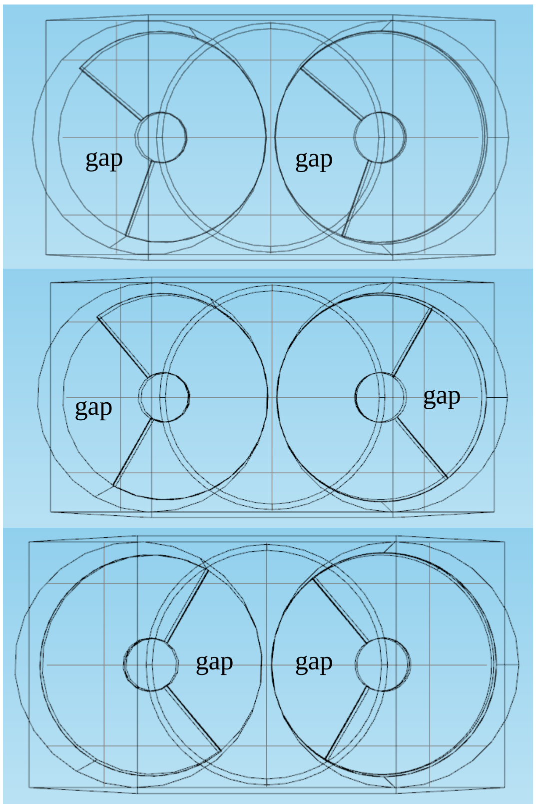

Figure 2. Investigated three cases of rotation angles of two identical helicoidal resonators arranged in parallel ducts

2.1. Acoustical model

Investigated in this paper acoustical models have the same parameters as in previous, well described studies under helicoidal resonators, as in example papers [2-7, 9-12, 14-17]. It was used the finite element method in Comsol Multiphysics-Acoustic Module numerical environment [18]. The transmission loss (*TL*) [19] was computed as the acoustic attenuation performance parameter. It was considered the sound propagation in air with temperature 20ºC without flow. The boundary conditions were established, as follows:

- hard walls of all elements of helicoidal resonators (perfect reflection) and cylindrical ducts,
- plane waves radiation - inlet (incident pressure p=1Pa) of a duct with diameter D=140mm and outlet surfaces of two cylindrical ducts with diameters d=125mm - that satisfies the anechoic terminations to calculate *TL*.

Free tetrahedral mesh [18] was created with satisfying the rule of minimum 5 finite elements per sound wave length [20] for maximum frequency- here it is f_{max}=2000Hz at

20 Celsius degrees. The considered speed of sound in air c_s=343m/s. Maximum finite element size equalled $h_e=0{,}2(c_s/f_{max})$. Example view on generated free tetrahedral mesh of investigated model is presented in Figure 3.

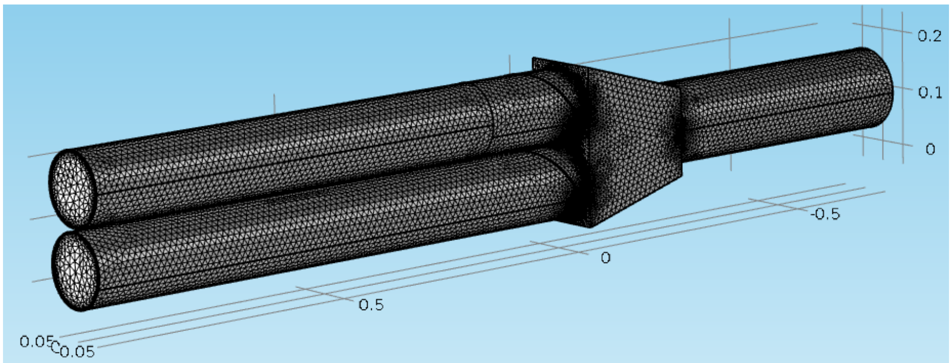

Figure 3. Example view on free tetrahedral mesh of investigated ducted acoustical system with two identical helicoidal resonators arranged in parallel

2.2. CFD turbulent flow model

CFD Module of Comsol Multiphysics [18] was used to solve investigated CFD turbulent flow model of ducted system analyzed as a single-phase flow *k-ω* turbulence RANS model [18, 21, 22] with compressible flow (Mach number lower than 0,3), as it was similarly considered in papers [8, 14, 16]. The main feature is fluid properties, that adds the Navier-Stokes equations and the transport equations for the turbulent kinetic energy *k* and the specific dissipation ω, and provides interface for defining the fluid material and its properties [14]. The basic fluid properties are: temperature *T*=20ºC, reference atmospherical pressure p_a=1atm, density and dynamic viscosity of air were calculated automatically from COMSOL material library [18]. The boundary conditions were described as follows:

– wall slip - there are no viscous effects at the slip wall at all surfaces of cylindrical duct and helicoidal resonators,
– normal inflow velocity at the inlet equaled 1m/s,
– no viscous stress at the outlet, pressure there equaled 0 Pa.

Finite element mesh was generated automatically as a free tetrahedral and controlled by physics-fluid dynamics. The stationary solver was used.

3. Results

This chapter contains the results of solved pressure acoustics in frequency domain (subchapter 3.1) and fluid dynamics problems (subchapter (3.2) for investigated models of two identical helicoidal resonators with constant ratio *s/d*=1,976 and numbers of helicoidal turns *n*=0,695 arranged in parallel ducts past the transition from one larger duct with diameter *D*.

3.1. Transmission Loss

Figure 4 presents the three *TL* characteristics of two identical helicoidal resonators with ratio *s/d*=1,976 and numbers of helicoidal turns *n*=0,695for three cases of rotation the helicoidal resonators and localisation of gaps.
The numerical calculation were made in the frequency range from 10Hz to 2000Hz with the calculation step of 10Hz.

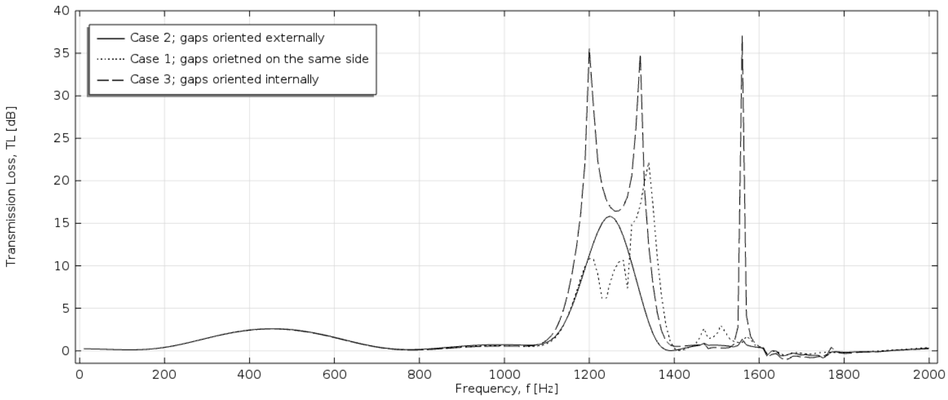

Figure 4.Transmission Loss of two identical helicoidal resonators with *s/d*=1,976 and *n*=0,671 arranged in parallel ducts for three cases of rotation.

As it can be observed from Figure 4 the specific narrow-band attenuation of sounds for investigated two identical helicoidal resonators arranged in parallel ducts is visible for all investigated cases. But only for case 3, when the gaps are oriented internally, there were obtained the highest *TL* levels (TL_1≈35dB and TL_2≈34dB) for characteristic resonance frequencies (f_1≈1200Hz and f_2≈1350Hz) of this type of helicoidal resonators (see results of researches in several authors publications, as for example in [9,12,16]).

For case 1 with gaps oriented on the same side it is observed, near the second resonance frequency of about 1350Hz,*TL* level of about 22dB. And for the case 2, when the gaps are oriented externally, there are visible only nearly symmetrical *TL* distribution for one characteristic frequency of about 1250Hz with *TL* level of about 17dB.

3.2. CFD turbulent flow

The numerically calculated pressure drop *Δp* [Pa],as a difference between surface average pressure in [Pa] at the inlet and outlet of the ducted system for three cases of investigated two identical helicoidal resonators with ratio *s/d*=1,976 and number of helicoidal turns *n*=0,695 arranged in parallel cylindrical ducts with diameter d past the transition from cylindrical duct with diameter D, are presented in Figure 5.

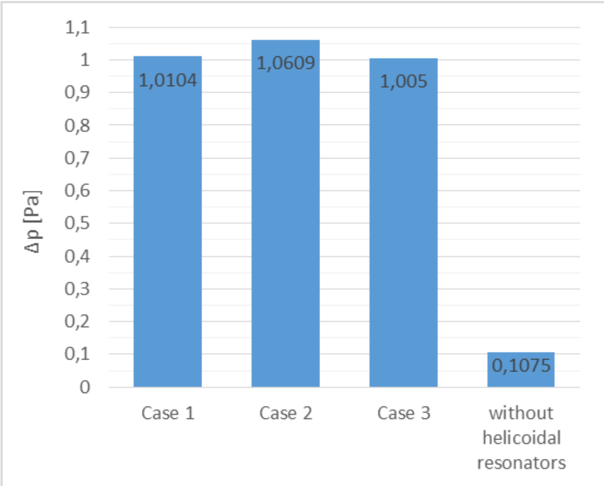

Figure 5. Pressure drop *Δp* [Pa] of investigated three cases of two identical helicoidal resonators with ratio *s/d*=1,976 and number of helicoidal turns *n=0,695*arranged in parallel ducts with different rotation angles

On the basis of performed CFD numerical analysis, there were calculated a total pressure drop coefficients ζ for three investigated cases in the same way as in previous papers [13,16], presented in Table 1.

Table 1. Total pressure drop coefficients ζ for three investigated cases

Case No.	ζ
1	1,4993
2	1,5832
3	1,4904

As it can be observed from Figure 5, the highest pressure drop *Δp*= 1,0609Pa (ζ=1,5832)occurs for case 2, when the gaps of two helicoidal resonators are oriented externally. The lowest pressure drop *Δp*= 1,005Pa (ζ=1,4904)occurs for case 3, when the gaps of two helicoidal resonators are oriented internally.

4. Conclusions

A numerical analysis of pressure drop and acoustic attenuation performance of two identical acoustic helicoidal resonators with *s/d*=1,976 and *n*=0,695 arranged in parallel cylindrical ducts with diameter *d*=125mm and different rotation angles past the transition from one cylindrical duct of a diameter *D*=140mm,was performed in this paper. Three cases of rotation angles and orientation of helicoidal resonators gaps were considered.

On the base of acoustical analysis, it can be found, that the specific narrow-band attenuation of sounds for investigated two identical helicoidal resonators arranged in parallel ducts with different rotation angles is visible for all investigated cases. But only for case 3, when the gaps are oriented internally, there were obtained the highest *TL* levels for (TL_1≈35dB and TL_2≈34dB) for characteristic resonance frequencies (f_1≈1200Hz and f_2≈1350Hz) of this type of helicoidal resonators.

On the base of fluid dynamics analysis, it can be found, that the lowest pressure drop Δp=1,005Pa(ζ=1,4904)occurs for case 3, when the gaps of two helicoidal resonators are oriented internally.

Obtained results are surprising, due to a fact that the case 3, when the helicoidal resonators gaps are oriented internally, provides the best acoustical attenuation performance and the lowest pressure drop.

Considered in this paper the three cases of rotation angles and orientation of gaps were selected intuitive in the manner of practical applications. There should be performed more acoustical and CFD analysis for ducted systems with helicoidal resonators placed past the transition to find the best solution.

Acknowledgments

The author gratefully acknowledges that this paper was financially supported in the year 2016 by the research project 02/21/DSPB/3478.

References

1. W. Łapka, C. Cempel, *Acoustic filter for suppressing the sound in the channel installations*, Polish Patent Office, Patent Number PL216176-B1, Publ. Date 31 MAR 2014.
2. W. Łapka, C. Cempel, *Noise reduction of spiral ducts*, International Journal of Occupational Safety and Ergonomics (JOSE), **13**(4) (2007) 419 – 426.
3. W. Łapka, *Acoustic attenuation performance of a round silencer with the spiral duct at the inlet*, Archives of Acoustics (Supplement), **32**(4) (2007) 247 – 252.
4. W. Łapka, C. Cempel, *Computational and experimental investigations of a sound pressure level distribution at the outlet of the spiral duct*, Archives of Acoustics (Supplement), **33**(4) (2008), 65 – 70.
5. W. Łapka, C. Cempel, *Acoustic attenuation performance of Helmholtz resonator and spiral duct*, Vibrations in Physical Systems, **23** (2008) 247 – 252.
6. W. Łapka, *Insertion loss of spiral ducts - measurements and computations*, Archives of Acoustics, **34**(4) (2009) 407 – 415.
7. W. Łapka, *Substitutional transmittance function of helicoidal resonator*, Vibrations in Physical Systems, **24** (2010) 265 – 270.
8. W. Łapka, *Comparison of numerically calculated pressure drop for selected helicoidal resonators*, Proceedings of the 59th Open Seminar on Acoustics joint with Workshop on Strategic Management of Noise including Aircraft Noise, Polskie Towarzystwo Akustyczne - Oddział Poznański, (2012) 145 – 148.
9. W. Łapka, *Numerical Aeroacoustic Research of Transmission Loss Characteristics Change of Selected Helicoidal Resonators due to Different Air Flow Velocities*, Vibrations in Physical Systems, **25** (2012) 267 – 272.

10. W. Łapka, *Multi resonant helicoidal resonator for passive noise control in ducted systems*, Experimental Mechanics- New Trends and Perspectives, Editors J.F. Silva Gomes, Mario A.P. Vaz, Proceedings of the 15th International Conference on Experimental Mechanics, ICEM15, Porto, Portugalia, 22-27 lipiec 2012, 995 – 996, 2012.
11. W. Łapka, *Helicoidal resonators for passive noise control in ducted systems with practical application*, Proceedings of Internoise 2012, New York, USA, 2012.
12. W. Łapka, *Numerical study of acoustic-structure interaction of selected helicoidal resonator with flexible helicoidal profile*, Postępy Akustyki, Polskie Towarzystwo Akustyczne - Oddział w Rzeszowie, Rzeszów, (2013) 194 – 205.
13. W. Łapka, M. Szymański, R. Górzeński, *Badania oporów przepływu w zależności od strumienia objętości powietrza w kanale dla wybranych rezonatorów helikoidalnych*, Postępy Akustyki, Polskie Towarzystwo Akustyczne - Oddział w Rzeszowie, Rzeszów, (2013) 168 – 180.
14. W. Łapka, *Transmission Loss and Pressure Drop of Selected Range of Helicoidal Resonators*, Vibrations in Physical Systems, **26** (2014) 121 – 128.
15. W. Łapka, *Fan duct noise elimination by the use of helicoidal resonators*, Proceedings of Inter-Noise 2014, 16-19 November 2014, Melbourne, Australia, 2014.
16. W. Łapka, P. Kędzia, *Numerical analysis of transmission loss and pressure drop of helicoidal resonators in straight cylindrical ducts*, Proceedings of Forum Acusticum 2014, 7-12 September 2014, Kraków, Poland, 6 pages in CD, 2014.
17. W. Łapka, *Acoustic attenuation performance of selected helicoidal resonators lined with an absorbent materials of different thickness and density*, Proceedings of Inter-Noise 2013, Innsbruck, Austria, 2013, 8 pages in CD, 2013.
18. COMSOL Multiphysics, *User's Guide and Model Library Documentation Set*, COMSOL AB, www.comsol.com, Stockholm, Sweden, 2016.
19. M. L. Munjal, *Acoustics of Ducts and Mufflers with Application to Exhaust and Ventilation System Design*, Inc., Calgary, Canada, John Wiley & Sons, 1987.
20. S. Marburg, B. Nolte, *Computational Acoustics of Noise Propagation in Fluids – Finite and Boundary Element Methods*, 578, Springer-Verlag, Berlin, Germany, 2008.
21. D. C. Wilcox, *Turbulence Modeling for CFD*, 3rd edition, DCW Industries, Inc., La Canada CA, 2006.
22. D. C. Wilcox, *Formulation of the k-omega Turbulence Model Revisited*, AIAA Journal, **46**(11) (2008) 2823 – 2838.

Application of the Continuous Dynamic Absorbers in Local and Global Vibration Reduction Problems in Beams

Waldemar ŁATAS
Cracow University of Technology, Institute of Applied Mechanics
Al. Jana Pawła II 37, 31-864 Kraków, latas@mech.pk.edu.pl

Abstract

The paper deals with the application of the continuous dynamic absorbers in vibration reduction problems in beams. The Euler-Bernoulli beam of variable cross-section is subjected to the concentrated and distributed harmonic excitation forces. The beam is equipped with a system of the continuous vibration absorbers. The problem of the forced vibration is solved employing the Galerkin's method and Lagrange's equations of the second kind. Performing time-Laplace transformation the amplitudes of displacement may be written in the frequency domain, similarly the time-averaged kinetic energy of any part of the beam. The results of some local and global vibration control optimization problems concerning the placement and parameters of the continuous vibration absorbers are presented.

Keywords: tuned mass damper, dynamic vibration absorber, continuous absorber, beam vibration, vibration control

1. Introduction

The main aim of dynamic vibration absorbers (DVA) and tuned mass dampers (TMD), properly located and tuned to the excitation force frequency, is the reduction of structure vibrations in the point of attachment [1,2]. The problem of vibration analysis and the proper selection of absorbers parameters was investigated in several theoretical studies [3-10].

Certain general rules concerning the proper location of dynamic absorbers can be given [7,18]. In continuous systems, such as beams, in case of its loading by a concentrated force the best place for the dynamic absorber attachment is usually the point of the applied load. The discrete absorbers efficiency depends significantly on the accuracy of their placement since even a slight deviation from the optimal position significantly decreases their effectiveness. Finding the optimal positions of absorbers for a distributed force applied is more complicated, especially for global problems of vibration reductions. Systems of dynamic absorbers tuned – in dependence of the excitation force bandwidth – into one [11-14] or into a few frequencies [3-5] are applied in several cases.

Continuous absorbers, in comparison with discrete absorbers, are efficient for various locations of excitation forces and at the appropriate tuning can be efficient within a wide frequency range. Continuous absorbers are especially suitable for damping the running structural waves in long one-dimensional continuous systems, such as beams [15]. This type dynamic absorbers are applied also for reducing vibrations of plates and shells at low frequencies [19] as well as for problems related to sound emission [20].

The computational algorithm, allowing to determine the amplitude-frequency characteristics of displacement and energy for the Euler-Bernoulli beam of a variable cross-section subjected to harmonic excitations of concentrated and distributed forces, with the system of continuous dynamic absorbers attached, is presented in the hereby paper. The presented examples of numerical calculations concern the application of the continuous absorbers in global vibration reduction problems in beams.

2. Theoretical model

The system considered in the paper is shown in Fig. 1. The beam of length l and with any given boundary conditions is given, its physical and geometrical parameters are functions of the position: mass density $\rho(x)$, cross-section area $A(x)$, geometrical moment of inertia $I(x)$, Young modulus $E(x)$, viscous damping coefficient $\alpha(x)$ (the Voigt-Kelvin rheological model was assumed). The beam subjected to harmonic excitations (both concentrated and distributed) is equipped with the system of continuous dynamic vibration absorbers.

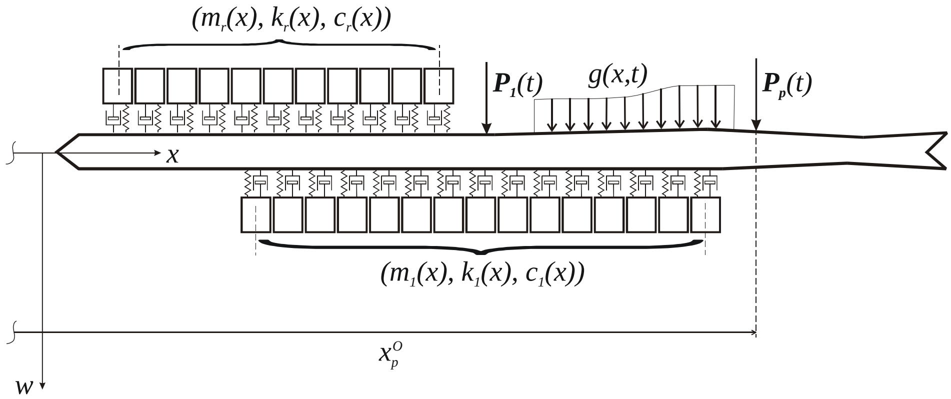

Figure 1. Beam with the system of ϱ continuous dynamic vibration absorbers

When the Euler-Bernoulli beam model is taken into account, the expressions for the kinetic and potential energy and for the dissipation potential take the following forms:

$$T = \frac{1}{2}\int_0^l \varrho(x)A(x)\left(\frac{\partial w}{\partial t}\right)^2 dx \tag{1}$$

$$V = \frac{1}{2}\int_0^l E(x)I(x)\left(\frac{\partial^2 w}{\partial x^2}\right)^2 dx \tag{2}$$

$$R = \frac{1}{2}\int_0^l E(x)I(x)\alpha(x)\left(\frac{\partial^3 w}{\partial t \partial x^2}\right)^2 dx \tag{3}$$

The beam deflection is described by the functional series

$$w(x,t) = \sum_{i=1}^{n} q_i(t)\varphi_i(x) \tag{4}$$

in which eigenfunctions of the beam of a constant cross-section (for boundary conditions of the given problem), without the attached dynamic absorbers, are assumed as basic functions $\varphi_i(x)$. Time functions $q_i(t)$ tare generalized coordinates which should be determined.

After the substitution of series (4) into equations (1)-(3) the expressions for the kinetic and potential energy and for the dissipation potential take the following forms:

$$T = \frac{1}{2}\sum_{i=1}^{n}\sum_{j=1}^{n} m_{ij}\dot{q}_i\dot{q}_j \tag{5}$$

$$V = \frac{1}{2}\sum_{i=1}^{n}\sum_{j=1}^{n} k_{ij}q_i q_j \tag{6}$$

$$R = \frac{1}{2}\sum_{i=1}^{n}\sum_{j=1}^{n} b_{ij}\dot{q}_i\dot{q}_j \tag{7}$$

Numerical factors m_{ij}, k_{ij}, b_{ij} occurring in the above shown expressions, are defined as follows:

$$m_{ij} = \int_0^l \rho(x)A(x)\varphi_\mathrm{i}(x)\varphi_\mathrm{j}(x)dx \tag{8}$$

$$k_{ij} = \int_0^l E(x)I(x)\varphi_i''(x)\varphi_\mathrm{j}''(x)dx \tag{9}$$

$$b_{ij} = \int_0^l E(x)I(x)\alpha(x)\varphi_i''(x)\varphi_\mathrm{j}''(x)dx \tag{10}$$

For the arbitrary beam load applied $H(x, t)$ the generalized force for the i-th generalized coordinate equals to:

$$H_i(t) = \int_0^l H(x,t)\,\varphi_i(x)dx \tag{11}$$

Using the Lagrange's equations of second kind the differential equations system for the generalized coordinates $q_i(t)$ is obtained:

$$\sum_{j=1}^{n} m_{ij}\ddot{q}_j + \sum_{j=1}^{n} b_{ij}\dot{q}_j + \sum_{j=1}^{n} k_{ij}q_j = H_i(t), \quad i = 1 \ldots n \tag{12}$$

Applying the time Laplace transform (with initial conditions being zero) to system (12) the linear system of algebraic equations is obtained, from which it is possible to obtain transforms $Q_i(s)$ of functions $q_i(t)$:

$$\sum_{j=1}^{n} m_{ij}s^2 Q_j(s) + \sum_{j=1}^{n} b_{ij}sQ_j(s) + \sum_{j=1}^{n} k_{ij}Q_j(s) = H_i(s), \quad i = 1 \ldots n \tag{13}$$

The transform of the beam deflection line is given by the series

$$W(x,s) = \sum_{i=1}^{n} Q_i(s)\varphi_i(x) \tag{14}$$

The load of the considered beam (Fig. 1) consists of p concentrated forces $P_k(t)$ applied in points of coordinates x_k^0, of a distributed load $g(x, t)$ and of r distributed loads $f_k(x, t)$ originated from continuous dynamic absorbers:

$$H(x,t) = \sum_{k=1}^{p} P_k(t)\,\delta(x - x_k^0) + g(x,t) + \sum_{k=1}^{r} f_k(x,t) \tag{15}$$

Thus, the generalized force $H_i(t)$ for the generalized coordinate $q_i(t)$ equals to:

$$H_i(t) = \sum_{k=1}^{p} P_k(t)\,\varphi_i(x_k^0) + \int_0^l g(x,t)\,\varphi_i(x)dx + \sum_{k=1}^{r}\int_0^l f_k(x,t)\,\varphi_i(x)dx, \quad i = 1 \ldots n \tag{16}$$

The Laplace transform of the generalized force is given by the expression:

$$H_i(s) = \sum_{k=1}^{p} P_k(s)\,\varphi_i(x_k^0) + \int_0^l g(x,s)\,\varphi_i(x)dx + \sum_{k=1}^{r}\int_0^l f_k(x,s)\,\varphi_i(x)dx, \quad i = 1 \ldots n \tag{17}$$

where $P_k(s)$, $g(x, s)$, and $f_k(x, s)$ are the Laplace transforms of functions: $P_k(t)$, $g(x, t)$, $f_k(x, t)$.

The Laplace transform of the continuous beam load originated from the k-th continuous dynamic absorber (with zero initial conditions) equals to:

$$f_k(x,s) = -\frac{\left(c_k(x)s + k_k(x)\right)m_k(x)s^2}{m_k(x)s^2 + c_k(x)s + k_k(x)} \sum_{j=1}^{n} Q_j(s)\varphi_j(x) \tag{18}$$

where by: $m_k(x)$, $k_k(x)$, $c_k(x)$ the linear densities of the mass, stiffness and damping coefficients (describing the continuous dynamic absorber) are marked, respectively. When expression (18) is inserted into (17), after rearrangements the system of linear algebraic equations is obtained from system (13). The transforms $Q_i(s)$ can be determined from the system:

$$\sum_{j=1}^{n}\left(m_{ij}s^2+b_{ij}s+k_{ij}+\sum_{k=1}^{r}F_{ij}^{k}(s)\right)Q_j(s)=\sum_{k=1}^{p}P_k(s)\varphi_i(x_k^0)+G_i(s)$$
$$i=1\ldots n \tag{19}$$

where the following notations are introduced:

$$F_{ij}^{k}(s)=\int_0^l\frac{\left(c_k(x)s+k_k(x)\right)m_k(x)s^2}{m_k(x)s^2+c_k(x)s+k_k(x)}\varphi_i(x)\varphi_j(x)dx$$
$$G_i(s)=\int_0^l g(x,s)\varphi_i(x)dx \tag{20}$$

The solution of equations system (19) provides in s-domain – after using equation (14) – the transform of the beam deflection line for arbitrary boundary conditions. When considering the steady state, substituting s = $j\omega$ ($j=\sqrt{-1}$)allows to determine the amplitude of the beam deflection line as the function of frequency. Analogous amplitude-frequency characteristics can be obtained for the bending moment, shear force and the time-averaged kinetic energy of the beam.

The developed computational algorithm allows to determine the mentioned above amplitude-frequency characteristics for the beam described by arbitrary functions (within the geometrical model applicability): $\rho(x)$, $A(x)$, $I(x)$, $E(x)$, $\alpha(x)$.

3. Numerical calculations – tunable continuous vibration absorber

A cantilever steel beam, with rectangular cross-section, excited by uniform distributed harmonic force: $g(x, t) = g_0 sin\omega t$ distributed along the segment $\langle 0.3l, 0.6l\rangle$ is considered, with the continuous absorber attached (Fig. 2). The parameters describing the system are collected in Table 1 (the internal damping in the beam is neglected).

Table 1. Parameters of the beam and absorber

Quantity	Symbol	Unit	Value
Mass density	ρ	kg/m^3	7800
Length	l	m	1.0
Young's modulus	E	N/m^2	2.1e11
Cross-section width	b	m	0.05
Cross section height	h	m	0.005
Total mass of the absorber	-	kg	0.098

The first four natural frequencies of the beam without the absorber attached are equal to: f_1 = 4.19 Hz, f_2 = 26.26 Hz, f_3 = 73.54 Hz, f_4 = 144.11 Hz.

It is assumed that the linear densities of the absorber mass, stiffness and damping coefficients are constant along its segment: $m(x)$ = const, $k(x)$ = const, $c(x)$ = const, the total mass of the continuous absorber is equal to 5% of the total beam mass, which means 0.098 kg.

Depending on whether the local optimization problem is considered (e.g. minimization of the vibration amplitude of the selected point of the beam) or the global one (e.g. minimization of the time-averaged kinetic energy of the selected part of the beam), the optimal solutions (i.e. width, location and physical absorber parameters) may be completely different. The solutions also depend on whether the problem of tuning the absorber around a selected frequency is considered (passive method) or the problem of tuning in real-time to the excitation frequency in a wider frequency band (semi-active method).

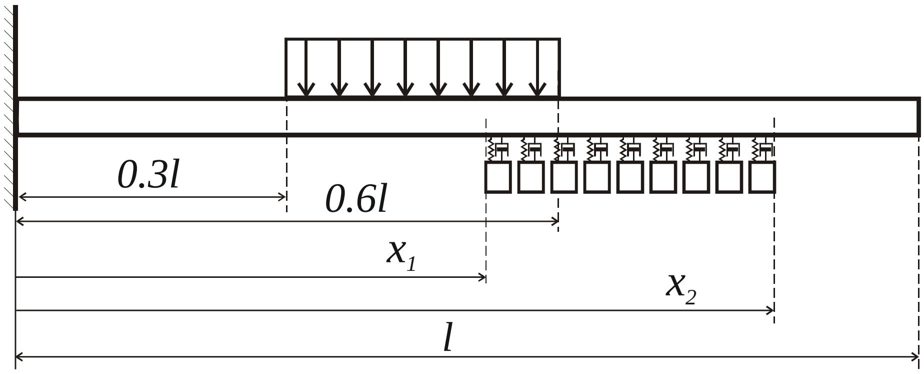

Figure 2. Beam with the attached dynamic continuous vibration absorber

For example, for the problem of passive minimization of the vibration amplitude of the free end of the beam shown in Fig. 2, in the bandwidth around the first natural frequency f_1 = 4.19 Hz, the best result is obtained for the discrete damper placed at the end of the beam. The calculated for this case the optimal stiffness and damping coefficients of the damper are: K_{OPT} = 47.70 N/m , C_{OPT} = 1.08 Ns/m.

Due to the first mode shape the problem of passive minimization of the time-averaged kinetic energy of the beam around the first natural frequency has a similar solution: the discrete damper placed at the end of the beam with the optimal parameters almost the same like given earlier.

The width and location of the optimal absorber in vibration reduction problems considered in a wider frequency band can be different depending on the criterion taken (local or global). In the case of the absorber tuned in real-time to the excitation frequency (semi-active method), the best solution for the problem of minimization the vibration amplitude of the beam free end may also occur the discrete absorber placed at the end of the beam. In this case, however, a new resonant frequency [18, 23-24] may appear with a node at the beam end, so such location of a discrete damper may be inadequate in the energy minimization problems. The vibration suppression efficiency may be improved by using several discrete translational and rotational absorbers [22-24].

In further calculations the continuous absorber (Fig. 2) is assumed to be tuned so that it is resonant at each frequency, without energy dissipating appliances ($c(x) = 0$).

The aim of calculations is to find the optimal width and placement of the continuous vibration absorber in a given frequency range, as a measure of vibration is used the time -averaged kinetic energy of the whole beam.

The results of the numerical calculations are presented in Fig. 3 and Fig. 4.

For comparison it is first shown in Fig. 3 the calculated time-averaged kinetic energy for the case with the single discrete absorber placed in different positions on the beam. The numbers in the figure represent the distance from the support (in meters).

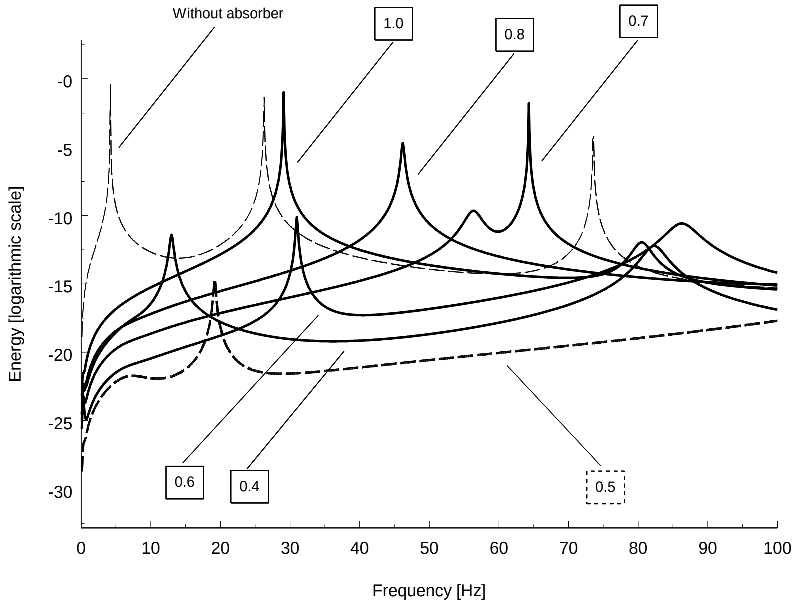

Figure 3. Time-averaged kinetic energy of the beam with the one discrete absorber attached in different positions – the absorber is tuned to be resonant at each frequency

It is visible that the vibration suppression efficiency of the discrete absorber (tuned to the excitation force frequency) depends largely upon the absorber position. Due to the appearing a new resonant frequency of the structure composed of the beam with absorber, there is no position of the absorber appropriate in the whole frequency band considered. Additionally the discrete absorber is very sensitive to inaccurate location and tuning.

In Fig. 4 is shown the time-averaged kinetic energy for the case with the single continuous absorber of different width and placed in different positions on the beam. The numbers in the figure represent the values of x_1 and x_2 (Fig. 2).

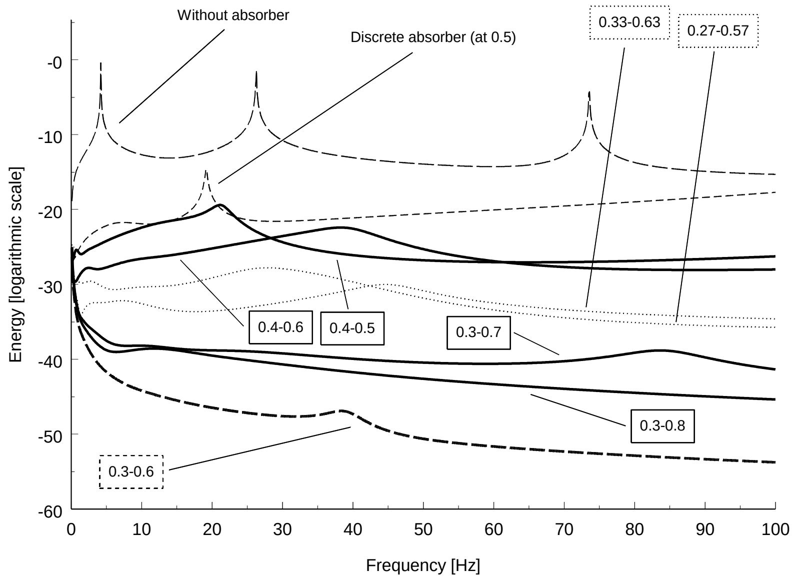

Figure 4. Time-averaged kinetic energy of the beam with the one continuous absorber attached in different positions and with different segment widths – the absorber is tuned to be resonant at each frequency

It results from the diagrams in Fig. 4 that the continuous absorbers may have the suppression efficiency many orders of magnitude higher than the discrete absorber.

It is possible to find the width and position of the continuous absorber segment which are considered optimal in the entire given bandwidth, because there doesn't appear any new resonant frequency in the system.

The continuous absorber is also sensitive to inaccurate location and tuning, but even when placed not exactly at the optimal location it can posses the vibration suppression efficiency much more higher than the discrete absorber.

For another type of loading optimization can give different results, as for the other frequency bands. A further improvement of the vibration reduction would be achievable, when the real time change not only of stiffness but also of damping was possible. Detuning the absorbers, both discrete and continuous, can also be beneficial [18].

4. Conclusions

Continuous dynamic absorbers can be efficient in cases when the points of loading attachment is not accurately determined as well as in cases of distributed loads. They can be applied in places where placements of one or a few absorbers of significant masses is technically impossible. By the appropriate tuning they can be efficient within a broad frequency band.

The computational model presented in the hereby paper can be used in local and global problems of the optimization the continuous dynamic absorbers locations and parameters in beams. The numerical algorithm created for calculation of the continuous absorbers may also be applied to calculation of the discrete absorbers. It can be obtained by taking the very narrow segment over which the continuous absorber is distributed or by describing the densities of the mass, stiffness and damping coefficients using the δ-Dirac distribution. The advantage of this approach is that the number of unknowns in the solved systems of equations does not depend on the number of discrete dampers used.

The computational model of the continuous dynamic absorber, presented in this study, can be adjusted to vibration reduction problems in more complex one-dimensional systems such as frames or curvilinear beams. It can be also expanded to problems of vibration reductions in plates or shells.

References

1. J. P. Den Hartog, *Mechanical Vibrations*, Dover Publications, Mineola, NY 1985.
2. C. M. Harris, A. G. Piersol, *Harris' Shock and Vibration Handbook*, McGraw-Hill, 2002.
3. M. Luu, V. Zabel, C. Könke, *An optimization method of multi-resonant response of high-speed train bridges using TMDs*, Finite Elements in Analysis and Design, **53** (2012) 13 – 23.
4. Q. Li, J. Fan, J. Nie, Q. Li, Y. Chen, *Crowd-induced random vibration of footbridge and vibration control using multiple tuned mass dampers*, Journal of Sound and Vibration, **329** (2010) 4068 – 4092.
5. E. Caetano, Á. Cunha, F. Magalhães, C. Moutinho, *Studies for controlling human-induced vibration of the Pedro e Inês footbridge, Portugal. Part 2: Implementation of tuned mass dampers*, Engineering Structures, **32** (2010) 1082 – 1091.
6. E. Esmalizadeh, N. Jalili, *Optimal design of vibration absorbers for structurally damped Timoshenko beams*, ASME Journal of Vibration and Acoustics, **120** (1998) 833 – 841.
7. M. J. Brennan, J. Dayou, *Global control of vibration using a tunable vibration neutralizer*, Journal of Sound and Vibration, **232**(3) (2000) 585 – 600.
8. D. Younesian, E. Esmailzadeh, R. Sedaghati, *Passive vibration control of beams subjected to random excitations with peaked PSD*, *Journal* of Vibration and Control, **12**(9) (2006) 941 – 953.
9. F. Yang, R. Sedaghati, *Vibration suppression of non-uniform curved beams under random loading using optimal tuned mass damper*, Journal of Vibration and Control, **15**(2) 2009) 233 – 261.
10. Y. L. Cheung, W. O. Wong, *Isolation of bending vibration in a beam structure with a translational vibration absorber and a rotational vibration absorber*, Journal of Vibration and Control, **14**(8) (2008) 1231 – 1246.
11. J. D. Yau, Y. B. Yang, *A wideband MTMD system for reducing the dynamic response of continuous truss bridges to moving train loads*, Journal of Structural Engineering, **26** (2004) 1795 – 1807.

12. J. D. Yau, Y. B. Yang, *Vibration reduction for cable-stayed bridges traveled by high-speed trains*, Finite Elements in Analysis and Design, **40** (2004) 341 – 359.
13. J. Li, M. Su, L. Fan, *Vibration control of railway bridges under high-speed trains using multiple tuned mass dampers*, ASCE Journal of Bridge Engineering, **10**(3) (2005) 312 – 320.
14. H. N. Li, X. L. Ni, *Optimization of non-uniformly distributed multiple tuned mass damper*, Journal of Sound and Vibration, **308** (2007) 80 – 97.
15. D. J. Thompson, *A continuous damped vibration absorber to reduce broad-band wave propagation in beams*, Journal of Sound and Vibration, **311** (2008) 824 – 842.
16. W. Łatas, P. Martynowicz, *Modeling of vibration of wind turbine tower-nacelle system with dynamic absorber*, Modelowanie Inżynierskie, **44**(13) (2012) 187 – 198.
17. W. Łatas, P. Martynowicz, J. Snamina, *Dynamic similarity of wind turbine's tower-nacelle system and its scaled model*, Solid State Phenomena, **208** (2014) 29 – 39.
18. J. Dayou, M. J. Brennan, *Global control of structural vibration using multiple-tuned tunable vibration neutralizers*, Journal of Sound and Vibration, **258**(2) (2002) 345 – 357.
19. R. L. Harne, *On the linear elastic, isotropic modeling of poroelastic distributed vibration absorbers at low frequencies*, Journal of Sound and Vibration, **332** (2013) 3646 – 3654.
20. H. Osman, M. E. Johnson, C .R. Fuller, P. Marcotte, *Interior noise reduction of composite cylinders using distributed vibration absorbers*, Proceedings of the Seventh AIAA/CEAS Aeroacoustics Conference, Maastricht, The Netherlands, **2** (2001) 2001 – 2230.
21. J. Spencer, S. Nagarajaiah, *State of the art of structural control*, Journal of Structural Engineering, **July** (2003) 845 – 856.
22. W. Łatas, *Multiple tuned tunable translational-rotational vibration absorbers in beam*, Vibrations in Physical Systems, **26** (2014) 145 – 152.
23. W. Łatas, Optimal positions of the tunable translational-rotational dynamic absorbers in global vibration control problems in beams, Journal of Theoretical and Applied Mechanics, **53**(2) (2014) 467 – 476.
24. W. Łatas, *Optimal tuning of the tunable translational-rotational dynamic absorbers in global vibration control problems in beams*, Journal of Civil Engineering, Architecture and Environment, **61**(2) (2014) 107 – 118.

Natural Frequencies of Layered Elongated Cylindrical Panels for Geometrically Nonlinear Deformation at Discrete Consideration of Components

Mykhailo MARCHUK
Pidstryhach Institute for Applied Problems of Mechanics and Mathematics, NASU
3 b Naukova Str., L'viv, 79053, Ukraine
and National University L'viv Polytechnic
12 Bandera Str., L'viv, 79013, Ukraine
mv_marchuk@ukr.net; marchuk@iapmm.lviv.ua

Taras GORIACHKO
Pidstryhach Institute for Applied Problems of Mechanics and Mathematics, NASU
3 b Naukova Str., L'viv, 79053, Ukraine
taras.horyachko@gmail.com

Vira PAKOSH
Pidstryhach Institute for Applied Problems of Mechanics and Mathematics, NASU
3 b Naukova Str., L'viv, 79053, Ukraine
v.pakosh@ukr.net

Abstract

The proposed and verified the technique of finding a finite number of first natural frequencies for geometrically nonlinear vibrations of layered elongated cylindrical panels at discrete consideration of components. The influence of the radius of curvature on the natural frequencies of three- and five-layered panels is investigated. The dependence between the volume of filler three-layer panels and the lowest natural frequency has been established.

Keywords: elongated layered panel, nonlinear vibrations, perturbations method, natural frequencies

1. Introduction

The flexible layered cylindrical panels constitute a significant part of various structures and hardware. The specificity of the functional purpose of components of layers causes a sharp difference in their physical and mechanical properties and thickness, causing the need for discrete consideration of the thickness of the structure, of the above mentioned objects, as the averaged approach can lead to significant errors when assessing the ability to support or determine their amplitude and frequency characteristics.

Effects of intensive dynamic (including cyclic) loads are usually the cause of geometrically non-linear stress-strain state. Therefore, there is a need for the development and verification of the methods for determining the parameters of free vibrations of geometrically nonlinear deformation of layered cylindrical panels for consideration of discrete components.

Free vibrations of the shell structural elements are studied using numerical and experimental methods [1–3] or only pliability to transversal shear [4]. Some analytical results for pliability to transversal compression are given in [8].

In this paper proposed the technique and with its using the investigated the free geometrically nonlinear vibrations of layered cylindrical panels with into account all the physical and mechanical properties of components in the spatial statement of the problem.

2. The problem statement for a particular component of a layered panel

A curved anisotropic elastic layer with thickness h we assume in a natural mixed system of coordinates $\alpha_1, \alpha_2, \alpha_3$ on the median surface. This surface is formed by the motion of the line $\alpha_1 = 0; \alpha_3 = 0$ on the segment of arbitrary guiding. We consider that the layer is significantly larger along the axis α_2 to the length of the section arc $\alpha_2 = 0$ of the median surface $\alpha_3 = 0$. So we have an elongated panel. If the conditions of fixing the ends of the panel $\alpha_1 = \pm\alpha_1^0$ and the initial conditions are independent of the coordinate α_2, then through a little influence of conditions of fixing the edges $\alpha_2 = \pm\alpha_2^0$, the functions, that determine the characteristics of geometrically nonlinear vibration processes in the plane of the median section, are dependent from α_1, α_3. To find these functions we have [9]:

– motion equations

$$div\,\hat{S} = \rho \frac{\partial^2 U}{\partial t^2}; \tag{1}$$

– elasticity relations

$$\hat{\Sigma} = \tilde{A} \otimes \hat{\varepsilon}; \tag{2}$$

– deformation relation between the strain tensor components $\hat{\varepsilon}$ and the components of the elastic displacement vector $\vec{U} = u_i \vec{e}_i \vec{e}_j$

$$\varepsilon_{ij} = \frac{1}{2}(\nabla_i u_j + \nabla_j u_i + \nabla_i u^k \nabla_j u_k); \tag{3}$$

– relation between the components S^{ij} of the nonsymmetrical Kirchhoff stress tensor $\hat{S}$ and the components σ^{ik} of the symmetric Piola stress tensor $\hat{\Sigma}$

$$S^{ij} = \sum_k \sigma^{ik} (\delta_k^j + \nabla_k u^j). \tag{4}$$

In equations (1) and (2) $\tilde{A}$ is the tensor of elastic properties of anisotropic layer, and ρ is its density.

Boundary conditions on the front surface of the panel $\alpha_3 = \pm h/2$ in the case of its belonging to the layered structure are shown below, and initial conditions have the form

$$u_i(\alpha_1, \alpha_3, t)\big|_{t=t_0} = v_i^0(\alpha_1, \alpha_3)\,, \quad \left.\frac{\partial u_i(\alpha_1, \alpha_3, t)}{\partial t}\right|_{t=t_0} = v_i^1(\alpha_1, \alpha_3)\,, \quad i = 1, 3\,, \tag{5}$$

$$\left|v_3^0(\alpha_1, \alpha_3)\right| >> \left|v_1^0(\alpha_1, \alpha_3)\right|, \quad (\alpha_1, \alpha_3) \in \Omega = [-\alpha_1^0, \alpha_1^0] \times [-h/2, h/2]\,. \tag{6}$$

3. The layered panels

Assume that a panel consists of N layers (see Fig. 1). Each k-th layer is considered as a separate thin panel with its own mechanical and material characteristics. Hooke's law is different for each layer:

$$\sigma^{(k)} = [Q^k]\varepsilon^k\,, \quad k = 1,\ldots,N, \tag{7}$$

where $[Q^k]$ is tensor of elastic properties of anisotropic k-th layer.

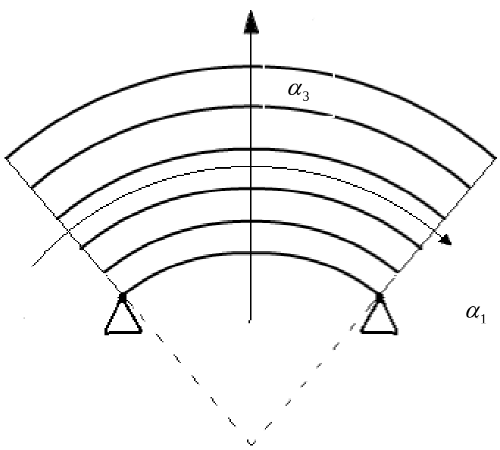

Figure 1. Layered cylindrical panel with hinges fixed on the elongated edges

Assuming that the value of α_3 coordinate at the top of k-th layer is h_k, and $h_0 = -h/2$, the equations (1) for a layered structure are written as

$$\sum_{i=1}^{3} \nabla_i S^{(k)ij} = \rho \frac{\partial^2 u_j^{(k)}}{\partial t^2}, \tag{8}$$

$$(\alpha_1, \alpha_3) \in \Omega = [-\alpha_1^0, \alpha_1^0] \times [h_{k-1}, h_k]\,, \quad k = 1,\ldots,N.$$

The contact conditions between the layers are

$$u_i^{(k-1)}(\alpha_1, h_{k-1}, t) = u_i^{(k)}(\alpha_1, h_k, t)\,, \quad i = 1, 2, 3, \tag{9}$$

$$S^{(k-1)3i}(\alpha_1, h_{k-1}, t) = S^{(k)3i}(\alpha_1, h_k, t), \quad |\alpha_1| \le \alpha_1^0, \quad k = 2,\ldots,N, \tag{10}$$

and on the lower and upper facial surfaces of the layered structure we have

$$S^{(m)31}(\alpha_1, h_m, t) = S^{(m)33}(\alpha_1, h_m, t) = 0, \quad |\alpha_1| \le \alpha_1^0, \quad m = 0, N. \tag{11}$$

At the elongated ends of the panel $\alpha_1 = \pm\alpha_1^0$ under the conditions of the fixing the hinge on the lower surface of the front $\alpha_2 = -h/2$ the boundary conditions have the form

$$S^{(k)1i}(a, \alpha_3, t) = 0, \quad k = 1, N, \tag{12}$$

$$u_i^{(N)}(a, \pm h/2, t) = 0, \quad |\alpha_3| \le h/2, \quad i = 1, 3, \quad a = \pm\alpha_1. \tag{13}$$

4. Approximations

Assuming that each *k*-th layer is thin, quadratic approximations along α_3 coordinate are used for components of elastic displacement vector u_1 and u_3 [10]:

$$u_i^{(k)}(\alpha_1, \alpha_3) = \sum_{j=0}^{2} u_{ij}^{(k)}(\alpha_1) p_j(\alpha_3), \quad i = 1, 3, \tag{14}$$

where

$$p_0(\alpha_3) = \frac{1}{2} - \frac{2\alpha_3 - h_{k-1} - h_k}{2(h_k - h_{k-1})},$$

$$p_1(\alpha_3) = \frac{1}{2} + \frac{2\alpha_3 - h_{k-1} - h_k}{2(h_k - h_{k-1})}, \quad p_2(\alpha_3) = 1 - \left(\frac{2\alpha_3 - h_{k-1} - h_k}{h_k - h_{k-1}}\right)^2, \quad \alpha_3 \in [h_{k-1}, h_k].$$

For finding the unknown coefficients $u_{ij}^{(k)}(\alpha_1)$ in (14), approximation by the tangential coordinate α_1 was used on one-dimensional isoperimetric linear finite elements [10]:

$$u_{ij}^{(k)(e)} = \sum_{j,m}^{2} u_{ijm}^{(k)(e)}(\alpha_1)\varphi_m^{(e)}(\xi), \quad \xi = \frac{2\alpha_1}{\alpha_{12}^{(e)} - \alpha_{11}^{(e)}} - 1, \tag{15}$$

where e is the number of finite elements of *k*-th layer; $u_{ijm}^{(k)(e)} = u_{ij}^{(k)}(\alpha_{1m}^{(e)})$, $m = 1, 2$ are the values on nodes $\alpha_{1m}^{(e)}(\alpha_1)$ of finite element; $\varphi_1^{(e)}(\xi) = \frac{1}{2}(1-\xi)$; $\varphi_2^{(e)}(\xi) = \frac{1}{2}(1+\xi)$.

5. The discretized problem

Considered above differential formulation of the problem of geometrically nonlinear free vibrations for single layer is equivalent to the problem of minimizing the functional L [10]:

$$L = -\int_{\Omega} \sum_i \sum_j u_i \frac{\partial S^{ij}}{\partial x_j} d\Omega - \int_{\Omega} \rho \frac{\partial^2 U^T}{\partial t^2} \cdot U d\Omega =$$

$$= -\int_{\Omega} \sum_i \sum_j S^{ij} \frac{\partial u_i}{\partial x_j} d\Omega - \int_{\Omega} \rho \frac{\partial^2 U^T}{\partial t^2} \cdot U d\Omega \to \min. \qquad (16)$$

Boundary conditions (11), (12) and contact conditions (9), (10) are a natural for the variation formulation of the problem (16) [10], but conditions (13) must be take into account during solving.

In a case layered panel we obtain:

$$L = \sum_{k=1}^{K} \left(-\int_{\Omega_k} \sum_i \sum_j S_k{}^{ij} \frac{\partial u_i}{\partial x_j} d\Omega - \int_{\Omega_k} \rho_k \frac{\partial^2 U^T}{\partial t^2} \cdot U d\Omega \right) \to \min. \qquad (17)$$

After substituting (14), (15), and using (4) into (8) in (17) and composing results together we obtain:

$$L^{\Delta} = \{u\}^T K_L \{u\} + \{u\}^T K_{NL}(u)\{u\} + \{u\}^T M\{\ddot{u}\} \to \min, \qquad (18)$$

where $\{u\} = \{u\}(t)$ – vector of values of the coefficients $u_{ijm}^{(k)(e)}$ at nodes on the finite-element of *k*-th layer; K_L – linear, and K_{NL} – nonlinear components of stiffness matrix; M – matrix of mass [5]. Stiffness and mass matrices composed from *M* matrices for each layer.

For solving discretized problem (18) perturbation method is used, that is described in [5, 6].

6. Numerical results

6.1. Verification of the proposed technique

Consider a cylindrical five-layer panel, the edges of which are fixed by hinges at the bottom of the front plane (see Fig. 1.) with geometrical $l = 1$ m; $h = 0,01$ m and physical-mechanical characteristics:

$$E_1 = 40E_2, \quad G_{12} = G_{13} = 0{,}6E_2, \quad G_{23} = 0{,}5E_2, \quad \nu_1 = 0{,}25.$$

For the analysis of reliability of the results we applied the proposed technique to the problem, the solutions of which are known [4]. Consider a cylindrical panel with radius curvature $K = 0$. For finding the values of natural frequencies apply partition at 50 finite elements by coordinate α_1.

In Table 1 compared the values ω_{NL} / ω_L obtained at the amplitudes $\frac{w_{\max}}{h}$ for free vibrations of five-layered panel with the results from the work [4].

Table 1.

$\frac{w_{\max}}{h}$	ω_{NL}/ω_L	
	[4]	Proposed technique
0,2	1,0313	1,0401
0,4	1,1198	1,1214
0,6	1,2536	1,2695
0,8	1,4199	1,4418
1,0	1,6086	1,6588
1,2	1,8127	1,8627

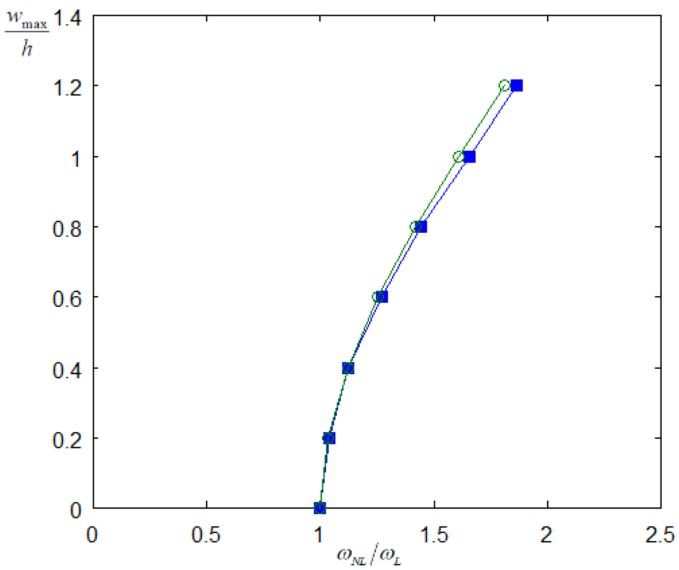

Figure 2. Comparison of amplitude-frequency characteristics obtained using the method of perturbation and results of work [4]

Fig. 2 shows the skeletal curves [11], constructed using the proposed technique (■) and the results given in the work [4] (o).

Also, the influence of the radius of curvature K on the free vibrations of the panel is investigation. Fig. 3 shows the dependence of the lowest natural frequency of the radius of curvature of five-layered panels from carbon fiber.

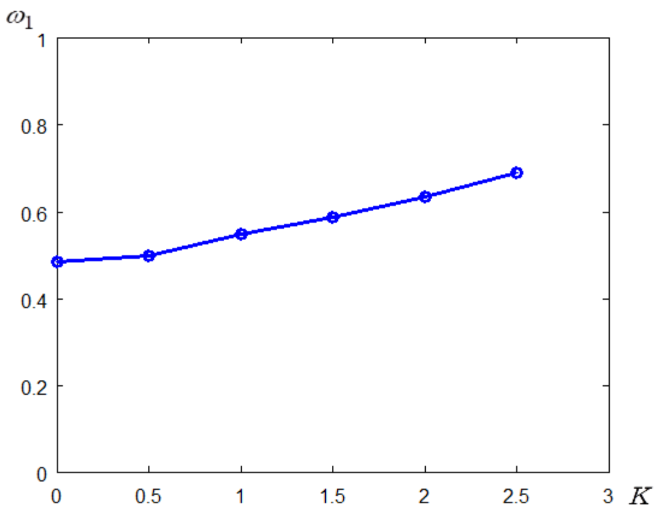

Figure 3. Dependence of the lowest natural frequency of the radius of curvature of the cylindrical panels

The maximum relative error in the Table 1 does not exceed 3%, which shows the effectiveness of the proposed technique. Comparative analysis of the graphs in Fig. 2 shows the reliability of the results obtained using proposed technique. Also established, that the main amplitude of natural vibrations increases with increasing radius curvature of the panel.

6.2. Three-layered panel

We considered a layered plate-strip with elongated edges that are fixed with stationary hinges on the lower plane (see Fig. 4). Geometrical characteristics of plane are $l = 1\,m$, $h = 0{,}1\,m$. It consists of three layers with following characteristics:

1) Rubber – $E = 0.1 \cdot 10^9\ N/m^2$, $\nu = 0{,}49$;
2) Steel – $E = 210 \cdot 10^9\ N/m^2$, $\nu = 0{,}3$.

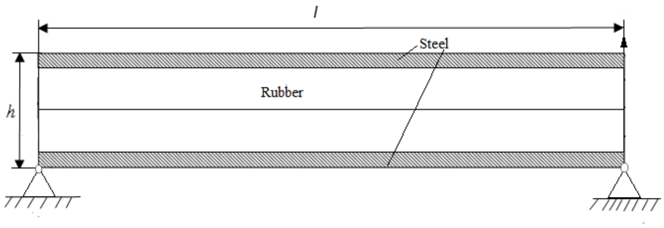

Figure 4. Panel with three layers

In Table 2 first five natural frequencies is shown for panel consisting of three layers where steel layers have thickness 0.01*m* and rubber has thickness 0.08*m*.

[1] Table 2.

n	ω_n
1	283000
2	1019000
3	1457300
4	1839600
5	2615200

In Table 3 dependency between first natural frequencies and thickness of middle layer (rubber layer) thickness is shown.

[2] Table 3.

$\frac{h_{rubber}}{h}$	ω_1
0.9	225650
0.8	283000
0.7	372770
0.6	490850
0.5	635100

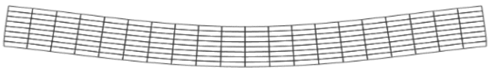

a)

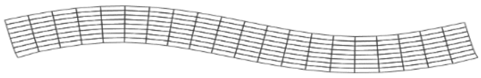

b)

Figure 5. View panels in different modes: a) – the first mode; b) – second

In the Fig. 5 we show the vibrations of the structure for first and second modes of the panel consisting of three layers where the steel layers have the thickness 0.01*m* and the rubber has the thickness 0.08*m.*

[3] Table 4.

K	ω_1
0	283000
0.5	254200
1	232000
2	218700

In Table 4 dependency between the radius of curvature and first natural frequency of the panel that consists of three layers where the steel layers have thickness 0.01*m* and the rubber has thickness 0.08*m* is shown.

For considered above panel we can make next conclusions:

1. the more matrix (rubber) component are included in the panel, the less is the first natural frequency;
2. the more radius curvature is the panel, the less is the first natural frequency of it.

7. Conclusion

We can make a conclusion that the method proposed in this paper is suitable for the layered panel because it provides logical results (Fig.5). Also this method can use at arbitrary amount of layers in the panel.

References

1. M. Amabili, *Nonlinear vibrations and stability of shells and plates*, Cambridge: Cambridge Univ. Press, 2008.
2. M. Amabili, *Nonlinear vibrations of rectangular plates with different boundary conditions: theory and experiments*, Comput. Struct., **82 (**2004) 2587 – 2605.
3. V. D. Kubenko, P. S. Kovalchuk, N. P. Podchasov, *Nonlinear vibrations of cylindrical shells*, K.: Vyshcha Shkola, 1989.
4. L. V. Kurpa, N. A. Budnikov, *Investigation of forced nonlinear vibrations of laminated shallow shells using a multimode approximation*, Bulletin of Donetsk Univ. Series A. Natural Sciences, **1** (2013) 55 – 60.
5. R. Lewandowski, *Analysis of strongly nonlinear free vibration of beams using perturbation method*, Civil and Env. Eng. Reports, **1** (2005) 153 – 168.
6. M. Marchuk, T. Goriachko, V. Pakosh *Geometrically Nonlinear Free Transversal Vibrations of Thin-Walled Elongated Panels with Arbitrary Generatrix*, Vibrations in Physical Systems, **26** (2014) 153 – 160.
7. M. Marchuk, I. Mukha, T. Goriachko, *A comparative analysis of the characteristics of geometrically nonlinear stress-strain state of composite plates and cylindrical panels on the basis refied model and elasticity theory*, Modeling and Stability: Abstracts of Conference Reports, K: Taras Shevchenko National Univ. of Kyiv, 2011.
8. M. Marchuk, V. Pakosh, O. Lesyk, I. Hurayewska, *Influence of Pliability to Transversal Deformations of Shear and Compression on Correlation Frequency from Amplitude for Nonlinear Oscillations of Composite Plates*, Vibrations in Physical Systems, **22** (2006) 251 – 256.
9. N. F. Morozov, *Selected two-dimensional problem of elasticity theory*, Leningrad: Publishing House of Leningrad. University Press, 1978.
10. J. N. Reddy, *An introduction to nonlinear finite element analysis*, Oxford Univ. Press, 2004.
11. S. Volmir, *Nonlinear dynamics of plates and shells*, M.: Nauka, 1972.

Vibrations of Periodic Sandwich Plates with Inert Core

Jakub MARCZAK
Department of Structural Mechanics, Łódź University of Technology
Al. Politechniki 6, 90-924 Łódź, jakub.marczak@p.lodz.pl

Jarosław JĘDRYSIAK
Department of Structural Mechanics, Łódź University of Technology
Al. Politechniki 6, 90-924 Łódź, jarek@p.lodz.pl

Abstract

In this note a free vibration analysis of periodic three-layered sandwich structures is performed. The equations of motion of such structures, which are derived basing on Kirchhoff's thin plate theory, contain periodic, non-continuous and highly oscillating coefficients, which makes them difficult to solve. In this work, the tolerance averaging technique is applied in order to transform the mentioned system of equations into a form with constant coefficients, which takes into account the effect of the microstructure size. The differences between two modelling procedures are shown and discussed. Eventually, formulas for free vibration frequencies of an exemplary 2D structure are derived and an analysis of influence of certain varying material properties is performed.

Keywords: *periodic sandwich plates, inert core, tolerance averaging, free vibrations, microstructure effect*

1. Introduction

Composites are more and more widely used in modern engineering. The possibility of combining several different materials into one heterogeneous structure, which material properties are outstanding when compared to 'classic' homogeneous materials, is very tempting for many researchers. All that is needed, is a proper model of such structures, which can be used in design and optimization process.

In this article three-layered sandwich structures are considered. A typical sandwich structure consists of external layers, which are made of materials characterised by high mechanical properties, hence, they are main bearing parts of the whole structure, and an inner layer, so called core, which is usually a light-weight, porous material, standing for thermal- and acoustic isolation. As a result, we obtain a highly durable structure, which, properly designed, can be used in many branches of engineering, such as aviation or even space ship construction.

On the other hand, sandwich structures also have disadvantages, such as vulnerability to local buckling, initial imperfections or concentrated loadings. Moreover, the mathematical models of such structures are complicated, with unclear and experimentally not proved assumptions connected with distribution of stresses and deflections. That is why, many different approaches towards the analysis of dynamic behaviour of such structures can be found in literature. Let us mention classic Euler-Bernoulli deflection hypothesis, Reissner-Mindlin's first order deformation theory, together with its extension to n^{th}-order deformation, or Zig-Zag hypothesis. For the exact description of above mentioned approaches, one should refer to Magnucki [1], Carrera [2] or Carrera and Brischetto [3], among others. In this work, let us concentrate on one of the most simple approach, which can be found in the works of Chonan [4], Oniszczuk [5] or Szcześniak [6], just to name few. In this approach, a three-layered sandwich structure is considered as a system of two Kirchhoff's type thin plates (outer layers), connected with each other by elastic Winkler's type material. Such assumption is well-fitted to our expectations, in which light-weight elastic core increase the stiffness of the structure by increasing its thickness, rather than being its bearing part.

In all above mentioned approaches, considered structures are characterised by constant geometry and are made of homogeneous or quasi-homogeneous materials. However, most recent sandwich structures contain certain varying geometry and/or material properties (especially the core can take very complicated shapes). As a result, governing equations of such structures have non-continuous and highly-oscillating coefficients, which make them difficult to solve. An answer to this problem can be the application of finite element method analysis. However, the optimization process with the use of such approach can be much time-consuming and ineffective. That is why, in this work one can find a mathematical model describing the vibrations of sandwich structure, which every layer can be characterised by periodic microstructure.

Solution to such problem was investigated by many researchers, for example by Brillouin [7], Mead [8] or Kohn and Vogelius [9], who created the basis of the asymptotic homogenisation method for plates. However, these models neglect the influence of microstructure on the behaviour of considered structures. The main aim of this paper is to derive a simple and useful model, which allows us to take into account this effect, with the use of the tolerance averaging technique, presented by Woźniak and Wierzbicki [10] or Woźniak et al. (eds.) [11], [12]. Eventually, as a result of two modelling procedures (*tolerance modelling* and *asymptotic-tolerance modelling*), free vibration frequencies of an exemplary rectangular sandwich plate are calculated.

2. Modelling foundations

Let $Ox_1x_2x_3$ be an orthogonal Cartesian coordinate system, where $\boldsymbol{x}\equiv(x_1,x_2)$, $x_3\equiv z$, and let us denote t as a time coordinate. The three-layered plate under consideration is assumed to have spans L_1 and L_2 in x_1 and x_2-axis directions, respectively, and total thickness $H(\boldsymbol{x})$. Hence, it can be stated, that undeformed structure occupies the region $\Omega\equiv[0,L_1]\times[0,L_2]\times[-\frac{1}{2}H(\boldsymbol{x}),\frac{1}{2}H(\boldsymbol{x})]$.

Let us assume, that both outer layers are Kirchhoff's type thin plates. Moreover they are made of the same set of materials and they have the same geometry, hence, all material and mechanical properties of these layers are the same, cf. Figure 1. Let us introduce their bending stiffness $B_{\alpha\beta\gamma\delta}(\boldsymbol{x},t)$ and mass density per unit area $\mu(\boldsymbol{x},t)$ as:

$$B_{\alpha\beta\gamma\delta}(\boldsymbol{x},z)=\int_{-h(\boldsymbol{x})/2}^{h(\boldsymbol{x})/2}C_{\alpha\beta\gamma\delta}(\boldsymbol{x},z)z^2dz,\qquad \mu(\boldsymbol{x},z)=\int_{-h(\boldsymbol{x})/2}^{h(\boldsymbol{x})/2}\rho(\boldsymbol{x},z)dz, \tag{1}$$

where $h(\boldsymbol{x})$ is the thickness of the outer layers, $C_{\alpha\beta\gamma\delta}(\boldsymbol{x},z)$ is their elastic modulus tensor and $\rho(\boldsymbol{x},z)$ is their mass density. Both outer layers are connected by an elastic Winkler's type material, so called *core*, characterized by elasticity modulus $k(\boldsymbol{x})$, mass density $\rho_c(\boldsymbol{x},z)$ and thickness $h_c(\boldsymbol{x})$.

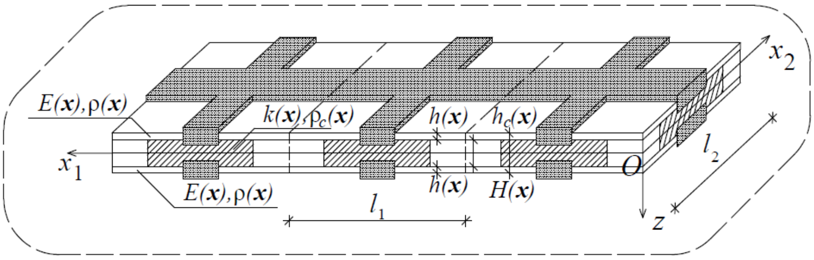

Figure 1. A part of periodic sandwich plate

The whole structure is build of small, repeatable elements, called *periodicity cells*. Every cell has dimensions l_1 and l_2 in x_1- and x_2-axis direction, respectively, while its diameter is referred to as to the *microstructure parameter l*. It is assumed, that dimensions of the plate and the microstructure parameter must satisfy following normalizing conditions: $h(\boldsymbol{x}) << l << \min(L_1, L_2)$, hence, the outer layers of the structure can be treated as thin plates not only in a macro-scale, but also when a single periodicity cell is considered.

Let us follow the simplified approach presented by Szcześniak [6]. According to the Kirchhoff's type thin plate theory, governing equations of this structure takes the form:

$$\begin{aligned}\partial_{\alpha\beta}(B_{\alpha\beta\gamma\delta}\partial_{\gamma\delta}u_1)+\mu\ddot{u}_1+k(u_1-u_2)=f_1,\\ \partial_{\alpha\beta}(B_{\alpha\beta\gamma\delta}\partial_{\gamma\delta}u_2)+\mu\ddot{u}_2+k(u_2-u_1)=f_2,\end{aligned} \tag{2}$$

where $u_1(\boldsymbol{x},t)$, $u_2(\boldsymbol{x},t)$ are deflections of upper and lower outer layers along z-axis direction, respectively, and $f_1(\boldsymbol{x},t)$, $f_2(\boldsymbol{x},t)$ are their loadings, defined as:

$$f_1 \equiv p_1 - \tfrac{1}{2}\mu_c\ddot{u}_1, \qquad f_2 \equiv p_2 - \tfrac{1}{2}\mu_c\ddot{u}_2, \qquad \mu_c = \int_{-h_c(\boldsymbol{x})/2}^{h_c(\boldsymbol{x})/2}\rho_c(\boldsymbol{x},z)dz, \tag{3}$$

where $p_1(\boldsymbol{x},t)$, $p_2(\boldsymbol{x},t)$ are external loadings applied to outer layers of the structure. It should be emphasized, that coefficients in system of equations (2) are periodic, non-continuous and highly oscillating. In order to derive a system of governing equations with constant coefficients, the tolerance averaging technique will be used.

3. Basic modelling assumptions of the tolerance averaging technique

The whole modelling procedure with the use of the tolerance averaging technique uses several introductory concepts, such as: *an averaging operator*, a *slowly varying function*, a *tolerance-periodic function* or a *highly oscillating function.* The idea standing behind those concepts, as well as a detailed description of the tolerance averaging technique, can be found in a various literature, for example by Woźniak and Wierzbicki [10] or by Woźniak et al. (eds.) [11], [12].

Let us introduce the definition of the *averaging operator*, which for an arbitrarily chosen basic periodicity cell $\Delta(\boldsymbol{x})$ can be formulated as follows:

$$<\partial^k f>(\boldsymbol{x}) = \frac{1}{|\Delta|}\int_{\Delta(\boldsymbol{x})} \tilde{f}^{(k)}(\boldsymbol{x},y)dy, \tag{4}$$

where $\tilde{f}^{(k)}(\boldsymbol{x},y)$ is periodic approximation of k^{th} gradient of certain function $f(\boldsymbol{x})$.

There are two main assumptions of the tolerance averaging technique. The first of them is *the micro-macro decomposition*, which stands, that the deflections of outer plates u_1, u_2 can be formulated as sums of macrodeflections $w_1(\boldsymbol{x},t)$, $w_2(\boldsymbol{x},t)$ and products of mode shape functions $g_1^A(\boldsymbol{x})$, $g_2^B(\boldsymbol{x})$ and fluctuation amplitudes $v_1^A(\boldsymbol{x},t)$, $v_2^B(\boldsymbol{x},t)$:

$$\begin{aligned} &u_1(\boldsymbol{x},t) = w_1(\boldsymbol{x},t) + g_1{}^A(\boldsymbol{x}) v_1{}^A(\boldsymbol{x},t), \\ &u_2(\boldsymbol{x},t) = w_2(\boldsymbol{x},t) + g_2{}^B(\boldsymbol{x}) v_2{}^B(\boldsymbol{x},t), \qquad A,B = 1,\ldots,N. \end{aligned} \tag{5}$$

Both macrodeflections $w_1(\boldsymbol{x},t)$, $w_2(\boldsymbol{x},t)$ and fluctuation amplitudes $v_1^A(\boldsymbol{x},t)$, $v_2^B(\boldsymbol{x},t)$ are basic unknowns, additionally assumed to be slowly varying functions for every t.

The second assumption contain *the tolerance averaging approximations*. By introducing certain given 'a priori' *tolerance parameter* δ and keeping in mind properties of functions mentioned as introductory concepts, it is possible to prove the following equations:

$$\begin{aligned} &< \Phi > (x) = < \overline{\Phi} > (x) + O(\delta), \qquad < \Phi F > (x) = < \Phi > (x) F(x) + O(\delta), \\ &< \Phi \partial_\alpha (gF) > (x) = < \Phi \partial_\alpha g > (x) F(x) + O(\delta), \end{aligned} \tag{6}$$

where Φ is tolerance-periodic function, $\overline{\Phi}$ is periodic approximation of Φ, F is slowly varying function, g is highly oscillating function and $O(\delta)$ is negligibly small term, $0<\delta<<1$.

4. Tolerance modelling procedure and model equations

The starting point of the tolerance modelling procedure is the system of equations (2) together with denotations (3). By applying *the averaging operator* to (2) and transforming it with the use of both *the micro-macro decompositions* and *the tolerance averaging approximations*, the averaged form of system of equations (2) can be obtained in the form:

$$\begin{aligned} &\partial_{\alpha\beta}(< B_{\alpha\beta\gamma\delta} > \partial_{\gamma\delta} w_1 + < B_{\alpha\beta\gamma\delta} \partial_{\gamma\delta} g_1^A > v_1^A) + < \mu + \tfrac{1}{2}\mu_c > \ddot{w}_1 + \\ &+ < k > (w_1 - w_2) + \underline{< k g_1^A >} v_1^A - \underline{< k g_2^B >} v_2^B = < p_1 >, \\ &< B_{\alpha\beta\gamma\delta} \partial_{\alpha\beta} g_1^A > \partial_{\gamma\delta} w_1 + < B_{\alpha\beta\gamma\delta} \partial_{\alpha\beta} g_1^A \partial_{\gamma\delta} g_1^B > v_1^A + \underline{< (\mu + \tfrac{1}{2}\mu_c) g_1^A g_1^B >} \ddot{v}_1^A + \\ &+ \underline{< k g_1^B >}(w_1 - w_2) + \underline{< k g_1^A g_1^B >} v_1^A - \underline{< k g_2^A g_1^B >} v_2^A = \underline{< p_1 g_1^B >}, \\ &\partial_{\alpha\beta}(< B_{\alpha\beta\gamma\delta} > \partial_{\gamma\delta} w_2 + < B_{\alpha\beta\gamma\delta} \partial_{\gamma\delta} g_2^A > v_2^A) + < \mu + \tfrac{1}{2}\mu_c > \ddot{w}_2 + \\ &+ < k > (w_2 - w_1) + \underline{< k g_2^A >} v_2^A - \underline{< k g_1^B >} v_1^B = < p_2 >, \\ &< B_{\alpha\beta\gamma\delta} \partial_{\alpha\beta} g_2^B > \partial_{\gamma\delta} w_2 + < B_{\alpha\beta\gamma\delta} \partial_{\alpha\beta} g_2^A \partial_{\gamma\delta} g_2^B > v_2^A + \underline{< (\mu + \tfrac{1}{2}\mu_c) g_2^A g_2^B >} \ddot{v}_2^A + \\ &+ \underline{< k g_2^B >}(w_2 - w_1) + \underline{< k g_2^A g_2^B >} v_2^A - \underline{< k g_1^A g_2^B >} v_1^A = \underline{< p_2 g_2^B >}. \end{aligned} \tag{7}$$

The above system of equations constitute *the tolerance model of the periodic sandwich structures under consideration*. It is the system of $2N$+2 partial differential equations with constant coefficients, where the exact number of equations depends on the amount of assumed mode shape functions g_1^A, g_2^B, A,B = 1,...,N. System of equation (7) should be followed by four boundary conditions for every macrodeflection and a two initial conditions for every unknown function. It can be also observed, that only the underlined terms in (7) are dependent on *the microstructure parameter l*.

5. Asymptotic-tolerance modelling procedure and model equations

The asymptotic-tolerance model can be obtained in two steps, which are described for example by Woźniak et al. [12] or for plates by Kaźmierczak and Jędrysiak [13]. In the first step, the asymptotic solution to the problem is derived. In our considerations it can be obtained by omitting the underlined terms in equations (7). As a result, we arrive at:

$$\begin{aligned}&\partial_{\alpha\beta}(<B_{\alpha\beta\gamma\delta}>\partial_{\gamma\delta}w_1+<B_{\alpha\beta\gamma\delta}\partial_{\gamma\delta}g_1^A>v_1^A)+<\mu+\tfrac{1}{2}\mu_c>\ddot{w}_1+<k>(w_1-w_2)=<p_1>,\\&<B_{\alpha\beta\gamma\delta}\partial_{\alpha\beta}g_1^A>\partial_{\gamma\delta}w_1+<B_{\alpha\beta\gamma\delta}\partial_{\alpha\beta}g_1^A\partial_{\gamma\delta}g_1^B>v_1^A=0,\\&\partial_{\alpha\beta}(<B_{\alpha\beta\gamma\delta}>\partial_{\gamma\delta}w_2+<B_{\alpha\beta\gamma\delta}\partial_{\gamma\delta}g_2^A>v_2^A)+<\mu+\tfrac{1}{2}\mu_c>\ddot{w}_2+<k>(w_2-w_1)=<p_2>,\\&<B_{\alpha\beta\gamma\delta}\partial_{\alpha\beta}g_2^B>\partial_{\gamma\delta}w_2+<B_{\alpha\beta\gamma\delta}\partial_{\alpha\beta}g_2^A\partial_{\gamma\delta}g_2^B>v_2^A=0.\end{aligned}\tag{8}$$

By analyzing the above system of equations, one can observe, that it can be easily transformed into a system of two equations with unknowns macrodeflections. Hence, macro-scale vibrations can be estimated regardless of the micro-scale fluctuations.

In the second step, an additional micro-macro decomposition, with the use of already known macrodeflections $w_1{}^0$, $w_2{}^0$, is applied to system of equations (2):

$$u_1(\boldsymbol{x},t)=w_1^0(\boldsymbol{x},t)+\hat{g}_1{}^A(\boldsymbol{x})V_1{}^A(\boldsymbol{x},t),u_2(\boldsymbol{x},t)=w_2^0(\boldsymbol{x},t)+\hat{g}_2{}^B(\boldsymbol{x})V_2{}^B(\boldsymbol{x},t).\tag{9}$$

Following the tolerance modelling procedure, after several manipulations, we arrive at the system of differential equations for fluctuation amplitudes $V_1{}^A(\boldsymbol{x},t)$, $V_2{}^B(\boldsymbol{x},t)$:

$$\begin{aligned}&<B_{\alpha\beta\gamma\delta}\partial_{\alpha\beta}\hat{g}_1^A\partial_{\gamma\delta}\hat{g}_1^B>V_1{}^A+\underline{<(\mu+\tfrac{1}{2}\mu_c)\,\hat{g}_1^A\hat{g}_1^B>}\ddot{V}_1{}^A+\underline{<k\hat{g}_1^A\hat{g}_1^B>}V_1{}^A+\\&-\underline{<k\hat{g}_2^A\hat{g}_1^B>}V_2{}^A=\underline{<p_1\hat{g}_1^B>}-<B_{\alpha\beta\gamma\delta}\partial_{\alpha\beta}\hat{g}_1^A>\partial_{\gamma\delta}w_1^0-\underline{<k\hat{g}_1^B>}(w_1^0-w_2^0),\\&<B_{\alpha\beta\gamma\delta}\partial_{\alpha\beta}\hat{g}_2^A\partial_{\gamma\delta}\hat{g}_2^B>V_2{}^A+\underline{<(\mu+\tfrac{1}{2}\mu_c)\,\hat{g}_2^A\hat{g}_2^B>}\ddot{V}_2{}^A+\underline{<k\hat{g}_2^A\hat{g}_2^B>}V_2{}^A+\\&-\underline{<k\hat{g}_1^A\hat{g}_2^B>}V_1{}^A=\underline{<p_2\hat{g}_2^B>}-<B_{\alpha\beta\gamma\delta}\partial_{\alpha\beta}\hat{g}_2^B>\partial_{\gamma\delta}w_2^0-\underline{<k\hat{g}_2^B>}(w_2^0-w_1^0).\end{aligned}\tag{10}$$

Systems of equations (8) and (10) together constitute *the asymptotic-tolerance model of the periodic sandwich structure under consideration.* As a result, using this modelling procedure allows to perform a simplified analysis of vibrations in only macro- or micro-scale without the necessity of evaluating both. The amount of boundary and initial conditions is the same as in the tolerance model.

6. Calculation example - the analysis of free vibrations

Let us consider a rectangular three-layered plate, which is simply supported on all four edges. It is assumed, that the relations between characteristic dimensions of the structure can be formulated as follows: $L_2/L_1=2$, $l_2/l_1=2$. The outer layers of the plate are assumed to be made of periodically varying isotropic materials, having different Young's modulus E_1, E_2 and densities ρ_1, ρ_2, but constant Poisson's ratio $\nu=0.2$ and thickness $h=0.1l_1$, cf. Figure 2.

Let us introduce only one mode-shape function, the same for both upper and lower outer layer. Moreover, in order to obtain comparable results, let it be the same function for both tolerance and asymptotic-tolerance models:

$$\begin{aligned}&G\equiv g_1{}^1=g_2{}^1=\hat{g}_1{}^1=\hat{g}_2{}^1=l_1{}^2\cos(2\pi x_1/l_1)\cos(2\pi x_2/l_2)+c,\\&c=l_1{}^2<\hat{\mu}\cos(2\pi x_1/l_1)\cos(2\pi x_2/l_2)>/<\hat{\mu}>,\qquad\qquad \hat{\mu}=\mu+\tfrac{1}{2}\mu_c.\end{aligned}\tag{11}$$

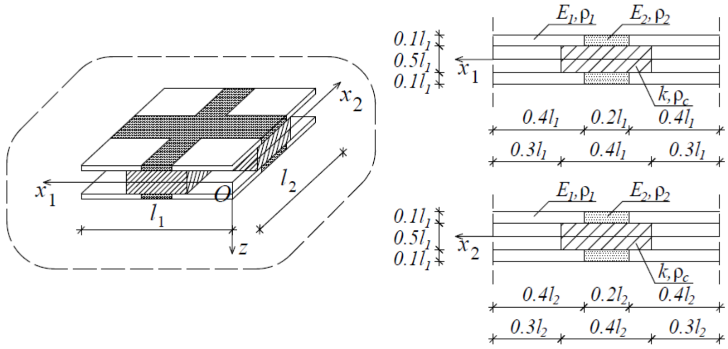

Figure 2. A periodicity cell of plate in the calculation example

By defining $A_{w_i}, A_{v_i}, A_{V_i}$ as amplitudes of unknowns, i = 1,2, λ_1, λ_2 as wave numbers and ω as a frequency, solutions to all governing equations can be assumed in the following forms, which satisfy boundary conditions:

$$
\begin{aligned}
&w_i(\boldsymbol{x},t) = A_{w_i}\sin(\lambda_1 x_1)\sin(\lambda_2 x_2)e^{i\omega t}, \\
&v_i(\boldsymbol{x},t) = A_{v_i}\sin(\lambda_1 x_1)\sin(\lambda_2 x_2)e^{i\omega t}, \qquad V_i(\boldsymbol{x},t) = A_{V_i}\sin(\lambda_1 x_1)\sin(\lambda_2 x_2)e^{i\omega t}.
\end{aligned} \tag{12}
$$

Let us neglect all external loadings. Free vibration frequencies are calculated by solving characteristic equations of homogeneous systems of equations (7) and (8), (10) and presented in dimensionless form, derived with the transformation below:

$$\overline{\omega} \equiv \omega[\rho_1 l_1^2 (E_1)^{-1}]^{0.5}. \tag{13}$$

Moreover, all calculations are performed for constant wave numbers: λ_1=0.1/l_1, λ_2=0.1/l_2. On charts in Figure 3 and 4 lower order frequencies are denoted as "*a*" and "*b*", while higher order frequencies as "*c*" and "*d*". Moreover, the tolerance model results are distinguished by subscript "1" and the asymptotic-tolerance model - by subscript "2".

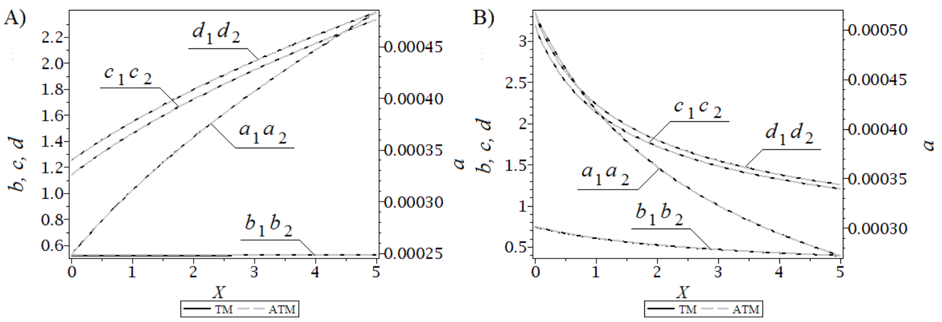

Figure 3. Dimensionless free vibrations frequencies' parameters $\overline{\omega}$ versus parameter X:
A) E_2=XE_1, ρ_2=2ρ_1, k=0.03E_1/l_1, ρ_c=0.03ρ_1,
B) E_2=2E_1, ρ_2=$X\rho_1$, k=0.03E_1/l_1, ρ_c=0.03ρ_1

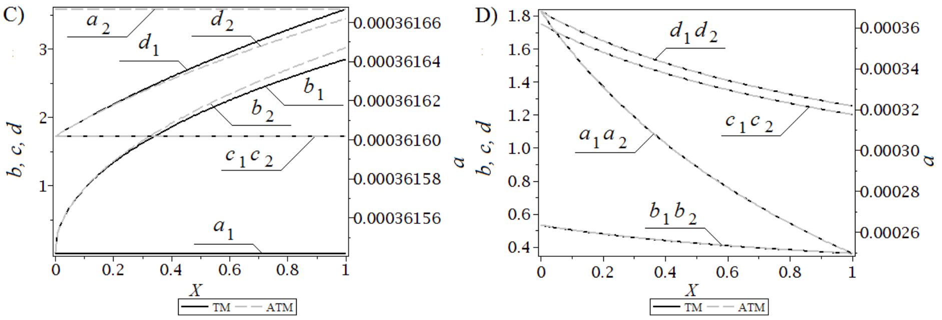

Figure 4. Dimensionless free vibrations frequencies' parameters $\overline{\omega}$ versus parameter X:
C) $E_2=2E_1$, $\rho_2=2\rho_1$, $k=XE_1/l_1$, $\rho_c=0.03\rho_1$,
D) $E_2=2E_1$, $\rho_2=2\rho_1$, $k=0.03E_1/l_1$, $\rho_c=X\rho_1$

7. Remarks

In this article, two averaged models describing vibrations of periodic three-layered plates are presented. The simple model of sandwich plate, described by Szcześniak [6], is extended and modified with the use of two modelling procedures of the tolerance averaging technique, so as structures with periodic microstructure can also be analyzed. As a result of these modifications, systems of governing equations with constant coefficients are obtained and solved.

Basing on the considered calculation examples, it can be observed that results of both models are comparable even for structures with much varying material properties. Hence, presented solutions can be used in the process of optimization of mechanical properties of considered sandwich structures, as a simple and convenient way of estimating the frequency of vibrations.

In the future investigations, the consistency of the proposed averaged models with finite element method will be presented. Moreover, a physical correctness of derived models will be described and justified.

References

1. K. Magnucki, W. Szyc (eds.), *Strength and stability of three-layered beams and plates with aluminum foam core*, Publ. House of Poznań Univ. Technol., Poznań 2012.
2. E. Carrera, *Historical review of Zig-Zag theories for multilayers plates and shells*, Appl. Mech. Rev., **56** (2003) 287 – 308.
3. E. Carrera, S. Brischetto, *A survey with numerical assessment of classical and refined theories for the analysis of sandwich plates*, Appl. Mech. Rev., **62** (2009) 1 – 17.
4. S. Chonan, *Dynamical behaviour of elastically connected double-beam systems subjected to an impulsive load*, Bull. JSME, **19** (1976) 595 – 603.

5. Z. Oniszczuk, *Forced transverse vibrations of an elastically connected complex simply supported double-beam system*, J. Sound. Vibr., **264** (2003) 273 – 286.
6. W. Szcześniak, *Vibration of elastic sandwich and elastically connected double-plate system under moving loads*, Publ. Warsaw Univ. Technol., **132** (1998) 153 – 172.
7. L. Brillouin, *Wave propagation in periodic structures*, Dover Pub. Inc., Dover 1953.
8. D.J. Mead, *Wave propagation in continuous periodic structures: research contributions from Southampton*, J. Sound. Vibr., **190** (1996) 495 – 524.
9. R.V. Kohn, M. Vogelius, *A new model of thin plates with rapidly varying thickness*, Int. J. Solids Struct., **20** (1984) 333 – 350.
10. Cz. Woźniak, E. Wierzbicki, *Averaging techniques in thermomechanics of microheterogeneous solids and structures: Tolerance averaging versus homogenization*, Publ. House of Częstochowa Univ. Technol., Częstochowa 2000.
11. Cz. Woźniak, B. Michalak, J. Jędrysiak (eds.), *Thermomechanics of microheterogeneous solids and structures: Tolerance averaging approach*, Technical University of Łódź Press, Łódź 2008.
12. Cz. Woźniak (eds.), *Mathematical modelling and analysis in continuum mechanics of microstructured media*, Pub. House of Silesian Tech. Univ., Gliwice 2010.
13. M. Kaźmierczak, J. Jędrysiak, *A new asymptotic-tolerance model of vibrations of thin transversally graded plates*, Engn. Struct., **46** (2013) 322 – 331.

A Semi-Active Control of Lateral Vibrations of the Overhung Rotor Using Dampers with the Magneto-Rheological Fluid

Maciej MICHAJŁOW, Robert KONOWROCKI and Tomasz SZOLC
Institute of Fundamental Technological Research of the Polish Academy of Sciences
ul. A. Pawińskiego 5B, 02-106 Warszawa, mmich@ippt.pan.pl, tszolc@ippt.pan.pl

Abstract

In the paper there is proposed an algorithm of an efficient semi-active control of steady-state periodic lateral vibrations of the overhung rotor-shaft system. This algorithm has been developed using fundamentals of the Optimal Control Theory. In the considered system the control is realized by means of the linear dampers with the magneto-rheological fluid built in the bearing housing. The computational example demonstrates possibilities of the applied approach resulting in an additional reduction of out-of-resonance and near-resonance harmonic oscillation amplitudes in comparison with an analogous passive control.

Keywords: overhung rotor-shaft, lateral vibrations, semi-active control, Optimal Control Theory

1. Introduction

Heavy rotors suspended in bearings in an overhung way constitute a wide class of rotating machinery. Typical examples of this group are pumps, compressors, blowers, gas turbines, crushers, beater mills, drums of washing machines and many others. As it follows e.g. from [1,2], at high rotational speeds they are sensitive to gyroscopic effects associated by their lateral vibrations excited mainly by residual unbalances as well as by assembly misalignments, rubbing effects in bearings, sealings or blade rims and by other sources. Such oscillations are usually very detrimental and a suppression of their amplitudes is an important challenge in order to assure precise motions of such rotor-shaft systems, possibly small bearing reactions, minimized danger of material fatigue and low level of generated noise. This target can be effectively achieved by means of a semi-active control of lateral vibrations affecting the rotor-shaft systems with overhung rotors. For this purpose, similarly as e.g. in [3], actuators with the magneto-rheological fluid (MRF) are going to be applied. Such an approach seems to be very convenient for rotor machines like vacuum pumps, turbo-chargers, washing machines, precise spindles and others rotating with high speeds in steady-steady state operating conditions under harmonic external excitations due to residual unbalances and the mentioned above dynamic effects. It is to emphasize that, contrary to a control of transient or resonant vibrations, for which many algorithms turned out to be effective, a suppression of forced, steady-state oscillations with frequencies far away from resonance zones is an extremely difficult task. Here, in cases of the abovementioned rotor machines even a few-percent minimization of fluctuation amplitudes can be very fruitful from the viewpoint of material fatigue, precision of motion, dynamic interaction with an environment, detrimental noise generation and many other factors. Thus, in order to achieve this target, in the paper for the actuators with the MRF a control strategy based on the

Optimal Control Theory (OCT) will be applied for the high-speed overhung rotor-shaft under steady-state harmonic lateral vibrations. The obtained results of simulations are going to be compared with the analogous ones determined for additional passive damping applied into the considered system as well as using the numerical optimization control algorithm.

2. Modelling of the rotor-shaft and mathematical formulation of the problem

In many cases the high-speed rotating machines are characterized by heavy, lumped overhung rotors attached on short, dumpy shafts suspended on relatively flexible bearing supports. Thus, deformations of such rotor-shafts can be neglected and then only rotor-shaft inertial parameters and bearing support visco-elastic properties play a predominant role in lateral vibrations of these objects. According to [1], if a maximal static deflection of such rotor-shaft is of the same order as the bearing clearances, its dynamic behaviour can be investigated by means of a rigid body model of four degrees of freedom. Then, the generalized coordinates corresponding to them describe two translational displacements of the rigid body mass center in the two mutually perpendicular directions with respect of the rotor-shaft rotation axis as well as two angular displacements with respect of mutually perpendicular axes passing the mass center of this rigid body. In order to take into consideration a rotor-shaft support in a possibly general way, the anisotropic and non-symmetrical visco-elastic properties of bearings have been assumed in the form of stiffness and damping coefficients containing also the proper cross-coupling terms. The proposed rigid body model of the overhung rotor shaft supported on two bearings is presented in Fig. 1.

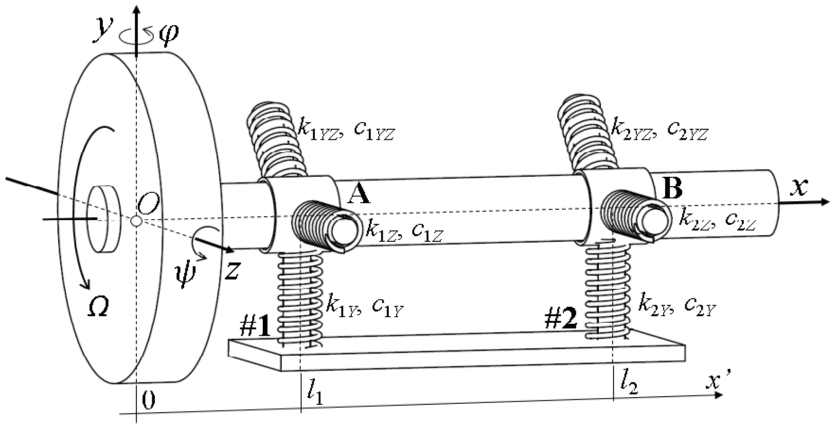

Figure 1. The rigid-body model of the double-bearing overhung rotor

Motion of the rotor-shaft has been described in the inertial orthogonal coordinate system *Oxyz* with the origin placed in the rigid body model center of gravity *O*. Axis *Ox* coincides with the bearing axis and axes *Oy*, *Oz* respectively determine the vertical and horizontal direction. The plains of bearing interaction cross *Ox* axis in points A and B distant of l_1 in the case of bearing #1 and of l_2 in the case of bearing #2, as shown in Fig.

1. The motion equation of the assumed rotor-shaft rigid body model have the following form:

$$\mathbf{M}\cdot\ddot{\mathbf{r}}(t)+\left(\mathbf{C}+\Omega\cdot\mathbf{G}\right)\cdot\dot{\mathbf{r}}(t)+\mathbf{K}\cdot\mathbf{r}(t)=\mathbf{F}\left(t,\Omega^2\right) \tag{1}$$

where $\mathbf{r}(t)$= col [$y(t)$, $z(t)$, $\psi(t)$, $\varphi(t)$] is the generalized coordinate vector with components corresponding respectively to the translational displacements along *Oy* and *Oz* axes and to the angular displacements around *Oz* and *Oy* axes. Symbol **M** denotes the diagonal inertial matrix, **C** and **K** are respectively the symmetrical bearing damping and stiffness matrices and **G** is the skew-symmetrical matrix of gyroscopic effects. The external excitation vector **F** has the following components:

$$\mathbf{F}\left(t,\Omega^2\right)=\begin{bmatrix} Mg+M\varepsilon\cdot\Omega^2\sin(\Omega t)+U(t) \\ M\varepsilon\cdot\Omega^2\cos(\Omega t)+V(t) \\ 0 \\ 0 \end{bmatrix} \tag{2}$$

where ε is the eccentricity of the rotor-shaft residual static unbalance, *M* denotes the entire mass of the rigid rotor and $U(t)$, $V(t)$ are the control forces acting in the vertical and horizontal direction, respectively. Such equations are very convenient here for a demonstration of relatively easy implementation of the proposed algorithm of semi-active control of the steady state forced lateral vibrations of the considered object.

The rotating machines usually operate in steady-state conditions at constant rotational speeds, more or less far away from the critical ones associated with the corresponding lateral eigenvibration modes. Thus, the goal of this paper is to propose a computationally effective numerical method for determination of the optimal control function applied here for the mechanical system under periodical vibrations due to the residual unbalance. In order to distinguish such successive mutually uncoupled eigenmodes of the considered gyroscopic, nonconservative rotor-shaft system, it is necessary to perform a complex modal analysis of Eqs. (1) according e.g. to the approach presented in [2,4]. Then, the investigations reduce to control of steady-state harmonic oscillations of simple single degree-of-freedom oscillators shown in Fig. 2 (a).

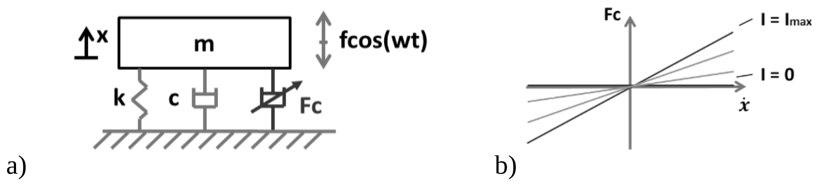

Figure 2. Single DOF dynamic oscillator (a), controllable damper force function (b)

An equation of motion of such oscillator has the following form:

$$m\cdot\ddot{x}(t)+c\cdot\dot{x}(t)+k\cdot x(t)=\kappa\cdot\left(f\cdot\cos(\Omega t-\varphi)-u(\dot{x}(t))\right) \tag{3}$$

where according to [4], the modal damping coefficient $c = 2\delta m$, the modal stiffness $k = \left(\delta^2 + \omega^2\right)m$, $\kappa = \left(\delta r - \omega s\right)$, m is the modal mass, δ, ω denote respectively the real and imaginary part of the complex eigenvalue corresponding to the considered eigenmode, r, s are respectively the real and imaginary part of the complex left eigenvector component, $x(t)$ denotes the modal displacement of the controlled eigenmode and φ is phase shift angle.

As shown in Fig. 2b, for the assumed linear relationship between the shaft/bearing vibratory velocity and the control force F_c generated by the MRF damper built in the bearing housing, one can express in (3): $F_c = u(\dot{x}(t))$, where u denotes the control variable. The slope of the damping force curve depends on the instant value of the control current I. Control current cannot exceed the boundary limits $I \in \langle 0, I_{max} \rangle$. Also, it is assumed that the control current can change its value instantly. Because the controllable damper characteristic is linear, it may be assumed that:

$$\begin{cases} u = I \\ u_{min} = I_{min} = 0 \\ u_{max} = I_{min} \end{cases} \tag{4}$$

For the simplification of further considerations it is convenient to transform Equation (3) into the state-space representation:

$$\begin{cases} \dot{q}_1 = q_2 \\ \dot{q}_2 = -\dfrac{k}{m}q_1 - \dfrac{c}{m}q_2 - \dfrac{\kappa}{m}(f\,cos(\Omega t) - uq_2) \end{cases} \tag{5}$$

where state variables are defined in the following form:

$$[\boldsymbol{q}] = \begin{bmatrix} x \\ \dot{x} \end{bmatrix} = \begin{bmatrix} q_1 \\ q_2 \end{bmatrix} \tag{6}$$

In order to define the optimal control problem it is necessary to introduce a performance index which will represent a measure of vibration level. One of possible choices is to select the performance index as a single scalar value that will represent the average motion mean energy of the considered system:

$$J = \int_0^{t_f} \left[\frac{1}{2}\left(kq_1^2 + mq_2^2\right) + ru^2 \right] dt = \int_0^{t_f} E dt \tag{7}$$

In the above equation, apart from the motion energy component$1/2(kq_1^2+mq_2^2)$, the other component has been added, namely ru^2. This expression refers to the amount of energy consumed by the controlled damping element. This component has been added into Eq. (7) in order to simplify further transformations. The term ru^2 should be treated as negligible, since a minimization of the control energy has not been considered as a primary goal for mechanical systems under periodical excitation. Therefore, it is assumed that scalar r nearly equals zero. Variable E denotes the integrand function.

Using the Optimal Control Theory (OCT) it is possible to derive the set of equations specifying the optimal control function profile u*, providing a minimization of functional *J*. For this purpose, it is necessary to apply the common OCT control function derivation procedure given in [5,6]. It starts with a definition of the Hamiltonian function:

$$H = E + \boldsymbol{\lambda}'\dot{\boldsymbol{q}} \tag{8}$$

Next, using the necessary condition for minimization of functional *J*, namely: $\delta J=0$, the following set of equations can be derived:

$$\begin{cases} \dot{\boldsymbol{q}} = \dfrac{\partial H}{\partial \lambda} \\ \dot{\boldsymbol{\lambda}} = -\dfrac{\partial H}{\partial \boldsymbol{q}} \\ H(\boldsymbol{q}^*, \boldsymbol{\lambda}^*, u^*) \le H(\boldsymbol{q}^*, \boldsymbol{\lambda}^*, u) \\ \boldsymbol{u} \in \langle 0, u_{max} \rangle \end{cases} \tag{9}$$

where $\boldsymbol{\lambda}$ denotes the costate vector. Upon an expansion of the third inequality standing in (9) and an application of the Pontryagin principle, finally the following set of equations defining the optimal control can be derived:

$$\begin{cases} \begin{cases} \dot{q}_1 = \dfrac{\partial H}{\partial \lambda_1} = q_2 \\ \dot{q}_2 = \dfrac{\partial H}{\partial \lambda_2} = -\dfrac{k}{m} q_1 - \dfrac{c}{m} q_2 + \dfrac{\kappa}{m}(f\, cos(\Omega t) - u q_2) \end{cases} \\ \begin{cases} \dot{\lambda}_1 = -\dfrac{\partial H}{\partial q_1} = -k q_1 + \dfrac{k}{m} \lambda_2 \\ \dot{\lambda}_2 = -\dfrac{\partial H}{\partial q_2} = -m q_2 - \lambda_1 + \dfrac{c}{m} \lambda_2 + \lambda_2 u \\ u^* = sat\left(sign\left(\lambda^*{}_2 q^*{}_2\right)\right) \end{cases} \end{cases} \tag{10}$$

In order to find exact function values, all equations of the above system have to be solved simultaneously. It requires a specification of boundary values of the state and costate vectors. For the considered vibrating system one can assume that under optimal control function this system will eventually fall into steady-state vibrations, starting from an arbitrary initial state condition. Different initial state conditions will only affect a duration time of the transient phase of motion up to the instant, when the steady-state vibration phase shall be established. Concluding, the initial condition for the state vector can be arbitrarily chosen as: $\boldsymbol{q}(0) = 0$.

The second condition follows directly from the fundamentals of the OCT. Provided that the considered system of Eqs. (10) has to be integrated in the finite time range $t \in \left\langle 0, T_f \right\rangle$, the optimal problem in the OCT nomenclature can be classified as *free-end*, *fixed-time* problem, [5]. The phrase "*free-end*" refers to a lack of constraints specified for the state vector at the end of the simulation time window. The phrase "*fixed-time*" refers to the finite value of the simulation time range T_f. For such kind of the optimal control problem the OCT provides the additional boundary condition, i.e.: $\boldsymbol{\lambda}(T_f)=0$.

Concluding, because the known boundary conditions are specified partially at the beginning and partially at the end of the simulation time window, this problem can be classified as the Two-Point Boundary Value Problem (TPBVP). The TPBVPs are generally considered as difficult numerical problems. In order to solve the TPBVP for the considered system, the following algorithm has been developed:

1. initialize the $\boldsymbol{\lambda}(0)$ vector with random values,
2. integrate the coupled state-costate equations on the time interval $\left\langle 0,T_f \right\rangle$ assuming $\boldsymbol{q}(0)=0$ and taking (0) from point 1,
3. after an integration check, whether terminal condition has been satisfied $\boldsymbol{\lambda}(T_f)=0$,
4. conditional step:
   a. if the terminal condition from step 3 has been satisfied, terminate the algorithm,
   b. if the terminal condition from step 3 has not been satisfied, find the new estimation of the (0) condition by means of the external, numerical optimization algorithm; then, repeat the steps 1-4 as long as terminal condition is not being satisfied.

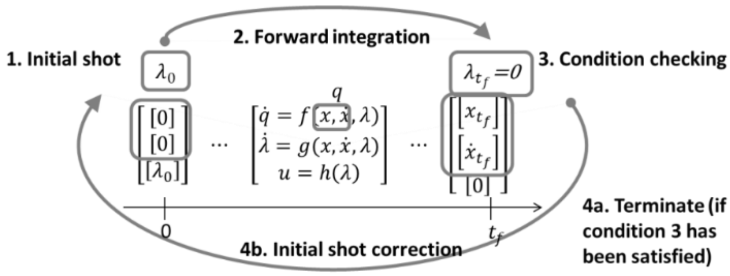

Figure 3. Optimal control problem computational algorithm

The algorithm described above can be illustrated by means of the following diagram presented in Fig. 3. It is important to choose the sufficiently large T_f value, so the steady-state phase of motion could be significantly longer than either transient phase at the beginning or at the end of the simulation time window.

3. Computational example

In the computational example the rigid overhung rotor-shaft of the industrial blower supported on two identical rolling bearings is used as an object of considerations. This rotor-shaft of a total weight ca. 60.13 kg and of the bearing span 0.275 m is characterized by a relatively heavy impeller and light shaft, as shown in Fig. 1. Its total polar and diametral mass moments of inertia are respectively equal to 7.02 and 12.75 kgm^2. It is assumed that bushings of the isotropic and radially stiff rolling bearings are embedded in the bearing housings by means of layers made of relatively soft and viscous vulcanized rubber. The bearing suspension stiffness coefficients are assumed constant within the entire shaft rotational speed range 0-7200 rpm.

In Fig. 4a there are presented the imaginary parts and in Fig. 4b the real parts of four eigenvalues of the considered rotor-shaft, where the grey lines correspond to the original system and the black ones to the system equipped with the MRF damper built in the bearing support #1 and operating passively. From the obtained plots it follows that

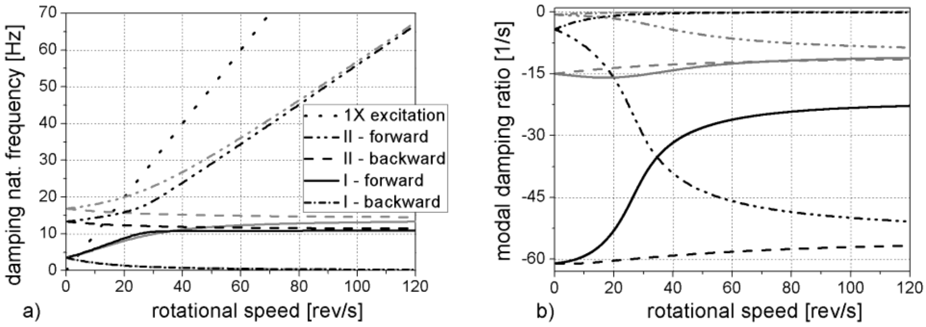

Figure 4. Imaginary (a) and real (b) parts of the rotor-shaft eigenvalues

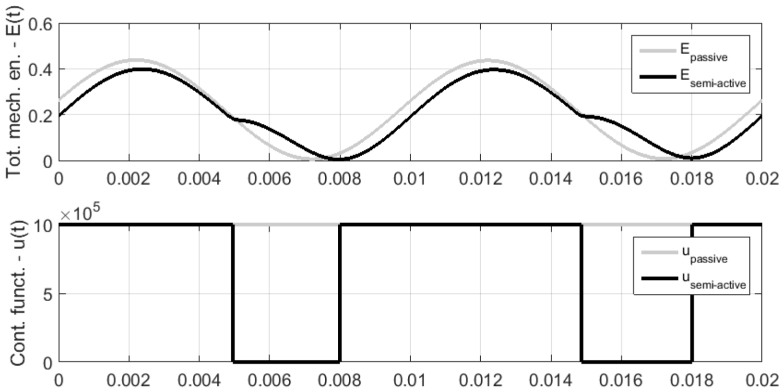

Figure 5. Entire vibratory mechanical energy profiles for the passive and semi-actively damped system for the 1st eigenmode backward precession of 6.1 Hz at 3000 rpm

the optimal passive control effectively stabilizes the backward and forward branches of the second eigenmode and the forward branch of the first eigenmode. But it has almost no influence on a stabilization of its backward branch characterized by the close to zero natural frequency and modal damping coefficient at greater rotational speeds, Fig. 4. However, the semi-active control realized using the MRF damper and the proposed control algorithm can result in an effective stabilization of this almost no damped backward precession of the 1st eigenmode excited here e.g. by means of periodic retarding frictional loads in the bearings. As shown in Fig. 5, the semi-active control minimizes fluctuation amplitudes of this backward mode by ca. 8%. Moreover, the semi-active control suppresses lateral vibration amplitudes even by 10% for the first eigenmode forward precession induced by unbalances at the overcritical rotational speed 110 rev/s, i.e. 6600 rev/min, as it follows from the time-history plots depicted in Fig. 6.

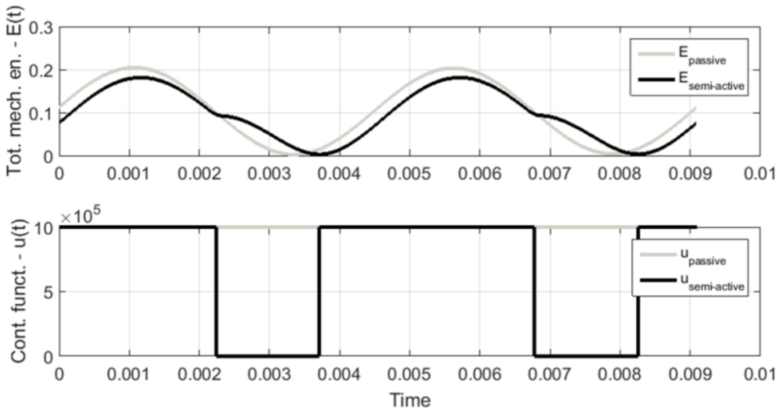

Figure 6. Entire vibratory mechanical energy profiles for the passive and semi-actively damped system for the 1st eigenmode forward precession of 13.67 Hz at 6600 rpm.

4. Conclusions

In the paper there were considered passively and semi-actively controlled periodic lateral vibrations of the rigid overhung rotor suspended on flexible bearings equipped with the MRF dampers. From the results of an eigenvalue analysis it follows that additional passive damping introduced into this system can effectively suppress its oscillation amplitudes and increase stability regions only for sufficiently stable eigenmodes. But it is not the case for unstable or almost stable eigenmodes, e.g. due to gyroscopic effects or skew-symmetrical bearing properties. Here, the semi-active control realized according to the proposed algorithm based on the Optimal Control Theory seems to be a very advantageous and universal tool for engineering applications tool for stabilization of vibrating mechanical systems and for an attenuation of their oscillation amplitudes.

References

1. R. Gryboś, *Dynamics of Rotor Machines*, Polish Sci. Publi. (PWN), Warsaw (1994).
2. G. Genta, *Dynamics of Rotating Systems*, Springer Science+Business Media, Inc. ISBN 0-387-20936-0, (2005).
3. P. Ferfecki, J. Zapoměl, *Investigation of vibration mitigation of flexibly support rigid rotors equipped with controlled elements*, Procedia Eng., **48** (2012) 135 – 142.
4. M. J. Patil, *Decoupled second-order equations and modal analysis of a general nonconservative system*, Proc. of the AIAA Dynamics Specialists Conference, Atlanta, Georgia, USA, April 3 – 6, (2000), AIAA-2000-1654.
5. E. G. Gilbert, *Optimal periodic control: A general theory of necessary conditions*, SIAM J. Control and Optimization, **15**(5) (1977).
6. M. Michajłow T. Szolc, Ł. Jankowski, R. Konowrocki, *Semi-active reduction of vibrations of periodically oscillating system*, Solid State Phen., **248** (2016) 111 – 118.

Influences of System Parameters on Energy Harvesting from Autoparametric Absorber. Numerical Research

Andrzej MITURA
Department of Applied Mechanics, Lublin University of Technology
Nadbystrzycka 36, 20-618 Lublin, a.mitura@pollub.pl

Krzysztof KECIK
Department of Applied Mechanics, Lublin University of Technology
Nadbystrzycka 36, 20-618 Lublin, k.kecik@pollub.pl

Abstract

In the paper a numerical analysis of an autoparametric system is presented. The two main elements of a tested system are the pendulum (tuned mass absorber) and an energy harvester. The electromechanical model takes into account these both effects. Numerical simulations are made in a MATLAB software environment. The obtained results allowed estimation of influence of the system parameters on efficiency of energy harvesting.

Keywords: Non-linear autoparametric system, Energy harvester, Vibration absorption, Magnetic induction

1. Introduction

Application of the pendulum to the vibration reduction is described in the literature as a tuned mass absorber. A gigantic pendulum (about 700 tons) is applied in skyscraper Taipei 101 building [1]. It is used to reduction of building's movement occurring during earthquakes and high winds. The similar problem was studied intensively at the Lublin University of Technology [2, 3]. The pendulum spring mass system shows regular or irregular (chaotic) responses. The irregular vibrations are very dangerous, especially for dynamic absorber devices.

In the last years the pendulum systems are intensively studied [2-4]. In application where the primary task of the pendulum is vibration reduction (buildings, ship, etc.) a special devices can be added to energy harvesting. An additional harvester can increase functionality of the original system. The new models take into account the possibility of recovery energy from the motion of the pendulum. Generally, in literature exists two different solutions: (I) the rotary harvester [4] and (II) the linear harvester [5]. The word *linear* describes the movement path of the magnet in relative to the pendulum. In this paper the second solution (linear) is proposed.

A strongly non-linear model of electromechanical system and results of simple numerical analysis are shown in paper [5]. In this paper more complex considerations are presented. Influence of the system parameters on induced current level is investigated in detail.

2. Electromechanical model of system

The total system consists of two main subsystems: mechanical and electrical parts. The parts are presented in Fig. 1(a) and (b), respectively. The mechanical subsystem has three basic elements:

- simple oscillator – mass *M* suspended on linear spring k_1 and damper *c*. It is excited kinematically by linear spring k_2.
- non-linear vibration absorber (tuned mass absorber)– pendulum mounted on the oscillator and applied to vibration reduction of mass *M*.
- energy harvester – generally, it is movable magnet located between two fixed magnets (polarity configurations: SN-NS-SN). In presented model this magnetic suspension of movable magnet is modelled as linear spring k_3, for small vibrations [6].

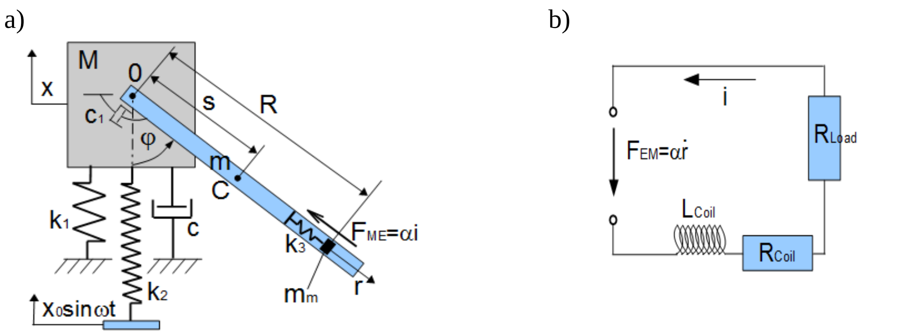

Figure 1. Model of a mechanical (a) and electrical (b) parts of the system

The movable magnet is moving inside the coil. This motion can generate current *i* in electrical circuit (Fig. 1(b)). Both parts, the electrical and the mechanical are coupled by equivalent forces F_{EM} and F_{ME}, which have the same values but opposite directions. These forces depend on the current and velocity of the moving magnet relative to the coil [7]. Differential equations of motion were derived using second kind of Lagrange's equations [5]. The final form of equation of motion has a form:

$$M\ddot{x} + m\ddot{x} + m\ddot{\varphi}s\sin\varphi + m\dot{\varphi}^2 s\cos\varphi + m_m\ddot{x} - m_m\ddot{r}\cos\varphi + 2m_m\dot{r}\dot{\varphi}\sin\varphi + \\ + m_m\ddot{\varphi}\left(R+r\right)\sin\varphi + m_m\dot{\varphi}^2\left(R+r\right)\cos\varphi + kx + c\dot{x} = Q\sin\omega t \tag{1}$$

$$I_0\ddot{\varphi} + m\ddot{x}s\sin\varphi + m_m\ddot{\varphi}\left(R+r\right)^2 + 2m_m\dot{\varphi}\dot{r}\left(R+r\right) + \\ + m_m\left(R+r\right)\ddot{x}\sin\varphi + mgs\sin\varphi + m_m g\left(R+r\right)\sin\varphi + c_1\dot{\varphi} = 0 \tag{2}$$

$$m_m\ddot{r} - m_m\ddot{x}\cos\varphi - m_m\dot{\varphi}^2\left(R+r\right) + k_3 r - m_m g\cos\varphi + \alpha i = 0 \tag{3}$$

and for the electrical part:

$$L_{Coil}\dot{i} + R_{Total}\,i = \alpha\dot{r}\,. \tag{4}$$

2. Numerical results

Numerical simulations of the equations (1-4) were made in MATLAB 2015 software using *ode15i* method. The mechanical and electrical parameters are shown in Tab. 1.

Table 1. Parameters of mechanical and electromechanical models

Description of parameter	Symbol	Unit	Value
The mass of the object main	M	kg	0.65
The mass of the pendulum	m	kg	0.265
The mass of the magnet	m_m	kg	0.02
The mass moment of inertia of the pendulum relative to the rotation axis	I_0	kgm^2	4.96e–4
Distance from the gravity center of the pendulum to the rotation axis	s	m	4.25e–2
Sum of stiffness coefficients of coil springs	$k = k_1 + k_2$	N/m	2700
The substitute stiffness of magnetic suspension of moving magnet	k_3	N/m	2000
Damping coefficient of linear damper	c	Ns/m	10
Damping coefficient of air resistance	c_1	Nms/rad	0.01
Distance from the gravity center of moving magnet to the rotation axis	R	m	3.75e-3
The coil inductance	L_{Coil}	H	1e-3
Sum of resistance of coil and external receiver	$R_{Total} = R_{Coil} + R_{Load}$	Ω	1200
Electromechanical coupling coefficient	α	N/A or Vs/m	3.5
Amplitude of periodic excitation	$Q = k_2 x_0$	N	110

All numerical simulations always start from the same initial conditions $[x, \dot{x}, \varphi, \dot{\varphi}, r, \dot{r}, i]_{initial} = [0, 0, \pi / 2, 0, 0, 0, 0]$. Non zero initial value of the pendulum steady variable φ or $\dot{\varphi}$ causes that semi-trivial solution becomes unstable (pendulum executes motion). This chapter presents influence of the electrical parameters on efficiency of energy harvesting. The following parameters were changed: L_{Coil} from 0 to 0.005 H (first analysis), R_{Total} from 500 to 2000 Ω (second analysis) and α from 0.5 to 5 N/A (third analysis) versus frequency of excitation ω from 20 to 50 rad/s. The efficiency of energy harvesting is described by the quality index. In this paper a simple form of index is proposed (root mean square of current i_{RMS}). RMS values were calculated in a time window $t \in \langle 0, 10 \rangle$ s.

a) b)

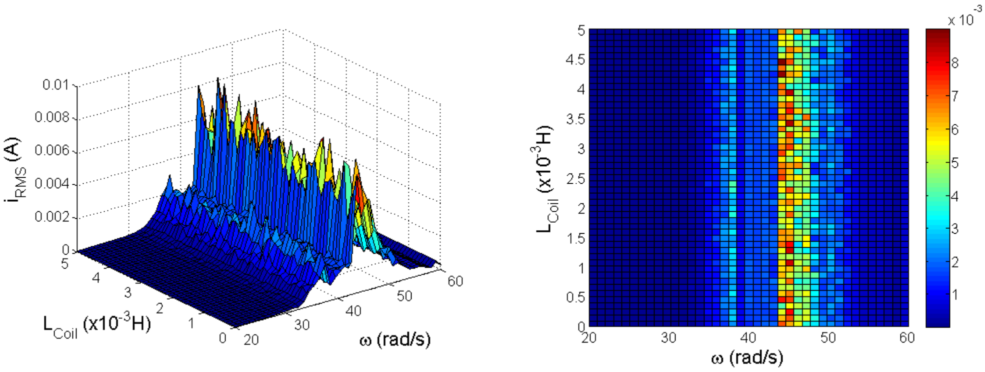

Figure 2. 3D characteristics i_{RMS} versus L_{Coil} and ω (a), and top view (b)

a) b)

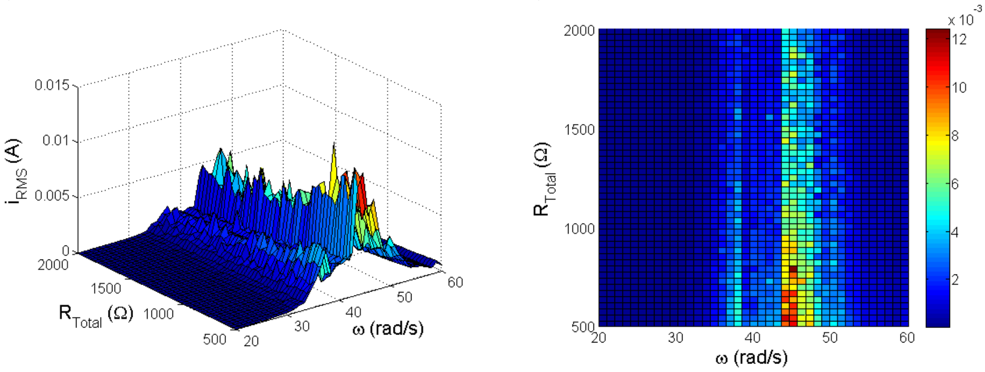

Figure 3. 3D characteristics i_{RMS} versus R_{Totall} and ω (a), and top view (b)

a) b)

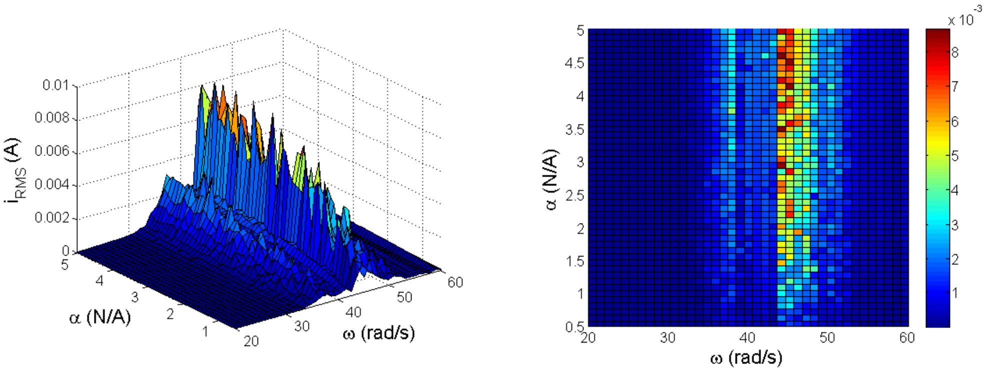

Figure 4. 3D characteristics i_{RMS} versus α and ω (a) and top view (b)

a) b)

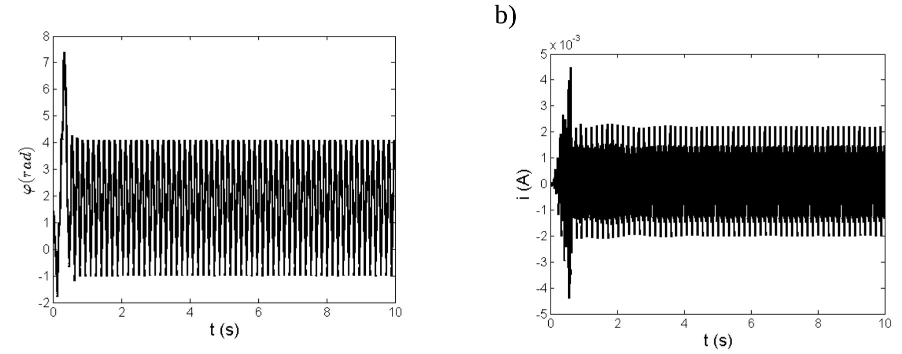

Figure 5. Time series of angle φ (a) and recovered current i (b), for ω=40rad/s

a) b)

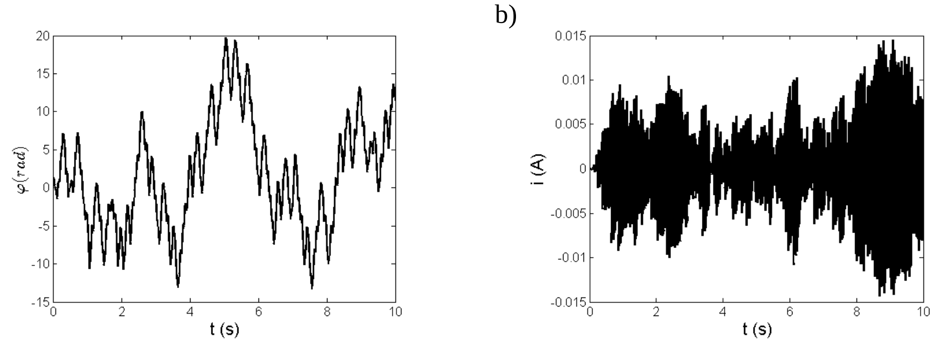

Figure 6. Time series of angle φ (a) and current i (b), for ω=45rad/s

a) b)

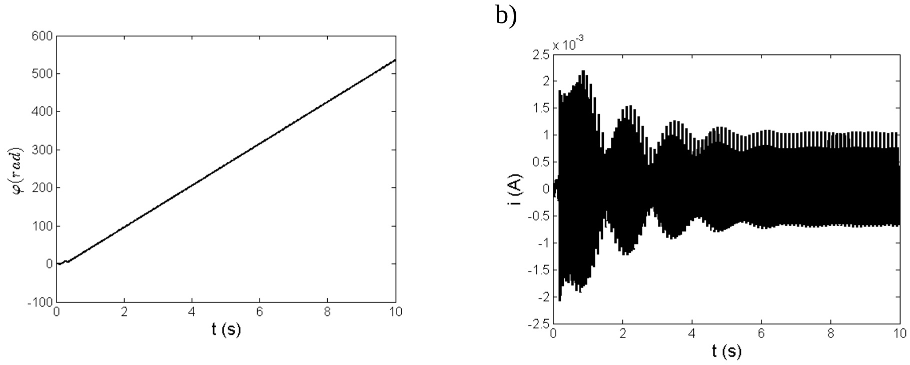

Figure 7. Time series of angle φ (a) and current i (b), for ω=55rad/s

Figures 2-4 present obtained 3D characteristics of recovered current. These results show trend of change the current flowing in the electrical circuit. We observe a significant change of the values i_{RMS} occurring with increasing the resistance R_{Total} and the coupling coefficient α. Increase in the resistance values causes that i_{RMS} decreased slowly (see at a frequency about 45 rad/s). Another trend is observed with an increase of the coefficient α, then the i_{RMS} increases. On the basis on Fig. 2 the definitive conclusions cannot be made. The inductance of electrical coil practically not influences on the energy recovery.

For selected values of the excitation frequency ω, the time series are presented (Figs. 5-7). These times series of the system responses show that pendulum can perform different kind of motion. Namely, pendulum swings (Fig. 5(a)), executes chaotic motion (Fig. 6(a)) and rotates (Fig. 7(a)). The maximal current recovered when the pendulum performs no regular motion (Fig. 6(b)).

3. Conclusions

In this paper numerical analysis of a pendulum vibration absorber with device to energy recovery is presented. The influences of the harvester parameters (L_{Coil}, R_{Total}, α) on value of the recovered current is presented. Energy harvester based on a movable magnet inside the coil, allows recover energy from different kind of the pendulum motion. The 3D characteristics give some information about proper tuning of the electrical parameters. The highest level of energy recovered for the small load resistance and high value of the coupling coefficient. Generally, efficiency of analyzed energy harvester system is low, the obtained current is in mA. However, it can be used to power of small electronic devices consume a little energy, for example sensor in monitoring system.

Acknowledgments

This work was financially supported under project of National Science Centre according to decision no. DEC-2013/11/D/ST8/03311.

References

1. K. Dhadse, S. Mishra, L. Mathew, S. Bhatt, *Case study of tuned mass damper and modeling of gyroscopic damper for corresponding effect,* International Journal of Applied Research, **1** (2015) 219 – 221.
2. K. Kecik, A. Mitura, D. Sado, J. Warminski, *Magnetorheological damping and semi-active control of an autoparametric vibration absorber*, Meccanica, **49** (2014) 1887 – 1900.
3. K. Kecik, A. Mitura, J. Warminski, *Efficiency analysis of an aotoparametric pendukum vibration absorber,* Eksploatacja i Niezawodnosc Maintenance and Reliability, **15** (2013) 221 – 224.
4. K. Kecik, M. Borowiec, An *autoparametric energy harvester,* European Physical Journal, **222** (2013) 1597 – 1605.
5. A. Mitura, K. Kecik, J. Warminski, W. Jarzyna, S. Lenci, *A numerical study of an autoparametric system with electromagnetic energy harvester,* Proceedings of the ECCOMAS Thematic Conference on Multibody Dynamics, (2015) 609 – 615.
6. B. P. Mann, N.D. Sims, *Energy harvesting from the nonlinear oscillations of magnetic levitation*, Journal of Sound and Vibration, **319** (2009) 515 – 530.
7. N. G. Stephen, *On energy harvesting from ambient vibration*, Journal of Sound and Vibration, **293** (2006) 409 – 425.

Influences of System Parameters on Energy Harvesting from Autoparametric Absorber. Experimental Research

Andrzej MITURA
Department of Applied Mechanics, Lublin University of Technology
Nadbystrzycka 36, 20-618 Lublin, a.mitura@pollub.pl

Krzysztof KECIK
Department of Applied Mechanics, Lublin University of Technology
Nadbystrzycka 36, 20-618 Lublin, k.kecik@pollub.pl

Abstract

In the paper an experimental analysis of an autoparametric system dedicated to vibration suppression and energy recovery is presented. The main part is an electromagnetic energy harvester. Its properties were defined by quasi static and dynamic tests. The obtained results show influence of selected parameters on energy recovery level. The experimentally identification of electromechanical coupling coefficient which couples mechanical and electrical systems is done.

Keywords: Non-linear autoparametric system, Energy harvester, Experimental research, Magnetic levitation

1. Introduction

In practice application of magnet and coil systems are often used in harvester construction. For example, Malaji and Ali [1] propose a concept in which the magnet is attached to the pendulum end. Both elements move together relative to the coil, which is mounted as the separated part. The similar concept is presented in the paper [2], where author presents a solution of the coil mounted on the pendulum tube. A movable magnet moves inside the tube and the coil and induced energy. This efficiency of the harvester device was studies numerically and experimentally in papers [2, 3]. The harvester application has fewer restrictions and can be used in the real object, for example mounted on existing nonlinear vibration absorbers in high buildings.

The paper presents preliminary experimental results of the magnetic levitation (maglev) harvester. The work is divided into two parts: the static (quasi-static) and the dynamic tests. The obtained results show, that coupling coefficient strongly depends on the magnet's position in the coil. In literature this coefficient usually assumed as a constant [2, 4].

2. Experimental setup

The experimental study has been made on a laboratory rig at the Lublin University of Technology (LUT) in the Department of Applied Mechanics. A scheme and general view of the real apparatuses in Fig. 1(a) and 1(b) is shown. This laboratory system consists of three main subsystems:

- the nonlinear oscillator (damped mass),
- the pendulum (vibration absorber),
- the energy harvester (maglev system) with the electrical circuit.

The system has three mechanical degree (x, φ and r) and one electrical *(i)* degrees of freedom. In this section more information about construction of energy harvester is presented (Fig. 1(c)).

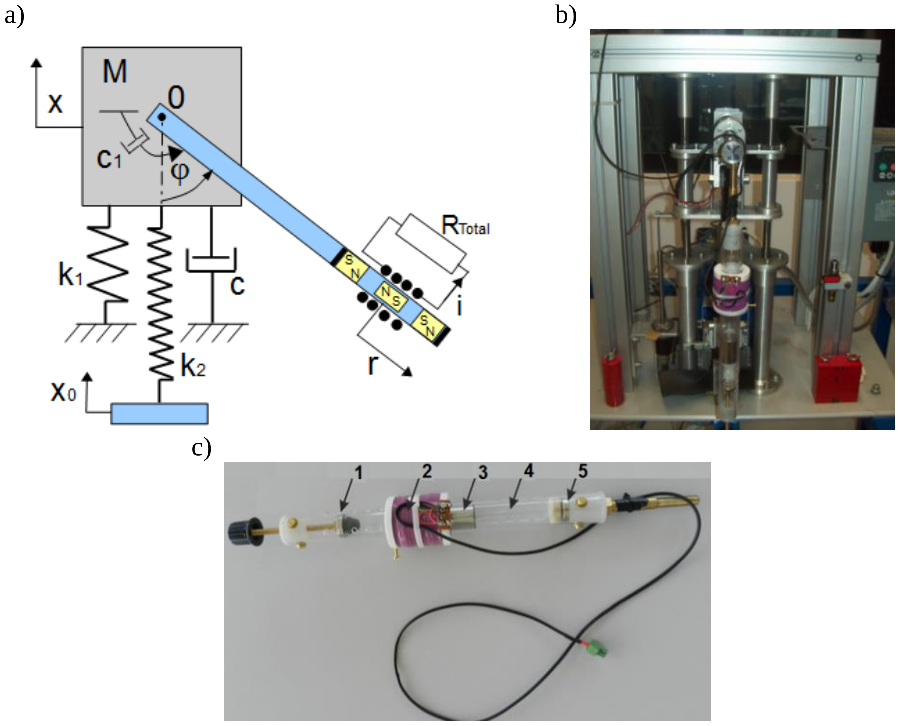

Figure 1. An autoparametric vibration absorber: scheme (a), a photo of the laboratory rig (b), and maglev harvester (c). The elements of harvester are: 1- lower fixed magnet, 2- coil, 3- movable magnet, 4- neutral magnetic tube, 5- top fixed magnet

The energy maglev harvester consists of the movable levitating magnet (3), which moves inside the coil (2). The motion of this magnet generate current flow i in the coil electrical circuit with the resistor (R_{Total}). The initial position of the movable magnet is determined by magnetic levitation suspension. It levitates between two fixed magnets (no. 1 and no. 5). The electrical circuit is provided with a receiver (resistor) and measurement system to recorder current, voltage and power of generated electrical signal. The tube of the pendulum (4) is made of non-magnetic material. The all parameters of electromagnetic harvester are listened in Table 1.

Table 1. Parameters of energy harvester.

Description of parameter	Unit	Value
Height of movable magnet	mm	35
Diameter of movable magnet	mm	20
Mass of movable magnet	g	98
Length of coil	mm	50
Coil resistance	Ω	1150
Coil inductance	H	1460e-3
Wire diameter	mm	0.14
Turn of winding	-	12740
Total length of tube	mm	340
Mass of tube with two fixed magnets	g	350

2. Experimental results. Static test

The first stage of experimental analysis was the quasi-static test. During this analysis, the tube, the coil with electrical equipment and the movable magnet mounted in the machine SHIMADZU (Fig. 2(a)) were used. The magnet was connected by a wooden rod with the upper handle, which is moved to a triangular signal (Fig. 2(b)). The handle moves with constant velocity ±500mm/min. The resistance of the receiver can be changed, set on a desired level.

a)

b)

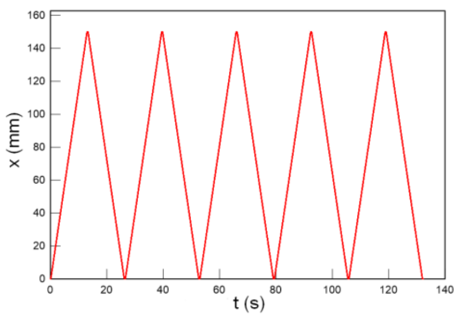

Figure 2. The system view for static tests (a), a displacement of an upper handle (b)

Tests were made for the three different values of receiver resistance (R=1.15kΩ, R=4kΩ and R=6kΩ). The obtained in Fig. 3 are shown. The coordinate r describes the distance from the coil center to center of the movable magnet. We can see, that the maximum current is generated when a center of the magnet is located on the end of the coil (r=±25mm). Generally, with increased resistance the values of the current flowing in the electrical circuit decreases.

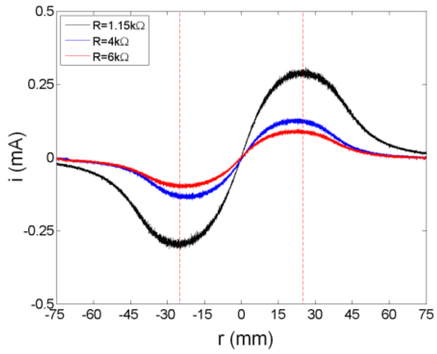

Figure 3. Experimental results: current versus magnet position from the static tests

3. Experimental results. Dynamic test

The second stage of experimental study was the dynamic tests. Research was made on the complete experimental rig. The relative motion of movable magnet was measured by the high speed camera MIRO 120 (Fig. 4(a)). The mechanical responses r and $\dot{r}$ were determined from the video information using TEMA software (Fig. 4(b)). The exemplary results are shown in Fig. 5. These signals were compared with the measured current i (Fig. 6).

a)

b)

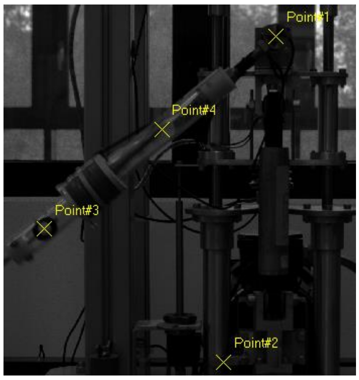

Figure 4. Photo during experiment test (a) and single picture with traced points from TEMA software (b)

Generally in literature [2, 4], the electromechanical coupling coefficient α can be assumed as the constant parameter. Their value depends on the construction of energy harvester. The electrical properties of the tested system can be written in the standard simple Kirchhoff law

$$L_{Coil}\dot{i} + R_{Total}i = a(r,\dot{r})\dot{r} \tag{1}$$

Based on the obtained results it is possible to determine values of the coupling coefficient α. Equation (1) was transformed to following form

$$a(r,\dot{r}) = (L_{Coil}\dot{i} + R_{Total}i)/\dot{r} \tag{2}$$

After a simple numerical calculations, the curve α=*f(r)* was prepared (Fig. 7).

a) b)

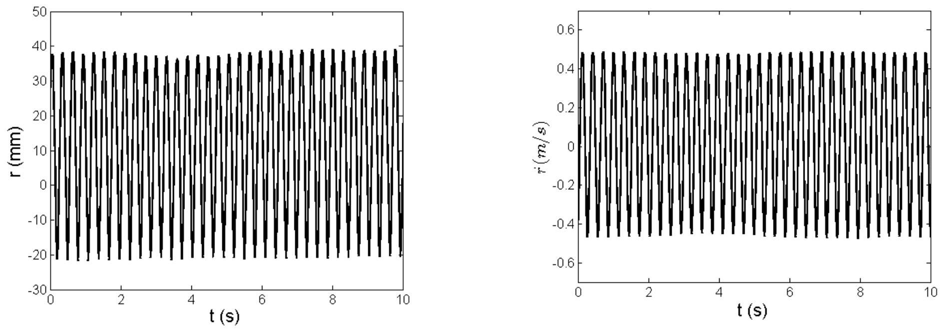

Figure 5. Experimental time series of the relative displacement r (a) and velocity $\dot{r}$ (b)

a) b)

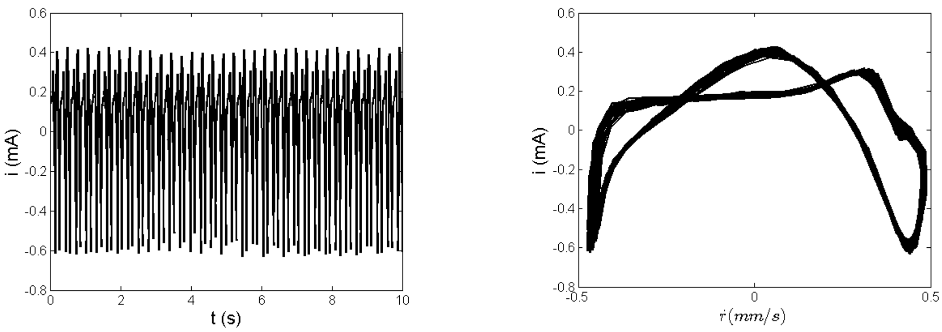

Figure 6. Time series of current *i* (a) and the phase portrait current - relative velocity (b)

The obtained experimental coupling coefficient results show that α value is not constant. The value depends on the distance from the coil center to center of the movable magnet, it is function of the coordinate *r*.

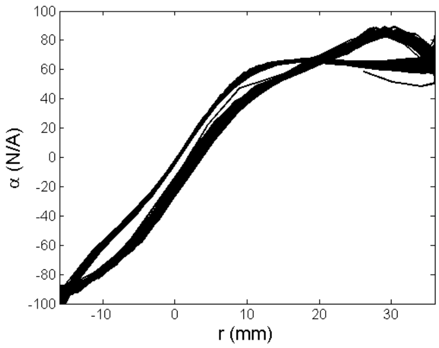

Figure 7. The experimental coupling coefficient characteristics

3. Conclusions

The paper presents experimental analysis of the selected electrical parameters in recovered current. The most important observation from the static and the dynamic tests is to detect a relationship between the electromechanical coupling $L_{Coil}\dot{i} + R_{Total}i$ coefficients α and the coordinate r. In future research will be planned to determine an empirical form of a new model of the coupling coefficient.

Acknowledgments

This work was financially supported under project of National Science Centre according to decision No. DEC-2013/11/D/ST8/03311.

References

1. P. V. Malaji, S. F. Ali, *Analysis of energy harvesting from multiple pendulums with and without mechanical coupling*, European Physical Journal, **224** (2015) 2823 – 2838.
2. A. Mitura, K. Kecik, J. Warminski, W. Jarzyna, S. Lenci, *A numerical study of an autoparametric system with electromagnetic energy harvester*, Proceedings of the ECCOMAS Thematic Conference on Multibody Dynamics, (2015) 609 – 615.
3. K. Kecik, A. Mitura, *Non linear dynamics of a vibration harvest-absorber system. Experimental study*, Dynamical systems: control and stability, Łódź, ARSA, (2015) 297 – 306.
4. N. G. Stephen, *On energy harvesting from ambient vibration*, Journal of Sound and Vibration, **293** (2006) 409 – 425.

Experimental Validation of the 3D Dynamic Unicycle-Unicyclist Model

Michał NIEŁACZNY
Division of Dynamics, Technical University of Łódź, Stefanowskiego 1/15
90-924 Łódź, Poland, nielaczek@gmail.com

Wiesław BARNAT
Department of Mechanics and Applied Computer Science
Military University of Technology, Gen. S. Kaliskiego 2, 00-908 Warszawa
wieslaw.barnat@wat.edu.pl

Abstract

The problem of motion of a unicycle – unicyclist system in 3D is studied. The equations of motion of system have been derived using the Boltzmann-Hamel equations. A description of the unicycle – unicyclist system dynamical model, simulation results and experimental validation of the system are presented in the paper.

Keywords: unicycle, 3D dynamic model, Boltzmann-Hamel equations

1. Introduction

1.1. Unicycle – one-wheel vehicle

Unicycle, one-wheel vehicle, is a specific type of single track, which is a bicycle. It has only one road wheel. Unicycle is shown in the figure below [1].

Figure 1. Typical unicycle [2]

The main feature of unicycle is fixed gear. Therefore, the rotation of the cranks directly controls the rotation of the wheel, and positions of unicyclist's legs. Riding without pedalling is impossible. Riding a unicycle is more difficult than on regular bicycle, due to the fact that there is only one point of support. For this reason, a balance must be simultaneously maintained in two planes, transverse and parallel to the direction of moving, so that the centre of gravity oscillates above the fulcrum of the wheel.

In technical aspect unicycle-unicyclist system, can be considered as a moving double inverted spherical pendulum with follow-up control system.

1.2. Boltzmann-Hamel equations

The Boltzmann-Hamel equations are rarely used because of complicated formulae containing Hamel coefficients and complex relationships for the determination of these coefficients [3, 4, 5, 6, 7]. The classic form of the Boltzmann-Hamel equations for a system with the number of coordinates equal to k is as follows [3, 4]

$$\frac{d}{dt}\left(\frac{\partial T^*}{\partial w_n}\right) - \frac{\partial T^*}{\partial \pi_n} + \sum_{m=1}^{m=k}\sum_{l=1}^{l=k}\sum_{i=1}^{j=k}\sum_{j=1}^{j=k} b_{li}b_{mj}\left(\frac{\partial a_{im}}{\partial q_l} - \frac{\partial a_{il}}{\partial q_m}\right)\frac{\partial T^*}{\partial w_i} w_j = \Pi_n, \quad (n = 1, \dots k) \tag{1}$$

Matrix form of Boltzmann-Hamel equations

$$\frac{\mathrm{d}}{\mathrm{dt}}\left(\frac{\partial \mathrm{T}^*}{\partial \mathbf{w}}\right) + \mathbf{B}^{\mathbf{T}}\left(\dot{\mathbf{A}}^{\mathbf{T}} - \mathbf{D}^{\mathbf{T}_0}\mathbf{B}\mathbf{w}\right)\frac{\partial T^*}{\partial \mathbf{w}} - \mathbf{B}^{\mathbf{T}}\frac{\partial \mathrm{T}^*}{\partial \mathbf{q}} = \mathbf{B}^{\mathbf{T}}\left(\mathbf{f} - \frac{\partial \mathrm{V}}{\partial \mathbf{q}}\right) \tag{2}$$

allows to automate generation of Hamel coefficients and eliminates all difficulties associated with a determination of these quantities [8].

2. Description of the analysed model

For the unicycle-unicyclist model description we use fixed inertial frame *Oxyz* (Fig. 2). We also use no inertial frames $x_iy_iz_i$, inertial frames $\xi_i\eta_i\zeta_i$ and parallel frames $x_i'y_i'z_i'$ or $\xi_i'\eta_i'\zeta_i'$ related to each link (i=1,…,7), attached at the end of it.

Table 1. Model of the unicycle-unicyclist system

i	1	2	3	4	5	6	7
mark	w	f	b	tir	thr	til	thl
link	wheel	frame	body	tibia right	thigh right	tibia left	thigh left

To consider motion of the system, we introduce the following generalized coordinates

$$\mathbf{q} = [x_w, y_w, z_w, \alpha_w, \beta_w, \gamma_w, \alpha_f, \alpha_b, \beta_b]^T, \tag{3}$$

where x_w, y_w, z_w are the coordinates of the wheel contact point, and the remaining ones are the Euler angles describing spatial orientation with respect to the particular frame, Fig. 2.

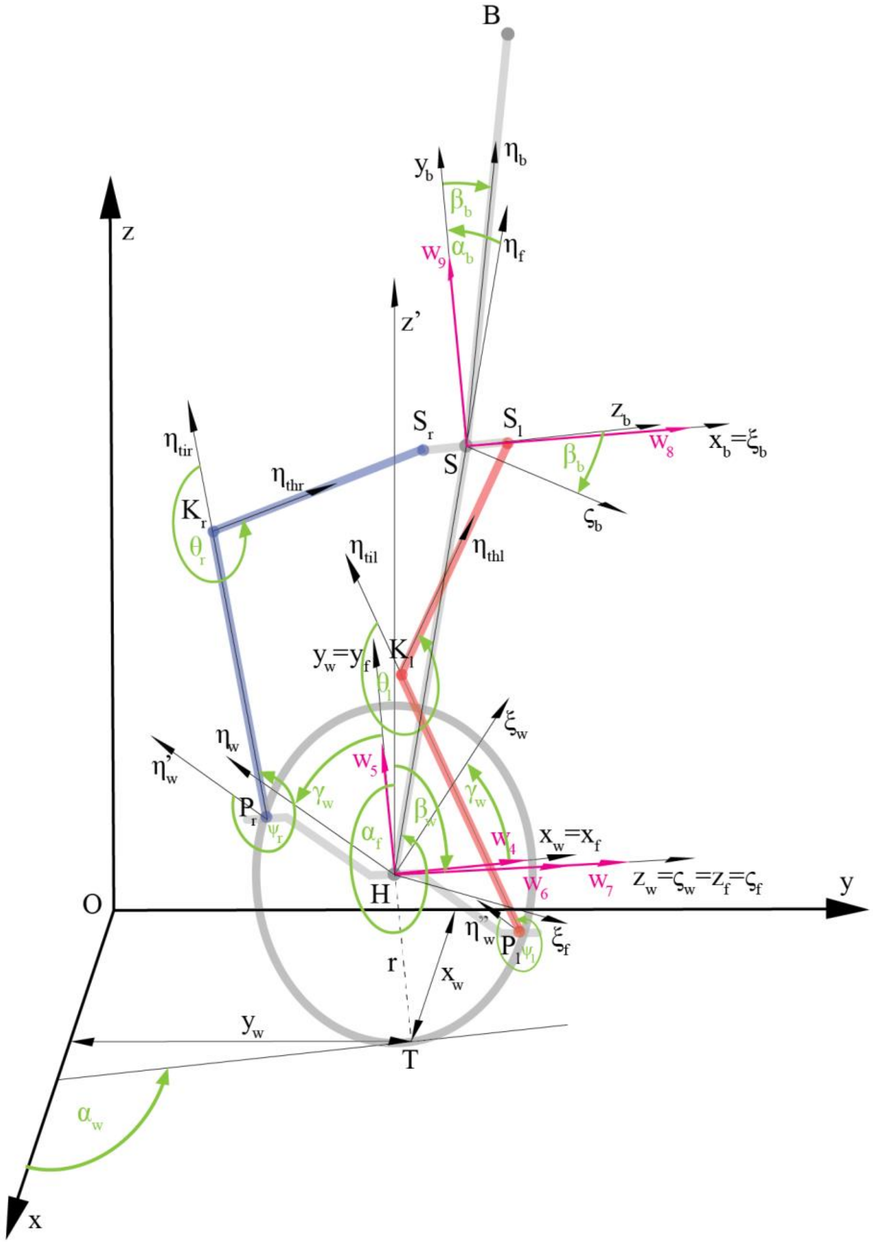

Figure 2. Model of the system (some axes are omitted for reasons of clarity)

A unicyclist leg which is used in this model consists of thigh and tibia. Foot is omitted due to the specific and complex motion in one rotational cycle, which does not aspect significantly in a ride. Thereby, pedal axes are covered up with ankle. Therefore, the leg can be treated as a crank mechanism and the leg position is clearly defined by γ_w and α_f [9].

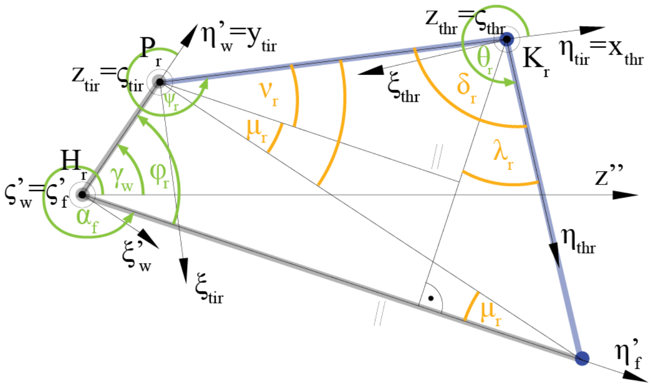

Figure 3. Leg positions and coordinates, on an example of the right leg

Quasi-velocities (Fig. 2) defining the model velocities are assumed in the form:

$$\mathbf{w}=\begin{bmatrix} w_1\\ w_2\\ w_3\\ w_4\\ w_5\\ w_6\\ w_7\\ w_8\\ w_9 \end{bmatrix}=\begin{bmatrix} 1 & 0 & 0 & 0 & 0 & r\cos\alpha_w & 0 & 0 & 0\\ 0 & 1 & 0 & 0 & 0 & r\sin\alpha_w & 0 & 0 & 0\\ 0 & 0 & 1 & 0 & 0 & 0 & 0 & 0 & 0\\ 0 & 0 & 0 & 0 & 1 & 0 & 0 & 0 & 0\\ 0 & 0 & 0 & \sin\beta_w & 0 & 0 & 0 & 0 & 0\\ 0 & 0 & 0 & \cos\beta_w & 0 & 1 & 0 & 0 & 0\\ 0 & 0 & 0 & \cos\beta_w & 0 & 0 & 1 & 0 & 0\\ 0 & 0 & 0 & 0 & 0 & 0 & 0 & 0 & 1\\ 0 & 0 & 0 & 0 & 0 & 0 & 0 & 1 & 0 \end{bmatrix}\begin{bmatrix} \dot{x}_w\\ \dot{y}_w\\ \dot{z}_w\\ \dot{\alpha}_w\\ \dot{\beta}_w\\ \dot{\gamma}_w\\ \dot{\alpha}_f\\ \dot{\alpha}_b\\ \dot{\beta}_b \end{bmatrix}=\mathbf{A}\,\dot{\mathbf{q}}. \tag{4}$$

where r is the radius of the wheel. Equations (4) are valid under assumption that the wheel is a rigid hoop making point contact with the road and it rolls without longitudinal slip on a flat surface. It means that the constraint equations for the wheel are: w_1=0, w_2=0 and w_3=0. Kinetic energy, with respect to mass canters of the system is obtained using the formula

$$T=\frac{1}{2}\sum_{i=1}^{n}\mathbf{v}_i^T\mathbf{M}_i\mathbf{v}_i+\frac{1}{2}\sum_{i=1}^{n}\boldsymbol{\omega}_i^T\mathbf{I}_i\boldsymbol{\omega}_i\,,\quad (n=1,\ldots,7). \tag{5}$$

where $\mathbf{v}_i$ is the vector of linear velocities, $\mathbf{M}_i$ is the mass matrix, $\boldsymbol{\omega}_i$ is the vector of angular velocities and $\mathbf{I}_i$ are the moments of inertia standing in the mass matrix.

The equations of model dynamics based on Boltzmann-Hamel equation (2) were generated automatically and solved using *Wolfram Mathematica*.

3. Simulation results

Results of numerical simulation for the unicycle-unicyclist model motion are shown in Figs. 4–6. The most important initial conditions for simulations are the vertical position and the constants of wheel velocity. It is a wire model; which means that every link is a rigid rod, except the wheel regarded here as a rigid circular hoop. Appropriate damping in the nodes provides that the system does not immediately collapse and small values of masses of legs epitomize control of the unicycle by a unicyclist.

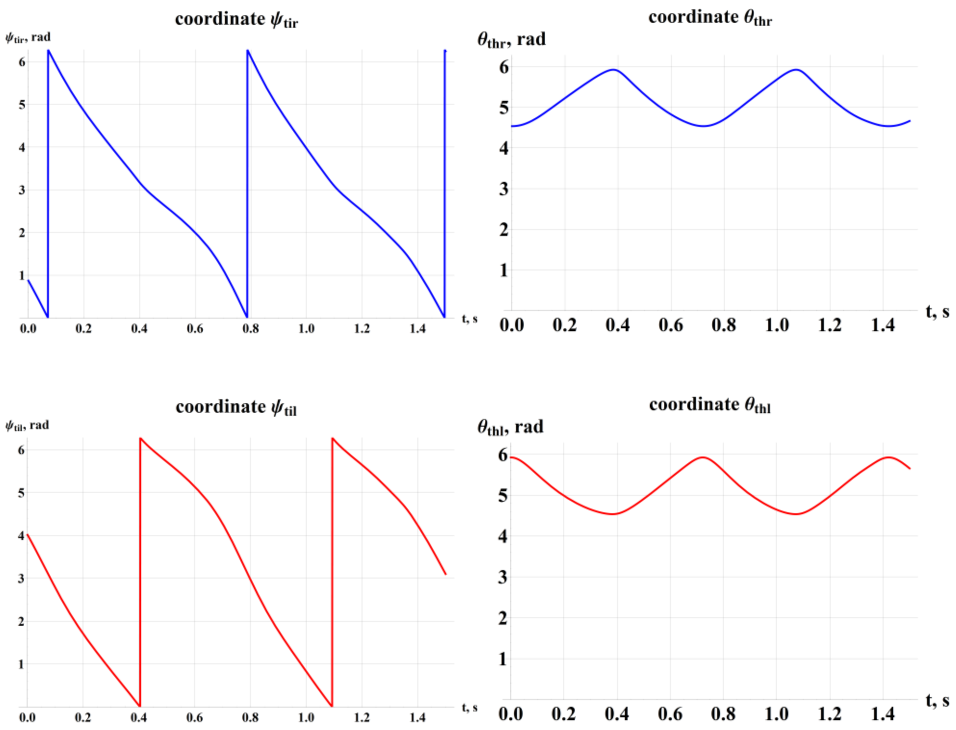

Figure 4. Time histories of legs coordinates. Right leg (blue) and left leg (red)

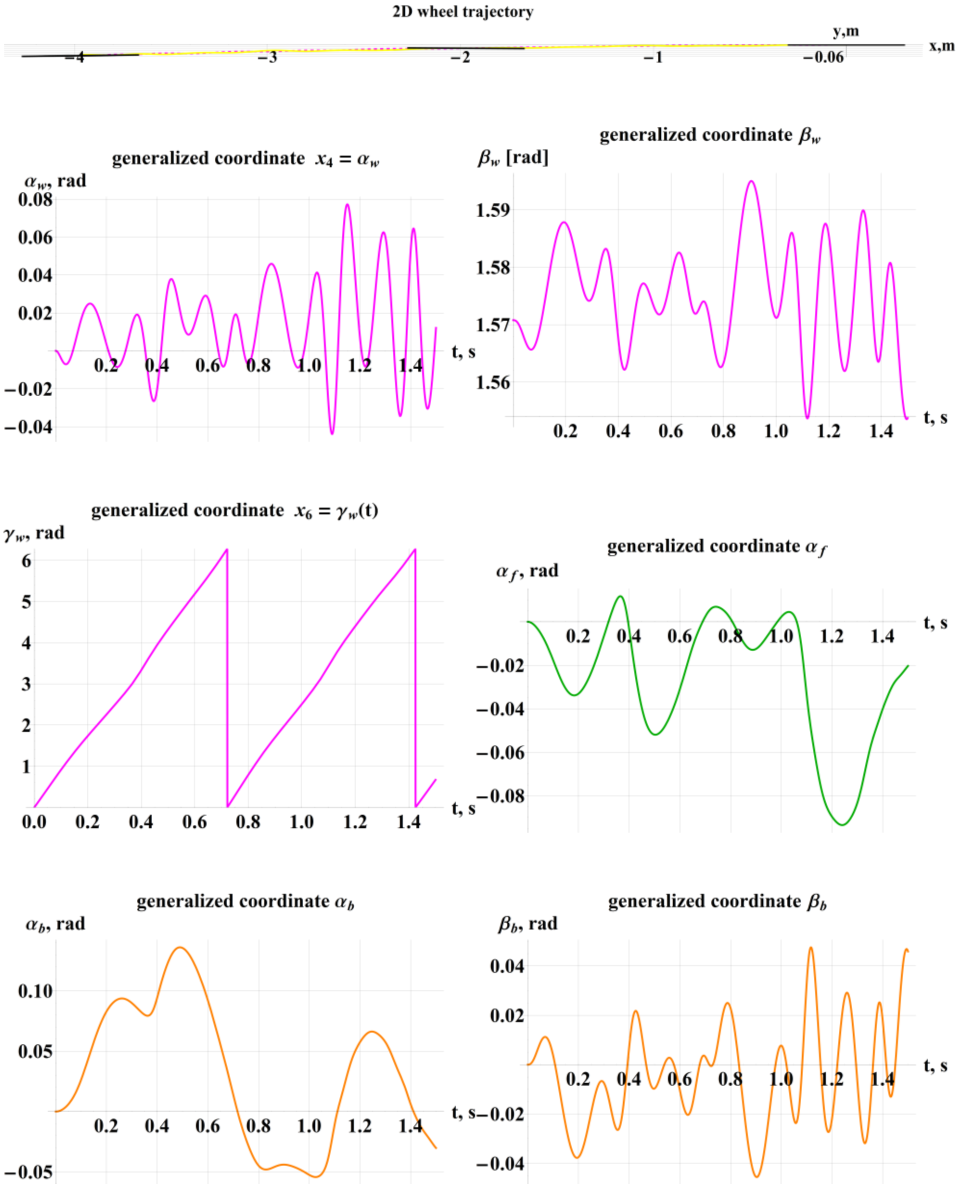

Figure 5. Wheel 2D trajectory and time histories of the system Euler angels

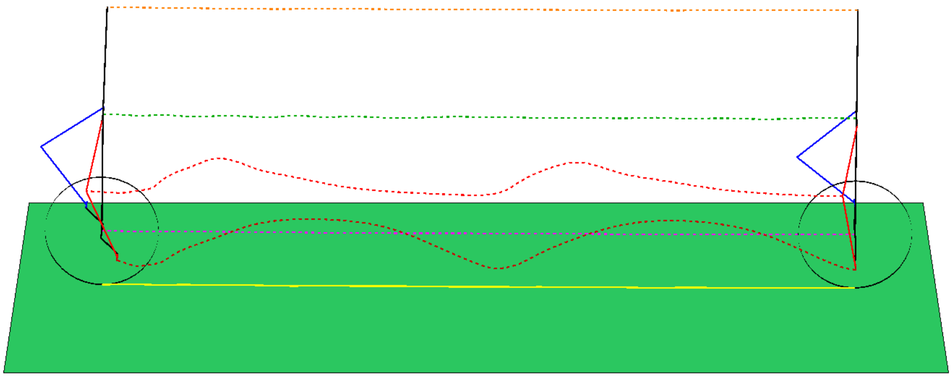

Figure 6. 3D trajectories of the system

4. Experimental validation

To capture motion of the real object, a high speed camera was used. A duration of single attempt is about two seconds. The quadrant symmetry markers were used. To process the movies, the *TEMA* software was used. An experiment in 2D was made in order to check, if the way of modelling is correct. Below there are shown the parametric plots of positions of the characteristics point of the model.

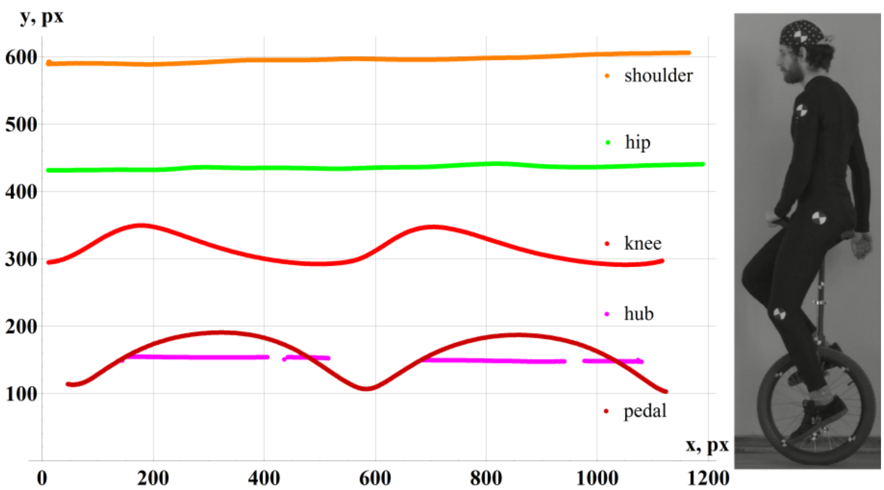

Figure 7. 2D trajectories of the motion capture of the real object

By comparing Fig. 6. with Fig. 7. it can be seen, that trajectories of characteristic points have very similar courses. Dissimilarities may be due to the fact that the experiment was made in 2D, while the real object moves in 3D.

5. Conclusions

The matrix notation of Boltzmann-Hamel equations eliminates drawbacks occurring with the classical formulation of these equations. Its application allows an automation of generation process of motion equations.

It is clearly shown that the model during movements swings around an unstable equilibrium. Because of unbalance caused by legs and cranks with pedals, the wheel moves in a “snake style”. To sum up, our model behaves like a real object. It is confirmed by a comparison of the trajectory of characteristic points, by 2D motion capture of the real object.

In the future, in this model also a tire will be taken into consideration as well as and a system control method are going to be introduced. Upon those steps, the 3D motion capture will be made to validate the final model.

References

1. M. Niełaczny, J. Grabski, J. Strzałko, *3D dynamic model of the unicycle – unicyclist system,* Journal of Vibrations in Physical Systems, Poznan, 2014.
2. [online] [access: 18-12-2011] http://qu-ax.com/en/products
3. R. Gutowski R, *Mechanika analityczna,* PWN Warszawa 1971.
4. J. I. Nejmark, N. A. Fufajew, *Dynamika układów nieholonomicznych,* PWN Warszawa 1971.
5. W. Blajer, *Metoda projekcyjna - teoria i zastosowania w badaniu nieswobodnych układów mechanicznych*, WSI Radom, 13/1994.
6. W. Blajer, Projective formulation of Lagrange's and Bolzmann-Hamel equations for multibody systems, ZAMM, **75** (1995) 107 – 108.
7. J. M. Maruskin, A. M. Bloch, *The Boltzmann's Hamel equations for the optimal control of mechanical systems with nonholonomic constraints*, Int. J. Robust. Nonlinear Control, **21** (2011).
8. J. Grabski, J. Strzałko, *Automatic Generation of Boltzmann-Hamel Coefficients for Mechanical Problems.* Mechanics and Mechanical Engineering International Journal, **1** (1997) 61 – 77.
9. JI. B. Берестов, *Сравнительный анализ реакций в кинематических парах механизма шарнирног четырехзвенника для различных схем уравновешивания*, Механика машин. – М.: Наука, (1977) 61 – 70.

The Analysis of the Impact of Different Shape Functions in Tolerance Modeling on Natural Vibrations of the Rectangular Plate with Dense System of the Ribs in Two Directions

Martyna RABENDA
Department of Structural Mechanics, Lodz University of Technology
al. Politechniki 6, 90-924 Łódź, martynarabenda@gmail.com

Abstract

The main concern of this paper are thin rectangular plates with dense system of the ribs in two directions. The aim of the analysis is the examination of the impact of different shape functions in tolerance modeling on natural vibrations of the plates.
The plate is made of two different materials, both for matrix and ribs. The thickness of the plate is comparable to the width of the ribs. This provides a powerful tool for getting a desirable frequency of natural vibrations of the plate. The tolerance averaging approach is the base for the formulation of averaged model equations. The most accurate readings presenting this method are described in Wozniak et al. [1].
By application of the tolerance averaging technique to the known differential equations of considered plates, the averaged equations of the tolerance model have been derived. The general results of the contribution are illustrated using the analysis of natural vibrations. The effect of different shape functions on free vibration frequencies is examined.

Keywords: dynamic, tolerance average technique, thin plates, natural vibrations

1. Introduction

The object of the contribution is thin composite plate with dense system of the ribs. The aim of the analysis is the diagnosis of the impact of different shape functions in tolerance modeling on natural vibrations of the plates.

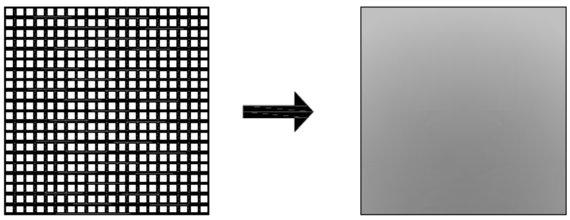

Figure 1. Composite plate at microscopic level and at macroscopic level

The space between the ribs is filled with a homogeneous matrix material (Figure 1). The analogous plate was examined in the paper [2]. The period $l = \sqrt{l_1 l_2}$ of heterogeneity is presumed to be sufficiently small versus the measure of the midplane of the plate. Simultaneously, it is assumed that the microstructure length parameter l is appropriately small in contrast with the minimum characteristic length dimension of the plate. The size of the microstructure l is comparable with the thickness of the plate h ($h \cong l$) (Figure 2). The differential equations of this kind of the plates have discontinuous and rapidly oscillating coefficients. The applications of those equations to engineering problems is not the most efficient tool. Thus, an averaged model has been proposed in which material properties are represented by functional but smooth effective stiffnesses.

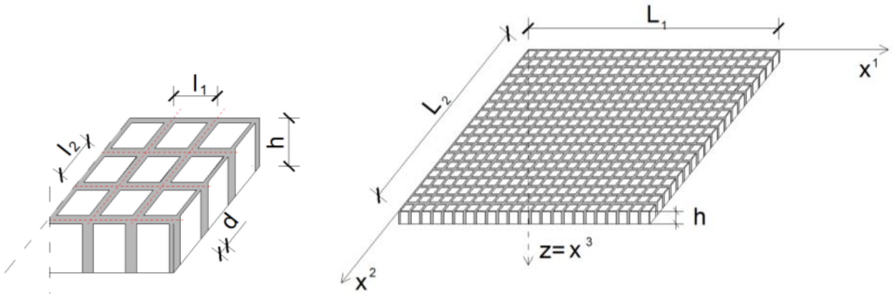

Figure 2. Detailed geometry of the plate

Analogous plate has been described in the paper [3] where it has been considered the influence of initial stress forces on the free vibrations of the plate. In this work the calculations were shown for different geometric and material properties.

The formulation of the averaged mathematical model for the analysis of dynamic behaviour of these plates is based on the tolerance averaging approach. This approach can be find in book Woźniak et al. [1]. This technique was applied in many papers. Some of the following papers can be mentioned here as examples: Baron [4] has analyzed the plates in which the period length is comparable with the thickness of the plate. In the work [5] propagation of harmonic wave in periodically laminated composites was analyzed. Furthermore, in the paper [6] the rectangular composite plate under the plane stress was analyzed. The elastic plate is reinforced by system of periodically distributed parallel ribs. Michalak [7] examined vibrations of thin plates with initial geometrical imperfections as a model of elastic wavy plates. In the contribution [8] the vibrations of periodic three-layered plates with inert core has been analysed.

In contrast to the previous works [9-10], where the gradation only in one direction is described, in the present paper it is analyzed in two directions. What is more, in the majority of above mentioned notes, in which the plates are considered, the thickness h of the plate is essentially smaller compared to the microstructure length parameter $l = \sqrt{l_1 l_2}$ (l_1, l_2 - dimensions of the cell). Baron [4] considered the thickness of the plate similar to the period length which is analogous to the current contribution. The difference is in the geometry of the plate which is reinforced in two directions not just in one (paper [4]). On a microscopic level we deal with the microheterogeneous plate while, after averaging, we deal with a special case of a functionally graded material on the macroscopic level (Figure 1).

2. Direct description and modelling technique

In this contribution the rectangular plates shown in Figure 2 are considered. The orthogonal Cartesian coordinate system is introduced $Ox_1x_2x_3$ and the time coordinate t. In all respects in the note, indices $i,k,l\dots$ run over $1,2,3$, indices $\alpha,\beta,\gamma,\dots$ and indices $A,B,C,\dots$ run over $1,2$. The summation convention holds all aforementioned sub-and superscripts. Adopting $x\equiv(x_1,x_2)$ and $z=x_3$ the undeformed plate occupies the region $\Omega\equiv\{(x,z):-h/2\le z\le h/2, x\in\Pi\}$, where Π is the rectangular plate midplane and h is the plate thickness.

In the framework of a well known theory of thin plates the averaged model equations of the dynamic behavior of microheterogeneous plate are obtained. The displacement field of the arbitrary point of the plate is given in form

$$w_3(x,z)=w_3(x) \qquad w_\alpha(x,z)=w_\alpha^0(x)-\partial_\alpha w_3(x)\,z \tag{1}$$

Denoting by $p(x,t)$ the external forces, ρ the mass density, $g_{\alpha\beta}$ the metric tensor, $\in_{\alpha\beta}$ a Ricci tensor. Setting $\partial_k=\partial/\partial x^k$ we also introduce gradient operators $\nabla\equiv(\partial_1,\partial_2)$. After application of the linear approximated theory for thin plates we obtain the following system of equations:

(i) strain-displacement relations

$$\varepsilon_{\alpha\beta}(x,z)=\kappa_{\alpha\beta}(x)\ z, \qquad \kappa_{\alpha\beta}=-\nabla_{\alpha\beta}w_3 \tag{2}$$

(ii) strain energy

$$E_z(x,z)=\tfrac{1}{2}C^{\alpha\beta\gamma\delta}\,\varepsilon_{\alpha\beta}\,\varepsilon_{\gamma\delta} \tag{3}$$

(iii) kinetic energy

$$K_z(x,z)=\tfrac{1}{2}\rho(\dot w_3\,\dot w_3+\dot w_\alpha\,\dot w_\beta\,\delta^{\alpha\beta}) \tag{4}$$

for $z\in(-h/2,h/2)$.

The strain energy averaged over the shell thickness is given by

$$E(x)=\tfrac{1}{2}B^{\alpha\beta\gamma\delta}\nabla_{\alpha\beta}w_3\,\nabla_{\gamma\delta}w_3 \tag{5}$$

where $B^{\alpha\beta\gamma\eta}=\dfrac{E\,h^3}{12(1-\nu^2)}0.5(\delta^{\alpha\eta}\,\delta^{\beta\gamma}+\delta^{\alpha\gamma}\delta^{\beta\eta}+\nu(e^{\alpha\gamma}e^{\beta\eta}+e^{\alpha\eta}e^{\beta\gamma})$.

The coefficients in the above equations are discontinuous and highly oscillating. The above equations will be used as a starting point of the modeling procedure.

Consequently, going to the modeling technique let us introduce the orthogonal coordinates system $O\xi^1\xi^2$ in the undeformed midplane. The midplane of the plate occupies the region $\Pi\equiv[0,L_1]\times[0,L_2]$ (Figure 2). Assuming that the number of ribs in ξ^1 and ξ^2 directions is respectively n and m $(1/n,1/m<<1)$. Hence $l_1=L_1/n$ and $l_2=L_2/m$ are the dimensions of the cell $\Delta\equiv(-l_1/2,l_1/2)\times(-l_2/2,l_2/2)$. We introduce, for the arbitrary cell $\Delta(\xi^\alpha)\equiv\Delta+\xi^\alpha$ with center situated at point (ξ^1,ξ^2), the orthogonal local coordinate system Oy_1y_2 which is local with its origin at $(\xi^1,\xi^2)\in\overline{\Pi}_\Delta$ where $\Pi_\Delta\equiv(l_1/2,L_1-l_1/2)\times(l_2/2,\,L_2-l_2/2)\subset\Pi$.

In order to derive averaged model equations for skeletonal plate under consideration we applied tolerance averaging approach [1]. There will be introduced some basic concepts of this technique: an averaging operator, a tolerance parameter, a tolerance periodic function, a slowly varying function and a highly oscillating function.
The starting point of the modeling procedure is a decomposition of displacement fields.

$$\begin{aligned} &w_3(\xi^\alpha,z,t)=V_3(\xi^\alpha,t)\\ &w_\alpha(\xi^\alpha,z,t)=(-\partial_\alpha V_3(\xi^\alpha,t)+h^{A}(\xi^\alpha)u_\alpha^A(\xi^\alpha,t))\,z \end{aligned} \tag{6}$$

for $\xi^\alpha=\Pi$, $z\in(-h/2,h/2)$, $A=I,II$ and every time t.
The governing equations derived from stationary action principle of the averaged lagragian [2,3] $<\mathrm{L}>=<K>-<E>+<F>$ have the form

$$\begin{aligned} &\nabla_{\alpha\beta}\left(\tilde{B}^{\alpha\beta\gamma\delta}\nabla_{\gamma\delta}V_3-\tilde{B}^{\gamma A\alpha\beta}u_\gamma^A\right)+\langle\tilde{\rho}\rangle\ddot{V}_3-\left\langle f^3\right\rangle=0\\ &\tilde{B}^{\alpha A\gamma\delta}\nabla_{\gamma\delta}V_3-\tilde{B}^{\alpha A\gamma B}u_\gamma^B=0 \end{aligned} \tag{7}$$

After simple manipulations we obtain finally the following equation for the averaged displacements $V_3(\xi^\alpha,t)$,

$$\nabla_{\alpha\beta}\left(F^{\alpha\beta\gamma\delta}\nabla_{\gamma\delta}V_3\right)+\langle\tilde{\rho}\rangle\ddot{V}_3=\left\langle f^3\right\rangle \tag{8}$$

where $\tilde{\rho}=\rho h$ is mass density related to plate midplane. In contrast to equations in direct description with the discontinuous and highly oscillating coefficients, the coefficients in the above equation are smooth and functional.

3. Applications - fluctuation shape functions

The key point of the tolerance modeling technique is to determine of fluctuation shape function (FSF). In dynamic problems, the system of fluctuation shape function can be taken to represent the principal modes of free vibrations of the cell $\Delta(x_\alpha)$ or a physically reasonable approximation of these modes. Our analysis is to investigate the impact of different shape functions on free vibrations of the plate. We are restricted to the case where we have two fluctuation shape functions, $h^I(x_\alpha,y_\alpha)$ and $h^{II}(x_\alpha,y_\alpha)$ (Figure 3)

$$h^I\left(x_\alpha,y_\alpha\right)=S_1\left(y_1\right)\cdot\left[1-\left(\frac{2y_2}{b_2}\right)^2\right],\qquad h^{II}\left(x_\alpha,y_\alpha\right)=S_2\left(y_2\right)\cdot\left[1-\left(\frac{2y_1}{b_1}\right)^2\right] \tag{9}$$

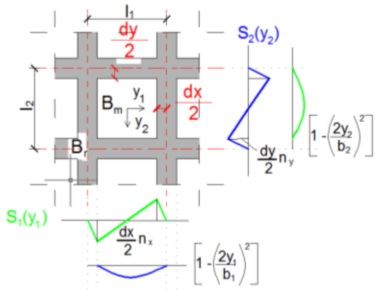

Figure 3. Fluctuation shape functions in the considered cell

$$S_1(y_1)=\begin{cases} -\left(y_1+\dfrac{l_1}{2}\right)\cdot\eta_x & y_1\in\left\langle -\dfrac{l_1}{2},-\dfrac{b_1}{2}\right\rangle \\ \dfrac{dx}{l_1-dx}\cdot y_1\eta_x & y_1\in\left\langle -\dfrac{b_1}{2},\dfrac{b_1}{2}\right\rangle \\ -\left(y_1-\dfrac{l_1}{2}\right)\cdot\eta_x & y_1\in\left\langle \dfrac{b_1}{2},\dfrac{l_1}{2}\right\rangle \end{cases}$$
$$S_2(y_2)=\begin{cases} -\left(y_2+\dfrac{l_2}{2}\right)\cdot\eta_y & y_2\in\left\langle -\dfrac{l_2}{2},-\dfrac{b_2}{2}\right\rangle \\ \dfrac{dy}{l_2-dy}\cdot y_2\eta_y & y_2\in\left\langle -\dfrac{b_2}{2},\dfrac{b_2}{2}\right\rangle \\ -\left(y_2-\dfrac{l_2}{2}\right)\cdot\eta_y & y_2\in\left\langle \dfrac{b_2}{2},\dfrac{l_2}{2}\right\rangle \end{cases} \tag{10}$$

where $b_1=l_1-dx(x_1)$ $\quad$ $b_2=l_2-dy(x_2)$.

We have considered for four different amplitudes of functions $S_1(y_1)$ and $S_2(y_2)$ as following (respectively *versions 1-4*):

1. $$\eta_x(x_1)=\frac{dx(x_1)}{l_1}\ ,\ \eta_y(x_2)=\frac{dy(x_2)}{l_2}$$

2. $$\eta_x(x_1)=\frac{dx(x_1)}{l_1}\cdot\frac{2(B_r-B_m)}{(B_r+B_m)}\ ,\ \eta_y(x_2)=\frac{dy(x_2)}{l_2}\cdot\frac{2(B_r-B_m)}{(B_r+B_m)} \tag{10b}$$

3. $$\eta=\eta_x(x_1)=\eta_y(x_2)=\frac{1}{l_1\cdot l_2}\sqrt{(l_1-dx(x_1))\cdot(l_2-dy(x_2))\cdot(l_1dy(x_2)+l_2dx(x_1)-dx(x_1)dy(x_2))}$$

$$\eta=\frac{1}{l_1\cdot l_2}\sqrt{\frac{2(B_r-B_m)}{(B_r+B_m)}(l_1-dx(x_1))\cdot(l_2-dy(x_2))\cdot(l_1dy(x_2)+l_2dx(x_1)-dx(x_1)dy(x_2))}$$ We have analyzed free vibrations of a simple supported square plate with the constant width of the ribs. Taking into the consideration *tolerance model*, we obtain from (8) differential equation describing dynamic behavior of the considered plate

$$F^{1111}\frac{\partial^4 V_3}{\partial x^4}+2(F^{1122}+2F^{1212})\frac{\partial^4 V_3}{\partial x^2 \partial y^2}+F^{2222}\frac{\partial^4 V_3}{\partial y^4}+<\tilde{\rho}>\ddot{V}_3=0 \tag{11}$$

where for square plate and $d_x = d_y = d$, $l_1 = l_2 = l$ we have

$$\begin{gathered}
F^{1111}=F^{2222}=\tilde{B}^{1111}-(1+\nu^2)(\tilde{B}^{1I11})^2 K^{1I1I}-2\nu(\tilde{B}^{1I11})^2 K^{1I2II}\ ,\\
F^{1122}=\nu B^{1111}-(1+\nu^2)(B^{1I11})^2 K^{1I2II}-2\nu(B^{1I11})^2 K^{1I1I}\ ,\\
F^{1212}=F^{1221}=\frac{1-\nu}{2}B^{1111}-2(\frac{1-\nu}{2})^2(B^{1I11})^2(K^{1II1II}+K^{1II2I})\ ,
\end{gathered} \tag{12}$$

Exemplified modulus:

$$K^{1I1I}=\frac{\tilde{B}^{2II2II}}{\tilde{B}^{1I1I}\tilde{B}^{2II2II}-(\tilde{B}^{1I2II})^2}\ ,\quad K^{1I2II}=\frac{-\tilde{B}^{1I2II}}{\tilde{B}^{1I1I}\tilde{B}^{2II2II}-(\tilde{B}^{1I2II})^2}\ ,$$

$$\tilde{B}^{1111}=B_r[(1-nd)(nd+\alpha(1-nd))+nd]\ ,\ <\tilde{\rho}>=\tilde{\rho}_r[(1-nd)(nd+\beta(1-nd))+nd]\ ,$$

$$\alpha=B_m/B_r\ ,\qquad \beta=\tilde{\rho}_m/\tilde{\rho}_r\ ,\qquad nd=d/l\ .$$

In the above formulae we have assume: Poisson's ratio $\nu=\nu_m=\nu_r$, B_m, B_r stiffness of the matrix and rib respectively, $\tilde{\rho}_m, \tilde{\rho}_r$ - mass density of the matrix and rib related to the plate midplane.

The equation (11) is in the form analogous to equation of motion of homogeneous orthotropic plate. This equation will be solved similar to known method for simply supported rectangular plates. Restricting our considerations to harmonic vibrations $V\left(x^1,x^2,t\right)=V\left(x^1,x^2\right)e^{i\omega t}$ we derive equation

$$\frac{\partial^4 V}{\partial x^4}+2\eta\varepsilon^2\frac{\partial^4 V}{\partial x^2\partial y^2}+\varepsilon^4\frac{\partial^4 V}{\partial y^4}-\frac{<\tilde{\rho}>}{F^{1111}}\omega^2 V=0 \tag{13}$$

where $\qquad \varepsilon^4=\dfrac{F^{2222}}{F^{1111}}\ ,\qquad \eta=\dfrac{F^{1122}+2F^{1212}}{\sqrt{F^{2222}/F^{1111}}}$

Substituting $V(x,y)=V_{mn}\sin(\frac{m\pi}{L_x}x)\sin(\frac{n\pi}{L_y}y)$ into equation (13) we derive formula for free vibration frequencies

$$\omega_{mn}=\frac{\pi^2}{{L_x}^2}\sqrt{\frac{F^{1111}}{<\tilde{\rho}>}}\sqrt{m^4+2\eta\varepsilon^2(\frac{mnL_x}{L_y})^2+\varepsilon^4(\frac{nL_x}{L_y})^4} \tag{14}$$

The results obtained above were compared to finite element method calculated by Abaqus program [11]. It was considered two-dimensional shell element with a thickness equal to 0,10m. The way of modeling of the plate in Abaqus program was described in the paper [2]. Ribs are represented by the slave and matrix by master surface. The boundary conditions were established as simply supported along the circumference of the plate. Calculations were provided for the linear perturbation (frequency). As mesh element we assume S4R element as a 4-node doubly curved thin (or thick) shell which provides reduced integration, hourglass control and finite membrane strains. The mesh was added to the matrix and ribs separately bearing in mind that for the slave surface the mesh needs to be denser. To verify model equations and Abaqus program there will be compared values of the first four vibration frequencies.

4. Results

Free vibrations frequencies for the plate with constant width of the ribs and geometric and material parameters shown below for different shape functions are in Table 1.

Geometric data: $h = 0{,}1m$, size of the plate: $L_1 = L_2 = 4{,}0m$, width of the ribs: $d = 0{,}05m$, size of the cell: $l_1 = l_2 = 0{,}20m$. Material data: $E_r = 210GPa,\ \nu_r = \nu_m = 0{,}3,\ \rho_r = 7800kg/m^3,\ E_m = 20GPa,\ \rho_m = 2400kg/m^3$

Table 1. First four free vibrations frequencies for different shape functions

	1st mode	**2nd mode**	**3rd mode**	**4th mode**	**Versions 1-4/ Abaqus**
	[Hz]	[Hz]	[Hz]	[Hz]	
Version 1	141,783	361,147	361,147	567,133	1,62%
Version 2	161,497	405,614	405,614	645,987	13,63%
Version 3	170,305	426,001	426,001	681,22	18,09%
Version 4	182,561	455,748	455,748	730,245	23,59%
Abaqus	139,490	357,32	357,32	555,060	

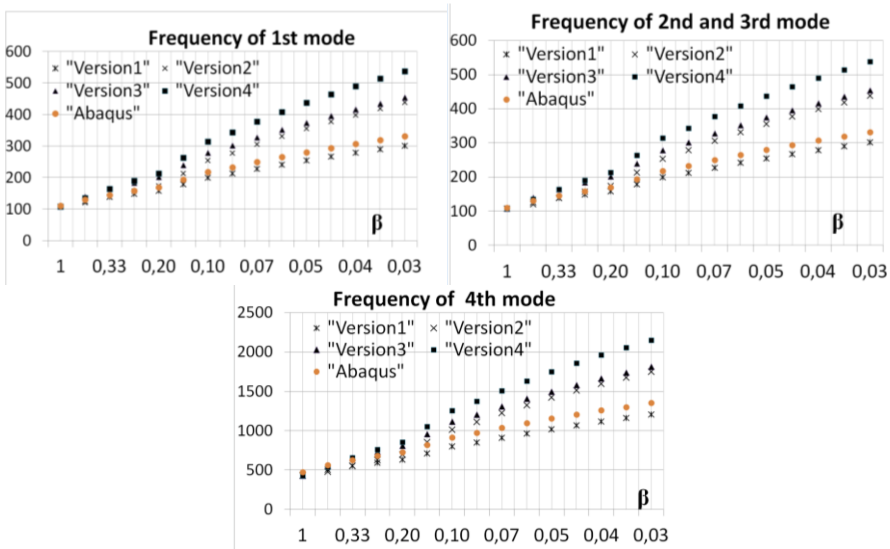

Figure 4. First four free vibrations frequencies depending on parameter β

In the Figure 4 there are shown free frequencies of the first four modes. On the horizontal axis is presented parameter $\beta = E_m / E_r$. The calculations are made for the constant density equal to $2400 kg / m^3$ and respectively for different amplitudes (10b).

5. Conclusion

It can be observed that free vibrations for different *versions* vary from 2% till 24%. Only the 2nd and 4th versions depend on Young's modulus, We can recognize that the results shown in the Figure 4 are convergent for homogenous plate $(\beta = 1)$. The higher the β parameter is, the higher is the difference between parameters**.** The most consistent with Abaqus' outcome is the 1st *version*. Further research, in which influence of different Young's modulus on the free vibrations will be investigated.

References

1. C. Woźniak, B. Michalak, J. Jędrysiak, (eds.), *Thermomechanics of Heterogeneous Solids and Structures*, Lodz University of Technology, Lodz 2008.
2. B. Michalak, M. Rabenda, *Tolerance modelling of dynamic behavior of thin plates with dense system of ribs in two direction*, paper under review in Archives of Civil and Mechanical Engineering.
3. M. Rabenda, B. Michalak, *Natural vibrations of prestressed thin functionally graded plates with dense system of ribs in two directions*, Composite Structures, **133** (2015) 1016 – 1023.
4. E. Baron , *On modelling of periodic plates with inhomogeneity period of an order of the plate thickness*, J.Theor. Appl. Mech., **44** (2006) 3 – 18.
5. S. J. Matysiak, W. Nagórko, *On the wave propagation in periodically laminated composites*, Bulletin of the Polish Academy of Science - Technical Sciences, **43** (1995) 1 – 12.
6. K. Jeleniewicz, W. Nagórko, *Free vibrations in periodically ribbed elastic plate*, Acta Scientiarum Polonorum, s. Architectura, **9**(2) (2010) 11 – 21.
7. B. Michalak, *Vibrations of plates with initial geometrical periodical imperfections interacting with a periodic elastic foundation*, Archive of Applied Mechanics, **70** (2000) 508 – 518.
8. J. Marczak, J. Jędrysiak, *Tolerance modelling of vibrations of periodic three-layered plates with inert core*, **134** (2015) 854 – 861.
9. B. Michalak, A. Wirowski, *Dynamic modeling of thin plate made of certain functionally graded materials*, Meccanica, **47** (2012) 1487 – 1498.
10. C. Woźniak, M. Wagrowska, O. Szlachetka, *Asymptotic modelling and design of some microlayered functionally graded heat conductors*, ZAMM, **92** (2012) 841 – 848.
11. https://portal.plgrid.pl/web/guest/home

The Dynamics of a Coupled Mechanical System with Spherical Pendulum

Danuta SADO
Warsaw University of Technology, Institute of Machine Design Fundamentals
Narbutta 84, 02-524 Warsaw, dsado@poczta.onet.pl

Jan FREUNDLICH
Warsaw University of Technology, Institute of Machine Design Fundamentals
Narbutta 84, 02-524 Warsaw, jfr@simr.pw.edu.pl

Anna DUDANOWICZ
International School of Gdansk, Sucha 29, 80-180 Gdansk
aniamil@wp.pl

Abstract

The nonlinear response of a three degree of freedom vibratory system with spherical pendulum in the neighbourhood internal and external resonance is investigated. It was assumed that spherical pendulum is suspended to the main body which is suspended by the element characterized by elasticity and damping and is excited harmonically in the vertical direction. The equation of motion have bean solved numerically. In this type system one mode of vibration may excite or damp another one, and for except different kinds of periodic vibrations there may also appear chaotic vibration.

Keywords: Spherical pendulum, energy transfer, coupled oscillators, chaos

1. Introduction

The subject of this work is investigation of initial conditions effect on dynamics of a three degree of freedom system with spherical pendulum. Dynamical systems with element of the mathematical or physical pendulum type have important applications. Different kind of coupled autoparametric oscillators with simply pendulums is presented in book [1]. The real pendulum is a spherical character. Spherical pendulum was investigated by a lot of researches. Spherical pendulum subject to parametric excitation was studied by Miles and Zou [2], and with kinematic external excitation by Naprstek and Fischer [3]. The bifurcation behaviour of a spherical pendulum where the suspension point is harmonically excited in both vertical and horizontal directions was presented by Leung and Kung [4], spherical pendulum with moving pivot by Mitrev and Grigorov [5], stochastic analysis of a spring spherical pendulum was done by Viet [6], the dynamics coupled spherical pendulums was studied by Witkowski at all [7].

In the present paper is assumed that the spherical pendulum is suspended to the flexible element, so in this system may occur the autoparametric excitation as a result of inertial coupling.

2. System description and equation of motion

The investigated system is shown in Figure 1.

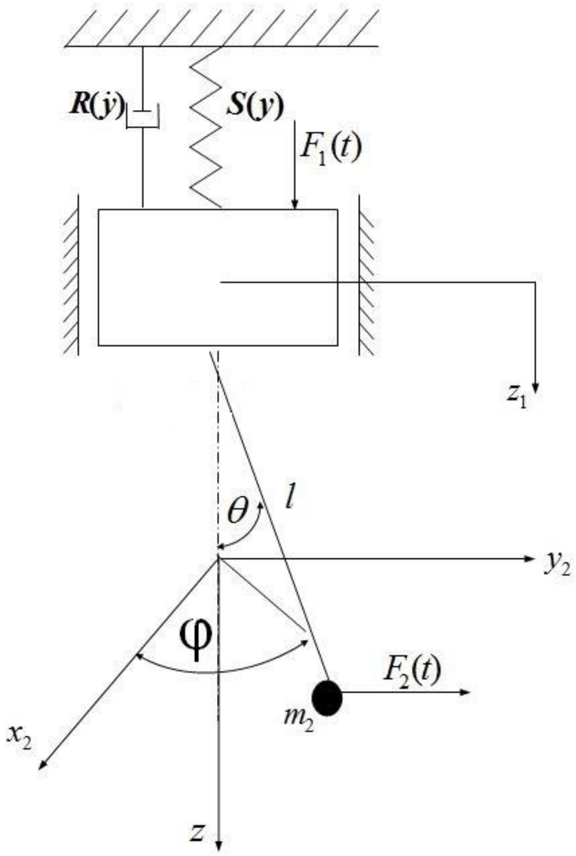

Figure 1. Schematic diagram of system

The system consists of a body of mass m_1 suspended on the flexible element of rigidity k and damping c and a spherical pendulum of length l and mass m_2 suspended on the body of mass m_1.The body of mass m_1 subjected to harmonic vertical excitation and the spherical pendulum subjected to harmonic horizontal excitation.

The spherical pendulum is similar to the simple pendulum, but moves in 3-dimensional space, so we need to introduce the new variable φ in order to describe the rotation of the pendulum in space xy. The position of the body of mass m1 is described by coordinate z and position of the pendulum is describe by coordinate z and two angles: Θ and φ. Angle Θ is the deflections of pendulum measured from the vertical line. This system has three degrees of freedom . The equations of motion are derived as Lagrange's equations.

The kinetic energy E_k is the sum of the energy two bodies

$$E_k = \frac{m_1 v_1^2}{2} + \frac{m_2 v_2^2}{2} = \frac{m_1 \dot{z}^2}{2} + \frac{m_2(\dot{x}_2^2 + \dot{y}_2^2 + \dot{z}_2^2)}{2} \tag{1}$$

where

$$\begin{aligned} x_2 &= l\sin\theta\cos\varphi \\ y_2 &= l\sin\theta\sin\varphi \\ z_2 &= z + l\cos\theta \end{aligned} \tag{2}$$

The kinetic energy E_k are given by the expression

$$E_k = \frac{1}{2}(m \ + m_2)\ \dot{z}^2 + \frac{1}{2} m_2 (l\ \dot{\theta}^2 + l^2 \dot{\varphi}^2 \sin^2\theta - 2\ l\ \dot{z}\ \dot{\theta}\sin\theta) \tag{3}$$

The potential energy E_p are given by the expression

$$E_p = -(m_1 + m_2) g (z + z_{st}) + m_2 g (l - l\cos\theta) + \frac{k(z + z_{st})^2}{2} \tag{4}$$

Assuming that the exciting forces are in form: $F\,(t) = P_1 \cos\nu_1 t \quad F_2(t) = P_2 \cos\nu_2 t$, the equations of motion of the system are in form

$$\begin{aligned} &(m_1 + m_2)\ \ddot{z} - m_2 l\ddot{\theta}\sin\theta - m_2 l\dot{\theta}^2\cos\theta + kz + c\dot{z} = P_1\cos\nu_1 t \\ &m_2 l^2\ddot{\theta} - m_2 l\ddot{z}\sin\theta - m_2 l^2\dot{\phi}^2\sin\theta\cos\theta + m_2 g l\sin\theta = l\cos\theta\sin\varphi\ P_2\cos\nu_2 t \\ &m_2 l^2\ddot{\varphi}\sin^2\theta + 2 m_2 l^2\dot{\varphi}\ \dot{\theta}\sin\theta\cos\theta = l\sin\theta\cos\theta\ P_2\cos\nu_2 t \end{aligned} \tag{5}$$

By introducing the dimensionless time and dimensionless parameters

$$\begin{aligned} &\tau = \omega_1 t, \quad \omega_1^2 = \frac{k}{m_1 + m_2}, \quad \omega_2^2 = \frac{g}{l}, \quad \beta = \frac{\omega_2}{\omega_1}, \quad \gamma = \frac{c}{(m_1 + m_2)\omega_1}, \quad \bar{z} = \frac{z}{l} \\ &a = \frac{m_2}{m_1 + m_2}, \quad A_1 = \frac{P_1}{(m_1 + m_2)\omega_1^2}, \quad A_2 = \frac{P_2}{m_2 l \omega_1^2}, \quad \mu_1 = \frac{\nu_1}{\omega_1}, \quad \mu_2 = \frac{\nu_2}{\omega_1} \end{aligned} \tag{6}$$

We can transform (5) into dimensionless form

$$\ddot{z} - a\ddot{\theta}\sin\theta - \dot{\theta}^2\cos\theta + z + \gamma\ \dot{z} = A_1\cos\mu_1\tau$$

$$\ddot{\theta} - \ddot{z}\ \sin\theta - \dot{\varphi}^2\sin\theta\cos\theta + \beta^2\sin\theta = A_2\cos\theta\sin\varphi\cos\mu_2\tau \qquad (7)$$

$$\ddot{\varphi}\sin\theta + 2\dot{\varphi}\ \dot{\theta}\cos\theta = A_2\cos\theta\cos\mu_2\tau$$

(where the overbars denoting nondimensionalisation are omitted for convenience).
After transformations equations of motion can be written in form easier to calculations

$$\ddot{z} = [(A_1\cos\mu_1\tau + a\dot{\theta}^2\cos\theta - z - \gamma\ \dot{z}) + a(\varphi^2\sin\theta\cos\theta - \beta^2\sin\theta)]\sin\theta/(1 - a\sin^2\theta)$$

$$\begin{aligned}\ddot{\theta} = \dot{\varphi}_2\sin\theta\cos\theta - \beta^2\sin\theta + [(A_1\cos\mu_1\tau + a\dot{\theta}^2\cos\theta - z - \gamma\ \dot{z}) + a(\dot{\varphi}_2\sin\theta\cos\theta + \\ - \beta^2\sin\theta)\sin^2\theta]\sin\theta/(1 - a\sin^2\theta)\end{aligned} \qquad (8)$$

$$\ddot{\varphi} = (A\ \cos\theta\cos\mu_2\tau - 2\ \dot{\varphi}\ \dot{\theta}\cos\theta)/\sin\theta$$

3. Numerical results

Equations (8) are solved numerically by using R-K method with step length variable. The calculations are carried out for different values of parameters of the system and for different initial conditions. Exemplary time histories of displacements z and θ obtained for the initial conditions for the body of mass m_1 are presented in Figure 2, where we can observe the energy transfer between the modes of vibration in a closed cycle. In this case spherical pendulum behaviour is the some than simple pendulum and the motion of pendulum is in vertical plane (angle φ is constant**)**. The diagram of internal resonance for initial conditions put on the displacements is presented in Figure 4 and it is similar to simple pendulum presented in work [1]. We observe resonance excitation for frequency ratio β=0.5. In this case assuming the simple pendulum results are good.

When the initial conditions are put on the displacements and on the velocities ($z(0) = 0;\ \dot{z}(0) = 0.;\ \theta(0) = 5^\circ, \dot{\theta}(0) = -0.04; \varphi(0) = 0;\ \dot{\varphi}(0) = -0.96$) we observe influence of angle φ. (Figures 3). Exemplary internal resonance in this case we observe for frequency ratio β=0.51 (Figure 5).

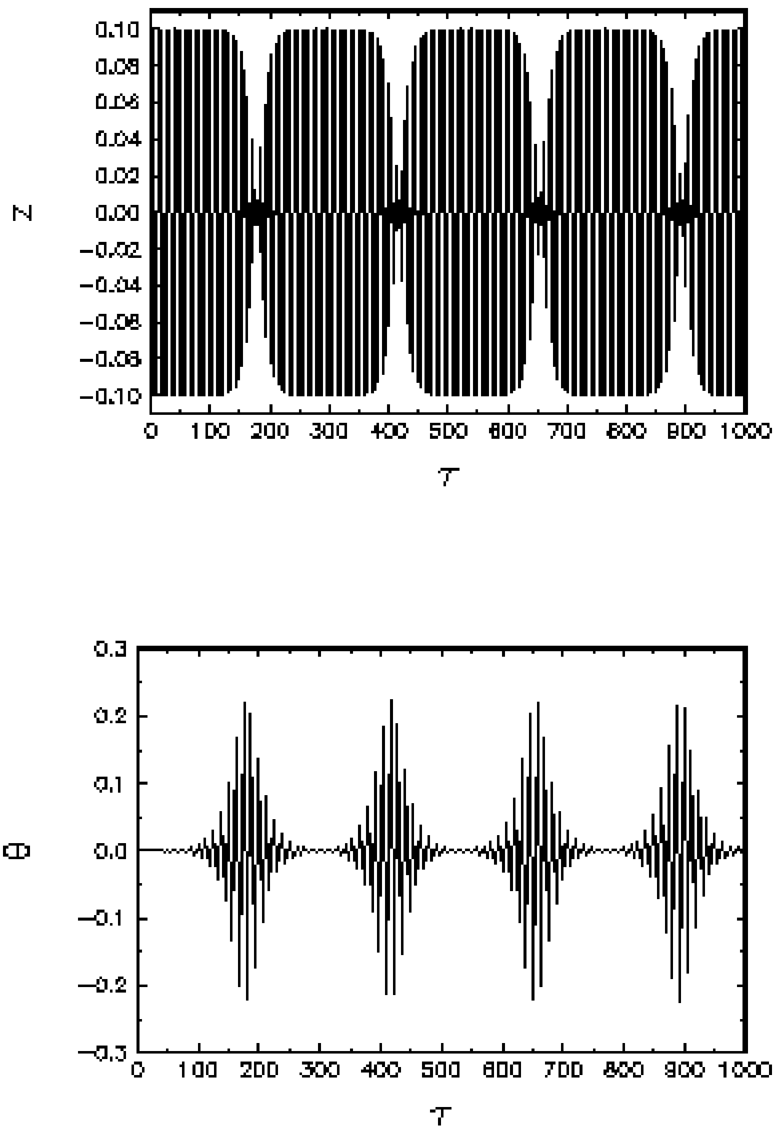

Figure 2. Time history for: a=0.8; β=0.5;γ=0; A_1=A_2=0;
z(0)=0.1;Θ(0)=0.005˚; φ(0)=0

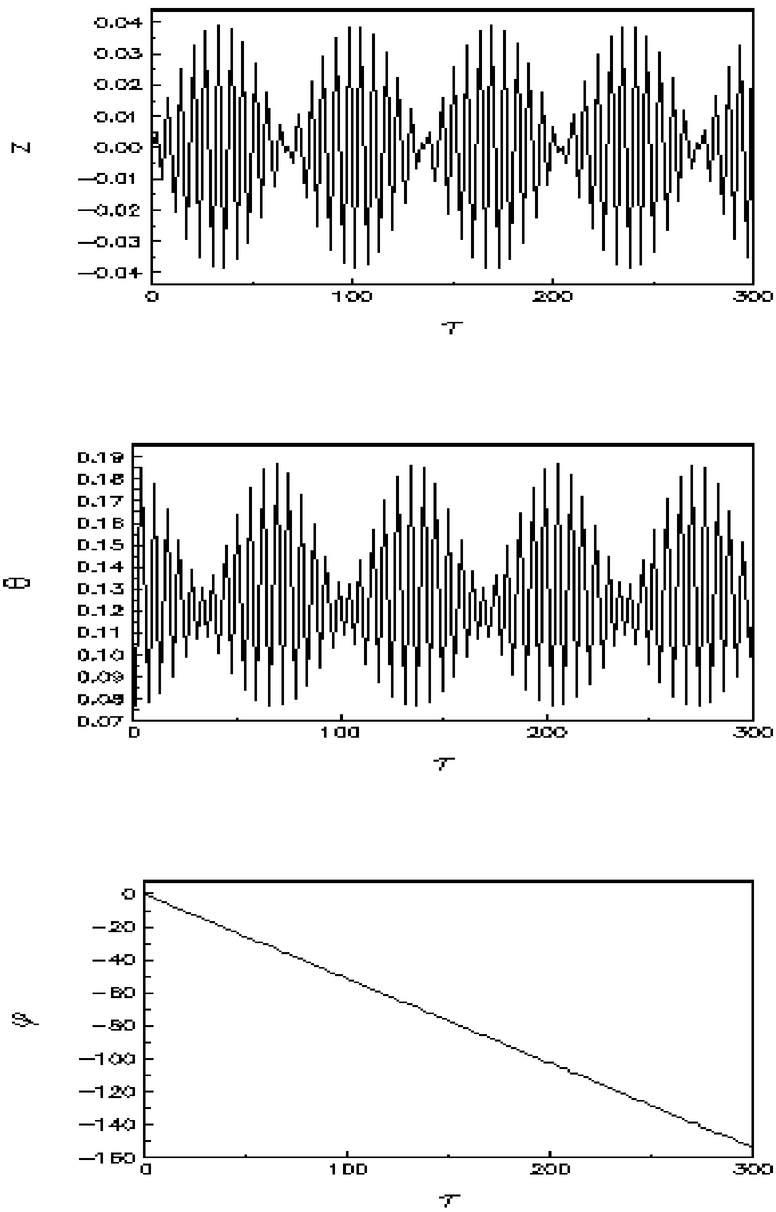

Figure 3. Time history for: a=0.5; β=0.51;γ=0; A_1=A_2=0;
$z(0)=0;\ \dot{z}(0)=0;\ \theta(0)=5^\circ,\ \dot{\theta}(0)=-0.04;\ \varphi(0)=0;\ \dot{\varphi}(0)=-0.96$

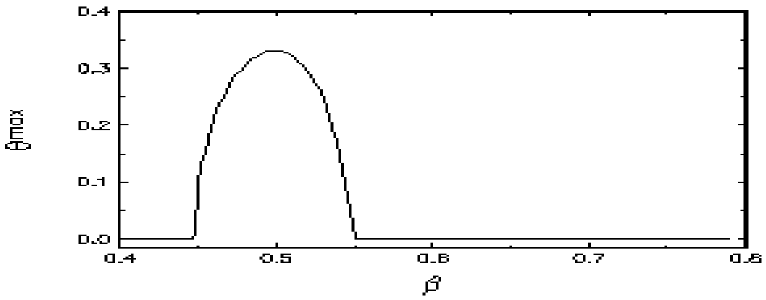

Figure 4. Internal resonance for: a=0.8;γ=0; A_1=A_2=0;
z(0)=0.1; Θ(0)=0.005˚; φ(0)=0

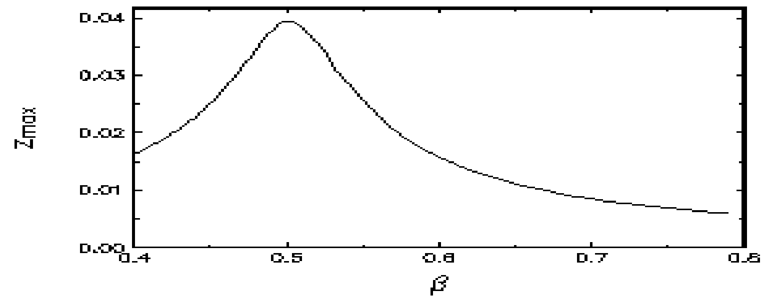

Figure 5. Internal resonance for: a=0.5;γ=0; A_1=A_2=0;
$z(0)=0;\ \dot{z}(0)=0;\ \theta(0)=5^{\circ},\ \dot{\theta}(0)=-0.04;\ \varphi(0)=0;\ \dot{\varphi}(0)=-0.96$

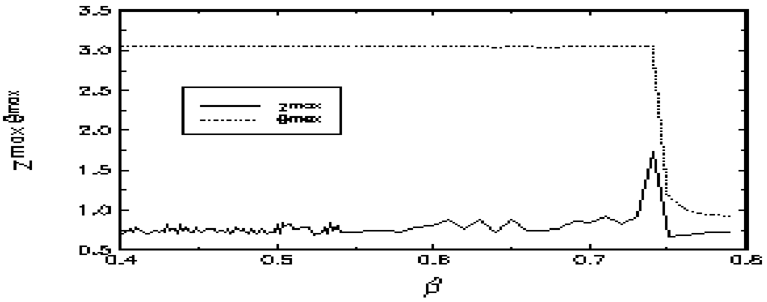

Figure 6. Internal resonance for: a=0.2;γ=0; A_1=A_2=0;
$z(0)=0;\ \dot{z}(0)=0.65;\ \theta(0)=50^{\circ},\ \dot{\theta}(0)=-0.04;\ \varphi(0)=0;\ \dot{\varphi}(0)=-0.296$

But when the initial conditions are put on the displacements and on the velocities ($z(0)=0;\ \dot{z}(0)=0.65;\ \theta(0)=50^{\circ},\dot{\theta}(0)=-0.04;\varphi(0)=0;\ \dot{\varphi}(0)=-0.296$) we observe influence of angle φ and internal resonance area in this case we observe for frequency ratio near β=0.75 (Figure 6). In this case φ described the rotation of the pendulum around axis z, so assuming the spherical pendulum we have the results more similar to the real system.

3. Conclusions

The influence of initial conditions on the behaviour of an autoparametric system with spherical pendulum is very interesting, because sometimes when initial conditions are put on the displacements spherical pendulum is similar to simple pendulum (angle φ is const.), but when the initial conditions are put on the velocities we observe influence of angle φ. It is important, because near internal and external resonance area can existence the different motion - regular or chaotic. The autoparametric systems are very sensitive on nonlinearities. The spherical pendulum is more similar to the real systems then the simply pendulum.

References

1. D. Sado, *Drgania regularne i chaotyczne w wybranych układach z wahadłami*, WNT Warszaw, 2010 (in Polish).
2. J. W. Miles and Q. P. Zou, *Parametric excitation of a detuned spherical pendulum,* Journal of Sound and Vibration, **164**(2) (1993) 237 – 250.
3. J. Naprstek and C. Fischer, *Auto-parametric semi-trival and post-critical response of a spherical pendulum damper,* Computers and Structures, **87** (2009) 1204 – 1215.
4. A. Y. T. Leung, J. L. Kuang, *On the chaotic dynamics of a spherical pendulum with a harmonically vibrating suspension*, Nonlinear Dynamics, **43** (2006) 213 – 238.
5. R. Mitrov, B. Grigorov, *Dynamic behaviour of a spherical pendulum with spatially moving pivoti*, Zeszyty Naukowe Politechniki Poznańskiej, **9** (2009) 81 – 91.
6. L. D. Viet, *Partial stochastic linearization of a spherical pendulum with coriolis damping produced by radial spring and damper*, Journal Vib. Acoust., **137**(5) 1 – 9, Paper No.VIB-14-1388; doi: 10.1115/1.4030663.
7. B. Witkowski at all, *The dynamics of co- and counter rotating coupled spherical pendulums,* EPJ, 2014.

Transverse and Longitudinal Damped Vibrations of Hydraulic Cylinder in a Mining Prop

Wojciech SOCHACKI
Institute of Mechanics and Fundamentals of Machinery Design
University of Technology, Czestochowa, sochacki@imipkm.pcz.pl

Marta BOLD
Institute of Mechanics and Fundamentals of Machinery Design
University of Technology, Czestochowa, bold@imipkm.pcz.pl

Abstract

This study presents the influence of different kinds of damping on transverse and longitudinal vibrations of hydraulic cylinder in a mining prop. The dissipation of vibration energy in the model is caused by simultaneous internal damping of viscoelastic material of beams that model the system, external viscous damping and constructional damping. Constructional damping (modelled by the rotational viscous dampers) occurs as a result of movement resistance in the cylinder supports. The eigenvalues of the system with respect to changes in system geometry with two values of load and for a selected and variable damping coefficient values were calculated.

Keywords: damped vibration, hydraulic cylinder, transverse vibration, longitudinal vibration

1. Introduction

A hydraulic cylinder as an object of research studies on dynamics of mechanical systems has been extensively investigated in the number of studies. Most of the published studies focused on the interactions between the cylinder tube and piston rod. Results of the investigations of the dynamic response of the model of a cylinder to axial impulse were presented in paper [1]. The work [2] presents an analysis of the effect of initial inaccuracy of connection between the piston and cylinder tube on critical loading force in the cylinder. Many authors analysed the effect of sealing or the medium on the cylinder's dynamics and dynamic stability of cylinder. In study [3] calculations of free vibration frequencies were extended with the investigations of the dynamic stability of the cylinder by means of determination of geometrical parameters and load at the time of losing the stability were presented. In paper [4] the problem of the stability and free vibrations of a slender system in the form of a hydraulic cylinder subjected to Euler's load was carried out. The studies [5] and [6] present the effect of internal damping on vibrations of a support beam with a mass attached to a free end of the beam and on stability of a support column loaded with a follower force, respectively. The influence of small internal and external damping on stability of non-conservative beam systems is described in paper [7]. Equally interesting publication concerning the effect of external damping on vibration of beams with stepped cross-section is the study [8]. The effect of structural damping of fixations on free vibration of the linear Bernoulli-Euler beam was presented in the study [9].

In study [10] dissipation of vibration energy in the model of hydraulic cylinder – boom crane system occurs as a result of simultaneous internal damping of the viscoelastic material of the beam used in the model and the constructional damping in the supports of the cylinder and crane boom. The constructional damping of supports was modelled using rotational viscous dampers. The problem to be considered in the study [11] is the natural vibration of the system consisting of two clamped-free rods carrying tip masses to which several double spring-mass systems are attached across the span. The study is concerned with longitudinal vibrations of this mechanical system and the major contribution of this study is to derive a general formulation for the exact solution of the system described by using the Green's function method.

This study analyses the simultaneous effect of the constructional damping, internal damping, external damping and the influence of changes in system geometry on the transverse and longitudinal vibrations of hydraulic cylinder in a mining prop. The results obtained in the study were presented in 2D figures and spatial presentations.

2. Mathematical Model

A scheme of the considered system is presented in Fig. 1. The model of a hydraulic cylinder is composed of four beams. Two of them model a cylinder tube (l_{11}, l_{12}) and two - piston rod (l_{21}, l_{22}) in the cylinder. The liquid in the cylinder was adopted as the medium of load transfer between the piston and the cylinder along the length filled with liquid. The liquid rigidity in the cylinder was modelled by the translational spring. Stiffness coefficient of spring was denoted by k_S.

In adopted model dissipation of vibration energy was caused by simultaneous internal damping, external damping and constructional damping. Internal damping of the viscoelastic material for individual parts of hydraulic cylinder was characterized by Young's modulus E_{mn} and viscosity coefficients E^*_{mn}. External damping of medium surrounding the system were denoted by coefficient c_e. Constructional damping occurs as a result of movement resistance in the piston and the cylinder supports and it was modelled by the rotational viscous dampers. Damping coefficients of rotational viscous dampers were denoted by c_R.

The boundary problem connected to the free vibrations of the considered non-conservative (due to damping) system was formulated on the basis of Hamilton's principle in the following form:

$$\delta\int_{t_1}^{t_2}(T-V)dt+\int_{t_1}^{t_2}\delta W_N\,dt=0 \tag{1}$$

where: T – kinetic energy, V – potential energy, δW_N – virtual work of non-conservative forces originating from damping.

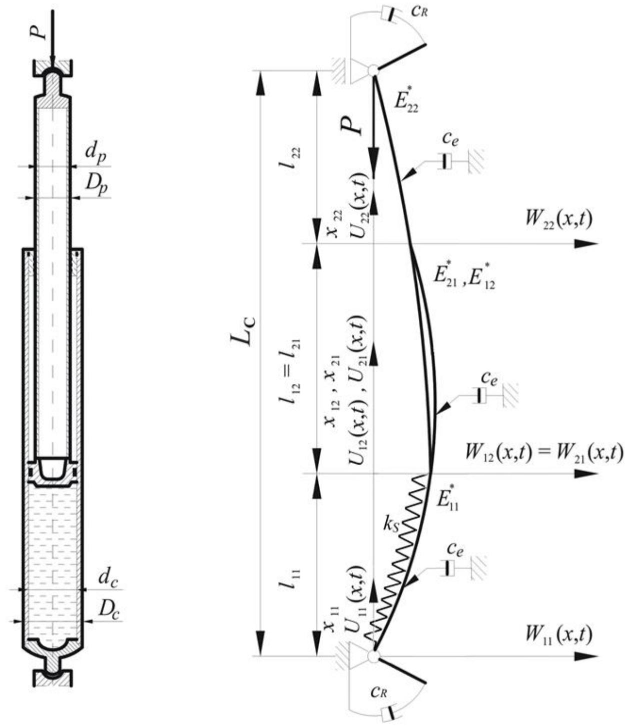

Figure 1. Diagram and beam model of a hydraulic cylinder with damping

The vibration equations for individual beams are known and have the following form:

$$J_{mn}\left(E_{mn}+E_{mn}^{*}\frac{\partial}{\partial t}\right)\frac{\partial^4 W_{mn}(x_{mn},t)}{\partial x_{mn}^4}+P\frac{\partial^2 W_{mn}(x_{mn},t)}{\partial x_{mn}^2}+ \\ +\rho_{mn}A_{mn}\frac{\partial^2 W_{mn}(x_{mn},t)}{\partial t^2}+c_e\frac{\partial W_{mn}(x_{mn},t)}{\partial t}=0 \tag{2}$$

where:

$$-A_{mn}\left(E_{mn}+E_{mn}^{*}\frac{\partial}{\partial t}\right)\frac{\partial^2 U_{mn}(x_{mn},t)}{\partial x_{mn}^2}+\rho_{mn}A_{mn}\frac{\partial^2 U_{mn}(x_{mn},t)}{\partial t^2}=0 \tag{3}$$

where: $m,n = 1,2$ ($c_e = 0$ for $m = 2$ and $n = 1$)
$W_{mn}(x_{mn}, t)$ – transverse displacement of beams that model cylinder and piston rod
$U_{mn}(x_{mn}, t)$ – longitudinal displacement of beams that model cylinder and piston rod
E_{mn} – Young's modulus for individual beams,
E^{*}_{mn} – material viscosity coefficient,
J_{mn} – moment of inertia in beam cross-sections,
A_{mn} – cross-sectional areas of the beams,

ρ_{mn} – beam material density,
c_e – viscous damping coefficient,
P – cylinder loading force (at the length l_{12} of the cylinder tube coverage with the piston rod in the cylinder P=0)
x_{mn} – spatial coordinates, t – time

Solutions of equations (2) and (3) are in the form:

$$W_{mn}(x_{mn},t)=w_{mn}(x_{mn})e^{i\omega^* t} \tag{4}$$

$$U_{mn}(x_{mn},t)=u_{mn}(x_{mn})e^{i\omega^* t} \tag{5}$$

where: ω^* – the complex eigenvalue of the system, $i=\sqrt{-1}$
Substitution of (4) and (5) into (2) and (3) leads to, respectively:

$$w_{mn}^{IV}(x_{mn})+\beta_{mn}^2 w_{mn}^{II}(x_{mn})-\gamma_{mn}w_{mn}(x_{mn})=0 \tag{6}$$

$$u_{mn}^{II}(x_{mn})+\alpha_{mn}^2 u_{mn}(x_{mn})=0 \tag{7}$$

where:

$$\begin{gathered}\gamma_{mn}=\frac{\rho_{mn}A_{mn}}{J_{mn}(E_{mn}+E_{mn}^* i\omega^*)}\left(\omega^{*2}-\frac{c_e}{\rho_{mn}A_{mn}}i\omega^*\right),\\ \alpha_{mn}=\frac{\rho_{mn}\omega^{*2}}{(E_{mn}+E_{mn}^* i\omega^*)},\ \beta_{mn}=\sqrt{\frac{P}{(E_{mn}+iE_{mn}^*\omega^*)J_{mn}}}\end{gathered} \tag{8}$$

Boundary conditions:

$$\begin{gathered}
w_{11}(0)=w_{12}^{II}(l_{12})=w_{21}^{II}(0)=w_{22}(l_{22})=0,\ w_{11}^{I}(l_{11})=w_{12}^{I}(0),\\
w_{21}^{I}(l_{21})=w_{22}^{I}(0),\ \ w_{11}(l_{11})=w_{12}(0)=w_{21}(0),\\
w_{12}(l_{12})=w_{21}(l_{21})=w_{22}(0),\ \ E_{11}J_{11}w_{11}^{II}(0)=c_R i\omega^* w_{11}^{I}(0),\\
(E_{12}+E_{12}^* i\omega^*)J_{12}w_{12}^{II}(0)=(E_{11}+E_{11}^* i\omega^*)J_{11}w_{11}^{II}(l_{11}),\\
(E_{22}+E_{22}^* i\omega^*)J_{22}w_{22}^{II}(0)=(E_{21}+E_{21}^* i\omega^*)J_{21}w_{21}^{II}(l_{21}),\\
E_{22}J_{22}w_{22}^{II}(l_{22})=-c_R i\omega^* w_{22}^{I}(l_{22}),\ \ (E_{11}+E_{11}^* i\omega^*)J_{11}w_{11}^{III}(l_{11})+\\
+Pw_{11}^{I}(l_{11})-(E_{12}+E_{12}^* i\omega^*)J_{12}w_{12}^{III}(0)+\\
-(E_{21}+E_{21}^* i\omega^*)J_{21}w_{21}^{III}(0)-Pw_{21}^{I}(0)=0,\\
(E_{12}+E_{12}^* i\omega^*)J_{12}w_{12}^{III}(l_{12})+(E_{21}+E_{21}^* i\omega^*)J_{21}w_{21}^{III}(l_{21})+\\
-(E_{22}+E_{22}^* i\omega^*)J_{22}w_{22}^{III}(0)=0,\ \ u_{21}(l_{21})=u_{22}(0),\ \ u_{11}(l_{11})=u_{12}(0),\\
u_{11}(0)=u_{21}(l_{21})=0,\ \ (E_{21}+E_{21}^* i\omega^*)A_{21}u_{21}^{I}(l_{21})=(E_{22}+E_{22}^* i\omega^*)A_{22}u_{22}^{I}(0),\\
(E_{21}+E_{21}^* i\omega^*)A_{21}u_{21}^{I}(0)=-k_S u_{21}(0),\ \ (E_{22}+E_{22}^* i\omega^*)A_{22}u_{22}^{I}(l_{22})=P,\\
(E_{12}+E_{12}^* i\omega^*)A_{12}u_{12}^{I}(0)=(E_{11}+E_{11}^* i\omega^*)A_{11}u_{11}^{I}(l_{11})
\end{gathered} \tag{9}$$

The solution of equations (6) and (7) are expressed in the form of functions:

$$w_{mn}(x) = C_{1mn}e^{\lambda_{mn}x} + C_{2mn}e^{-\lambda_{mn}x} + C_{3mn}e^{i\bar{\lambda}_{mn}x} + C_{4mn}e^{-i\bar{\lambda}_{mn}x} \tag{10}$$

$$u_{mn}(x) = D_{1mn}e^{i\bar{\delta}_{mn}x} + D_{2mn}e^{-i\bar{\delta}_{mn}x} \tag{11}$$

where:

$$\lambda_{mn} = \sqrt{-\frac{\beta_{mn}^2}{2} + \sqrt{\frac{\beta_{mn}^4}{4} + \gamma_{mn}}}\ ,\ \bar{\lambda}_{mn} = \sqrt{\frac{\beta_{mn}^2}{2} + \sqrt{\frac{\beta_{mn}^4}{4} + \gamma_{mn}}}\ ,\ \bar{\delta}_{mn} = \sqrt{\alpha_{mn}} \tag{11}$$

The boundary problem is solved numerically for the eigenvalues ω^*. Depending on the solution adopted, the roots ω^* are complex numbers (that represent the damped vibration frequencies $Re(\omega^*)$ and damping $Im(\omega^*)$ in the considered system) and they may accept positive or negative value. In this paper, presentation of the results was based on positive values of the real and imaginary parts of solutions.

3. Numerical Calculation Results

Calculations were carried out for a cylinder used in a mining prop. Computations were carried out for the data contained in Table 1. Dimensionless damping parameters: η for internal damping, μ for constructional damping, and ν for external damping were placed below the table.

Table 1. Geometrical and material data adopted in the study

Quantity	Symbol	Unit	Value
Cylinder tube - external diameter	$D_{11} = D_{12}$	mm	290
Cylinder tube - internal diameter	$d_{11} = d_{12}$	mm	250
Piston rod - external diameter	$D_{21} = D_{22}$	mm	160
Piston rod - internal diameter	$d_{21} = d_{22}$	mm	120
Cylinder tube and piston rod density	ρ_{mn}	kg/m^3	7.86e3
Young's modulus	E_{mn}	Pa	21e11

Damping parameters:

$$\eta = \frac{E_{mn}^*}{hE_{mn}}\ ,\ \nu = \frac{c_e\, L_C^{\ 3}}{d}\ ,\ \mu = \frac{C_R}{d}\ ,\ p = \frac{P}{P_C}\ ,$$

$$h^2 = L_C^{\ 4}\,\frac{\sum\limits_{m,n=1}^{2}\rho_{mn}A_{mn}}{\sum\limits_{m,n=1}^{2}E_{mn}J_{mn}}\ ,\ d = L_C\sqrt{\sum_{m,n=1}^{2}\rho_{mn}A_{mn}E_{mn}J_{mn}}\ , \tag{11}$$

where: P_C – the critical load of the cylinder extended to L_C=4m and $L_C = l_{11} + l_{12} + l_{22}$.

The results of the calculations are presented in Figures 2 to 5. The system was loaded with the longitudinal force P (p=0 and p=0.3). The dependency of the eigenvalues (real parts $Re(\omega_1^*)$ and imaginary parts $Im(\omega_1^*)$) on coefficients of constructional damping μ, external damping v, internal damping η and total length of cylinder that ranged from L_C=2.6m to L_C=4m was also determined. The relationships between the first eigenvalue of cylinder and changes its total length L_C and coefficient of constructional damping μ at p=0.3 without internal and external damping in the system are presented in the form of spatial diagrams in Figure 2.

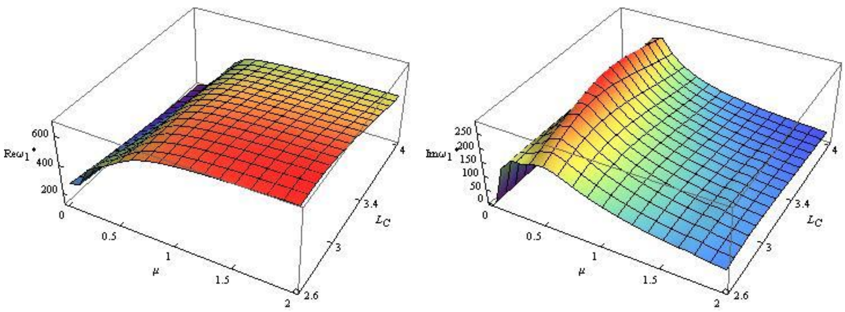

Figure 2. The dependency of the first eigenvalue ($Re(\omega^*)$ and $Im(\omega^*)$) for the cylinder on total length L_C and constructional damping μ at η=0, v =0 and p=0.3

As can be seen in the figure above, the higher value of $Im(\omega_n^*)$ then the more the amplitudes of a particular (n) mode of vibration are damped. Figure 3 presents the maximum values of $Im(\omega^*_{max})$ for the first mode of vibration in the examined system depending on the hydraulic cylinder length L_C for two values of loading.

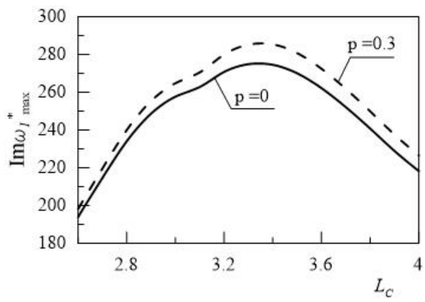

Figure 3. The relationships between the maximum values of $Im(\omega^*_{max})$ for the first mode of vibration in the cylinder and the extension total length L_C (for η=0 and v=0)

Next investigations focused on consideration of effect of different kind of damping on cylinder vibration. The dependency of real and imaginary parts of the first eigenvalue of the hydraulic cylinder on extension total length L_C for selected values of damping (η=0.02, v=0.5, μ=0.5) and for two values of loading are presented in Figure 4.

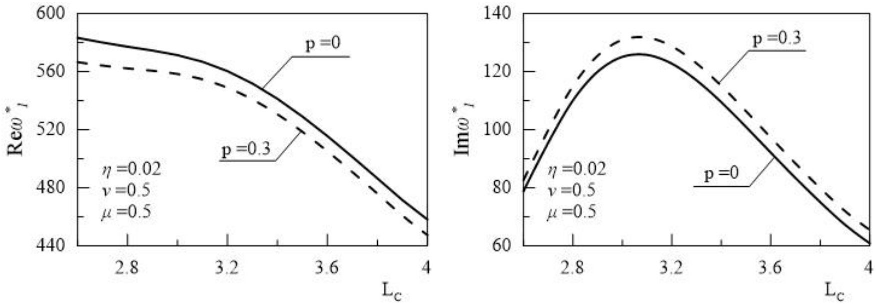

Figure 4. The dependency of the first eigenvalue ($Re(\omega^*)$ and $Im(\omega^*)$) for the cylinder on extension total length L_C

The next figure (Figure 5) presents the change in the first eigenvalue of the hydraulic cylinder depending on the external damping ν and internal damping η without loading and loaded with the force p=0.3 for selected length of cylinder L_C=3m. The investigations were carried out for optimal constructional damping value μ=0.5.

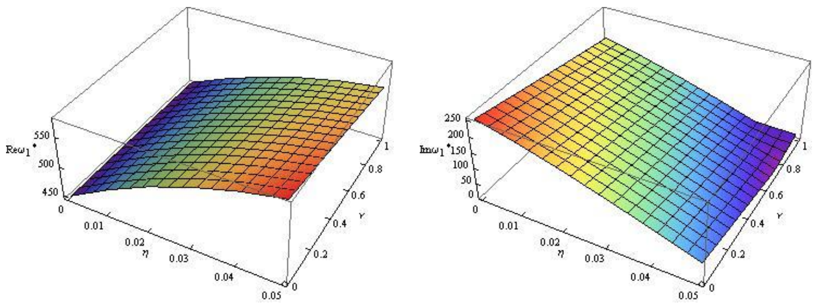

Figure 5. The dependency of the first eigenvalue ($Re(\omega^*)$ and $Im(\omega^*)$) for the cylinder on internal damping η and external damping ν at μ=0.5 and L_C =3

4. Conclusions

This study presents a beam model of a hydraulic cylinder based on the system used in mining props. The computations for the model of transverse and longitudinal vibrations in a hydraulic cylinder with damping were carried out. The model of damping took into consideration the internal damping of the beams that modelled a cylinder tube and a piston rod, external damping and constructional damping that modelled motion resistance in the supports. Substantial changes can be observed in the damped frequencies $Re(\omega_1^*)$ and in degree of amplitude decay $Im(\omega_1^*)$ in the case of changes the length of hydraulic cylinder L_C and coefficient of constructional damping μ (Figure 2). An increase in constructional damping causes the increase in the values of degree of amplitude decay $Im(\omega_1^*)$ to maximum values, followed by $Im(\omega_1^*)\to 0$ where $\mu\to\infty$. These substantial changes in both $Re(\omega^*)$ and $Im(\omega^*)$ are caused by considerable intervention in the conditions of system fixation (in extreme cases, the fixation points are changed from joint mountings into rigid mountings). The length of hydraulic cylinder extension for which the degree of vibration amplitude decay is the highest allows for determination of optimum lengths of the hydraulic cylinder with respect to minimum vibration amplitudes in the system (Figure 3). It can be concluded based on the calculations that introduction of the internal and external damping causes only insignificant changes in the first eigenvalue (Figure 5). The results presented in the study help determine the geometric parameters and values of the coefficients that characterize damping of the system for which the maximum degree of amplitude decay is maintained.

Acknowledgments

This research was supported by the Ministry of Science and Higher Education in 2016, Warsaw, Poland.

References

1. L. Tomski, S. Kukla, *Dynamical response of bar-fluid-shell system simulating hydraulic cylinder subjected to arbitrary axial excitation*, Journal of Sound and Vibration, **92**(2) (1984) 273 – 284.
2. P. J. Gamez-Montero, E. Salazar, R. Castilla, J. Freire, M. Khamashta, E. Codina, *Misalignment effects on the load capacity of a hydraulic cylinder*, International Journal of Mechanical Sciences, **51** (2009) 105 – 113.
3. W. Sochacki, L. Tomski, *Free vibration and dynamic stability of hydraulic cylinder set*, Machine Dynamics Problems, **23**(4) (1999) 91 – 104.
4. L. Tomski, S. Uzny, *A hydraulic cylinder subjected to Euler's load in aspect of the stability and free vibrations taking into account discrete elastic elements*, Archives of Civil and Mechanical Engineering, **11**(3) (2011) 769 – 785.
5. M. Gürgöze, A. N. Doğruoğlu, S. Aeren, *On the eigencharacteristics of a cantilevered visco-elastic beam carrying a tip mass and its representation by a spring-damper-mass system*, Journal of Sound and Vibration, **301** (2007) 420 – 426.
6. S. U. Ryu, Y. Sugiyama, *Computational dynamics approach to the effect of damping on stability of cantilevered column subjected to a follower force*, Computers & Structures, **81**(4) (2003) 265 – 271.
7. O. N. Kirrllov, A. O. Seyranin, *The effect of small internal and external damping on the stability of distributed non-conservative systems*, Journal of Applied Mathematics and Mechanics, **69** (2005) 529 – 552.
8. M. I. Friswell, A. W. Lees, *The modes of non-homogeneous damped beams*, Journal of Sound and Vibration, **242**(2) (2001) 355 – 361.
9. G. Oliveto, A. Santini, E. Tripodi, *Complex modal analysis of flexural vibrating beam with viscous end conditions*, Journal of Sound and Vibration, **200** (1997) 327 – 345.
10. W. Sochacki, M. Bold, *Damped vibration of the system of changing the crane boom radius*, Journal of Applied Mathematics and Computational Mechanics, **14**(2) (2015) 111 – 122.
11. S. Inceoğlu, M. Gürgöze, *Longitudinal vibrations of rods coupled by several spring-mass system*, Journal of Sound and Vibration, **234**(5) (2000) 895 – 905.

Load by a Force Directed Towards a Positive Pole in the Aspect of Studies on Vibrations of a Column with Crack

Krzysztof SOKÓŁ
Częstochowa University of Technology, Dąbrowskiego 73
42-200 Częstochowa, sokol@imipkm.pcz.pl

Sebastian UZNY
Częstochowa University of Technology, Dąbrowskiego 73
42-200 Częstochowa, uzny@imipkm.pcz.pl

Abstract

In this paper the results of numerical studies on natural vibration frequency and stability of a slender supporting system loaded by external force directed towards a positive pole are presented. In the investigated structure the failure in the form of crack is present. The boundary problem is formulated on the basis of the principle of minimum action – Hamilton's principle. The results in the non-dimensional form are plotted as the characteristic curves in the external load – natural vibration frequency plane as well as the maximum loading capacity is discussed.

Keywords: column, crack, natural vibration, instability, characteristic curves

1. Introduction

The studies on cracks which can appear in the supporting systems are very important. The columns are classified as slender structures due to much greater length than cross section area. In slender systems the unwanted phenomena like flutter instability, buckling or non-axially applied load should be avoided. The presence of cracks reduces loading capacity and has an influence on dynamic behavior of the structure that is why an engineers must take care of this very dangerous problem before it is too late.

The investigations on cracks have been performed in recent years by inter alia Arif Gurel M. [1], Bergman [2], Binici [3], Chondros [4], Dimarogonas [5], Sokół [6] and Sokół and Uzny [7]. In the literature cracks are divided into always open and breathing cracks. In the first type is a linear problems - static deflection of the structure is much greater than an amplitude of vibrations while breathing cracks are the non-linear problem - crack opens and closes in time as vibration amplitude dependent. The simulation of cracks are mostly done as reduced cross section area or rotational springs. The studies presented in [4] and [1] show that the use of rotational spring leads to the good results accuracy (numerical simulation and experiment) despite their simplicity.

The presented in this paper slender supporting system is loaded by a force directed towards a positive pole (comp [8, 9 , 10]). This load is induced by a force with the line of action described by two points. The points are: loaded end of the column and a pole – point on the undeformed axis of the column. It is assumed that the positive pole is place below the loaded end. If the point is localized above the loaded end the pole is negative. The same nomenclature about the poles is used when the specific load introduced by

Tomski [11 – 14] is taken into account. Depending on the location of the pole (positive or negative) the different deflection angles of the loaded end can be obtained.

In this paper the results of numerical studies on a column subjected to external compressive load taking into account a defect in the form of a crack are presented. The discussed simulation data are concerned on external load – vibration frequency relationship, loading capacity, transom length and crack size.

2. Boundary problem formulation

The investigated slender system is shown in the figure 1. Structure is loaded by external force P which is placed on the free end of the column. The presented type of load is called the load with a force directed towards a positive pole. The column is composed of one element in which the crack is present. It is assumed that crack is open and the rotational spring C is used as a discreet element in the simulations. The presence of crack divides a structure into two elements as shown in the figure 1. In the common point the continuity of transversal as well as bending moments and shear forces are met by means of natural boundary conditions. The free end of a column is reinforced by a transom of length l_c. The donations shown in the figure 1 are as follows: E_i – Young's modulus, J_i – moment of inertia, A_i – cross section area, ρ_i – material density, C – rotational spring stiffness (crack size), P – external load, l_c – transom length, m – loading head mass. The total length of a column is $l = l_1+l_2$.

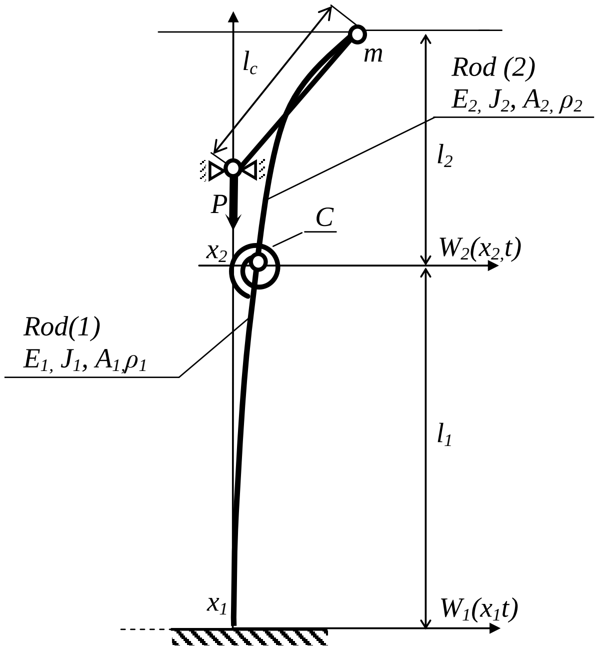

Figure 1. Investigated system

The boundary problem has been formulated on the basis of the Hamilton's principle

$$\delta\int_{t_1}^{t_2}(\mathrm{T}-V)dt=0 \tag{1}$$

according to which the kinetic T and potential V energies are described as follows:

$$T=\frac{1}{2}\sum_{i=1}^{2}\rho A_i\int_0^{l_i}\left(\frac{\partial W_i(x_i,t)}{\partial t}\right)^2 dx+\frac{1}{2}m\left(\left.\frac{\partial W_2(x_2,t)}{\partial t}\right|^{x_2=l_2}\right)^2 \tag{2}$$

$$\begin{aligned}V=&\frac{1}{2}\sum_{i=1}^{2}EJ_i\int_0^{l_i}\left(\frac{\partial^2 W_i(x_i,t)}{\partial x_i^2}\right)^2 dx_i+\frac{1}{2}C\left(\left.\frac{\partial W_1(x_1,t)}{\partial x_1}\right|^{x_1=l_1}-\left.\frac{\partial W_2(x_2,t)}{\partial x_2}\right|_{x_2=0}\right)^2+\\&-P\frac{1}{2}\sum_{i=1}^{2}\int_0^{l_i}\left(\frac{\partial W_i(x_i,t)}{\partial x_i}\right)^2 dx_i+\frac{1}{2}P\frac{1}{l_c}W_2(l_2,t)^2\end{aligned} \tag{3}$$

On (1) the integration and variation operations are performed and finally inter alia the differential equations of motion in transversal direction (4) are found:

$$EJ_iW_i^{''''}(x_i,t)+PW_i^{''}(x_i,t)+\rho A_i\ddot{W}_i(x_i,t)=0 \quad i=1{,}2 \tag{4}$$

As well as the natural boundary conditions. The complete set of natural and geometrical boundary conditions is presented by 4(a-h):

$$\begin{gathered}W_1(0,t)=W_1^{I}(0,t)=0 \qquad W_1(l_1,t)=W_2(0,t) \qquad W_2^{II}(l_2,t)=0\\EJ_1W_1^{III}(l_1,t)+PW_1^{I}(l_1,t)-EJ_2W_2^{III}(0,t)+PW_2^{I}(0,t)=0\\-EJ_2W_2^{II}(0,t)+C\left[W_2^{I}(0,t)-W_1^{I}(l_1,t)\right]=0\\EJ_1W_1^{II}(l_1,t)-C\left[W_2^{I}(0,t)-W_1^{I}(l_1,t)\right]=0\\EJ_2W_2^{III}(l_2,t)+P\left[W_2^{I}(l_2,t)-\frac{1}{l_c}W_2(l_2,t)\right]-m\ddot{W}_2(l_2,t)=0\end{gathered} \tag{4a-h}$$

On the basis of solution of formulated boundary problem connected with free vibrations characteristic curves on the plane: external load – natural vibration frequency for given parameters such as crack size/location or position of pole can be calculated.

3. Results of numerical simulations

The results of numerical simulations are shown in the non-dimensional form:

$$p=\frac{Pl^2}{EJ_1},c=\frac{Cl}{EJ_1+EJ_2},d=\frac{l_1}{l},\mu=\frac{EJ_2}{EJ_1},m_b=m\rho A_1l,l_{CB}=\frac{l_c}{l} \tag{5(a-f)}$$

The use of non-dimensional parameters does not require to specify the material properties or cross section area.

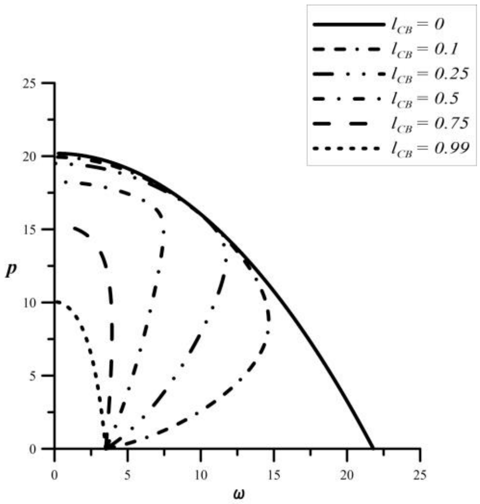

Figure 2. Characteristic curves of reference structure at different transom length; d = 0.5, μ = 1, m_b = 0.15, $c = \infty$

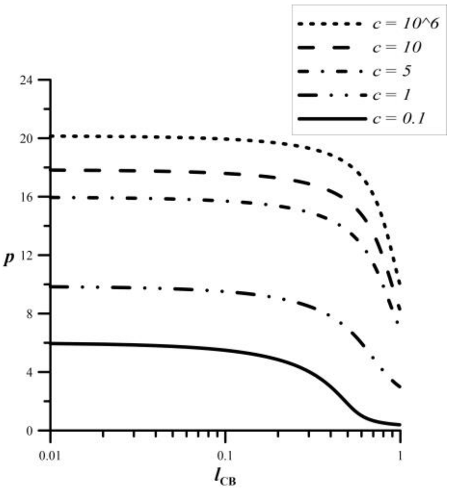

Figure 3. An influence of transom length on loading capacity at different crack size; d = 0.5, μ = 1, m_b = 0.15

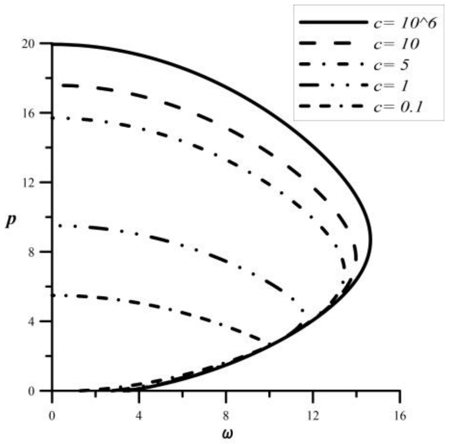

Figure 5. Characteristic curves of at different crack size; d = 0.5, μ = 1, m_b = 0.15, l_{CB} = 0.1

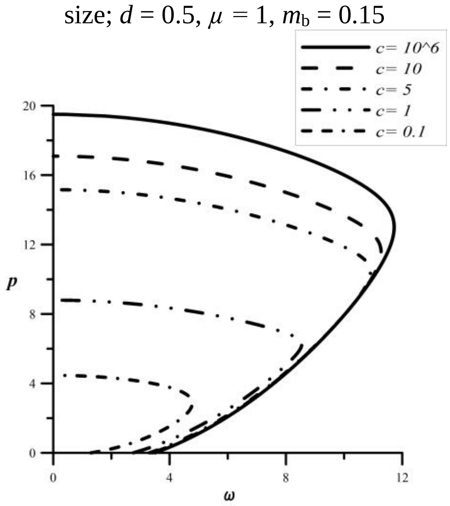

Figure 6. Characteristic curves of at different crack size; d = 0.5, μ = 1, m_b = 0.15, l_{CB} = 0.25

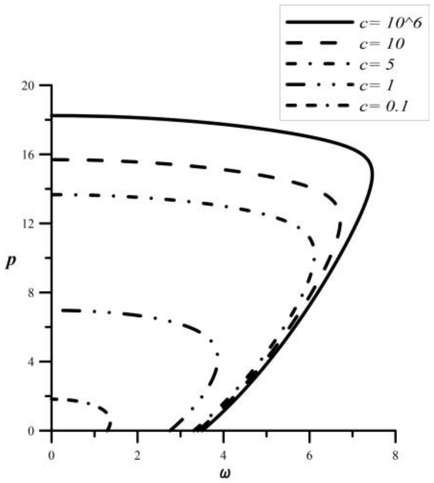

Figure 6. Characteristic curves of at different crack size; d = 0.5, μ = 1, m_b = 0.15, l_{CB} = 0.5

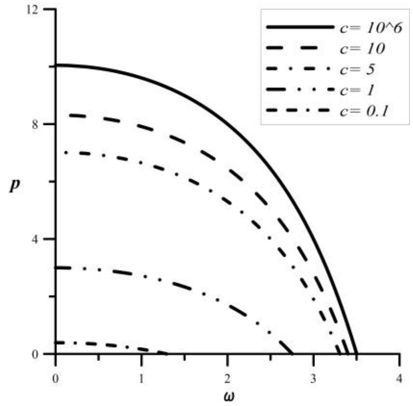

Figure 7. Characteristic curves of at different crack size; d = 0.5, μ = 1, m_b = 0.15, l_{CB} = 0.99

In the figures 2, 3 an influence of the transom length on the natural vibrations and loading capacity are presented. An analysis of the figure 2 allows one to conclude that if no transom is used the column behaves like a fixed - pinned system. The use of short transom results in change of the dynamic behaviour in relation to the reference (l_{CB} = 0) column. Furthermore the characteristic curve of the column with short transom has initially positive slope what results in increase of the natural vibration frequency along with increase of the external load magnitude. After reaching the highest natural vibration frequency magnitude point the frequency decreases while the external load is getting greater. This type of characteristic curve relates to the structures with divergence – pseudo flutter instability type. The vibration modes are being changed along the characteristic curves – see table 1 at $c = \infty$ a) p = 0.97, b) p = 14.6. As shown in the figure 2 an installation of the transom leads to the reduction of vibration frequency by reduction of transversal displacements of the free end of the column. An increase of its length finally leads to the very rapid decrease of the loading capacity in the structure without any defects and causes the change of instability into divergence one (refer to figure 2 and 3). There exists such transom length above which the change of instability can be observed. If in the column the crack appears its loading capacity is reduced. The size and nature of this reduction highly depends on transom length. The greater the crack and the longer transom the more smooth loading capacity reduction can be observed (see figure 3). When the characteristic curves of the cracked system are taken into account (figures 5 – 8) it allows one to state that at short transom (figure 5) an appearance of the crack does not affect the initial shape of the investigated curves – the curves are overlapping each other. Along with external load increase the curves are being shifted in relation to the reference curve (continues one) and the loading capacity drop is observed. The size of this reduction highly depends on crack size and transom length. At longer transom (figures 6, 7) the smaller crack causes the shift of the characteristic curve in relation to the reference one. When the transom length is equal to the one of the column's (figure 8) the system has divergence instability type. The crack appearance shifts the characteristic curves even at small size of the defect. It can be stated that the crack does not affect the type of instability. The first and second vibration modes are plotted in the table 1. The plots are done at different crack sizes of the divergence – pseudo flutter system. Due to large number of the results the table 1 corresponds only to one configuration of the investigated system. An analysis of the vibration modes can easily lead to detection of the structure defect but it must cover at least first and second modes.

Table 1. Vibration modes of the divergence – pseudo flutter system:
$d = 0.5$, $\mu = 1$, $m_b = 0.15$, $l_{CB} = 0.1$

$c = \infty$ a) $p = 0.97$, b) $p = 14.6$	$c = 5$ a) $p = 0.97$, b) $p = 14.6$
a) 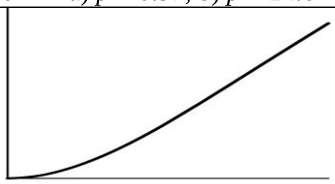	a) 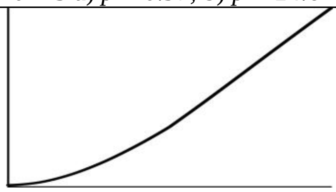
b) 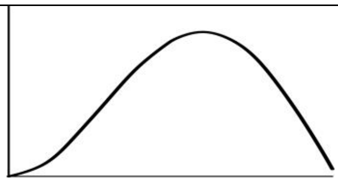	b) 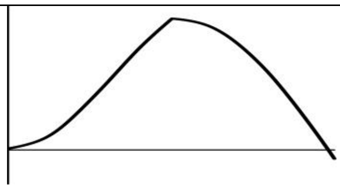
$c = 1$ a) $p = 0.97$, b) $p = 8.75$	$c = 0.1$ a) $p = 0.97$, b) $p = 4.85$
a) 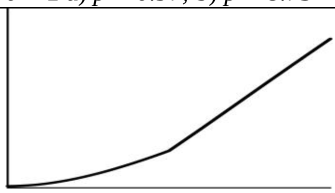	a) 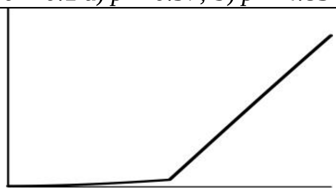
b) 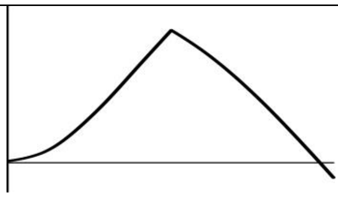	b) 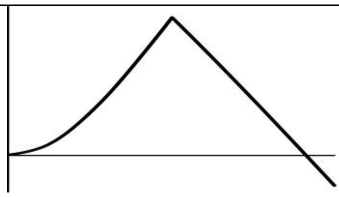

Taking into account the results from table 1 it can be concluded that the loading structure by means of which the load by a force directed towards a positive pole is created has an influence on the vibration modes. The size of an influence depends on crack size as well as on the parameters of the loading structure which are present in the boundary condition (4h).

4. Conclusions

In this paper the studies on natural vibration frequency and loading capacity of a column subjected to a force directed towards a positive pole are done. Additionally an influence of the defect in the form of crack is taken into account. On the basis of the results of numerical simulations it can be concluded that:

- in the reference structure an installation of transom of greater length causes a decrease of maximum loading capacity in relation to the shorter elements,
- in relation to transom length the divergence or divergence – pseudo flutter characteristic curves can be obtained,
- presence of a crack causes a reduction of maximum loading capacity. This change highly depends on transom length – the shorter transom the more rapid loading capacity decrease can be observed,
- the crack affects the shape of characteristic curves but doesn't change the type of instability (divergence or divergence – pseudo flutter),
- at short transom the appearance of the crack doesn't change the initial shape of characteristic curve of divergence – pseudo flutter system,
- the crack presence and location can be found on the basis of the analysis of the vibration modes. An analysis of the higher modes allows on to indicate the crack even if it is unseen the lower modes.

The obtained results can be used in the structure health monitoring in order to find a defect which can lead to the destruction of the column. The presented studies should be expanded by an analysis of the crack location on the instability and natural vibrations of the slender system as well as by the experimental verification of the proposed mathematical model. Additionally the investigations of the parameters of the loading structure at which the column is the least sensitive to the crack presence can be performed.

Acknowledgments

The study has been carried out within the statutory funds of the Czestochowa University of Technology (BS/PB-1-101-3020/11/P).

References

1. M. Arif Gurel., *Buckling of slender prismatic circular columns weakened by multiple edge cracks*, Acta Mechanica, **188** (2007) 1 – 19.
2. L. A. Bergman, J. Lee., *The vibration of stepped beams and rectangular plates by an elemental dynamic flexibility method*, J. Snd. and Vib, **171** (1994) 617 – 640.
3. B. Binici., *Vibration of beams with multiple open cracks subjected to axial force*, J. Snd. and Vib., **287** (2005) 277 – 295.
4. T. G. Chondros, A. D. Dimarogonas., J. Yao., *A continuous cracked beam vibration theory*, J. Snd. and Vib., **215** (1998) 17 – 34.

5. A. D. Dimarogonas, N. Anifantis, *Stability of columns with a single crack subjected to follower and axial loads*, Int. J. Sld. and Struc., **19** (1999) 281 – 291.
6. K. Sokół, *Linear and nonlinear vibrations of a column with an internal crack,* J. Eng. Mech., **140** (2014) http://dx.doi.org/10.1061/(ASCE)EM.1943-7889.0000719.
7. K. Sokół, S. Uzny., *Instability and vibration of multi-member columns subjected to Euler's load*, Arch. App. Mech. DOI 10.1007/s00419-015-1068-6.
8. A. Gajewski, *Pewne problem optymalnego kształtowania pręta ściskanego siłą skierowaną do bieguna*, Mechanika Teoretyczna i Stosowana, **2**(8) (1970) 159 – 173.
9. A. Gajewski, M. Życzkowski, *Optymalne kształtowanie pręta ściskanego siłą skierowaną do bieguna*, Rozprawy inżynierskie, **2**(17) (1969) 299 – 329.
10. J. Szmidla, *Free vibrations of a gamma type planar frame loaded by a follower force directed towards the positive pole,* Vib. in Phys. Sys., **24** (2010) 405 – 410.
11. L. Tomski, J. Przybylski, M. Gołębiowska-Rozanow, J. Szmidla., *Vibration and stability of a cantilever column subjected to a follower porce passing through a fixed point,* J. Snd. And Vib, **214**(1) (1998) 67 – 81.
12. L. Tomski, J. Szmidla., *Free vibrations and stability of discrete systems subjected to the specific load,* J. Theoret. App. Mech., **45**(4) (2007) 873 – 892.
13. L. Tomski, S. Uzny., *Free vibrations and the stability of a geometrically non-linear column loaded by a follower force directed towards the positive pole*, Int. J. of Sol. Struct., **45**(1) (2008) 1 – 24.
14. S. Uzny., *Free vibrations of an elastically supported geometrically nonlinear column subjected to a generalized load with a force directed towards the positive pole,* J. Eng. Mech. ASCE, **137**(11) (2011) 740 – 748.

Vibration of the Oscillator Exchanging Mass with Surroundings

Roman STAROSTA
Poznan University of Technology, Institute of Applied Mechanics
ul. Jana Pawła II 24, 60-965 Poznań, roman.starosta@put.poznan.pl

Grażyna SYPNIEWSKA-KAMIŃSKA
Poznan University of Technology, Institute of Applied Mechanics
ul. Jana Pawła II 24, 60-965 Poznań, grazyna.sypniewska-kaminska@put.poznan.pl

Jan AWREJCEWICZ
Technical Universityof of Łódź, Department of Automatics and Biomechanics,
ul. Stefanowskiego 90-924, Łódź, jan.awrejcewicz@p.lodz.pl

Abstract

Vibration of two simple open systems (namely the linear mass-sprins oscillator and the mathematical pendulum) are investigated. During the motion, the body absorbs matter through its boundary. In both cases, mechanism of mass absorption is modeled as a perfectly 'inelastic' collision and constant rate of mass change is assumed. The paper is focused on the influence of mass change on the kinematic aspects of oscillations.

Keywords: vibration of open systems, mass variable, reactive force

1. Introduction

Mass is generally not conserved when a supply of mass is present, or when open systems with a flow of mass through their surface are to be considered. Mass of the mechanical system then is said to be variable. In such a situation, the general methodological approaches of mechanics have to be properly modified. In solid mechanics, the systems with a variable mass appear as the result of a problem-oriented modelling, e.g., when mass is expelled or captured by a structure or machine. The finite discontinual mass variation in a very short time was not of special interest for a long time and was not intensively discussed. Meshchersky was the first who considered the velocity change of a translatory moving body during step-like mass variation [1]. The motion of the continuously mass variable systems is much more investigated due to its application in rocket theory [2] and astronomy [3]. The motion is described with differential equations with variable parameters. For the case when the mass is varies continuously in time, the influence of the reactive force on the motion is investigated by Cvecitanin and Kovacic[4].

Mathematically the reactive force is the product of the mass variation function and the relative velocity of mass separated from or added to the particle. Usually, two special cases were considered: the first one for zero relative velocity and the second for zero absolute velocity of separated or added mass. In case of zero relative velocity, i.e. when the absolute velocity of the separated or added particle is equal to the velocity of the basic particle, the reactive force is also zero.

Based on the dynamics of the particle with time-varying variable mass and the basic laws of dynamics, the theoretical consideration of the dynamics of the body with time variable mass is presented in this paper. Two mechanical systems are considered: one dimensional oscillator and a mathematical pendulum.

The process of the mass increase is considered as the perfectly inelastic impact of a small mass on the main body. Based on the general equations of motion, the mathematical model for the oscillatory motion is formed.

2. Linear oscillator

In this section the open mechanical system is considered which absorbs matter from the surroundings. Its physical model is presented in Fig.1.

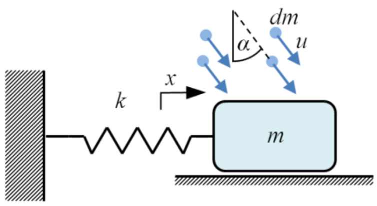

Figure 1. One-dimensional linear oscillator exchanging mass with the surrounding

Let us assume that the mass $m(t)$ of the body changes with time proportionally to the area of its surface with a constant rate – Γ. Mass change is described by the evolution equation

$$\dot{m}(t) = \Gamma \tag{1}$$

and at the beginning $m(0) = m_0$.

In this way the mass of the body changes in time linearly

$$m(t) = m_0 + \Gamma t\,,\ \ t > 0\,. \tag{2}$$

The added mass *dm* drops at the body with the absolute velocity **u** (see Fig.1).

The momentum principle in the case of mass exchanging body is

$$m(t)\dot{\mathbf{v}} = \mathbf{F} + \dot{m}(t)(\mathbf{u} - \mathbf{v}), \tag{3}$$

where **F** is the resultant force, **v** velocity of the body and **u** velocity of the added particles of mass *dm*. In the case of free vibration, the mathematical model of the one-degree-of-freedom oscillator with time variable mass is

$$(m_0 + t\,\Gamma)\ddot{x}(t) = -k\,x(t) + \Gamma(u_x - \dot{x}(t)), \tag{4}$$

Where x(t) is the coordinate describing the position of the body, $u_x = |\mathbf{u}|\sin(\alpha)$ is the x – component of the velocity **u**, m_0 is the initial mass of the body and k denotes the stiffness coefficient.

After rearranging, the equation of motion (4) takes the form

$$(m_0 + t\,\Gamma)\ddot{x}(t) + \Gamma\dot{x}(t) + k\,x(t) = \Gamma\,u_x\,, \tag{5}$$

The second term on the left hand side of (6) can be recognized as a damping of viscous type, and a constant force occurs on the right side.
The equation of motion (5) is supplemented by the initial conditions

$$x(0) = x_0, \;\; \dot{x}(0) = v_0 . \tag{6}$$

The analytical solution of the problem (5) – (6) is as follows

$$x(t) = AJ_0\left(2\sqrt{\frac{k}{\Gamma}}\sqrt{\frac{m_0}{\Gamma}+t}\right) + BY_0\left(2\sqrt{\frac{k}{\Gamma}}\sqrt{\frac{m_0}{\Gamma}+t}\right) + \frac{\Gamma}{k}u_x , \tag{7}$$

where $J_0(.)$ and $Y_0(.)$ are the Bessel functions of the first and second kind, respectively, A and B are the unknown constants which fulfil the following equations resulting from initial conditions (6)

$$AJ_0\left(2\sqrt{\frac{k\,m_0}{\Gamma^2}}\right) + BY_0\left(2\sqrt{\frac{k\,m_0}{\Gamma^2}}\right) + \frac{\Gamma}{k}u_x = x_0 \tag{8}$$

$$-\sqrt{\frac{k}{m_0}}AJ_1\left(2\sqrt{\frac{k\,m_0}{\Gamma^2}}\right) - \sqrt{\frac{k}{m_0}}BY_1\left(2\sqrt{\frac{k\,m_0}{\Gamma^2}}\right) = v_0 . \tag{9}$$

Some results of calculations are presented for the chosen values of parameters m_0=1 kg,Γ=0.01kg/s,k=10N/m, u_x=2m/s, and initial values: x_0=0.1 m,v_0=0m/s.
The solution (7) is presented in Fig.2.

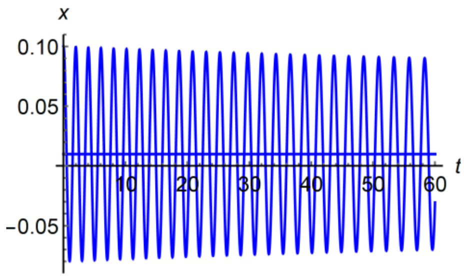

Figure 2. Time history of the body motion

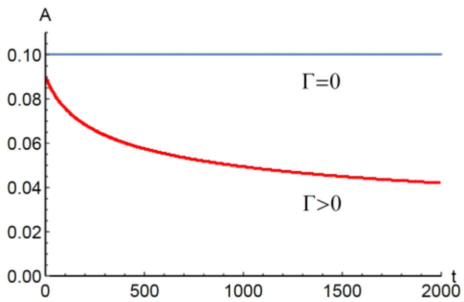

Figure 3. Amplitude vs. time for constant and varying mass oscillator

The system oscillates around the equilibrium state given by the particular solution $u_x \Gamma / k$. The shift, in the time history in Fig. 2, appears due to the spring extension caused by the constant momentum supply of the added mass. The amplitude decreases in time while the mass of the oscillator grows, which is illustrated in Fig. 3.

The amplitude – frequency spectra, obtained using the discrete Fourier transform for the system with constant and varying mass are shown in Fig. 4.

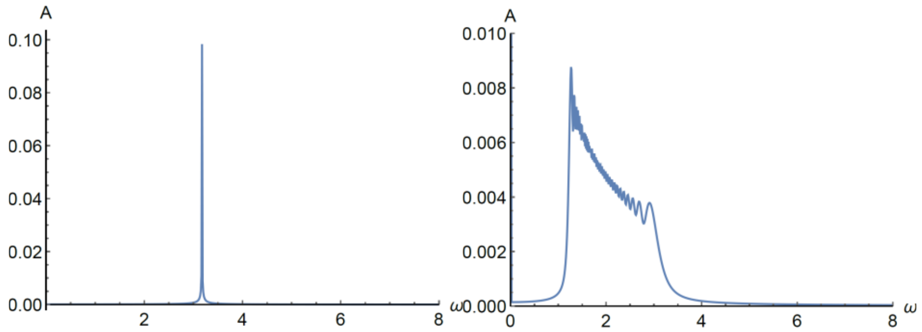

Figure 4. The amplitude spectra of the oscillations with constant and variable mass

The amplitude spectra in the case of mass exchange and those with constant mass are quite different. This effect is connected with variation of the self-frequency of the system in time.

3. Pendulum exchanging mass with surroundings

The problem of motion of the pendulum which exchanges mass with surroundings is investigated in this section. The process of mass exchanging is the same as described above. In this case, the governing equation of pendulum motion is

$$(m_0 + t\Gamma)\ddot{\varphi}(t) + \Gamma\dot{\varphi}(t) + u\Gamma L \sin(\alpha - \varphi(t)) + g(m_0 + t\Gamma)L\sin\varphi(t) = 0 \tag{10}$$

with the initial conditions

$$\varphi(0) = \varphi_0,\ \ \dot{\varphi}(0) = \omega_0\,, \tag{11}$$

where L and m_0 are length of the pendulum and its initial mass respectively.

The problem (10) – (11) is solved only numerically due to geometric nonlinearities in considered problem described by Eq. (10).

Results of two simulations concerning small and large oscillations are presented hereafter. Calculations have been made for the following values of parameters:m_0=1kg,Γ=0.01kg/s,u=2m/s,L=0.7m andα=π/3.

In Fig. 5 time histories of two regimes of motion are presented. One of them, caused by the initial values φ_0=0.1, ω_0=0,is related to the small oscillations and the second one, caused byφ_0=1.3, ω_0=0, concerns the large oscillations.

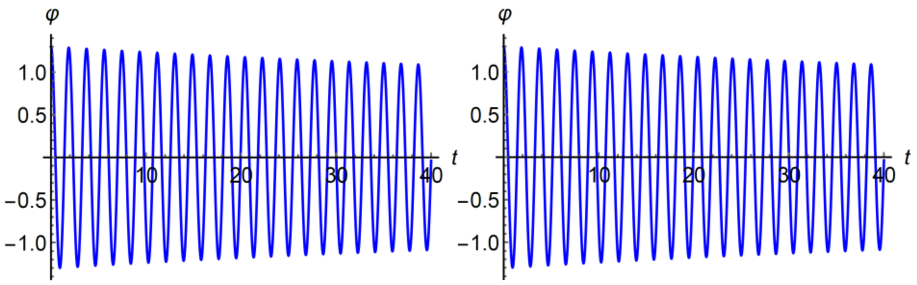

Figure 5. Time histories of small (left) and large (right) oscillations

The character of vanishing amplitude of the pendulum which absorbs mass in comparison to constant amplitude in the case of pendulum with constant mass is presented in Fig. 6.

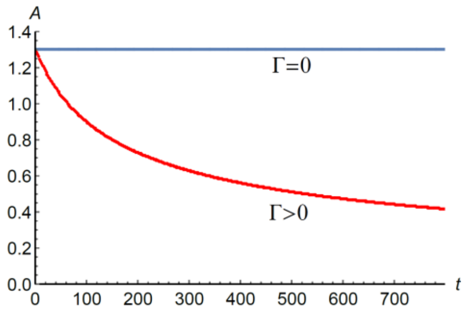

Figure 6. Amplitude vs. time for constant and varying mass pendulum

In Fig. 7 the amplitude-frequency spectra for the case of small and large oscillations are presented.

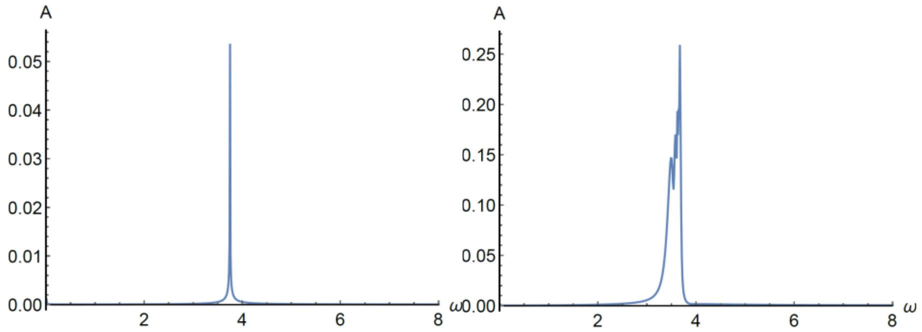

Figure 7. Amplitude spectra for the case of small and large oscillations

Similarly as for the linear oscillator the amplitude spectrum is strongly affected by the effect of mass variation.

4. Conclusions

Two open systems with one degree of freedom have been investigated. One of them described by the linear differential equation and the second one described by the nonlinear equation. Nonlinearities in the pendulum equation are of geometrical type. In the governing equations some time depending coefficients appear due to changing mass of the system. One additional term has the same form as viscous damping, and appears in the both discussed structures. Other additional term can be recognized in the linear oscillator as a constant force, whereas in the pendulum its counterpart term is time dependent and nonlinear.

The analytical solution of the initial value problem describing motion of the linear oscillator of variable mass has been achieved. The pendulum oscillation might have been analyzed only numerically due to nonlinearities.

The mass increase causes decreasing amplitude of oscillation in both tested structures. The mass exchange with surroundings affects the amplitude-frequency spectra both for the linear oscillator and pendulum.

Acknowledgments

This paper was financially supported by: the National Science Centre of Poland under the grant MAESTRO 2, (No. 2012/04/A/ST8/00738, for years 2013-2016) and by the grant of the Ministry of Science and Higher Education in Poland realized in Institute of Applied Mechanics of Poznan University of Technology (DS-PB: 02/21/DSPB/3477).

References

1. I. V. Meshchersky, *Rabotji po mehanike tel peremennoj massji.* Gos. Izd. tehniko-teoret. lit, Moscow, 1952.
2. T. Tran, F.O. Eke, *Effects of internal mass flow on the attitude dynamics of variable mass systems.* J. Astronaut. Sci., **119** (2005) 1297 – 1316.
3. Ya. F. Kayuk, V. I. Denisenko, *Motion of a mechanical system with variablemass - inertial characteristics*. Int. Appl. Mech., **40**(7) (2004) 814 – 820.
4. L. Cveticanin, I. Kovacic, *On the dynamics of bodies with continual mass variation*. Trans ASME, J. Appl. Mech., **74** (2007) 810 – 815.

Effect of the Sleeve Profile on the Stability of Rotor Operating in Multilobe Journal Bearings

Stanislaw STRZELECKI
Research Development Institute of Textile Machinery "POLMATEX-CENARO"
Wolczańska 55/591/15, 90-924 Lodz, Poland
stanislaw.strzelecki@p.lodz.pl

Abstract

Multilobe journal bearings with the sleeve of the 2-, 3 or 4- sliding lobes of cylindrical profile are applied in different types of rotating machinery. The design of such journal bearings, the number of lobes and oil grooves improves thermal state of bearing at higher speeds and the stability of operation.
The paper describes the results of the calculations of dynamic characteristics and determination of stability ranges of simple symmetric rotor operating in the offset types of multilobe journal bearings. The dynamic characteristics of supporting bearings are defined by four stiffness and damping coefficients of oil film. The iterative solution of Reynolds, energy and viscosity equations allows the obtaining of the load capacity of bearings and the required dynamic coefficients of oil film. Adiabatic, laminar oil film and the static equilibrium position of journal were assumed. The oil film pressure, temperature, viscosity fields and the oil film forces were the basis of the bearing dynamic characteristics and stability determination.

Keywords**:** multilobe, offset journal bearings, stability of rotor

1. Introduction

The stability of rotor operating in journal bearings can be determined on the basis of supporting bearings dynamic characteristics expressed by the stiffness and damping coefficients of oil film [1-6]. The multilobe bearings, mostly used in slightly loaded, high speed rotating machines are characterised by good damping of vibrations and good stability of operation [1-3]. Exemplary types of such bearings are the 2- (offset-halves) [6], 3-and 4-lobe offset bearings [7-11] that are applied in the turbine gearboxes [6].
The design of 2-, 3- or 4-lobe journal bearings, the number of lobes and oil grooves improves the thermal state of bearing and stability of operation [1-3]. These multilobe journal bearings can be manufactured as the bearings with cylindrical sliding surfaces [5], with pericycloid profile of bearing bore [7,8] or as the offset ones [6,9].
Typical multilobe (classic) journal bearing is composed of single circular sections whose centres of curvature are not in the geometric centre of the bearing. The geometric configuration of the bearing as a whole is discontinuous and not circular. The multilobe pericycloid journal bearings ("wave bearings" [7,8]) is characterised by continuous profile and multihydrodynamic oil films on the journal perimeter.
The characteristic feature of multilobe, offset journal bearings are that the circle inscribed in the bearing profile touches the end of the convex gap of the bearing [5,6] in the direction of journal rotation (Fig. 1)**.**
The paper presents the effect of sleeve profile on the stability of simple symmetric, elastic rotor operating in 2-, 3- and 4-lobe offset journal bearings The oil film pressure,

temperature and viscosity fields that are required for the calculations of the bearing static and dynamic characteristics, have been obtained by iterative solution of the Reynolds', energy and viscosity equations. Adiabatic, laminar oil film and the static equilibrium position of journal were assumed. The dynamic characteristics of journal bearing are the basis of stability ranges determination [1-3]. All the stiffness and damping coefficients were calculated by means of perturbation method [1,6].

2. Stability of elastic rotor

Considered multilobe, offset type journal bearings are presented in Fig. 1. Their geometry can be found in [5,6].

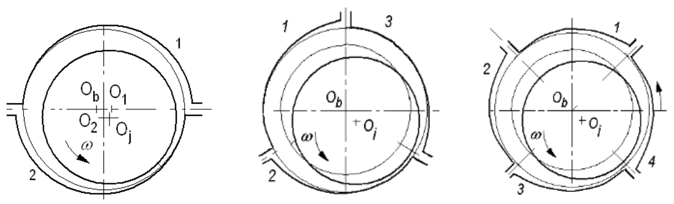

Figure 1. Lay-out of the 2-, 3-, and 4-lobe offset journal bearings; O_b, O_j, O_1, O_2 – centres of bearing, journal, upper and bottom lobe (2-lobe offset bearing), 1 ÷ 4 number of lobes

The journal bearing static and dynamic characteristics for adiabatic or diathermal model of oil film can be determined by the numerical solution of the oil film geometry, Reynolds, energy, viscosity [2,6] equations. The stiffness g_{ik} and damping b_{ik} coefficients allow the determination of stability ranges [1-8].

The equations of motion for the journal and the centre of elastic shaft are given in matrix form by Eqn. (1) [4].

$$M \cdot \ddot{x} + B \cdot \dot{x} + C \cdot x = \hat{a}\cos \omega t + \hat{b}\sin \omega t \tag{1}$$

where: *M*, *B*, *C* –matrices of mass, damping and stiffness, $\hat{a}, \hat{b}$ - coefficients of dynamic constraints, ω- angular velocity, (s^{-1}).

After transformations of Eqn. (1) the real and imaginary part was obtained [1,4]. The stability of elastic rotor-bearing system is analysed based on the following characteristic frequency equation of 6-th order with regard to (λ/ω) [1-6].

$$c_6 \lambda^6 + c_5 \lambda^5 + c_4 \lambda^4 c_3 \lambda^3 + c_2 \lambda^2 + c_1 \lambda + c_0 = 0 \tag{2}$$

1.

2. Solution assumption for Eqn. (2) is $\lambda_j = - u_j + iv_j$ ($1 \le j \le 6$), with u as damping and v representing the self-vibrations. Stability of the linear vibrations of system occurs only when all real parts of eigenvalues λ_j are negative. The coefficients c_0 through c_6 in Eqn. (2) are the functions of a_0 , b_0 , g_{ik}, b_{ik}.

$$c_0 \div c_6 = f(a_0, b_0, g_{ik}, b_{ik}) \tag{3}$$

where: a_0 - ratio of angular velocity ω to the angular self-frequency of stiff shaft, $a_0=(\omega / \omega_c)^2$, ω_c - angular self frequency of stiff rotor, $\omega_c = \sqrt{c^* / m}$, b_0 - ratio of Sommerfeld number to the relative elasticity of shaft, $b_0 = So/c_s$, c* - shaft stiffness, (N m^{-1}), c_s - relative elasticity of shaft, $c_s = f/\Delta R = g/(\omega_c^2 \cdot \Delta R)$, f- static deflection of shaft, (m), F.- resultant force of oil film (N), F_{stat} - static load of bearing, (N), g - acceleration of gravity, (m s^{-2}), g_{ik} - dimensionless stiffness coefficients, g_{ik} = So($\Delta R/F_{stat}$), g'_{ik}, - stiffness coefficients, (N/m), b_{ik}- dimensionless damping coefficients, b_{ik} =So($\Delta R/F_{stat}$) $\omega \cdot b'_{ik}$, b'_{ik} - damping coefficients, (N s/ m), *m* - mass of the rotor, (kg), *So* - Sommerfeld number, $So = F \cdot \psi^2 /(L \cdot D \cdot \eta \cdot \omega)$, S_{ok} -critical Sommerfeld number, S_{ok} = So ω/ω_c

Coefficients of characteristic Eqn. (2) depend on the stiffness and damping coefficients, Sommerfeld number So, relative elasticity of shaft c_s and the ratio of angular velocity to the critical angular velocity of stiff rotor. The expression determining the ratio of boundary angular speed Ω_b to the critical ω_c one, and the stability of rotor [1-4], is:

$$\left(\frac{\Omega_b}{\omega_c}\right)^2 = \frac{1}{1+b_0 \cdot \dfrac{A_3}{A_1}} \; \frac{A_2 \cdot A_3^2}{A_1^2 + A_1 \cdot A_3 \cdot A_4 + A_0 \cdot A_3^2} \tag{4}$$

where: A_0, A_1, A_2, A_3, A_4, consist the stiffness g_{ik} (i=1,2 and k=1,2) and damping b_{ik} (i=1,2 and k=1,2) coefficients [1-6], Ω_b - boundary angular velocity (s^{-1})

3. Results of calculations

The stability of simple elastic, symmetric rotor (Jeffcott rotor) was determined with the use of the calculated dynamic characteristics The calculations included the non-dimensional load capacity S_0 and journal displacement ε as well as the static equilibrium position angles α_{eq}, too. The offset journal bearings under consideration have the length to diameter ratio L/D=0.6, L/D=0.75 and L/D=0.8. Different lobe relative clearances ψ_s (for the 3-lobe pericycloid bearing its relative eccentricity was λ^* = 0.25 [6,7]) and rotational speeds were assumed. The bearing relative clearances were ψ = 0,9‰, ψ = 1.5‰ and ψ = 2.7‰. The feeding oil temperature was T_0=40^{0}C and the corresponding thermal coefficients K_T [2,8] were 0.139, 0.215 and 0.315; K_T = $\omega \cdot \eta_0 /(c_t \cdot \rho \cdot g \cdot T_0 \cdot \psi^2)$ where: c_t - specific heat of oil, (J/kgK), g - acceleration of gravity (m/s^2), η_0 - dynamic viscosity of supplied oil (Ns/m^2), ρ - oil density, (kg/m^3), ψ - bearing relative clearance, (‰).

Exemplary results of the calculations of dynamic characteristics and stability are shown in Fig. 2 through Fig. 15. The stiffness g_{ik} and damping b_{ik} coefficients are given in Fig.2 through Fig.7. The stability ranges can be observed in Fig. 8 through Fig. 15.

Fig. 2 and Fig. 3 show the stiffness and damping coefficients of the offset-halves bearing with the lobe relative clearance ψ_s =2. The largest values have the coefficient g_{22} for the Sommerfeld numbers over 0.44. The values of the coupled damping coefficients b_{12} and b_{21} are very close (e.g. Fig. 3). The damping coefficient b_{11} is larger than the ones b_{12} and b_{21} in the range of Sommerfeld numbers S_0 from 0 to about 0,6. At increasing values of Sommerfeld numbers, the coefficient b_{11} is smaller than the coupled terms b_{12} and b_{21} (Fig. 3).

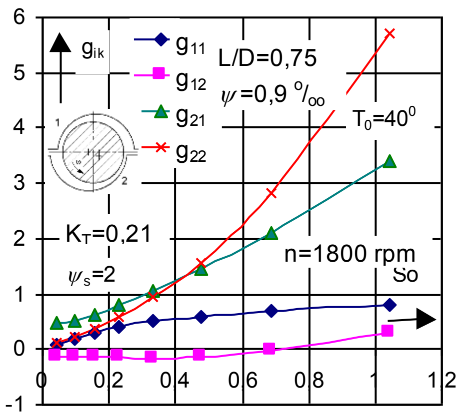

Figure 2. Stiffness coefficients of offset-halves offset- journal bearing

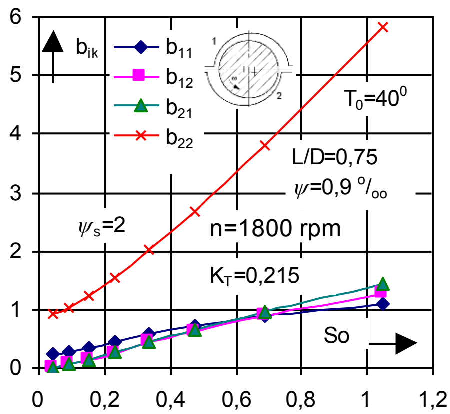

Figure 3. Damping coefficients of halves journal bearing

The stiffness and damping coefficients of the 3-lobe offset journal bearing are presented in Fig. 4 and Fig. 5. The bearing length to diameter ratio L/D=0.8, clearance ratio ψ = 1.5 ‰ and lobe relative clearance ψ_s=2 were assumed. Heat number K_T was K_T=0.315.
The largest values have the coefficients g_{22} and b_{22} but the smallest g_{12} and b_{21} (Fig. 4 and Fig.5). The values of the coupled damping coefficients b_{12} and b_{21} are very close and b_{11} is larger than the coupled coefficients (Fig. 5).
The stiffness and damping coefficients of 4-lobe offset bearing are given in Fig. 6 and Fig. 7. The largest values has the stiffness coefficient g_{21} and the smallest value the coefficient g_{11} (Fig. 6); In the range of Sommerfeld number from nil to about 0.12 the coefficient g_{22} is larger than g_{12} but at higher Sommerfeld numbers there is reverse dependence. The damping coefficient b_{22} is the largest and the coupled coefficients have the smallest, equal values, i.e. b_{12}=b_{21} (Fig. 7).
The stability ranges of symmetric rotor operating in 2-lobe offset bearings with the lobe relative clearance ψ_s =1 (Fig. 8 - cylindrical sliding surfaces) and ψ_s =2 (Fig. 9 - lemon shaped sliding surfaces) show the difference. The rotor running in the bearings characterized by the value of lobe relative clearance ψ_s =2 shows larger range of stability (e.g. Fig. 8 and Fig. 9).
Exemplary results of stability ranges that were obtained for 3-lobe offset journal bearing at different values of lobe relative clearance ψ_s and at different relative elasticity of shaft

c_s are shown in Fig. 10 and Fig. 11. At the values of the relative elasticity of shaft under consideration there is an increase in the stability at the increase in the lobe relative clearance ψ_s (e.g. the curves for c_s=0.1 in Fig. 10 and Fig. 11). The coefficient tg τ in the range of larger critical Sommerfeld numbers S_{ok} is the measure of stability properties of bearing [2,3]. Larger values of angle τ mean the larger range of stability, i.e. at assumed load of bearing there is higher boundary of stability Ω_b/ω_C [2,3].

For the comparison task, the stability ranges of rotor operating in 3-lobe pericycloid journal bearing and in classic 3-lobe bearing are shown in Fig.12 and Fig. 13. It results from the comparison that the 3-lobe offset bearing has better stability properties than the 3-lobe pericycloid and 3-lobe classic bearings.

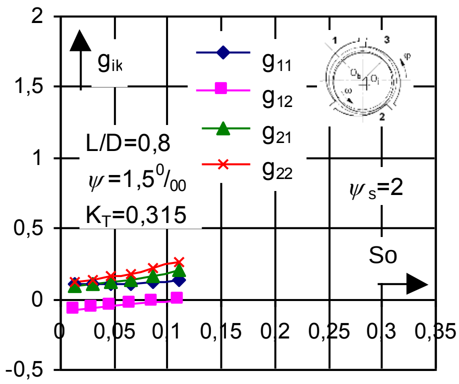

Figure 4. Stiffness coefficients of 3-lobe offset journal bearing

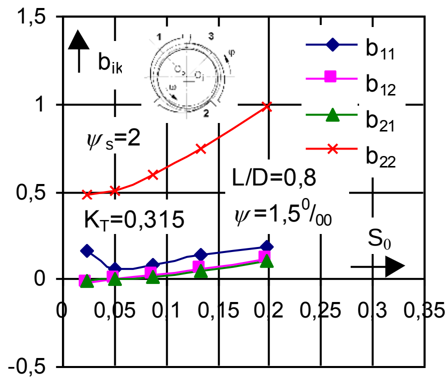

Figure 5. Damping coefficients of 3-lobe offset journal bearing

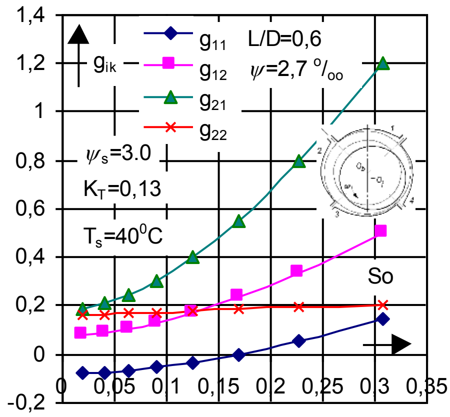

Figure 6. Stiffness coefficients of 4-lobe offset journal bearing

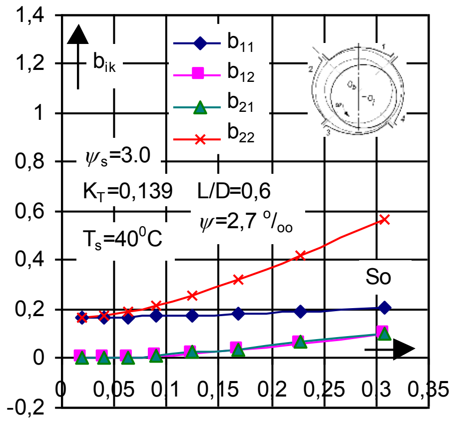

Figure 7. Damping coefficients of 4-lobe offset journal bearing

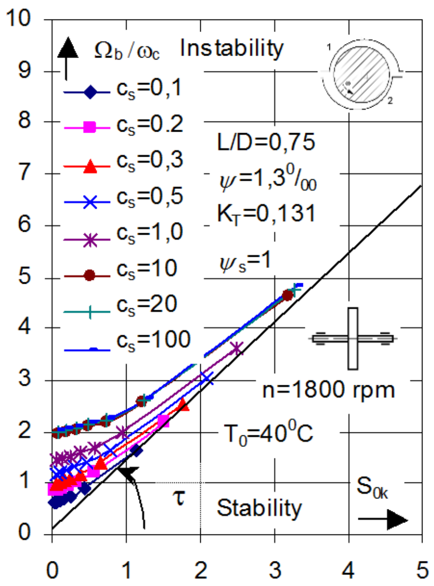

Figure 8. Stability chart of rotor operating offset-halves journal bearings (ψ_s =1)

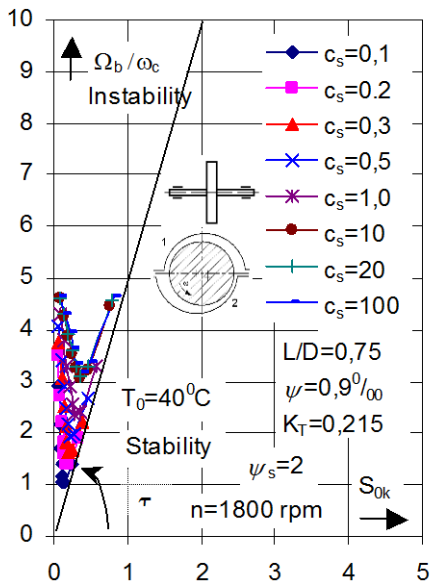

Figure 9. Stability chart of rotor operating in offset-halves journal bearings (ψ_s =2)

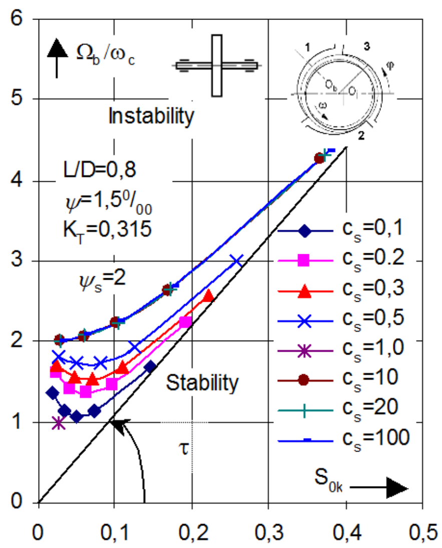

Figure 10. Stability chart of rotor operating 3-lobe offset journal bearing

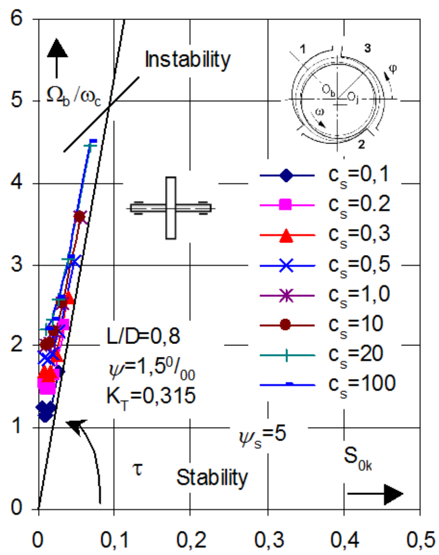

Figure 11. Stability chart of rotor operating in in 3-lobe offset journal bearing

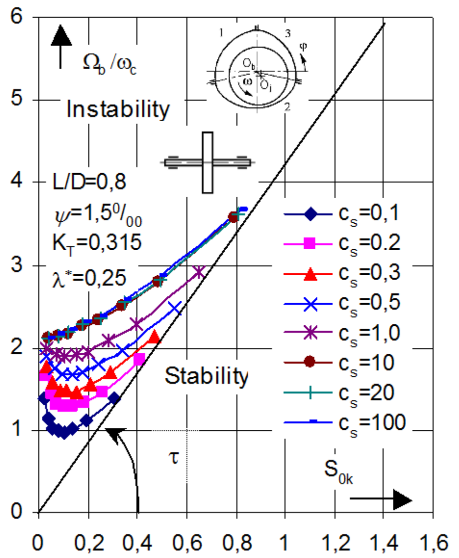

Figure 12. Stability chart of rotor operating in 3-lobe pericycloid journal bearing

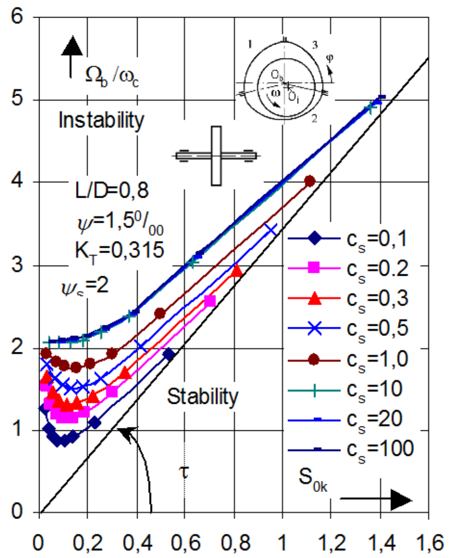

Figure 13. Stability chart of rotor operating in 3-lobe journal bearing

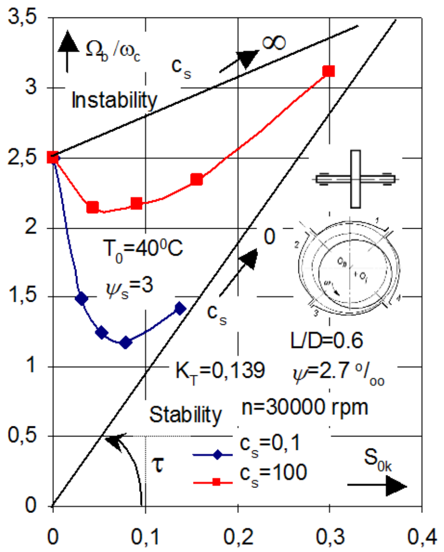

Figure 14. Stability of elastic rotor operating in 4- lobe offset journal bearing at the lobe relative clearance $\psi_s = 3$

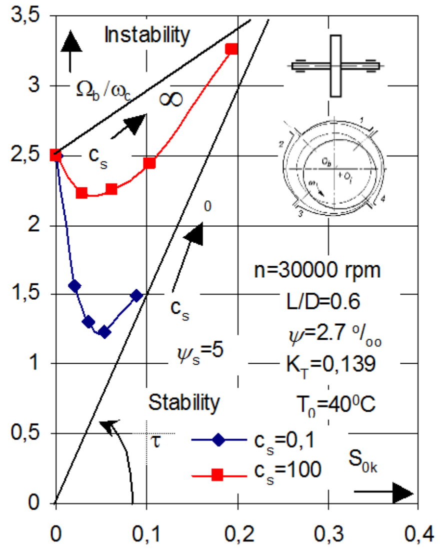

Figure 15. Stability of elastic rotor operating in 4-lobe offset journal bearing at the lobe relative clearance $\psi_s = 5$

4. Conclusions

Dynamic characteristics including the stability ranges of the chosen types of offset bearing with different sleeve profiles and on the assumption of adiabatic model of oil film, were obtained by means of perturbation method. Investigation that were carried out at assumed geometric and operating parameters, various relative shaft elasticity values, allows to draw the following conclusions:

1. Static and dynamic characteristics of the considered journal bearings of different sleeves profiles can be obtained from developed program of numerical calculations.
2. The offset type multilobe journal bearings show better stability than the classic multilobe bearings.
3. An increase in the relative elasticity of shaft increases the range of rotor stability.
4. The results of developed program form the input data for the investigation and analysis into the stability of different types of multilobe journal bearings.

References

1. T. Someya, *Stabilität einer in zylindrischen Gleitlagern laufenden, unwuchtfreien Welle-Beitrag zur Theorie des instationär belasteten Gleitlagers*. Diss. Techn. Universität Karlsruhe 1962.
2. D. C. Han, *Statische und dynamische Eigenschaften von Gleitlagern bei hohen Umfangsgeschwindigkeiten und bei Verkantung*. Diss. Univeristät Karlsruhe 1979.
3. J. Glienicke, *Feder- und Dämpfungskonstanten von Gleitlagern für Turbomaschinen und deren Einfluß auf das Schwingungsverhalten eines einfachen Rotors*. Diss. Techn. Universität Karlsruhe .1962.
4. R. Gasch, H. Pfützner, *Rotordynamik*, Springer-Verlag 1975.
5. T. Someya, *Journal-Bearing Databook*, Springer-Verlag, Berlin, Heidelberg, New York, London, Paris, Tokyo, Heidelberg 1989.
6. S. Strzelecki, *Stability of rotor operating in offset halves journal bearings*, Synopsis. TAE, Technische Akademie Esslingen, Esslingen, Germany, 14-16.01.2008.
7. F. Dimofte, *Wave Journal Bearing with Compressible Lubricant- Part I: The Wave Bearing Concept and a Comparison to the Plain Circular Bearing*, Tribology Transaction, **38** (1995) 153 – 160.
8. S. Strzelecki, *Effect of geometric parameters on the dynamic characteristics of 3-lobe pericycloid journal bearing*, Technical University of Ostrava, Czech Republic, 7–9 September 2005, SESSION 8 - APPLIED MECHANICS 225 – 230.
9. S. Strzelecki, H. Kapusta, *Dynamic characteristics and stability of 3-lobe offset journal bearing*, Machine Dynamics Problems, **30**(4) (2006) 131 – 139.
10. S. Strzelecki, *Stability of elastic rotor operating in 3-lobe journal bearings of different sleeves profile*, 7th IFToMM- Conference on Rotor Dynamics, Vienna, Austria, September 25–28, 2006, Paper ID-317 (1 – 10) CD.
11. S. Strzelecki, *Stability of Jeffcott rotor operating in 4-lobe offset journal bearings*, XVI Int. Conference TEMAG 2008, 23–24.10.2008, Ustroń Zawodzie, 263 – 273.

Timber-Frame House Resistant to Dynamic Loads - Analysis of Wall Panel Filled with Polyurethane Foam

Marcin SZCZEPAŃSKI
Politechnika Gdańska, Wydział Inżynierii Lądowej i Środowiska
ul. Narutowicza 11/12, 80-233 Gdańsk; marszcze@pg.gda.pl

Wojciech MIGDA
Politechnika Gdańska, Wydział Inżynierii Lądowej i Środowiska
ul. Narutowicza 11/12, 80-233 Gdańsk; wmigda@pg.gda.pl

Robert JANKOWSKI
Politechnika Gdańska, Wydział Inżynierii Lądowej i Środowiska
ul. Narutowicza 11/12, 80-233 Gdańsk; jankowr@pg.gda.pl

Abstract

The present study shows the experimentally and numerically determined response of a single timber-frame house wall panel filled with polyurethane (PU) foam under dynamic loads. The harmonic tests were conducted for the following frequencies: 0.5 Hz, 1.0 Hz, 2.0 Hz and 5.0 Hz for various values of the specified displacement. Based on the results of the comparison between the experimental tests and the numerical analyses, the numerical model has been verified to be correct. The model can be used in further analyses so as to investigate the behaviour of the whole building under dynamic loads, including seismic and paraseismic excitations. Using such a numerical model, it will be possible to evaluate the improvement in resistance against dynamic loads for the case when PU foam is used instead of mineral wool.

Keywords: timber-frame house, earthquake resistance, dynamic loads, numerical model

1. Introduction

The use of timber-frame houses is very popular in many places around the world. The resistance of small building, including wooden houses, under seismic and paraseismic excitations (see, for example, [12, 11]), in terms of cost effectiveness is one of the most attractive aspects. The possibility of improving the dynamic resistance in existing houses is another positive and desired issue (see [5, 2]).

Correctly designed structures are marked by good resistance against dynamic loads, for example extreme earthquakes [9]. OSB/3 and MFP waterproof boards are used as slab, wall and roof sheathing. Those boards increase the structural stiffness of the building due to their relative high strength and because of their good resistance against shear forces and they reduce the forces transmitted to the structure during dynamic loads [9, 10, 11].

With the experience gained in North America and Japan, it can be stated that wooden houses are able to survive the catastrophic earthquake with little damage. In many cases, extremely effective design solution is to use a plywood wall panels. This material has a beneficial effect on the level of shear forces due to stiffening effect [5, 6]. Structures with such walls panels are relatively rigid and therefore resistant to dynamic actions, such as earthquakes, paraseismic excitations or impact loads [7, 1].

The use of thermal insulation in form of wool in sheathed timber-frame elements shows almost none influence on the timber-frame in terms of dynamic resistance [8].

The purpose of this article is to present the results of experimental studies of the wall panel of a skeletal wooden building of traditional technology filled with polyurethane (PU) foam, that have been adopted to create a whole building numerical model. This model was subjected to horizontal forces so as to verify the behaviour of a PU foam filled building in comparison to a mineral wool filled structure.

2. Experiment setup

The experimental setup consisted of especially designed steel frame, in which the tested specimen were mounted - see Fig 2 and Fig. 3. A PARKER dynamic actuator was used to generate harmonic excitation. For the purpose of this study, a typical timber frame house wall panel was built with dimension as shown in Fig. 1. The frame was covered with OSB3 sheaths and then the space inside was filled with PU foam. This frame was then mounted into the previously fabricated steel frame and connected with the actuator.

Figure 1. Example of real size wooden house with basic element (shown in red)

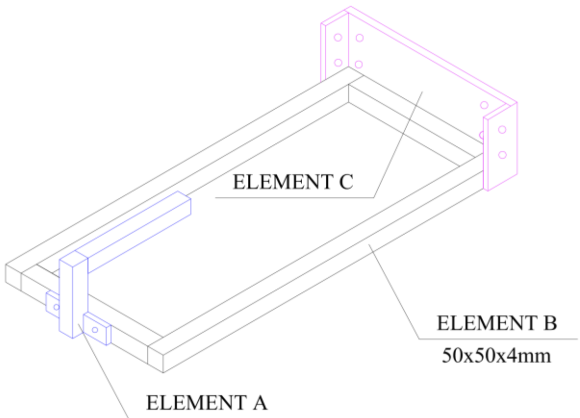

Figure 2. Steel frame used in the experiment

3. Analysis Description

During the test, the specimen has been exposed to harmonic loads with the following frequencies: $f = 0.5$ Hz; $f = 1.0$ Hz; $f = 2.0$ Hz; $f = 5.0$ Hz and different displacements. During the tests, force has been recorded with a force meter KMM40 with a range up to 50 kN as well as the resulting displacement (for the induced dynamic displacement) was recorded by a laser meter optoNCDT1302 with a range of +-100 mm (see Fig 3).

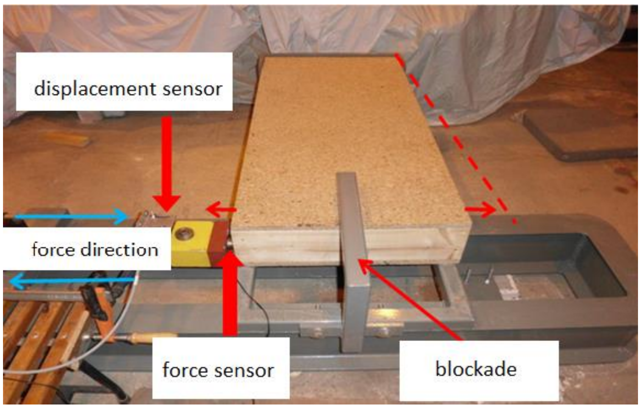

Figure 3. Experiment setup details (see [12])

The test was conducted with traditionally constructed wall panels, as described before. The panels have been fixed at one end, while the other end was subjected to displacement from 8 mm to 75 mm. The examples of the results, for the frequency of 2 Hz, are shown in Fig. 4 and Fig. 5.

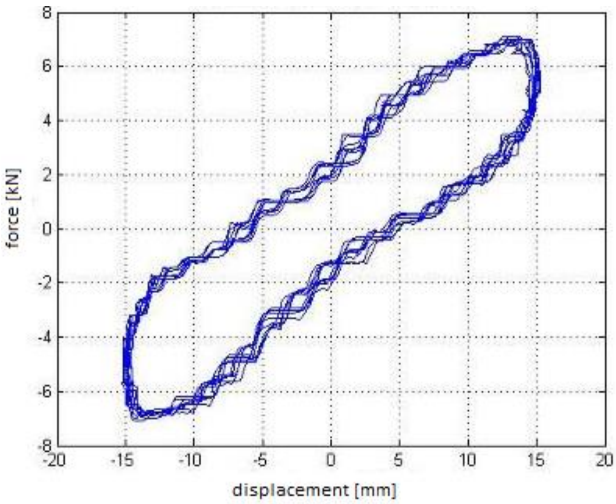

Figure 4. Hysteresis loop at 2 Hz (PU foam filling)

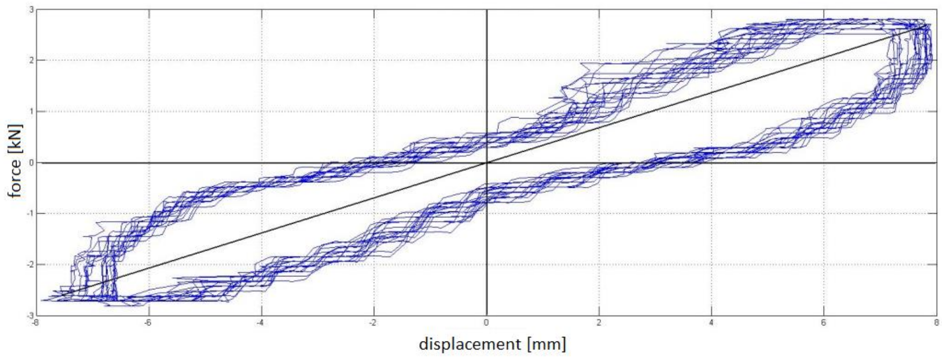

Figure 5. Hysteresis loop at 2 Hz (mineral wool filling)

The tested specimen filled with PU was able to withstand higher frequencies as well as a larger force in comparison to a wool filled wall panel, where a frequency of 2 Hz and a displacement of 28 mm caused the OSB3 sheathing to break from the wood frame as well as cracking in the connection in the wood frame itself (see [12]).

4. Numerical Model of the Polyurethane Foam Filled Panel

The program RFEM was used to create a numerical model of the tested panel (see Fig. 6). The geometry as well as the material characteristics and support conditions have been considered to be identical as in the experimental specimen. Shell elements have been used with material properties as for C30 wood. The thickness of the shell elements was 45 mm for the frame parts and 18 mm for the OSB3 sheaths and one shell with a thickness of 145 mm for the mineral wool filling. Polyurethane foam material parameters (see Fig. 7) have been established through the experimental tests. The support conditions have been modelled as shown in Fig. 6 – all translations were fixed but all rotations were free. Those support conditions have been considered as best approximation of the conditions of the experimental setup. The numerical model was calibrated by changing only the stiffness of the OSB3 sheathing in order to reflect the character of the connection between the frame and sheathing. In order to use damping, the following formulas were used in order to obtain the damping coefficents:

$$a_0 = 2\zeta\omega_1\omega_2/(\omega_1 + \omega_2) \tag{1}$$

$$a_1 = 2\zeta/(\omega_1 + \omega_2) \tag{2}$$

where:
a_0 – Rayleigh's damping factor,
a_1 – Rayleigh's damping factor,
ζ – damping coefficient obtained by experimental investigations [%],
$\omega_{1,2}$ – angular frequency [rad/s].

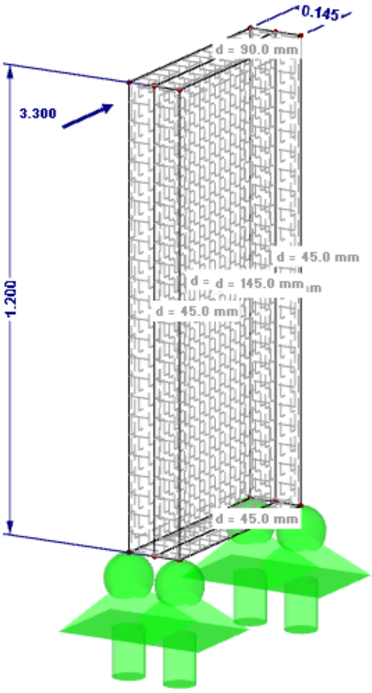

Figure 6. Numerical wall panel model

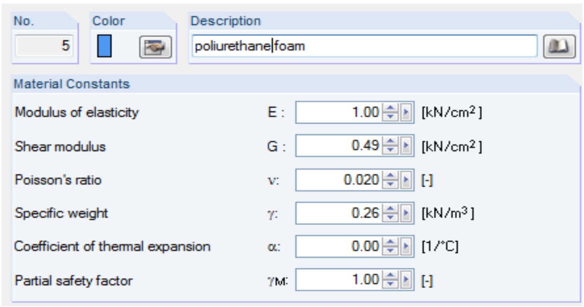

Figure 7. Polyurethane foam parameters

5. Numerical Analysis

The created numerical model was tested in order to verify its accuracy by subjecting it to the same loads as applied in the experiment and by comparing the resulting displacements. For example, for the hysteresis loop received at the frequency of 2 Hz, the resulting force was 3.30 kN and the displacement was U = 6.4 mm (see Fig. 8). Exactly the same results were obtained from the numerical analysis (see Fig. 9 and Fig. 10).

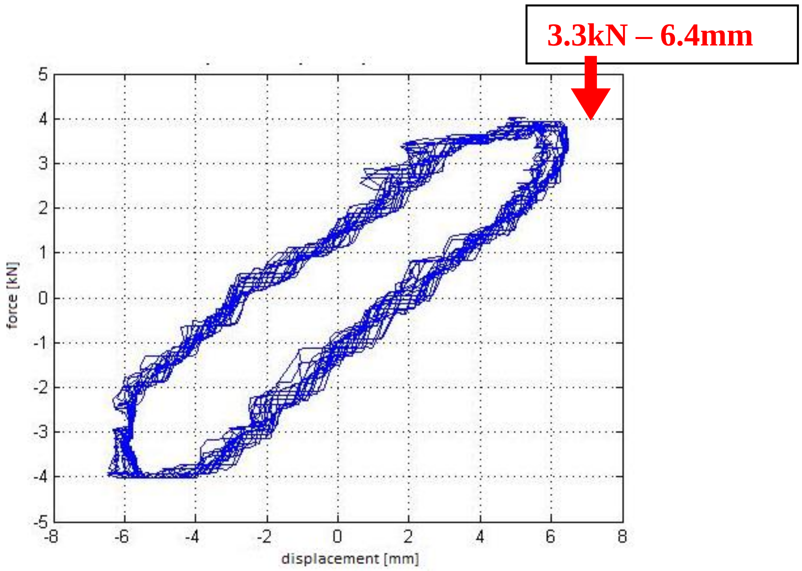

Figure 8. Hysteresis loop – maximum displacement and corresponding force

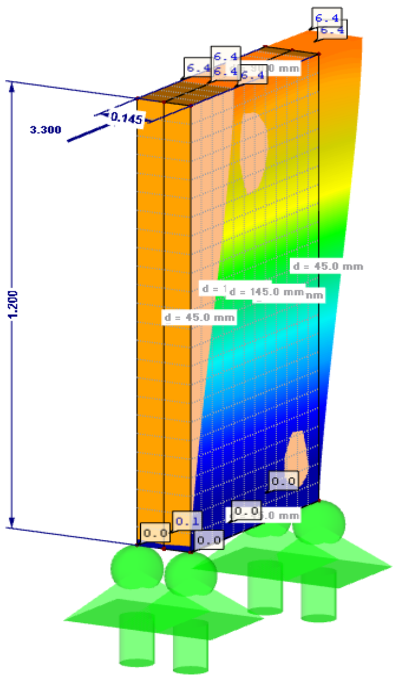

Figure 9. Deformation of the numerical model

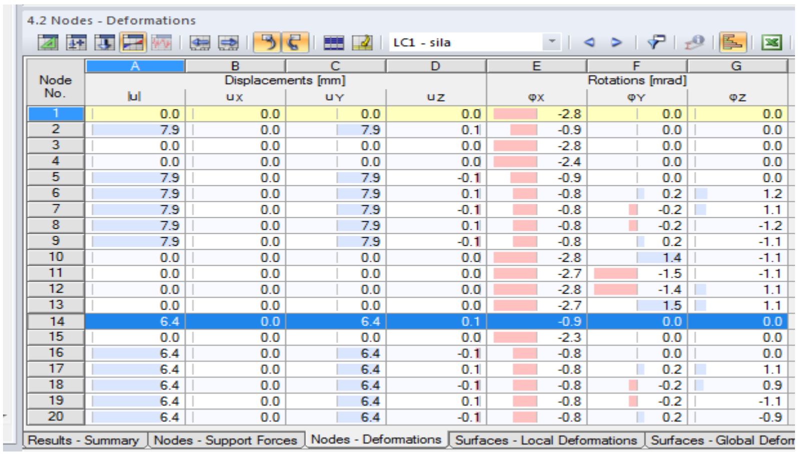
4.2 Nodes - Deformations

LC1 - sila

Node No.	A	B	C	D	E	F	G
	Displacements [mm]				Rotations [mrad]		
	|u|	uX	uY	uZ	φX	φY	φZ
1	0.0	0.0	0.0	0.0	-2.8	0.0	0.0
2	7.9	0.0	7.9	0.1	-0.9	0.0	0.0
3	0.0	0.0	0.0	0.0	-2.8	0.0	0.0
4	0.0	0.0	0.0	0.0	-2.4	0.0	0.0
5	7.9	0.0	7.9	-0.1	-0.9	0.0	0.0
6	7.9	0.0	7.9	0.1	-0.8	0.2	1.2
7	7.9	0.0	7.9	-0.1	-0.8	-0.2	1.1
8	7.9	0.0	7.9	0.1	-0.8	-0.2	-1.2
9	7.9	0.0	7.9	-0.1	-0.8	0.2	-1.1
10	0.0	0.0	0.0	0.0	-2.8	1.4	-1.1
11	0.0	0.0	0.0	0.0	-2.7	-1.5	-1.1
12	0.0	0.0	0.0	0.0	-2.8	-1.4	1.1
13	0.0	0.0	0.0	0.0	-2.7	1.5	1.1
14	6.4	0.0	6.4	0.1	-0.9	0.0	0.0
15	0.0	0.0	0.0	0.0	-2.3	0.0	0.0
16	6.4	0.0	6.4	-0.1	-0.8	0.0	0.0
17	6.4	0.0	6.4	0.1	-0.8	0.2	1.1
18	6.4	0.0	6.4	-0.1	-0.8	-0.2	0.9
19	6.4	0.0	6.4	0.1	-0.8	-0.2	-1.1
20	6.4	0.0	6.4	-0.1	-0.8	0.2	-0.9

Results - Summary | Nodes - Support Forces | Nodes - Deformations | Surfaces - Local Deformations | Surfaces - Global Defor

Figure 10. Results of the numerical analysis indicating the same displacement value as during experimental test

6. Conclusions

Based on the results of the comparison between the experimental tests and the numerical analyses, the numerical model has been verified to be correct. On this basis, it can be concluded that not only the material properties and characteristics but also the support conditions have been properly modelled. Therefore, the numerical model can be used in further analyses so as to investigate the behaviour of the whole building (see Fig. 11) under dynamic loads, including seismic and paraseismic excitations. Using such a numerical model, it will be possible to evaluate the improvement in resistance against dynamic loads for the case when PU foam is used instead of mineral wool.

Figure 11. Numerical model of the whole wood-frame house

Acknowledgments

The authors would like to thank Mr. Maciej Wysokinski from STOLKAL for building the specimen used in the tests and Mr. Bohdan Kowalewski for his help during the tests. Huge thanks also goes to dr. Łukasz Piszczyk for the help in polyurethane studies.

References

1. B. Dujic, R. Zarnic, *Study of Rateral Resistance of Massive X-Lam Wooden Wall System Subjected to Horizontal Loads*, Earthquake Engineering on Timber Structures, Portugal 2006.
2. R. Jankowski, *Impact force spectrum for damage assessment of earthquake-induced structural pounding*, Key Engineering Materials, **293-294** (2005) 711 – 718.
3. J. Kiyono, A. Furukawa, *Casuality Occurence Mechanism in the Collapse of Timber-Frame House During an Earthquake*, Earthquake Engineering and Structural Dynamics, **33** (2004) 1233 – 1248.
4. S. Mahmoud, R. Jankowski, *Elastic and inelastic multi-storey buildings under earthquake excitation with the effect of pounding*, Journal of Applied Sciences, **9**(18) (2009) 3250 – 3262.
5. S. Pei, J. W. Van de Lindt, *Coupled Shear-Bending Formulation for Seismic Analysis of Stacked Wood Shear Wall Systems*, Earthquake Engineering and Structural Dynamics, **38** (2009) 1631 – 1647.
6. J-M. Seo, I-K Choi, J-R Lee, *Experimental Study on the Aseismic Capacity of a Wooden House Using Shaking Table*, Earthquake Engineering and Structural Dynamics, **28** (1999) 1143 – 1162.
7. M. Szczepański, R. Jankowski, *Experimental dynamic study on a timber-frame house using shaking table*, In: Current Scientific Challenges in Concrete and Steel Structures and Concrete Technology, Gdansk University of Technology, Gdańsk (2011) 155 – 162.
8. M. Szczepański, W. Migda, R. Jankowski, *Construction technology of timber-frame houses resistant to dynamic loads - study on models of exterior walls*, Advances in Science and Technology - Research Journal, **9**(28) (2015) 75 – 80.
9. T. Toratti, *Seismic Design of Timber Structures*, FEMA, 1994.
10. J. Vessby, *Analysis of shear walls for multi-storey timber buildings*, Linnaeus University Dissertations, **45** (2011).
11. Z. Zembaty, R. Jankowski, A. Cholewicki, J. Szulc, *Trzęsienie ziemi 30 listopada 2004 r. na Podhalu oraz jego wpływ na obiekty budowlane*, Inżynieria i Budownictwo, **61**(9) (2005) 507 – 511.
12. Z. Zembaty, A. Cholewicki, R. Jankowski, J. Szulc, *Trzęsienia ziemi 21 września 2004 r. w Polsce północno-wschodniej oraz ich wpływ na obiekty budowlane*, Inżynieria i Budownictwo, **61**(1) (2005) 3 – 9.

Free Vibrations of Geometrically Nonlinear Column Locally Resting on the Winkler Elastic Foundation under the Specific Load

Janusz SZMIDLA
Institute of Mechanics and Machine Design Foundations
Częstochowa University of Technology, szmidla@imipkm.pcz.czest.pl

Ilona CIEŚLIŃSKA-GĄSIOR
Institute of Mechanics and Machine Design Foundations
Częstochowa University of Technology, cieslinskailona@wp.pl

Abstract

The results of theoretical and numerical studies concerning continuous system subjected to the follower force directed towards the positive pole, locally resting on Winkler elastic foundation are presented in this paper.

The load by follower force directed towards the positive pole is guaranteed by loading structure built of loading and receiving heads made of elements of circular outlines. Abovementioned heads are real constructions, used in experimental research of continuous systems.

Taking into account total mechanical energy of the system, the Hamilton's principle and the small parameter method, the differential equations of motion and boundary conditions of the considered column were determined. On the basis of a solution of the issue of dynamics of the system, an appropriate formulas were formulated and then the trajectory of curves on the plane frequency of free vibrations – the value of external load were calculated taking into considerations physical and geometrical parameters of the structure, including parameter of loading head and parameters describing Winkler elastic foundation.

Keywords: frequency of free vibrations, Winkler elastic foundation, slender systems

1. Introduction

The issue of stability and free vibrations of slender geometrically nonlinear bar systems [1] lying on the Winkler elastic foundation is the subject of many scientific publications, where an influence of elastic base parameters on the value of bifurcation load and the scope of changes in the frequency of free vibrations was analysed.

Taking into account the physical models, the following types of arrangement of elastic foundation are defined:
– along the full length of each rod of the system (total foundation – linear systems [2]),
– along the full length of selected rod of the system (partial foundation – geometrically nonlinear systems [3]),
– at a certain distance along the axis of the system (local foundation for the rod- linear structures [4] or for the selected rods - geometrically nonlinear structures [5]).

2. The Physical Model of the System

The physical model of geometrically nonlinear column (**NW**) subjected to the follower force directed towards the positive pole locally resting on the Winkler elastic foundation is presented in Figure 1.

The column (Figure 1a) is built of two external prismatic rods ①,② of length l_1 and l_2 and one prismatic internal rod mounted symmetrically in relation to the external rods. In order to model the local elastic foundation of stiffness K, the internal rod was divided into three segments ③,④,⑤ of constant flexural stiffness and lengths l_3, l_4, l_5 respectively.

Taking into consideration presented description, the following relations relating to the lengths l_i (i = 1…5), distribution of the flexural stiffness $(EJ)_i$, compressive stiffness $(EA)_i$, and mass per unit length $(\rho A)_i$ are assumed:

– in the case of external rods of the system:

$$l_1 = l_2 \tag{1}$$

$$(EJ)_1 = (EJ)_2 \tag{2}$$

$$(EA)_1 = (EA)_2 \tag{3}$$

$$(\rho A)_1 = (\rho A)_2 \tag{4}$$

– in the case of the internal rod:

$$l_1 = l_2 = l_3 + l_4 + l_5 \tag{5}$$

$$(EJ)_3 = (EJ)_4 = (EJ)_5 \tag{6}$$

$$(EA)_3 = (EA)_4 = (EA)_5 \tag{7}$$

$$(\rho A)_3 = (\rho A)_4 = (\rho A)_5 \tag{8}$$

The internal rod, which is supported on the elastic foundation (member ④) is characterised by lower flexural stiffness $(EJ)_3$ as compared to the flexural stiffness of external rods of the column, that is:

$$(EJ)_3 \le (EJ)_1 + (EJ)_2 \tag{9}$$

Rods ①,②,③ are mounted rigidly (cantilevered) ($x_1 = x_2 = x_3 = 0$). The free ends of the rods ①,②,⑤ ($x_1 = l_1$, $x_2 = l_2$, $x_5 = l_5$) of the system are connected by the element of concentrated mass m that ensures the equality of longitudinal and transverse displacements as well as the equality of angles of deflection of these rods. The follower force directed towards the positive pole (see Figure 1a) is realised by loading ⑥ and receiving heads ⑦,⑧ of circular outlines (constant curvature) [6]. The direction of external load P ⑨ passes through a stationary point O lying on the non-deformed axis of the column and is tangential to the line of deflection of free end of the system. It is assumed in this paper that the elastic foundation does not effect the symmetry of the structure. The free end of the column is connected with the receiving head by the infinitely rigid element ⑧ of length l_0 that is a part of loading structure. Consideration of this element jest necessary due to real constructional solution of head realising the load [7]. The flexural stiffness of abovementioned element is many times higher than the flexural stiffness of the essential system. The pole O is located at a distance of (R-l_0) from the free end of the column.

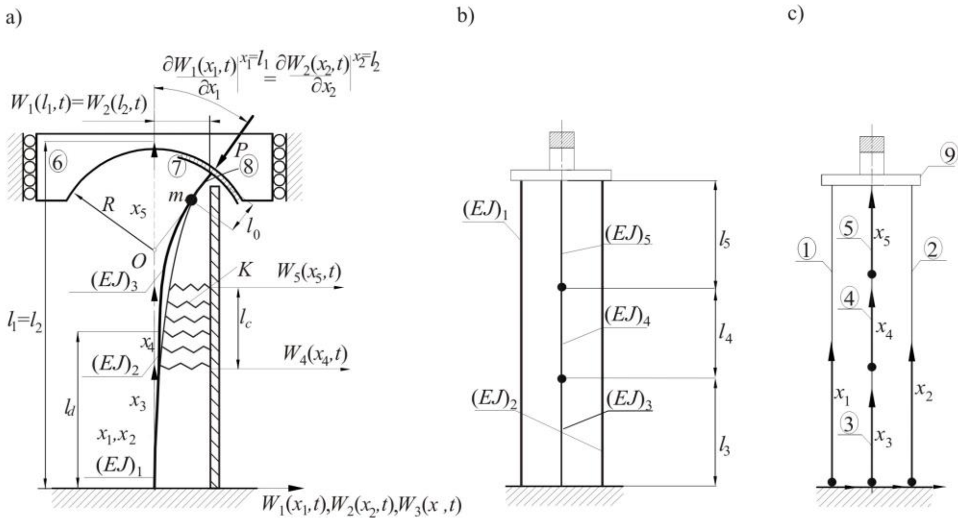

Figure 1. a) The physical model of geometrically nonlinear column (**NW**) locally resting on Winkler elastic foundation,
b, c) The physical model of rods of the geometrically nonlinear column

Taking into account the elastic foundation, the following parameters describing a location and a size of the elastic base relative to the total length of the analysed structure were determined:

$$l_c^* = \frac{l_4}{l_1} = \frac{l_c}{l_1}, \; l_d^* = \frac{l_3 + \frac{l_4}{2}}{l_1} = \frac{l_d}{l_1} \tag{10}$$

Assuming that the sum of the total flexural stiffness of the geometrically nonlinear system (**NW**) is constant:

$$\sum_{n=1}^{3} (EJ)_n = idem, \tag{11}$$

the asymmetry of flexural stiffness coefficient μ was defined in the form:

$$\mu = \frac{(EJ)_3}{(EJ)_1 + (EJ)_2} \tag{12}$$

Taking into consideration the physical model of the column, a components of kinetic energy and potential energy were specified. The kinetic energy T is a sum of the kinetic energy of particular rods and the kinetic energy of concentrated mass m :

$$T = \frac{1}{2}\sum_{i=1}^{5} (\rho A)_i \int_0^{l_i} \left(\frac{\partial W_i(x_i,t)}{\partial t} \right)^2 dx_i + \frac{1}{2} m \left(\frac{\partial W_1(l_1,t)}{\partial t} \right)^2 \tag{13}$$

The components of the potential energy V refer to the energy of bending elasticity, the potential energy resulting from external load and the energy of elastic foundation:

$$V = \frac{1}{2}\sum_{i=1}^{5}(EJ)_i\int_0^{l_i}\left[\frac{\partial^2 W_i(x_i,t)}{\partial x_i^{\,2}}\right]^2 dx_i + \frac{1}{2}\sum_{i=1}^{5}(EA)_i\int_0^{l_i}\left[\frac{1}{2}\left(\frac{\partial W_i(x_i,t)}{\partial x_i}\right)^2 + \frac{\partial U_i(x_i,t)}{\partial x_i}\right]^2 dx_i + \\ + PU_1(l_1,t) + \frac{1}{2}P(R-l_0)\left[\frac{\partial W_1(x_1,t)}{\partial x_1}\right]^2 + \frac{1}{2}K\int_0^{l_4}\Big(W_4(x_4)\Big)\,dx_4 \tag{14}$$

3. Problem Formulation, Differential Equations of Motion, Boundary Conditions

The issue of the stability and free vibrations of the geometrically nonlinear column was formulated using the Hamilton's principle [6]:

$$\delta\int_{t_1}^{t_2}(T-V)\,dt = 0 \tag{15}$$

where: δ – variation operator.

Using the formulas (13) and (14), after computation of the variation of the kinetic and potential energies, the following equations were obtained:

– the differential equations of transverse displacements

$$(EJ)_j\frac{\partial^4 W_j(x_j,t)}{\partial x_j^4} + S_j(t)\frac{\partial^2 W_j(x_j,t)}{\partial x_j^2} + (\rho A)_j\frac{\partial^2 W_j(x_j,t)}{\partial t^2} = 0,\; j = 1,2,3,5 \tag{16}$$

$$(EJ)_4\frac{\partial^4 W_4(x_4,t)}{\partial x_4^4} + S_4(t)\frac{\partial^2 W_4(x_4,t)}{\partial x_4^2} + (\rho A)_4\frac{\partial^2 W_4(x_4,t)}{\partial t^2} + KW_4(x_4,t) = 0 \tag{17}$$

where longitudinal forces in external rods and particular members of the internal rod are defined as:

$$S_i(t) = -(EA)_i\left[\frac{\partial U_i(x_i,t)}{\partial x_i} + \frac{1}{2}\left(\frac{\partial W_i(x_i,t)}{\partial x_i}\right)^2\right],\quad i = 1..5 \tag{18}$$

– the equations on motion in the longitudinal direction:

$$\frac{\partial}{\partial x_i}\left[\frac{\partial U_i(x_i,t)}{\partial x_i} + \frac{1}{2}\left(\frac{\partial W_i(x_i,t)}{\partial x_i}\right)^2\right] = 0,\; i = 1..5 \tag{19}$$

Double integration of the formulas (19) over an adequate ranges and taking account of the relationships (18) allowed the determination of the formulas describing the longitudinal displacements of the each rod of the system:

$$U_i(x_i,t) - U_i(0,t) = -\frac{S_i(t)}{(EA)_i}x_i - \frac{1}{2}\int_0^{x_i}\left(\frac{\partial W_i(x_i,t)}{\partial x_i}\right)^2 dx_i \tag{20}$$

Known geometrical boundary conditions of the considered structure are written as follows:

$$W_1(0,t) = W_2(0,t) = W_3(0,t) = U_1(0,t) = U_2(0,t) = U_3(0,t) = 0$$

$$W_1(l_1,t) = W_5(l_5,t), \qquad W_2(l_2,t) = W_5(l_5,t),$$

$$U_1(l_1,t) = U_2(l_2,t) = U_5(l_5,t),$$

$$\left.\frac{\partial W_1(x_1,t)}{\partial x_1}\right|_{x_1=0} = \left.\frac{\partial W_2(x_2,t)}{\partial x_2}\right|_{x_2=0} = \left.\frac{\partial W_3(x_3,t)}{\partial x_3}\right|_{x_3=0} = 0,$$

$$\left.\frac{\partial W_1(x_1,t)}{\partial x_1}\right|_{x_1=l_1} = \left.\frac{\partial W_5(x_5,t)}{\partial x_5}\right|_{x_5=l_5}, \left.\frac{\partial W_2(x_2,t)}{\partial x_2}\right|_{x_2=l_2} = \left.\frac{\partial W_5(x_5,t)}{\partial x_5}\right|_{x_5=l_5} \tag{21-35}$$

$$W_3(l_3,t) = W_4(0,t), \qquad W_4(l_4,t) = W_5(0,t),$$

$$U_3(l_3,t) = U_4(0,t), \qquad U_4(l_4,t) = U_5(0,t),$$

$$\left.\frac{\partial W_3(x_3,t)}{\partial x_3}\right|_{x_3=l_3} = \left.\frac{\partial W_4(x_4,t)}{\partial x_4}\right|_{x_4=0}, \qquad \left.\frac{\partial W_4(x_4,t)}{\partial x_4}\right|_{x_4=l_4} = \left.\frac{\partial W_5(x_5,t)}{\partial x_5}\right|_{x=0},$$

$$W_1(l_1,t) = (R - l_0)\left.\frac{\partial W_1(x_1,t)}{\partial x_1}\right|_{x_1=l_1}$$

Substituting of conditions (21-35) into the equation (15) allowed to determine remaining natural boundary conditions that are expressed by the following formulas:

$$(EJ)_1 \left.\frac{\partial^3 W_1(x_1,t)}{\partial x_1^3}\right|_{x=l_1} + (EJ)_2 \left.\frac{\partial^3 W_2(x_2,t)}{\partial x_x^3}\right|_{x=l_2} + (EJ)_5 \left.\frac{\partial^3 W_5(x_5,t)}{\partial x_5^3}\right|_{x=l_5} +$$

$$- \frac{1}{R - l_0}\left[(EJ)_1 \left.\frac{\partial^2 W(x_1,t)_1}{\partial x_1^2}\right|_{x=l_1} + (EJ)_5 \left.\frac{\partial^2 W_5(x_5,t)}{\partial x_5^2}\right|_{x=l_5}\right] - m\,\frac{\partial^2 W_1(x_1,t)}{\partial t^2} = 0$$

$$\left.\frac{\partial^2 W_3(x_3,t)}{\partial x_3^2}\right|_{x_2=l_3} = \left.\frac{\partial^2 W_4(x_4,t)}{\partial x_4^2}\right|_{x_3=0}, \qquad \left.\frac{\partial^2 W_4(x_4,t)}{\partial x_4^2}\right|_{x_4=0} = \left.\frac{\partial^2 W_5(x_5,t)}{\partial x_5^2}\right|_{x_5=0}, \tag{32-37}$$

$$\left.\frac{\partial^3 W_3(x_3,t)}{\partial x_3^3}\right|_{x_3=l_3} = \left.\frac{\partial^3 W_4(x_4,t)}{\partial x_4^3}\right|_{x_4=0}, \qquad \left.\frac{\partial^3 W_4(x_4,t)}{\partial x_4^3}\right|_{x_4=0} = \left.\frac{\partial^3 W_5(x_5,t)}{\partial x_5^3}\right|_{x_5=0}$$

$$\sum_{n=1}^{3} S_n - P = 0$$

4. Results of Numerical Computations

Taking into account the solution of the boundary problem, the numerical calculations were carried out relating to the free vibrations of the considered system.

An exemplary scope of change in the value of the first frequency of vibrations (parameter Ω^*) as a function of external load (parameter λ_c^*) for given parameters of Winkler elastic foundation (K^*, l_c^*, l_d^*) and parameter of the loading head R^* was presented in Figure 2.

$$\lambda_c^* = \frac{P l_1^2}{\sum_{n=1}^{3} (EJ)_n}, \quad \Omega^* = \frac{\sum_{n=1}^{3} (\rho A)_n l_n^4 \omega^2}{\sum_{n=1}^{3} (EJ)_n}, \quad K^* = \frac{K l_1^{\,4}}{\sum_{n=1}^{3} (EJ)_n}, \quad R^* = \frac{R - l_0}{l_1}, \tag{38a-d}$$

Depending on the external load, the curve representing eigenvalues may be positively or negatively inclined to the axis of ordinates. In order to compare the results, besides the trajectories of curves relating to the frequencies of vibrations of **NW** system, the scope of changes in frequencies for **L** and **N** columns were presented too. The geometrically nonlinear column **N** is built of three rods (two external and one internal rods). The physical model of geometrically nonlinear column is identical as the physical model of **NW** column (without considering the Winkler elastic foundation). The linear column **L** consists of two external rods ①,② of the column **N-** the flexural stiffness of these elements is the same as the flexural stiffness of external rods of the nonlinear column **N** for given value of the asymmetry of flexural stiffness coefficient μ. The linear system is treated in this paper as a comparative system.

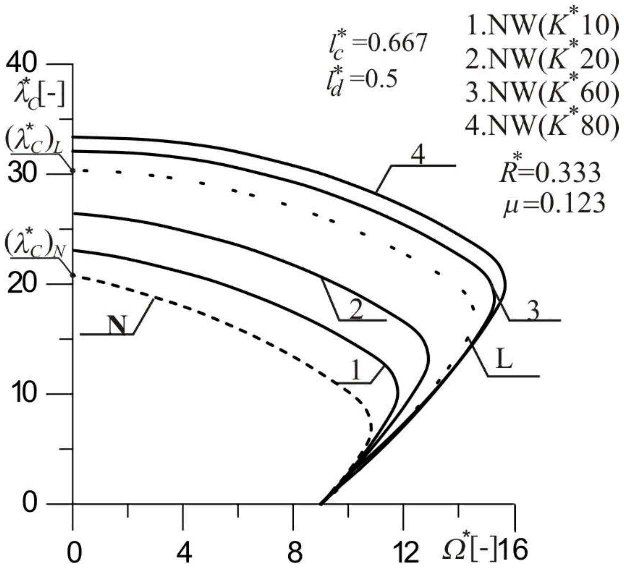

Figure 2. The curves representing the first frequency of free vibrations of the **NW**, **N** and **L** columns - the changes in frequencies of nonlinear and linear systems

The value of the bifurcational load parameter λ_c^* for each of the courses of curves of the free vibrations occurs while $\Omega^* = 0$. On the basis of the obtained results it has been proved that there are such a parameters of Winkler elastic foundation, for which the system can "exit" from the range of local loss of stability ($\lambda_c^*>\lambda_L^*$, compare curves 3, 4 in Figure 2.). The detailed results of studies were presented during the 27th Symposium on vibrations in physical systems.

5. Conclusions

The analysis of the free vibrations of the geometrically nonlinear column **NW** locally resting on the Winkler elastic foundation subjected to the follower force directed towards the positive pole was the subject of this paper. The Winkler elastic foundation, its length and location effect on the value of frequency of free vibrations of the examined system. Consideration of the Winkler elastic foundation in the physical model of the column causes an increase in the value of frequency of vibrations of the system. The value of bifurcational load is rising with the increase in elastic base stiffness. The elastic foundation of sufficiently large stiffness causes an "exit" from the range of the local loss of stability.

Acknowledgments

The study has been carried out within the framework of project BS/PB-1-101-3021/11/P realized at Częstochowa University of Technology.

References

1. S. Uzny, *An elastically supported geometrically nonlinear slender system subjected to a specific load in respect of bifurcational load and free vibrations*, International Journal Bifurcation and Chaos, **21**(10) (2011) 2983 – 2992.
2. D. Thambiratnam, Y. Zhuge, *Free vibration analysis of beams on elastic fundation*, Computers and Structures, **60** (1996) 971 – 980.
3. J. Szmidla, *Drgania swobodne i stateczność układów smukłych poddanych obciążeniu swoistemu* (rozdział III) w: Drgania swobodne i stateczność kolumny geometrycznie nieliniowej niecałkowicie spoczywającej na podłożu sprężystym typu Winklera. Częstochowa: Wyd. Politechnika Częstochowska 2009.
4. Elishakoff, X. Wang, *Controversy associated with the so – called „Follower Forces"*, Critical Overview, Applied Mechanics Reviews, (2005) 117 – 139.
5. J. Szmidla, A. Jurczyńska, *Drgania swobodne wstępnie sprężonej kolumny geometrycznie nieliniowej poddanej obciążeniu siłą śledzącą skierowaną do bieguna dodatniego miejscowo spoczywającej na podłożu typu Winklera*, Modelowanie inżynierskie, **54**(23) (2015) 87 – 93.

6. L. Tomski, J. Szmidla, *Drgania swobodne i stateczność obiektów smukłych, jako układów liniowych lub nieliniowych* (rozdział VIII) w: Drgania swobodne i stateczność kolumny geometrycznie nieliniowej częściowo spoczywającej na podłożu sprężystym typu Winklera, Praca zbiorowa wykonana pod kierownictwem naukowym i redakcją L. Tomskiego, Wydawnictwo Naukowo- Techniczne Fundacja Książki Naukowo-Techniczna Warszawa 2007.
7. L. Tomski, J. Szmidla, *Drgania swobodne i stateczność obiektów smukłych, jako układów liniowych lub nieliniowych* (rozdział II) w: Opis techniczny struktur obciążenia kolumny. Praca zbiorowa wykonana pod kierownictwem naukowym i redakcją L. Tomskiego, Wydawnictwo Naukowo- Techniczne Fundacja Książki Naukowo-Techniczna Warszawa 2007.

Free Vibrations of Non-Prismatic Slender System Subjected to the Follower Force Directed Towards the Positive Pole

Janusz SZMIDLA
Institute of Mechanics and Machine Design Foundations
Częstochowa University of Technology, szmidla@imipkm.pcz.pl

Anna JURCZYŃSKA
Institute of Mechanics and Machine Design Foundations
Częstochowa University of Technology, a.jurczynska@imipkm.pcz.pl

Abstract

The paper contains the results of theoretical and numerical studies within the scope of kinetic criterion of stability loss of slender non-prismatic column subjected to the follower force directed towards the positive pole (the case of specific load). Shape of the system approximation by a linear function and polynomial of degree 2 was considered. On the basis of the Bernoulli – Euler's theory, the mechanical energy was defined. The differential equations of motion and natural boundary conditions were determined according to the Hamilton's principle. The issue of free vibrations was solved using the small parameter method. Within the range of numerical calculations, the changes in the eigenvalues were presented as a function of external load with variable geometrical parameters of the system, including parameters resulting from the shape approximation and parameters of loading structure.

Keywords: slender systems, non-prismatic systems, free vibrations, specific load

1. Introduction

Non-prismatic systems are commonly used in mechanics and mechanical constructions. Due to increasing technical requirements for the designers, an optimal shapes of structures, that will ensure an increase in transferred load or mass reduction are looked for. The issue of dynamics of slender non-prismatic systems is the subject of many scientific publications.

The dynamic analysis of Bernoulli – Euler's beam with stepped variable flexural stiffness with discrete elements was presented in work [1]. The problem was solved on the basis of the mode summation method. The results regarding to the issue of stability and free vibrations of non-prismatic column under Euler's load were shown in publication [2]. The solution of vibration problem of beam with stepped variable cross-section was presented in [3].

In scientific papers, the shape optimization was based on different methods, such as the Lagrange multiplier formalism [4], modified simulated annealing algorithm [5], finite element method [6], cellular automata method [7] or using Green's function properties [8].

2. The physical model of the system

A slender non-prismatic column of rectangular cross-section subjected to the chosen case of specific load is considered in this paper. The physical model of analysed system is presented in Figure 1. To model cross-section variable along the axis, the structure was divided into *n* segments of constant length *l* and thickness *h* and variable width *b*. It is assumed that total volume of each segments V_{obj}, total length of the column $L = l \cdot n = const.$ and the values of material density ρ as well as Young's modulus *E* of each parts are constant. In addition, the value of width *b* of segments must satisfy the condition that $b \geq h$. The column's shape was described by linear function $b(x) = 2a(Z) \cdot x + d$ and by polynomial of degree 2 $b(x) = 2\left[a(p,q) \cdot [x-p]^2 + q\right]$, where $0 \leq x \leq L$.

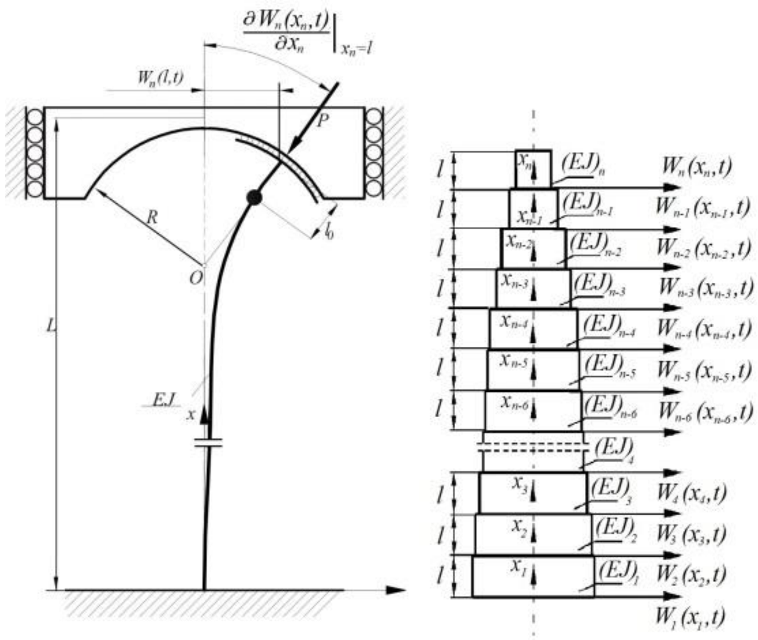

Figure 1. The scheme of physical model of considered column

The load by follower force directed towards the positive pole (the case of specific load, see [9]) is achieved by loading and receiving heads of circular outlines. The direction of the force *P* is tangential to the line of deflection of end of system ($x = L$) and additionally passes through stationary point *O* located on the non-deformed axis of the column at the distance of *R* from its free end (positive pole). The system is connected with receiving head through infinitely rigid element l_0, which consideration is necessary for reasons relating to the construction.

3. The mathematical model

On the basis of the physical model of non-prismatic column (comp. Figure 1), the total mechanical energy of the system was defined. The potential energy V consists of:

- energy of bending elasticity:

$$V_1 = \sum_{i=1}^{n} \frac{(EJ)_i}{2} \int_0^l \left(\frac{\partial^2 W_i(x_i,t)}{\partial x_i^2} \right)^2 dx_i \tag{1}$$

- potential energy V_2 resulting from the external load:

$$V_2 = -\frac{P}{2} \int_0^l \left(\frac{\partial W_i(x_i,t)}{\partial x_i} \right)^2 dx_i + PU_n(l,t) + \frac{1}{2} P(R-l_0) \left(\left. \frac{\partial W_n(x_n,t)}{\partial x_n} \right|_{x_n=l} \right)^2 \tag{2}$$

$$V = V_1 + V_2 \tag{3}$$

The kinetic energy T of the system is formulated in the following form:

$$T = \sum_{i=1}^{n} \frac{(\rho A)_i}{2} \int_0^l \left(\frac{\partial W_i(x_i,t)}{\partial t} \right)^2 dx_i + \frac{1}{2} m \left(\frac{\partial W_n(l,t)}{\partial t} \right)^2 \tag{4}$$

The solution of the problem of free vibrations of column was obtained on the basis of Hamilton’s principle (see [2,9]), using the properties of the calculus of variation:

$$\delta \int_{t_1}^{t_2} (T - V) dt = 0 \tag{5}$$

where t_1, t_2 – coordinates of time, δ – variation operator.
Known a priori geometrical boundary conditions and continuity conditions were written as follows:

$$W_1(0,t) = \left. \frac{\partial W_1(x_1,t)}{\partial x_1} \right|_{x_1=0} = 0, \tag{6-7}$$

$$W_i(l,t) = W_{i+1}(0,t) \tag{8}$$

$$\left. \left(\frac{\partial W_i(x_i,t)}{\partial x_i} \right) \right|_{x_i=l} = \left. \left(\frac{\partial W_{i+1}(x_{i+1},t)}{\partial x_{i+1}} \right) \right|_{x_i+1=0}, \tag{9}$$

$$W_n(l,t) = (R-l_0) \left. \frac{\partial W_n(x_n,t)}{\partial x_n} \right|_{x_n=l}, \tag{10}$$

where the condition (10) results from the geometry of loading head.

Taking into account the variation of mechanical energy (1-4) and conditions (6-10) in the equation (5), the following relations were obtained:
– differential equations of motion:

$$(EJ)_i \frac{\partial^4 W_i(x_i,t)}{\partial x_i^4} + P \frac{\partial^2 W_i(x_i,t)}{\partial x_i^2} + (\rho A)_i \frac{\partial^2 W_i(x_i,t)}{\partial t^2} = 0 \tag{11}$$

– missing natural boundary condition and continuity conditions:

$$\left.\frac{\partial^3 W_n(x_n,t)}{\partial x_n{}^3}\right|_{x_n=l} - \frac{1}{(R-l_0)}\left.\frac{\partial^2 W_n(x_n,t)}{\partial x_n{}^2}\right|_{x_n=l} - \frac{m}{(EJ)_n}\left.\frac{\partial^2 W_n(x_n,t)}{\partial t^2}\right|_{x_n=l} = 0 \tag{12}$$

$$(EJ)_i\left.\left(\frac{\partial^2 W_i(x_i,t)}{\partial x_i{}^2}\right)\right|_{x_i=l} = (EJ)_{i+1}\left.\left(\frac{\partial^2 W_{i+1}(x_{i+1},t)}{\partial x_{i+1}{}^2}\right)\right|_{x_i+1=0} \tag{13}$$

$$(EJ)_i\left.\left(\frac{\partial^3 W_i(x_i,t)}{\partial x_i{}^3}\right)\right|_{x_i=l} = (EJ)_{i+1}\left.\left(\frac{\partial^3 W_{i+1}(x_{i+1},t)}{\partial x_{i+1}{}^3}\right)\right|_{x_i+1=0} \tag{14}$$

The solution of the differential equations of motion was obtained on the basis of small parameter method, which consists of expanding of nonlinear members of differential equations into the power series with respect to the amplitude parameter ε ($\varepsilon \ll 1$).

4. The Results of Numerical Calculations

To compare the results, the following dimensionless parameters were determined:
– external load parameter

$$\lambda = \frac{PL^2}{(EJ)_{pr}} \tag{15}$$

– parameter of frequency of natural vibrations

$$\Omega = \frac{\omega^2(\rho A)_{pr} L^4}{(EJ)_{pr}} \tag{16}$$

– parameters describing cross-section variable along the axis of the column

$$Z^* = \frac{b_1 - b_n}{L}\cdot 100\%, \quad p^* = \frac{p}{L}, \quad q^* = \frac{q}{L}, \tag{17-20}$$

– radius of loading head parameter

$$R^* = \frac{R-l_0}{L}\,, \tag{21}$$

where the subscript „*pr*" refers to the geometrical parameters of prismatic column (a comparative system).

The results of numerical computations in the scope of kinetic criterion of stability loss were shown in Figures 2 and 3.The considerations are limited to presentation of changes in two first frequencies of natural vibrations of column (Ω_1, Ω_2) as a function of the parameter of external load. In Figure 2., the changes in first frequency of natural vibration of non-prismatic system for different values of taper parameter Z (shape approximation by linear function) was illustrated. The results regarding to the approximation by quadratic function were presented in Figure 3., taking into account variable location of a vertex of parabola (p^*, q^* parameters).

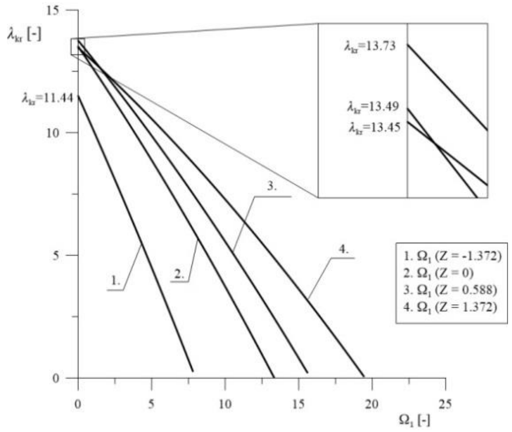

Figure 2.The first frequency of vibration of non-prismatic column approximated by linear function (R^*=1.3) for selected values of taper parameter Z

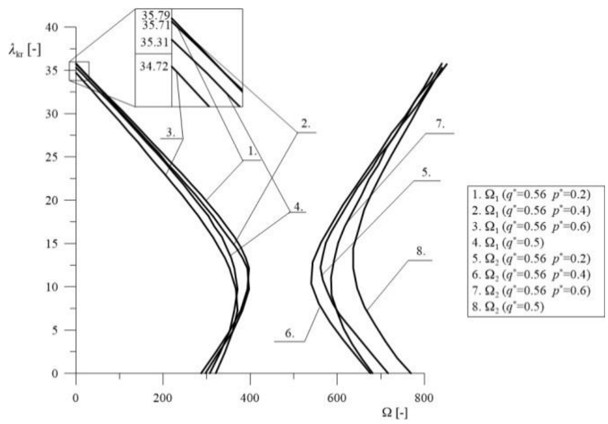

Figure 3. The characteristic curves of column approximated by quadratic function (R^*=0.3) for chosen values of parameters p^* and q^*

The value of critical load for presented curves on the plane dimension less parameter of external load – dimensionless parameter of frequency of free vibrations is determined for $\Omega = 0$. The results regarding to the values of critical load parameter, obtained on the basis of the kinetic criterion of stability loss, show compliance with the results from the energetic method (the static criterion of loss of stability).Presented courses of changes in eigenvalues have the positive, zero or negative slope, depending on the value of external load and radius of loading head. Therefore, considered structures may be classified as a divergent or divergent pseudo fluttering type of system.

5. Conclusions

The analysis of free vibrations of non-prismatic column subjected to the follower force directed towards the positive pole was presented in this paper. On the basis of conducted numerical calculations, the following conclusions were formulated:
– shape of system approximation effects the value of frequency of vibration. The value of critical load of the system depends on the parameters describing shape of the column and geometrical parameters of loading structure,
– depending on the value of radius of the loading head parameter, the system under consideration may be classified as the divergent or divergent pseudo fluttering type of system,
– approximation of the shape of the considered column is restricted by the condition which states that the value of width b of each segments of system must be greater than or equal to the thickness h of segments.

Acknowledgments

The study has been carried out within the framework of project BS/PB-1-101-3021/11/P realized at Częstochowa University of Technology.

References

1. W. Sochacki, *The dynamic stability of a stepped cantilever beam with attachments*, Journal of Vibroengineering, **15**(1) (2013) 280 – 290.
2. J. Szmidla, M. Kluba, *Stateczność i drgania swobodne niepryzmatycznego układu smukłego poddanego obciążeniu eulerowskiemu*, Modelowanie Inżynierskie, **41** (2011) 385 – 394.
3. A. P. Seyranian, E. Lund, N. Olhoff, *Multiple eigenvalues in structural optimization problems*, Struct. Optimization, **8** (1994) 207 – 227.
4. D. Cekus, P. Waryś, *Identification of parameters of discrete-continuous models*, AIP Conf. Proc., **1648** (2015).
5. J. Szmidla, A. Wawszczak, *Optymalizacja kształtu kolumn realizujących wybrane przypadki obciążenia Eulera za pomocą zmodyfikowanego algorytmu symulowanego wyżarzania*, Zeszyty Naukowe Politechniki Rzeszowskiej, **258**(74) (2008) 333 – 344.
6. G. J. Simitses, M. P. Kamat, C. V. Smith, *Strongest column by the finite element displacement method*, AIAA Journal, **11**(9) (1973) 1231 – 1232.
7. B. Bochenek, K. Tajs-Zielińska, *Optimization of beams and columns using cellular automata*, CzasopismoTechniczne. Mechanika, **105**(4) (2008) 19 – 30.
8. S. Kukla, I. Zamojska, *Frequency analysis of axially loaded stepped beams by Green's function method*, Journal of Sound and Vibrations, **300** (2007) 1034 – 1041.
9. L. Tomski, J. Szmidla, *Theoretical and experimental investigations of the natural vibrations of the divergence and divergence pseudo flutter type systems*, PAMM, **4**(1) (2004) 418 – 419.

A Study on Natural Frequencies of Timoshenko Beam with Rapidly Varying Stiffness

Michał ŚWIĄTEK[1], Łukasz DOMAGALSKI[2], Jarosław JĘDRYSIAK[3]
Department of Structural Mechanics, Lodz University of Technology
al. Politechniki 6, 90-924 Lodz, Poland,
email: 800778@edu.p.lodz.pl[1], lukasz.domagalski@p.lodz.pl[2], jarek@edu.p.lodz.pl[3]

Abstract

Vibrations of Timoshenko beams with properties periodically varying along the axis are under consideration. The tolerance method of averaging differential operators with highly oscillating coefficients is applied to obtain the governing equations with constant coefficients. The dynamics of Timoshenko beam with the effect of the cell length is described. A asymptotic model is then constructed, which is further studied in analysis of the low order natural frequencies. The proposed model is able to describe dynamics of beams made of non-slender cells.

Keywords: beam vibrations, periodic beams, tolerance modelling

1. Introduction

The analysis will be restricted to the linear free vibrations of elastic shear-deformable beam with rotational inertia. Considered structure consists of many small, identical and ordered pieces of length *l*, called periodicity cells. The geometric and material properties are varying periodically along longitudinal axis of the beam. A fragment of such beam is shown in Figure 1.

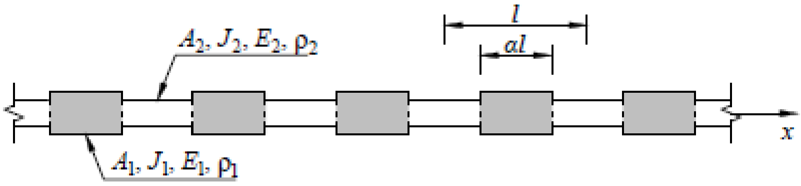

Figure 1. A fragment of periodically inhomogeneous Timoshenko beam

The direct analytical formulation of considered Timoshenko beam model leads to equations of motion which usually do have non-continuous, highly oscillating, periodic coefficients. Many methods have been developed in analysis of periodically inhomogeneous solids and structures. The most advanced are the analytical methods based on asymptotic homogenization of differential operators [1-2].

Here, the tolerance averaging technique [9-10] is applied in order to replace the differential equations with highly oscillating coefficients by equations with constant coefficients. The presented method enables continuous analysis of an equivalent homogeneous medium with effective properties. The model reduces the computational cost and disposes of numerical difficulties. The approach used here has been applied in analysis of many thermo-mechanical problems of periodic and almost-periodic solids and structures. To name only few, tolerance models of beams with periodically variable parameters are considered in [3, 8]. In [6] some aspects of modelling of dynamic problems of thin functionally graded plates with a special tolerance–periodic microstructure in planes parallel to the plate midplane are considered.

Detailed analytical solution of homogeneous Timoshenko beam is considered in [6]. A numerical example is shown for a non-slender beam to signify the differences among the Timoshenko, Bernoulli, shear and Rayleigh beam models.

2. Formulation of the problem

The strain-displacement relations in Timoshenko beam theory are assumed as

$$\kappa = \partial\theta, \quad \gamma = \partial w - \theta, \tag{1}$$

where w, θ, κ and γ represent the deflection, the cross-section rotation, the bending curvature, and the shear strain, respectively. The strain energy U and the kinetic energy K for a Timoshenko beam can be written as

$$U = \frac{1}{2}\int_0^L \left(EJ\kappa^2 + kGA\gamma^2\right)dx, \quad K = \frac{1}{2}\int_0^L \rho A\dot{w}^2 dx + \frac{1}{2}\int_0^L \rho J\dot{\theta}^2 dx, \tag{2}$$

where ρ, A, J, E, G and k are the mass density per unit volume, cross-section area of the beam, the area moment of the inertia, Young's modulus and shear modification coefficient, respectively. The equations of motion may be derived from Hamiltons principle (3).

$$\delta\int_{t_0}^{t_1} (U - K)dt = 0. \tag{3}$$

3. Introductory concepts, fundamental assumptions

The domain occupied by the beam is given by one-dimensional $\Lambda = (0,L)$, where L is the beam length. It is assumed that the cell length is much smaller than the beam length, $l \ll L$. Following the book edited by Woźniak cf. [9], some introductory concepts of the tolerance modelling are used, i.e. the averaging operator, tolerance system, slowly-varying function $SV^{\alpha}_{\xi}(\Lambda,\Delta)$, tolerance-periodic function $TP^{\alpha}_{\xi}(\Lambda,\Delta)$, highly oscillating function $HO^{\alpha}_{\xi}(\Lambda,\Delta)$, fluctuation shape function $FS^{\alpha}_{\xi}(\Lambda,\Delta)$, where ξ is the tolerance parameter and α is a positive constant determining kind of the function. The basic concept of the modelling technique is the averaging operator, for an integrable function f defined by:

$$\langle f \rangle(x) = \frac{1}{l}\int_{\Delta(x)} f(x)dx. \tag{4}$$

The unknown deflection w, and rotation θ are decomposed into their averaged and fluctuating part:

$$
\begin{aligned}
&w(x,t) = W(x,t) + h^A(x) V^A(x,t), \quad A = 1,\ldots,N,\\
&\theta(x,t) = \Theta(x,t) + p^R(x) Z^R(x,t), \quad R = 1,\ldots,M\,,\\
&W(\cdot), V^A(\cdot), \Theta(\cdot), Z^R(\cdot) \in SV_d^1(\Lambda,\Delta), \quad h^A(\cdot), p^R(\cdot) \in FS_d^1(\Lambda,\Delta),
\end{aligned}
\tag{5}
$$

The new basic kinematic unknowns $W(x,t)$ and $\Theta(x,t)$ are called the transverse macro-displacement and the macro-rotation; $V^A(x,t)$, $Z^R(x,t)$ are additional kinematic unknowns, called the fluctuation amplitudes. The unknown functions are assumed to be slowly-varying (*SV*) together with their first derivatives. The highly oscillating fluctuation shape functions (*FSF*s) h^A and p^R are assumed a priori in every problem under consideration in order to describe the unknown fields oscillations caused by the structure inhomogeneity. Apart from the restriction of *l*-periodicity, the *FSF*s have to satisfy the following conditions:

$$
\langle \rho A h^A \rangle = 0, \quad \langle \rho J p^K \rangle = 0. \tag{6}
$$

4. The tolerance model of a Timoshenko beam

The Lagrange function for considered problem is given as follows:

$$
L = U - K = \frac{1}{2}\left[EJ\partial\theta\partial\theta + kGA(\partial w\partial w - 2\partial w\theta + \theta\theta) - \rho A\dot{w}\dot{w} - \rho J\dot{\theta}\dot{\theta}\right]. \tag{7}
$$

As the basic modelling assumption micro-macro decompositions (5) of the unknown deflection w, longitudinal displacement u_0 and shear angle θ are introduced into Lagrangian. Applying averaging operator (4) and the tolerance averaging approximations, the tolerance averaged form $\langle \mathcal{L} \rangle$ of Lagrangian (7) is obtained in the form:

$$
\begin{aligned}
\langle \mathcal{L} \rangle = \frac{1}{2}\Big[&\langle EJ \rangle \partial\Theta\partial\Theta + 2\langle EJ\partial p^R \rangle \partial\Theta Z^R + \langle EJ\partial p^R \partial p^S \rangle Z^R Z^S + \langle kGA \rangle \partial W\partial W +\\
&+ 2\langle kGA\partial h^A \rangle \partial W V^A + \langle kGA\partial h^A \partial h^B \rangle V^A V^B - 2\langle kGA \rangle \partial W\Theta - 2\langle kGAp^R \rangle \partial W Z^R +\\
&- 2\langle kGA\partial h^A \rangle \Theta V^A + -2\langle kGA\partial h^A p^R \rangle V^A Z^R + \langle kGA \rangle \Theta\Theta + 2\langle kGAp^R \rangle \Theta Z^R +\\
&+ \langle kGAp^R p^S \rangle Z^R Z^S - \langle \rho A \rangle \dot{W}\dot{W} + -2\langle \rho A h^A \rangle \dot{W}\dot{V}^A - \langle \rho A h^A h^A \rangle \dot{V}^A \dot{V}^B +\\
&- \langle \rho J \rangle \dot{\Theta}\dot{\Theta} - 2\langle \rho J p^R \rangle \dot{\Theta}\dot{Z}^R - \langle \rho J p^R p^S \rangle \dot{Z}^R \dot{Z}^S
\end{aligned}
\tag{8}
$$

Subsequently, variation of above Lagrangian leads to four equations of motion with constant coefficients.

$$
\begin{aligned}
&\langle kGA \rangle (\partial^2 W - \partial\Theta) + \langle kGA\partial h^A \rangle \partial V^A - \underline{\langle kGAp^R \rangle} \partial Z^R - \langle \rho A \rangle \ddot{W} - \underline{\langle \rho A h^A \rangle} \ddot{V}^A = 0,\\
&\langle kGA\partial h^A \rangle (\partial W - \Theta) + \langle kGA\partial h^A \partial h^B \rangle V^B - \underline{\langle kGA\partial h^A p^R \rangle} Z^R + \underline{\langle \rho A h^A \rangle} \ddot{W} +\\
&\qquad + \underline{\langle \rho A h^A h^B \rangle} \ddot{V}^B = 0,
\end{aligned}
\tag{9}
$$

$$
\begin{gathered}
\langle EJ\rangle\partial^2\Theta+\langle EJ\partial p^R\rangle\partial Z^R+\langle kGA\rangle(\partial W-\Theta)+\langle kGA\partial h^A\rangle V^A-\underline{\langle kGAp^R\rangle}Z^R+\\
-\langle\rho J\rangle\ddot{\Theta}-\underline{\langle\rho Jp^R\rangle}\ddot{Z}^R=0,\\
\langle EJ\partial p^R\rangle\partial\Theta+\langle EJ\partial p^R\partial p^S\rangle Z^S-\underline{\langle kGAp^R\rangle}(\partial W-\Theta)-\underline{\langle kGA\partial h^A p^R\rangle}V^A+\\
+\underline{\langle kGAp^R p^S\rangle}Z^S+\underline{\langle\rho Jp^R\rangle}\ddot{\Theta}+\underline{\langle\rho Jp^R p^S\rangle}\ddot{Z}^S=0.
\end{gathered}
\tag{9}
$$

The underlined terms depend on the microstructure size.

5. Asymptotic model equations

Neglecting the terms dependent on the cell length l, we obtain the system of equations of the asymptotic model. It describes the behaviour of Timoshenko beam only in the macroscale:

$$
\begin{gathered}
\langle kGA\rangle(\partial\partial W-\partial\Theta)+\langle kGA\partial h^A\rangle\partial V^A-\langle\rho A\rangle\ddot{W}=0,\\
\langle kGA\partial h^A\rangle(\partial W-\Theta)+\langle kGA\partial h^A\partial h^B\rangle V^B=0,\\
\langle EJ\rangle\partial\partial\Theta+\langle EJ\partial p^R\rangle\partial Z^R+\langle kGA\rangle(\partial W-\Theta)+\langle kGA\partial h^A\rangle V^A-\langle\rho J\rangle\ddot{\Theta}=0,\\
\langle EJ\partial p^R\rangle\partial\Theta+\langle EJ\partial p^R\partial p^S\rangle Z^S=0.
\end{gathered}
\tag{10}
$$

Equations $(10)_2$ and $(10)_4$ can be rewritten as

$$
V^A=-\frac{\langle kGA\partial h^A\rangle}{\langle kGA\partial h^A\partial h^B\rangle}(\partial W-\Theta),\quad Z^R=-\frac{\langle EJ\partial p^R\rangle}{\langle EJ\partial p^R\partial p^S\rangle}\partial\Theta.
\tag{11}
$$

We can further define the effective shear stiffness H^{eff} and effective bending stiffness D^{eff} which are constant:

$$
\langle kGA\rangle-\frac{\langle kGA\partial h^A\rangle\langle kGA\partial h^B\rangle}{\langle kGA\partial h^A\partial h^B\rangle}=H^{eff},\quad \langle EJ\rangle-\frac{\langle EJ\partial p^R\rangle\langle EJ\partial p^S\rangle}{\langle EJ\partial p^R\partial p^S\rangle}=D^{eff}.
\tag{12}
$$

Combining equations (10-12), we obtain the following system of differential equations which represents the asymptotic model of considered Timoshenko beam:

$$
\begin{gathered}
H^{eff}(\partial\partial W-\partial\Theta)-\langle\rho A\rangle\ddot{W}=0,\\
D^{eff}\partial\partial\Theta+H^{eff}(\partial W-\Theta)-\langle\rho J\rangle\ddot{\Theta}=0.
\end{gathered}
\tag{13}
$$

It can be noted that the above equations have the same form as the equations for a homogeneous beam, cf. [4].

6. Asymptotic model solution

We assume that functions W, Θ share the same time solution $T(t)$:

$$
\begin{bmatrix} W(x,t)\\ \Theta(x,t)\end{bmatrix}=\begin{bmatrix} W(x)\\ \Theta(x)\end{bmatrix}T(t).
\tag{14}
$$

After substitution of (14), equations (13) can be rewritten in matrix form:

$$0=\begin{bmatrix} H^{eff} & 0 \\ 0 & D^{eff}\end{bmatrix}\begin{bmatrix}\partial\partial W \\ \partial\partial\Theta\end{bmatrix}+\begin{bmatrix} 0 & -H^{eff} \\ H^{eff} & 0\end{bmatrix}\begin{bmatrix}\partial W \\ \partial\Theta\end{bmatrix}+ \\ +\begin{bmatrix}\langle\rho A\rangle\omega^2 & 0 \\ 0 & -H^{eff}+\langle\rho J\rangle\omega^2\end{bmatrix}\begin{bmatrix} W \\ \Theta\end{bmatrix}. \tag{15}$$

These equations can be decoupled to yield

$$\partial\partial\partial\Theta+\left(\frac{\langle\rho A\rangle}{H^{eff}}+\frac{\langle\rho J\rangle}{D^{eff}}\right)\omega^2\partial\partial\Theta-\frac{\langle\rho A\rangle}{D^{eff}}\left(1-\frac{\langle\rho J\rangle}{H^{eff}}\omega^2\right)\omega^2\Theta=0, \\ \partial\partial\partial W+\left(\frac{\langle\rho A\rangle}{H^{eff}}+\frac{\langle\rho J\rangle}{D^{eff}}\right)\omega^2\partial\partial W-\frac{\langle\rho A\rangle}{D^{eff}}\left(1+\frac{\langle\rho J\rangle}{H^{eff}}\omega^2\right)\omega^2 W=0. \tag{16}$$

The differential equations for $W(x)$ and $\Theta(x)$ have the same form, so that it is assumed that he solutions also have the same form and differ by a constant as

$$\begin{bmatrix} W(x) \\ \Theta(x)\end{bmatrix}=d\mathbf{u}e^{rx}. \tag{17}$$

The characteristic equation is given by

$$r^4+\left(\frac{\langle\rho A\rangle}{H^{eff}}+\frac{\langle\rho J\rangle}{D^{eff}}\right)\omega^2 r^2-\frac{\langle\rho A\rangle}{D^{eff}}\left(1-\frac{\langle\rho J\rangle}{H^{eff}}\omega^2\right)\omega^2=0, \tag{18}$$

therefore the eigenfrequencies can be expressed as:

$$r_i=\pm\sqrt{-\left(\frac{\langle\rho A\rangle}{H^{eff}}+\frac{\langle\rho J\rangle}{D^{eff}}\right)\omega^2\pm\sqrt{\left(\frac{\langle\rho A\rangle}{H^{eff}}+\frac{\langle\rho J\rangle}{D^{eff}}\right)^2\omega^4+\frac{\langle\rho A\rangle}{D^{eff}}\left(1-\frac{\langle\rho J\rangle}{H^{eff}}\omega^2\right)\omega^2}}\,, \tag{19}$$

i = 1, 2, 3, 4, and from the following equation:

$$\begin{bmatrix} H^{eff}r^2+\langle\rho A\rangle\omega^2 & -H^{eff}r \\ H^{eff}r & D^{eff}r^2-H^{eff}r+\langle\rho J\rangle\omega^2\end{bmatrix}\mathbf{u}=0, \tag{20}$$

the corresponding eigenvectors $\mathbf{u}$ are obtained:

$$\mathbf{u}_i=\begin{bmatrix} H^{eff}r \\ H^{eff}r^2+\langle\rho A\rangle\omega^2\end{bmatrix}\ \text{lub}\ \begin{bmatrix} D^{eff}r^2-H^{eff}r+\langle\rho J\rangle\omega^2 \\ -H^{eff}r\end{bmatrix}. \tag{21}$$

The spatial solutions are given by

$$\begin{bmatrix} W_m(x) \\ \Theta_m(x)\end{bmatrix}=\sum_{i=1}^{4}d_i\mathbf{u}_ie^{r_ix}=d_1\mathbf{u}_1e^{bx}+d_2\mathbf{u}_2e^{-bx}+d_3\mathbf{u}_3e^{\mathrm{i}ax}+d_4\mathbf{u}_4e^{-\mathrm{i}ax}, \tag{22}$$

where

$$a=\sqrt{\left(\frac{\langle\rho A\rangle}{H^{eff}}+\frac{\langle\rho J\rangle}{D^{eff}}\right)\omega^2+\sqrt{\left(\frac{\langle\rho A\rangle}{H^{eff}}+\frac{\langle\rho J\rangle}{D^{eff}}\right)^2\omega^4+\frac{\langle\rho A\rangle}{D^{eff}}\left(1-\frac{\langle\rho J\rangle}{H^{eff}}\omega^2\right)\omega^2}}\,, \tag{23}$$

$$b=\sqrt{-\left(\frac{\langle\rho A\rangle}{H^{eff}}+\frac{\langle\rho J\rangle}{D^{eff}}\right)\omega^2+\sqrt{\left(\frac{\langle\rho A\rangle}{H^{eff}}+\frac{\langle\rho J\rangle}{D^{eff}}\right)^2\omega^4+\frac{\langle\rho A\rangle}{D^{eff}}\left(1-\frac{\langle\rho J\rangle}{H^{eff}}\omega^2\right)\omega^2}}\,. \tag{23}$$

Spatial solution (22) can be also written in terms of the sinusoidal and hyperbolic functions with real arguments:

$$\begin{bmatrix}W(x)\\ \Theta(x)\end{bmatrix}=\begin{bmatrix}C_1\\ D_1\end{bmatrix}\sin ax+\begin{bmatrix}C_2\\ D_2\end{bmatrix}\cos ax+\begin{bmatrix}C_3\\ D_3\end{bmatrix}\sinh bx+\begin{bmatrix}C_4\\ D_4\end{bmatrix}\cosh bx, \tag{24}$$

and only four from the constants C_1-C_4 and D_1-D_4 are independent, cf. [4].

Substituting (24) into the boundary conditions for W and Θ, we obtain a system of linear homogeneous equations for the suitable constants C and D. Then, the frequency equation is derived from the condition that the determinant of coefficients matrix has to vanish.

7. Application

In this section, analysis of influence of geometrical parameters in a cell on the first natural frequency of hinged-hinged beam with periodically varying cross-section, cf. Figure 1, is performed. The boundary conditions for considered beam are:

$$\partial\Theta=0 \quad \text{and} \quad W=0 \quad \text{for} \quad x=0,L. \tag{25}$$

The frequencies were obtained in the framework of the proposed model and compared with the results from a finite element model (30 elements, 60 degrees of freedom) with Hermite polynomials as shape functions.

The fluctuation shape functions defining the fluctuating parts of unknown displacements were assumed in the form of trigonometric series:

$$h^A(y)=l\sin\frac{2A\pi y}{l}, \quad p^R(y)=l\sin\frac{2R\pi y}{l}, \tag{26}$$

to ensure non-zero correctors in calculating the effective shear and bending stiffness (12). The conditions (6) are satisfied for considered symmetric unit cell. The number of functions (26) has been selected by the analysis of the effective stiffness convergence, and the satisfactory results were obtained for $N = M = 10$.

The beam length is $L = 1$ m, shear factor $k = 5/6$, the mass density of the material $\rho = 7860$ kg/m^3, Young modulus $E = 210$ GPa. The cross-section is rectangular, piecewise constant. The saturation parameter α changes in range 0.1-0.9, section width is $b_1 = b_2 = 20$ mm, section height is $h_1 = 20$ mm, $h_2 = a\ h_1 = \{0.95,0.9,0.85,0.8,0.75\}\ h_1$. The number of the cells is 10, $h_1 / l = 1/5$, hence the cell can be considered as moderately thick. Dependence of the first natural frequency ω for asymptotic model (lines) and finite element model (dots) is depicted in Figure 2, and the relative difference between these models, versus parameter α is shown in Figure 3. As it can be seen from the Figure 3, the results differ no more than 0.5% in the considered cases.

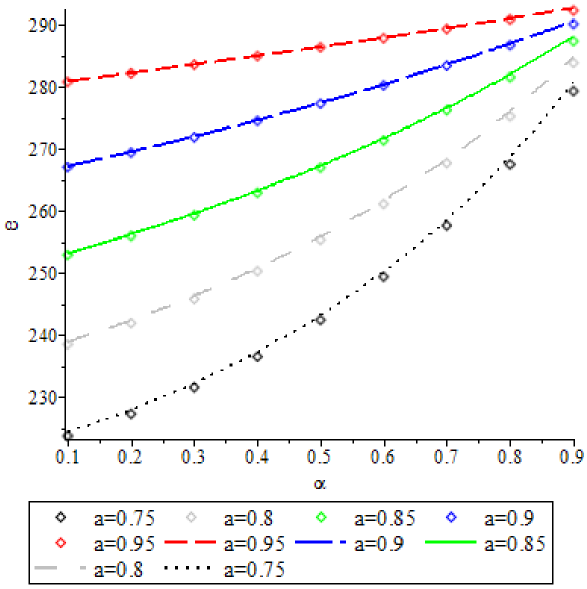

Figure 2. First natural frequency for various values of cross section height, dots - finite element model, lines – asymptotic model; $a=h_2/h_1$

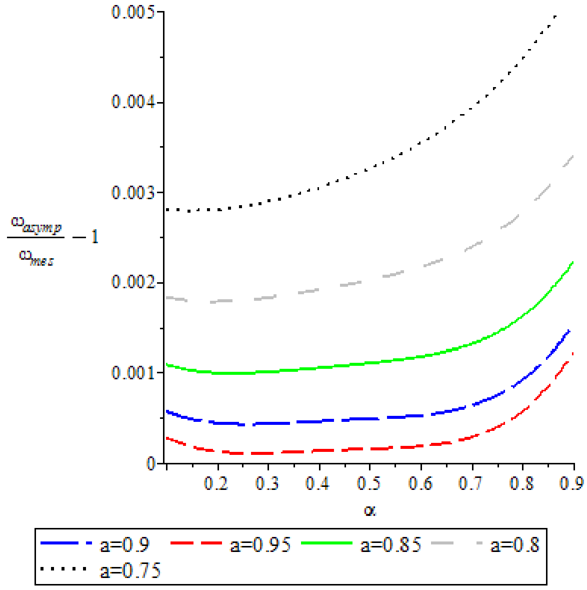

Figure 3. Relative difference between asymptotic and fem results

8. Conclusions

The natural vibration analysis of a periodic beam has been performed in the framework of tolerance modelling technique. The Timoshenko beam theory, including first order kinematic correction for shear strain, have been applied in order to analyse beams consisting of non-slender repetitive cells. The obtained system of differential equations with constant coefficients and additional degrees of freedom makes it possible to describe the dynamics of the beam in the macro-scale. The coefficients of these equations depend on so-called fluctuation shape functions which describe the vibrations of a periodicity cell.

A simplified version of the proposed model has been applied in analysis of first natural frequency of a variable cross-section beam. From the obtained results it can be concluded that application of approximate fluctuation shape functions leads to satisfactory results.

Acknowledgement

The authors are grateful for the support provided by the National Science Centre, Poland (Grant No. 2014/15/B/ST8/03155).

References

1. N. S. Bakhvalov, G. P. Panasenko, *Averaging of processes in periodic media*, Nauka, Moskwa 1984.
2. A. Bensoussan, J. L. Lions, G. Papanicolaou, *Asymptotic analysis for periodic structures*, North-Holland, Amsterdam 1978.
3. Ł. Domagalski, J. Jędrysiak, *Geometrically nonlinear vibrations of slender meso-periodic beams. The tolerance modelling approach,* Comp. Struct., **136** (2016) 270 – 277.
4. S. M. Han, H. Benaroya, T. Wei, *Dynamics of transversely vibrating beams using four engineering theories,* Journal of Sound and Vibration, **225**(5) (1999) 935 – 988.
5. W. M. He, W. Q. Chen, H. Qiao, *Frequency estimate and adjustment of composite beams with small periodicity*, Composites: Part B, **45** (2013) 742 – 747.
6. J. Jędrysiak, *Modelling of dynamic behaviour of microstructured thin functionally graded plates, Thin-Walled Structures*, **71** (2013) 102 – 107.
7. V. V. Jikov, S. M. Kozlov, O. A. Oleinik, *Homogenization of differential operators and integral functionals,* Springer Verlag, Berlin-Heidelberg-New York 1994.
8. K. Mazur-Śniady, *Macro-dynamics of micro-periodic elastic beams*, J. Theor. Appl. Mech., **31** (1993) 34 – 46.
9. C. Wozniak et al (eds.), *Mathematical modelling and analysis in continuum mechanics of microstructured media*, Silesian University of Technology Press, Gliwice 2010.
10. Cz. Woźniak, E. Wierzbicki, *Averaging techniques in thermomechanics of composite solids*, Wydawnictwo Politechniki Częstochowskiej, Częstochowa 2000.

Influence of Substructure Properties on Natural Vibrations of Periodic Euler-Bernoulli Beams

Marcin ŚWIĄTEK
Department of Structural Mechanics, Łódź University of Technology
al. Politechniki 6, 90-924 Łódź, 800777@edu.p.lodz.pl

Jarosław JĘDRYSIAK
Department of Structural Mechanics, Łódź University of Technology
al. Politechniki 6, 90-924 Łódź, jarek@p.lodz.pl

Łukasz DOMAGALSKI
Department of Structural Mechanics, Łódź University of Technology
al. Politechniki 6, 90-924 Łódź, lukasz.domagalski@p.lodz.pl

Abstract

In this paper there are considered vibrations of Euler-Bernoulli beams with geometrical and material properties periodically varying along the axis. The basic exact equations with highly oscillating periodic coefficients are replaced by the system of averaged equations with constant coefficients. The new model is based on the tolerance modelling technique, which describes macro-dynamics of the beam including the effect of the microstructure size. The purpose of this paper is to present an approximately equivalent model, which describe vibrations of periodic beams taking into account length of the periodicity cell.

***Keywords*:** periodic beams, Euler-Bernoulli beams

1. Introduction

This paper is related to certain problems, which are met in the analysis of periodic beams. Dynamics of such beams is described by differential equations with non-continuous highly oscillating periodic coefficients. Therefore, various approximate models, introducing effective beam properties are proposed. Amongst them, can be mentioned those, based on the asymptotic homogenization, cf. [1, 2, 7]. However, in many technical problems, number of cells is finite. Thus, neglecting the microstructure size may lead to erroneous results, especially in the range of high frequencies.

In order to include the effect of microstructure size, the tolerance modelling technique is introduced (cf. the book edited by Cz. Woźniak, Michalak and Jędrysiak [10]). The preceding method is very general and convenient for modelling problems, described by differential equations with highly oscillating coefficients, e.g. modelling of dynamic behaviour of microstructured thin functionally graded plates [6] and dynamic problems for plates with a periodic structure [8]. In contrary to the exact solutions, the obtained relations have constant coefficients, some of which explicitly depend on the microstructure size.

Wave propagation and linear vibrations in periodic beams are revised in many research papers. For a periodic Euler-Bernoulli beam it is considered in [3] and [9].

Frequency band gaps were analyzed by the differential quadrature method in [11]. The transfer matrix method was applied in [12] in analysis of flexural wave propagation in the beam on elastic foundation. In [4] a wide literature study on composite beam vibration can be found. In order to determine a homogenized model of a composite beam with small periodicity the two-scale asymptotic expansion method is used in [5].

In this paper the tolerance model of Euler-Bernoulli beam with geometrical and material properties periodically varying along the axis is presented and discussed. The tolerance averaging model is applied to investigate free vibration frequencies for an Euler-Bernoulli beam. Obtained results are compared with finite element method.

2. Formulation of the problem

Let *Oxyz* be an orthogonal Cartesian coordinate system, the *Ox* axis coincides with the axis of the beam. It is assumed that considered elastic periodically inhomogeneous Euler-Bernoulli beam consists of many small repetitive elements called periodicity cells. It is also assumed that every such element can be treated as an Euler-Bernoulli beam. Hence, it is defined the region $\Omega \equiv [0, L]$, where L is the beam length. The considered cells are defined as $\Delta \equiv [-l/2, l/2]$, where $l \ll L$ is the dimension of the cell, called microstructure parameter. It is assumed that the beam possesses principal planes and that the vibration takes place in one of the principal planes. Let $w = w(x,t)$ denote the small deflection of the neutral axis of the beam from its initial, straight configuration. The following notation is introduced: $\partial^k = \partial^k / \partial x^k$ is the k-th derivative with respect to the x coordinate and overdot stands for the derivative with respect to time. For small deflections of the beam strain and kinetic energy are:

$$U = \tfrac{1}{2}\int_0^L EJ\partial^2 w \partial^2 w dx, \quad K = \tfrac{1}{2}\int_0^L \mu \dot{w}\dot{w} dx, \tag{1}$$

where $E = E(x)$, $J = J(x)$, $\mu = \mu(x)$ are the Young's modulus of the beam material, the cross-sectional moment of inertia, the mass per unit length of the beam, respectively. Since only free vibrations are considered, the potential energy of the external load is assumed to be zero.

The equation of motion is derived from Hamilton's principle:

$$\delta \int_{t_0}^{t_1} \mathcal{L}\, dt = \delta \int_{t_0}^{t_1} (U - K)\, dt = 0. \tag{2}$$

The Lagrange function for the problem can be written as:

$$\mathcal{L} = \tfrac{1}{2} EJ\partial^2 w \partial^2 w - \tfrac{1}{2}\mu \dot{w}\dot{w}. \tag{3}$$

Following the usual procedure of the calculus of variations, the Euler equation of motion is obtained:

$$\partial^2\left(EJ\partial^2 w\right) + \mu \ddot{w} = 0. \tag{4}$$

The coefficients E, J, μ, are in considered cases highly oscillating, non-continuous functions of the x-coordinate.

3. The tolerance averaging approach – introductory concepts and basic assumptions

The main concept of tolerance averaging approach is the tolerance reflexive relation. Amongst the fundamental ideas of the technique the most remarkable are certain classes of functions such as the tolerance-periodic (*TP*), slowly-varying (*SV*), highly oscillating (*HO*) and fluctuation shape (*FS*) function.

A cell at $x \in \Omega_\Delta$ is denoted by $\Delta(x) = x + \Delta,\ \Omega_\Delta = \{x \in \Omega : \Delta(x) \subset \Omega\}$. The averaging operator for an arbitrary integrable function *f* is defined by

$$\langle f \rangle(x) = \frac{1}{l} \int_{\Delta(x)} f(y)dy, \quad x \in \Omega_\Delta, \quad y \in \Delta(x). \tag{5}$$

The basic assumption of micro-macro decomposition plays imperative role in tolerance modelling technique. The unknown transverse deflection can be decomposed into their averaged and fluctuating part:

$$\begin{aligned} &w(x,t) = W(x,t) + h^A(x)V^A(x,t), \quad A = 1,\ldots,N, \\ &W(\cdot), V^A(\cdot) \in SV_d^2(\Omega,\Delta), \quad h^A(\cdot) \in FS_d^2(\Omega,\Delta), \end{aligned} \tag{6}$$

where $W(\cdot)$ (macrodeflection) and $V^A(\cdot)$ (fluctuation amplitudes of the deflection) functions are the basic unknowns; h^A is the known fluctuation shape function. The tolerance parameter, associated with the tolerance relation, is denoted by d, $0<d<<1$. It is assumed that the unknown functions are slowly-varying (*SV*) up to the second derivative, which is denoted by the top index.

The highly oscillating fluctuation shape functions (*FSFs*) h^A, proposed *a priori* for every considered problem, are assumed to describe the unknown fields oscillations caused by the structure inhomogeneity. What is more, *FSFs* have to ensure the *l*-periodicity constraint and provide the conditions below:

$$\left\langle \mu h^A \right\rangle = 0, \quad \left\langle \mu h^A h^B \right\rangle = 0 \ \text{ for A} \neq \text{B}; \quad \partial^m h^A \in O\left(l^{2-m}\right), \quad A,B = 1,\ldots,N. \tag{7}$$

4. Governing equations of the model

4.1. Tolerance model equations

In the first place, the micro-macro decomposition (6) of Lagrangian (3) is performed. Next, averaging over an arbitrary periodicity cell is performed (5), applying the aforementioned approximations (7).

The variation of averaged functional has the specified form:

$$\delta \int_{t_0}^{t_1} \int_0^L \langle \mathcal{L}_h \rangle dxdt = \int_{t_0}^{t_1} \int_0^L \delta \langle \mathcal{L}_h \rangle dxdt. \tag{8}$$

Therefore, after expanding we obtain:

$$\begin{aligned} \delta \int_{t_0}^{t_1} \int_0^L \langle \mathcal{L}_h \rangle dxdt = \delta \tfrac{1}{2} \int_{t_0}^{t_1} \int_0^L \Big[&\langle EJ \rangle \partial^2 W \partial^2 W + 2\left\langle EJ\partial^2 h^A \right\rangle \partial^2 W V^A + \\ + \left\langle EJ\partial^2 h^A \partial^2 h^B \right\rangle V^A V^B - \langle \mu \rangle \dot{W}\dot{W} - 2\left\langle \mu h^A \right\rangle \dot{W}\dot{V}^A &- \left\langle \mu h^A h^B \right\rangle \dot{V}^A \dot{V}^B \Big] dxdt. \end{aligned} \tag{9}$$

From the principle of stationary action, applied to the averaged Lagrangian, the averaged Euler-Lagrange equations are obtained:

$$\begin{aligned} \langle EJ\rangle\partial^4 W + \left\langle EJ\partial^2 h^A\right\rangle\partial^2 V^A + \langle\mu\rangle\ddot{W} + \underline{\left\langle\mu h^A\right\rangle}\ddot{V}^A = 0, \\ \left\langle EJ\partial^2 h^A\right\rangle\partial^2 W + \left\langle EJ\partial^2 h^A\partial^2 h^B\right\rangle V^B + \underline{\left\langle\mu h^A\right\rangle}\ddot{W} + \underline{\left\langle\mu h^A h^B\right\rangle}\ddot{V}^B = 0. \end{aligned} \tag{10}$$

In contrast to the exact formulation (4), obtained system of 1+N differential equations for the macrodisplacement $W(\cdot)$ and fluctuation amplitudes of deflection $V^A(\cdot)$ has constant coefficients. Underlined coefficients depend on the microstructure parameter l. In order to present (10) in more convenient form, let us denote coefficients by:

$$\begin{Bmatrix} D \\ D^A \\ D^{AB} \end{Bmatrix} \equiv \begin{Bmatrix} \langle EJ\rangle \\ \left\langle EJ\partial^2 h^A\right\rangle \\ \left\langle EJ\partial^2 h^A\partial^2 h^B\right\rangle \end{Bmatrix}, \quad \begin{Bmatrix} M \\ M^A \\ M^{AB} \end{Bmatrix} \equiv \begin{Bmatrix} \langle\mu\rangle \\ \left\langle\mu h^A\right\rangle \\ \left\langle\mu h^A h^B\right\rangle \end{Bmatrix}. \tag{11}$$

After taking into account (11) we get:

$$\begin{aligned} D\partial^4 W + D^A\partial^2 V^A + M\ddot{W} = 0, \\ D^A\partial^2 W + D^{AB} V^B + \underline{M^{AB}}\ddot{V}^B = 0, \end{aligned} \tag{12}$$

where M^{AB} depends on microstructure size.

4.2. Asymptotic model equations

The asymptotic tolerance model is obtained by neglecting coefficients dependent on microstructure size l. If matrix D^{AB} is nonsingular, then there exists an inverse matrix $(D^{AB})^{-1}$.Thus, let us denote the effective stiffness of the beam by:

$$D_0 = D - D^A\left(D^{AB}\right)^{-1} D^B. \tag{13}$$

Therefore the asymptotic model equations become

$$\begin{aligned} D_0\partial^4 W + M\ddot{W} = 0, \\ V^A = -\left(D^{BA}\right)^{-1} D^B\partial^2 W. \end{aligned} \tag{14}$$

5. Natural frequencies

We can transform system of PDEs (12) into system of ODEs using separation of variables. Let us expand macrodeflection and fluctuation amplitudes of the deflection into series of eigenfunctions of a simply supported beam:

$$\begin{Bmatrix} W(x,t) \\ V^A(x,t) \end{Bmatrix} = \sum_{m=1}^{\infty} \begin{Bmatrix} w_m(t) \\ v_m^A(t) \end{Bmatrix} \sin\xi_m x, \quad \xi_m = \frac{m\pi}{L}. \tag{15}$$

Substituting (16) into (13) and limiting the analysis for one *FSF* we obtain:

$$\begin{aligned} \xi_m^4 D w_m - \xi_m^2 D^1 v_m^1 + M\ddot{w}_m = 0, \\ -\xi_m^2 D^1 w_m + D^{11} v_m^1 + \underline{M^{11}}\ddot{v}_m^1 = 0. \end{aligned} \tag{16}$$

There can be assumed the following solutions:

$$\begin{Bmatrix} w_m \\ v_m^A \end{Bmatrix} = \begin{Bmatrix} A_m^W \\ A_m^{V^1} \end{Bmatrix} \cos \omega t. \tag{17}$$

In order to find free vibrations frequencies, we introduce subsequent symbols:

$$\tilde{a}_m \equiv \frac{\xi_m^4 D}{M}, \quad \tilde{b}_m \equiv -\frac{\xi_m^2 D^1}{M}, \quad \tilde{c}_m \equiv -\frac{\xi_m^2 D^1}{M^{11}}, \quad \tilde{d} \equiv \frac{D^{11}}{M^{11}}. \tag{18}$$

System of equations (17) is in fact, an eigenvalue problem:

$$\begin{bmatrix} \tilde{a}_m - \omega^2 & \tilde{b}_m \\ \tilde{c}_m & \tilde{d} - \omega^2 \end{bmatrix} \begin{Bmatrix} w_m \\ v_m^1 \end{Bmatrix} = \begin{Bmatrix} 0 \\ 0 \end{Bmatrix}. \tag{19}$$

We can obtain expressions for high and low natural frequencies by finding the roots of characteristic polynomial:

$$\left(\omega_m^{-,+}\right)^2 = \frac{1}{2}\left[\tilde{a}_m + \tilde{d} \mp \sqrt{\left(\tilde{a}_m - \tilde{d}\right)^2 + 4\tilde{b}_m \tilde{c}_m}\right]. \tag{20}$$

6. Examples of applications

6.1. Introduction

The object under consideration is a hinged-hinged beam, which fragment is shown in Fig. 1. The beam's cross section, moment of inertia, Young's modulus and mass per unit length are periodically varying along the axis. It is assumed that cross section of the beam is rectangular. Considered periodicity cell, presented in Fig. 2, has symmetrical shape. Length of its segments depends on an α parameter.

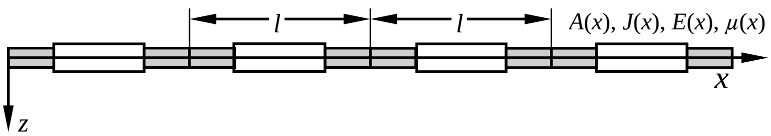

Figure 1. Fragment of considered periodic Euler-Bernoulli beam

The fluctuation shape functions represent the oscillations of displacements within the periodicity cell. For a purposes of this paper there were used approximate l-periodic trigonometric functions: $h^1(y) = l^2[\cos(2\pi y/l)+c]$.

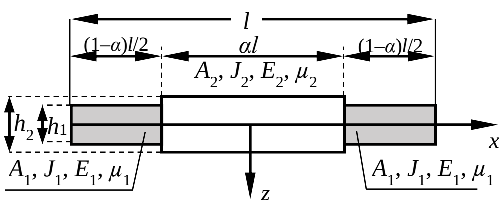

Figure 2. Periodicity cell

6.2. Results and discussion

The free vibrations of a slender periodic beam depending on the α parameter are considered. The calculations are carried out for two cases:

1. Constant geometrical properties and periodically varying values of mass density and Young's modulus.
2. Constant material properties and periodically varying height of beam's cross section.

In both cases it is assumed that considered beam has following properties: length $L = 1.0$ m; periodicity cell's length $l = 1/10L = 10$ cm.

For the first problem it is assumed that Young's modulus $E_1 = E = 210$ GPa; $E_2 = [0.25, 0.50, 0.75]E$; mass density $\rho_1 = \rho = 7860$ kg/m^3; $\rho_2 = [0.25, 0.50, 0.75]\rho$; cross section width and height: $b = 2$ cm, $h = 2$ cm. The results are shown in Fig. 3 and Fig. 4. It is evident that TAT has the best agreement with FEM for less disproportion of material parameters. For $E_2 = 0.75E$ and $E_2 = 0.50E$ the solutions are almost equal.

In the second case we declare following properties: $E = 210$ GPa, $\rho = 7860$ kg/m^3; $b = 2$ cm; $h_1 = h = 2$ cm, $h_2 = [0.50, 0.70, 0.90]h$. Figure 4(a) shows the results for this particular case. It is evident that difference in stiffness of the beam's segments is noticeably high. Similarly, as it was earlier, the proposed method delivered the best results for less disproportion of given properties. It is evident that tolerance model in cases with high disproportion is stiffer that FEM. The maximum value of obtained frequencies from both tolerance averaging method and FEM is denoted by $\omega_{\max}$. What is more, TAT gives the opportunity to analyse higher natural frequencies, as it is shown in Fig. 4(b). Study based on the finite element method does not provide such a possibility.

The assumed tolerance averaging model has 2 degrees of freedom and approximate fluctuation shape functions. It is worth noting, that comparative finite element model has 30 elements and 60 degrees of freedom.

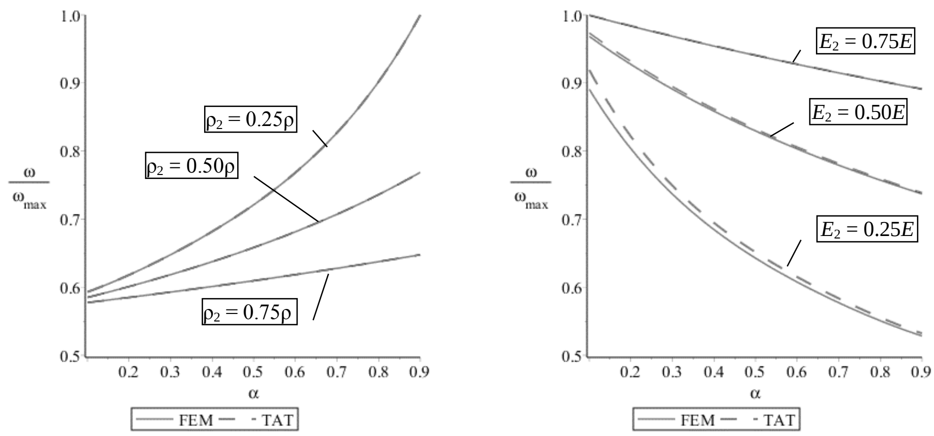

Figure 3. First natural frequencies for various values of mass density and Young's modulus

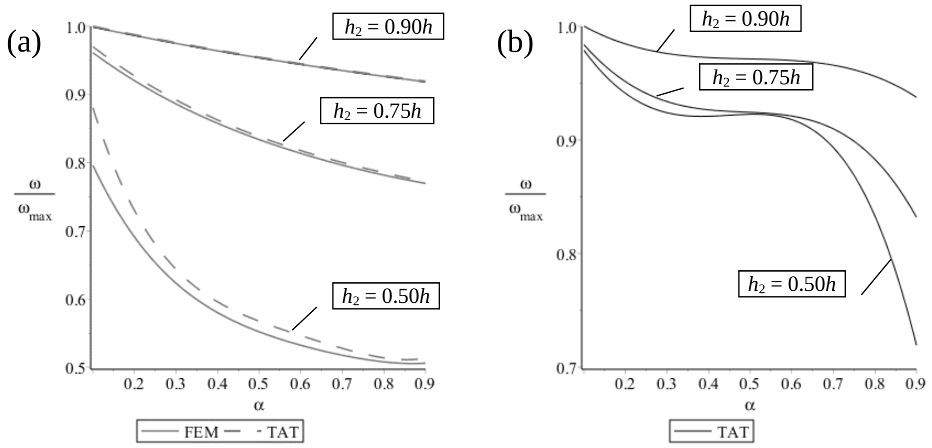

Figure 4. First lower (a) and higher (b) natural frequencies for various values of cross section height

7. Conclusions

The free vibrations of Euler-Bernoulli beams, with geometrical and material properties periodically varying along the axis have been considered. The model equations are obtained by implementing the tolerance averaging technique. Derived differential equations have constant coefficients. The main advantage of this approach is that it includes the effect of the period lengths on the overall behaviour of these beams. Despite the use of the approximate fluctuation shape functions the results are consistent with finite element method.

References

1. N. S. Bakhvalov, G. P. Panasenko, *Averaging of processes in periodic media*, Nauka, Moskwa 1984 (in Russian).
2. A. Bensoussan, J. L. Lions, G. Papanicolaou, *Asymptotic analysis for periodic structures*, NorthHolland, Amsterdam 1978.
3. T. Chen, *Investigations on flexural wave propagation of a periodic beam using multi-reflection method*, Archive of Applied Mechanics, **83**(2) (2013) 315 – 329.
4. M. Hajianmaleki, M.S. Quatu, *Vibrations of straight and curved composite beams: A review*, Composite Structures, **100** (2013) 218 – 232.
5. W. M. He, W. Q. Chen, H. Qiao, *Frequency estimate and adjustment of composite beams with small periodicity*, Composites: Part B, **45** (2013) 742 – 747.
6. J. Jędrysiak, *Modelling of dynamic behaviour of microstructured thin functionally graded plates*, Thin-Walled Structures, **7** (2013) 71 – 102.
7. V. V. Jikov, S. M. Kozlov, O. A. Oleinik, *Homogenization of differential operators and integral functionals*, Springer Verlag, Berlin-Heidelberg-New York 1994.

8. K. Mazur-Śniady, C. Woźniak, E. Wierzbicki, *On the modelling of dynamic problems for plates with a periodic structure*, Archive of Applied Mechanics, **74** (2004) 179 – 190.
9. K. Mazur-Śniady, *Macro-dynamics of micro-periodic elastic beams*, Journal of Theoretical and Applied Mechanics, **31** (1993) 781 – 793.
10. Cz. Woźniak et al (eds.), *Mathematical modelling and analysis in continuum mechanics of microstructured media*, Silesian University of Technology Press, Gliwice 2010.
11. H. J. Xiang, Z. F. Shi, *Analysis of flexural vibration band gaps in periodic beams using differential quadrature method*, Computers and Structures, **87** (2009) 1559 – 1566.
12. D. L. Yu, J. H. Wen, H. J. Shen, Y. Xiao, X.S. Wen, *Propagation of flexural wave in periodic beam on elastic foundations*, Physics Letters A, **376** (2012) 626 – 630.

Analysis of Vibration Transmission in an Air-Operated Demolition Hammer

Maciej TABASZEWSKI
Poznan University of Technology, Institute of Applied Mechanics
24 Jana Pawła II Street, 60-965 Poznan, maciej.tabaszewski@put.poznan.pl

Małgorzata WOJSZNIS
Poznan University of Technology, Institute of Applied Mechanics
24 Jana Pawła II Street, 60-965 Poznan, malgorzata.wojsznis@put.poznan.pl

Abstract

The paper presents an analysis of vibrations of a ram, body and handle of a heavy, air-operated demolition hammer. The research was conducted in order to determine the character of dynamic inputs and resulting vibrations at the tool handle which were necessary to build a structural model of local influences on an operator taking the hammer design into account. The experiment was carried out on a test stand without participation of an operator, which guaranteed repeatability of measurements and elimination of ontogenetic characteristics. The displacements of selected structural elements of the tool were recorded by means of a camera and the accelerations at the handle were recorded by means of a standard measuring apparatus. The recorded signals were subjected to the spectral analysis and the short-time Fourier transform (STFT) using dedicated software in MATLAB environment.

Keywords: vibrations, dynamic inputs, short-time Fourier transform (STFT)

1. Introduction

As part of the conducted research an analysis of vibrations of a ram, body and handle of a heavy air-operated demolition hammer was performed. Such type of tools are commonly used e.g. in building industry, and their negative influence on an operator is well known [1, 4, 5]. The source of the harmful interaction are vibrations originating both in the driving unit and in the working process itself [2, 3].

The research was conducted in order to recognize vibration transmission in the hammer structure, to determine the main direction of their propagation, and to determine the character of dynamic inputs and resulting vibrations at the tool handle. The analysis of motion of individual parts of the tool is necessary for proper modeling and enables to interfere in the tool structure selectively. The recognition of the main direction of propagation enables to eliminate small influences and to limit the investigations to significant directional interactions. As a result of the performed analyses of vibrations at the tool handle it will be possible to create a structural model of a human being – tool object (with consideration and modeling of the hammer structure), which, in turn, will enable to model the influence of local vibrations on the tool operator. It should be remembered that the correct model of the system should include both the operator and the tool, because there exist mutual interactions between these elements [3, 6, 7].

2. Research object – test stand

Measurements were performed on a dedicated stand equipped with a holder to fix heavy hand-held tools (Fig. 1). The holder had been designed and made specially for the performed investigations in order to eliminate the participation of an operator, and hence to be independent of operator's ontogenetic characteristics (body mass, pressure force on the hammer, clamping force on the handle etc.). Foundation and positioning of the hammer in the test stand reflected its position during work in real environment. For the investigations a standard foundation in the form of an impact energy absorber was used – see Fig. 1.

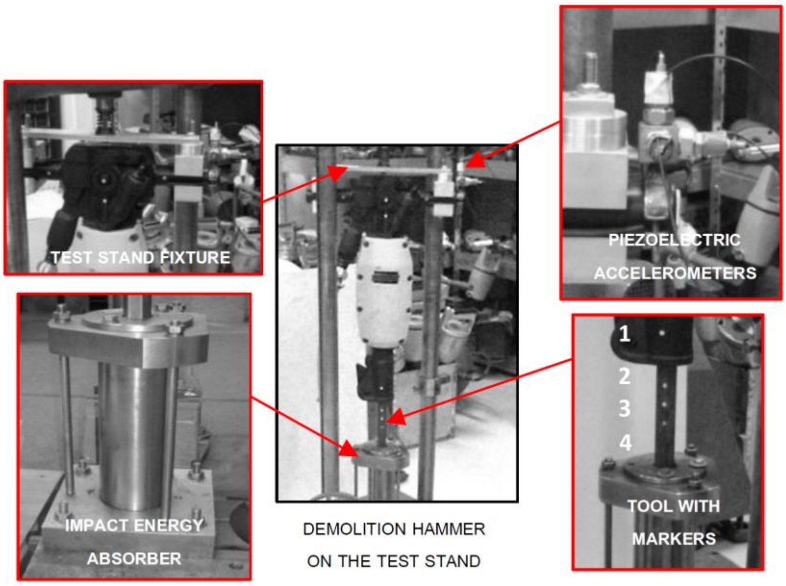

Figure 1. Research object in the test stand

As the research object a demolition hammer TEX 140 (Fig.1) was used, which is usually used in building industry for crushing asphalt, concrete, frozen soil etc.

3. Methodology of research

The research being the subject of this work was based on the analysis of the recordings of motions of the ram and casing of the investigated hammer and its handle, an operator is in contact with. For measurements of motion of the ram (and additionally the tool casing) a high-speed camera 1024 PCI [8] was used, which enabled to record displacements of vibrations. For this purpose several markers were placed on the tool, which motion was analyzed with the dedicated software. Additionally, three markers were placed on the ram to average its motion in time synchronously – Fig.1. The recordings enabled to identify the motion in the plane of the filmed picture.

During the test vibration accelerations of the handle in three perpendicular directions **X-Y-Z** were recorded as well. To do this, a measuring head with three piezoelectric absolute vibration accelerometers was used (Fig.1).

The results obtained from both methods enabled to determine vibrations at the handle and transmission of vibrations from the ram to the handle. As the measurements with the camera enabled to record the displacements, and with the accelerometers – vibration accelerations, the obtained results had to be subjected to an appropriate transformation and brought to one physical quantity. Integration of the acceleration signal was performed numerically after initial high-pass filtration.

4. Results

Figure 2 shows the comparison of displacements and spectra in **Z**-axis direction (the direction of work of the tool): for the hammer casing (point 1 – Fig.1) and the ram, computed by synchronous averaging of displacements of three points on the ram, marked as 2, 3 and 4 (Fig.1).

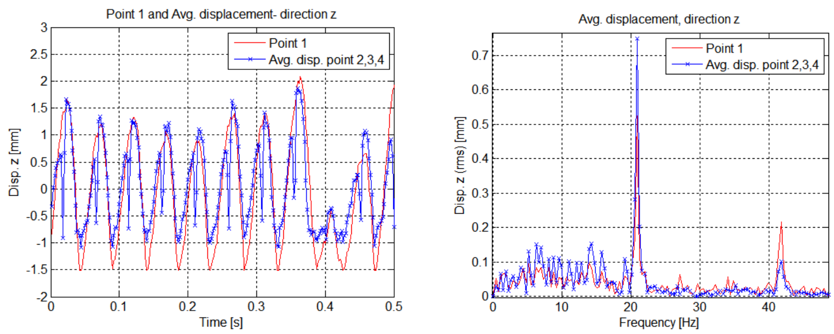

Figure 2. Displacements of the casing and the ram of the investigated air-operated hammer in time and frequency domains (enlarged sections)

In the range below 20 Hz and for the frequency of work of the tool (about 22 Hz) the tool casing vibrates generally with lower amplitudes than the ram. The differences are, however, not so big as one could have expected. One can say, that the amplitudes of displacements are comparable even for higher frequency ranges than those shown in the picture, which means that the casing of this hammer is not separated from the source. Moreover, as one can see, the vibrations of both elements are cophasic. A question may arise here, whether when building a dynamic model it is worthwhile to take both elements into consideration. This seems purposeless. Hence, in the case of the investigated tool, the model being created may be limited to a model with fewer degrees of freedom, taking the tool casing and the ram together into account.

Analyzing the motion of the casing at a measuring point placed near the ram (Fig. 3a) and the motion of the ram itself (Fig. 3b) in the **Y-Z** plane one can see, that these motions in the axis perpendicular to the impact direction are significant and cannot be omitted in the modeling of interactions of vibrations on the operator.

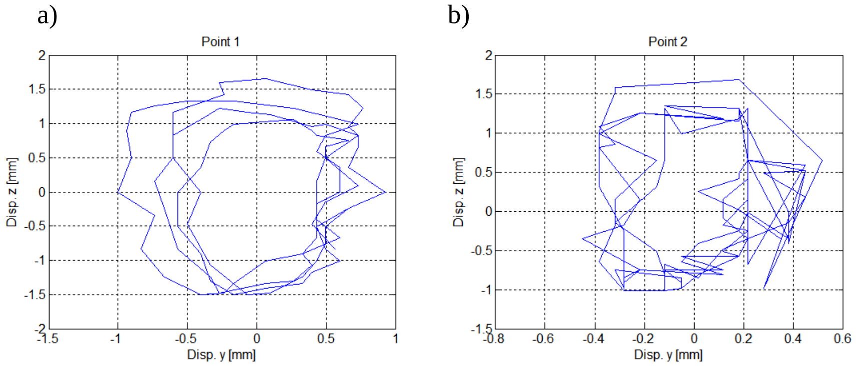

Figure 3. Movements of a selected point on the casing near the ram (Fig. a)
and the ram itself in its middle point (Fig. b)

What is the most important this indicates the character of fixing the hammer in the test stand. At points placed at longer distance from the ram their lateral movements are not so important. This results from the fact, that the hammer is fixed well in its upper part, and that the collisions between the ram and the absorber are not central. To a degree this simulates real working conditions of the tool held by an operator. Hence, it seems to be important that forces perpendicular to the hammer axis are also taken into account in the model.

The performed analysis of vibrations of the hammer handle shows a reduction in vibration amplitudes (Fig. 4).

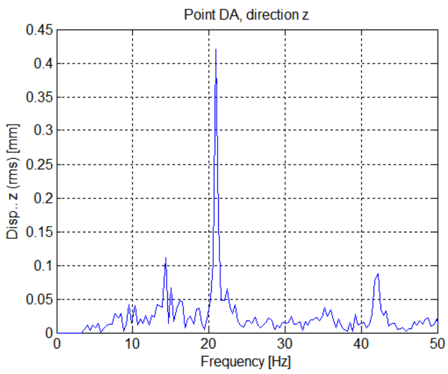

Figure 4. A section of an amplitude spectrum of vibration displacements of the handle. The result has been obtained by double integration of the recorded signals of vibration accelerations

In comparison to the amplitudes of the ram movements at the frequency of work of the tool (about 22 Hz) this drop equals almost 50%. Unfortunately it is not a lot when protection of the operator against excessive vibrations is considered.

To work out guidelines for building a proper model of the investigated air-operated hammer a time and frequency analysis of the signals was performed as well. The work of the hammer is non-stationary. This results at least from the fact that the collision process and possible fluctuations of working frequency of the tool are unrepeatable. That is why the short-time Fourier transform (STFT) was applied, which is defined as [9]:

$$X(f,\tau) = \int_{-\infty}^{\infty} w(t-\tau)x(t)e^{-i2\pi ft}dt, \tag{1}$$

where: t is time, $x(t)$ is the analyzed signal, w(t, τ) is a moving window function, τ is the shift of the window in time domain, f is frequency, and i is the imaginary unit.

Examples of results of such a time and frequency analysis are shown in Fig. 5.

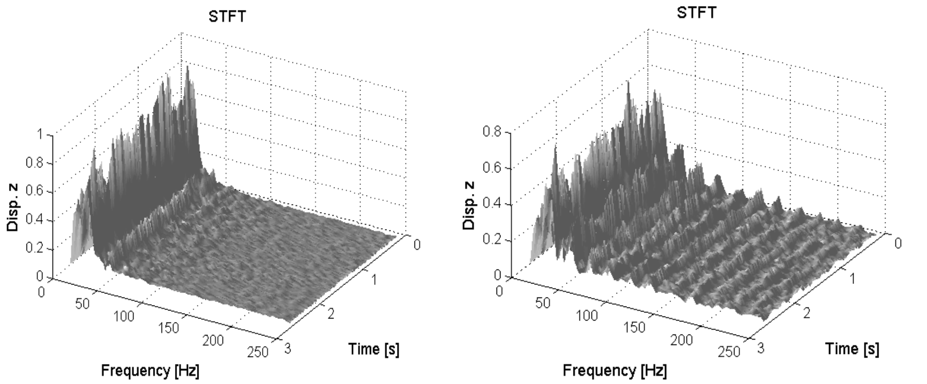

Figure 5. STFT analysis for two points. On the left: motion of a point on the casing near the ram; on the right: motion of a point on the ram near the casing

As it can be seen from the figures the input itself is non-stationary regarding amplitudes, the spectral composition of the signals, however, remains invariable. Moreover, it seems that only two or three components of the signal frequency should be essential in the analysis (see vibrations of the casing in Fig. 5), especially if the ram itself will be omitted in the model. This enables to define well the input in the dynamic model as regards both its average amplitude and its frequency composition. To assume, however, the input as a harmonic function with the working frequency of the ram, which sometimes is done, would be a too big simplification.

5. Conclusions

As a result of the conducted experimental research information enabling to build a dynamic model of the considered air-operated hammer was obtained. The results show that the modeling can be done by taking only the hammer casing and handle into account and omitting the ram. Additionally, it is essential to limit the complex frequency composition of the input to two or three harmonic frequencies. It also seems important to assume such a model, which takes also lateral input forces into account. This also determines the choice of the model of the operator of the hammer. Non-stationarity of the work of the hammer and, what follows, of the inputs may be taken into consideration by using the average amplitude of each component of the input or by modeling the system using stochastic differential equations.

Acknowledgments

The study was partly financed by the Ministry of Science and Higher Education as a project 02/21/DSPB/3465

References

1. K. Marek, *Choroby zawodowe*, Wydawnictwo Lekarskie PZWL, Warszawa 2003.
2. M. W. Dobry, M. Wojsznis, *Oddziaływanie drgań miejscowych na organizm ludzki-ocena analizy dynamicznej i energetycznej*, Diagnostyka, Polskie Towarzystwo Diagnostyki Technicznej, **30**(1) (2004) 151 – 154.
3. M. Wojsznis, M. W. Dobry, *Drgania w strukturze Człowiek-Narzędzie*, Wybrane zagadnienia analizy modalnej konstrukcji, Praca zbiorowa pod redakcją Tadeusza UHLA, (2010) 301 – 308.
4. L. Markiewicz, *Fizjologia i higiena pracy*, Wibracja. Instyt. Wyd. CRZZ, 1980.
5. I. M. Lidström, *Effect of local vibration on the upper extremity*, Arbete och Hälsa (Work and Health); **8** (1974) 1 – 127.
6. M. W. Dobry, M. Wojsznis (Miszczak), *Dynamiczny model systemu człowiek-maszyna w przypadku posługiwania się dużymi narzędziami zmechanizowanymi*, Acta of Bioengineering and Biomechanics, Oficyna Wydawnicza Politechniki Wrocławskiej, **2**(1) (2000) 125 – 130.
7. M. W. Dobry, *Postawy diagnostyki energetycznej systemów mechanicznych i biomechanicznych*, Wydawnictwo Naukowe Instytutu Technologii Eksploatacji – PIB, Radom 2012.
8. M. Wojsznis, M. Tabaszewski, M. W. Dobry, *Vibration research on a Demolition Hammer Using a High-speed Camera*, Vibrations in Physical Systems, Poznan University of Technology; **25** (2012) 453 – 458.
9. R. Barczewski, *Diagnostycznie zorientowane metody krótkoczasowego przetwarzania sygnałów wibroakustycznych*, Rozprawy Nr 504, Wydawnictwo Politechniki Poznańskiej Poznań; p. 152, 2013.

Dynamics Analysis of a Truck-Mounted Crane with the LuGre Friction Model in the Joints

Andrzej URBAŚ
University of Bielsko-Biala, Department of Mechanics
43-309 Bielsko-Biała, Willowa 2, aurbas@ath.eu

Grzegorz STANCLIK
University of Bielsko-Biala, Ph.D. student
43-309 Bielsko-Biała, Willowa 2, gstanclik@ath.eu

Jacek KŁOSIŃSKI
University of Bielsko-Biala, Department of Mechanical Engineering Fundamentals
43-309 Bielsko-Biała, Willowa 2, jklosinski@ath.eu

Andrzej HARLECKI
University of Bielsko-Biala, Department of Mechanics
43-309 Bielsko-Biała, Willowa 2, aharlecki@ath.eu

Abstract

A dynamics analysis of a selected truck-mounted crane is presented in this article. A mathematical model of the crane, considered in a form of an open-loop kinematic chain, allows to take into account flexibility of its support system, hoist rope and drives of particular links, and also friction in the joints. The geometry of the crane model is described using the Denavit-Hartenberg notation based on joint coordinates and homogeneous transformation matrices. Its equations of motion were derived on basis of the Lagrange formalism. The LuGre model was used to describe friction in the joints.

1. Introduction

In the today's era of computer systems a development of virtual complex models of mechanical systems is achieved using commercial or proprietary calculation programs. Computerization of a designing process of these systems shortens time significantly from determining design assumptions to making a final product.

In the literature there are lots of publications devoted to the dynamics analysis of different types of cranes. Unfortunately, there are hardly any publications devoted strictly to issues of the dynamics analysis of the truck-mounted cranes. This scope of investigations can be deemed – according to the authors of this publication – as poorly advanced. While making an overview of the literature the authors want to draw attention to a few selected works devoted to the dynamics analysis of cranes taking into account flexibility of their support systems (e.g. [1, 2, 3, 4]), flexibility of a hoist rope (e.g. [2, 3]), and also occurring of friction in joints (e.g. [5, 6]). All the issues mentioned are also a subject of the analysis presented in this work.

In the work it is assumed that the links of the modeled crane are driven directly by torques, whereas the retractable link by a force. It is a simplification, because in the real system the links are driven by three hydraulic cylinders (two of them are jib cylinders, and the third one is a telescopic cylinder). The assumed crane model is an open-loop kinematic chain, like models of robot manipulators. For this reason the Denavit-Hartenberg notation [7], taken from robotics, based on use of joint coordinates and homogeneous transformation matrices was applied to describe its geometry. Equations of the model motion were assumed using the Lagrange formalism [8]. Transported load was modeled in a form of a material point. In all the revolute joints, and also in the prismatic joint of the crane between the links moving on each other friction is taken into account. The friction phenomenon is described by the advanced LuGre model [9] based on bristle interpretation of friction [10]. This model allows to take into account the both phases of friction in the joints, that is the static and kinetic friction, and more precisely such phenomena as: a preliminary displacement, the Stribeck effect and a frictional lag.

2. Mathematical model of the crane

The model of the crane in question is presented in Fig. 1. This model consists of five links $\left(n_l = 5\right)$. First of them constitutes a truck chassis on which the crane is mounted. This chassis is settled flexibly by six supports $\left(n_s = 6\right)$, out of which four are the wheels of the truck.

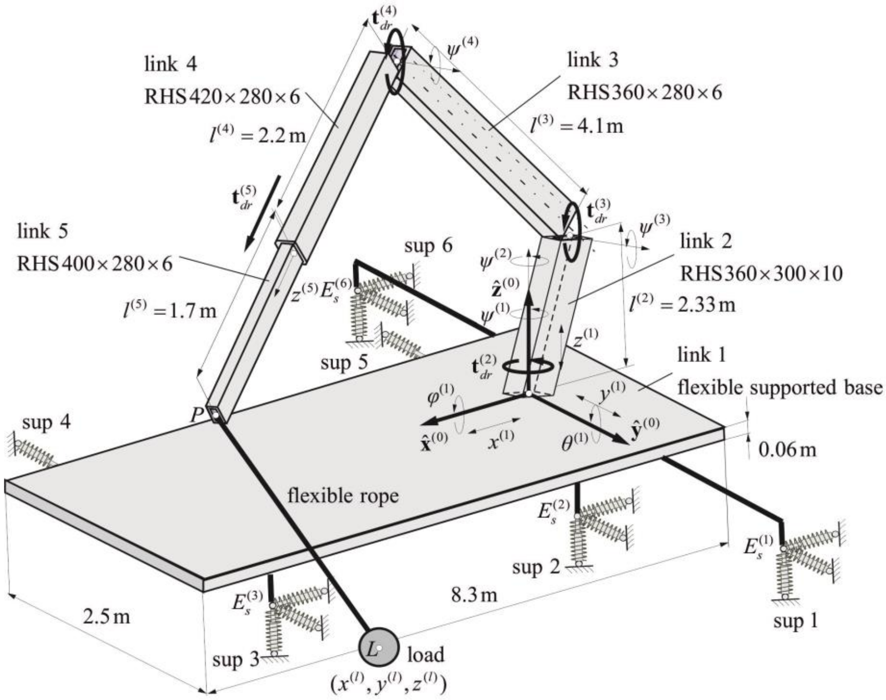

Figure 1. Model of the truck-mounted crane

A vector of the generalised (joint) coordinates of the developed model was determined in a form:

$$\mathbf{q} = \begin{bmatrix} \mathbf{q}^{(c)^T} & \mathbf{q}^{(l)^T} \end{bmatrix}^T = \begin{bmatrix} \tilde{\mathbf{q}}^{(1)^T} & \tilde{\mathbf{q}}^{(2)^T} & \tilde{\mathbf{q}}^{(3)^T} & \tilde{\mathbf{q}}^{(4)^T} & \tilde{\mathbf{q}}^{(5)^T} & \mathbf{q}^{(l)^T} \end{bmatrix}^T, \tag{1}$$

where: $\tilde{\mathbf{q}}^{(1)} = \begin{bmatrix} x^{(1)} & y^{(1)} & z^{(1)} & \psi^{(1)} & \theta^{(1)} & \varphi^{(1)} \end{bmatrix}^T$, $\tilde{\mathbf{q}}^{(2)} = \begin{bmatrix} \psi^{(2)} \end{bmatrix}$, $\tilde{\mathbf{q}}^{(3)} = \begin{bmatrix} \psi^{(3)} \end{bmatrix}$,

$$\tilde{\mathbf{q}}^{(4)} = \begin{bmatrix} \psi^{(4)} \end{bmatrix}, \quad \tilde{\mathbf{q}}^{(5)} = \begin{bmatrix} z^{(5)} \end{bmatrix}, \ \mathbf{q}^{(l)} = \begin{bmatrix} x^{(l)} & y^{(l)} & z^{(l)} \end{bmatrix}^T.$$

The matrices of the homogeneous transformations from the local coordinate systems of particular links of the model to the assumed reference system can be presented as:

$$\mathbf{T}^{(p)}\Big|_{p=1,\dots,n_l} = \mathbf{T}^{(p-1)}\tilde{\mathbf{T}}^{(p)}, \tag{2}$$

where: $\mathbf{T}^{(0)} = \mathbf{I}$,

$$\tilde{\mathbf{T}}^{(1)} = \begin{bmatrix} 1 & -\psi^{(1)} & \theta^{(1)} & x^{(1)} \\ \psi^{(1)} & 1 & -\varphi^{(1)} & y^{(1)} \\ -\theta^{(1)} & \varphi^{(1)} & 1 & z^{(1)} \\ 0 & 0 & 0 & 1 \end{bmatrix}, \ \tilde{\mathbf{T}}^{(2)} = \begin{bmatrix} \mathrm{c}\psi^{(2)} & -\mathrm{s}\psi^{(2)} & 0 & 0 \\ \mathrm{s}\psi^{(2)} & \mathrm{c}\psi^{(2)} & 0 & 0 \\ 0 & 0 & 1 & 0 \\ 0 & 0 & 0 & 1 \end{bmatrix},$$

$$\tilde{\mathbf{T}}^{(3)} = \begin{bmatrix} \mathrm{c}\psi^{(3)} & -\mathrm{s}\psi^{(3)} & 0 & -l^{(2)}\,\mathrm{c}\alpha^{(2)} \\ 0 & 0 & 1 & 0 \\ -\mathrm{s}\psi^{(2)} & -\mathrm{c}\psi^{(2)} & 0 & l^{(2)}\,\mathrm{s}\alpha^{(2)} \\ 0 & 0 & 0 & 1 \end{bmatrix}, \tilde{\mathbf{T}}^{(4)} = \begin{bmatrix} \mathrm{c}\psi^{(4)} & -\mathrm{s}\psi^{(4)} & 0 & l^{(3)} \\ \mathrm{s}\psi^{(4)} & \mathrm{c}\psi^{(4)} & 0 & 0 \\ 0 & 0 & 1 & 0 \\ 0 & 0 & 0 & 1 \end{bmatrix},$$

$$\tilde{\mathbf{T}}^{(5)} = \begin{bmatrix} 1 & 0 & 0 & 0 \\ 0 & 0 & 1 & z^{(5)} \\ 0 & -1 & 0 & 0 \\ 0 & 0 & 0 & 1 \end{bmatrix}, \ \mathrm{s}\alpha^{(\beta)} = \sin\alpha^{(\beta)}, \ \mathrm{c}\alpha^{(\beta)} = \cos\alpha^{(\beta)}.$$

Models of a revolute joint and a prismatic joint with friction were developed for the needs of the analysis and they are presented in Figs. 2a and 2b, respectively.

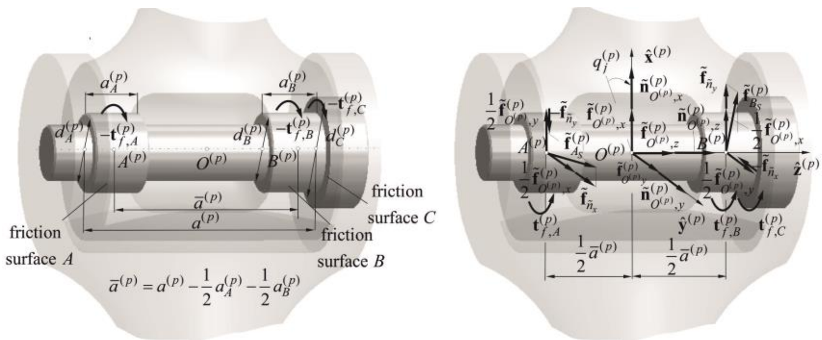

Figure 2a. Model of a revolute joint

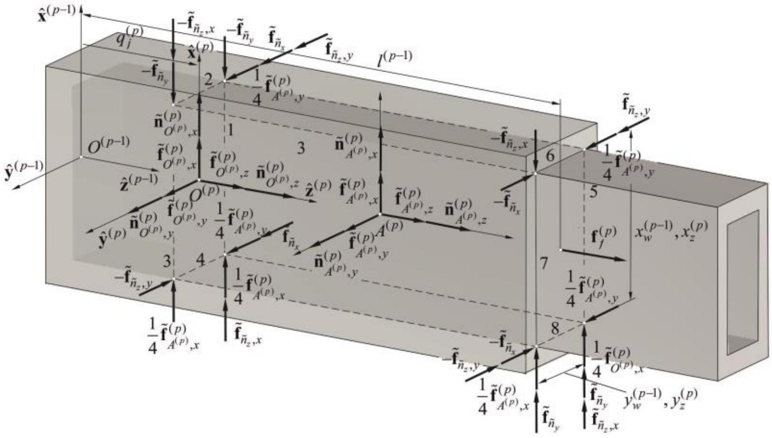

Figure 2b. Model of a prismatic joint

Values of friction torques $t_f^{(p)}$ in the revolute joints and friction force $f_f^{(p)}$ in the prismatic joint are calculated on basis of knowledge about joint forces and torques $\tilde{\mathbf{f}}_{O^{(p)}}^{(p)}$, $\tilde{\mathbf{n}}_{O^{(p)}}^{(p)}$ in those joints determined by the Newton-Euler recursive algorithm [7].

The equations of the crane model motion can be presented as:

$$\mathbf{A}\ddot{\mathbf{q}} = \mathbf{e} + \mathbf{f}_s + \mathbf{t}_{dr} - \mathbf{s}_f \ , \tag{3}$$

where:

$$\mathbf{A} = \begin{bmatrix} \mathbf{A}^{(c)} & 0 \\ 0 & \mathbf{A}^{(l)} \end{bmatrix}, \quad \mathbf{A}^{(c)} = \begin{bmatrix} \mathbf{A}_{1,1} & \cdots & \mathbf{A}_{1,j} & \cdots & \mathbf{A}_{1,n_l} \\ \vdots & \ddots & \vdots & \iddots & \vdots \\ \mathbf{A}_{i,1} & \cdots & \mathbf{A}_{i,j} & \cdots & \mathbf{A}_{i,n_l} \\ \vdots & \iddots & \vdots & \ddots & \vdots \\ \mathbf{A}_{n_l,1} & \cdots & \mathbf{A}_{n_l,j} & \cdots & \mathbf{A}_{n_l,n_l} \end{bmatrix}, \quad \mathbf{A}^{(l)} = \begin{bmatrix} m^{(l)} & 0 & 0 \\ 0 & m^{(l)} & 0 \\ 0 & 0 & m^{(l)} \end{bmatrix},$$

$$\mathbf{A}_{i,j} = \sum_{p=\max\{i,j\}}^{n_l} \tilde{\mathbf{A}}_{i,j}^{(p)}, \ \tilde{\mathbf{A}}_{i,j}^{(p)}\Big|_{i,j=1,\ldots,p} = \left(\tilde{a}^{(p)}_{n_{dof}^{(i-1)}+k,\, n_{dof}^{(j-1)}+l}\right)_{\substack{k=1,\ldots,\tilde{n}_{dof}^{(i)} \\ l=1,\ldots,\tilde{n}_{dof}^{(j)}}}, \ \tilde{a}_{i,j}^{(p)} = \operatorname{tr}\left\{\mathbf{T}_i^{(p)}\mathbf{H}^{(p)}\mathbf{T}_j^{(p)^T}\right\},$$

$$\mathbf{T}_i^{(p)} = \frac{\partial \mathbf{T}^{(p)}}{\partial q_i^{(p)}}, \quad \mathbf{H}^{(p)}$$ – pseudo-inertia matrix of link p,

$$\mathbf{e} = \begin{bmatrix} \mathbf{e}^{(c)} \\ \mathbf{e}^{(l)} \end{bmatrix}, \ \mathbf{e}^{(c)} = \begin{bmatrix} \mathbf{e}_1 \\ \vdots \\ \mathbf{e}_i \\ \vdots \\ \mathbf{e}_{n_l} \end{bmatrix}, \ \mathbf{e}^{(l)} = \begin{bmatrix} 0 \\ 0 \\ m^{(l)} g \end{bmatrix}, \ \mathbf{e}_i = -\sum_{p=i}^{n_l}\left(\tilde{\mathbf{h}}_i^{(p)} + \tilde{\mathbf{g}}_i^{(p)}\right),$$

$m^{(l)}$ – mass of the load, g – acceleration of gravity,

$$\tilde{\mathbf{h}}_i^{(p)}\Big|_{i=1,\dots,p} = \left(\tilde{h}^{(p)}_{n_{dof}^{(i-1)}+k}\right)_{k=1,\dots,\tilde{n}_{dof}^{(p)}},\ \tilde{h}_i^{(p)} = \sum_{m=1}^{n_{dof}^{(p)}}\sum_{n=m}^{n_{dof}^{(p)}} \operatorname{tr}\left\{\mathbf{T}_i^{(p)}\mathbf{H}^{(p)}\mathbf{T}_{m,n}^{(p)^T}\right\}\dot{q}_m^{(p)}\dot{q}_n^{(p)},\ \mathbf{T}_{m,n}^{(p)} = \frac{\partial^2\mathbf{T}^{(p)}}{\partial q_m^{(p)}\partial q_n^{(p)}},$$

$$\tilde{\mathbf{g}}_i^{(p)}\Big|_{i=1,\dots,p} = \left(\tilde{g}^{(p)}_{n_{dof}^{(i-1)}+k}\right)_{k=1,\dots,n_{dof}^{(i)}},\quad \tilde{g}_i^{(p)} = m^{(p)} g \begin{bmatrix}\mathbf{j}_3^T & 0\end{bmatrix}\mathbf{T}_i^{(p)}\mathbf{r}_{C^{(p)}}^{(p)},$$

$m^{(p)}$ – mass of link p, $\mathbf{r}_{C^{(p)}}^{(p)}$ – vector of the position of mass centre $C^{(p)}$ of link p,

$$\mathbf{f}_s = \begin{bmatrix}\mathbf{f}_s^{(c)}\\ \mathbf{f}_s^{(l)}\end{bmatrix},\ \mathbf{f}_s^{(c)} = \mathbf{f}_{s,s}^{(c)} + \mathbf{f}_{s,r}^{(c)},\ \mathbf{f}_{s,s}^{(c)} = \begin{bmatrix}-\left(\dfrac{\partial E_{p,s}}{\partial\tilde{\mathbf{q}}^{(1)}} + \dfrac{\partial R_s}{\partial\dot{\tilde{\mathbf{q}}}^{(1)}}\right)^T & \mathbf{0}\end{bmatrix}^T,\ \mathbf{f}_{s,r}^{(c)} = \begin{bmatrix}-\left(\dfrac{\partial E_{p,r}}{\partial\mathbf{q}^{(c)}} + \dfrac{\partial R_r}{\partial\dot{\mathbf{q}}^{(c)}}\right)\end{bmatrix}^T,$$

$$\mathbf{f}_s^{(l)} = \begin{bmatrix}-\left(\dfrac{\partial E_{p,r}}{\partial\mathbf{q}^{(l)}} + \dfrac{\partial R_r}{\partial\dot{\mathbf{q}}^{(l)}}\right)\end{bmatrix}^T,$$

$$\frac{\partial E_{p,s}}{\partial\tilde{\mathbf{q}}^{(1)}} = \sum_{i=1}^{n_s}\sum_{\alpha\in\{x,y,z\}} s_{s,\alpha}^{(i)}\frac{e_{s.\alpha}^{(i)}}{l_{s,\alpha}^{(i)}}\mathbf{U}_{E_s}^{(i)^T}\mathbf{U}_{E_s}^{(i)}\tilde{\mathbf{q}}^{(1)},\ \frac{\partial R_s}{\partial\dot{\tilde{\mathbf{q}}}^{(1)}} = \sum_{i=1}^{n_s}\sum_{\alpha\in\{x,y,z\}} d_{s,\alpha}^{(i)}\mathbf{U}_{E_s}^{(i)^T}\mathbf{U}_{E_s}^{(i)}\dot{\tilde{\mathbf{q}}}^{(1)},$$

$$e_{s,\alpha}^{(i)} = l_{s,\alpha}^{(i)} - l_{s,\alpha,0}^{(i)},\ l_{s,\alpha}^{(i)} = \left|\mathbf{U}_{E_s}^{(i)}\tilde{\mathbf{q}}^{(i)}\right|,\ \mathbf{U}_{E_S}^{(i)} = \left[\begin{array}{ccc:ccc} 1 & 0 & 0 & 0 & z_{E_S}^{(i)} & -y_{E_S}^{(i)}\\ 0 & 1 & 0 & -z_{E_S}^{(i)} & 0 & x_{E_S}^{(i)}\\ 0 & 0 & 1 & y_{E_S}^{(i)} & -x_{E_S}^{(i)} & 0\end{array}\right],$$

$s_{s,\alpha}^{(i)}, d_{s,\alpha}^{(i)}$ – stiffness and damping coefficient of support i in direction α,

$l_{s,\alpha}^{(i)},\ l_{s,\alpha,0}^{(i)}$ – current and initial length of support i in direction α,

$$\frac{\partial E_{p,r}}{\partial q_j^{(c)}} = s_r\delta_r\frac{e_r}{l_r}\mathbf{r}_{PL}^T\mathbf{J}\mathbf{T}_j^{(5)}\mathbf{r}_P^{(5)},\ \frac{\partial R_r}{\partial\dot{q}_j^{(c)}} = d_r\delta_r\frac{\dot{\mathbf{r}}_{PL}}{l_r}\mathbf{r}_{PL}^T\mathbf{J}\mathbf{T}_j^{(5)}\mathbf{r}_P^{(5)},$$

$$\frac{\partial E_{p.r}}{\partial q_j^{(l)}} = -s_r\delta_r\frac{e_r}{l_r}\mathbf{r}_{PL}^T\mathbf{j}_j,\ \frac{\partial R_r}{\partial\dot{q}_j^{(l)}} = -d_r\delta_r\frac{\dot{\mathbf{r}}_{PL}}{l_r}\mathbf{r}_{PL}^T\mathbf{j}_j,$$

s_r, d_r – stiffness and damping coefficient of the hoist rope,

$\mathbf{r}_P^{(5)}$ – vector of the position of point P in the coordinate system of link 5,

$$\mathbf{r}_{PL} = \mathbf{J}\left(\mathbf{r}_P^{(0)} - \mathbf{r}_L^{(0)}\right),\ l_r = \mathbf{r}_{PL}^T\mathbf{r}_{PL},\ e_r = l_r - l_{r,0},\ \delta_r = \begin{cases}1, & e_r > 0\\ 0, & e_r \le 0\end{cases},$$

$\mathbf{r}_\alpha^{(0)}\Big|_{\alpha\in\{P,L\}}$ – vector of the position of points P and L in the reference system,

l_r, $l_{r,0}$ – current and initial length of the hoist rope,

$$\mathbf{J} = \left[\begin{array}{c:c:c:c} 1 & 0 & 0 & 0\\ 0 & 1 & 0 & 0\\ 0 & 0 & 1 & 0\end{array}\right] = \left[\begin{array}{c:c:c:c}\mathbf{j}_1 & \mathbf{j}_2 & \mathbf{j}_3 & \mathbf{0}\end{array}\right],\ \mathbf{t}_{dr} = \begin{bmatrix}\mathbf{0} & t_{dr}^{(2)} & t_{dr}^{(3)} & t_{dr}^{(4)} & t_{dr}^{(5)} & \mathbf{0}\end{bmatrix}^T,$$

$$t_{dr}^{(p)} = -\left(\frac{\partial E_{p,dr}^{(p)}}{\partial q_j^{(p)}} + \frac{\partial R_{dr}^{(p)}}{\partial \dot{q}_j^{(p)}} \right), \ \frac{\partial E_{p,dr}^{(p)}}{\partial q_j^{(p)}} = -s_{dr}^{(p)} \left(q_{dr}^{(p)} - q_j^{(p)} \right), \ \frac{\partial R_{dr}^{(p)}}{\partial \dot{q}_j^{(p)}} = -d_{dr}^{(p)} \left(\dot{q}_{dr}^{(p)} - \dot{q}_j^{(p)} \right),$$

$s_{dr}^{(p)}, d_{dr}^{(p)}$ – stiffness and damping coefficient of the drive,

$q_{dr}^{(p)}$ – assumed driving functions,

$$\mathbf{s}_f = \begin{bmatrix} \mathbf{0} & t_f^{(2)} & t_f^{(3)} & t_f^{(4)} & f_f^{(5)} & \mathbf{0} \end{bmatrix}^T, \ t_f^{(p)} = t_{f,A}^{(p)} + t_{f,B}^{(p)} + t_{f,C}^{(p)}, \ f_f^{(p)} = \mu^{(p)} \tilde{f}^{(p)},$$

$$t_{f,A}^{(p)} = \frac{1}{2} \mu_A^{(p)} \tilde{f}_{A^{(p)}}^{(p)} d_A^{(p)}, \ t_{f,B}^{(p)} = \frac{1}{2} \mu_B^{(p)} \tilde{f}_{B^{(p)}}^{(p)} d_B^{(p)}, \ t_{f,C}^{(p)} = \frac{1}{2} \mu_C^{(p)} \left| \tilde{f}_{O^{(p)},z}^{(p)} \right| \frac{d_C^{(p)^3} - d_B^{(p)^3}}{d_C^{(p)^2} - d_B^{(p)^2}},$$

$$\tilde{f}_{A^{(p)}}^{(p)} = \sqrt{\left(\frac{1}{2} \tilde{f}_{O^{(p)},x}^{(p)} - \tilde{f}_{\tilde{n}_y} \right)^2 + \left(\frac{1}{2} \tilde{f}_{O^{(p)},y}^{(p)} + \tilde{f}_{\tilde{n}_x} \right)^2},$$

$$\tilde{f}_{B^{(p)}}^{(p)} = \sqrt{\left(\frac{1}{2} \tilde{f}_{O^{(p)},x}^{(p)} + \tilde{f}_{\tilde{n}_y} \right)^2 + \left(\frac{1}{2} \tilde{f}_{O^{(p)},y}^{(p)} - \tilde{f}_{\tilde{n}_x} \right)^2}, \ \tilde{f}_{\tilde{n}_x} = \frac{\tilde{n}_{O^{(p)},x}^{(p)}}{\overline{a}^{(p)}}, \ \tilde{f}_{\tilde{n}_y} = \frac{\tilde{n}_{O^{(p)},y}^{(p)}}{\overline{a}^{(p)}},$$

$$\tilde{f}^{(p)} = \sum_{i=1}^{8} \tilde{f}_i^{(p)}, \ \tilde{f}_1^{(p)} = \left| \frac{1}{4} \tilde{f}_{A^{(p)},x}^{(p)} - \tilde{f}_{\tilde{n}_y} + \tilde{f}_{\tilde{n}_z,x} \right|, \ \tilde{f}_2^{(p)} = \left| \frac{1}{4} \tilde{f}_{A^{(p)},y}^{(p)} + \tilde{f}_{\tilde{n}_x} + \tilde{f}_{\tilde{n}_z,y} \right|,$$

$$\tilde{f}_3^{(p)} = \left| \frac{1}{4} \tilde{f}_{A^{(p)},x}^{(c,p)} - \tilde{f}_{\tilde{n}_y} - \tilde{f}_{\tilde{n}_z,x} \right|, \ \tilde{f}_4^{(p)} = \left| \frac{1}{4} \tilde{f}_{A^{(p)},y}^{(p)} + \tilde{f}_{\tilde{n}_x} - \tilde{f}_{\tilde{n}_z,y} \right|, \ \tilde{f}_5^{(p)} = \left| \frac{1}{4} \tilde{f}_{A^{(p)},x}^{(p)} + \tilde{f}_{\tilde{n}_y} + \tilde{f}_{\tilde{n}_z,x} \right|,$$

$$\tilde{f}_6^{(p)} = \left| \frac{1}{4} \tilde{f}_{A^{(p)},y}^{(p)} - \tilde{f}_{\tilde{n}_x} + \tilde{f}_{\tilde{n}_z,y} \right|, \ \tilde{f}_7^{(p)} = \left| \frac{1}{4} \tilde{f}_{A^{(p)},x}^{(p)} + \tilde{f}_{\tilde{n}_y} - \tilde{f}_{\tilde{n}_z,x} \right|, \ \tilde{f}_8^{(p)} = \left| \frac{1}{4} \tilde{f}_{A^{(p)},y}^{(p)} - \tilde{f}_{\tilde{n}_x} - \tilde{f}_{\tilde{n}_z,y} \right|,$$

$$\tilde{f}_{\tilde{n}_x} = \frac{1}{2} \frac{\tilde{n}_{A^{(p)},x}^{(p)}}{l^{(p-1)} - \left| q_j^{(p)} \right|}, \ \tilde{f}_{\tilde{n}_y} = \frac{1}{2} \frac{\tilde{n}_{A^{(p)},y}^{(p)}}{l^{(p-1)} - \left| q_j^{(p)} \right|}, \ \tilde{f}_{\tilde{n}_z,x} = \frac{1}{2} \frac{y_z^{(p)}}{\left(x_z^{(p)^2} + y_z^{(p)^2} \right)} \tilde{n}_{A^{(p)},z}^{(p)},$$

$$\tilde{f}_{\tilde{n}_z,y} = \frac{1}{2} \frac{x_z^{(p)}}{\left(x_z^{(p)^2} + y_z^{(p)^2} \right)} \tilde{n}_{A^{(p)},z}^{(p)}, \ \tilde{f}_{A^{(p)},\alpha}^{(p)} = \tilde{f}_{O^{(p)},\alpha}^{(p)} \Big|_{\alpha \in \{x,y,z\}},$$

$$\tilde{n}_{A^{(p)},x}^{(p)} = \tilde{n}_{O^{(p)},x}^{(p)} + \frac{1}{2} \tilde{f}_{O^{(p)},y}^{(p)} \left(l^{(p-1)} - \left| q_j^{(p)} \right| \right), \ \tilde{n}_{A^{(p)},y}^{(p)} = \tilde{n}_{O^{(p)},y}^{(p)} - \frac{1}{2} \tilde{f}_{O^{(p)},x}^{(p)} \left(l^{(p-1)} - \left| q_j^{(p)} \right| \right),$$

$$\tilde{n}_{A^{(p)},z}^{(p)} = \tilde{n}_{O^{(p)},z}^{(p)}.$$

The LuGre friction model adopted by the authors of this work, describing friction coefficients $\mu\Big|_{\substack{\mu=\mu_\alpha^{(p)}\big|_{\alpha\in\{A,B,C\}} \\ \mu=\mu^{(p)}}}$ in a form of two differential equations of a first order, has already been presented in details in other works by them, namely in the publication devoted to dynamics of spatial linkages [11], and also in the article dealing with the grab crane [6].

The formulated equations of motion were solved by the Runge-Kutta method of the fourth order with a fixed-step.

3. Results of numerical calculations

Some results of the numerical calculations presenting a trajectory of the load moved, determined in plane $\hat{\mathbf{x}}^{(0)}\hat{\mathbf{y}}^{(0)}$ of the reference system in the case of taking into account or omitting friction in the crane joints, are presented in Fig. 3.

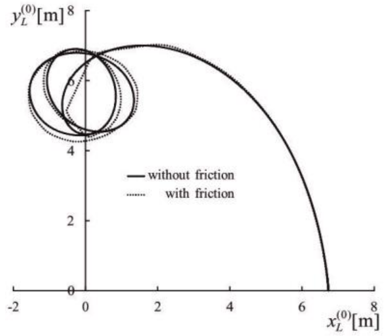

Figure 3. Trajectory of the load

An influence of friction on time courses of the values of the drive torques in the revolute joints and the drive force in the prismatic joint is presented in Fig. 4.

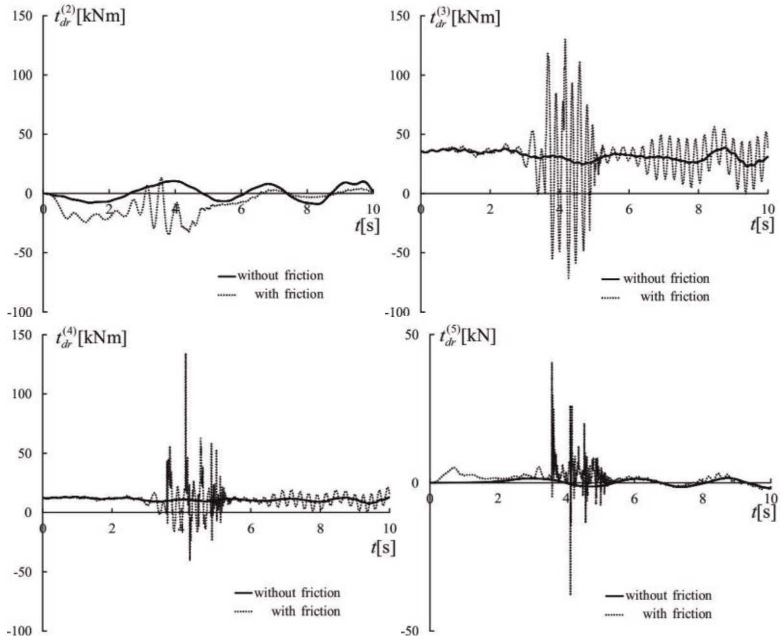

Figure 4. Courses of the values of the drive torques and the drive force

The performed calculations showed that friction in the joints of the modeled crane and also – as it was to be expected – flexibility of its support system and hoist rope had a significant influence on the crane dynamics, changing significantly courses of the determined parameters.

4. Conclusions

A dynamics analysis of the selected truck-mounted crane is presented in the work. The developed mathematical model can be treated as a virtual prototype of a real crane helpful while performing a process of its designing, and also while developing control algorithms. High degree of advancement of the prepared model provides – according to the authors – a possibility of a precise reflection of real system behavior in the dynamics conditions, what should make correctness of the calculation results reliable. However, the final verification of correctness of the prepared model can be made by experimental tests of a real system.

References

1. R. M. Ghigliazza, P. Holmes, *On the dynamics of crane, or spherical pendula with moving supports*, International Journal of Non-Linear Mechanics, **37** (2002) 1211 – 1221.
2. J. Kłosiński, *Swing-free stop control of the slewing motion of the mobile crane*, Control Engineering Practice, **13** (2005) 451 – 460.
3. A. Trąbka, *Influence of flexibilities of cranes structural components on load trajectory*, Journal of Mechanical Science and Technology, **30**(1) (2016) 1 – 14.
4. A. Urbaś, *Analysis of flexibility of the support and its influence on dynamics of grab crane*, Latin American Journal of Solid and Structures, **10**(1) (2013) 109 – 121.
5. B. Posiadała, *Modeling and analysis of the dynamics of load carrying system*, Proc. of World Congress on Engineering and Computer Science, San Francisco, USA 2012.
6. A. Urbaś, A. Harlecki, *Dynamics analysis of the grab crane with the LuGre friction model in the joints*, Proc. of XXIX Conference "Engineering Machines Problems", Zakopane, Poland 2016 (in Polish).
7. J. J. Craig, *Introduction to robotics. Mechanics and control*, Addison-Wesley Publish Company, Inc., (1989), (1986).
8. E. I. Jurevič (ed.), *Dynamics of robot control*, Nauka, Moscow 1984 (in Russian).
9. C. Canudas de Wit, H. Olsson, K. J. Åström, P. Lischinsky, *A new model for control of system with friction*, IEEE Transactions on Automatic Control, **40**(3) (1995) 419 – 425.
10. D. A. Haessig, B. Friedland, *On the modeling and simulation of friction*, Journal of Dynamical Systems, Measurements and Control Trans. of ASME, **113**(3) (1991) 354 – 362.
11. A. Harlecki, A. Urbaś, *Modelling friction in dynamics of selected one-DOF spatial linkage mechanisms*, Meccanica, February (2016), DOI 10.1007/s11012-016-0390-6

Free Vibrations of the Partially Tensioned Geometrically Non-Linear System Subjected to Euler's Load

Sebastian UZNY
Częstochowa University of Technology
Institute of Mechanics and Machine Design Foundations
ul. Dąbrowskiego 73, 42-200 Częstochowa, uzny@imipkm.pcz.pl

Krzysztof SOKÓŁ
Częstochowa University of Technology
Institute of Mechanics and Machine Design Foundations
ul. Dąbrowskiego 73, 42-200 Częstochowa, sokol@imipkm.pcz.pl

Michał OSADNIK
Częstochowa University of Technology
Institute of Mechanics and Machine Design Foundations
ul. Dąbrowskiego 73, 42-200 Częstochowa, osadnik@imipkm.pcz.pl

Abstract

In this study the fixed-fixed column subjected to axial Euler's load has been investigated. The load is placed between the fixed ends of the structure and its location can be changed along column's length. The boundary problem of free vibrations of the mentioned system has been formulated on the basis of Bernoulli – Euler theory and taking into account non-linear axial deformation relationship. Due to non-linear expressions the solution of the problem was done with small parameter method. In the paper the change of the first vibration frequency in relation to location and magnitude of the loading force was obtained. The relationship between natural vibration frequency and the amplitude is also discussed.

Keywords: column, Bernoulli-Euler's theory, free vibrations frequency, nonlinear system, characteristic curves, amplitude of vibrations, nonlinear component of free vibrations frequency

1. Introduction

In the literature the papers in which the vibrations of beams [1, 3, 4, 5, 11], columns [6, 12, 7, 8, 9, 15-21] and frame [10, 13, 14] are investigated can be found. In the boundary problem formulation process of these systems the theory of Bernoulli – Euler is mostly used. (see [2, 8-22]). This theory is sufficient when slender systems are taken into account (structures in which the total length is much greater than transverse dimensions) and when the system is not connected to mass elements with translational and rotational inertia. In the other cases (especially then higher order vibration frequencies are considered) the theory of beams proposed by Timoshenko should be used in which the shear energy and the rotational inertia energy of cross section are considered [1, 3-7]. The second problem which is present in the boundary problems are the linear and nonlinear theories. When the non-linear one is taken into account the deformation of the elastic element at moderately large deflections is written in the form:

$$\varepsilon_i(x_i,t)=\frac{\partial U_i(x_i,t)}{\partial x_i}+\frac{1}{2}\left(\frac{\partial W_i(x_i,t)}{\partial x_i}\right)^2 \tag{1}$$

where: $U_i(x_i,t)$, $W_i(x_i,t)$ longitudinal and transversal displacements respectively.

In non-linear systems in which the boundary problem is described by non-linear differential equations [2, 8, 15, 16, 19-22] the components of vibration frequency can be computed as dependent on amplitude of vibration (non-linear components of vibration frequency). The non-linear components may have great influence on vibration frequency and can't be omitted. In relation to the method of solution of the boundary problem the estimation of the non-linear component may be hard and time consuming. Nonlinear components of vibration frequencies of complex non-linear systems were investigated by Tomski and Przybylski [16], Przybylski [9] and Sokół [12] in relation to the conservative and non-conservative loads. The estimated components of vibration frequency were computed at rectilinear components of static equilibrium. The non-linear component of vibration frequency at rectilinear as well as at curvilinear form of static equilibrium of the column loaded by Euler's force were discussed in [21, 22]. At specific load studies on an influence of an amplitude on natural vibration frequency can be found in the following publications [19, 20]. The results were discussed at rectilinear and curvilinear form of static equilibrium. It has been shown that an influence of an amplitude on vibration frequency highly depends on the magnitude of external load. The use of specific load allows one to choose such load magnitude along with the parameters of the loading structure that an influence of an amplitude is negligible.

The main purpose of this paper is to present the results of the studies on the magnitude and location of the external force on natural vibration frequency (both linear and non-linear components) of the partially tensioned geometrically non-linear column.

2. Boundary problem

The considered column is presented in the figure 1. The column is fixed on both ends and loaded by a force P with constant line of action regardless to the deflection of the host element. The line of action of the force is compatible to the undeformed axis of the column. The point of location of the force is described by ζ parameter which is calculated as a relationship between length l_1 to total length l:

$$\zeta=\frac{l_1}{l} \tag{2}$$

The bending stiffness and compression stiffness and mass of the tensioned part (above the point of external force location) and compressed one are as follows: $((EA)_1 = (EA)_2 = (EA)$; $(EJ)_1 = (EJ)_2 = (EJ)$; $(\rho A)_1 = (\rho A)_2 = (\rho A))$.

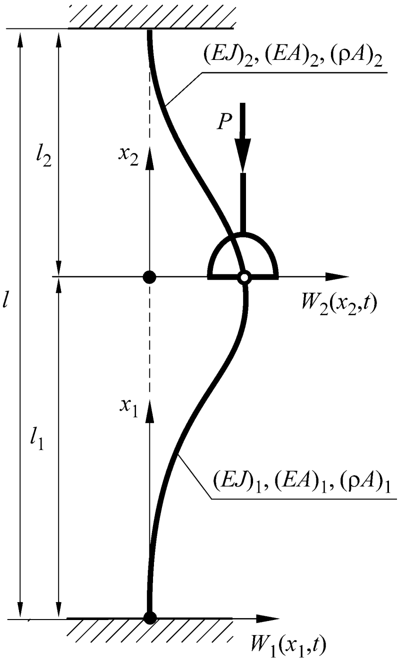

Figure 1. Considered column

The boundary problem is formulated on the basis of relation (1) and Bernoulli – Euler theory. The differential equations (in transversal and longitudinal direction) of vibration of the column are as follows:

$$\frac{\partial^4 W_i(x_i,t)}{\partial x_i^4} + S_i(t)\frac{\partial^2 W_i(x_i,t)}{\partial x_i^2} + (\rho A)_i\,\frac{\partial^2 W_i(x_i,t)}{\partial t^2} = 0 \tag{3}$$

$$U_i(x_i,t) - U_i(0,t) = -\frac{S_i(t)}{(EA)_i}x_i - \frac{1}{2}\int_0^{x_i}\left(\frac{\partial W_i(x_i,t)}{\partial x_i}\right)^2 dx_i \tag{4}$$

where: $S_i(t)$ – force in i – th element, $U_i(x_i,t)$, $W_i(x_i,t)$ – longitudinal and transversal displacements of the cross section of the i – th element described by coordinate x_i.

The boundary conditions of the considered system are presented below (5a-l):

$$U_1(0,t) = U_2(l_2.t) = W_1(0,t) = \left.\frac{\partial W_1(x_1,t)}{\partial x_1}\right|_{x_1=0} = W_2(l_2,t) = \left.\frac{\partial W_2(x_2,t)}{\partial x_2}\right|^{x_2=l_2} = 0 \quad \text{(5a-f)}$$

$$U_1(l_1,t) = U_2(0,t),\ W_1(l_1,t) = W_2(0,t),\ S_1 - S_2 = P \quad \text{(5g-i)}$$

$$(EJ)_1\left.\frac{\partial^3 W_1(x_1,t)}{\partial x_1^3}\right|^{x_1=l_1} - (EJ)_2\left.\frac{\partial^3 W_2(x_2,t)}{\partial x_2^3}\right|_{x_2=0} + P\left.\frac{\partial W_2(x_2,t)}{\partial x_2}\right|_{x_2=0} = 0 \quad \text{(5j)}$$

$$\left(EJ\right)_1 \frac{\partial^2 W_1\left(x_1,t\right)}{\partial x_1^2}\Bigg|^{x_1=l_1} - \left(EJ\right)_2 \frac{\partial^2 W_2\left(x_2,t\right)}{\partial x_2^2}\Bigg|_{x_2=0} = 0 \tag{5k}$$

$$\frac{\partial W_1\left(x_1,t\right)}{\partial x_1}\Bigg|^{x_1=l_1} = \frac{\partial W_2\left(x_2,t\right)}{\partial x_2}\Bigg|_{x_2=0} \tag{5l}$$

The further consideration are performed in non-dimensional form with the following relations:

$$\xi_i = \frac{x_i}{l_i},\ w_i\left(\xi_i,\tau\right) = \frac{W_i\left(x_i,\tau\right)}{l_i},\ u_i\left(\xi_i,\tau\right) = \frac{U_i\left(x_i,\tau\right)}{l_i},\ k_i^2\left(\tau\right) = \frac{S_i\left(\tau\right)l_i^2}{\left(EJ\right)_i}, \tag{6a-d}$$

$$\Omega_i^2 = \frac{\left(\rho A\right)_i \omega^2 l_i^4}{\left(EJ\right)_i},\ \tau = \omega t,\ \Theta_i = \frac{A_i l_i^2}{J_i},\ i = 1, 2. \tag{6e-g}$$

where ω is the natural vibration frequency.

The parameters presented in (6) are substituted into differential equations and boundary conditions what leads to their non-dimensional forms. The non-linear elements of the differential equations and boundary conditions are written into power series of the small parameter of an amplitude. In this study only the rectilinear form of static equilibrium is investigated at which the series are as follows:

$$w_i\left(\xi,\tau\right) = \sum_{j=1}^{N} \varepsilon^{2j-1} w_{i2j-1}\left(\xi,\tau\right) + O\left(\varepsilon^{2(N+1)}\right), \tag{7a}$$

$$u_i\left(\xi,\tau\right) = u_{i0}\left(\xi\right) + \sum_{j=1}^{N} \varepsilon^{2j} u_{i2j}\left(\xi,\tau\right) + O\left(\varepsilon^{2(N+1)}\right) \tag{7b}$$

$$k_i^2\left(\tau\right) = k_{i0}^2 + \sum_{j=1}^{N} \varepsilon^{2j} k_{i2j}^2\left(\tau\right) + O\left(\varepsilon^{2(N+1)}\right), \tag{7c}$$

$$\Omega_i^2 = \Omega_{i0}^2 + \sum_{j=1}^{N} \varepsilon^{2j} \Omega_{i2j}^2 + O\left(\varepsilon^{2(N+1)}\right) \tag{7d}$$

where:

$$w_{i1}\left(\xi,\tau\right) = \overset{(1)}{w}_{i1}\left(\xi\right)\cos\tau,\ w_{i3}\left(\xi,\tau\right) = \overset{(1)}{w}_{i3}\left(\xi\right)\cos\tau + \overset{(3)}{w}_{i3}\left(\xi\right)\cos 3\tau;\ \ldots \tag{8a,b}$$

$$u_{i2}\left(\xi,\tau\right) = \overset{(0)}{u}_{i2}\left(\xi\right) + \overset{(2)}{u}_{i2}\left(\xi\right)\cos 2\tau;\ \ldots \tag{8c}$$

$$k_{i2}^2\left(\tau\right) = \overset{(0)}{k}{}_{i2}^2 + \overset{(2)}{k}{}_{i2}^2 \cos 2\tau;\ \ldots \tag{8d}$$

On the basis of the obtained equations and boundary conditions the distribution of the external load on the elements of the structure can be found as well as magnitudes of the axial forces during vibrations and basic (ω_0) and nonlinear (ω_2) components of natural vibrations.

3. Results of numerical simulations

The results of numerical simulations are presented with the use of the following parameters:

$$\zeta_{\Omega} = \frac{\Omega - \Omega_0}{\Omega_0} 100\%, \ \lambda = \frac{Pl^2}{(EJ)}, \ \Omega = \frac{\omega^2 (\rho A) l^4}{(EJ)}, \tag{9a-c}$$

$$\Omega_i = \frac{\omega_i^2 (\rho A) l^4}{(EJ)}; \ i = 0, 2; \ \omega^2 = \omega_0^2 + \varepsilon^2 \omega_2^2 \tag{9d,e}$$

The parameters expressed by the formulas (9a-e) are the non-dimensional ones. Wherefore no information about material properties and cross-section area of the column can be found in this paper.

In the numerical calculations of an influence of a non-linear component ω_2 on natural vibration frequency ω the magnitude of the small parameter of an amplitude was defined as $\varepsilon = 0.008$.

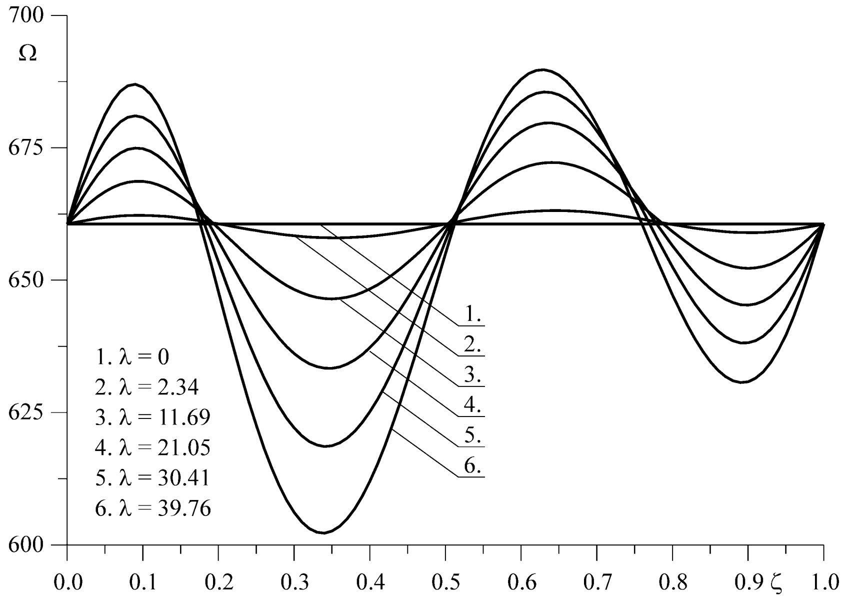

Figure 2. Magnitude of vibration frequency Ω parameter in relation to the point of location of external load ζ

In the figure 2 the change of vibration frequency parameter Ω (taking into account the non-linear component) in relation to the point of location of external load ζ has been presented. The calculations were performed at different magnitudes of external load parameter - λ. The vibration frequency highly depends on the magnitude and point of location of the external load. An increase of the magnitude of the external load causes an increase of the difference between the highest and the lowest magnitudes of vibrations in the investigated range of ζ. In this range the three points along the length of the column can be found in which the natural vibration frequency is not highly dependent on external load.

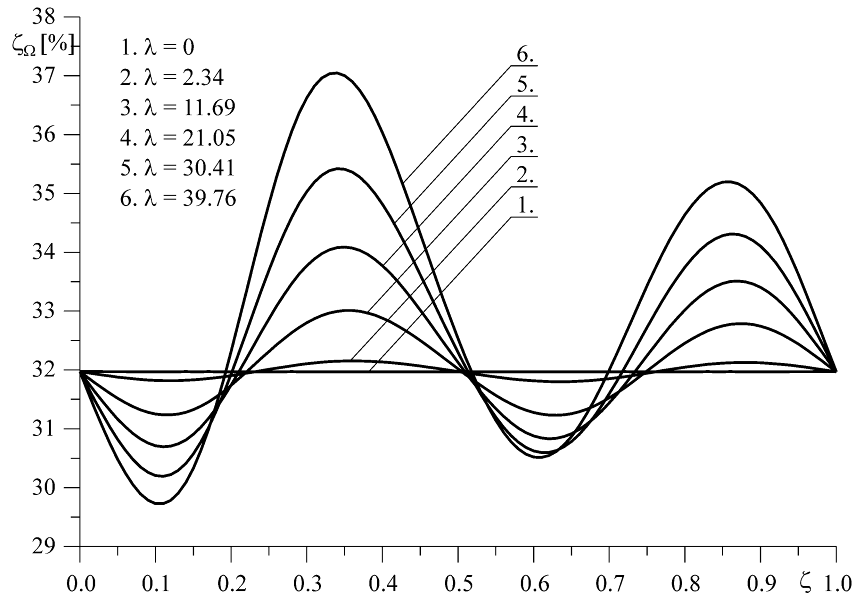

Figure 3. Magnitude of an influence on an amplitude on vibration frequency ζ_ω parameter in relation to the point of location of external load ζ

In the figure 3 the change of ζ_Ω parameter along length of the column at different magnitudes of external load has been plotted. It has been shown that an influence of an amplitude on natural vibrations depends on both external load magnitude and point of location of the external force. The highest magnitude of ζ_Ω has been found at $\zeta \approx 0.34$. In the unloaded system an influence of the second component of vibrations on vibration frequency is about 31.97 % at given amplitude corresponding to small parameter ε = 0.008.

4. Conclusions

In this paper the non-linear column fixed on both ends subjected to Euler's load (the load with constant line of action) has been investigated. The loading force was placed between the fixed ends of the structure. The boundary problem has been formulated on the basis of the Bernoulli – Euler theory and with taking into account the non-linear relationship of the axial deformation. In the final step of formulation of the boundary problem the small parameter method was used on the basis of which the computations of natural vibration frequency with consideration of linear and non-linear components (which depends on amplitude) were done. It has been shown that the natural vibration frequency of the investigated structure depends on both point of location and magnitude of the external force. The similar relationship can be observed at component which depends on amplitude of vibrations. It has been stated that the non-linear component of vibration can't be omitted especially at higher magnitudes of external load as well as at some point of location of external load. It's influence on final magnitude of vibration frequency can be significant but on the other hand it depends on amplitude.

In the future it is planned to develop of the studies started in this paper by addition of the elements which can have an influence on the behavior of the column during vibrations. The presented in this study results of numerical simulations may have engineering importance in investigation on the systems in which the point of location of the external load changes along their length (for example the screw along which the nut transferring loads changes position).

Acknowledgments

The study has been carried out within the statutory funds of the Czestochowa University of Technology (BS-1-101-302/99/P).

References

1. H. Abramovich, O. Hamburger, *Vibration of a cantilever Timoshenko beam with a tip mass*, Journal of Sound and Vibration, **148**(1) (1991) 162 – 170.
2. J. Awrejcewicz, O. A. Saltykova, Yu. B. Chebotyrevskiy, V. A. Krysko, *Nonlinear vibrations of the Euler-Bernoulli beam subjected to transversal load and impact actions*, Nonlinear Studies, **18**(3) (2011) 329 – 364.
3. J. C. Bruch Jr., T. P. Mitchell, *Vibrations of a mass-loaded clamped-free Timoshenko beam*, Journal of Sound and Vibration, **114**(2) (1987) 341 – 345.
4. W. Glabisz, *O granicach obszarów stateczności pręta pod dwuparametrowym obciążeniem niepotencjalnym*, Mechanika Teoretyczna i stosowana, **1**(29) (1991) 173 – 188.
5. L. Y. Jiang, Z. Yan, *Timoshenko beam model for static bending of nanowires with surface effects*, Physica E, **42** (2010) 2274 – 2279.
6. A. N. Kounadis, J. T. Katsikadelis, *Shear and rotary inertia effect on Beck's columns*, J. Sound and Vib., **49**(2) (1976) 171 – 178.
7. S. Nemat-Nasser, *Instability of a cantilever under a follower force according to Timoshenko beam theory*, J. Appl. Mech., **34** (1967) 484 – 485.
8. J. Przybylski, L. Tomski, *Vibration of an initially prestressed compound column under axial compression*, Elsevier Science Publishers B.V., (1992) 263 – 268.
9. J. Przybylski, *Drgania i stateczność dwuczłonowych układów prętowych wstępnie sprężonych przy obciążeniach niezachowawczych*, Seria Monografie, Nr 92, Wydawnictwo Politechniki Częstochowskiej, Częstochowa, 2002.
10. W. Sochacki, P. Rosikon, S. Topczewska, *Constructional damping mounting influence on T type frame vibrations*, Journal of Vibroengineering, **15**(4) 1866 – 1872.
11. W. Sochacki, *The dynamic stability of a simply supported beam with additional discrete elements*, Journal of Sound and Vibration, **314**(1-2) 180 – 193.

12. K. Sokół, *Linear and nonlinear vibrations of a column with an internal crack*, J. Eng. Mech., **140** (2014), http://dx.doi.org/10.1061/(ASCE)EM.1943-7889.0000719.
13. J. Szmidla, Free *Vibrations of a gamma type planar frame loaded by a follower force directed towards the positive pole*, Vibrations in Physical Systems, **24** (2010) 405 – 410.
14. J. Szmidla, *Vibrations and stability of t type frame loaded by longitudinal force in relation to its bolt*, Thin-Walled Structures, **45**(10-11) (2007) 931 – 935.
15. L. Tomski, S. Kukla, *Vibration of a prestressed two-member compound column*, Journal of Theoretical and Applied Mechanics, **30**(3) (1992) 625 – 638.
16. L. Tomski, J. Przybylski, *Flutter instability of a two member compound column*, Journal of Sound and Vibration, **146**(1) (1991) 125 – 133.
17. L. Tomski, S. Uzny, *Free vibrations and stability of a new slender system subjected to a conservative or non-conservative load,* Journal of Engineering Mechanics-ASCE, **139**(8) (2013) 1133 – 1148.
18. L. Tomski, S. Uzny, *The regions of flutter and divergence instability of a column subjected to Beck's generalized load, taking into account the torsional flexibility of the loaded end of the column*, Research Mechanics Communications, **38** (2011) 95 – 100.
19. S. Uzny, *Drgania i stateczność kolumny geometrycznie nieliniowej poddanej uogólnionemu obciążeniu z siłą skierowaną do bieguna dodatniego podpartej na obciążonym końcu liniową sprężyną* (rozdział 6) w: Drgania swobodne i stateczność układów smukłych poddanych obciążeniu konserwatywnemu i niekonserwatywnemu, praca zbiorowa wykonana pod kierunkiem naukowym i redakcją L. Tomskiego, PWN, Warszawa 2012, 107 – 158.
20. S. Uzny, *Drgania i stateczność kolumny geometrycznie nieliniowej poddanej obciążeniu siłą śledzącą skierowaną do bieguna dodatniego podpartej na obciążonym końcu liniową sprężyną* (rozdział 7) w: Drgania swobodne i stateczność układów smukłych poddanych obciążeniu konserwatywnemu i niekonserwatywnemu, praca zbiorowa wykonana pod kierunkiem naukowym i redakcją L. Tomskiego, PWN, Warszawa 2012, 159 – 176.
21. S. Uzny, *Nieliniowa składowa częstości drgań własnych kolumny poddanej obciążeniu Eulera (prostoliniowa postać równowagi statycznej)*, Modelowanie Inżynierskie, **11**(42) (2011) 449 – 457.
22. S. Uzny, *Nieliniowa składowa częstości drgań własnych kolumny poddanej obciążeniu Eulera (krzywoliniowa postać równowagi statycznej)*, Modelowanie Inżynierskie, **11**(42), 2011, 441 – 448.

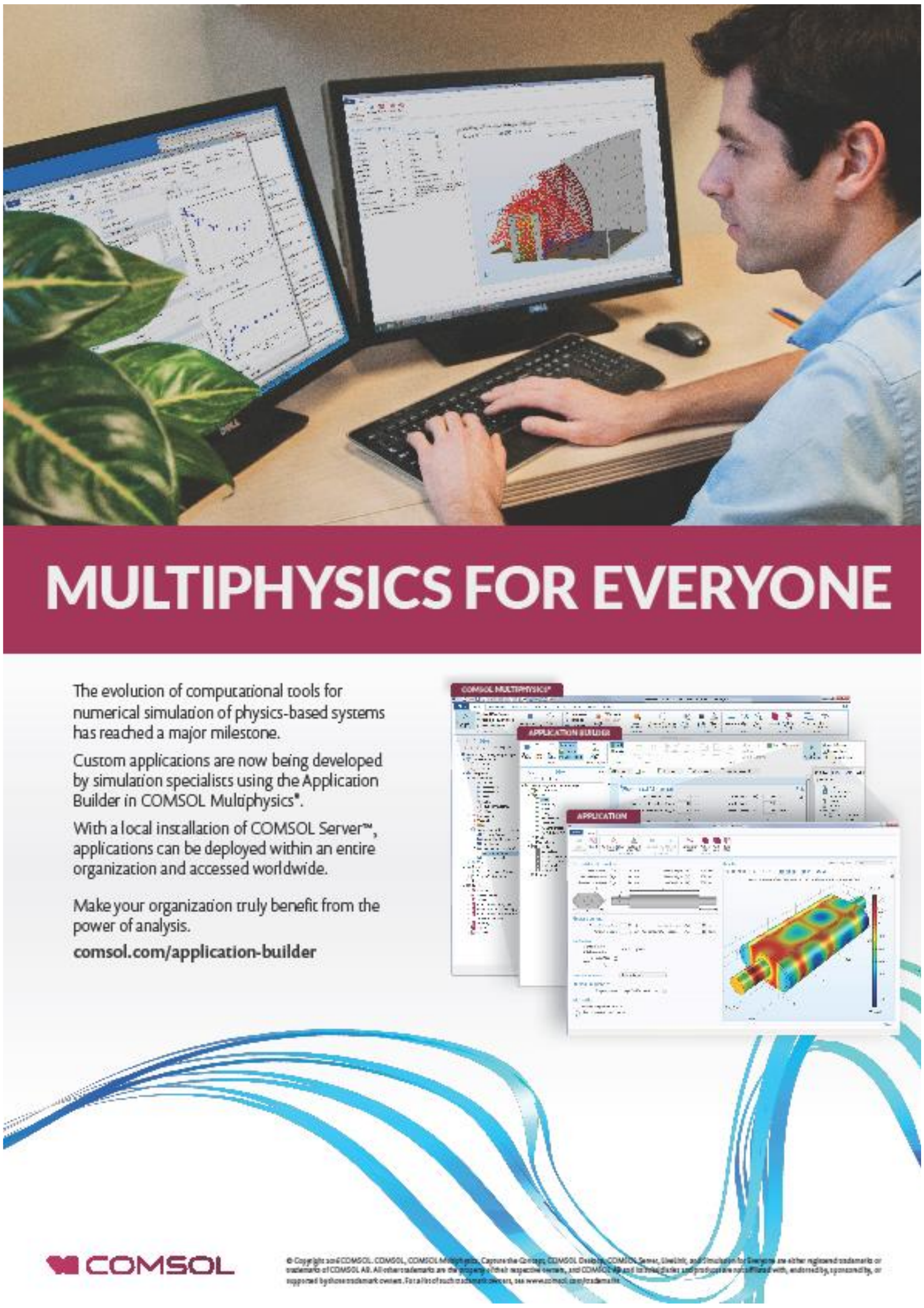
MULTIPHYSICS FOR EVERYONE
The evolution of computational tools for numerical simulation of physics-based systems has reached a major milestone.
Custom applications are now being developed by simulation specialists using the Application Builder in COMSOL Multiphysics®.
With a local installation of COMSOL Server™, applications can be deployed within an entire organization and accessed worldwide.
Make your organization truly benefit from the power of analysis.
comsol.com/application-builder
COMSOL MULTIPHYSICS®
APPLICATION BUILDER
APPLICATION
COMSOL